



**HAL**  
open science

# Experimental and theoretical studies of incompatibility and dislocation pile-up stresses at grain boundaries accounting for elastic and plastic anisotropies

Xiaolei Chen

► **To cite this version:**

Xiaolei Chen. Experimental and theoretical studies of incompatibility and dislocation pile-up stresses at grain boundaries accounting for elastic and plastic anisotropies. Materials. Université de Lorraine; Universität des Saarlandes, 2020. English. NNT : 2020LORR0089 . tel-02969946

**HAL Id: tel-02969946**

**<https://hal.univ-lorraine.fr/tel-02969946v1>**

Submitted on 17 Oct 2020

**HAL** is a multi-disciplinary open access archive for the deposit and dissemination of scientific research documents, whether they are published or not. The documents may come from teaching and research institutions in France or abroad, or from public or private research centers.

L'archive ouverte pluridisciplinaire **HAL**, est destinée au dépôt et à la diffusion de documents scientifiques de niveau recherche, publiés ou non, émanant des établissements d'enseignement et de recherche français ou étrangers, des laboratoires publics ou privés.



## AVERTISSEMENT

Ce document est le fruit d'un long travail approuvé par le jury de soutenance et mis à disposition de l'ensemble de la communauté universitaire élargie.

Il est soumis à la propriété intellectuelle de l'auteur. Ceci implique une obligation de citation et de référencement lors de l'utilisation de ce document.

D'autre part, toute contrefaçon, plagiat, reproduction illicite encourt une poursuite pénale.

Contact : [ddoc-theses-contact@univ-lorraine.fr](mailto:ddoc-theses-contact@univ-lorraine.fr)

## LIENS

Code de la Propriété Intellectuelle. articles L 122. 4

Code de la Propriété Intellectuelle. articles L 335.2- L 335.10

[http://www.cfcopies.com/V2/leg/leg\\_droi.php](http://www.cfcopies.com/V2/leg/leg_droi.php)

<http://www.culture.gouv.fr/culture/infos-pratiques/droits/protection.htm>



UNIVERSITÉ  
DE LORRAINE

DOCTORAT



UNIVERSITÄT  
DES  
SAARLANDES

DISSERTATION

Presented at

Université de Lorraine and Universität des Saarlandes

**Xiaolei CHEN**

To obtain the doctor's degree of  
University of Lorraine and Saarland University

SPECIAL FIELD: Material Mechanics

---

**Experimental and theoretical studies of  
incompatibility and dislocation pile-up  
stresses at grain boundaries accounting  
for elastic and plastic anisotropies**

---

Defended on July 16<sup>th</sup>, 2020 in front of the jury:

Benoit Devincre	Senior Research Scientist, LEM, CNRS, ONERA, France	<i>Reviewer</i>
Stefan Diebels	Professor, LTM, Universität des Saarlandes, Germany	<i>Reviewer</i>
Thomas Böhlke	Professor, ITM, Karlsruhe Institute of Technology, Germany	<i>Reviewer</i>
Céline Gérard	Research Scientist, Pprime, CNRS, EN-SMA, France	<i>Jury member</i>
Thiebaud Richeton	Research Scientist - HDR, LEM3, CNRS, Université de Lorraine, France	<i>Co-Supervisor</i>
Christian Motz	Professor, MWW, Universität des Saarlandes, Germany	<i>Supervisor</i>
Stéphane Berbenni	Senior Research Scientist, LEM3, Université de Lorraine, France	<i>Supervisor</i>

*Laboratoire d'Etude des Microstructures et de Mécanique des Matériaux, LEM3  
UMR CNRS 7239 - Université de Lorraine  
7 rue Félix Savart, 57050 Metz, France*



---

Experimentelle und theoretische  
Untersuchungen zu Inkompatibilitäts-  
und Versetzungsaufstauungsspannungen  
an Korngrenzen unter Berücksichtigung  
der elastischen und plastischen  
Anisotropie

---

Dissertation

zur Erlangung des Grades  
des Doktors der Naturwissenschaften  
der Naturwissenschaftlich-Technischen Fakultät  
der Universität des Saarlandes

Von

**Xiaolei CHEN**

Metz

Juli, 2020

**Tag des Kolloquiums: 16.07.2020**

**Dekan: Prof. Dr. Guido Kickelbick**

**Berichterstatter: Prof. Dr. Christian Motz**  
**Prof. Dr. Thomas Böhlke**  
**Prof. Dr. Stefan Diebels**

**Voritz: Prof. Dr. Martin Müser**

**Akad. Mitarbeiter: Dr. Frank Aubertin**

献给我的爷爷 陈国财

想念您，愿您□切安好

慎□微观 涉广研深

*“Le mieux est l’ennemi du bien”*  
*Merci Stéphane*





# Acknowledgement

This thesis was carried out in the Laboratory of Microstructure Studies and Mechanics of Materials (LEM3 for “Laboratoire d’Étude des Microstructures et de Mécanique des Matériaux” in French) at University of Lorraine in Metz, France and in the Department of Materials Science and Engineering (MWW for ”Experimentelle Methodik der Werkstoffwissenschaften” in German) at Saarland University in Saarbrücken, Germany.

I would like to express my deepest thanks to my thesis supervisor Stéphane Berbenni, CNRS senior research scientist, and to my co-supervisor Thiebaud Richeton, CNRS research scientist (HDR), for having supervised me during my thesis work and for having given me the benefit of their knowledge and experience. I would like to thank them for their trust, their support, their availability and their patience. I would like to thank them for their valuable time to have a deep discussion with me at any time when I need it and driving me to Saarbrücken for the PhD meetings each time. I would like to thank them for the precious advice that helped me move forward and overcome the difficulties I encountered. I would like to thank them for helping me to find the funding for the extra period of the thesis. Especially, I would like to thank them for the corrections of all my reports, presentations and thesis, not only for the scientific part, but also for the language part due to my poor English and French. That is a hugely extra and bored work for them, but they always friendly and careful help me to correct every mistake word by word.

I would also like to thank my thesis supervisor Prof. Dr. Christian Motz for teaching me all the experimental skills and sharing his knowledge and experience with me. I want to thank him for his trust, his openness, his advances and his support to let me try all of my experimental ideas. Let me thank him for his kindly patience of my poor English and unknown of German, especially for having changed one German lecture into English just for me. Let me thank him for many interesting discussions in the PhD meetings. Especially, Let me thank him for providing me the funding support of my thesis for the four extra months.

The Franco-German University deserves my thanks for the financial support without which this work would not be possible.

I would also like to thank all the members of the jury who make me feel honour for reading my dissertation and evaluating my work. I would like to thank Dr. Benoît Devincré, CNRS senior research scientist at CNRS-ONERA, for chairing my thesis jury and report my thesis. My thanks also go to Prof. Dr.-Ing. habil. Thomas Böhlke, Professor at Karlsruhe Institute of Technology, and Prof. Dr. Stefan Diebels, Professor at the University of Saarland, who accepted the heavy

task of reporting my work, as well as to Dr. Céline Gérard, CNRS research scientist at PPRIME-ENSMA for having carefully examined this work. Their criticisms were pertinent and constructive. Special thanks go to Prof. Dr. Martin Müser and Dr. Frank Aubertin at the University of Saarland who organized my PhD defense.

My colleagues at the MWW Institute: Jorge, Michael, Mohammad, Florian, Andreas, Rita, Stefan, Peter, Patrick, Marc, Killang, Jutta, Jonas, Dominic, Matthias, Eric, Dominik, Rouven and David made a very significant contribution to the success of this work. I am very grateful to all of them for their professional contributions and for the friendly and constructive working atmosphere. In particular, I want to thank Stefan and Peter for helping me to develop the rotation stage. Also thank to Andreas for the support of computer science. My special thanks go to my colleague Jorge Rafael Velayarce for his generous help of all of my experimental studies, for his useful discussions, for his kind help for proofreading the manuscript in German, and also for his deep friendship.

I would like to thank all the people working at LEM3 for contributing to the successful completion of my thesis. Special thanks to Meriem, Nabila, Nathalie and Antoine for the discussions of ECCI and AFM. I would also like to thank my fellow PhD students, Zhengtian Yang, Yajun, Wenjing, Rui, Qian, Fengming, Ke, Meishuai, Qianfeng, Dan, Xiaomeng and Komlavi for their support and friendship. Special thanks go to Zhengtian Yang, for all of his support, not only academically, but more important, for my daily life.

I would like to thank Arlette Jacquierre, Anne-Martine Blum, Stoll Nicolas, Elvire Meyer, Aurore Aubry, Florence Drouot, Jacqueline Decker for their availability and their help with administrative procedures.

I would like to thank Isabelle Wagner for helping me to handle all the German documents.

I would like to thank Julien Oury for his precious help concerning computer science.

Thanks to all the people I have met and who have participated in one way or another in this beautiful adventure, especially to all the teachers in my past life. Without them, this work cannot be possible.

Finally, my greatest thanks go to my family, who have supported me even in difficult times: my parents, my grandparents and my aunt. Special thanks to my grandfather Guocai CHEN, who has guided me into the science and taught me to think independently. This memoir is dedicated to them.

# Abstract

The mechanical properties of metallic materials strongly depend on the dislocation behavior, such as the density, the distribution, the nucleation and the mobility of dislocations as well as the interactions between dislocations and grain boundaries (GB). The main objective of this thesis is to study the effects of elastic and plastic anisotropies on the dislocation-GB interaction considering complex properties of GBs, misorientation effects and free surfaces effects. To reach this objective, an analytical approach based on the L-E-S formalism was investigated, which provides the elastic fields of single straight dislocations and different dislocation pile-ups at GBs in anisotropic homogeneous media, half-spaces, bi- and tri-materials while possibly considering free surface effects. The tri-material configuration allows considering a non-zero thickness in the nanometer range and a specific stiffness tensor for the GB region. The configuration with two free surfaces was used to study size effects. The effects of anisotropic elasticity, crystallographic orientation, GB stiffness and free surfaces were studied in the case of a single dislocation and dislocation pile-ups in a Ni bi-crystals with image forces and pile-ups length analyses, respectively. In parallel, in-situ compression tests on micron-sized Ni and  $\alpha$ -Brass bi-crystals produced from FIB machining and observations coupling SEM, AFM and EBSD were performed. The compression test was performed with a low strain until slip lines were observed or yield stress was reached. Then, step height spatial variations due to localized slip bands terminating at GB were measured by AFM to determine the Burgers vector distribution in the dislocation pile-up. This distribution was then simulated by dislocation pile-up configuration in bi-crystals with the experimentally measured parameters by considering the effect of misorientation, GB stiffness, free surfaces, incompatibility stresses and critical force. In particular, the incompatibility stresses were analyzed using CPFEM simulations and the thickness of GB was simulated using atomistic simulations with LAMMPS.

## Keywords

Bi-crystal, Grain boundary, Free surface, Anisotropic elasticity, Image force, Dislocation pile-up, Micromechanical testing



# Résumé

Les propriétés mécaniques des matériaux métalliques dépendent fortement du comportement des dislocations, telles que la densité, la distribution, la nucléation et la mobilité des dislocations ainsi que les interactions entre les dislocations et les joints de grain (JDGs). L'objectif principal de cette thèse est d'étudier les effets des anisotropies élastiques et plastiques sur l'interaction de dislocations-JDG en considérant les propriétés complexes des JDGs, les effets de désorientation et les effets de surfaces libres. Pour atteindre cet objectif, une approche analytique basée sur le formalisme L-E-S a été étudiée, qui fournit les champs élastiques des dislocations droites simples et des différents empilements de dislocations aux JDGs dans des milieux homogènes anisotropes, des demi-espaces, des bi- et tri-matériaux tout en considérant éventuellement les effets de surface libre. La configuration tri-matériaux permet d'envisager une épaisseur non nulle de l'ordre du nanomètre et un tenseur de rigidité spécifique pour la région du JDG. La configuration à deux surfaces libres a été utilisée pour étudier les effets de taille. Les effets de l'élasticité anisotrope, de l'orientation cristallographique, de la rigidité du JDG et des surfaces libres ont été étudiés dans le cas d'une seule dislocation et des empilements de dislocations dans un bi-cristal de Ni avec l'analyse des forces images et de la longueur d'empilements, respectivement. En parallèle, des essais in-situ de compression sur des bi-cristaux de Ni et de  $\alpha$ -laiton de taille micronique réalisés par usinage au FIB et des observations couplant MEB, AFM et EBSD ont été effectués. L'essai de compression a été réalisé avec une faible déformation jusqu'à ce que les lignes de glissement soient observées ou que la limite d'élasticité soit atteinte. Ensuite, les variations spatiales de la hauteur des marches dûs aux bandes de glissement localisées se terminant au JDG ont été mesurées par AFM pour déterminer la distribution du vecteur de Burgers dans l'empilement de dislocations. Cette distribution a ensuite été simulée par la configuration de l'empilement de dislocations dans des bi-cristaux avec les paramètres mesurés expérimentalement en considérant l'effet de la désorientation, de la rigidité du JDG, des surfaces libres, des contraintes d'incompatibilités et de la force critique. En particulier, les contraintes d'incompatibilités ont été analysées à l'aide de simulations CP-MEF et l'épaisseur du JDG a été simulée à l'aide de simulations atomistique avec LAMMPS.

## Mot-clés

Bi-cristal, Joint de grains, Surface libre, Élasticité anisotrope, Force image, Empilement de dislocations, Essais micromécaniques



# Zusammenfassung

Die mechanischen Eigenschaften von metallischen Materialien hängen stark vom Versetzungsverhalten ab, wie z.B. der Dichte, der Verteilung, der Nukleation und der Beweglichkeit von Versetzungen, sowie den Wechselwirkungen zwischen Versetzungen und Korngrenzen (KG). Das Hauptziel dieser Arbeit ist die Untersuchung der Auswirkungen von elastischen und plastischen Anisotropien auf die Versetzungs-KG Wechselwirkung unter Berücksichtigung der komplexen Eigenschaften von KG, sowie der Einflüsse der Misorientierung und der freien Oberflächen. Um dieses Ziel zu erreichen, wurde ein auf dem L-E-S-Formalismus basierender analytischer Ansatz verwendet, der die elastischen Felder einzelner gerader Versetzungen und unterschiedlicher Versetzungskonfigurationen an KG in anisotropen homogenen Medien, Halbräumen, Bi- und Tri-Materialien unter möglicher Berücksichtigung freier Oberflächeneffekte liefert. Die Tri-Material-Konfiguration erlaubt die Berücksichtigung einer KG mit der Dicke ungleich Null im Nanometerbereich und eines spezifischen Steifigkeitstensors für die KG. Die Konfiguration mit zwei freien Oberflächen wurde zur Untersuchung von Größeneffekten verwendet. Die Auswirkungen der anisotropen Elastizität, der kristallographischen Orientierung, der KG-Steifigkeit und der freien Oberflächen wurden für den Fall einer einzelnen Versetzung sowie für einen Versetzungsaufstau in einem Ni-Bikristall mit Bildkraft- bzw. Aufstaulängenanalysen untersucht. Parallel dazu wurden in-situ Mikrodruckversuche an Ni und  $\alpha$ -Messung Bikristallen, welche durch FIB-Bearbeitung hergestellt wurden, kombiniert mit SEM, AFM und EBSD Untersuchungen durchgeführt. Die Druckversuche wurde mit einer geringen Dehnung durchgeführt, bis Gleitlinien beobachtet wurden oder die Fließspannung erreicht wurde. Dann wurden die räumlichen Variationen der Gleitstufenhöhe an den lokalisierten Gleitbändern, welche an der KG endeten, mittels AFM gemessen und die Verteilung der Burgers-Vektoren in dem Versetzungsaufstau bestimmt. Diese Versetzungsverteilung wurde dann mit den experimentell gemessenen Parametern simuliert, indem die Auswirkungen von Misorientierung, KG-Steifigkeit, freien Oberflächen, Inkompatibilitätsspannungen und kritischer Kraft berücksichtigt wurden. Insbesondere wurden die Inkompatibilitätsspannungen mit Hilfe von CPFEM-Simulationen analysiert und die Dicke der KG wurde mit atomistischen Simulationen mittels LAMMPS bestimmt.

## Schlüsselwörter

Bi-Kristall, Korngrenze, freie Oberfläche, anisotrope Elastizität, Bildkraft, Versetzungsaufstau, mikromechanische Prüfverfahren





# Contents

<b>Abstract</b>	<b>1</b>
<b>Résumé</b>	<b>3</b>
<b>Zusammenfassung</b>	<b>5</b>
<b>tableofcontents</b>	<b>7</b>
<b>Notations</b>	<b>12</b>
<b>General introduction</b>	<b>14</b>
<b>1 State of the art</b>	<b>19</b>
1.1 Dislocation and crystal plasticity . . . . .	19
1.1.1 Introduction to dislocations . . . . .	19
1.1.2 Slip mechanism . . . . .	27
1.1.3 Deformation Twinning . . . . .	33
1.2 Grain boundary and free surface . . . . .	34
1.2.1 Definition of a grain boundary . . . . .	34
1.2.2 Definition and classification of grain boundaries . . . . .	35
1.2.3 Free surface effects . . . . .	47
1.3 Interaction between dislocation and grain boundary . . . . .	48
1.3.1 Experimental observations . . . . .	48
1.3.2 Dislocation pile-up . . . . .	51
1.3.3 Image force and image dislocation . . . . .	53
1.3.4 Slip transmission and geometrical criteria . . . . .	55
1.3.5 Grain boundary strength . . . . .	58
1.4 Experimental methods . . . . .	61
1.4.1 SEM and EBSD . . . . .	61
1.4.2 Ion Milling . . . . .	63
1.4.3 Focused Ion Beam technique . . . . .	65
1.4.4 Atomic Force Microscopy . . . . .	67

1.4.5	Micro-beam size effects . . . . .	69
1.5	Theoretical and numerical multi-scale modelling methods . . . . .	71
1.5.1	Continuum dislocation mechanics . . . . .	71
1.5.2	3D incompatibility stresses in bi-crystals . . . . .	73
1.5.3	Two dimensional L-E-S (Leknitskii-Eshelby-Stroh) formalism for anisotropic elasticity . . . . .	79
1.5.4	Crystal Plasticity Finite Element Method (CPFEM) . . . . .	81
1.5.5	Discrete Dislocation Dynamics method (DDD) . . . . .	86
1.5.6	Molecular Dynamics simulation (MD) . . . . .	88
<b>2</b>	<b>Experimental part: Nickel and <math>\alpha</math>-Brass bicrystalline micro-pillar compression test</b>	<b>94</b>
2.1	Introduction . . . . .	94
2.2	Material choice . . . . .	96
2.3	Sample preparation . . . . .	96
2.3.1	Metallographic preparation . . . . .	96
2.3.2	Heat treatment . . . . .	97
2.3.3	Grain boundary choice . . . . .	105
2.3.4	Micro-beam preparation . . . . .	107
2.4	Preanalyses of slip information . . . . .	110
2.5	Micro-pillar compression tests . . . . .	114
2.6	Stress-strain analysis . . . . .	116
2.7	Slip analysis by SEM and AFM . . . . .	117
<b>3</b>	<b>Elastic fields due to single dislocations and dislocation pile-ups in heterogeneous and anisotropic media</b>	<b>122</b>
3.1	Introduction . . . . .	122
3.2	Elastic fields due to one single dislocation in different configurations	123
3.2.1	Homogeneous anisotropic medium . . . . .	123
3.2.2	Heterogeneous anisotropic medium: bi-material . . . . .	124
3.2.3	Anisotropic half-space with rigid or free surface . . . . .	127
3.2.4	Heterogeneous anisotropic medium: tri-material . . . . .	128
3.2.5	Heterogeneous anisotropic medium: multilayer material with free surfaces . . . . .	132
3.3	Discrete dislocation pile-ups theory . . . . .	140
3.4	Computational procedure . . . . .	143
<b>4</b>	<b>Results and discussions</b>	<b>148</b>
4.1	Introduction . . . . .	148
4.2	Theoretical results . . . . .	149
4.2.1	Computation configurations . . . . .	149

4.2.2	Convergence of the series solutions within the tri-material configuration . . . . .	152
4.2.3	Displacements and stresses distribution due to one single dislocation . . . . .	156
4.2.4	Image force on dislocation in heterogeneous media . . . . .	158
4.2.5	Results for discrete dislocation pile-ups . . . . .	163
4.3	Prediction of stress-strain curves and study of incompatibility stresses using Crystal Plasticity Finite Element Method (CPFEM) . . . . .	174
4.3.1	CPFEM configuration: geometry and mesh . . . . .	174
4.3.2	Calibration of displacement and determination of material parameters . . . . .	177
4.3.3	Incompatibility stresses . . . . .	178
4.4	Computations of slip step height compared with experimental observations . . . . .	186
4.4.1	Simulation configuration for experiment . . . . .	186
4.4.2	Results of Ni micro-beam . . . . .	188
4.4.3	Results of $\alpha$ -Brass micro-beam . . . . .	199
4.5	Conclusions of Chapter 4 . . . . .	201
<b>Conclusions and Perspectives</b>		<b>204</b>
<b>Appendix</b>		<b>207</b>
A	Equivalence between the formulations of T.C.T. Ting and Z. Suo for the elastic fields of a dislocation in bi-materials with perfectly bonded interface . . . . .	207
B	Full coefficient matrix of image decomposition method . . . . .	211
C	GB thickness and structure analyzed by Molecular Statics (MS) / Molecular Dynamics (MD) simulations . . . . .	220
C.1	MD configuration . . . . .	220
C.2	Results and discussions . . . . .	222
<b>Bibliographie</b>		<b>227</b>
<b>English abstract</b>		<b>1</b>
1.1	Introduction . . . . .	1
1.2	Experiments . . . . .	1
1.2.1	Materials . . . . .	2
1.2.2	Sample preparation and choice of bi-crystals . . . . .	2
1.2.3	Micro-pillars compression test . . . . .	7
1.2.4	Slip analyses by AFM . . . . .	8
1.3	Theory . . . . .	9

1.3.1	2D anisotropic elasticity framework . . . . .	9
1.3.2	Dislocation in homogeneous media . . . . .	10
1.3.3	Dislocation in bi-materials . . . . .	10
1.3.4	Dislocation in tri-materials . . . . .	11
1.3.5	Dislocation in tri-materials with free surfaces . . . . .	13
1.3.6	Application to discrete dislocation pile-up . . . . .	17
1.4	Preliminary theoretical results and discussions with single dislocation and dislocation pile-ups for Ni bi-crystals . . . . .	19
1.5	Experimental results for Ni and $\alpha$ -Brass bi-crystals . . . . .	26
1.6	Simulation of slip step height profile using discrete dislocation pile-up calculations and discussions . . . . .	30
1.7	Conclusions and perspectives . . . . .	37
<b>Résumé français</b>		<b>1</b>
1.1	Introduction . . . . .	1
1.2	Expériences . . . . .	2
1.2.1	Matériaux . . . . .	2
1.2.2	Préparation des échantillons et choix des bi-cristaux . . . . .	2
1.2.3	Essai de compression sur micro-piliers . . . . .	7
1.2.4	Analyses des lignes de glissement par AFM . . . . .	8
1.3	Théorie . . . . .	9
1.3.1	Cadre de l'élasticité anisotrope bi-dimensionnelle . . . . .	9
1.3.2	Dislocation dans un milieu homogène . . . . .	10
1.3.3	Dislocation dans un bi-matériau . . . . .	10
1.3.4	Dislocation dans un tri-matériau . . . . .	11
1.3.5	Dislocation dans un tri-matériau avec surfaces libres . . . . .	13
1.3.6	Applications à un empilement de dislocations discrètes . . . . .	17
1.4	Résultats théoriques préliminaires et discussion pour des dislocations simples et des empilements de dislocations dans des bi-cristaux de Ni . . . . .	20
1.5	Résultats expérimentaux pour les bi-cristaux de Ni et de $\alpha$ -Brass . . . . .	27
1.6	Simulation des profils de hauteur de marche de glissement en utilisant les calculs d'empilement de dislocations discrètes et discussion . . . . .	31
1.7	Conclusions et perspectives . . . . .	39
<b>Deutsche Zusammenfassung</b>		<b>1</b>
1.1	Einführung . . . . .	1
1.2	Experimente . . . . .	1
1.2.1	Materialien . . . . .	2
1.2.2	Probenvorbereitung und Auswahl von Bikristallen . . . . .	2
1.2.3	Druckversuche der Mikro-Bikristalle . . . . .	7

1.2.4	Gleitlinienanalyse mit Hilfe vom AFM . . . . .	8
1.3	Theorie . . . . .	9
1.3.1	2D anisotropes Elastizitätsgerüst . . . . .	9
1.3.2	Versetzung in einem homogenen Medium . . . . .	10
1.3.3	Versetzungen in Bi-Materialien . . . . .	10
1.3.4	Versetzung in Tri-Materialien . . . . .	11
1.3.5	Versetzung in Tri-Materialien mit freien Oberflächen . . . . .	13
1.3.6	Anwendung auf diskrete Versetzungs-Pile-ups . . . . .	17
1.4	Vorläufige theoretische Ergebnisse und Diskussion der einzelnen Versetzungen und Versetzungs-Pile-ups in Ni-Bikristalle . . . . .	19
1.5	Experimentelle Ergebnisse für Ni und $\alpha$ -Brass Bikristalle . . . . .	27
1.6	Simulation des Stufenhöhenprofils mit Hilfe diskreter Versetzungs-Pile-up-Berechnungen und Diskussionen . . . . .	31
1.7	Schlussfolgerungen und Perspektiven . . . . .	39
<b>Curriculum Vitae</b>		<b>1</b>



# Notations

A bold lowercase letter like  $\mathbf{v}$  denotes a vector and a bold uppercase letter like  $\mathbf{W}$  denotes a second-order tensor. In particular,  $\mathbf{C}$  denotes the elastic stiffness tensor, which is a fourth-order tensor with classic symmetries:  $C_{ijkl} = C_{jikl} = C_{ijlk} = C_{klij}$ .

The incompatible part of a second-order tensor  $\mathbf{W}$  is marked as  $\mathbf{W}_\perp$ .

The compatible part of a second-order tensor  $\mathbf{W}$  is marked as  $\mathbf{W}_\parallel$ .

The unit second-order tensor is  $I_{ij} = \delta_{ij}$  where  $\delta_{ij} = 1$  if  $i = j$  and  $\delta_{ij} = 0$  if  $i \neq j$ .

The unit fourth-order tensor is  $I_{ijkl} = \frac{1}{2}(\delta_{ik}\delta_{jl} + \delta_{il}\delta_{kj})$ .

The imaginary unit is  $\mathbf{i} = \sqrt{-1}$ .

“.” represents the inner product between:

- two vectors  $\mathbf{w}$  and  $\mathbf{v}$ ,  $\mathbf{w} \cdot \mathbf{v} = w_i v_i$ ,
- two second-order tensors  $\mathbf{W}$  and  $\mathbf{V}$ ,  $\mathbf{W} \cdot \mathbf{V} = W_{ij} V_{jl}$ ,
- a second-order tensor  $\mathbf{W}$  and a vector  $\mathbf{v}$ ,  $\mathbf{W} \cdot \mathbf{v} = W_{ij} v_j$ .

“:” represents the double inner product between:

- two second-order tensors  $\mathbf{W}$  and  $\mathbf{V}$ ,  $\mathbf{W} : \mathbf{V} = W_{ij} V_{ij}$ ,
- a fourth-order tensor  $\mathbf{C}$  and a second-order tensor  $\mathbf{W}$ ,  $\mathbf{C} : \mathbf{W} = C_{ijkl} W_{kl}$ .

“ $\otimes$ ” represents the tensorial product such as  $\mathbf{w} \otimes \mathbf{v} = w_i v_j$ .

The component of third-order alternating Levi-Civita tensor is marked as  $\epsilon_{ilm}$  with  $\epsilon_{123} = \epsilon_{231} = \epsilon_{312} = 1$ ,  $\epsilon_{321} = \epsilon_{213} = \epsilon_{132} = -1$  and  $\epsilon_{ilm} = 0$  if two indices are identical.

The “gradient” operator is marked as *grad* such as  $(grad \mathbf{v})_{ij} = v_{i,j}$ .

The “divergence” operator is marked as *div* such as  $(div \mathbf{W})_i = W_{ij,j}$ .

The “curl” operator is marked as *curl* such as  $(curl \mathbf{W})_{ij} = \epsilon_{jlm} W_{im,l}$ .

The “cross product” is marked as  $\times$  such as  $(\mathbf{w} \times \mathbf{v})_i = \epsilon_{ijk} w_j v_k$  and  $(\mathbf{W} \times \mathbf{v})_{ij} = \epsilon_{jlk} W_{il} v_k$ .

The superscript T denotes the transpose of a matrix such as  $(\mathbf{W}^T)_{ij} = W_{ji}$ .

The Einstein convention over repeated indices is used when indices are underlined, such as:  $A_{\underline{ij}}f_{\underline{j}}(z_j) = A_{i1}f_1(z_1) + A_{i2}f_2(z_2) + A_{i3}f_3(z_3)$  but  $f_{\underline{j}}(z_j) \neq f_1(z_1) + f_2(z_2) + f_3(z_3)$  and  $\mathbf{f} = [f_1(z_1), f_2(z_2), f_3(z_3)]^T$  is a vector function, while the  $f_i$  are arbitrary functions of their arguments.

The notation  $\overline{f}(z) = \overline{f(\bar{z})}$  is used for the conjugate of a complex function.

The jump of a mechanical field or a materials property  $g$  at an interface between two crystals I and II towards to  $\mathbf{n} = x_2$  and from I to II is marked as  $\llbracket \cdot \rrbracket$  such as  $\llbracket g \rrbracket = g^{\text{II}}(x_2 \rightarrow 0^+) - g^{\text{I}}(x_2 \rightarrow 0^-)$

The average of a mechanical field or a materials property  $g$  at an interface between two crystals I and II towards to  $\mathbf{n} = x_2$  is marked as  $\langle \langle \cdot \rangle \rangle$  such as  $\langle \langle g \rangle \rangle = \frac{1}{2}(g^{\text{I}}(x_2 \rightarrow 0^-) + g^{\text{II}}(x_2 \rightarrow 0^+))$

The average of a mechanical field or a materials property  $g$  in a volume  $V$  is marked as  $\langle \cdot \rangle_V$  such as  $\langle g \rangle_V = \frac{1}{V} \int_V g dV$

Besides, the following reduction convention is adopted for the writing of the Hooke's law in matrix notation as the Voigt notation [1] (11  $\rightarrow$  1, 22  $\rightarrow$  2, 33  $\rightarrow$  3, 23  $\rightarrow$  4, 13  $\rightarrow$  5, 12  $\rightarrow$  6) for the fourth-order tensor, like elastic stiffness or elastic compliance.

$$\begin{bmatrix} \sigma_{11} \\ \sigma_{22} \\ \sigma_{33} \\ \sigma_{23} \\ \sigma_{13} \\ \sigma_{12} \end{bmatrix} = \begin{bmatrix} c_{11} & c_{12} & c_{13} & c_{14} & c_{15} & c_{16} \\ c_{12} & c_{22} & c_{23} & c_{24} & c_{25} & c_{26} \\ c_{13} & c_{23} & c_{33} & c_{34} & c_{35} & c_{36} \\ c_{14} & c_{24} & c_{34} & c_{44} & c_{45} & c_{46} \\ c_{15} & c_{25} & c_{35} & c_{45} & c_{55} & c_{56} \\ c_{16} & c_{26} & c_{36} & c_{46} & c_{56} & c_{66} \end{bmatrix} \begin{bmatrix} \varepsilon_{11} \\ \varepsilon_{22} \\ \varepsilon_{33} \\ 2\varepsilon_{23} \\ 2\varepsilon_{13} \\ 2\varepsilon_{12} \end{bmatrix} \quad (1)$$

$$\begin{bmatrix} \varepsilon_{11} \\ \varepsilon_{22} \\ \varepsilon_{33} \\ 2\varepsilon_{23} \\ 2\varepsilon_{13} \\ 2\varepsilon_{12} \end{bmatrix} = \begin{bmatrix} s_{11} & s_{12} & s_{13} & s_{14} & s_{15} & s_{16} \\ s_{12} & s_{22} & s_{23} & s_{24} & s_{25} & s_{26} \\ s_{13} & s_{23} & s_{33} & s_{34} & s_{35} & s_{36} \\ s_{14} & s_{24} & s_{34} & s_{44} & s_{45} & s_{46} \\ s_{15} & s_{25} & s_{35} & s_{45} & s_{55} & s_{56} \\ s_{16} & s_{26} & s_{36} & s_{46} & s_{56} & s_{66} \end{bmatrix} \begin{bmatrix} \sigma_{11} \\ \sigma_{22} \\ \sigma_{33} \\ \sigma_{23} \\ \sigma_{13} \\ \sigma_{12} \end{bmatrix} \quad (2)$$

where  $\sigma_{ij}$  are the Cauchy stresses with  $\sigma_{ij} = \sigma_{ji}$ ,  $\varepsilon_{ij}$  the elastic strain defined by  $\varepsilon_{ij} = \frac{1}{2}(u_{i,j} + u_{j,i})$  with  $u_i$  the displacement,  $c_{ij}$  the  $6 \times 6$  components of elastic stiffness tensor and  $s_{ij}$  are the  $6 \times 6$  components of elastic compliance tensor.



# General introduction

The present PhD thesis is a cotutelle thesis which is part of a scientific collaboration between France and Germany. The work was carried out, on the French side, within the APLI research team (Auto-organisation, Plasticité et Longueurs Internes) in the Laboratory of Microstructure Studies and Mechanics of Materials (LEM3 for “Laboratoire d’Étude des Microstructures et de Mécanique des Matériaux” in French) at University of Lorraine in Metz, and on the German side, in the Department of Materials Science and Engineering (MWW for “Experimentelle Methodik der Werkstoffwissenschaften” in German) at Saarland University in Saarbrücken.

The plasticity of crystalline materials results primarily from the dislocation motion and the multiplication of dislocations. Dislocations are line defects that were introduced by Volterra [2] at the beginning of the 20th century. Both theoretical and experimental investigations show that the mechanical properties of metals depend on the density, the distribution, the nucleation and the mobility of dislocations. In particular, the mechanical properties of polycrystals depend on the presence of grain boundaries (GBs), such as the elastic limit and strain hardening. More specifically, these properties greatly are dependent on the interaction mechanisms between dislocations and GBs (dislocation transmission or absorption at GB, formation of a dislocation pile-up, etc). Indeed, GBs generally present themselves as obstacles to dislocation motion.

In the case of grain size reduction, which means the increase of GB fraction in the material, the material will be harder following the Hall-Petch’s law [3, 4]. Experimental observations of dislocation distributions in the neighborhood of GBs have also made it possible to study these phenomena thanks to slip lines characterization, observation in Transmission Electron Microscopes (TEM) and Scanning Electron Microscopes (SEM), Electron Back Scattered Diffraction (EBSD) measurements in SEM and more recently thanks to Atomic Force Microscopy (AFM) and Electron Channelling Contrast Imaging (ECCI). The evolution of slip mechanism and the interaction between individual dislocations and GB can be directly observed through an in-situ mechanical test in TEM. It is also possible to obtain

the position of each dislocation in the case of dislocation pile-ups, which can be used to calculate elastic fields produced by these dislocations and thus the stress concentrations at GB coming from a dislocation pile-up [5]. EBSD measurements reveal the microstructure and micro-texture of the materials. It is able to measure the local crystallographic orientations during deformation and therefore the evolution of intra-granular lattice rotations and dislocation densities [6, 7]. Recently, the AFM technique makes it possible to analyze the topography and surface roughness of a material following the emergence of dislocations (slip step heights) during mechanical loading [8]. Moreover, the coupling of ECCI and EBSD permits to characterize single dislocations, dislocation densities and dislocation substructures in deformed bulk materials [9].

Based on experimental observations and the analysis of experimental results, multi-scale simulations have been developed these last decades in order to deeply understand slip mechanisms and the interactions between dislocations and GBs, and to predict mechanical properties of metallic materials. First of all, based on continuum mechanics, Crystal Plasticity Finite Element Method (CPFEM) is usually employed to describe the elastic-plastic deformation of anisotropic heterogeneous crystalline materials at the mesoscale [10]. Combined with various constitutive laws for plastic flow and hardening at the slip system level, the evolution of crystallographic texture and material's strength during mechanical loading can be obtained. CPFEM is also a powerful method to investigate geometrical and boundary influences on the mechanical properties of materials. Meanwhile, considering the effect of strain gradient, size effects [11] can be predicted by Strain Gradient CPFEM (SG-CPFEM), in which the hardening is assumed to result from the accumulation of both statistically stored dislocations (SSDs) and geometrically necessary dislocations (GNDs). Then, different from continuum theory, Discrete Dislocation Dynamics simulation (DDD) is another powerful tool to investigate plastic deformation of crystalline materials based on dislocation motion and Peach-Koehler driving force at the microscale. In DDD, the GB is usually considered as an impenetrable obstacle for which a dislocation pile-up can be created or as to be totally penetrable to dislocations. Furthermore, the dislocation transmission across GB can be represented by the annihilation of incoming dislocation and the activation of a Frank-Read source in the adjacent grain [12]. In some special cases, the GB can be modeled by a dislocation wall [13]. In that case, the dislocation-GB interaction can be regarded as the interaction between dislocations. Finally, Molecular Dynamics (MD) simulations can give a more realistic observation for deformation mechanisms at the nanoscale. MD simulations can represent the structure of dislocation cores and the complexion of GBs at atomic scale. It focuses on the motion of each individual atoms. Thus, the different mechanisms of dislocation-GB interactions can be directly observed using MD simulations [14].

However, CPFEM can only consider continuum mechanics, which cannot be used to investigate the discrete interaction between one single dislocation with GBs in details. DDD can perform the motion of each individual dislocation, but the complex properties of GB are missing in this method and elastic anisotropy calculations remain tedious. MD can show the precise structure of dislocation cores and GBs, thus it can perform the dislocation-GB interactions in details at atomic scale. However, MD can be only used for simulations with small dimensions at the nanoscale and within a small period of time due to intensive required computing resources.

The objective of this thesis is to develop a new method suitable for investigating the effects of elastic and plastic anisotropies on the dislocation-GB interactions considering complex properties of GBs, misorientation effects and free surfaces effects. In order to reach this objective, both an experimental study based on compression tests on bi-crystal micro-beams and a theoretical investigation of dislocations in heterogeneous anisotropic media are performed in the present thesis. Among the different possible mechanisms involving collective dislocation behavior, dislocation pile-ups at GBs and slip transfer are essentially studied.

In experiments, the studied materials are Nickel (Ni) and  $\alpha$ -Brass. The low stacking fault energy of  $\alpha$ -Brass can promote planar slip and thus facilitate the observation of slip lines. Meanwhile, planar slip is also observed in Ni bi-crystals during compression test even though it has a higher stacking fault energy. The in-situ compression test is performed with a low strain in order to create a single slip interacting with GBs. GBs are carefully chosen based on several critical conditions to form a dislocation pile-up at GBs. Then, the dislocation distributions in the pile-up and the dislocation transmission at GB can be determined from AFM measurements of the slip step height on the external surface of the micro-beam.

Regarding the theoretical studies, beyond the specific details of different mechanisms of dislocation-GB interaction, dislocations always interact with GBs through their elastic fields. In heterogeneous media like bi-crystals containing grains with different orientations, image stresses are indeed appended to the self dislocation stress field (i.e. the one for an infinite homogeneous medium) in order to satisfy the boundary conditions at interfaces. The image forces can either attract the dislocation towards the GB or conversely repel the dislocation away. In case of a dislocation pile-up, image forces can especially influence the positions of the dislocations and the stress field caused in the adjacent crystal. Such forces can be considered as configurational forces [15, 16]. Meanwhile, real GBs have finite width and their specific elastic properties may then constitute an additional source of image forces. Moreover, the presence of surfaces (finite sized specimen) can also create strong image forces on dislocations. Thus, the elastic fields of single straight

dislocations and different dislocation pile-ups in anisotropic homogeneous media, half-spaces, bi- and tri-material [17], while possibly considering free surface effects [18], are performed. Furthermore, the equilibrium positions of dislocations in a pile-up are determined through minimizing the Peach-Koehler (P-K) force (produced by all other dislocations and heterogeneities) on each dislocation with respect to a critical force.

As an application of the present theoretical studies, the slip step height profiles of slip lines measured by AFM are simulated by the dislocation pile-up configuration and the effects of anisotropic elasticity, incompatibility stresses, crystallographic misorientation, GB thickness and stiffness considered as interphase, free surface, lattice friction and transmitted dislocations are discussed. In particular, the incompatibility stresses in bi-crystalline micro-beams considering complex boundary conditions are analyzed with the Crystal Plasticity Finite Element Method (CPFEM). Furthermore, the GB thickness used in the theoretical model is determined from Molecular Statics (MS) / Molecular Dynamics (MD) in Ni bi-crystals configuration by LAMMPS using an EAM potential for Ni.

The organization of the thesis manuscript is the following:

- In Chapter 1, a state of the art of crystal plasticity and GB in face-centered cubic (FCC) metals is presented. The dislocation, slip mechanism, GB and its interactions with dislocations are described. Furthermore, some experimental methods used for the characterization of micro-mechanical tests are briefly discussed. At the end, incompatibility stresses at GB and CPFEM, DDD and MD modeling methods are also introduced.
- In Chapter 2, the experimental procedure of an in-situ micro-compression test on Ni and  $\alpha$ -Brass bi-crystals is presented. Slip lines height profiles analyzed by SEM and AFM are presented.
- In Chapter 3, the theoretical elastic fields due to a single dislocation in heterogeneous anisotropic media such as bi-material [19], tri-material [17] and multilayered configurations [18] are presented. The theory is based on two-dimensional anisotropic elasticity with L-E-S formalism (Leknitskii [20] - Eshelby [21] - Stroh [22]), which allows to consider the effect of GB with/without thickness, the GB stiffness, misorientation dependence and free surface effects. Meanwhile, the equilibrium positions of discrete dislocations in pile-ups and the stress concentrations produced by these pile-ups are computed and discussed.
- In Chapter 4, some theoretical results obtained from the models developed in Chapter 3 are first presented and discussed. Then, the simulations of the

experimental configurations are performed. The dislocation distributions in the pile-up are computed and compared with experimental observations. The influences of some parameters of the model are deeply discussed, such as the role of anisotropic elasticity, applied stress, misorientation, GB stiffness, presence of free surfaces, and critical force. Furthermore, incompatibility stresses from analytical expressions are verified by CPFEM calculations. The thickness, as well as the dislocation structure of GBs with different misorientations are also analyzed using MD simulations.

- Finally, a summary of the main results obtained during the thesis is presented as a conclusion of the manuscript in the last Chapter, as well as a set of future research directions that may be investigated.

# Chapter 1

## State of the art

### 1.1 Dislocation and crystal plasticity

#### 1.1.1 Introduction to dislocations

##### 1.1.1.1 Dislocation definition

As proposed by Volterra [2] at the beginning of the 20th century, dislocations have been studied for many years. From a geometric point of view, dislocations belong to line defects, which can be regarded as the boundary line between the slipped part and the unslipped part of the crystal, and its existence has a great influence on the physical properties of the material, especially the mechanical properties. There are mainly two types of dislocations: edge dislocation and screw dislocation. If a crystal plane suddenly terminates at a certain line inside the crystal, this irregular arrangement is called an edge dislocation as shown in Figure 1.1 (a). The atomic region near the edge dislocation will distort in the direction of the dislocation line. The edge dislocation can be determined by two quantities: the first one is the dislocation line  $\mathbf{t}$ , that is, the line ending with the excess half-atomic plane; the second one is the Burgers vector  $\mathbf{b}$ , which describes the magnitude and direction of displacement caused by dislocations. For edge dislocations, the direction of the Burgers vector is perpendicular to the direction of the dislocation line. Now imagine a regularly arranged crystal plane as a stack of paper with a fixed lattice distance. If the paper is cut into two parts along the direction perpendicular to the paper plane (but not completely cut), then one part is moved up by half the fixed lattice distance and the other part is moved down by half the fixed distance to form an arrangement similar to the corner of a stairway. The atomic region near this corner will distort at the end of this “cut line” (where a dislocation line perpendicular to the paper plane has been formed). This kind of irregular arrangement is called a screw dislocation as shown in Figure 1.1 (b). For

a screw dislocation, the Burgers vector  $\mathbf{b}$  is parallel to the dislocation line direction  $t$ .

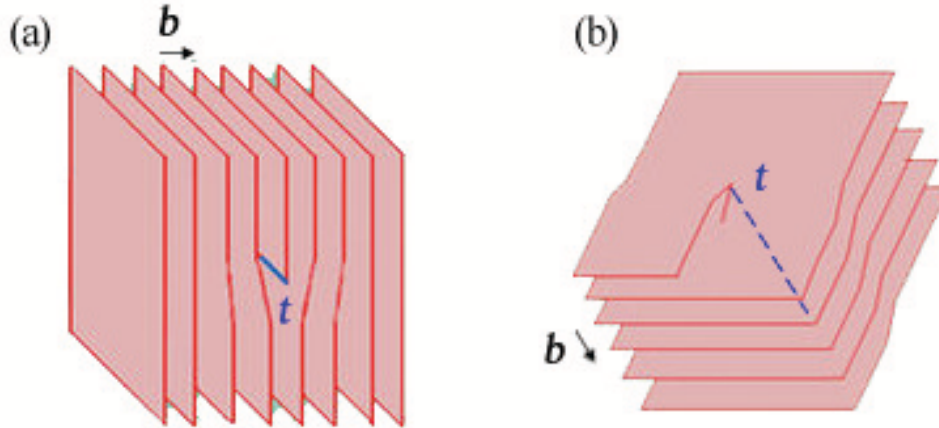


Figure 1.1: (a) Edge dislocation and (b) Screw dislocation.

As described above, the Burgers vector of the edge dislocation is perpendicular to the direction of the dislocation line, and it is parallel to the direction of the dislocation line for the screw dislocation. However, the Burgers vector of dislocations in actual materials can normally be neither parallel nor perpendicular to the direction of the dislocation lines. These dislocations have both the characteristics of edge and screw dislocations, and are called mixed dislocations (Figure 1.2 (a)). So the Burgers vector of mixed dislocations is not perpendicular, nor parallel to the dislocation line, but retains a fixed direction in space as shown in Figure 1.2 (b).

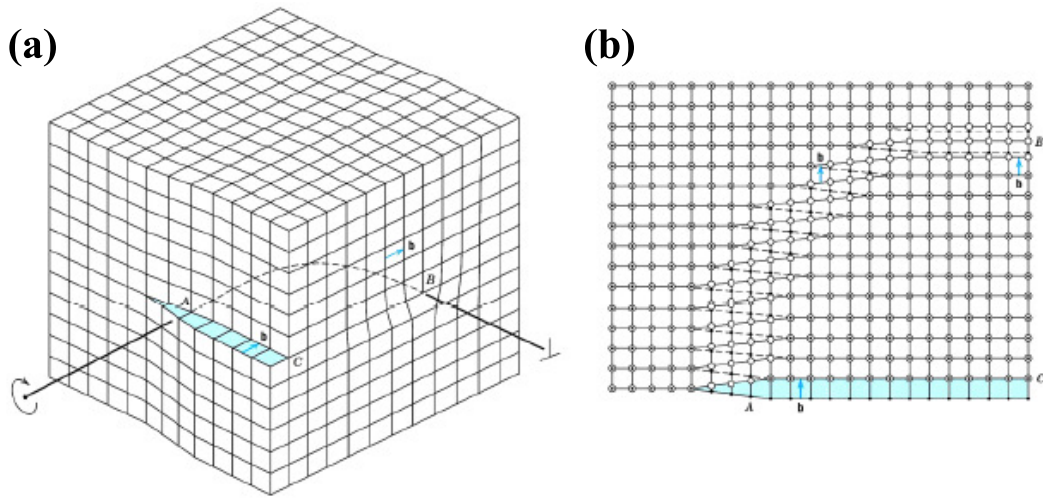


Figure 1.2: (a) Mixed dislocation configuration and (b) The Burgers vector is not perpendicular, nor parallel to the dislocation line, but retains a fixed direction in space.

### 1.1.1.2 Perfect and partial dislocations

In Face Centered Cubic (FCC) structures (Ni, Al, Cu, Au, Fe<sub>γ</sub>, etc.), the shortest translation vector defined by the Burgers vector is  $\frac{1}{2} \langle 110 \rangle$ . The glide due to the passage of this Burgers vector leaves, at long distance, a perfect crystal. In this case, the dislocation is called a perfect dislocation. This type of dislocation glides in the densest planes of the crystalline lattice, so in the family of (111) planes. Perfect dislocations can be divided into two imperfect dislocations, also called partial dislocations. Unlike perfect dislocations, partial dislocations form, after their passage, an imperfect crystal containing a two-dimensional defect called a stacking fault. The stack of atoms in the FCC structure can be modeled by rigid spheres in a QRSQRS... sequence as shown schematically in Figure 1.3 (a). In this structure, the compact stack of atoms lies in the plane (111). The Burgers vector of perfect dislocations QQ, which is the vectors  $\frac{1}{2} \langle 110 \rangle$ , thus occupy a regular tetrahedron ABCD which is shown in Figure 1.3 (b). The four different planes of the family (111) are parallel to each of the 4 faces of this tetrahedron called Thompson's tetrahedron.



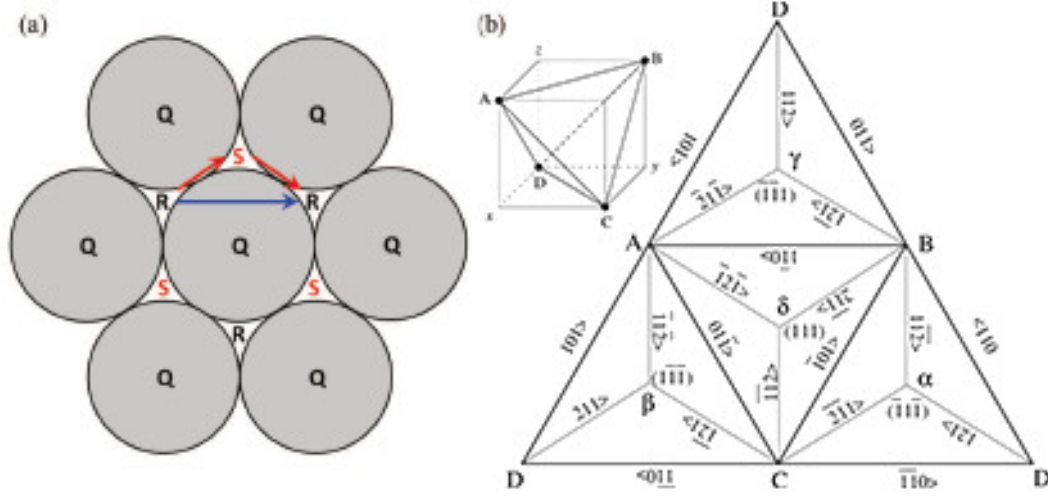


Figure 1.3: (a) (111) slip plane in FCC crystals. (b) Perfect and partial dislocations described by the Thompson's Tetrahedron [23].

The edges of the tetrahedron (AB, BC, ...) are parallel to the directions of Burgers vectors of type  $\langle 110 \rangle$  specific to perfect dislocations. The shear motion of the two planes Q and R produces a displacement in the slip direction. It can be seen that the motion of the R atoms is first through the passage to the S sites along the valley between two Q atoms and then to the R site via the second valley as shown in Figure 1.3 (a). Similarly, the Burgers vectors of partial dislocations  $\frac{1}{6} \langle 112 \rangle$  are defined by the lines, which link each vertex to the center of each face (A $\beta$ , D $\gamma$ , ...). This dislocation brings the atoms R in position S and transforms the stack QRSQRS... to QRSQSQRS.... This passage through the planes S introduces therefore a stacking fault in the crystal delimited by partial dislocations called Shockley partials. For example, the dissociation of a perfect dislocation AB into two partial dislocations in the plane (111) is defined by the reaction  $AB = A\delta + \delta B$  in the plane ABC and  $AB = A\gamma + \gamma B$  in the plane ABD.

Inserting or removing a region of close packed (111) plane creates another stacking fault, so called Frank partial dislocation as shown in Figure 1.4 (a). Frank partial dislocation has a Burgers vector  $\frac{1}{3} \langle 111 \rangle$  which is normal to the (111) plane. As the Burgers vector of a Frank partial dislocation is not contained in one of the (111) glide plane, so it is a sessile dislocation which can only climb but cannot glide. Depending on whether the partial (111) plane is added or removed, the stacking fault is called extrinsic for adding partial plane, giving the stack QRSQRQRS... which is presented in Figure 1.4 (a), or is called intrinsic for removing partial plane, giving the stack QRSQSQRS... which is the same as the stacking fault due

to Shockley partial dislocations and is presented in Figure 1.4 (b).

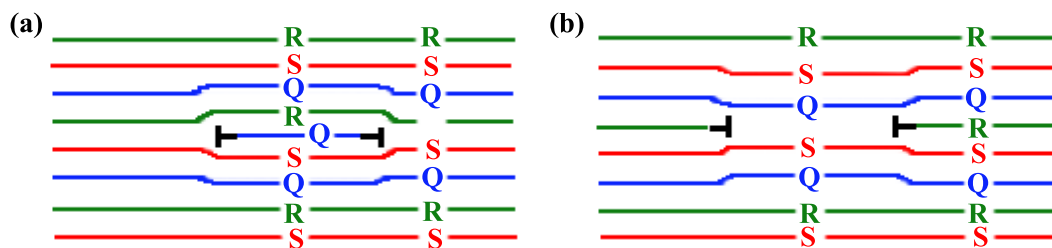


Figure 1.4: (a) Loop of positive Frank partial dislocation and (b) Loop of negative Frank partial dislocation.

It should be noted that partial dislocations can be activated indifferently from one to another in the case where the stacking fault energy is very low [24, 25]. In this case, the collective movement of the same partials does not lead to any crystallographic slip in the  $\langle 112 \rangle$  directions but to the twin formation (see subsection 1.1.3).

### 1.1.1.3 Dislocation motion

The plastic deformation in crystalline materials is mostly caused by the movement of dislocations. With enough force applied to the material structure, the atoms at the dislocation line pass through the atomic plane, breaking and reforming bonds with atoms on this plane, to create a dislocation motion. There are two types of dislocation motion: glide and climb. Under shear stress, atoms near the dislocation line move on a plane containing their Burgers vector, called dislocation glide. Its movement is similar to the worm crawling, which gradually spreads and moves along the slip plane as shown in Figure 1.5. Both edge and screw dislocations can glide.

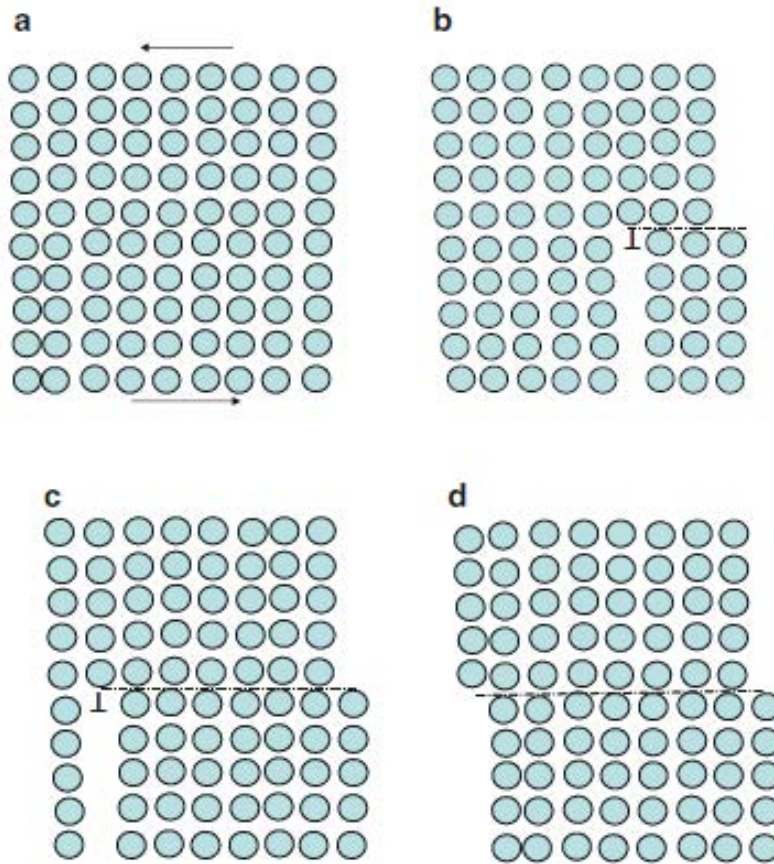


Figure 1.5: Glide motion of an edge dislocation on its slip plane under shear stress. The lattice is deformed through (a) to (d). When the dislocation comes out of the surface of the crystal, a step with the Burgers vector dimension is formed [26].

In addition to gliding along the slip plane, the edge dislocation can also climb perpendicular to the slip plane, which is equivalent to the movement of the semi-atomic plane perpendicular to the slip plane. This is an important property of the edge dislocation. The screw dislocation cannot climb. Dislocation climbing is a diffusion process. By means of the diffusion and movement of vacancies or particles, the edge dislocations move up and down a certain atomic distance as shown in Figure 1.6. This phenomenon is often encountered in the heat treatment of materials.

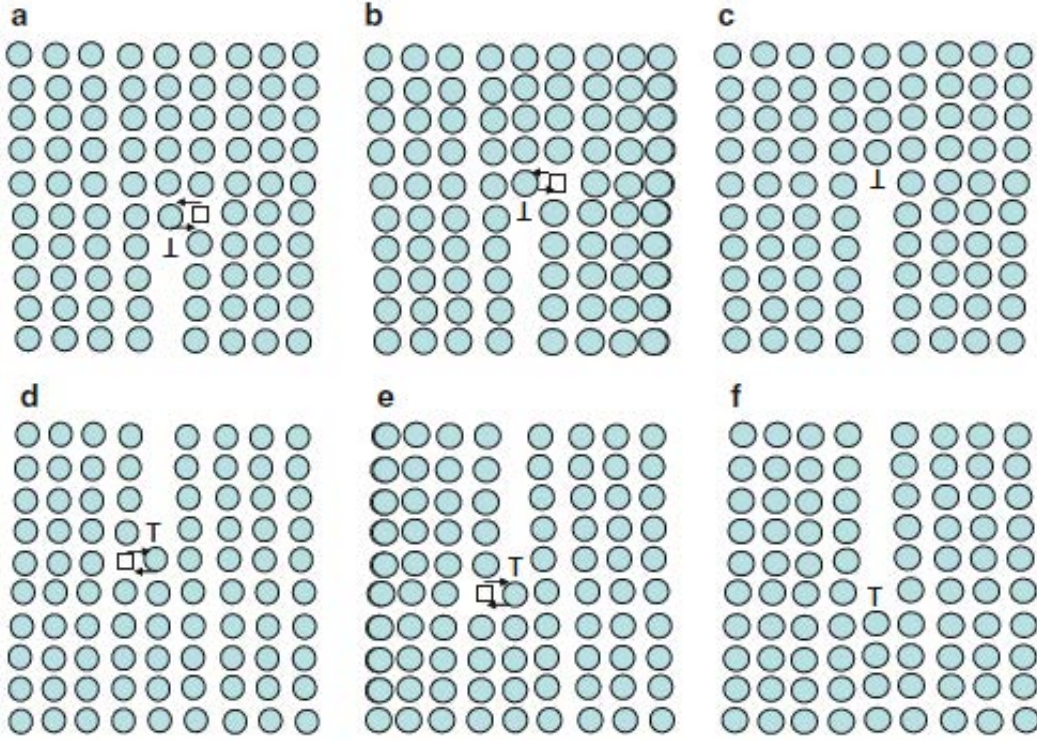


Figure 1.6: Climb motion of edge dislocation in positive and negative directions. When a point defect, like vacancy reaches at the vicinity of a dislocation line, it changes the position with the atom at dislocation and climb occurs. Dislocation climb means a part of the dislocation has left its slip plane [26].

The driving force for dislocation motion can be calculated by Peach-Koehler (P-K) force formula [27]:

$$\mathbf{f} = \boldsymbol{\sigma} \cdot \mathbf{b} \times \mathbf{t} \quad (1.1)$$

where  $\mathbf{f}$  is the subjected force per unit length of dislocation,  $\boldsymbol{\sigma}$  the stress field which includes internal stress fields. Internal stresses come from other defects, like interaction force between dislocations.  $\mathbf{b}$  is the Burgers vector and  $\mathbf{t}$  is the parallel vector to the dislocation line. The P-K force is always normal to the dislocation line.

#### 1.1.1.4 Elastic fields of single straight edge and screw dislocations

Dislocations cause misalignment of atoms in the crystal, which in turn causes elastic distortion of the crystal lattice, so dislocations are sources of internal stresses. For an infinite straight dislocation, the elastic fields can be regarded to be constant along the dislocation line. Thus, it is a two dimensional problem.

When the dislocation line is taken to be parallel to  $\mathbf{x}_3$  as shown in Figure 1.7, all the elastic fields are only functions of  $(x_1, x_2)$  [15].

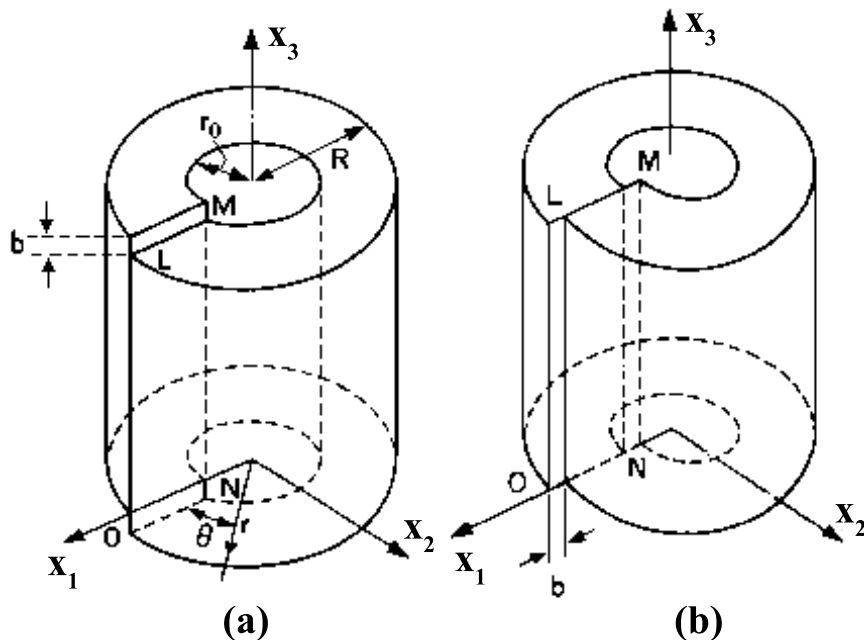


Figure 1.7: Schematic figure of (a) a screw dislocation and (b) an edge dislocation in Cartesian coordinate system.

in Figure 1.7 (a) an infinite straight screw dislocation is presented in a Cartesian coordinate system. The Burgers vector is taken as  $\mathbf{b} \cdot \mathbf{t} = +b$  which is called a right-handed screw dislocation. In an elastic isotropic medium, the displacement  $\mathbf{u}$  increases uniformly with the discontinuity of the Burgers vector  $\mathbf{b} \parallel \mathbf{x}_3$  [28]:

$$\begin{cases} u_1 = 0 \\ u_2 = 0 \\ u_3 = \frac{b}{2\pi} \tan^{-1} \left( \frac{x_2}{x_1} \right) \end{cases} \quad (1.2)$$

The stress fields can be then determined from the gradients of displacements and the Hooke's law with the shear modulus  $G$ :

$$\begin{cases} \sigma_{13} = -\frac{Gb}{2\pi} \frac{x_2}{x_1^2 + x_2^2} \\ \sigma_{23} = \frac{Gb}{2\pi} \frac{x_1}{x_1^2 + x_2^2} \\ \sigma_{11} = \sigma_{22} = \sigma_{33} = \sigma_{12} = 0 \end{cases} \quad (1.3)$$

For an infinite straight edge dislocation, the Burgers vector is taken as  $\mathbf{b} = b\mathbf{x}_1$  as shown in Figure 1.7 (b). The corresponding displacement fields are [28]:

$$\left\{ \begin{array}{l} u_1 = \frac{b}{2\pi} \tan^{-1} \left( \frac{x_2}{x_1} \right) + \frac{b}{2\pi(1-\nu)} \frac{x_1 x_2}{x_1^2 + x_2^2} \\ u_2 = -\frac{b}{2\pi} \frac{1-2\nu}{4(1-\nu)} \ln(x_1^2 + x_2^2) - \frac{x_1^2 - x_2^2}{4(1-\nu)(x_1^2 + x_2^2)} \\ u_3 = 0 \end{array} \right. \quad (1.4)$$

where  $\nu$  is the Poisson ratio. Meanwhile the stresses fields are given by:

$$\left\{ \begin{array}{l} \sigma_{11} = -\frac{Gb}{2\pi(1-\nu)} \frac{x_2(3x_1^2 + x_2^2)}{(x_1^2 + x_2^2)^2} \\ \sigma_{22} = \frac{Gb}{2\pi(1-\nu)} \frac{x_2(x_1^2 - x_2^2)}{(x_1^2 + x_2^2)^2} \\ \sigma_{12} = \frac{Gb}{2\pi(1-\nu)} \frac{x_1(x_1^2 - x_2^2)}{(x_1^2 + x_2^2)^2} \\ \sigma_{33} = -\frac{Gbv}{\pi(1-\nu)} \frac{x_2}{x_1^2 + x_2^2} = \nu(\sigma_{11} + \sigma_{22}) \end{array} \right. \quad (1.5)$$

### 1.1.2 Slip mechanism

From the experimental point of view, plastic deformation was firstly characterized by the observation of slip lines or slip bands at the surface of crystalline specimens as presented in Figure 1.8 [29, 30, 31]. It was observed that plastic deformation occurs by slip on special planes and in specific crystallographic directions. A slip system is defined by a slip plane and a slip direction. Slip lines or slip bands can be observed by several different experimental techniques, such as SEM (Scanning electron microscope), TEM (Transmission electron microscopy), EBSD (Electron Back Scattered Diffraction) [32] or AFM (Atomic Force Microscopy) [33, 34, 8, 35, 36]. As the slip line is the trace of a specific slip plane and the surface, the active slip plane can be determined by identification if the orientation of the crystal is known.

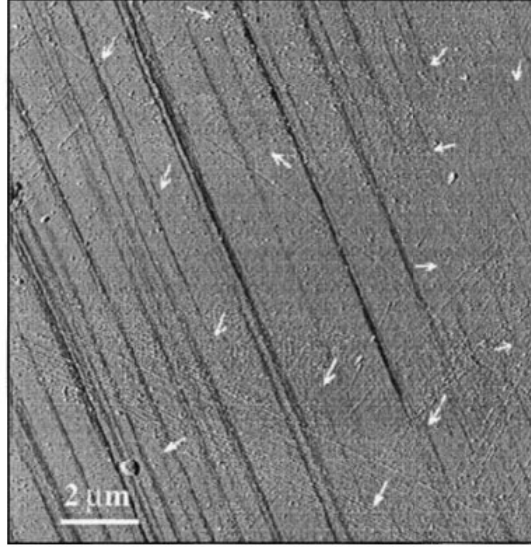


Figure 1.8: An AFM image of slip lines at the surface of  $\text{Ni}_3\text{Al}$ . The white arrows indicate short slip traces [29].

The slip steps observed on the surface of these materials reflect the cooperative movement of dislocations leading to highly localized deformation [30, 37, 38]. Dislocations can indeed multiply in a crystal during plastic deformation as observed by AFM [33]. The collective role of dislocations is thus predominant in determining the internal mechanical fields. The latter can be computed by using a micro-mechanical approach as done in Perrin's thesis [39, 8] where the slip line distribution within grains was considered through a distribution of intra-granular dislocation loops constrained at grain boundary.

### 1.1.2.1 Slip systems

In most crystalline materials, (a) the slip plane is the plane with the most densely atom packed plane; (b) the slip direction is the direction with the most closely atom packed direction; (c) between several possible slip systems in the structure, the first active slip system is the one with the largest resolved shear stress which should be larger than a critical resolved shear stress (CRSS). In FCC materials, there are 12 slip systems for perfect dislocations: 4 planes of type  $(111)$  with each 3 directions of type  $\langle 110 \rangle$ . These slip systems are listed in Table 1.1 using the Schmid and Boas notation [40]. The letter (A, B, C, D) designates the slip plane and the number (1 to 6) the slip direction. The Burgers vector of dislocations is parallel to the slip direction and the slip plane where dislocation can glide necessarily contains both the Burgers vector and the dislocation line.

System	Plane	Direction
<b>A2</b>	$(\bar{1}11)$	$\langle 0\bar{1}1 \rangle$
<b>A3</b>	$(\bar{1}11)$	$\langle 101 \rangle$
<b>A6</b>	$(\bar{1}11)$	$\langle 110 \rangle$
<b>B2</b>	$(111)$	$\langle 0\bar{1}1 \rangle$
<b>B4</b>	$(111)$	$\langle \bar{1}01 \rangle$
<b>B5</b>	$(111)$	$\langle \bar{1}10 \rangle$
<b>C1</b>	$(\bar{1}\bar{1}1)$	$\langle 011 \rangle$
<b>C3</b>	$(\bar{1}\bar{1}1)$	$\langle 101 \rangle$
<b>C5</b>	$(\bar{1}\bar{1}1)$	$\langle \bar{1}10 \rangle$
<b>D1</b>	$(1\bar{1}1)$	$\langle 011 \rangle$
<b>D4</b>	$(1\bar{1}1)$	$\langle \bar{1}01 \rangle$
<b>D6</b>	$(1\bar{1}1)$	$\langle 110 \rangle$

Table 1.1: Schmid and Boas's notations of slip systems in FCC crystals [40].

### 1.1.2.2 Frank-Read source

Among many different dislocation source models, such as Frank-Read source, condensation of point defects, particles and inclusions, grain boundary sources, surface sources and crack sources, etc. [41], the Frank-Read source is an important mechanism of dislocation multiplication and has been largely studied [42]. This mechanism involves the curvature of a dislocation wedged between two points under the effect of its line tension, and the subsequent instability of the curved dislocation which leads to the formation of a dislocation loop and the maintenance of the original trapped dislocation (see Figure 1.9). This source was observed experimentally by Dash in a silicon sample with Copper (Cu) precipitates [43]. This phenomenon has also been observed in other materials, particularly in Aluminum (Al) (see Figure 1.10) [44].



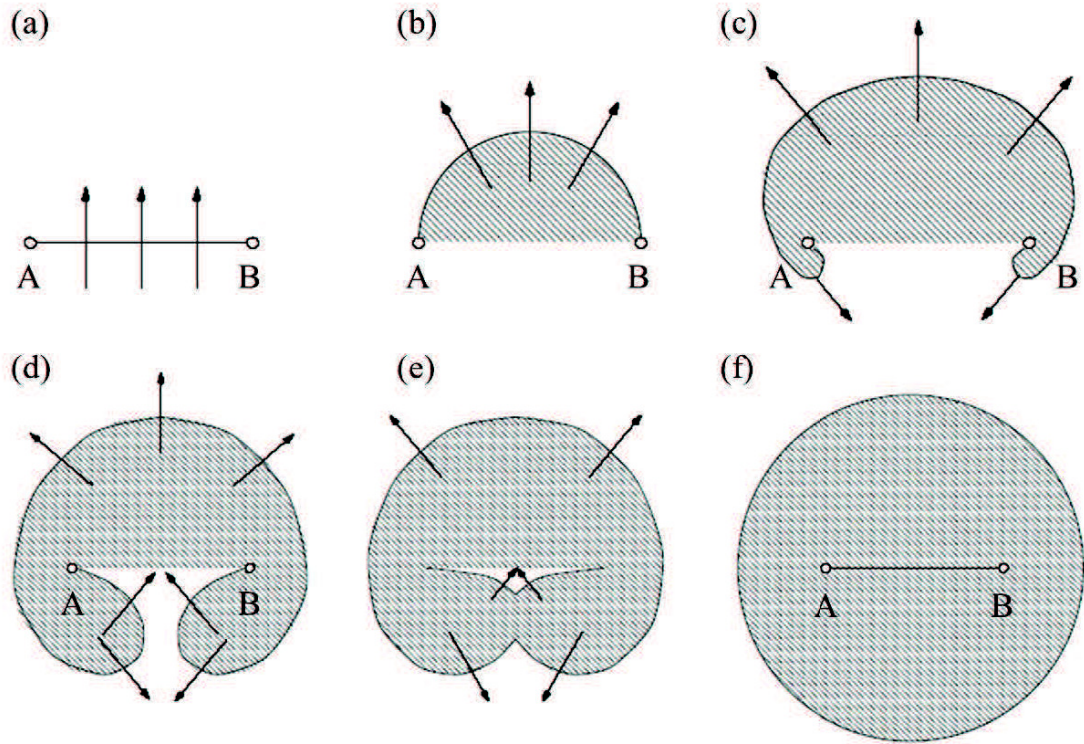


Figure 1.9: Principle of the Frank-Read source. (a) A dislocation line is anchored between two points A and B. (b) The external applied stress allows to form a curvature at the dislocation line to reach a critical position under the effect of its line tension. (c,d) After this configuration, the lines below points A and B attract each other and (e) annihilate each other to form a closed loop and (f) a new segment. The arrows represent the direction of loop movement.

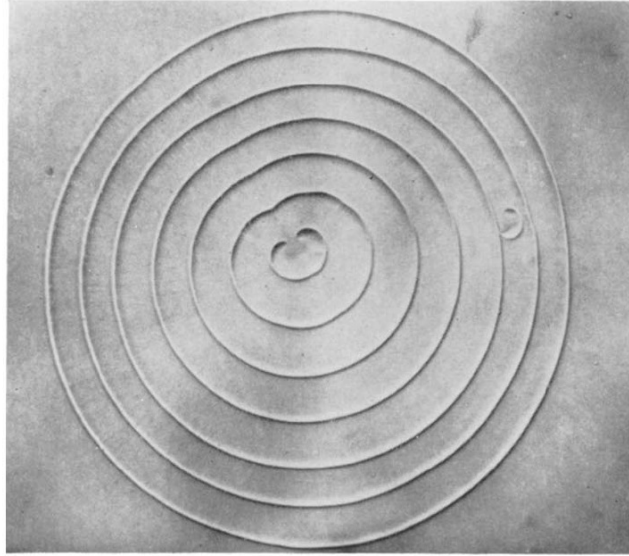


Figure 1.10: Experimental observation of a Frank-Read source having emitted a large number of loops on Al surface [44].

### 1.1.2.3 Stacking fault energy

As discussed in subsection 1.1.1.2, a perfect dislocation can be separated into several partial dislocations when certain conditions are met. However, the energy before decomposition must be greater than the sum of the energy of each part after decomposition, i.e. the process should be thermodynamically favorable. When a perfect dislocation is decomposed on a certain crystal plane, a stacking fault is formed. The perfect lattice structure between the dislocations of the various faces on the crystal face is further broken, which causes the rise of systematic energy. This energy is called stacking fault energy. Only when the metal stacking fault energy is low, the decomposition of complete dislocations will appear.

In a crystal, when two or more different slip planes slide simultaneously or alternately along a common slip direction, the slip is called cross-slip. Only screw dislocations can be transferred from one slip plane to another one. The stacking fault energy has a significant influence on the formation of dislocations and the cross slip phenomenon. When the stacking fault energy is low, dislocations are easily decomposed into partial dislocations and cross-slip cannot occur, thus planar slip is promoted. However, when the stacking fault energy is high, cross-slip is promoted and it will cause more homogeneous slip.

#### 1.1.2.4 Flow by dislocation motion

The plastic deformation of crystalline material can be regarded as the motion of dislocations, and the strain rate  $\dot{\gamma}$  caused by dislocation motion can be described by Orowan's equation as follows [45]:

$$\dot{\gamma} = \rho b v \quad (1.6)$$

where  $b$  is the magnitude of the Burgers vector,  $\rho$  is the mobile dislocation density and  $v$  is the dislocation velocity. Based on experimental observations, the dislocation density  $\rho$  mainly depends on applied stress, so the density of mobile dislocations can be described by a mechanistic law:

$$\rho = \alpha \left( \frac{\sigma}{b} \right)^2 \quad (1.7)$$

where  $\alpha$  is a material constant. However, dislocation velocity  $v$  is a function of temperature  $T$  and applied stress, which can be estimated by an Arrhenius law:

$$v = \beta \exp \left( \frac{-\Delta G(\sigma)}{kT} \right) \quad (1.8)$$

where  $\beta$  is a material constant,  $k$  is the Boltzmann constant which is equal to  $1.381 \times 10^{-23}$  J/K and  $\Delta G(\sigma)$  is the Gibbs free energy of thermal activation for dislocations overcoming obstacles. Furthermore, the activation energy can be described by [46]:

$$\Delta G(\sigma) = \Delta F \left( 1 - \left( \frac{\sigma}{\sigma_b} \right)^p \right)^q \quad (1.9)$$

where  $\Delta F$  is the activation energy needed to overcome energy barrier without help of stress and  $\sigma_b$  is the stress needed to overcome barrier without help of thermal vibration (thermal stress). Combining all the equations from Eqs. 1.6 to 1.9, the expression of the flow law is:

$$\dot{\gamma} = \frac{\alpha \beta \sigma^2}{b} \exp \left( \frac{-\Delta F}{kT} \left( 1 - \left( \frac{\sigma}{\sigma_b} \right)^p \right)^q \right) \quad (1.10)$$

Thus the strain rate is a function of material properties, applied stress and temperature. When considering the absolute zero temperature, there is no contribution of thermal vibration, and with an applied stress  $\sigma = \sigma_b$ , we get the strain hardening coefficient:

$$\dot{\gamma}_0 = \frac{\alpha \beta \sigma^2}{b} \exp(-0) = \frac{\alpha \beta \sigma^2}{b} \quad (1.11)$$

Inserting this coefficient into Eq. 1.10, we can get the final expression:

$$\dot{\gamma} = \dot{\gamma}_0 \exp \left( \frac{-\Delta F}{kT} \left( 1 - \left( \frac{\sigma}{\sigma_b} \right)^p \right)^q \right) \quad (1.12)$$

### 1.1.3 Deformation Twinning

Besides slip mechanism, plastic deformation may also occur due to mechanical twinning. Twinning consists in a shear of the crystal lattice such that the twinned structure has a mirror crystallographic orientation within the parent structure with respect to the twin plane (Figure 1.11). Twinning is due to the cooperative motion of partial dislocations. This is experimentally observed in recrystallized FCC structures like Ni, with the presence of twin bands with parallel sides in the grains as shown in Figure 1.12.

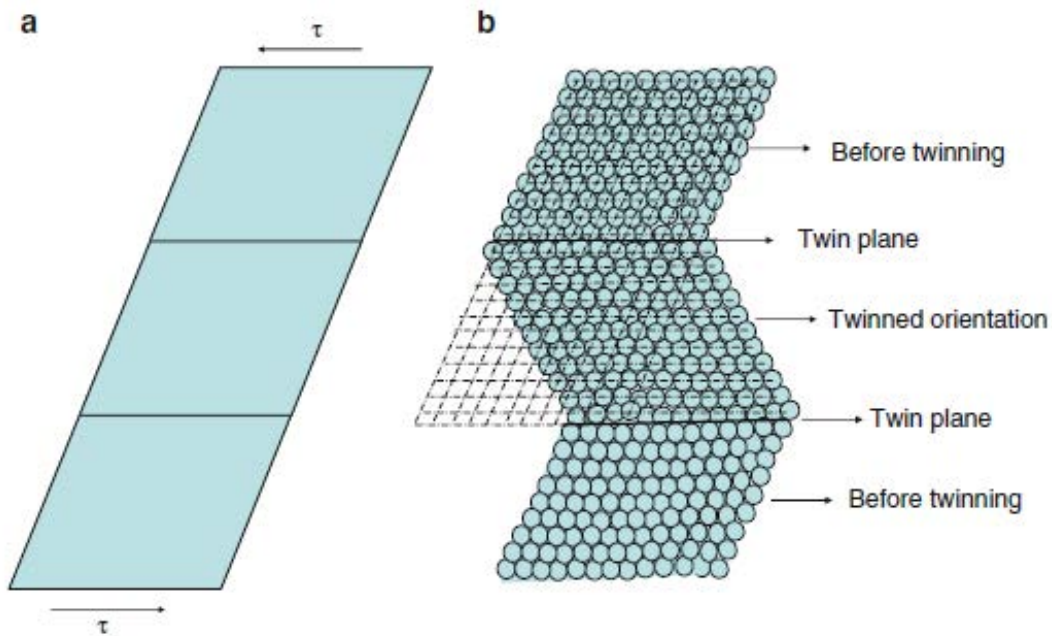


Figure 1.11: Schematic figure of twinning area in lattice: (a) original lattice form before application of shear stress and (b) after twinning deformation [26].

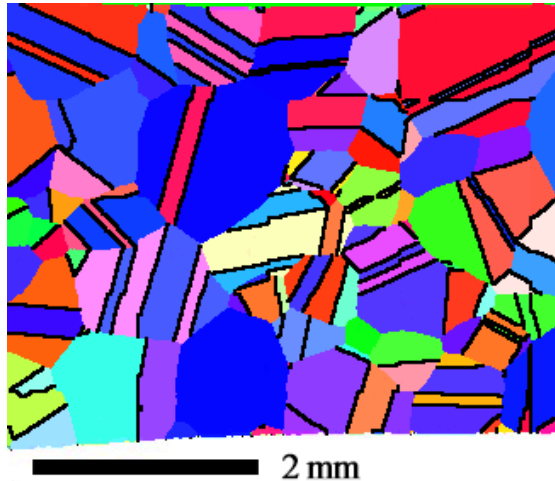


Figure 1.12: EBSD observation of twinning in Ni sample after heat treatment, in which the black lines indicate twin boundaries.

Compared to slip mechanism, twinning deformation is directional and, in addition to accommodate strain, provides also a significant reorientation of the crystal lattice. Hence, only a local positive resolved shear can normally activate a twinning system. Twinning is promoted in materials where the number of easy slip systems is limited like in HCP metals, or when the decomposition into partials is facilitated due to a low stacking fault energy like in TWIP steels. The main twinning system in FCC crystals is defined as: twin plane  $(111)$ , twin direction  $\langle 11\bar{2} \rangle$  and twin shear magnitude  $1/\sqrt{2}$ .

## 1.2 Grain boundary and free surface

### 1.2.1 Definition of a grain boundary

The grain boundary (GB) is the interface between the grains having the same structure and different orientations. Thus, for a single crystal as shown in Figure 1.13 (a), there is no GB. At GB the atomic arrangement is in a transitional state. Due to the irregular arrangement of atoms, GBs have different characteristics from the grains. The arrangement of atoms in GBs makes GB easily exposed to corrosion (thermal erosion, chemical corrosion). Due to their loose structure, GBs are channels through which atoms (ions) rapidly diffuse. Therefore, GBs are liable to cause segregation of impurity atoms (ions). At the same time, the melting point of GBs is lower than that of the grain. The atoms in GBs are disorderly arranged, and there are many defects such as vacancies, dislocations, disclinations, and bond deformations which cause lattice distortion. Therefore, the atoms in GBs

tend to have higher energy than the atoms in the grains. The greater the difference of orientation between grains, the more irregular is generally the arrangement of atoms at GB. However, for some special high symmetric GBs, the atoms at GB are still at their original positions as shown in Figure 1.13 (b), but the energy of these atoms are still higher than the regular atoms. As a conclusion, the structure, composition and amount of GBs have a major impact on various properties of crystalline materials and various processes within them (such as recrystallization, diffusion, deformation, etc.). In polycrystals, there are a large number of GBs that cross each other as shown in Figure 1.13 (c). A GB is cut off by other GBs to create a finite GB area. Furthermore, three or more GBs intersecting together produce triple or multi junctions.

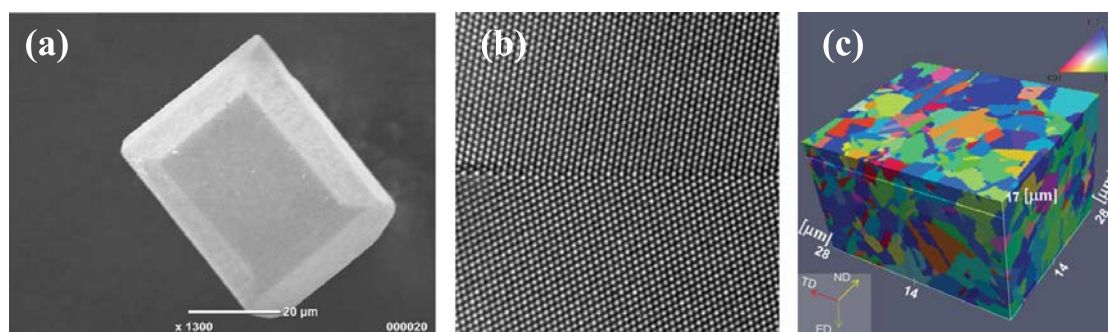


Figure 1.13: (a) SEM photograph of  $\text{La}_2\text{Li}_{0.5}\text{Al}_{0.5}\text{O}_4$  single crystal [47], (b) TEM photograph of a  $\Sigma_{11}$  (113) /  $[\bar{1}00]$  GB in Al bi-crystal configuration [48] and (c) 3D microstructure of the Cu-0.17wt%Zr polycrystal obtained by 3D EBSD measurement, which shows GBs in a polycrystal [49].

## 1.2.2 Definition and classification of grain boundaries

### 1.2.2.1 GB geometry and bi-crystallography

The classical GB is regarded as a plane interface defined by a normal vector between two crystals of different orientations, while the atoms distortion close to GB is disregarded. This GB is just an infinitely thin geometrical boundary separating two grains without any specific properties.

A complete geometrical characterization of GB can be specified by 9 geometrical degrees of freedom which include five macroscopic degrees of freedom and four microscopic degrees of freedom [50, 51]. The macroscopic degrees of freedom include misorientation and interfacial plane which are required to define a bi-crystal from given crystals:

- Three degrees of freedom are necessary to describe the misorientation between grains: one to define the rotation angle  $\theta$ , two to define the rotation

axis  $\mathbf{r} = \langle uvw \rangle$ . The misorientation angle is the smallest rotation angle to get from crystal to another.

- Two degrees of freedom are necessary to describe the inclination of the GB plane defined by its unit normal  $\mathbf{n}$ .

The microscopic degrees of freedom are needed to describe the atomic structure of GB which are determined by relaxation processes:

- Three degrees of freedom are necessary to describe the translation of one crystal to another one. The rigid body translation vector  $\tau$  includes two translations in the GB plane and one for expansion perpendicular to the GB plane.
- One degree of freedom is necessary to describe the position  $d$  of the GB plane along its normal. The value of  $d$  should be less than 1.

Depending on the misorientation angle  $\theta$ , GBs can be separated into low angle GBs (LAGB) with  $\theta < 10^\circ$  and high angle GBs (HAGB) with  $\theta > 15^\circ$ .

### 1.2.2.2 Coincidence Site Lattice

For certain angles around the axis of rotation, there is a three-dimensional periodic network of nodes which are common to both networks: this network is called coincidence site lattice (CSL) [52]. It is therefore the smallest network included in the networks of the two crystals. The CSL is characterized by an integer named the coincidence index  $\Sigma$  as the ratio between the volume of the primitive mesh of the coincidence network and that of the primitive mesh of the single crystal:

$$\Sigma = \frac{\text{Coincidence unit cell volume}}{\text{Crystal primitive unit cell volume}} \quad (1.13)$$

The CSL index is a purely geometric construction based on the geometry of the network and on the rotation of a network B with respect to a network A which brings about the coincidence of a point of B with a point of A as shown in Figure 1.14. Therefore, the precise atomic positions in the GB (due to internal relaxations) are not taken into account by this CSL approach. The geometry is such that the turned point (in network B) and the superimposed point in network A are connected by a mirror plane in the non-turned state.

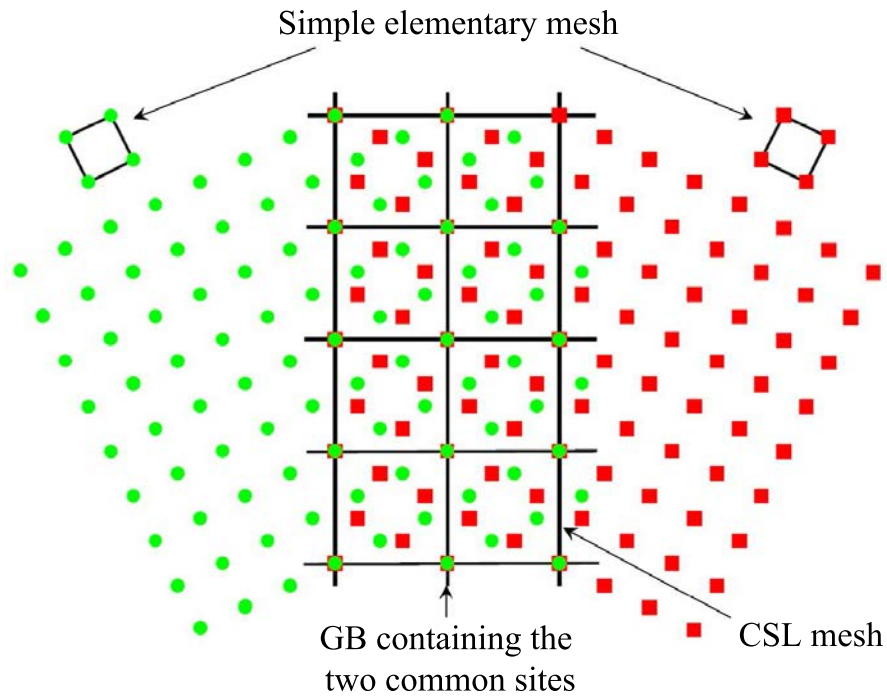


Figure 1.14: Schematic figure of CSL  $\Sigma = 5$  with the rotation angle  $\theta = 36.9^\circ$  across rotation axis  $[100]$  in simple cubic structure (SC).

### 1.2.2.3 Twist and tilt grain boundaries

The GB can be firstly categorized by the relationship between the rotation axis  $\mathbf{r}$  to get from grain to another and the GB normal vector  $\mathbf{n}$ . If the rotation axis is parallel to GB normal ( $\mathbf{r} \parallel \mathbf{n}$ ), the GB is called a twist GB as shown in Figure 1.15 (a). In contrast, if the rotation axis is perpendicular to the GB normal ( $\mathbf{r} \perp \mathbf{n}$ ), the type GB is called a tilt GB as shown in Figure 1.15 (b). A real GB is generally neither pure twist nor pure tilt, but combines the two types together. This last case is called a fixed GB as shown in Figure 1.15 (c).



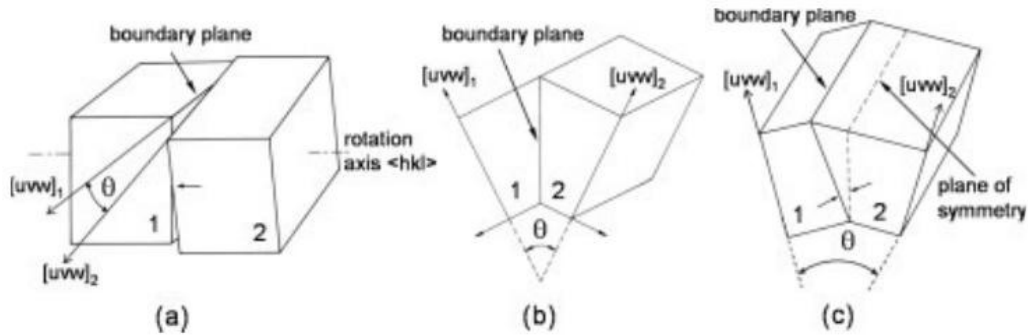


Figure 1.15: Schematic figure of (a) a pure twist GB, (b) a pure tilt GB and (c) a fixed GB.

The structure of a pure twist (with respect to tilt) GB can be regarded as the composition of screw (with respect to edge) dislocations which intersect each other. For a pure tilt GB, when both grains can be deduced from a same rotation angle around the rotation axis, then it is called symmetrical tilt GB (STGB). STGB is a mirror for the microstructure of the two adjacent grains. For a small rotation angle  $\theta$ , the STGB can be regarded as a wall of parallel edge dislocations, which will be discussed in subsection 1.2.2.6. However, if the STGB rotates another angle  $\varphi$  across the rotation axis, it is still a pure tilt GB with the same misorientation angle  $\theta$ , but in that case the GB is asymmetric with respect to the two adjacent grains and is called an asymmetric tilt GB (ATGB). ATGB's structure can be regarded as being formed by staggered arrangement of two sets of edge dislocations with Burgers vectors perpendicular to each other.

#### 1.2.2.4 Coherent and incoherent grain boundaries

Considering the atom matching at GB, GBs can also be classified into another three types: coherent GB, semicoherent GB and incoherent GB [51]. It should be pointed out that this classification is generally used for interphase boundaries, which are boundaries between two different phases. Two different phases may have different compositions, crystal structure and/or lattice parameter.

- Definition of coherent GB: Both crystals match perfectly at the interface plane as shown in Figure 1.16 (a). The interfacial plane has the same atomic configuration in both crystals like twin boundaries as shown in Figure 1.17. The energy of a perfectly coherent interface is very low: on the order of a few  $\text{mJ} \cdot \text{m}^{-2}$ . Small lattice mismatch at GB can be accommodated by elastic strain and coherent interface can be maintained as shown in Figure 1.16 (b).

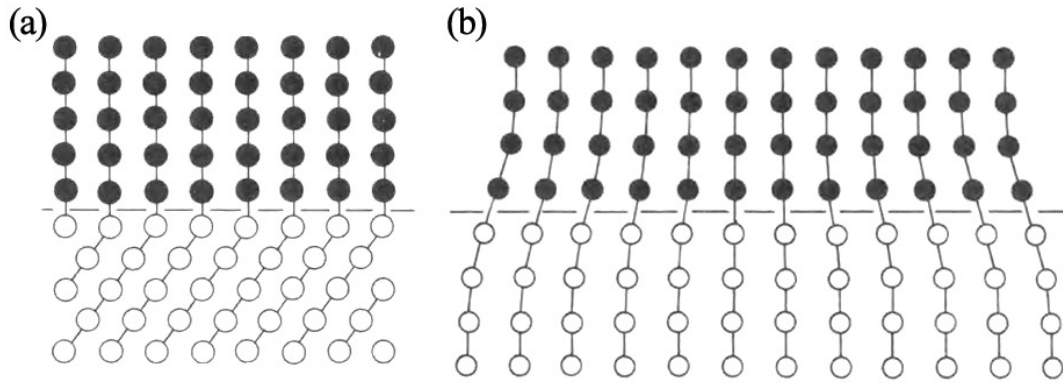


Figure 1.16: Schematic figure of a coherent GB (a) perfectly matching and (b) with small elastic strain [51].

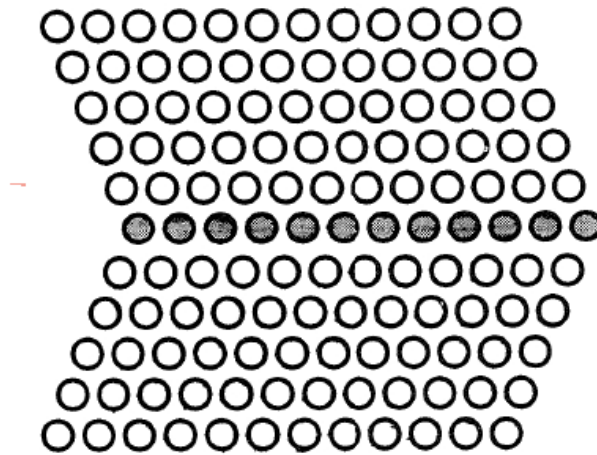


Figure 1.17: Schematic figure of a coherent twin boundary.

- Definition of semicoherent GB: Here, lattice mismatch is accommodated by a periodic array of misfit dislocations as shown in Figure 1.18. When the elastic coherency strain at GB becomes too large, a semicoherent GB is formed to reduce elastic energy. Uniform elastic strains are then replaced by localized strains due to such array of dislocations which do not create long-range strain fields.

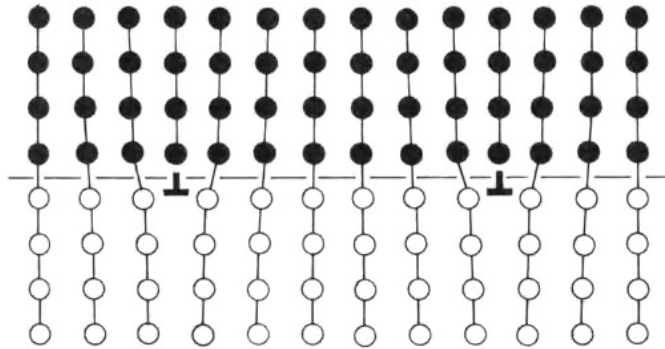


Figure 1.18: Schematic figure of a semicoherent GB.

- Definition of incoherent GB: Here, the atomic structure at GB is disordered as shown in Figure 1.19. An incoherent GB generally comes from a random misorientation relationship between the two grains. It can also come from a twin boundary if the GB has an inclination from the twinning plane as shown in Figure 1.20.

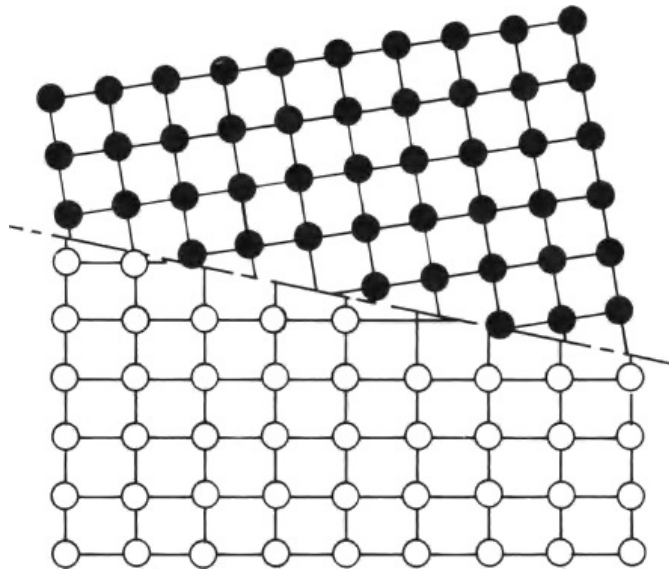


Figure 1.19: Schematic figure of an incoherent GB.

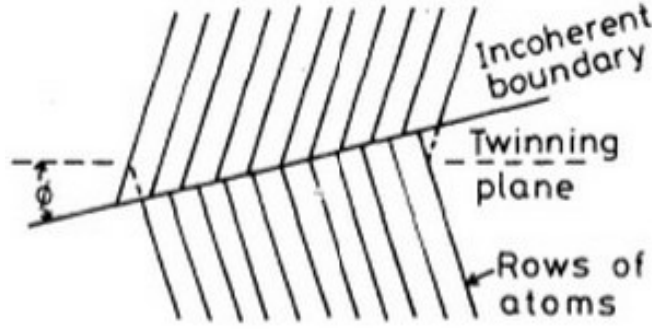


Figure 1.20: Schematic of an incoherent twin boundary.

### 1.2.2.5 Continuum based GB dislocation model

A GB can be described as a GB dislocation characterized by a Burgers vector density through the continuous Frank-Bilby (FB) approach [51]. This Burgers vector density  $\mathbf{b}_p$  which is necessary to realize the compatibility at GB between two crystals I and II can be calculated by the Frank-Bilby equation [53, 54]:

$$\mathbf{b}_p = (\mathbf{S}_I^{-1} - \mathbf{S}_{II}^{-1}) \cdot \mathbf{p} \quad (1.14)$$

where  $\mathbf{p}$  is a periodic vector in GB plane,  $\mathbf{S}_I$  and  $\mathbf{S}_{II}$  are the transform matrices that generate the lattice of crystal I and crystal II from a reference lattices as shown in Figure 1.21.  $\mathbf{b}_p$  is the Burgers vector content of all the dislocations that are crossed by the vector  $\mathbf{p}$ . The FB equation can be also used for HAGB even though discrete dislocation model cannot be defined anymore due to dislocation overlap.

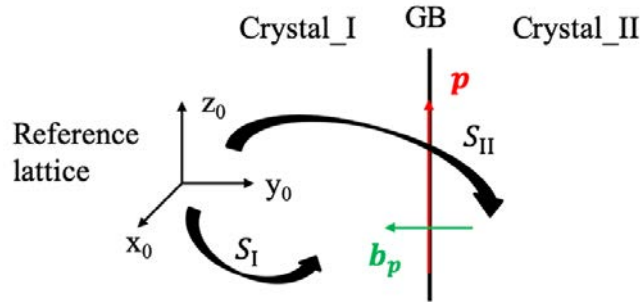


Figure 1.21: Continuum dislocation model of GB. Lattices of crystals I and II are generated from a reference system  $(x_0, y_0, z_0)$  by the transformations  $\mathbf{S}_I$  and  $\mathbf{S}_{II}$ , respectively. The vector  $\mathbf{b}_p$  is the Burgers vector density necessary to realise the compatibility at the GB and the vector  $\mathbf{p}$  is a periodic vector in GB plane [51].

In the case where the two crystalline lattices are connected by an axis / angle of disorientation and taking their median lattice as the reference lattice, this general equation is reduced to the Frank equation which is used for symmetrical LAGB (Eq. 1.15):

### 1.2.2.6 Discrete intrinsic dislocations model: Read-Schockley equation

A STGB can be described by a periodic network of edge dislocations characterized by a spacing, so-called Frank equation:

$$d = b/\theta \quad (1.15)$$

where  $b$  is the amplitude of the Burgers vector and  $\theta$  is the misorientation angle as shown in Figure 1.22. These dislocations are called intrinsic because they form a GB.

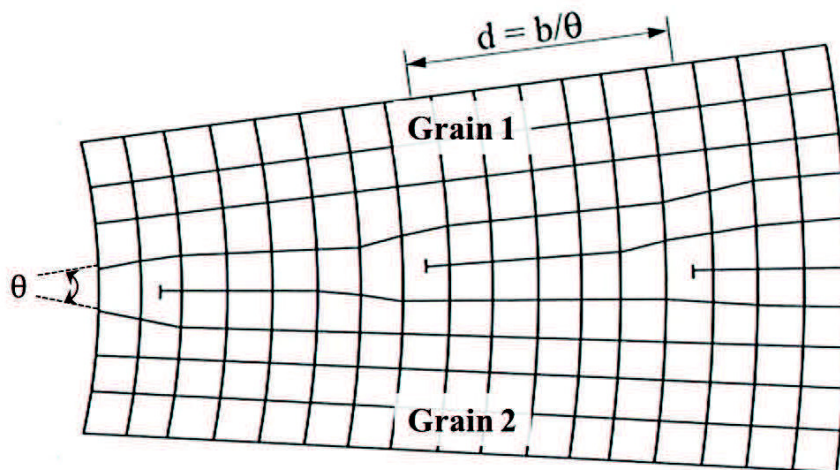


Figure 1.22: Schematic figure of a STGB formed by a dislocation arrangement [55].

The energy of a LAGB can be obtained in the case of linear elasticity from the Read-Schockley equation [55]:

$$E = E_0\theta (A - \ln \theta) \quad (1.16)$$

where  $E_0$  depends on the elastic stiffness of the studied material and  $A$  depends on the dislocation core radius and the Burgers vector magnitude. For low misorientation ( $\theta < 15^\circ$ ), this relationship shows that the GB energy increases as the misorientation angle increases which is presented in Figure 1.23 (dotted line). The formula 1.16 is actually valid in the case where the GB dislocations are arranged

in a periodic manner. Otherwise the variation of the energy as a function of the angle is very disordered and can contain many minima as shown in Figure 1.23 (solid line).

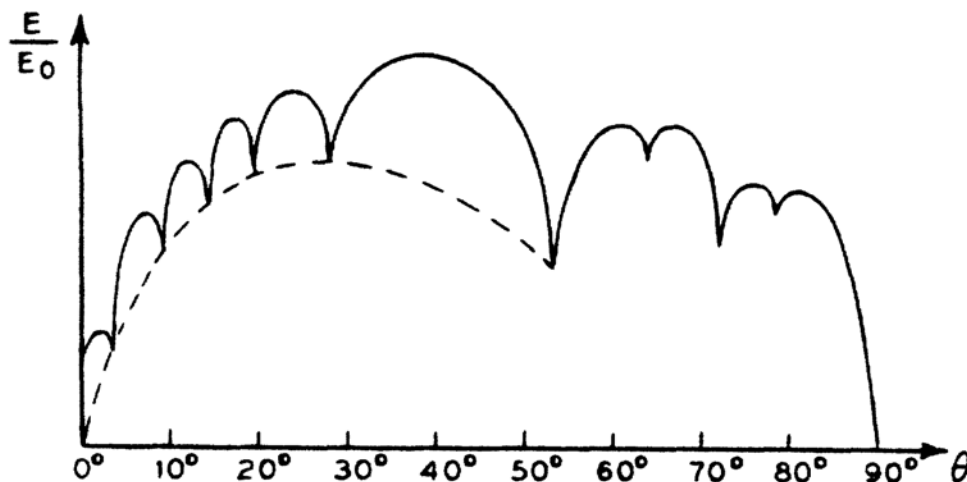


Figure 1.23: Evolution of the intergranular energy as a function of the disorientation angle  $\theta$ , deduced from the classical formula of Read and Shockley (Eq 1.16) (bridged line) and in the general case taking into account the distribution of non-periodic dislocations (solid line) showing the presence of level minima [55].

### 1.2.2.7 Structural Unit Model

The longer the periodic period on GB, the worse the atomic matching on both sides of the interface, and the higher the GB energy. Thus, GBs of any long-period structure tend to decompose into short-period structures with a certain strain. Short periods can be described by the structural unit model (SUM). It is the extension of the Read-Shockley model to LAGB with secondary dislocations [56]. For a certain range of disorientation  $\theta$ , the GB decomposes (over a period of the GB) alternately into two possible “structural units” called major units A (favored) and minor ones B (unfavored), such as  $\theta_A < \theta < \theta_B$ . The geometry of the GB is obtained by molecular statics (MS) using energy minimization where the core radius of interfacial dislocations is unknown. For example, three typical structural units in BCC bi-crystals are shown in Figure 1.24.

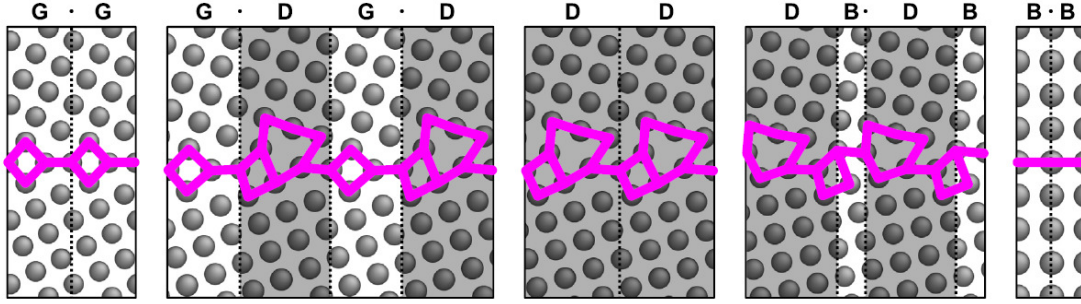


Figure 1.24: GB structure represented by G, D and B units in BCC bi-crystals. These structures are generated by STGB with corresponding misorientation angles across  $\langle 100 \rangle$  axis. [57]

The GB energy can be calculated through SUM by:

$$\gamma = \gamma_{el} + \gamma_C \quad (1.17)$$

where  $\gamma_{el}$  is the elastic energy (Read-Schockley) and  $\gamma_C$  is the core energy due to the interactions between units. For example, in the case of a GB composed by a major unit A with number  $m$  and a minor unit B with number  $n$  ( $m > n$ ), there are two types of interactions: A-A and A-B-A. Then the core energy can be calculated by:

$$\gamma_C = \frac{(m - n) d_A \gamma_C^A + n d_{AB} \gamma_C^{AB}}{(m - n) d_A + n d_{AB}} \quad (1.18)$$

where  $d_A$ ,  $d_{AB}$  are the radius of the cores and  $\gamma_C^A$ ,  $\gamma_C^{AB}$  are the core energies for units A and A-B, respectively. The radius of the cores are found by atomistic simulation. The energy of GBs can then be computed for different misorientations.

### 1.2.2.8 GB as an interphase model in monocrystalline materials

As discussed in subsection 1.2.2.4, except for perfectly coherent GB, the atomic arrangement in the vicinity of a GB is normally distorted due to crystalline lattice misorientation. This phenomenon is more evident when the grain size is reduced to nanoscale, such as in nanocrystalline materials. In that case, the volume fraction of GBs becomes non-negligible and the material can be divided into two parts: grain cores and GBs. GBs may have a different mechanical property from grain core and can be described as an interphase. The influence of the GBs on the overall mechanical property of the bulk material will increase when the grain size decreases [58, 59]. The GBs are usually treated as an isotropic amorphous interphase [60, 61, 62, 63]. Furthermore, the GB area can also be divided into two parts: GB and triple junctions as shown in Figure 1.25 [60, 64, 65]. These authors used

some mixture-based models to compute the overall behavior of monocrystalline materials considering grain size and GB effect in order to predict the inverse Hall-Petch relationship.

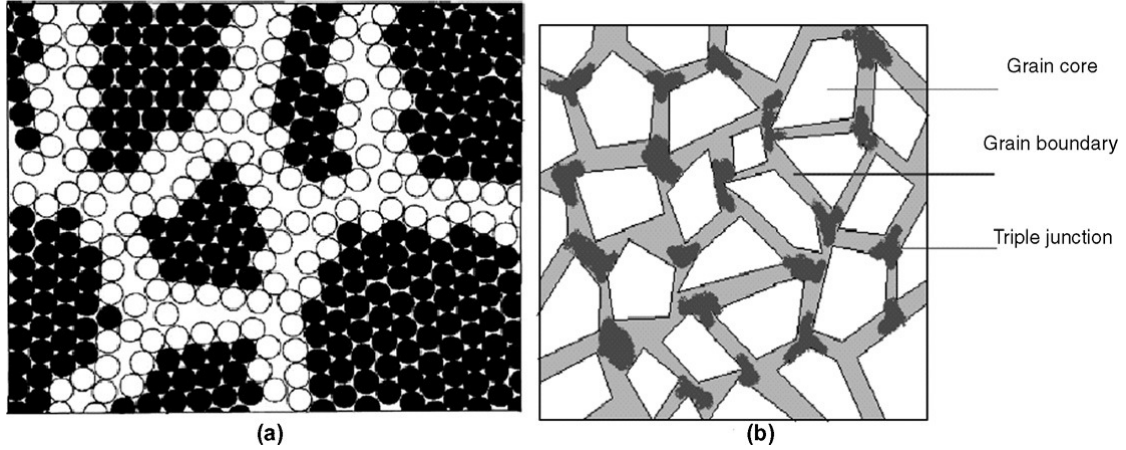


Figure 1.25: Two-dimensional model of a nanocrystalline solid with a separated area of GBs as interphase [65].

Molecular dynamics (MD) is a powerful method to investigate nanocrystals at atomic scale which will be more discussed in section 1.5.6. As the atomic arrangement is distorted within GBs, it is helpful to use MD simulations to analyze the structure and the property of GBs. The effective elastic modulus and strength of a bulk nanocrystal have been investigated by considering the grain size effect, the temperature effect and the volume fraction of interphase (GB volume fraction) [66, 67, 58, 68, 69, 70, 71]. A two-dimensional atomic crystalline structure of Cu nanocrystals is shown in Figure 1.26 [67]. Two different grain sizes  $d = 3$  nm in Figure 1.26 (a) and  $d = 7$  nm in Figure 1.26 (b) are compared. It is evident that the smaller grain size, the larger the thickness of GBs. Figure 1.26 (c) shows that as grain size decreases, the volume fraction of grain core decreases too. That means that the volume fraction of interphase increases. Considering temperature effects, it was evidenced that when temperature is increasing, the volume fraction of interphase is larger with the same grain size as shown in the Figure 1.26 (c).



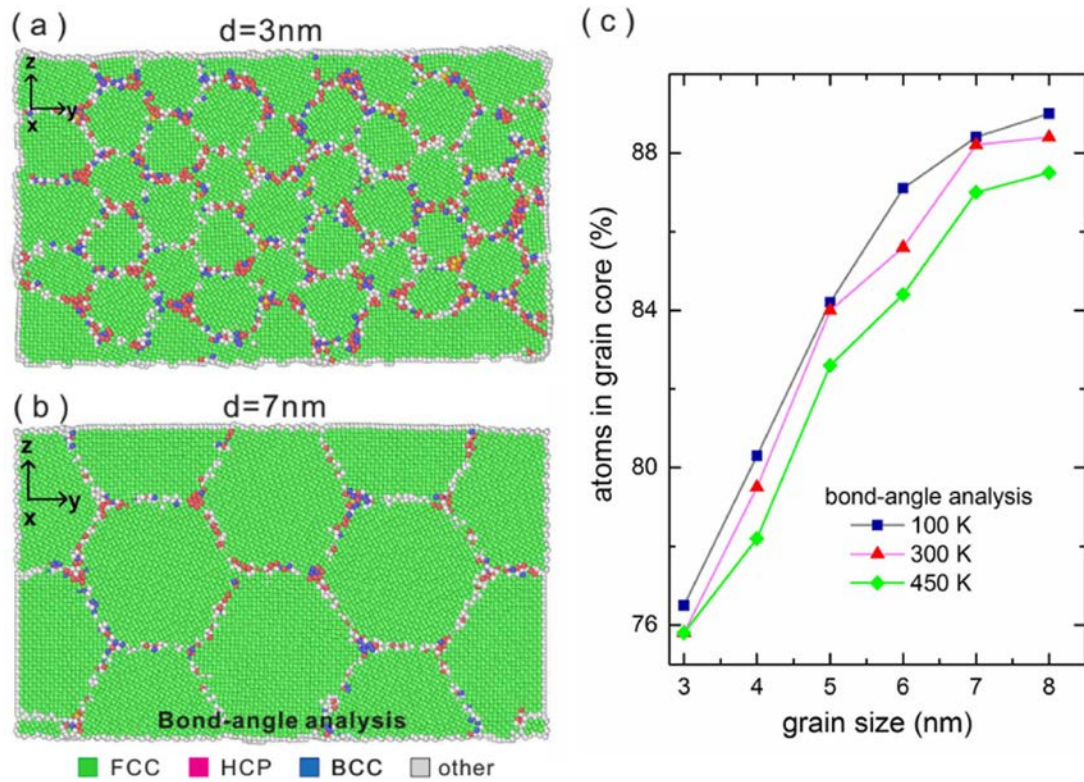


Figure 1.26: (a) and (b) show the atomic structure in Cu nanocrystalline material. (c) shows the fraction of atoms in grain core as a function of grain size [67].

A three-dimensional atomic crystalline structure of Cu nanocrystals is shown in Figure 1.27 [67]. The interphase structure is evidently different between grains with different misorientations.

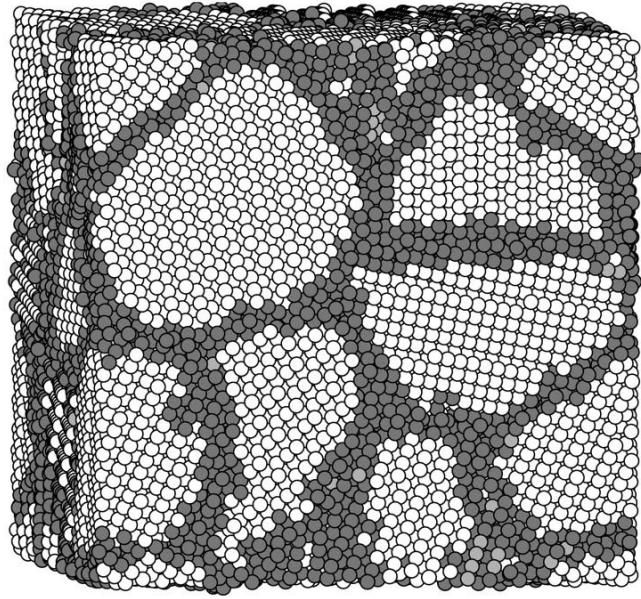


Figure 1.27: The initial configuration of a Cu nanocrystalline system at 300K with approximately 100 000 atoms arranged in 16 grains, giving an average grain diameter of 5.2 nm. White atoms are in a perfect FCC environment and atoms in GBs are colored as dark grey [69].

Furthermore, Kowalczyk-Gajewska et al. [72] have fully considered the anisotropy of a single crystal to estimate the effective elastic properties of nanocrystalline Cu. A series of molecular statics simulations were performed to find the all 21 components of the anisotropic stiffness tensor of polycrystals. It should be pointed out that all of the above researches studied overall properties of a bulk nanocrystal by considering interphase effect.

### 1.2.3 Free surface effects

In addition to GBs, free surfaces also have obvious effects on the mechanical properties of metallic materials. A free surface is traction free [73]. A free surface exerts an attractive force on a dislocation [73]. This force is called an image force [28] and will be deeply discussed in subsection 1.3.3. As it is always attractive, dislocations may exit the crystal and make a step on the surface. Such visible surface steps are called slip traces. For nanocrystalline materials, the dislocation density is quite low. These dislocations will be pulled out of grain by attractive force coming from free surface and the crystal is defect-free. In that case the strength of material will increase, which is called dislocation starvation mechanism [74, 75]. As this attractive force on dislocation is distance (between dislocation

and free surface) dependent, the free surface effect could be one of the explanation for size effect, which will be discussed in section 4.2.4. In addition to induce dislocation starvation, free surfaces can also act as dislocation sources during mechanical deformation. This phenomenon was studied by atomistic simulations in an Al specimen, which showed that dislocation nucleation occurs at surface steps [76]. This mechanism could be also studied by discrete dislocation dynamics simulations. For instance, the size-dependent plasticity of FCC micro-pillars under torsion was investigated by three dimensional discrete dislocation dynamics simulations that considered the mechanism of dislocation nucleation at free surfaces [77].

## 1.3 Interaction between dislocation and grain boundary

### 1.3.1 Experimental observations

With the development of microscopy techniques and micro-/nanomechanical testing methods, the dislocation-GB interactions have been largely experimentally studied using SEM, TEM, ECCI, EBSD, focused ion beam (FIB), nanoindentation, etc. During in-situ micro-/nanomechanical tests, the interaction between dislocations and a GB can be observed in time at atomic scale. Dehm et al. [78] have reported a comprehensive review on micro-/nanomechanical testing at small scale, especially for the GB effect in plasticity, such that the interaction between dislocations and GBs. Here only some significant results are presented.

Based on many experimental results, there are mainly four mechanisms of dislocation-GB interactions which have been studied:

- Dislocation transmission across GB [79].
- GB as a dislocation source for lattice dislocation [80]
- Formation of a dislocation pile-up [5]
- Dislocation absorption at GB [81].

From the mechanical tests on micro-size or nano-size samples, a size effect was observed due to dislocation source distribution [82]. The yield stress is increased with size decreasing at micro scale. Besides the increase of yield stress, the stress-strain curve of single crystals is also characterized by a jerky flow and scatter in the stress-strain measurement due to dislocation intermittent and critical behavior as shown by black curves in Figure 1.28. Similar size effect can be observed on

stress-strain measurement in bi-crystals. Figure 1.28 illustrates these size effects following the different mechanisms of dislocation-GB interaction. For a bi-crystal system with some special misorientation, a direct slip transfer without the storage a residual Burgers vector in GB is possible as shown in Figure 1.28 (a). However, this requires that the interaction lines between GB and both incoming/outgoing slip plane are parallel which is for instance the case with coherent  $\Sigma 3$  twin GB. It is believed that a breakthrough stress is needed for the dislocation to get from one grain to the other grain across the GB. The GB will dominate the overall material behaviour when this breakthrough stress is higher than the size-dependent single crystalline flow stress. However, Imrich et al. [83] showed that at a critical small sample size the coherent  $\Sigma 3$  twin GB does not have an impact on the overall mechanical property of micro-beam since the breakthrough stress is low in this case as shown by Malyar et al. [84] (17 MPa in Cu), but a large angle random GB does have an evident influence. The GB can also be the source of dislocation as shown in Figure 1.28 (b). In this mechanism, dislocations are emitted from GB in either one of the grains during mechanical deformation. In the case of a stable configuration, a lower flow stress for the bi-crystal with respect to the single crystal is possible which was observed by Kheradmand et al. [85]. Furthermore, it is believed that this mechanism occurs only in the case where there are already GB dislocations. When the GB strength is too large for dislocation motion due to slip incompatibility geometries or GB complexity, the boundary is regarded as an impenetrable obstacle. In this case, a dislocation pile-up is produced as shown in Figure 1.28 (c). The stress-strain curve shows a significant hardening effect and the dislocation density is normally higher than in the single crystalline counterparts. The GB strength can be calculated on the basis of dislocation pile-up distribution and anisotropic elasticity [5]. The stress concentration coming from dislocation pile-up can also activate dislocations in adjacent grain such that the GB can be regarded as a dislocation source. If some dislocations could enter into GB as GB dislocations, then these dislocations can overcome the obstacle and an indirect slip transfer mechanism is activated. The incorporated GB dislocation moves by non-conservative motion, like dislocation climb in the boundary, until its dislocation line is parallel with an outgoing slip system in adjacent grain as shown in Figure 1.28 (d) [86]. Kunz et al. [87] investigated this mechanism in micro pillars. They found that some bi-crystalline pillars exhibit smaller hardening and larger strain bursts than their single crystalline references, which could be explained by the annihilation of dislocations in the GB. Ng et al. [88] and Kim et al. [89] found the same mechanism and similar strain bursts behavior in bi-crystalline pillars of Al compared to the single crystalline pillars. They also indicated that it is hard to strictly discriminate the behavior between dislocations emitted by stress concentration coming from dislocation pile-up and those coming from indirect

slip transfer. It should be pointed out that several of these mechanisms may be simultaneously present in the same material with different misorientation of GBs.

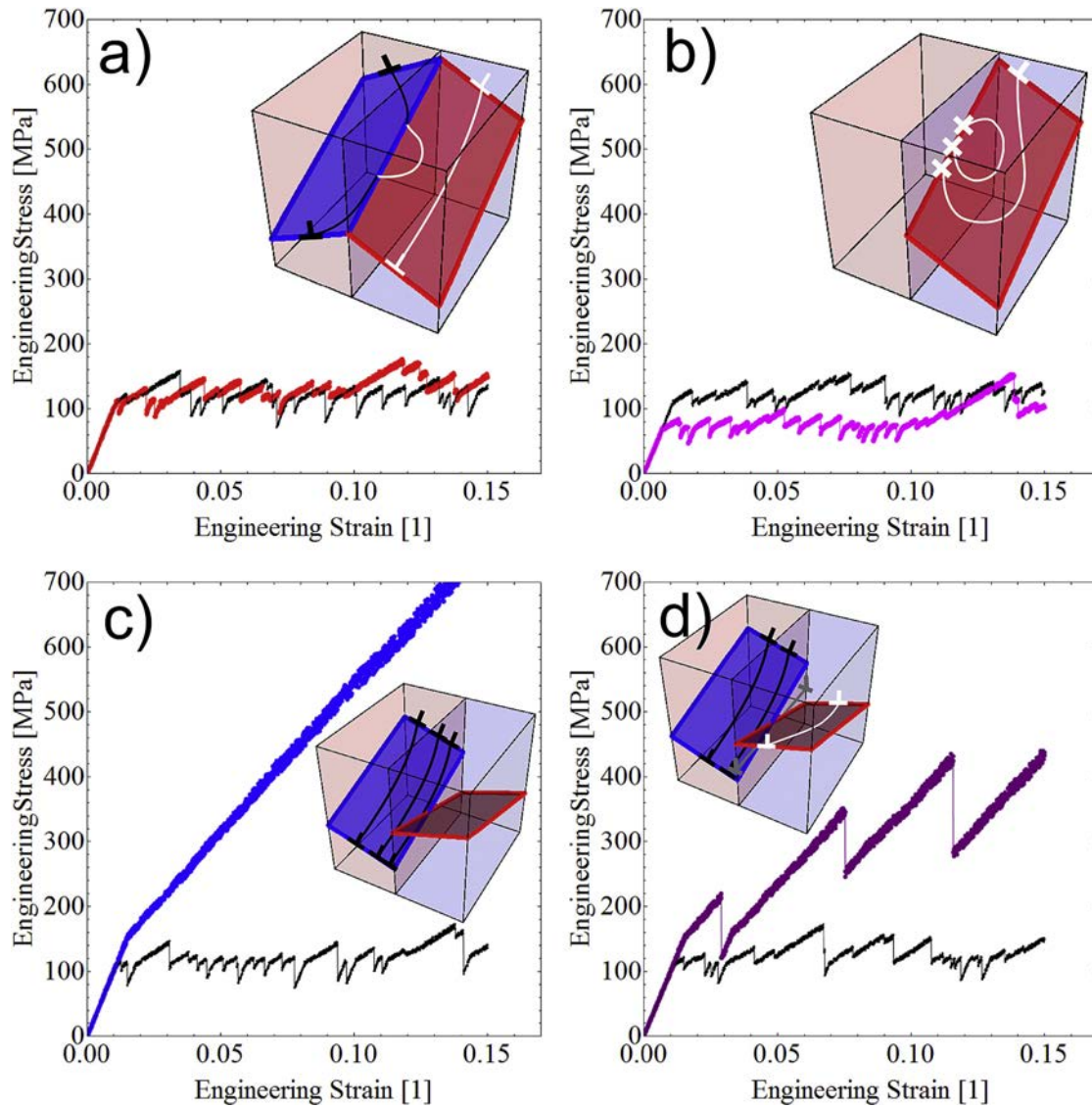


Figure 1.28: Engineering stress-strain curves related to different possible size dependent dislocation-GB interaction mechanisms with the single crystalline behavior in black and the corresponding bi-crystal colored: (a) slip transmission from single dislocations; in this case the activation stresses of dislocation-source can dominate over the stresses required for slip transmission. (b) GB acting as dislocation source, which may lead to a reduction in yield stress compared to single crystalline samples. (c) Dislocations forming a pile-up at an impenetrable GB. (d) Slip transfer via non-conservative dislocation motion in the GB [78].

### 1.3.2 Dislocation pile-up

Dislocation pile-up at GBs is an important inelastic deformation mechanism in polycrystalline materials that has been observed in metals using TEM [90, 91] as shown in Figure 1.29 or using stage-I fatigue crack experiment [92]. Both discrete and continuous-based theories of pile-ups were developed [93, 94]. The calculation of equilibrium positions of discrete dislocations in a pile-up was firstly performed by Eshelby et al. [95] in an isotropic homogeneous elastic crystal. The equilibrium position solutions were described as the roots of a generalized Laguerre polynomial. On the other hand, Leibfried [96] studied continuous pile-ups where discrete dislocations were replaced by a continuously distributed dislocation density. From Eshelby's work, Mitchell et al. [97] computed the equilibrium positions of discrete dislocations in pile-up within anisotropic homogeneous crystals.

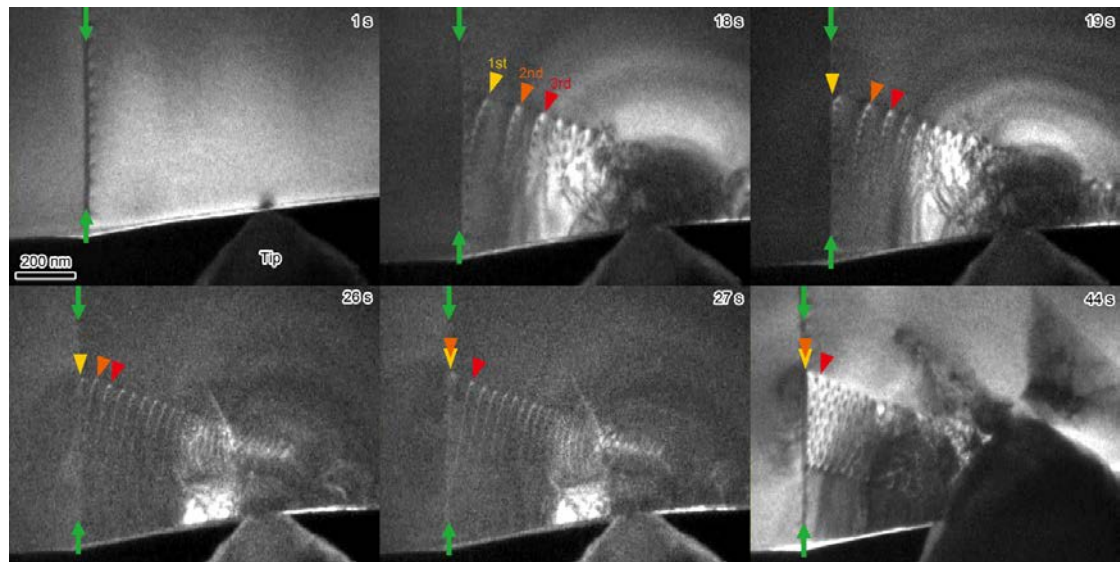


Figure 1.29: TEM images during nanoindentation experiment for the  $\Sigma 5$  GB of  $\text{SrTiO}_3$ . The line contrasts indicated by the green arrows correspond to the  $\Sigma 5$  GB. The positions of the leading three lattice dislocations are indicated by the triangles. The dislocation motion was strongly impeded by GB, which resulted in the dislocation pile-up. In this experiment, the first and second dislocations and the lower part of the third dislocation were trapped on GB plane even after the external stress was removed [91].

The stresses caused by dislocation pile-ups at GBs constitute the main explanation for the grain size dependence of the yield stress of polycrystals [95], well known as the Hall-Petch relationship [3, 4]:

$$\sigma_y = \sigma_0 + kd^{-1/2} \quad (1.19)$$

where  $\sigma_y$  is the yield stress of polycrystals,  $\sigma_0$  the applied stress,  $k$  a constant characterizing the resistance of GB and  $d$  is the average size of grains. In order to compute the elastic fields of dislocation pile-ups at GBs, two-dimensional elasticity is generally considered and dislocations are represented as a set of identical parallel straight infinite dislocations lying in the same slip plane. According to the theoretical work of Eshelby et al. [95] performed in isotropic elasticity, a lower bound estimate of the resolved shear stress on the slip system from a pile-up of straight dislocations is:

$$\tau = \tau_0 \sqrt{\frac{L}{d}} = \sqrt{2A\tau_0} \sqrt{\frac{N}{d}} \text{ for } \frac{1}{15}l \ll d \ll L \quad (1.20)$$

where  $d$  is the distance beyond the leading (locked) dislocation,  $\tau_0$  the applied resolved shear stress,  $A = \frac{G|b|}{2\pi(1-\nu)}$  for edge dislocation [95],  $L$  the pile-up length which can be approximated by  $\frac{2NA}{\tau_0}$ ,  $N$  the number of dislocations in pile-up and  $l$  the distance between the locked and the nearest free dislocation as shown in Figure 1.30. Furthermore, at short distance, the effect of the locked dislocation becomes predominant and the shear stress approximation is given by:

$$\tau = \frac{A}{d} \quad (1.21)$$

whereas at long distance, the stress can be approximated as the sum of the applied stress and that due all the dislocations regarded as congregated at the origin:

$$\tau = \tau_0 + N \frac{A}{d} \quad (1.22)$$

The stress concentration built up at the head of dislocation pile-ups may be the driving force for slip transfer and activation of new dislocation sources in the neighboring grain.

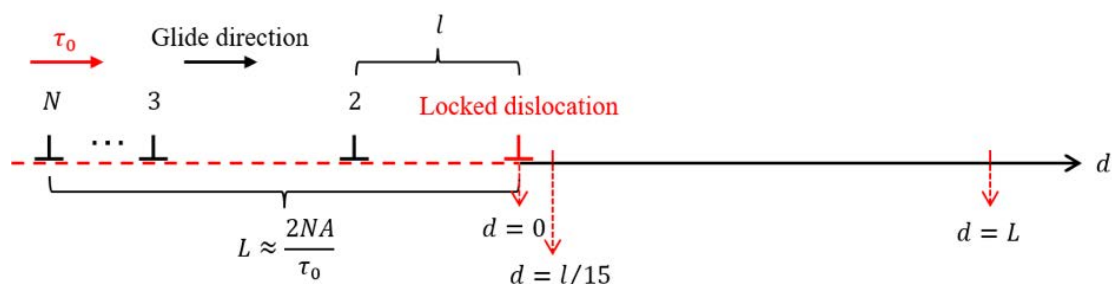


Figure 1.30: Discrete edge dislocation pile-up configuration in isotropic elasticity [95].

About dislocation pile-ups in heterogeneous media, many works dealt with planar or circular bimetallic interfaces but mostly in isotropic elasticity [98, 99, 100, 101, 102, 103]. In particular, Lubarda [102] recently studied the effect of the number of dislocations, the applied shear stress, the size of the inhomogeneity and the degree of mechanical contrast on the equilibrium position of edge dislocation pile-up against a circular inhomogeneity or a bimetallic interface. He also evaluated the configurational force on a circular inhomogeneity and the stress concentration caused by the pile-up against different interfaces, which is of importance for the study of interface cracking. A few works about pile-ups are however concerned with heterogeneous anisotropic elasticity, as the ones of Vagera [104] for continuous pile-ups and Wagoner [105] for discrete pile-ups. Wagoner [105] found dislocation positions of an equilibrated pile-up in an anisotropic bicrystal using a numerical iterative relaxation scheme with a first locked dislocation at small distance from GB. The iterative relaxation scheme minimizes the Peach-Koehler force acting on each dislocation along the glide direction. Up to now, a few discrete dislocation dynamics studies incorporate elastic anisotropy framework to integrate image forces in bi- and tri-materials, see e.g. Shishvan et al. [106]. Whereas the Hall-Petch relationship was obtained by discrete dislocation dynamics using isotropic elasticity assumption [107].

### 1.3.3 Image force and image dislocation

When a dislocation is close to a GB, it is subjected to five types of forces as shown in Figure 1.31:

- Applied forces
- Forces between dislocations  $F_d$
- Image forces from GB due to heterogeneous elasticity  $F_i$
- Lattice friction force  $F_f$
- Interaction forces between the cores of both dislocation and GB  $F_c$



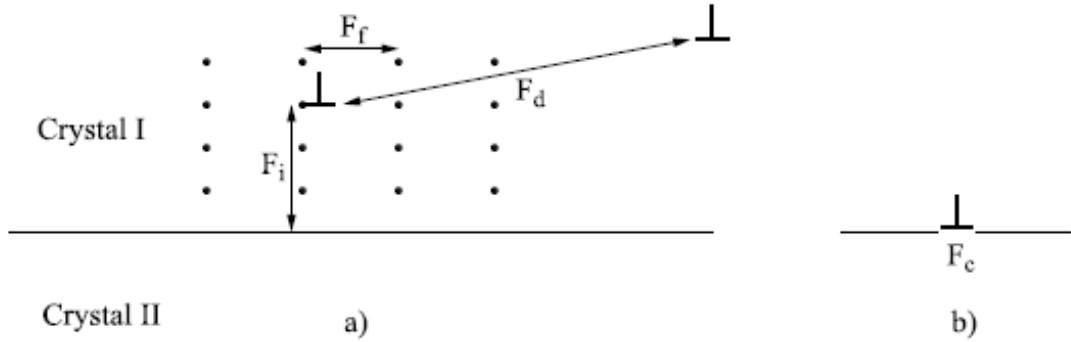


Figure 1.31: Schematic figure of the forces acting on a dislocation close to a GB [108].

In presence of a GB in anisotropic heterogeneous media like bi-crystals containing grains with different orientations, image stresses are appended to the self dislocation stress field (the one for an infinite homogeneous medium) in order to satisfy the boundary conditions at the interface through their elastic fields. According to Barnett and Lothe [109] the image force on a dislocation parallel to GB plane can be equivalently computed as:

$$F_i = -\frac{E^\infty - E^{I-II}}{d} \cdot \mathbf{n} \quad (1.23)$$

where  $\mathbf{n}$  is the inner normal to GB,  $d$  is the distance between dislocation and the GB plane,  $E^\infty$  is the prelogarithmic factor of the dislocation energy in an infinite crystal I and  $E^{I-II}$  is the same factor for the dislocation in the GB between crystal I and II. The image force on a dislocation corresponds to the Peach-Koehler force at the dislocation position. The image forces can either attract the dislocation towards the GB ( $E^{I-II} < E^\infty$ ) or on the contrary push the dislocation away ( $E^{I-II} > E^\infty$ ).

Based on a large number of numerical studies of different geometrical configurations with  $\mathbf{b}$  the Burgers vector,  $\mathbf{t}$  the dislocation line direction vector,  $\mathbf{r}$  the misorientation axis and  $\theta$  misorientation angle, the main properties are listed as follows [108]:

- The image force is null when the dislocation line  $\mathbf{t}$  is parallel to a high symmetry rotation axis  $\mathbf{r}$ : quaternary  $\langle 100 \rangle$  and ternary  $\langle 111 \rangle$  for all dislocation Burgers vectors, but it is not validated for a binary  $\langle 110 \rangle$  axis.
- The image force is null for all dislocations parallel to the twin plane (100) in symmetrical tilt boundaries of FCC crystals.

- When the dislocation line  $\mathbf{t}$  is parallel to  $\langle 100 \rangle$  or  $\langle 111 \rangle$  crystalline axis in second crystal, the image force is constant when the second crystal rotates around these two axis, respectively.
- The image force varies continually with the rotation angle around a fixed axis and for a fixed dislocation.
- For cubic structure, the intensity of the image force for a fixed dislocation/GB configuration increases with the anisotropic factor  $H = C_{44} - (C_{11} - C_{12})$  but not with the anisotropic ratio  $A = C_{44}/(C_{11} - C_{12})$ .

The image force on a dislocation due to GB or free surface can be regarded as the interaction force between this dislocation and other image dislocations through Green's function. The locations of these image dislocations in isotropic half-space were explicitly presented by Ma [110]. It was found that the Green's function for isotropic half-space consisted of four or five Green's functions for the infinite space. One of them is the analyzed dislocation itself inside the half-space. The other represent image dislocations located outside the half-space with the same distance from the surface as that of the analyzed dislocation as shown in Figure 1.32.

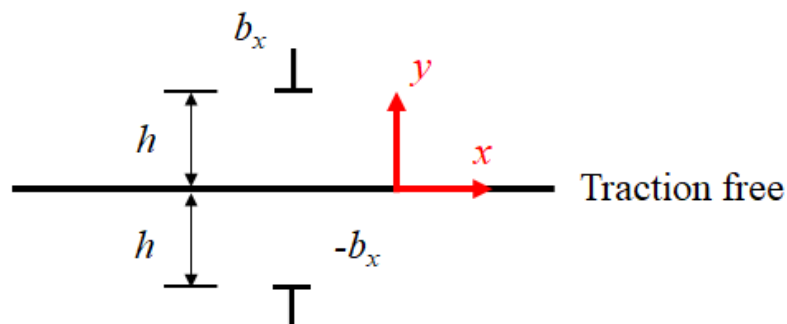


Figure 1.32: Image dislocation  $-b_x$  of the Green's function for a free half-space subjected to a dislocation  $b_x$  [110].

#### 1.3.4 Slip transmission and geometrical criteria

Slip primarily occurs on slip systems of special orientation. Even during the process of slip transmission across GB. At GB, slip generally comes from one incoming slip system and continues into an outgoing slip system. The possibility of slip transmission can thus be investigated by geometrical transmission factors [111, 112, 113, 114, 115, 116, 117, 118, 119, 120, 121, 122, 123]. Bayerschen et

al. [124] reported a complete review on slip transmission phenomenon. Here, only the different geometrical transmission factors are reviewed below from their paper meanwhile the notations of all used symbols are presented in Figure 1.33.

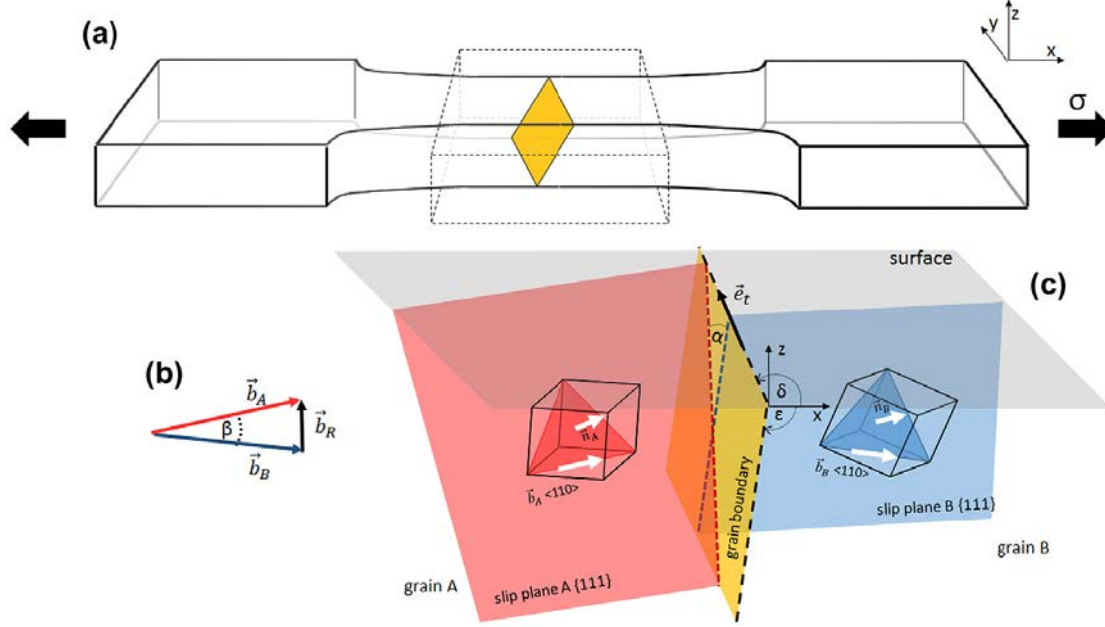


Figure 1.33: (a) Configuration of a bi-crystal sample with a random oriented GB under external applied stress, (b) the angle  $\beta$  between the incoming Burgers vector and the outgoing Burgers vector in both grain representing the slip directions with a residual Burgers vector  $\vec{b}_R$ , (c) Orientation of slip systems in both grains A and B: normalized Burgers vector  $\vec{b}$ , normal vector of slip plane  $\vec{n}$ , angle  $\alpha$  between the intersection line of GB plane and slip planes in both grains and GB orientation relative to surface: angle  $\delta$  between GB trace on surface and  $x$  direction, inclination angle  $\epsilon$  between GB plane and surface and GB surface trace unit vector  $\vec{e}_t = \langle \cos \delta, \sin \delta, 0 \rangle$  [125].

- Geometric criteria considering only slip system orientations:  
The geometric transmission factor was firstly proposed by Livingston and Chalmers [126] to investigate slip activation in an adjacent grain caused by a dislocation pile-up. This geometric transmission factor is based on slip directions and slip planes, and is defined as:

$$T_{pq} = (\mathbf{n}_A^p \cdot \mathbf{n}_B^q) (\mathbf{b}_A^p \cdot \mathbf{b}_B^q) + (\mathbf{n}_A^p \cdot \mathbf{b}_B^q) (\mathbf{n}_B^q \cdot \mathbf{b}_A^p) \quad (1.24)$$

where  $p$  and  $q$  indicate slip systems. This transmission factor is based on the approximation that the stress state in the adjacent grain due to the pile-up is of pure shear type. It was used to predict slip activation in adjacent grain

due to dislocation pile-up [111]. Based on Eq. 1.24, a simplified version was later employed by Luster and Morris [117]:

$$T_{pq} = (\mathbf{n}_A^p \cdot \mathbf{n}_B^q) (\mathbf{b}_A^p \cdot \mathbf{b}_B^q) \quad (1.25)$$

where the second term is dropped. This transmission factor was combined with stress intensity factor and Schmid factor to analyze slip activation in adjacent grain due to a dislocation pile-up [113]. It was found that the alignment of slip systems on both sides of the GB is more important than a high Schmid factor.

- Geometric criteria considering both slip system and GB orientation: The interaction between incoming and outgoing slip systems occurs at GB. In order to take into account the orientation of GB, a new transmission factor was proposed by Shen et al. [5]:

$$T_{pq} = \cos \alpha^{pq} \cos \beta^{pq} \quad (1.26)$$

This transmission factor considers both alignment of slip planes and minimization of residual Burgers vector at the same time. Combined with resolved shear stress calculation, this transmission factor successfully predicted slip activation due to a dislocation pile-up in a 304 stainless steel [5].

Furthermore, Lee et al. [114] have proposed a process to predict slip transmission by taking account the residual Burgers vector separately from alignment of slip systems. First, for a certain incoming slip system with slip plane  $\mathbf{n}_A$  and Burgers vector  $\mathbf{b}_A$ , a slip plane  $\mathbf{n}_B$  in the adjacent grain must be found with minimum angle  $\alpha$  combined with incoming slip plane  $\mathbf{n}_A$ . It should be pointed out that for one slip plane, there are three slip systems with different slip directions for (111)  $\langle 110 \rangle$  slip systems. Second, the resolved shear stress for different slip directions in the outgoing plane due to incoming dislocations is calculated, and the slip direction with the maximum resolved shear stress is picked up. For this slip direction, two opposite Burgers vectors are possible. The Burgers vector  $\mathbf{b}_B$  which provides the smallest residual Burgers vector  $\mathbf{b}_R$  with incoming Burgers vector  $\mathbf{b}_A$  is finally chosen. Then, the most likely transmitted slip system is determined.

- geometric criteria considering threshold angles for the slip system and GB. From previous discussion, it is known that the slip transmission is not favorable when the angle between intersection lines on GB or between two slip directions of incoming / outgoing slip systems is too large. Thus, it is believed that the slip transfer is not expected if at least one of these two

angles is bigger than a critical angle [123, 115]. Based on this hypothesis, a new transmission factor was proposed extending Eq. 1.26 [115]:

$$T_{pq} = \cos\left(\frac{90^\circ}{\omega_c}\alpha^{pq}\right) \cos\left(\frac{90^\circ}{\kappa_c}\beta^{pq}\right) \quad (1.27)$$

where  $\omega_c$  and  $\kappa_c$  are critical angles. In the calculation, the transmission factor is set to zero once at least one of these two angles is larger than the critical angle. Some critical angles were proposed for Brass [123]:  $\omega_c = 15^\circ$  and  $\kappa_c = 45^\circ$  for  $\alpha/\alpha$  and  $\alpha/\beta$  phase boundaries.

### 1.3.5 Grain boundary strength

Because GB is an obstacle to dislocation motion, it has a huge influence on plastic deformation of materials, especially for nanocrystals. The existence of GBs usually increases material strength as it needs an extra force to move dislocations across GBs [4, 3]. That extra force is called GB resistance against slip transmission which is also called as the GB strength [127, 128, 5]. Many experimental and simulation, from atomistic simulations to simple geometrical models or continuum mechanical models [129, 130, 131, 132, 133, 134, 135] studies tried to estimate it.

#### 1.3.5.1 TEM observation and anisotropic elasticity calculation

The GB strength in 304 stainless steel was investigated by Shen et al. [5] by using TEM observation of dislocation pile-ups close to GB and anisotropic elasticity calculation. The resolved shear stress  $\tau$  at the leading dislocation in a stable dislocation pile-up at vicinity of a GB was calculated based on anisotropic elasticity by considering the number of dislocations in pile-ups observed in TEM as shown in Figure 1.34. As the position of the leading dislocation was stable during the experiment, it was considered that  $\tau$  was a lower bound estimate of the back-stress from GB.  $\tau$  was then designated as a lower bound estimate of the GB strength. After computing  $\tau$  for different GBs, the value of the GB strength for 304 stainless steel was found to vary from 280 to 870 MPa.

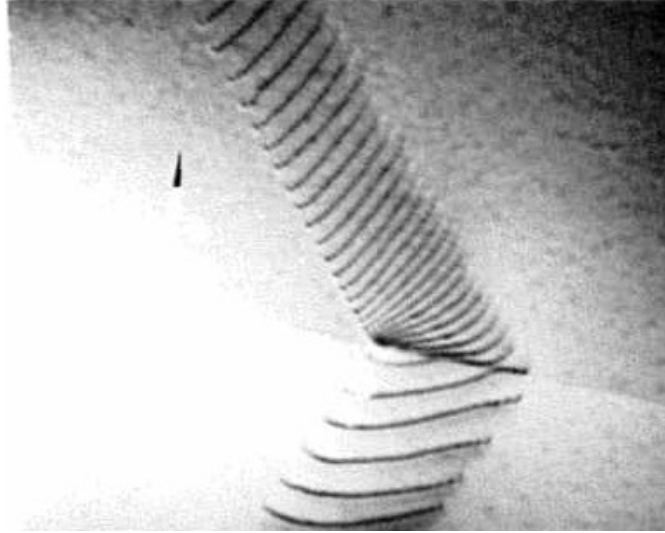


Figure 1.34: Dislocation pile-up at GB in 304 stainless steel from TEM observation [5].

### 1.3.5.2 Geometrical GB strength factor

The GB strength can also be described by a geometrical factor based on the discrepancy of slip systems in the two crystals which could impede slip transmission. Because of the inverse meaning of the GB strength factor and transmission factor, the transmission factor  $T_n$  can be translated into a strength factor  $R_n$  between 0 and 1 thanks to the normalization [125]:

$$R_n = 1 - T_n \quad (1.28)$$

Except inverse calculation from transmission factor, a direct strength factor was proposed by Blochwitz et al. [136] based on an incompatibility factor which incorporates the trace of GB on surface  $\mathbf{e}_t$ . A rotation vector is defined for the grain to characterize the effect of its slip system on GB:

$$\mathbf{r}^p = \mathbf{n}^p \times \mathbf{b}^p \quad (1.29)$$

The difference between the rotation vectors causes the incompatibilities across GB, such that the strength factor is defined as the projection of this rotation vector's difference on surface trace of GB:

$$R^{pq} = \Delta \mathbf{r}^{pq} \cdot \mathbf{e}_t = [(\mathbf{n}_A^p \times \mathbf{b}_A^p) - (\mathbf{n}_B^q \times \mathbf{b}_B^q)] \cdot \mathbf{e}_t \quad (1.30)$$

### 1.3.5.3 Stage-I-fatigue cracks and continuous dislocation density distribution method

In the work of Schäfer et al. [125], stage-I-fatigue cracks method was used to investigate the interactions between dislocations and GB in Nickel-based superalloy as shown in Figure 1.35. A stress intensity factor of the dislocation pile-up, used to characterize the critical breakthrough stress for slip across GB, was calculated based on a continuous dislocation distribution model:

$$K_m = \pi A \sqrt{2\pi} \lim_{x \rightarrow c} (\sqrt{c-x} D(x)) \quad (1.31)$$

where  $A = Gb/(2\pi)$  for screw dislocations and  $A = Gb/(2\pi(1-\nu))$  for edge dislocations,  $G$  the shear modulus,  $\nu$  the Poisson ratio,  $D(x)$  is the continuous dislocation density distribution that stands for the symmetric crack of length  $2a$  and a linear plastic zone of length  $c-a$  in front of each crack tip as shown in Figure 1.36. The value of  $K_m$  depends on the continuous dislocation density distribution, which can be estimated by dislocation-free zone model of fracture (DFZ-model), see Figure 1.36.

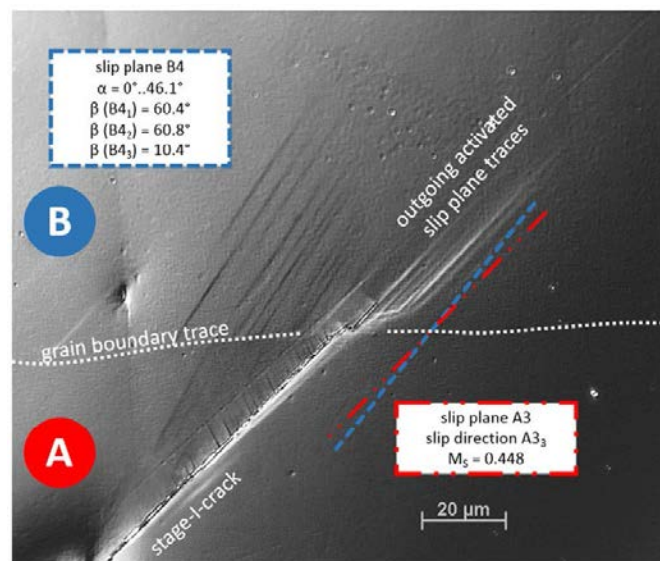


Figure 1.35: Slip and crack transfer through a GB produced by stage-I-fatigue cracks method [125].

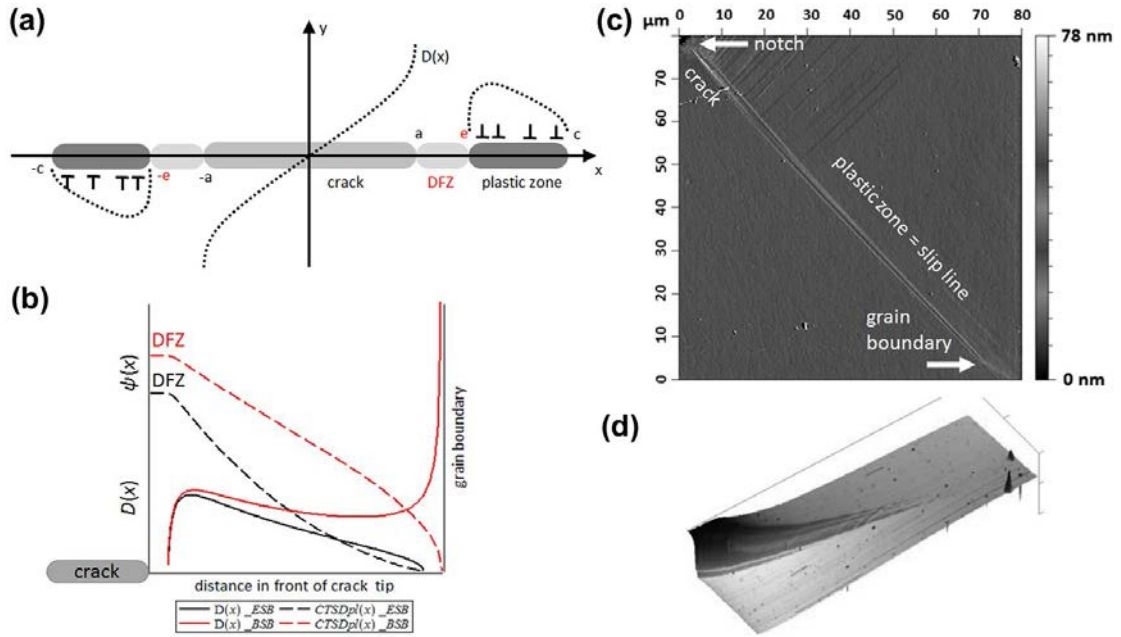


Figure 1.36: (a) DFZ-model configuration with a symmetric crack, a DFZ and a plastic zone with edge dislocations distribution  $D(x)$ , (b) examples of plastic displacement in the plastic zone  $\psi(x)$  and corresponding continuous dislocation density distribution  $D(x)$  for blocked slip band (BSB, red) and equilibrium slip band (ESB, black), (c) 2D AFM topography image of a BSB case and (d) 3D AFM topography image of a plastic zone for an ESB case, the left plateau area indicates the DFZ zone [125].

In comparison with geometrical transmission factors discussed in section 1.3.4, they found that the transmission factors in Eqs. 1.24 and 1.25 are not suitable to predict slip resistance. Meanwhile, the GB strength factor in Eq. 1.30 is not enough to predict the GB strength because of the lack of GB inclination's information. However, they found an evident correlation between stress intensity factor and the transmission factor in Eq. 1.26. Hence, the knowledge of orientations of grains and boundary plane is necessary to predict the GB resistance effect from geometrical parameters only.

## 1.4 Experimental methods

### 1.4.1 SEM and EBSD

The Scanning Electron Microscopy (SEM) technique involves scanning the surface of the sample with electrons. Interactions between electrons and matter generate different signals: secondary electrons that are used to form topographic contrast, backscattered electrons for crystallographic contrast, and energy dispersive



X-rays (EDX) for chemical microanalysis.

The Electron Back Scattered Diffraction technique (EBSD) allows the determination of the local crystallographic orientations within the SEM. This method then makes it possible to deduce the mean orientation over a given area, the misorientations between two points, the grain size and shape (in 2D), the presence of specific GBs (like twin boundaries), most components of the dislocation density tensor [7] as well as to have a rough estimate of the plastic deformation within the grain [137]. It relies mainly on the indexing of diffraction patterns of backscattered electrons or Kikuchi photos. The principle of measurement consists in focusing an electron beam on the studied grain. The backscattered electrons in Bragg incidence with the surrounding reflective crystalline planes diffract along two diffraction cones. The intersection of these cones with a detection screen, forms hyperbolas assimilable to straight lines at the observation scale. The set of lines resulting from the electron diffraction on the different planes of the lattice constitutes the Kikuchi diagram (see Figure 1.37). A rational indexing of the different lines makes it possible to determine the crystalline structure and the crystallographic orientation of the grain. Furthermore, a high angular resolution electron back scattered diffraction (HR-EBSD) can improve the angular precision of measurement, thus it can be used to measure the elastic deformation and so to estimate the local stress by Hooke's law [138].

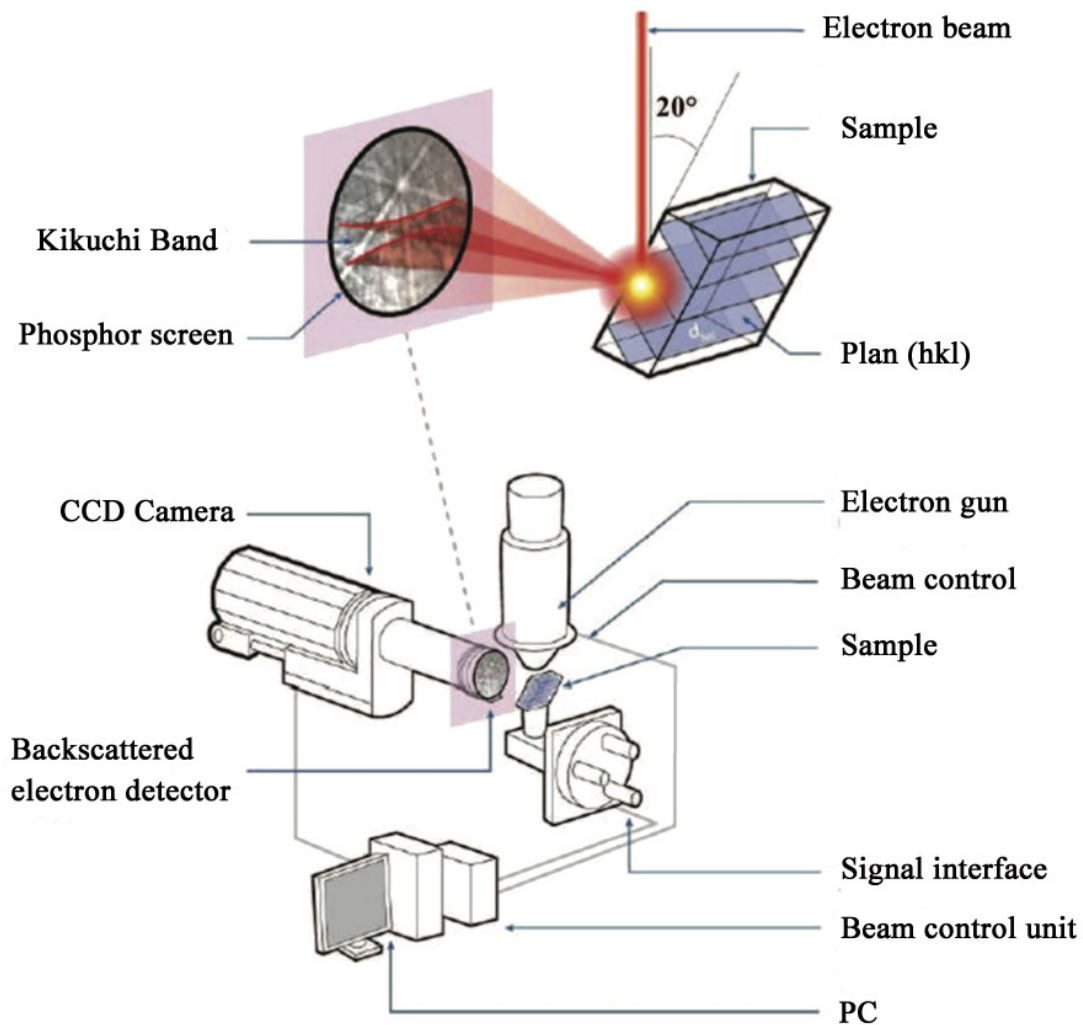


Figure 1.37: Principle of EBSD in the SEM: schematic representation of sample position for orientation measurements and principle of Kikuchi lines formation [137].

### 1.4.2 Ion Milling

In order to observe and analyze the internal structure of the sample, the internal structure of the sample must be revealed. However, by cutting or mechanically grinding the cross section, deformations and damages are unavoidable due to machining stresses. Thus, it is difficult to obtain a smooth surface required for SEM analysis. The ion milling device uses a large area and low energy Ar ion beam to process a cross section without stress damage, and provides an effective pretreatment method for the SEM observation. As an example, the IM4000 Ion Milling System (see Figure 1.38) is presented below which has been used in the present

thesis.



Figure 1.38: Ion Milling System IM4000 from Hitachi High-Technologies.

There are two different models in IM4000 system: cross section milling and flat surface milling. In the cross section milling, a mask is placed between the sample and the ion gun as shown in Figure 1.39 (a). The upper end of the sample slightly protrudes from the shielding plate, and the ion beam is irradiated onto the sample from above the shielding plate, so a flat cross section is processed along the edge of the shielding plate. The principle of flat surface milling is presented in Figure 1.39 (b). It uses a certain amount of eccentricity between the central axis of the ion beam and the central rotation axis of the sample stage in order to obtain a uniform and large-scale processing surface. When the ion beam irradiation angle is small, the processing rate of the ion beam is highly correlated with the crystal orientation and composition of the sample, so the difference in the processing rate can be used to process a plane shaped like a relief. However, when the ion beam irradiation angle is large, the processing rate of the ion beam is not related to the crystal orientation and composition of the sample, and a flat sample surface can be processed.

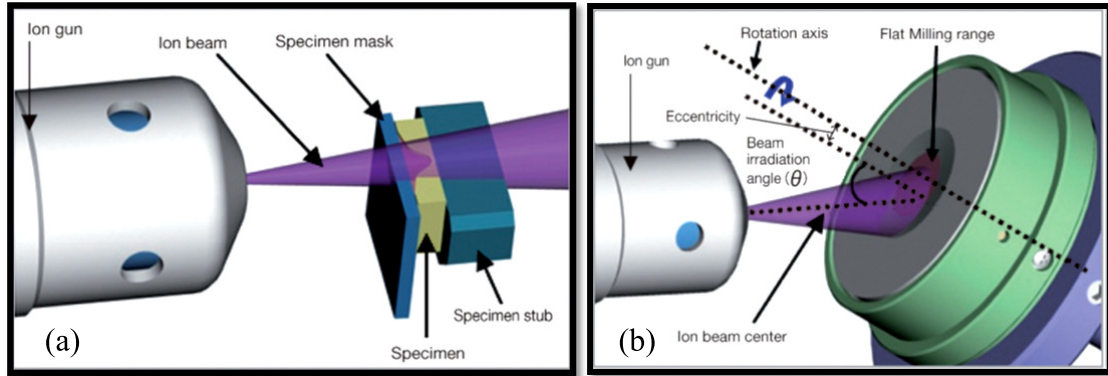


Figure 1.39: Principle of (a) cross section milling and (b) flat surface milling.

In the present thesis, the cross section milling is used to remove large amounts of material in order to bring the GBs close to the sample side surface. That is helpful for producing the micro-beam by FIB which will be discussed in subsection 2.3.4.

### 1.4.3 Focused Ion Beam technique

The Focused Ion Beam (FIB) is a technical instrument that was commercially produced in the 1980s. It was initially developed for the needs of the microelectronics industry (such as semiconductors) and later for basic research. This type of equipment operates in a similar way as the SEM (see section 1.4.1). Instead of electrons, it uses focused ions of Gallium ( $\text{Ga}^+$ ). Unlike the SEM, the FIB is equipped with two guns forming an angle of  $52^\circ$  between them as shown in Figure 1.40: a column of electrons and an ion column (it is thus a device of type “Dual Beam”). The electron source is used to make images according to the same principle as the SEM. The  $\text{Ga}^+$  ion beam makes it possible, on the one hand, to cut the sample and, on the other hand, to scan the surface of the sample in order to obtain an image. This image is either electronic or ionic (thanks to the ions and secondary electrons emitted) to follow the removal procedure (see Figure 1.40). This ion beam will allow us in this thesis to cut bi-crystalline micro-beam at the selected GB as shown in Figure 1.40.

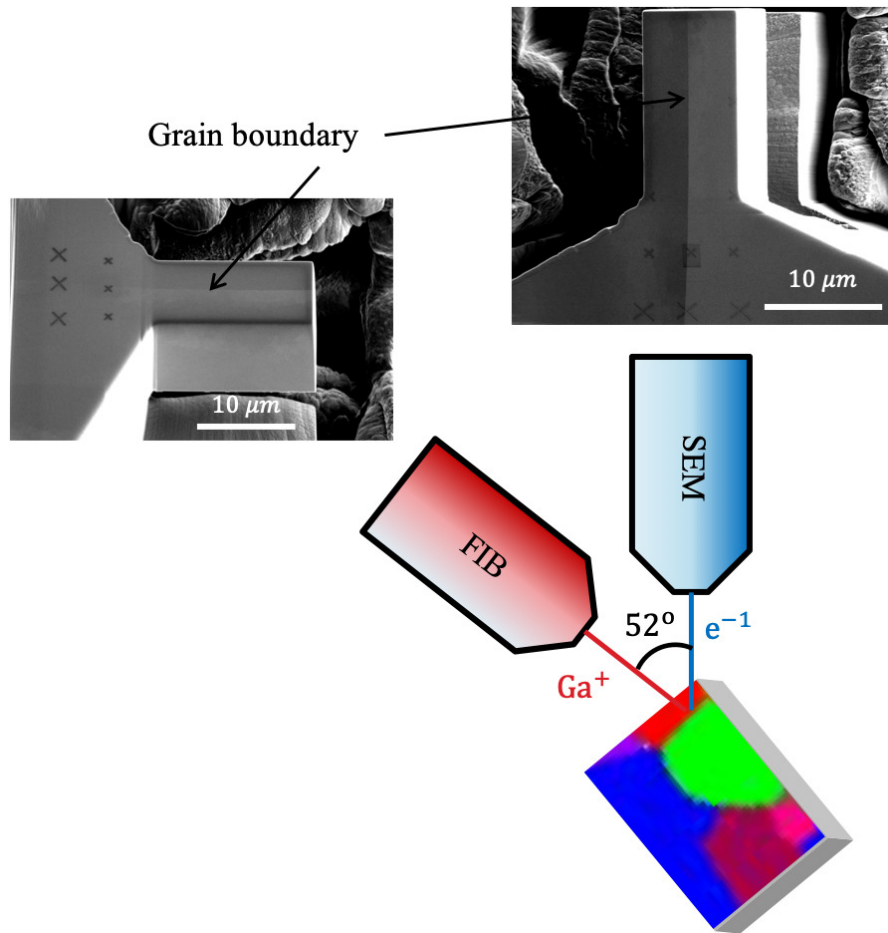


Figure 1.40: Principle of FIB operation. The micro-beam containing a GB produced by FIB is also presented.

The FIB preparation technique has an effect on the micro-pillars due to the dispersion of  $\text{Ga}^+$  ions on the surface of the micro-beam. The emission of  $\text{Ga}^+$  ions on the surface of a sample causes the formation of a layer on it which can modify its structure, and therefore, its surface mechanical properties. The thickness of this layer is in the order of a few tens of nanometers which depends essentially on the material, the intensity and the angle of incidence of the ions. Kheradmand et al. [139] estimated the thickness of the layer damaged by  $\text{Ga}^+$  ions by high resolution EBSD measurements on Ni micro-pillars. They produced the micro-pillars by different techniques: lithography, FIB, a combination of these last two techniques and the heavy bombardment with ions. These four methods have a damage level of 6 nm, 11 nm, 15 nm and 107 nm, respectively. Some authors mentioned that using the low-intensity in finishing step for the first two methods (lithography and FIB) hardly changes the result. This last observation was also

confirmed by nanoindentation tests. Indeed, this layer deposited by the FIB may be a new barrier for the mobility of dislocations which can then stack at the interface between the two different materials [137]. Furthermore, the  $\text{Ga}^+$  ions can create scratches within nanometers on the surface of micro-beam even with small ions density, as observed by SEM with high magnification and AFM measurement (it will be shown in section 2.3.4).

#### 1.4.4 Atomic Force Microscopy

Atomic Force Microscopy (AFM) is an atomic-level high-resolution analytical instrument invented by G. Binnig in 1986 based on Scanning Tunneling Microscope (STM). It can perform nano-scale studies of physical properties including topographies in various materials. Compared with STM, AFM has a wider applicability because it can observe non-conductive samples. It has been widely used in the fields of semiconductor, nano-functional materials, biological, chemical, medical research and research institutes in various nano-related disciplines, and has become a basic tool for nanoscience research. Especially, slip lines or slip bands heights can be observed and analyzed by this technique [33, 34, 8, 35, 36]. Furthermore, based on the analyses of slip bands, the dislocation distribution of a pile-up against GB can be reformed considering a continuous distribution [125] or a discrete one in anisotropic elasticity as it will be discussed in the present PhD thesis.

The principle of AFM is described below. The one end of a weakly sensitive cantilever is fixed, with another side as a microprobe which is in light contact with the sample surface. Due to the distance-dependent weak repulsion between the atoms on the probe tip and those on the sample surface, by keeping this force constant (which corresponds to a constant distance) during scanning, the probe's undulating motion perpendicular to the sample surface reflects the height of sample surface. The topographic information of sample surface is thus obtained based on this surface height profile. The tip motion corresponding to each scanning point can be measured by optical detection as shown in Figure 1.41.

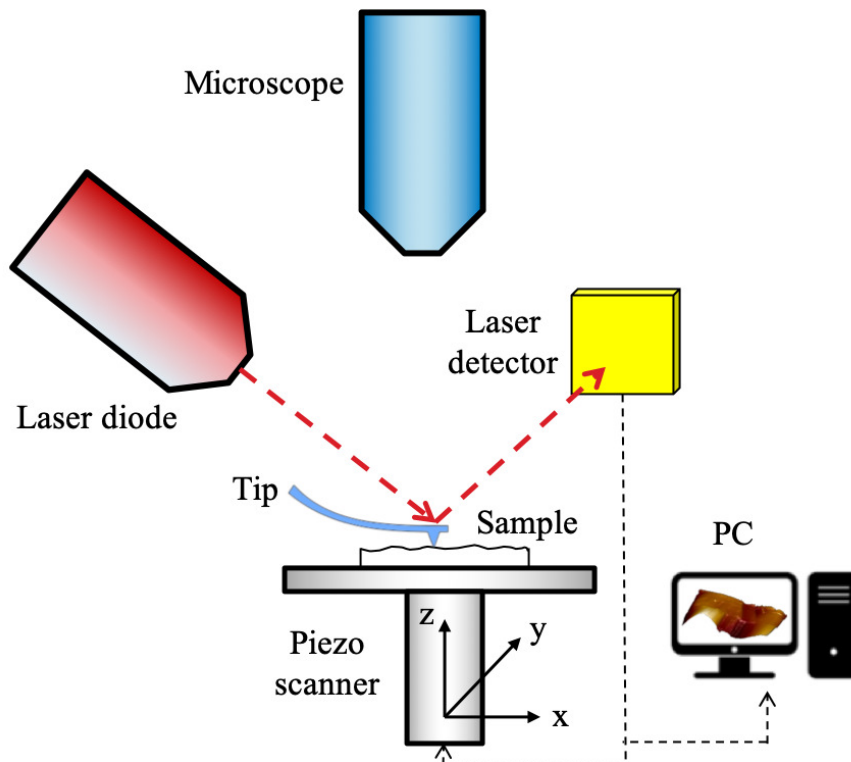


Figure 1.41: Schematic principle of AFM.

There are three types of contact models.

- The contact AFM mode uses the interaction of atomic force between the probe and the surface of analyzed object where they must be in contact. This atomic repulsive force is small, but an excessive force can still damage the sample due to the small contact area, especially for soft materials. However, a larger force gives a better resolution, so choosing a more appropriate force is very important. Since the repulsive force is very sensitive to distance, it is easier to obtain atomic resolution.
- The non-contact AFM mode was developed to solve the shortcomings of the contact AFM mode which may damage the sample. This was done by using the long-distance attraction between atoms. Since the probe and the sample are not in contact, the sample is not damaged. However, this force has a very small change in distance, so modulation techniques must be used to increase the signal-to-noise ratio.
- The frequently beating AFM mode modifies the non-contact AFM mode to make the probe and sample surface closer and increases the amplitude of tip

vibration, so that the probe will contact the sample when it oscillates to the valley. Since the surface of the sample is undulating, the amplitude of the probe is changed, then the contact feedback control method is used to obtain an image of height information. The resolution of this method is between the ones of contact and non-contact mode, and the probability of destroying the sample is greatly reduced. Furthermore, the result is not interfered by lateral forces. However, for very hard samples, the tip may still be damaged.

### 1.4.5 Micro-beam size effects

The size effects of micro-pillars have been thoroughly studied in the recent years as discussed in subsection 1.3.1. The hardening effects were found to be associated with the decrease of the diameter of the micro-pillar as shown in Figure 1.42 for Ni [140, 141], Au [74], Al [142] and Cu [143]. These methods allowed to show that the flow stress increases as the diameter of the micro-pillars decreases. The size effect is strongly related to the distribution of the dislocation density in the sample. The relationship between dislocation density and the size of micro-pillar was analyzed and resumed by D. Kiener [144] as shown in Figure 1.42. It was found that with a normal dislocation density  $10^{12}\text{m}^{-2}$ , the number of dislocations is less than 100 for a micro-pillar with a diameter within  $10\ \mu\text{m}$ . If the deformed volume is large, many sources of dislocations are present and the deformation is uniformly distributed. However, if the deformed volume is small, only a few dislocations are available and the deformation is concentrated on some slip planes. In that case, if there is an interface that causes stacking of dislocations like GBs, the induced internal stresses can then disable other sources of dislocations. Therefore, the Schmid law might be broken in some small size pillars, i.e. the first activated slip system is not the one with maximum Schmid factor [145]. Thus, the micro-pillar flow stress is highly dependent on GB and on the diameter of the micro-pillar.



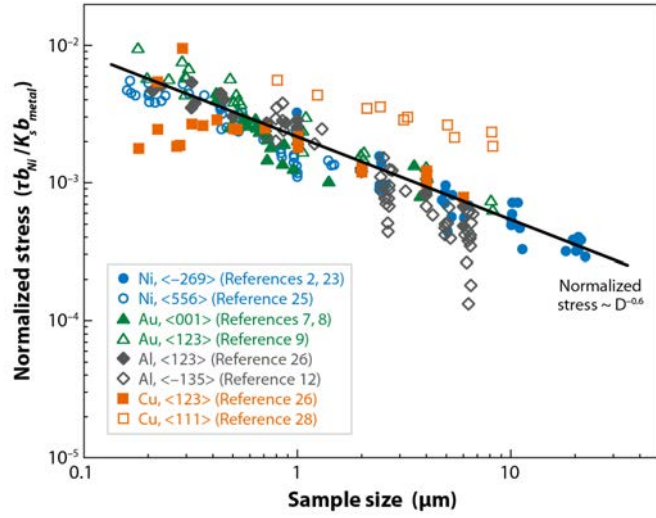


Figure 1.42: Evolution of the flow stress, normalized by the anisotropic shear modulus  $K_s$ , defined in [144] and the Burgers vector  $|\mathbf{b}|$  for corresponding metal, as a function of the diameter of the micro-pillars  $D$  for different FCC metals. The scaling law shows that the best fitting of the data is with  $D^{-0.6}$  [144].

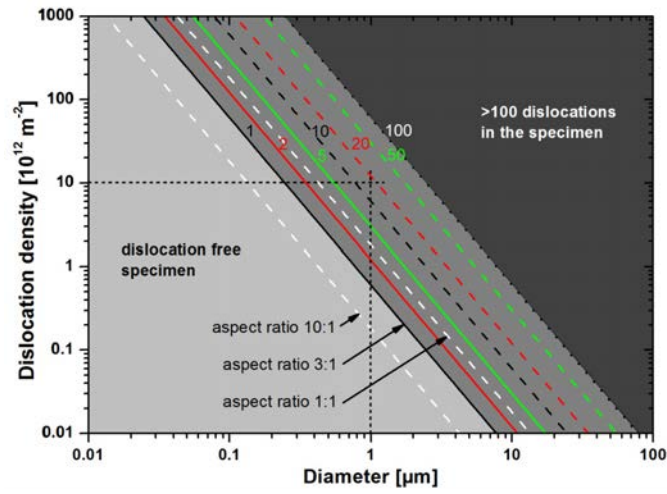


Figure 1.43: Average number of straight dislocations in a miniaturized cylindrical specimen for an aspect ratio between height and diameter of 3:1 [146].

## 1.5 Theoretical and numerical multi-scale modelling methods

### 1.5.1 Continuum dislocation mechanics

The dislocation density tensor  $\boldsymbol{\alpha}$  was initially introduced by Nye [147]. Operating on a unit area  $S$  of normal vector  $\mathbf{n}$  and delimited by the circuit  $C$ ,  $\boldsymbol{\alpha}$  provides the net Burgers vector  $\mathbf{b}$  of all the dislocation lines piercing through  $S$  (see Figure 1.44), i.e., the closing fault of the circuit  $C$  due to the presence of dislocations. If the size of  $C$ , i.e., the resolution scale, is small and only one dislocation passes through  $S$ , the closing fault is simply the Burgers vector of the dislocation [137]. If  $C$  is large enough and  $S$  is crossed by a large number of dislocations, the latter can either compensate statistically in which case the net Burgers vector is zero (they do not create any lattice incompatibility at the considered resolution scale) and are called statistically stored dislocations (SSD), or can collectively create a lattice incompatibility linked to a non-zero Burgers vector and are called geometrically necessary dislocations (GND) [148]. In conventional crystalline plasticity, only SSD are considered [149, 150].

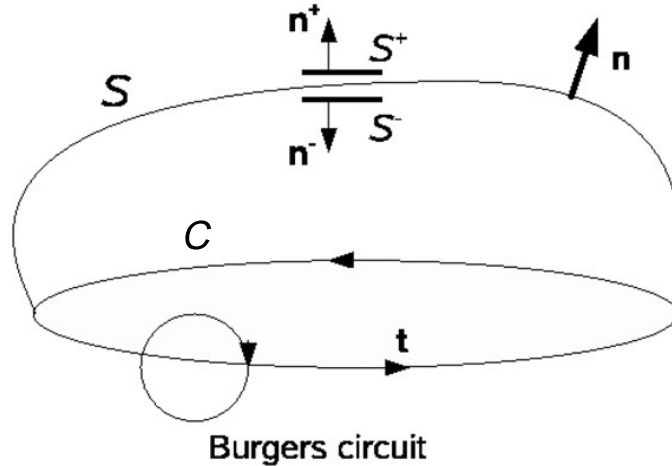


Figure 1.44: Dislocation loop  $C$  formed after piercing through a unit area  $S$  of normal vector  $\mathbf{n}$  [151].

The elastic theory of continuously distributed dislocations (ECDD) was initially developed by Kröner [152, 153], Indenbom [154] and Willis [155]. This theory was then rethought by Acharya [156] to become the so-called field dislocation mechanics (FDM). Acharya [157] decomposed in a unique way the elastic distortion into compatible and incompatible parts and added the evolution equation of GND. The FDM theory [156, 158] can operate on an intermediate scale of resolution,

where the net  $\mathbf{b}$  Burgers vector (hence  $\boldsymbol{\alpha}$  which reflects the density of GND) is non-zero, while some of the involved dislocations statistically contribute to a defect with null closure defect.

Within the formalism of small deformations (linear theory), the static version of the FDM theory includes the following field equations [156, 159, 158, 160]:

$$\text{grad } \mathbf{u} = \boldsymbol{\beta} = \boldsymbol{\beta}^e + \boldsymbol{\beta}^p \quad (1.32)$$

$$\boldsymbol{\beta}^e = \boldsymbol{\beta}_{\parallel}^e + \boldsymbol{\beta}_{\perp}^e; \quad \boldsymbol{\beta}^p = \boldsymbol{\beta}_{\parallel}^p + \boldsymbol{\beta}_{\perp}^p \quad (1.33)$$

$$\text{curl } \boldsymbol{\beta}_{\parallel}^e = \text{curl } \boldsymbol{\beta}_{\parallel}^p = \mathbf{0} \quad (1.34)$$

$$\boldsymbol{\alpha} = \text{curl } \boldsymbol{\beta}_{\perp}^e = -\text{curl } \boldsymbol{\beta}_{\perp}^p \quad (1.35)$$

$$\text{div } \boldsymbol{\beta}_{\perp}^e = \mathbf{0} \text{ in } V \text{ and } \boldsymbol{\beta}_{\perp}^e \cdot \mathbf{n} = \mathbf{0} \text{ on } \partial V \quad (1.36)$$

$$\boldsymbol{\sigma} = \mathbf{C} : (\boldsymbol{\beta}_{\parallel}^e + \boldsymbol{\beta}_{\perp}^e) \quad (1.37)$$

$$\text{div } \boldsymbol{\sigma} = \mathbf{0} \text{ in } V \quad (1.38)$$

where  $\mathbf{u}$  is the displacement field and  $\boldsymbol{\beta}$  is the total distortion field (i.e. the gradient of displacement). In the formalism of small deformations, this last tensor decomposes into an elastic part and a plastic part (Eq. 1.32). Because of the lattice incompatibility, the elastic and plastic distortion tensors are not gradients and therefore their curl is non-zero. Involving the Stokes-Helmholtz decomposition, they have a compatible part  $(\boldsymbol{\beta}_{\parallel}^e, \boldsymbol{\beta}_{\parallel}^p)$  and an incompatible part  $(\boldsymbol{\beta}_{\perp}^e, \boldsymbol{\beta}_{\perp}^p)$  (Eq. 1.33). While the compatible part is a gradient (Eq. 1.34), the incompatible part results from the distributions of GND and  $\boldsymbol{\alpha}$  is thus the solution of the incompatibility equation (Eq. 1.35). Eq. 1.36 makes it possible to ensure the uniqueness of the Stokes-Helmholtz decomposition which means that the  $\boldsymbol{\beta}_{\perp}^e$  tensor is a curl part. As a consequence of this decomposition, the incompatible elastic distortion must exactly compensate for the incompatible plastic distortion in order to ensure the continuity of the material given by  $\text{curl } \boldsymbol{\beta} = \mathbf{0}$ :

$$\boldsymbol{\beta}_{\perp}^e + \boldsymbol{\beta}_{\perp}^p = \mathbf{0} \leftrightarrow \boldsymbol{\beta} = \boldsymbol{\beta}_{\parallel}^e + \boldsymbol{\beta}_{\parallel}^p \quad (1.39)$$

The Cauchy stress tensor  $\boldsymbol{\sigma}$  is obtained from the Hooke's law (Eq. 1.37), with  $\mathbf{C}$  the elastic stiffness tensor. It satisfies the static equilibrium condition without volume force (Eq. 1.38). Hence, given a distribution of  $\boldsymbol{\alpha}$ , this set of equations allows

to solve for the associated stress fields in any kind of heterogeneous anisotropic medium. The numerical resolution can be performed by Finite Element Methods or by spectral methods such as Fast Fourier Transform (FFT).

### **1.5.2 3D incompatibility stresses in bi-crystals**

GBs can be obstacles for plastic slip or sources of dislocations, but also sources of additional stresses (internal stresses) related to elastic and plastic deformation incompatibilities between neighboring grains. As for image stresses, the presence of incompatibility stresses is necessary to ensure the continuity conditions at GBs. The presence of GBs in elastically or plastically deformed material can change the plasticity activation phenomena around the GBs.

#### **1.5.2.1 Experimental observations**

The notion of incompatibility in the bi-crystal was introduced by Hook and Hirth [161, 162, 163]. In addition, studies were conducted on Cu [164], Al [165, 166, 126] and Ag [167] bi-crystals to illustrate the effects of incompatibility stresses on intra-granular plastic activity. They proved that incompatibility stresses cause the activation of secondary slip systems around GB which favor the hardening of bi-crystal (see Figure 1.45). Figure 1.45 (a) shows the presence of a domain in a bi-crystal which illustrates the appearance of secondary slip [164]. The presence of secondary slip becomes more and more marked when the macroscopic deformation is increased. This phenomenon characterizes the effects of plastic incompatibilities. These mechanisms were also observed in the case of body centered cubic bi-crystals (BCC) by Hook and Hirth [161] as shown in Figure 1.45 (b).

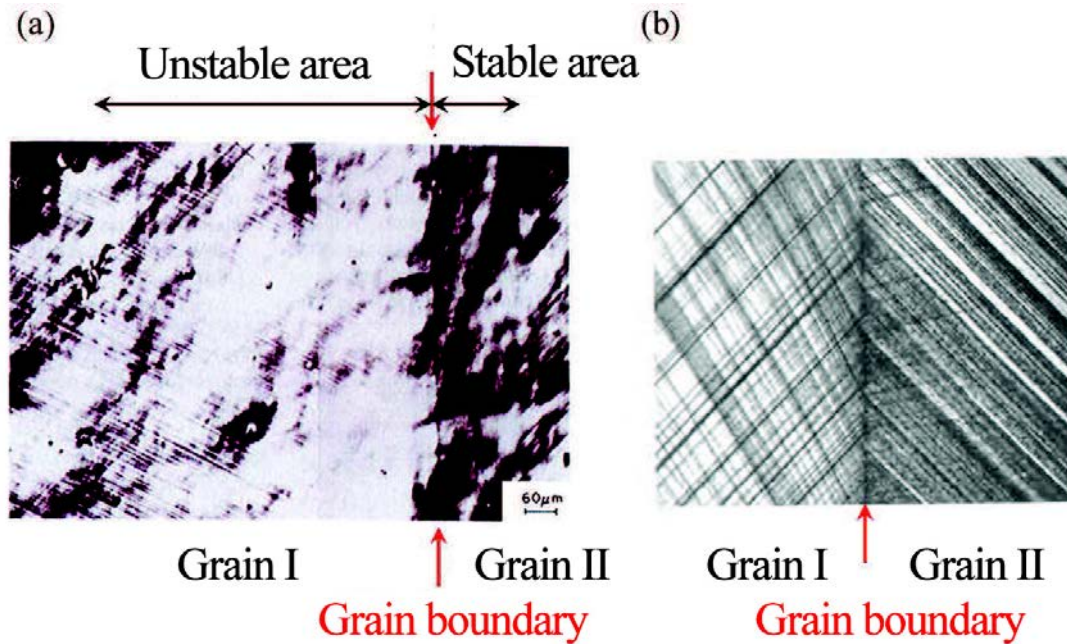


Figure 1.45: (a) Observation of multislip in an unstable area in grain I of a Cu bi-crystal after 2% deformation [164]. (b) The appearance of secondary slip system around GB in Fe-3%Si bi-crystal [161].

Based on the experimental observations cited above, several theoretical studies were conducted to determine the stresses due to elastic and plastic incompatibilities. These calculations were carried out in particular cases considering elastic anisotropy alone in a 1D model [161, 162], heterogeneous plastic deformation alone [165, 164, 168, 169, 170] and finally heterogeneous elasticity and plasticity [171, 160]. These models are successively described thereafter.

### 1.5.2.2 Elastic incompatibilities

To analyze the effect of elastic anisotropy, Hook and Hirth [161, 162] considered the particular case of a bi-crystal schematized in Figure 1.46. The reference  $(x_1, x_2, x_3)$  is defined such that the  $x_2$ -axis is perpendicular to the GB. It is a purely uniaxial approach where only the Young modulus describes the elastic properties of the material (no Poisson effect is considered).

The model is defined such that both crystals have a different Young modulus. The normal stresses along the  $x_3$ -direction in each component of the bi-crystal are computed by [162]:

$$\sigma_{33}^I = \frac{A^T}{A^I + rA^{II}} \Sigma_{33}, \quad \sigma_{33}^{II} = \frac{A^T}{A^{II} + \frac{A^I}{r}} \Sigma_{33}, \quad (1.40)$$

with  $A^I$  and  $A^{II}$  the cross-sectional areas of crystal I and II, respectively, that are perpendicular to  $x_3$  and  $A^T$  denotes the total cross-sectional area of the bi-crystal.  $r$  is the ratio of the directional elastic modulus  $E^I$  and  $E^{II}$  in the loading direction such that  $r = \frac{E^{II}}{E^I}$ . For a given single cubic crystal  $c$  ( $c = I, II$ ), the directional elastic modulus  $E^c$ , can be written according to the elastic compliance  $S_{ij}^c$  and the Miller indices  $(hkl)^c$  [172]:

$$\frac{1}{E^c} = S_{11}^c + \frac{(S_{44}^c - 2(S_{11}^c - S_{12}^c))(k^2l^2 + h^2l^2 + h^2k^2)^c}{((h^2 + k^2 + l^2)^2)^c} \quad (1.41)$$

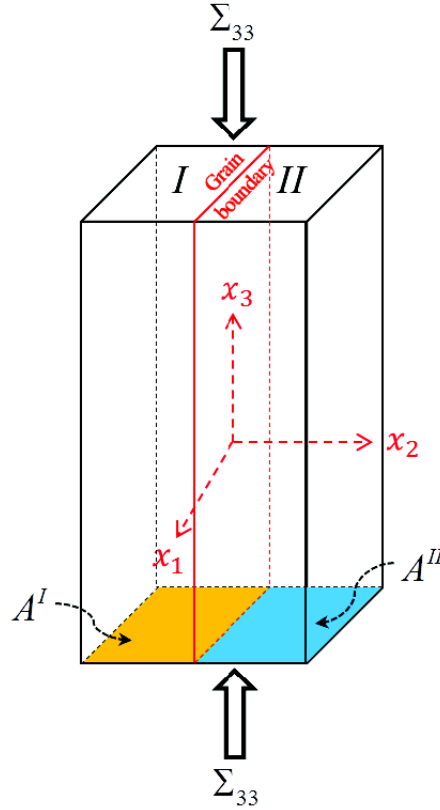


Figure 1.46: Bi-crystal geometry defined by Livingston and Chalmers [126] and Hauser and Chalmers [167] and used by Hook and Hirth [161, 162].

### 1.5.2.3 Plastic incompatibilities

Unlike the model of Hook and Hirth [161, 162], the model first developed in [168, 169, 165], takes into account plastic incompatibilities at GB between two semi-infinite crystals of same volume fraction, under the assumption of isotropic elasticity. This model can be derived by using the continuous dislocation theory and the Kröner stress potential [173].

The elasticity is assumed to be homogeneous and isotropic. The plastic strain tensors in the crystal I,  $\boldsymbol{\varepsilon}^{p^I}$ , and in the crystal II,  $\boldsymbol{\varepsilon}^{p^{II}}$ , are assumed to be uniform on both sides of the GB. Therefore, the stress tensor varies along the  $x_2$ -axis as [168, 169, 165]:

$$\begin{aligned}\sigma_{11} &= \Sigma_{11} + \frac{G}{1-\nu} ([\varepsilon_{11}^p] + \nu [\varepsilon_{33}^p]) \operatorname{sgn}(x_2), \\ \sigma_{33} &= \Sigma_{33} + \frac{G}{1-\nu} ([\varepsilon_{33}^p] + \nu [\varepsilon_{11}^p]) \operatorname{sgn}(x_2), \\ \sigma_{13} &= \Sigma_{13} + G [\varepsilon_{13}^p] \operatorname{sgn}(x_2), \\ \sigma_{12} &= \Sigma_{12}, \\ \sigma_{22} &= \Sigma_{22}, \\ \sigma_{23} &= \Sigma_{23}.\end{aligned}\tag{1.42}$$

with  $\Sigma_{ij}$  is the applied (external) stress tensor and

$$[\varepsilon_{ij}^p] = \varepsilon_{ij}^{p^{II}} - \varepsilon_{ij}^{p^I}\tag{1.43}$$

which defines the jump of the plastic strain at GB.  $\operatorname{sgn}(x_2)$  denotes the sign of  $x_2$  ( $\operatorname{sgn}(x_2) = 1$  if  $x_2 > 0$  (in crystal II) and  $\operatorname{sgn}(x_2) = -1$  if  $x_2 < 0$  (in crystal I)). It should be noted that in this problem, the stress field is uniform in each grain but it is discontinuous at GB. The predictions of this model are in agreement with experimental studies on Al [165] and Cu [164] bi-crystals to predict secondary slip systems that may be activated around GB. However, the approach described in [168, 169, 165] does not take into account the elastic anisotropy of the material. These formulas are therefore acceptable for Al which has a coefficient of elastic anisotropy  $A$  close to the unity ( $A = \frac{2C_{44}}{C_{11} - C_{12}}$ ) but not necessary for Ni or Cu where the coefficient of anisotropy  $A$  is much greater than 1 (typically  $A = 2.37$  for Ni and  $A = 3.26$  for Cu).

### 1.5.2.4 Elastic and plastic incompatibilities

Gemperlova et al. [171] were the first to consider both elastic and plastic incompatibilities in a bi-crystal with planar GB and same volume fraction of its

component crystals. Then, Richeton and Berbenni [160] used the static FDM theory to derive explicit analytical solutions of stress and elastic rotation fields for a bi-crystal with random volume fraction of its component crystals. In both models, uniform elastic properties and plastic distortions are assumed in each crystal. As this last method gives analytical expressions, the contribution of different incompatibility sources could be quantified as elastic incompatibilities alone, plastic incompatibilities alone and coupling of elastic and plastic incompatibilities. These analytical expressions were validated by crystal plasticity finite element method (CPFEM) on a bi-crystal with periodic boundary conditions [160]. This method is not only suitable for heterogeneous elastic anisotropy, but can be also used for heterogeneous elastic isotropy in the presence of plastic deformation.

The static configuration of this problem is shown in Figure 1.47. The infinite GB plane is in the  $(O, x_1, x_3)$  plane. Crystal I and crystal II are separated by this discontinuity GB with a normal vector  $\mathbf{n}$  pointing to crystal II from crystal I along the  $(O, x_2)$  direction. The bi-crystal is subjected to a macroscopic homogeneous stress  $\Sigma_{ij}$  with a volume fraction  $f$  of crystal I and thus  $1 - f$  for crystal II.

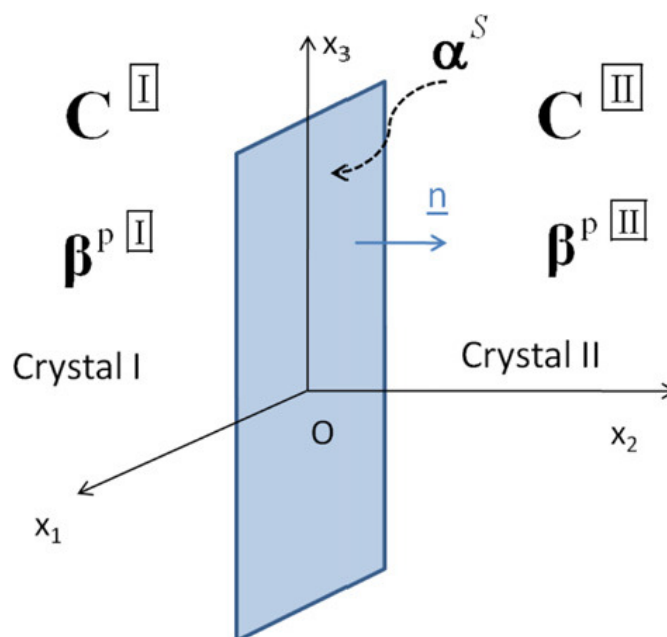


Figure 1.47: Bi-crystal configuration with an infinite planar GB which is characterized by an interface dislocation density tensor  $\alpha^s$  [160].

Following [160], and using the Voigt notation [1] ( $11 \rightarrow 1, 22 \rightarrow 2, 33 \rightarrow 3, 23 \rightarrow 4, 13 \rightarrow 5, 12 \rightarrow 6$ ), the expressions of the stress fields in each crystal are:



$$\begin{aligned}
\sigma_1^I &= \Sigma_1 - (1-f)(G_{11}[\varepsilon_1^*] + G_{13}[\varepsilon_3^*] + G_{15}[\varepsilon_5^*]), \\
\sigma_3^I &= \Sigma_3 - (1-f)(G_{13}[\varepsilon_1^*] + G_{33}[\varepsilon_3^*] + G_{35}[\varepsilon_5^*]), \\
\sigma_5^I &= \Sigma_5 - (1-f)(G_{15}[\varepsilon_1^*] + G_{35}[\varepsilon_3^*] + G_{55}[\varepsilon_5^*]), \\
\sigma_2^I &= \Sigma_2, \quad \sigma_4^I = \Sigma_4, \quad \sigma_6^I = \Sigma_6
\end{aligned} \tag{1.44}$$

$$\begin{aligned}
\sigma_1^II &= \Sigma_1 + f(G_{11}[\varepsilon_1^*] + G_{13}[\varepsilon_3^*] + G_{15}[\varepsilon_5^*]), \\
\sigma_3^II &= \Sigma_3 + f(G_{13}[\varepsilon_1^*] + G_{33}[\varepsilon_3^*] + G_{35}[\varepsilon_5^*]), \\
\sigma_5^II &= \Sigma_5 + f(G_{15}[\varepsilon_1^*] + G_{35}[\varepsilon_3^*] + G_{55}[\varepsilon_5^*]), \\
\sigma_2^II &= \Sigma_2, \quad \sigma_4^II = \Sigma_4, \quad \sigma_6^II = \Sigma_6
\end{aligned} \tag{1.45}$$

where  $[\varepsilon_i^*] = [s_{ij}] \Sigma_j + [\varepsilon_i^p]$ ,  $s_{ij}$  are the elastic compliances and the non-zero components of the symmetric matrix  $G_{ij}$  in Eqs. 1.44 and 1.45 are given by:

$$\begin{aligned}
G_{11} &= (\tilde{s}_{33}\tilde{s}_{55} - \tilde{s}_{35}^2) / D, \quad G_{13} = (\tilde{s}_{15}\tilde{s}_{35} - \tilde{s}_{13}\tilde{s}_{55}) / D \\
G_{33} &= (\tilde{s}_{11}\tilde{s}_{55} - \tilde{s}_{15}^2) / D, \quad G_{15} = (\tilde{s}_{13}\tilde{s}_{35} - \tilde{s}_{15}\tilde{s}_{33}) / D \\
G_{55} &= (\tilde{s}_{11}\tilde{s}_{33} - \tilde{s}_{13}^2) / D, \quad G_{35} = (\tilde{s}_{13}\tilde{s}_{15} - \tilde{s}_{35}\tilde{s}_{11}) / D
\end{aligned} \tag{1.46}$$

with  $\tilde{s}_{ij} = (1-f)s_{ij}^I + fs_{ij}^II$  and  $D = \tilde{s}_{11}\tilde{s}_{35}^2 + \tilde{s}_{33}\tilde{s}_{15}^2 + \tilde{s}_{55}\tilde{s}_{13}^2 - \tilde{s}_{11}\tilde{s}_{33}\tilde{s}_{55} - 2\tilde{s}_{13}\tilde{s}_{15}\tilde{s}_{35}$ . The above explicit solutions include coupling effects of elastic and plastic incompatibilities at GB. It is then possible to consider only the case of elastic incompatibilities by taking  $[\varepsilon^p] = \mathbf{0}$  or to consider only the case of plastic incompatibilities by taking  $[\mathbf{s}] = \mathbf{0}$ .

In the case of uniform isotropic elasticity, the stress fields in each crystal are derived as follows in agreement with Eq. 1.42:

$$\begin{aligned}
\sigma_1^I &= \Sigma_1 + \frac{2\mu}{1-\nu}(1-f)([\varepsilon_1^p] + \nu[\varepsilon_3^p]), \\
\sigma_3^I &= \Sigma_3 + \frac{2\mu}{1-\nu}(1-f)([\varepsilon_3^p] + \nu[\varepsilon_1^p]), \\
\sigma_5^I &= \Sigma_5 + \mu(1-f)[\varepsilon_5^p], \\
\sigma_2^I &= \Sigma_2, \quad \sigma_4^I = \Sigma_4, \quad \sigma_6^I = \Sigma_6
\end{aligned} \tag{1.47}$$

$$\begin{aligned}
\sigma_1^II &= \Sigma_1 - \frac{2\mu}{1-\nu}f([\varepsilon_1^p] + \nu[\varepsilon_3^p]), \\
\sigma_3^II &= \Sigma_3 - \frac{2\mu}{1-\nu}f([\varepsilon_3^p] + \nu[\varepsilon_1^p]), \\
\sigma_5^II &= \Sigma_5 - \mu f[\varepsilon_5^p], \\
\sigma_2^II &= \Sigma_2, \quad \sigma_4^II = \Sigma_4, \quad \sigma_6^II = \Sigma_6
\end{aligned} \tag{1.48}$$

### 1.5.3 Two dimensional L-E-S (Leknitskii-Eshelby-Stroh) formalism for anisotropic elasticity

Many physical problems can be reduced from three-dimensional to two-dimensional space, in order to make analytical forms and modelling easier to find and faster. That is suitable for the problems of infinite straight line defects in materials (e.g. dislocations) as the mechanical fields are constant along the defect line, thus they could be regarded as a two-dimensional problem. A general solution for two-dimensional anisotropic elasticity was firstly developed by Eshelby et al. [21], Stroh [22] and Leknitskii [20]. The so-called L-E-S (Leknitskii-Eshelby-Stroh) analytical formalism (or sextic equation formalism) involves solving a six-dimensional equation and considers complex variable techniques. It is very efficient but cannot handle the case of a completely isotropic crystal since the problem becomes singular due to repeated eigenvalues. In that case, some authors [174, 175] extended the formalism with pure isotropic elasticity.

#### 1.5.3.1 Sextic equation formalism

In a Cartesian reference frame  $(\mathbf{e}_1, \mathbf{e}_2, \mathbf{e}_3)$  such that  $\mathbf{e}_3 = \mathbf{e}_1 \times \mathbf{e}_2$ , the balance of linear momentum equation in the absence of body forces reads:

$$\sigma_{ij,j} = 0 \quad (1.49)$$

As a consequence of the symmetries of elastic stiffness  $\mathbf{C}$ , the generalized Hooke's law in linear anisotropic elasticity can be written as:

$$\sigma_{ij} = C_{ijkl} u_{k,l} \quad (1.50)$$

The combination of these two equations leads then to:

$$C_{ijkl} u_{k,lj} = 0 \quad (1.51)$$

Since it is assumed as a two-dimensional problem that the displacements are only the function of  $x_1$  and  $x_2$ , Eq. 1.51 can be rewritten in the form:

$$C_{i1k1} u_{k,11} + (C_{i1k2} + C_{i2k1}) u_{k,12} + C_{i2k2} u_{k,22} = 0 \quad (1.52)$$

Without loss of generality, it has been shown that the solution of Eq. 1.52 can be expressed as [21, 22]:

$$u_k = a_k f(z) \quad \text{with } z = x_1 + px_2 \quad (1.53)$$

Here  $f$  is an arbitrary scalar function of  $z$  and  $a_k$  and  $p$  are constants to be determined. Eq. 1.52 together with Eq. 1.53 yield:

$$(C_{i1k1} + p(C_{i1k2} + C_{i2k1}) + p^2 C_{i2k2}) a_{\underline{k}} = 0 \quad (1.54)$$

A nontrivial solution of  $a_{\underline{k}}$  exists if the determinant of Eq. 1.54 is zero. Such condition gives a sextic equation for  $p$  [21, 22]. It has been proven that the six roots (defined hereafter as the material eigenvalues) actually consist of three pairs of complex conjugate roots due to the positive definiteness of the strain energy [21]. If  $p_\alpha$  and  $a_{k\alpha}$  ( $\alpha = 1..6$ ) denote the eigenvalues and the associated eigenvector components, it is hereafter considered that:

$$\text{Im}(p_\alpha) > 0, \quad p_\alpha = \overline{p_{\alpha+3}}, \quad a_{k\alpha} = \overline{a_{k(\alpha+3)}} \quad \text{with } \alpha = 1, 2, 3 \quad (1.55)$$

### 1.5.3.2 Displacement and stress solutions

Assuming generally that the roots  $p_\alpha$  are distinct, the displacement vector is then obtained by the superposition of the six solutions, which can be put into the following form:

$$u_i = 2\text{Re} \left[ A_{i\underline{j}} f_{\underline{j}} \left( z_{\underline{j}} \right) \right] \quad (1.56)$$

where  $\mathbf{A}$  is a  $3 \times 3$  matrix containing the eigenvector components  $a_{k\alpha}$  ( $\alpha = 1, 2, 3$ ) and  $z_j = x_1 + p_j x_2$ . Finally, the stresses can be derived from a stress function vector  $\phi_i$  obtained as:

$$\phi_i = 2\text{Re} \left[ B_{i\underline{j}} f_{\underline{j}} \left( z_{\underline{j}} \right) \right] \quad (1.57)$$

where  $\mathbf{B}$  is a  $3 \times 3$  matrix defined as:

$$B_{ij} = (C_{i2k1} + p_j C_{i2k2}) A_{kj} \quad (1.58)$$

such that the  $\mathbf{e}_3$ -independent stresses are:

$$\sigma_{i1} = -\partial\phi_i/\partial x_2, \quad \sigma_{i2} = \partial\phi_i/\partial x_1 \quad (1.59)$$

If needed, component  $\sigma_{33}$  can be also computed from the generalized Hooke's law. It is noteworthy that  $p_\alpha$ , as well as the matrices  $\mathbf{A}$  and  $\mathbf{B}$ , are complex quantities, which depend only on the anisotropic elastic stiffness tensor  $\mathbf{C}$ . Matrices  $\mathbf{A}$  and  $\mathbf{B}$  are non-singular when the six complex roots  $p_\alpha$  are all distinct or for specific non-degenerate cases [176]. Properties of  $\mathbf{A}$  and  $\mathbf{B}$  (normalization, orthogonality) were discussed by Stroh [22, 177], Barnett and Lothe [109] and Chadwick and Smith [178].

## 1.5.4 Crystal Plasticity Finite Element Method (CPFEM)

### 1.5.4.1 Conventional CPFEM

Based on classic continuum mechanics, CPFEM describes the elastic-plastic deformation of anisotropic heterogeneous crystalline materials. This method is largely used to investigate orientation stability, micro-beam bending and deformation of single, bi and multi-crystals at the micro- and mesoscales. This method was reviewed by Roters et al. [10]. In particular, mechanisms at GBs were studied by many researchers [179, 180, 181, 182, 183, 184, 185, 186, 187, 188, 189, 190, 191, 192].

The kinematical theory for the mechanics of crystalline elastic-plastic deformation was described by Hill and Rice [193] in limit strains. In this theory, following Lee [194], Kröner [173] and Gurtin [195] the total deformation gradient  $\mathbf{F}$  can be multiplicatively decomposed into two components  $\mathbf{F}^e$  and  $\mathbf{F}^p$ :

$$\mathbf{F} = \frac{\partial \mathbf{x}}{\partial \mathbf{X}} = \mathbf{F}^e \cdot \mathbf{F}^p \quad (1.60)$$

where  $\mathbf{x}$  indicates the position of material point in the deformed configuration,  $\mathbf{X}$  the position of the same material point in initial undeformed configuration,  $\mathbf{F}^e$  the elastic distortion which includes the stretching and rotation of the crystalline lattice and  $\mathbf{F}^p$  is the plastic part due to crystallographic slip on slip systems. The velocity gradient  $\mathbf{L}$  can be calculated by:

$$\mathbf{L} = \dot{\mathbf{F}} \cdot \mathbf{F}^{-1} \quad (1.61)$$

It can be then separated into two parts: a symmetric part  $\mathbf{D}$  that represents the rate of stretching and an antisymmetric part  $\mathbf{\Omega}$  that represents the spin tensor.

$$\mathbf{L} = \mathbf{D} + \mathbf{\Omega} \text{ with } \mathbf{D} = \frac{1}{2} (\mathbf{L} + \mathbf{L}^T), \mathbf{\Omega} = \frac{1}{2} (\mathbf{L} - \mathbf{L}^T) \quad (1.62)$$

Each of these tensors can be continually separated into elastic and plastic two parts as shown in Eq. 1.63.

$$\begin{cases} \mathbf{D} = \mathbf{D}^e + \mathbf{D}^p \\ \mathbf{\Omega} = \mathbf{\Omega}^e + \mathbf{\Omega}^p \end{cases} \quad (1.63)$$

where  $\mathbf{D}^p$  and  $\mathbf{\Omega}^p$  can be described in function of the slip direction  $\mathbf{s}_\alpha$ , the normal of slip plane  $\mathbf{n}_\alpha$  of slip systems and slip rate  $\dot{\gamma}_\alpha$  as:

$$\begin{cases} \mathbf{D}^p = \sum_{\alpha=1}^N \frac{1}{2} \dot{\gamma}_\alpha (\mathbf{s}_\alpha \otimes \mathbf{n}_\alpha + \mathbf{n}_\alpha \otimes \mathbf{s}_\alpha) \\ \mathbf{\Omega}^p = \sum_{\alpha=1}^N \frac{1}{2} \dot{\gamma}_\alpha (\mathbf{s}_\alpha \otimes \mathbf{n}_\alpha - \mathbf{n}_\alpha \otimes \mathbf{s}_\alpha) \end{cases} \quad (1.64)$$

Therefore, the plastic part of velocity gradient can be calculated by:

$$\mathbf{L}^p = \mathbf{D}^p + \mathbf{\Omega}^p = \sum_{\alpha=1}^N \dot{\gamma}_{\alpha} \mathbf{s}_{\alpha} \otimes \mathbf{n}_{\alpha} \quad (1.65)$$

where subscript  $\alpha$  indicates the slip system. For FCC crystals, there are 12 slip systems as presented in Table 1.1, so  $N = 12$ .

The constitutive models of CPFEM can be classified into two types: phenomenological and physics-based constitutive models. With phenomenological constitutive models, the material's behavior is only described in terms of the critical resolved shear stress [196, 197]. However, with physics-based constitutive models, like dislocation-based constitutive laws, the lattice defect populations such as dislocation densities are required. Therefore, path- and size-dependent crystal plasticity can be investigated [198, 191]. Here, only a very common the phenomenological crystal plasticity constitutive model is presented [197, 199]. The rate-dependent hardening model can be described as:

$$\dot{\gamma}_{\alpha} = \dot{\gamma}_{\alpha}^0 \text{sgn}(\tau_{\alpha}) \left| \frac{\tau_{\alpha}}{\tau_{\alpha}^c} \right|^n \quad (1.66)$$

where  $\dot{\gamma}_{\alpha}^0$ ,  $\tau_{\alpha}^c$ ,  $\tau_{\alpha}$  and  $n$  are reference shear strain rate, critical resolved shear stress (CRSS), current resolved shear stress and rate sensitivity exponent, respectively. The rate of the change of the critical resolved shear stress is described by:

$$\dot{\tau}_{\alpha}^c = \sum_{\beta=1}^N h_{\alpha\beta} |\dot{\gamma}_{\beta}| \quad (1.67)$$

where  $h_{\alpha\beta}$  is the hardening matrix, which can be calculated as follows [196, 197]:

$$h_{\alpha\beta} = qh_{\alpha\alpha}, \quad h_{\alpha\alpha} = h_0 \text{sech}^2 \left| \frac{h_0 \gamma}{\tau^s - \tau^0} \right| \quad \text{with } \gamma = \sum_{\alpha=1}^N \int_0^t |\dot{\gamma}_{\alpha}| dt \quad (1.68)$$

where  $q$ ,  $h_0$ ,  $\tau^0$  and  $\tau^s$  are latent hardening effect, initial hardening modulus, initial CRSS and saturated shear stress at stage I, respectively.

#### 1.5.4.2 Strain gradient CPFEM (SG-CPFEM)

The conventional CPFEM do not consider material length scale and so no size effects are predicted. However, several observed plasticity phenomena display a size effect whereby the smaller is the size the stronger is the response [11]. Under this condition, it is necessary to introduce one or more intrinsic material length

scales into the conventional plasticity model with considering strain gradient, so-called strain gradient plasticity (SGP) which was reviewed by Voyiadjis and Song [200].

Aifantis [201, 202] first attempted to combine a material length scale parameter with the conventional plasticity theory. He modified the conventional yield function by adding the plastic strain gradient term to resolve the issues related to the thickness of the localization regions which is typically measured at the microscopic scale. He showed that the inclusion of higher-order deformation gradient into the expression of flow stress or strain energy function for hyper elastic materials was adequate to determine the width of shear bands and to preserve ellipticity in the governing equilibrium relations in the strain softening regime [200]. In particular, Aifantis [203] theoretically captured the occurrence of dislocation pile-ups across GBs, as well as subsequent emission to the adjacent grains by gradient plasticity and confirmed experimentally by nanoindentation. Inspired by the micro torsion experiment with the polycrystalline copper wires, Fleck and Hutchinson [11, 204] proposed a strain gradient theory of rate independent plasticity using dislocation theory. They paid more attention to the role of GNDs in the gradient of plastic strain and proposed the deformation and flow theory versions of SGP model. In this theory, the hardening is assumed to result from the accumulation of both SSDs and GNDs and the density of GNDs scales with the gradient of plastic strain [11]. Then, Gudmundson [205] and Gurtin and Anand [206] proposed another class of SGP theories which decompose the higher-order stresses into energetic and dissipative parts. This theory is constrained to plastically irrotational flow for small deformation framework [200]. Meanwhile, Gurtin [207] developed another SGP theory that accounts for the plastic dissipation caused by plastically rotational flow. Different from phenomenological SGP theories, Nix, Gao, Huang and co-workers [208, 209, 210, 211, 212, 213, 214] developed a mechanism-based SGP (MSGP) theory based on the multiscale framework linking the microscale dislocation mechanism to the mesoscale plasticity theory. From a microscopic point of view, the flow is defined as the critical stress to move a glide dislocation through a forest of obstacles, whereas in mesoscopic point of view, it is possible to connect the notion of GNDs to the gradient of the strain field and to institute a thermodynamically consistent framework. In this way, the concept of GNDs become a coherent part of the constitutive formulation. The Taylor hardening model relating the flow stress to the interactions of the mobile dislocations is also used in the MSGP theory [200].

Based on theoretical investigations of SGP, a variety of numerical applications of the SGP theory in the context of the FEM and FFT (highly efficient alternative to FEM) have been carried out. In particular, Lebensohn and Needleman [215] proposed a numerical implementation of a non-local polycrystal plasticity theory

using the FFT-based formulation. They incorporated the Gurtin [216] non-local formalism in the elasto-viscoplastic-FFT (EVP-FFT) algorithm of Lebensohn et al. [217]. Then, Djaka et al. [218] proposed an enhanced crystal plasticity EVP-FFT formulation coupled with a phenomenological Mesoscale Field Dislocation Mechanics (MFDM) theory, so-named MFDM-EVP-FFT formulation. In contrast with classic crystal plasticity EVP-FFT, this model is able to tackle plastic flow and hardening due to polar dislocation density distributions or GNDs in addition to SSDs. It also considers GND mobility through a GND density evolution law coupled with stress equilibrium.

#### 1.5.4.3 Dislocations-GB interactions analysis using CPFEM

Furthermore, the interaction between dislocations and GBs were also studied by CPFEM. Two types of dislocation-based constitutive model are discussed hereafter [186, 191]. The first type of model describes GB as a perfect obstacle that does not allow dislocation penetration events [186] (impenetrable GB). This assumption can be implemented in finite element simulations with an additional set of boundary conditions: a zero shear condition perpendicular to GB. Evers et al. [186] found that these boundary conditions can lead to an increase of hardening but not an increase of the initial yield stress. Thus they proposed to introduce GB dislocations (GBDs) as an initial GNDs at the position of the GBs. These GBDs can be calculated from the crystallographic misorientation across the interface with the schematic representation reported in Figure 1.48:

$$|\rho_{\text{GBD}}^{\alpha}| = \frac{1}{h^{\alpha^2}} = \left( \frac{1}{b^{\alpha}} - \frac{1}{b^{\beta}} \right)^2 \quad (1.69)$$

$$\rho_{\text{GBD}}^{\alpha} = \text{sign}(\mathbf{n}_0^{\alpha} \cdot \mathbf{n}_0^{\text{GB}}) \frac{\left( |\mathbf{n}_0^{\alpha} - \mathbf{n}_0^{\text{GB}}| - |\mathbf{n}_0^{\beta} - \mathbf{n}_0^{\text{GB}}| \right)^2}{b^2} \quad (1.70)$$

where  $\mathbf{n}_0^{\alpha}$  and  $\mathbf{n}_0^{\beta}$  are slip directions for incoming and outgoing slip systems, and  $\mathbf{n}_0^{\text{GB}}$  is the normal vector of GB. The slip system  $\beta$  has to be chosen to minimize  $\rho_{\text{GBD}}^{\alpha}$ .

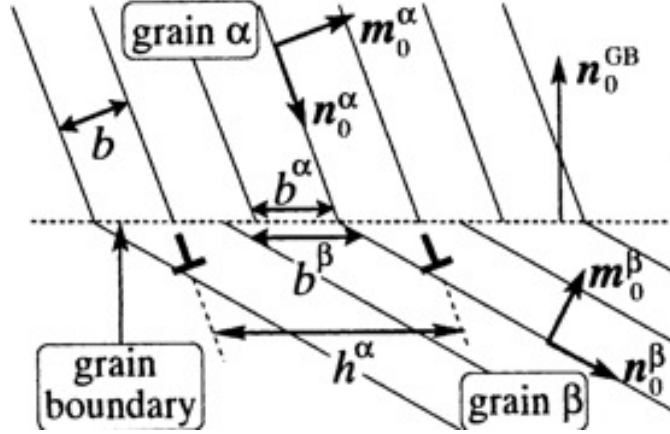


Figure 1.48: GB dislocations produced by different Burgers vectors according to different slip system in grains  $\alpha$  and  $\beta$  [186].

The second type of GB model in CPFEM was proposed by Ma et al. [191] who assumed partial penetrability of the GB to dislocations. An activation concept was used to treat the transmission probability of incoming dislocations to penetrate a GB. During slip transmission, the residual dislocations are formed as debris in the GB. An elastic energy is required to form these residual dislocations upon the slip systems in both grains. It is likely that each transmission event occurs at the smallest possible energy consumption which provides a selection criterion for the involved slip systems. As discussed in the section 1.3.1 and the section 1.3.4, the most likely outgoing slip system in adjacent grain is the slip system that has the smallest misalignment on GB with the incoming slip system, so the one with the smallest energy barrier of GB. However, perfect alignment is rare for general GBs. Residual dislocations are thus created in the GB in order to satisfy the conservation of the lattice defect vector when a dislocation crosses an GB. Thus, an additional energy is required to produce these residual dislocations which is regarded as a penalty energy barrier for the thermally activated slip transmission event. Ma et al. [191] proposed a mathematical treatment of this penalty energy based on the minimization of the activation energy with an outgoing slip system  $\beta$ :

$$E_{GB}^{\alpha} = \min_{\beta} c'_9 \frac{1}{2} G b^2 l^{\alpha} R^{\alpha\beta} \quad (1.71)$$

where  $c'_9$  is a fitting constant,  $l^{\alpha}$  the length of the incoming dislocation and  $R^{\alpha\beta}$  a geometrical factor describing the correlation of the incoming system  $\alpha$  and the outgoing system  $\beta$ .

Even if CPFEM is a powerful method, it does not resolve dislocations individually and miss therefore the effects of discrete mechanisms.



### 1.5.5 Discrete Dislocation Dynamics method (DDD)

DDD method is a powerful tool to investigate plastic deformation of crystalline material based on the motion of discrete dislocations. The principle of this method is that the dynamics of each discrete dislocation segment is controlled by a Newtonian-type equation of motion which includes an inertia term, a drag term and a driving force as [219]:

$$m\dot{v} + Bv = F \quad (1.72)$$

where  $v$ ,  $m$ ,  $B$  and  $F$  are the dislocation velocity, the effective mass density, the drag coefficient and the driving force, respectively. The driving force is composed by various sources: applied force, interaction forces between dislocations or with GB, line tension and thermal force, etc. It is supposed that when the driving force is larger than the Peirels force (lattice friction force), the dislocation can slip. If not, the velocity of dislocation is set to be zero. By solving Eq. 1.72, the position of each dislocation segment and the stress-strain relation of bulk crystalline materials can be obtained.

DDD is a significant method to study the interaction between dislocations and GBs which is well reviewed by Burbery et al. [220]. First studies used two-dimensional simulations. In the most simple models, the GBs were regarded as impenetrable barriers to dislocations [221, 222, 223, 224, 225, 226, 227, 228]. Later, more complex DDD models were proposed to consider slip transmission through GBs [229, 12, 230]. Biner and Morris [229] have shown the effect of dislocation pile-ups at GB on activation and shut-down of dislocation sources. Quek et al. [12] proposed a methodology where slip transmission is modeled by the annihilation of incoming dislocation and the activation of a Frank-Read source in the adjacent grain. Li et al. [230] proposed a method where the slip transmission criterion was defined in terms of the line energy of the incoming, outgoing and residual Burgers vector. An additional term was also included in their approach to compensate for the energy used to penetrate the GB structure. In that case, the crystallographic orientation could be considered and a dislocation re-emission mechanisms was proposed. Furthermore, other approaches for slip transmission study considered the effects of line tension [231] and conservation of Burgers vector [232]. The stress fields were also evaluated in bi-crystals containing a low angle GB modeled by a dislocation array [221, 13]. However, in two-dimensional DDD, only 1, 2 or maximum 3 slip systems can be considered [223] and these models do not account for crystallographic changes at GBs and line tension effects. Robbins and Voth [233] proposed a DDD simulation combined with generalized finite element method (GFEM) to model dislocation dynamics in finite heterogeneous anisotropic materials based on the superposition method. Dislocation arrays, GB, free surfaces and polycrystalline microstructure can be all considered in DDD-GFEM. It can also

consider the effect of GB stiffness by defining a GB stiffness tensor which depends on anisotropic misorientation of two adjacent grains. The elastic incompatibility and activation of secondary slip due to this incompatibility in a bi-crystal configuration were studied by DDD-GFEM as presented in Figure 1.49. Furthermore, researchers also developed three-dimensional DDD models. An impenetrable GB model was used for polycrystal DDD simulation in thin films with free surface effect to investigate grain size effect [228, 224]. A 3D thin film with penetrable GBs was proposed by Zhou and Lesar [234], where the transmission stress was defined by a line tension. However, these models cannot account for crystallographic changes at GBs, and cannot determine the appropriate outgoing slip system, because no interactions between incoming and outgoing dislocations are considered.

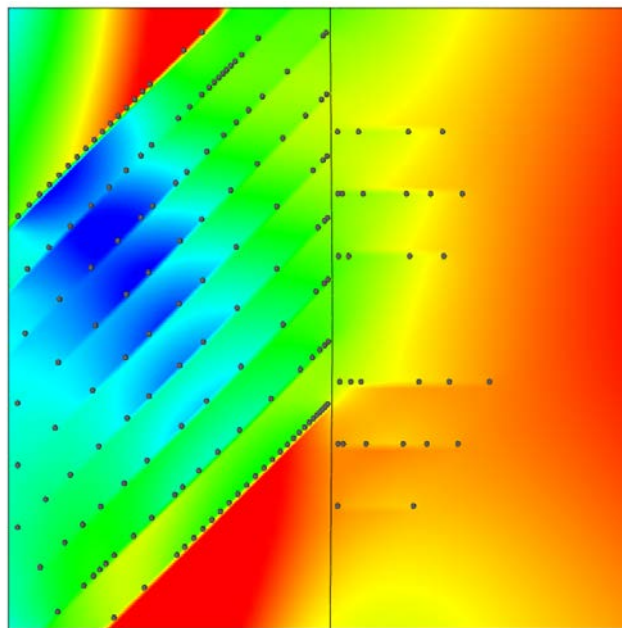


Figure 1.49: Activation of secondary slip and dislocation motion in the grain on right hand side due to a horizontal tensile load in a bi-crystal. There are nine initial dislocation sources distributed in the left hand grain. The color corresponds to displacement magnitude from 0 to 35b [233].

There are several different codes for DDD simulations, such as microMegas (mM) [235], ParaDis [236], TRIDIS [237], MDDP [219] and MoDEL [238, 239, 240], etc. In DDD simulations, the boundary conditions are generally set as two types of periodic conditions: (a) Transparent boundary (TB) condition where dislocations are free to cross the simulated volume borders and enter the simulation volume from the opposite face. (b) Impenetrable boundary (IB) condition where dislocations can only move inside the grain as shown in Figure 1.50. Combined

with a finite element code, DDD can be used to investigate complex materials configuration and loading conditions, such as bi-crystals or poly-crystals [241].

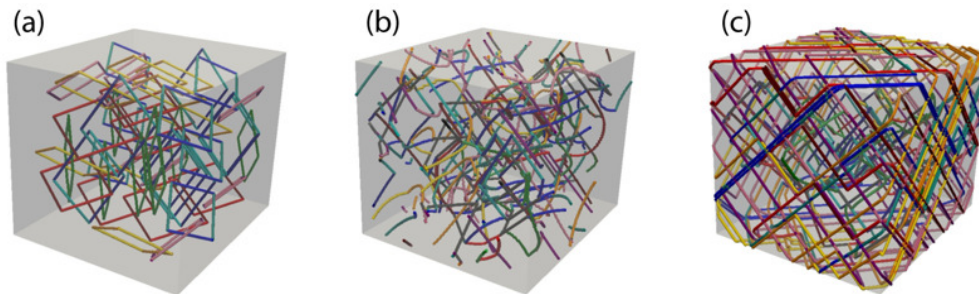


Figure 1.50: (a) Schematic figure of an initial dislocation configuration with a random distribution of dislocation loops, where the different colors indicate different slip systems. Dislocation microstructures were obtained after deformation with (b) the transparent boundaries (TBs) and (c) the impenetrable boundaries (IBs) [242].

A small angle tilt GB can be regarded as a dislocation array [13] as shown in Figure 1.51 in order to investigate this GB effect. Furthermore, this dislocation array can be obtained from molecular dynamics simulations [220], which can be also used for a HAGB, but with a reduced spacing between GB dislocations through Stukowshi's dislocation extraction algorithm [243].

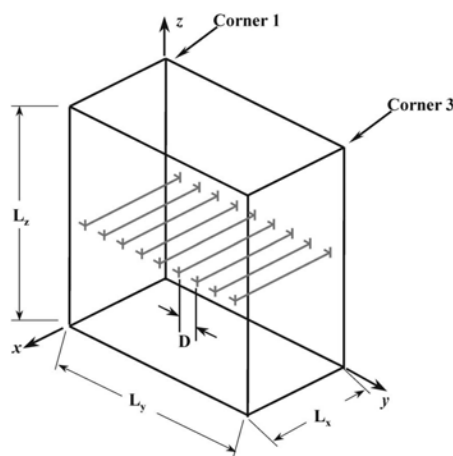


Figure 1.51: Small angle tilt GB, represented by a dislocation array [13].

## 1.5.6 Molecular Dynamics simulation (MD)

MD simulations can give a fine and realistic observation for deformation mechanism at the atomic scale. This method is used to analyze the physical movements of atoms and molecules by allowing them to interact during a fixed period

of time, giving the dynamic evolution of the system. In most common codes, such as LAMMPS [244], the movement of atoms are determined by numerically solving Newton's equations of motion for all interacting atoms in a unit cell. The force and the potential energies between these atoms can be calculated based on interatomic potentials or molecular mechanics force fields. The most common method to determine interatomic potentials for metals is the embedded-atom method (EAM). The total energy  $E_i$  of an atom I is given by [245]:

$$E_i = F_\alpha \left( \sum_{j \neq i} \rho_\beta(r_{ij}) \right) + \frac{1}{2} \sum_{j \neq i} \phi_{\alpha\beta}(r_{ij}) \quad (1.73)$$

where  $F$  is the embedding energy which is a function of the atomic electron density  $\rho$ ,  $\phi$  a pair potential interaction, and  $\alpha$  and  $\beta$  are the element types of atoms I and J. Both summations in the formula are over all neighbors J of atom I within the cutoff distance. Meanwhile, other potentials which can be used for metals simulation, such as the modified embedded-atom method (MEAM).

As MD simulations take into account the structure of dislocation core and the complexion of GBs at atomic scale, it can be used for many domains, such as GB structure and energy, GB sliding, GB migration and dislocation-GB interactions, which are well reviewed by Zhang et al. [14]. Here, only some significant results of dislocation-GB interactions are presented. Koning et al. [246, 247] verified the three conditions of slip transmission proposed by Lee et al. [114] by using MD simulations at a temperature of 0 K. Their results concerned transmitted dislocations nucleated from a crack tip near a series of pure tilt GBs. The nature of GB has an evident influence of dislocation-GB interactions. They found that the resistance of dislocation transmission depends on the mismatch of interaction lines between GB and incoming/outgoing slip systems, stress concentrations and residual Burgers vector. Finally, they determined the critical stress of dislocation activation for each pair of incoming and outgoing slip systems. Meanwhile, Bachurin et al. [248] found that the misorientation between two crystals, the sign of residual Burgers vector and the position of interaction line between dislocation and GB are important parameters to determine the ability of a dislocation to penetrate into GB at a temperature of 0 K. With the increasing of shear strain, the incoming leading partial dislocation was firstly absorbed by GB and then the entire dislocation was transmitted through the GB as shown in Figure 1.52 [248].

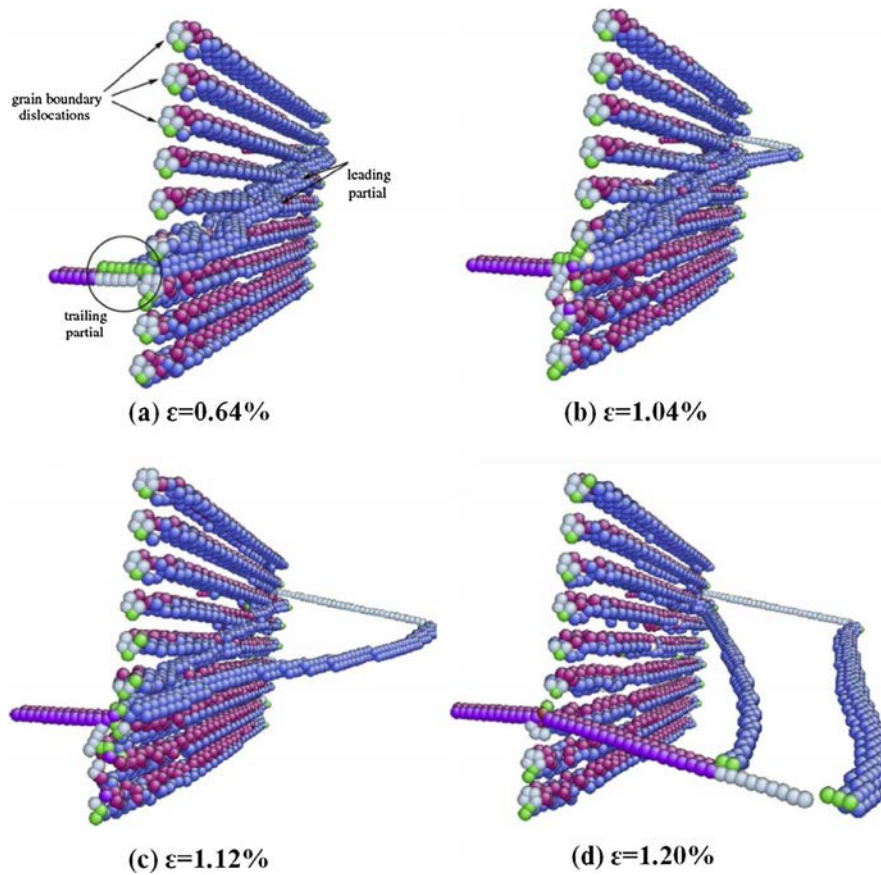


Figure 1.52: Process of dislocation transmission through a  $\Sigma 57$  symmetric tilt GB [14].

In some cases, when the energy barrier of GB is too high or when there are already too many residual Burgers vectors [249, 250, 251, 252, 120, 90, 114], the dislocation will stop in front of the GB without absorption or transmission. With the increasing of applied stress, there will be more and more dislocations in the same slip system and a dislocation pile-up will be created. Dewald and Curtin investigated the interaction of edge dislocation pile-up [250], screw dislocation pile-up [249] and  $60^\circ$  mixed dislocation pile-up [252] with  $\Sigma$  tilt GB in Al. They found that the nucleation of GB dislocation or original GB dislocation has an influence on dislocation pile-ups. Yu and Wang [253] studied the interactions between specified numbers of lattice dislocations and  $\Sigma 11$  ( $\bar{3}1\bar{1}$ ) symmetrical tilt GB in Cu by using quasicontinuum method. They proposed the definitions of positive and negative dislocation-GB interactions and also an unified geometrical criterion to predict “hard” and “easy” dislocation transmission. They observed that the incoming dislocation pile-up will activate outgoing dislocation with both “positive” and “negative” interactions.

The dislocation nucleation mechanism was also observed by MD simulations [254, 255, 256, 257, 258, 259, 260, 261] and was well introduced by Van Swygenhoven and Derlet [262] and Tschopp et al. [263] in bi-crystal model. Spearot et al. [258, 264] found that the mechanical failure along the boundaries was initiated by the dislocation nucleation from GB for the  $\langle 100 \rangle$  and  $\langle 110 \rangle$  symmetrical tilt GBs in Al and Cu. After the emission of partial dislocations into grain, the atoms at GB rearranged themselves, which increases local stress concentrations. Tschopp and McDowell [257] studied dislocation nucleation from  $\Sigma 3$  asymmetric tilt GBs under uniaxial tension that applied perpendicular to the boundary. They found a significant influence of inclination angle of GB on dislocation nucleation mechanism with the same misorientation in Cu as shown in Figure 1.53. For different ranges of inclination angle, the mechanisms for dislocation nucleation in Cu asymmetric GBs were divided into three regimes. At low inclination angles:  $\Phi \leq 35.26^\circ$ , the dissociation and nucleation processes occurred on different slip planes as shown in Figure 1.53 (a), and the stress required for dislocation nucleation was relatively high. At intermediate inclination angles:  $35.26^\circ < \Phi < 70.53^\circ$ , the dislocation dissociation and nucleation occurred on the same slip plane as shown in Figure 1.53 (b), and a relatively low stress was required to induce the dislocation nucleation from GB plane. At high inclination angles:  $\Phi \geq 70.53^\circ$  (see Figure 1.53 (c)), the extended dissociation of the boundary resulted in an increased volume of the 9R phase as shown in Figure 1.54 which is explained by Ernst et al. [265].

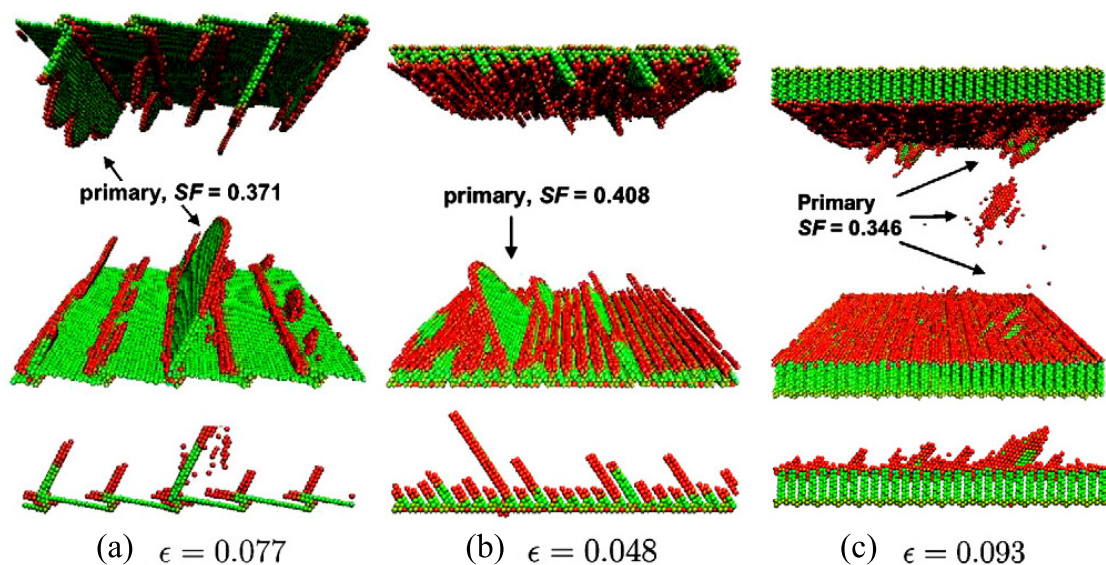


Figure 1.53: Dislocation nucleation from  $\Sigma 3$  asymmetric tilt GB in Cu at 10K with inclination angle (a)  $10.02^\circ$ , (b)  $54.74^\circ$  and (c)  $79.98^\circ$  [257].

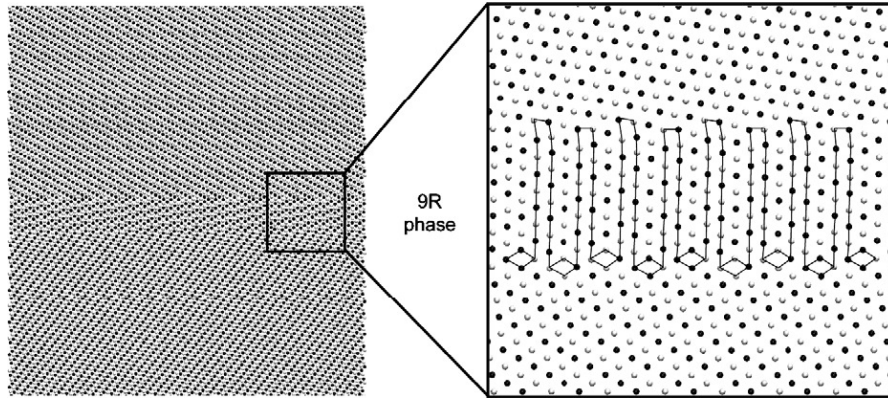


Figure 1.54: Detailed image of 9R phase structure in  $\Sigma 3$  asymmetric tilt GB in Cu at 10K with inclination angle  $79.98^\circ$  [257].

Meanwhile, the difference between symmetric and asymmetric GBs was studied by Zhang et al. [266] with  $\Sigma 5$  GBs in Cu bi-crystals. They found that for symmetric GB, dislocations can be emitted into both grains at the same time as shown in Figure 1.55 (a-b), while for asymmetric GB, dislocations were firstly emitted into one grain and then the slip systems in another grain can be activated as shown in Figure 1.55 (c-d).

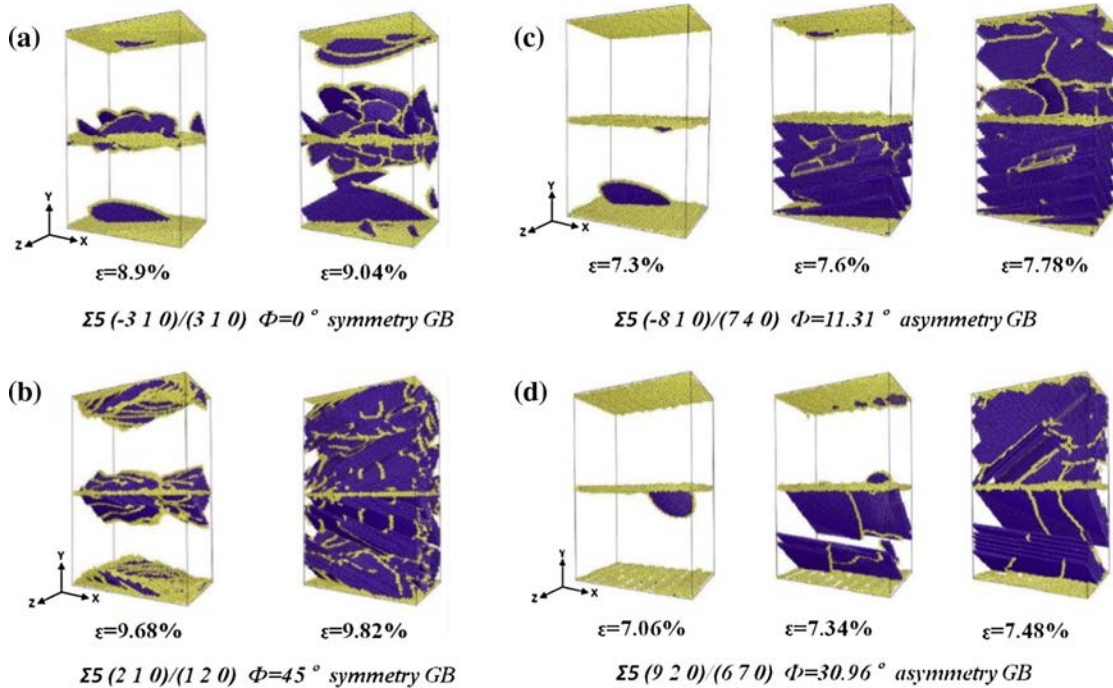


Figure 1.55: Dislocation nucleation from  $\Sigma 5$  symmetric and asymmetric GBs under uniaxial tension [14].

As a conclusion, by using MD simulations, the GB structure and local interactions between dislocations and GBs can be clearly investigated at atomic scale. However, MD simulations cannot be performed for a large system due to computing resources and time consuming.



# Chapter 2

## Experimental part: Nickel and $\alpha$ -Brass bicrystalline micro-pillar compression test

### 2.1 Introduction

In order to study the interactions between dislocations and GBs and the effect of heterogeneous crystallographic slip on elastic fields, mechanical tests on micro-bi-crystals were performed. In this context, it is decided to work on bi-crystalline micro-beams with plane surfaces. The advantage of this geometry is the ability to analyze slip lines on the upper surface by atomic force microscopy (AFM) as described in subsection 1.4.4. In this chapter, the different experimental methods involved in the fabrication and the characterization of micro-beams are described. The procedure of this experience is the following. First macro-samples were homogenized through heat treatment in order to reduce the internal stresses and increase the grain size. An interesting GB was then chosen from a macroscopic sample based on EBSD results. Then, a micro-beam of bi-crystals containing this GB was realized by FIB. After that, a micro-pillar compression test was performed on this micro-beam by a flat punch along GB direction with a low strain in order to create single slip in one of the crystal. At the end of the experimental campaign, the topography of the external surface containing the slip step height was measured by AFM. The whole process is schematically presented in Figure 2.1. The topography of slip lines can be used to analyze the distribution of dislocations in a discrete dislocation pile-up and slip transfer at GB. As a part of this cotutelle thesis, experiences were performed in the Department of Materials Science and Technology (MWW) at the Saarland University in Saarbrücken.

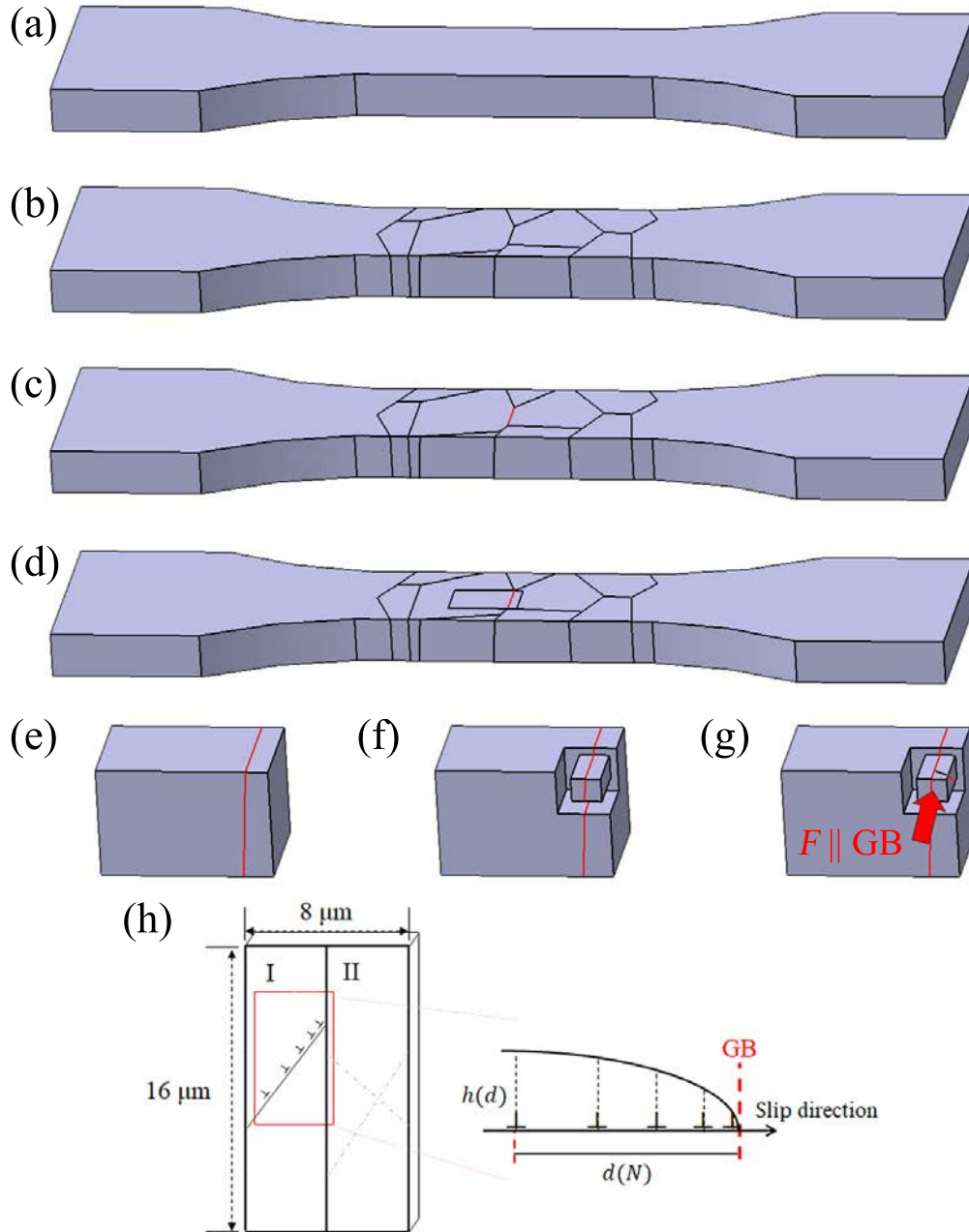


Figure 2.1: Schematic figure of the different experimental procedures: (a) The surfaces of polycrystalline macro-samples were polished after heat treatment. (b) Microstructure analysis based on EBSD measurement: the orientations of grains were determined. (c) The interesting GB was selected according to several criteria. (d) A bi-crystal area containing the interesting GB was selected. (e) The selected area was cut out with the GB close to side surface. (f) A micro-beam containing the interesting GB was realized by FIB, and the orientations of the two grains were determined again by EBSD measurement. (g) An in-situ micro-pillar compression test was performed on the micro-beam by a flat punch indenter with a low strain in order to create a single slip. The loading direction is parallel to GB. (h) The slip lines were analyzed by SEM and AFM, so the direction of their traces and the topographic distribution were obtained.  $h(d)$  and  $d(N)$  are the height of slip line and the distance of  $N^{th}$  dislocation from GB along the slip direction, respectively.

## 2.2 Material choice

The materials for this experimental study are Nickel (Ni) with very high purity (99.999%) and  $\alpha$ -Brass (70%Cu-30%Zn, wt%) with impurities (Fe, Pb, P and As, etc.) less than 0.001%. A chemical analysis by energy dispersive spectroscopy (EDX) was performed to check the purity of the samples before and after the sample preparation procedures. The elastic stiffness moduli of Ni are  $C_{11} = 246.5$  GPa,  $C_{12} = 147.3$  GPa,  $C_{44} = 124.7$  GPa [28] and those of  $\alpha$ -Brass are  $C_{11} = 139.21$  GPa,  $C_{12} = 104.51$  GPa,  $C_{44} = 71.3$  GPa [267, 268]. Thus these two materials have an elastic anisotropy factor  $A = \frac{2C_{44}}{C_{11} - C_{12}}$  which is 2.51 for Ni and 4.11 for  $\alpha$ -Brass. Therefore, the chosen materials have different anisotropy factors which can be used to analyze the effects of anisotropic elasticity. In the case of elastic isotropy, the considered elastic constants are  $G = 86.16$  GPa,  $\nu = 0.294$  for Ni and  $G = 40.75$  GPa,  $\nu = 0.343$  for  $\alpha$ -Brass. The latter are deduced from the anisotropic elastic stiffness moduli by applying the Voigt-Reuss-Hill average [269, 270]. Furthermore, the stacking fault energy for  $\alpha$ -Brass and Ni are about 14 mJ/m<sup>2</sup> [271] and 90 mJ/m<sup>2</sup> [272], respectively. The stacking fault energy of  $\alpha$ -Brass is low which promotes planar slip and thus facilitates the observation of slip lines. While the stacking fault energy of Ni is higher, slip lines were also well observed in Ni bi-crystals during compression tests [137]. Thus, Ni is also suitable for the present experiments.

## 2.3 Sample preparation

### 2.3.1 Metallographic preparation

The samples, usually in the form of cubes of  $20 \times 20 \times 5$  mm<sup>3</sup>, were cut by electrical discharge machining (EDM) using a bronze wire. This cutting process generates phenomena of temperature localization on the sample surfaces during which elements of copper and zinc in the bronze wire are diffused inside the samples and can thus modify the chemical composition on the surface. Besides the contamination by bronze wire, the high temperature accelerates the oxidation of materials on the surface. To remedy all these impurities, a mechanical polishing was performed on the whole samples. The six faces of the samples were mechanically polished with coarse abrasive papers up to the particle size index P2500 with water. This polishing phase was followed by a polishing using a diamond suspension of particle sizes 6, 3, and 1 micron on zeta cloth to eliminate hardening and damage achieved during the mechanical polishing, including scratches. At the end, the sample surfaces were finally polished by OP-U-NonDry solution with water on

chem-cloth for 5 mins. After the polishing of macro-samples, the thickness was around 2.0 ~ 2.5 mm. With this range of thickness, it is possible to keep GBs relatively perpendicular to the upper surface thanks to a heat treatment process.

### 2.3.2 Heat treatment

The purpose of the heat treatment is to reduce the internal stresses resulting from the manufacturing process of the raw material. It also allows us to regenerate a homogeneous microstructure with coarse grains.

For Ni, the produced samples were homogenized at 1100 °C for three days. The heat treatment was performed in a vacuum oven to minimize the risk of contamination and oxidation of the samples. The vacuum was obtained using a pump allowing a vacuum of less than  $10^{-6}$  mbar. At the end of heat treatment, the samples were submitted a relatively slow cooling process.

For  $\alpha$ -Brass however, the heat treatment is more complicated. The heat treatment of the  $\alpha$ -Brass sample was firstly done with the same process for the Ni sample. It was homogenized at 800 °C during four days in vacuum condition. After the heat treatment, there were lots of holes on the sample surface as shown in Figure 2.2 (a). Then, the sample surface was polished and analyzed by EDX, which showed that the chemical composition on surface was on average 87.5%Cu-12.5%Zn as shown in Figure 2.2 (b). At the location of a hole, it was about 87.8%Cu-12.2%Zn as shown in Figure 2.2 (c). The original chemical compositions of this  $\alpha$ -Brass is 70%Cu-30%Zn. These results show that the sample has lost about 20% Zn during the heat treatment on the whole sample surface.

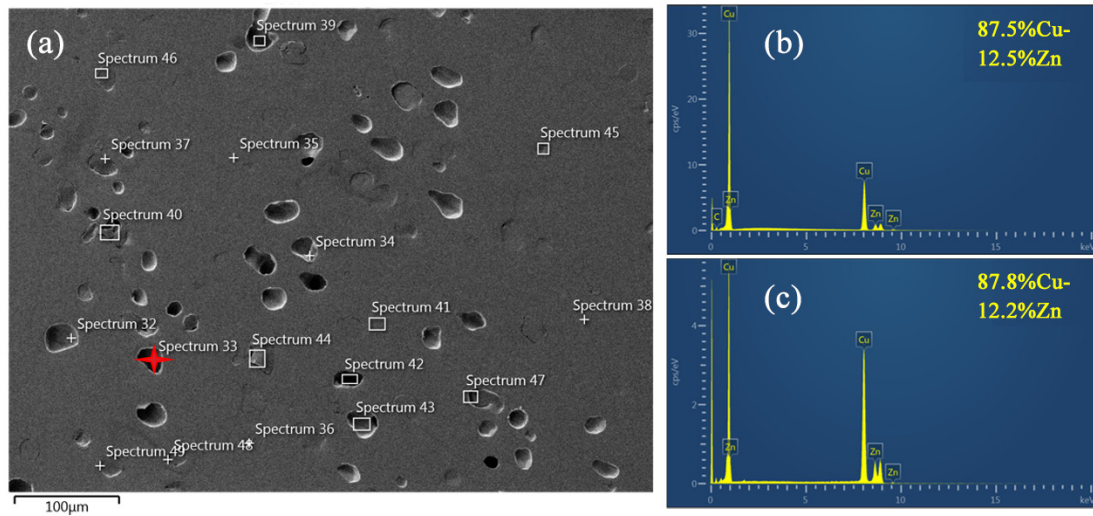


Figure 2.2: (a) SEM picture taken on the upper surface of the  $\alpha$ -Brass sample after heat treatment in vacuum showing many holes on the surface, (b) EDX analysis on the whole upper surface, and (c) EDX analysis of a hole on the sample upper surface which is marked as a red cross in (a).

This phenomenon was already observed and investigated by Itoh and Hikage in 1976 [273]. They found dezincified phenomenon during heat treatment of Brass samples with different zinc contents in vacuum condition as shown in Figure 2.3. Their results show that for a  $\alpha$ -Brass specimen with 33.5% Zn, the sample lose about 15% Zn after a heat treatment at 800 °C during 1 hour.

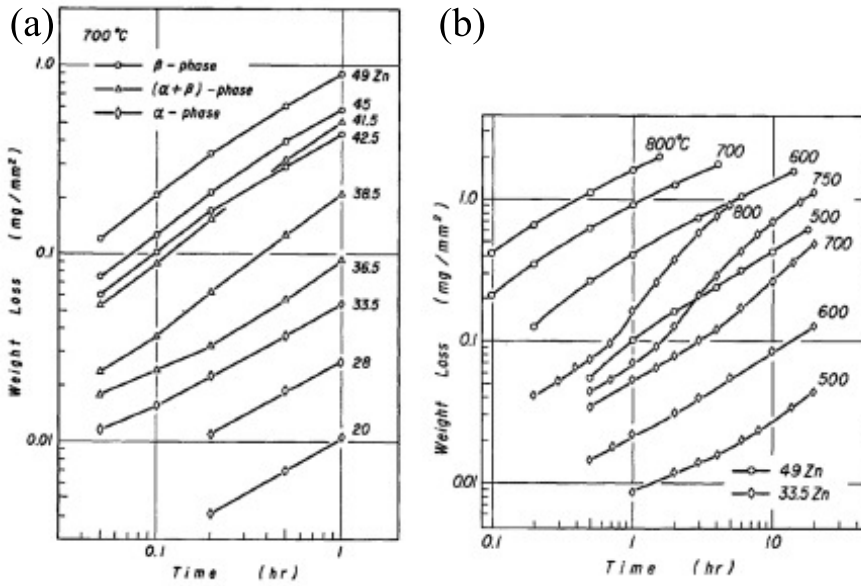


Figure 2.3: (a) The relation between weight loss and reaction time for the specimens with different zinc contents dezincified at 700 °C, where ( $\alpha$ ), ( $\alpha + \beta$ ) and ( $\beta$ ) indicate the specimens with  $\alpha$ -phase, both  $\alpha$ - and  $\beta$ -phase and  $\beta$ -phase, respectively. (b) The relations between weight loss and reaction time for the specimens with 33.5%Zn and 49%Zn over the temperature range 500-800 °C [273].

It is believed that the dezincification is due to the huge difference of melting temperature, which is about 500 °C, between pure Zn and  $\alpha$ -Brass as shown in Figure 2.4.

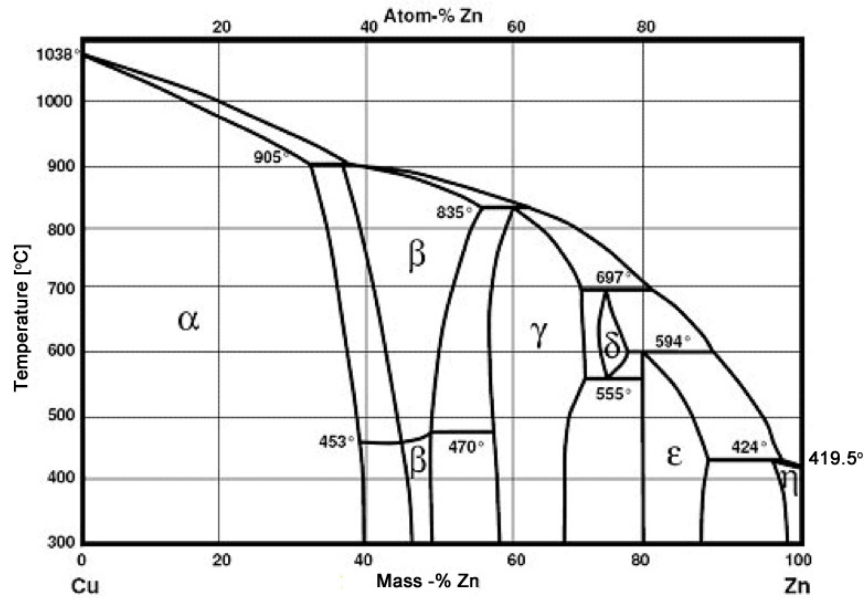


Figure 2.4: Phase diagram of Brass. The melting point of pure Zn is 419.5 °C and of  $\alpha$ -Brass (70%Cu-30%Zn) is about 920 °C [274].

Thus, it is crucial to prevent sample surface from dezincification. In order to do that, three different methods were proposed and tested as shown in Figure 2.5.

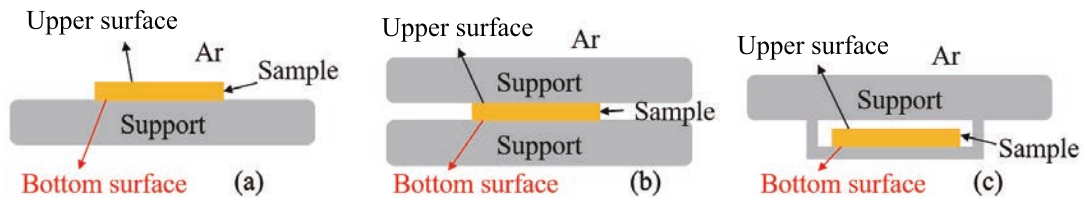


Figure 2.5: Schematic figures of three different methods to prevent from dezincification: (a) sample is placed on a ceramic plate in the argon environment, (b) sample is sandwiched between two ceramic plates in the argon environment, and (c) sample is stored in a closed ceramic box in the argon environment, however the ceramic cover does not touch the sample surface.

The first method consisted in doing the heat treatment in argon environment. The  $\alpha$ -Brass sample was placed on a ceramic plate in the oven, and the oven was filled with argon at ordinary pressure as shown in Figure 2.5 (a). During the heat treatment, the whole system was connected to the atmosphere with liquid seal of silicone oil at the system outlet and the argon was continually filled into the oven in order to keep the pressure constant. With this method, after a heat treatment at 700 °C for 80 hours, the dezincified intensity had receded on the upper surface

which is open to the argon as shown in Figure 2.6 (a). However, there were still some small holes on the upper surface and it has lost about 11.4% Zn of the whole sample. While for the bottom surface, there was no hole and the Zn content was 29.6%, nearly no dezincified event. These results show that compared to a vacuum environment, the argon environment with atmospheric pressure can thus recede dezincification, but it still needs a solid cover protection on the surface in order to eradicate dezincification, such as for the case of bottom surface.

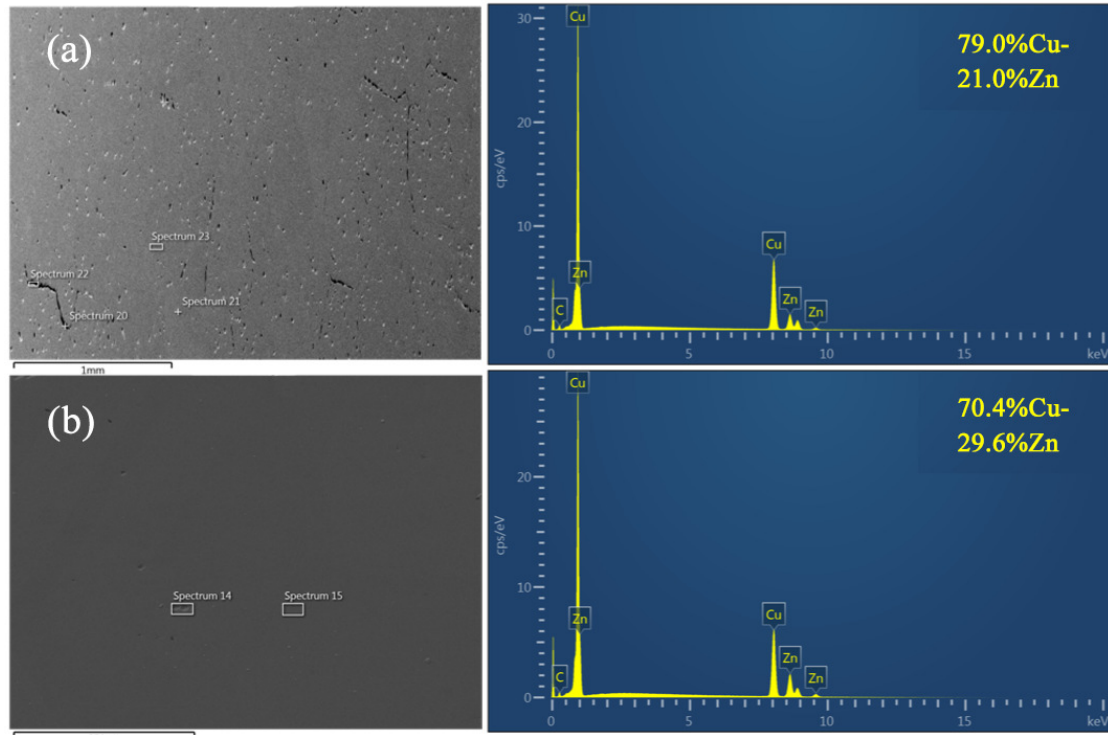


Figure 2.6: SEM picture of  $\alpha$ -Brass sample after heat treatment in argon environment and its EDX analysis on (a) the upper surface which was open to the argon and (b) the bottom surface which was protected by ceramic plate support.

Furthermore, an EBSD measurement was performed on the bottom surface in order to determine the grain size. The result is presented in Figure 2.7. It was found that the average grain diameter is about  $109 \mu\text{m}$ . The homogenization is not obvious. With this grain size, it is difficult to prepare the micro-beam as described in Figure 2.1.



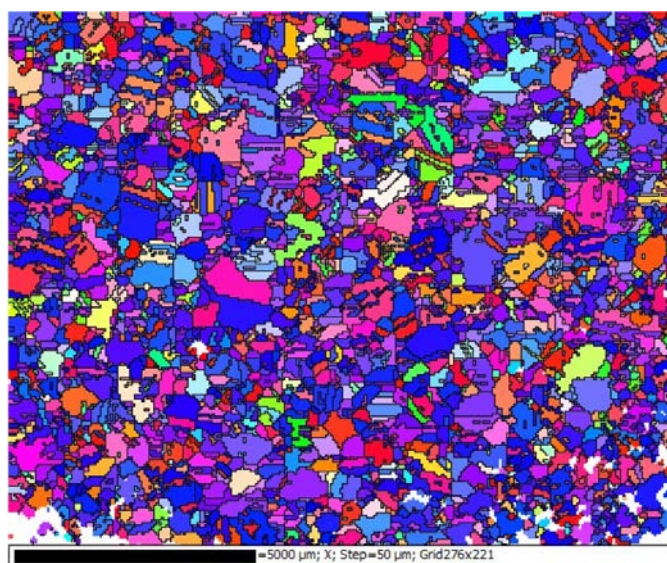


Figure 2.7: EBSD measurement of  $\alpha$ -Brass sample after heat treatment in argon environment on the bottom surface which was protected by ceramic plate support.

In order to further weaken the dezincification, the second system was designed as shown in Figure 2.5 (b). From the analyses made on the first system, it is believed that the argon environment can reduce dezincification and a solid cover on the surface can prevent dezincification. So in the second system, the macro-sample was sandwiched between two ceramic plates and the heat treatment was performed in argon environment. After heat treatment at  $700^{\circ}\text{C}$  for 45 h and at  $750^{\circ}\text{C}$  for 4 days, the EDX analysis and the EBSD measurement were performed on the bottom surface. The results are presented in Figure 2.8. From the EDX results, it was found that there is the zinc content percentage lost 2 ~ 3 points on the bottom surface. Compared to the first system, the dezincification is even more serious. About microstructure characterization, it was found that the grain size is still small and there are some unrecrystallized areas. One reason is that the temperature of recrystallization  $700 \sim 750^{\circ}\text{C}$  is not high enough compared to the melting point of studied  $\alpha$ -Brass ( $920^{\circ}\text{C}$ ). Another reason comes from the pressure of the upper plate which hinders the crystallization.

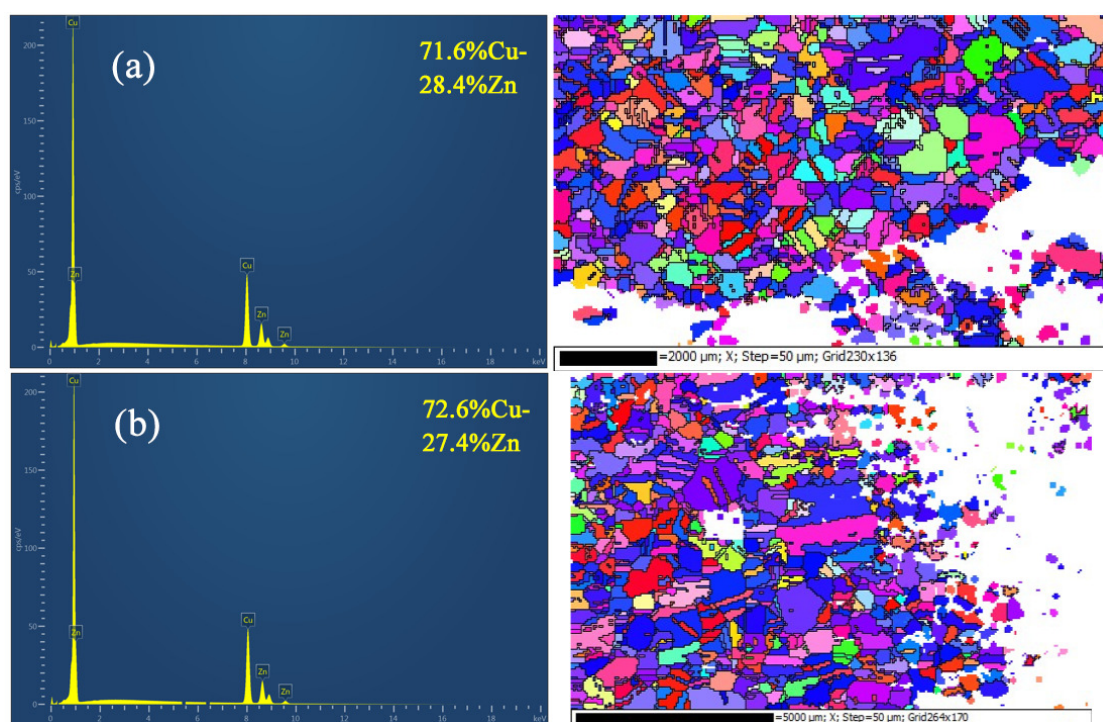


Figure 2.8: EDX analysis (on left side) on the bottom surface of  $\alpha$ -Brass sample after heat treatment in argon environment with a sandwich structure protection and its EBSD measurement (on right side) (a) at 700°C for 45 h and (b) at 750°C for 4 days.

Based on all the previous experiments, the third system was designed as shown in Figure 2.5 (c). The sample was stored in a closed ceramic box with the upper cover not touching the sample, but as close as possible to the upper surface of sample. The system was still in the argon environment. This system should reduce the dezincification without destroying the microstructure. Furthermore, in order to get recrystallization, the temperature of heat treatment was set to be 980°C during a short period of time. As this temperature is higher than the liquefaction temperature of the studied material, there should be recrystallization during the cooling process. Meanwhile the period of heat treatment is set to be short, so the sample can be kept in its original form. The results of EDX analysis and EBSD measurement on the bottom surface are shown in Figure 2.9 for the heat treatment of 1 min. It was found that the chemical composition was 69.9% of Cu and 30.1% of Zn which is nearly the same as the original chemical composition 70%Cu-30%Zn. Thus the dezincification is successfully suppressed. Based on the microstructure analysis, the grain size successfully increases compared to other systems. In particular, the length of GBs is about 1 ~ 2 mm, which is long enough for the present experiment.

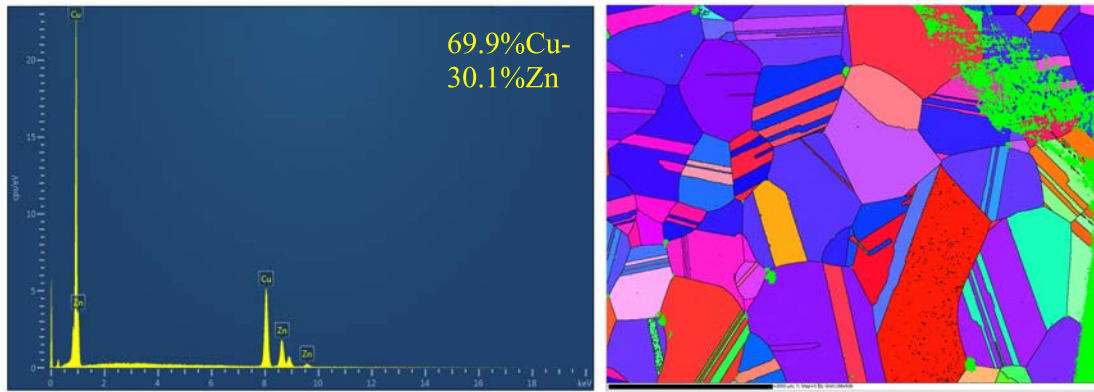


Figure 2.9: EDX analysis (on left side) on the bottom surface of  $\alpha$ -Brass sample after heat treatment at 980°C for 1 min in argon environment within closed ceramic box protection and its EBSD measurement (on right side).

At the same time, a heat treatment at 980°C during 15 min was also tried and the result is presented in Figure 2.10. It was found that the grain size is larger compared to the 1 min treatment, but the GBs are not clear and not straight due to excessive melting. Thus, this heat treatment cannot be used for the present experiment. As a conclusion, the chosen heat treatment of  $\alpha$ -Brass is at 980°C during 1 min in a closed box with the upper cover not touching the upper surface of sample within argon environment at atmospheric pressure.

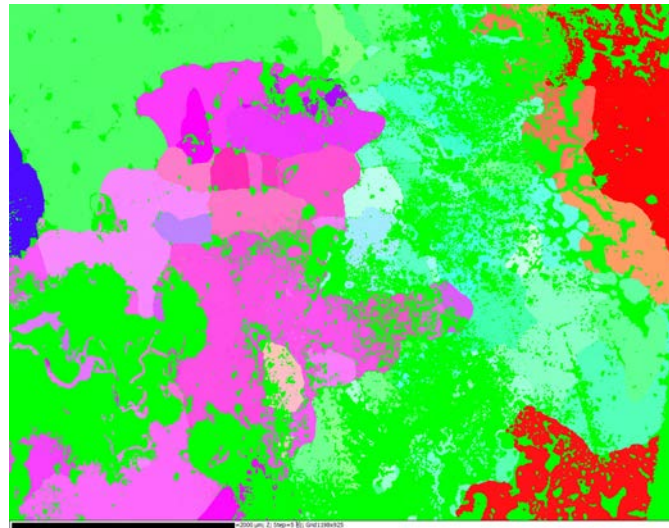


Figure 2.10: EBSD measurement on the bottom surface of  $\alpha$ -Brass sample after heat treatment at 980°C for 15 min in argon environment within closed ceramic box protection.

After the heat treatment, Ni and  $\alpha$ -Brass samples were mechanically polished

again until getting a “mirror surface”. At the end, the samples were electropolished at a voltage of 24V for 20s. The electrolyte for Ni is composed of 65~86% Ethanol, 10~15% 2-Butoxyethanol and 5~15% water, while for  $\alpha$ -Brass, it is composed of 15~35% Phosphoric acid, 15~25% Ethanol, <10% Propane-1-OL, <1% urea and 50~70% water. At the end, the GBs can be clearly observed under optical microscopy.

### 2.3.3 Grain boundary choice

The orientation of each grain was measured by EBSD in a SEM. It was carried out with a high resolution camera from Oxford Instruments in Zeiss Sigma VP SEM. For the acquisition of the orientation maps, the SEM was set with a 20 kV acceleration voltage, a working distance of 15 mm. The sample was tilted 70° with respect to the axis of the incident beam. Orientation maps were acquired with a spatial step size of 20  $\mu\text{m}$ . The orientation of a grain is given by the Euler angles  $(\phi_1, \Phi, \phi_2)$  defined according to the notation of Bunge [275]. The angular resolution of the EBSD orientation measurements and the array orientation variation within each grain produces a maximum variation of  $\pm 1^\circ$  in the Euler angle measurements. Data processing was performed by Flamenco Channel 5 software (HKL Technology) with the indexing rate always greater than 99%. The microstructures of the sample were represented by inverse pole figures (IPF) as shown in Figures 2.11. The GBs are marked as black lines in the EBSD orientation mapping and correspond to misorientation angle between adjacent pixels higher than  $2^\circ$ . In that case, the main GB can be detected and avoid the detection of small sous-grains.

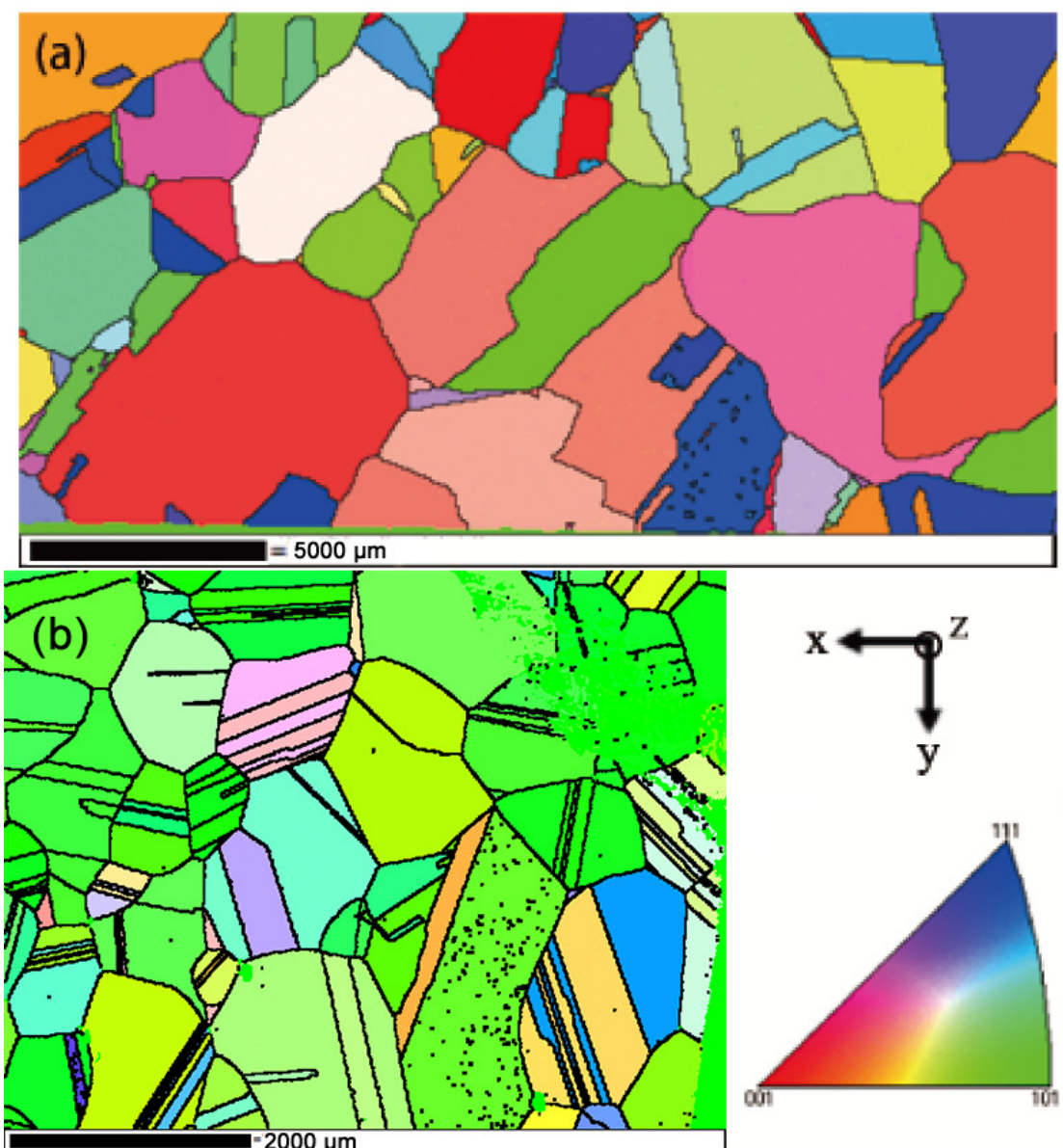


Figure 2.11: EBSD orientation mapping of the macroscopic sample: (a) Ni and (b)  $\alpha$ -Brass. The orientations are given in the IPF in the direction of Z axis which is perpendicular to upper surface. The black lines represent GBs and correspond to misorientation angles between adjacent pixels higher than  $2^\circ$ .

Based on orientation of each grain, the interesting GBs in the present study were chosen from the following conditions with the surface configuration presented in Figure 2.12:

- GB is or is close to be perpendicular to the upper surface.

- With a mechanical loading parallel to GB plane, for the target grain, the Burgers vector of the slip system with the maximum Schmid factor must not be perpendicular to GB. Meanwhile the slip plane of this slip system must not be parallel to the upper surface. These conditions ensure that the Burgers vector has a component perpendicular to the upper surface where AFM measurements will be performed.

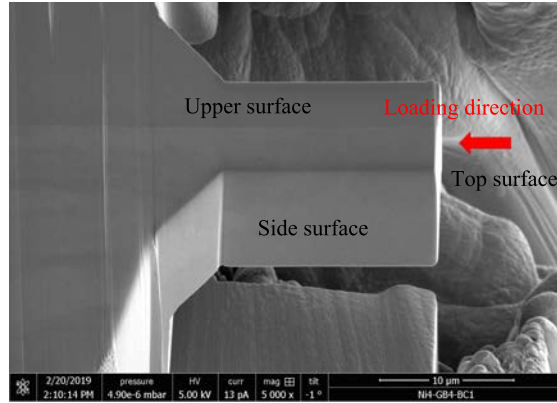


Figure 2.12: The upper surface is defined as the surface containing the GB where AFM measurements will be performed. The top surface is the one contacted by the flat punch during the compression test. The side surface is the lateral surface which does not contain the GB.

Then, it is better that the ratio between the maximum Schmid factor and the second maximum Schmid factor is higher than 1.1 in order to get a high probability to only activate single slip at low strain. Furthermore, when considering incompatibility stresses due to heterogeneous anisotropic elasticity [160] (see Eqs. 1.44 and 1.45 in subsection 1.5.2.4 of Chapter 1), the most favourable active slip system can be different from the one predicted by a simple Schmid analysis. This condition can be used to identify the effect of incompatibility stresses. Thus, twin GBs are disregarded in the present study as there is no elastic incompatibility stresses if type-I twin boundaries are parallel or perpendicular to the loading axis [276].

Based on all the above conditions, several GBs were chosen. However, due to a matter of time, only one GB of each material was used to analyze the distribution of dislocations in single slip and slip transmission. These GBs are presented in Figure 2.14 and 2.15.

### 2.3.4 Micro-beam preparation

The macro-sample was cut into pieces containing the interesting GB by EDM (electrical discharge machining). The side surface of small piece was mechanically

polished in order to make the GB close and parallel to side surface which is helpful for FIB cutting. During the FIB process, the top surface should indeed be polished from two sides in order to ensure that it is perpendicular to the upper surface. Only in that case, it is a pure compression test. If not, there will be some bending stresses. In the present thesis, it is crucial to have a pure compression in order to get the precise loading stresses which will be used in the simulations. In order to do that, the mechanical polishing was stopped when the distance between GB and side surface was reduced to about 1 mm in order to prevent GB damage. Then, this side surface was polished again by ion slicing technique with low energy  $\text{Ar}^+$  ions in the IM4000 system until the distance from GB to side surface was reduced to about  $40 \mu\text{m}$  as shown in Figure 2.13.

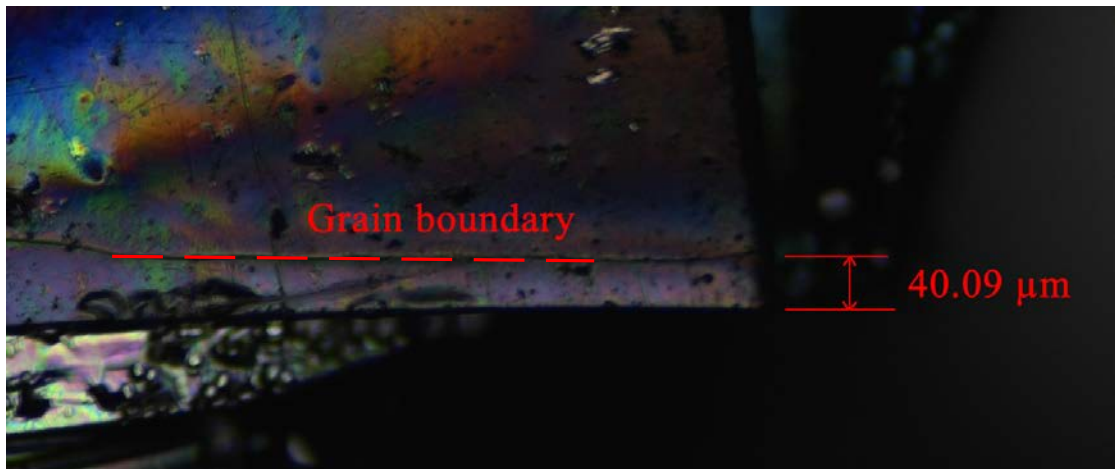


Figure 2.13: After ion milling, the GB was close to the side surface of Ni sample with a distance  $40.09 \mu\text{m}$ .

Finally the pre-prepared sample was cut into a micro-beam with length of about  $16 \mu\text{m}$ , width of about  $8 \mu\text{m}$  and thickness of about  $8 \mu\text{m}$  by FIB with FEI Versa 3D Dual Beam system using ion beam currents of  $15 \text{ nA}$  for rough cutting and  $1 \text{ nA}$  at  $30 \text{ kV}$  for fine polishing as shown in Figure 2.14 (c) for Ni and in Figure 2.15 (c) for  $\alpha$ -Brass. The orientations of the bi-crystal were acquired again by EBSD with a spatial step resolution of  $0.1 \mu\text{m}$ . Data processing was performed by AZtec software with an indexing rate greater than  $99\%$ . The microstructures of the micro-beam are presented by IPF in Figure 2.14 (a-b) for Ni and in Figure 2.15 (a-b) for  $\alpha$ -Brass.

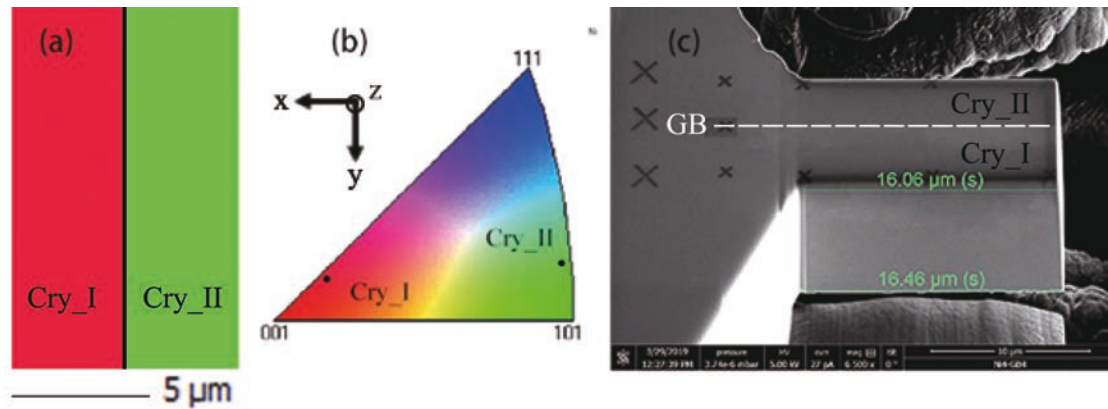


Figure 2.14: (a) EBSD mapping of Ni bi-crystal, orientation of crystal I:  $\phi_1^I = 63.8^\circ$ ,  $\Phi^I = 14.3^\circ$ ,  $\phi_2^I = 18.6^\circ$ , orientation of crystal II:  $\phi_1^{II} = 331.1^\circ$ ,  $\Phi^{II} = 9.0^\circ$ ,  $\phi_2^{II} = 75.1^\circ$ . (b) The crystallographic orientations of both crystals, Cry\_I and Cry\_II, are given on the standard IPF in the direction of y-axis which is parallel to GB and is also the loading direction of the compression test. (c) SEM micrograph of a micro-beam containing GB cut by FIB. The average length of micro-beam is about  $15.46 \mu\text{m}$  and the average section area is about  $71.80 \mu\text{m}^2$  with  $46.67 \mu\text{m}^2$  for crystal I and  $25.13 \mu\text{m}^2$  for crystal II. The GB inclination angle is  $0^\circ$  as defined in Figure 2.17.

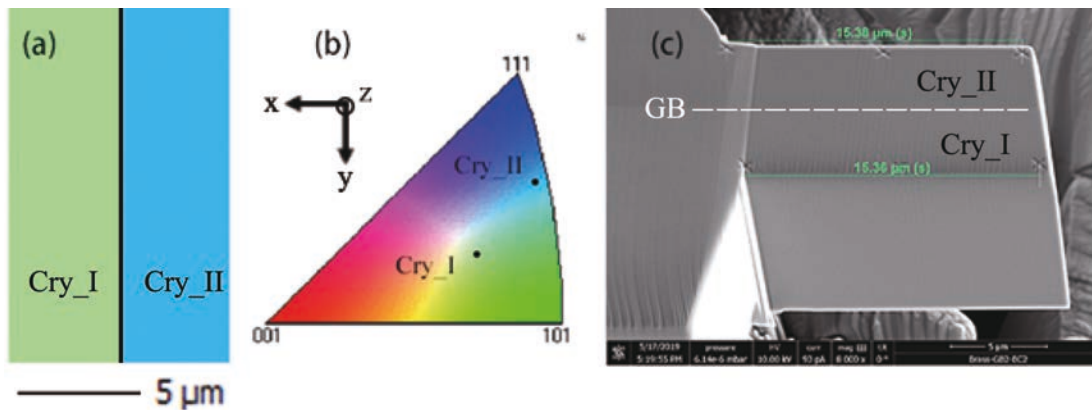


Figure 2.15: (a) EBSD mapping of  $\alpha$ -Brass bi-crystal, orientation of crystal I:  $\phi_1^I = 27.7^\circ$ ,  $\Phi^I = 35.7^\circ$ ,  $\phi_2^I = 66.1^\circ$ , orientation of crystal II:  $\phi_1^{II} = 219.5^\circ$ ,  $\Phi^{II} = 28.4^\circ$ ,  $\phi_2^{II} = 2.4^\circ$ . (b) The crystallographic orientations of both crystals, Cry\_I and Cry\_II, are given on the standard IPF in the direction of y-axis which is parallel to GB and is also the loading direction of the compression test. (c) SEM micrograph of a micro-beam containing GB cut by FIB. The average length of micro-beam is about  $15.37 \mu\text{m}$  and the average section area is about  $88.91 \mu\text{m}^2$  with  $42.02 \mu\text{m}^2$  for crystal I and  $46.89 \mu\text{m}^2$  for crystal II. The GB inclination angle is  $6.4^\circ$  as defined in Figure 2.17.

It should be pointed out that even with small ions density of  $\text{Ga}^+$  at the end of FIB polishing, there ions still created scratches within nanometers on the surface



of Ni micro-beam as presented in Figure 2.16 by SEM with high magnification.

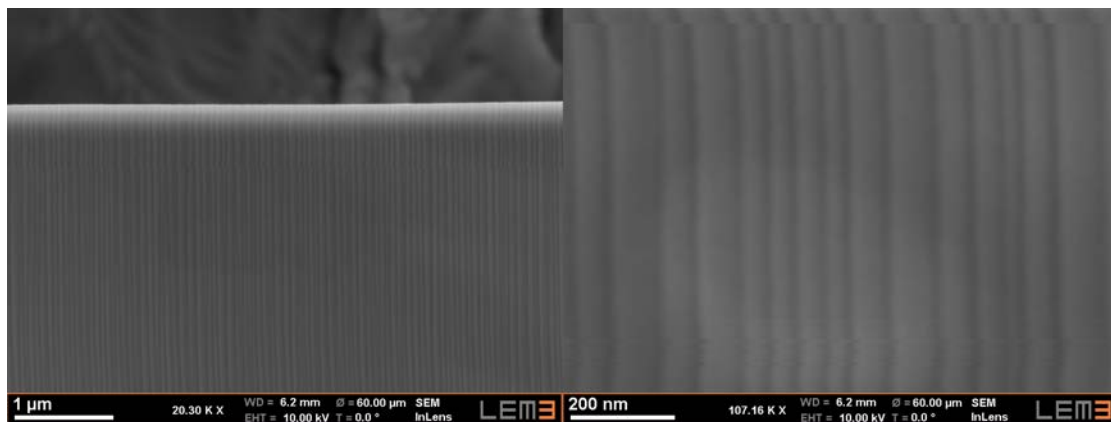


Figure 2.16: SEM micrograph with high magnification on the surface of Ni micro-beam after FIB fine polishing. It shows there are scratches produced by  $\text{Ga}^+$  ions.

## 2.4 Preanalyses of slip information

Based on the local crystalline orientation, the mechanical and geometrical information of each slip system in the studied grain were firstly analyzed. The slip analysis results for Ni and  $\alpha$ -Brass sample are presented in Table 2.1 and Table 2.2, respectively. The results include the Burgers vector presented in sample coordinates (see Figure 2.17), the unit normal vector of slip plane, the Schmid factor, the resolved shear stress normalized by applied stress considering elastic incompatibility stresses [160] (see Eqs. 1.44 and 1.45 in Chapter 1), the angle between slip line and GB line on the upper surface  $\theta_{\text{Up}}$  (see Figure 2.17), the angle between slip line and the upper edge of sample on the side surface  $\theta_{\text{Side}}$  (see Figure 2.17), the image force on a dislocation located at a distance  $5|\mathbf{b}|$  from GB due to misorientation effect in bi-crystal configuration with perfect planar GB (see subsection 3.1 in Chapter 3) and the transmission factor based on Eq. 1.26 in Chapter 1 with the corresponding slip system in the adjoining grain. The analysis of Schmid factor and resolved shear stress can be used to predict the primarily active slip system (with the maximum Schmid factor or the maximum resolved shear stress) with compressive loading. In some cases, the primarily active slip system with maximum Schmid factor can be different from the one when considering incompatibility stresses [121]. Furthermore, combining the analysis of Burgers vector and normal vector of slip plane can be used to choose the interesting GB as described in subsection 2.3.3. After the mechanical tests, the activated slip lines can be observed by SEM picture (see Figures 2.22 (a) and 2.23 (a)) and by AFM measurement (see Figures 2.25 and 2.27). Then, the two angles with slip

line  $\theta_{Up}$  and  $\theta_{Side}$  can be experimentally determined as shown in Figure 2.22 (a) right for Ni sample and in Figure 2.23 (a) right for  $\alpha$ -Brass sample. By comparing these angles to the theoretical analyses as described in Table 2.1 and 2.2 which are also schematically presented in Figure 2.22 (b) and 2.23 (b), the active slip plane can be identified. The image force presented in Table 2.1 and 2.2 indicates the misorientation effect on dislocation behavior which will be deeply discussed in subsection 4.2.4 of Chapter 4. As a simple summary, the negative image force indicates the repulsive misorientation effect which means the dislocation is repelled by the GB. On the contrary, the positive image force indicates the attractive misorientation effect and thus the dislocation is attracted by the GB. With a positive image force, as the dislocation is attracted by the GB, it is easier to get dislocation transfer across the GB. Furthermore, in combination with transmission factor, the dislocation transfer can be more comprehensively predicted.

For the present experiment, the interesting grain for Ni sample is the crystal II and for  $\alpha$ -Brass sample is the crystal I. For these two interesting GBs, the primarily active slip system is always the same either considering a simple Schmid analysis or considering the incompatibility stress formula as marked in red in Table 2.1 for Ni and in Table 2.2 for  $\alpha$ -Brass sample. However, for  $\alpha$ -Brass sample, combining the analyses of Schmid factor and incompatibility stresses, the mainly observed slip lines in crystal I was determined as the slip system A6 which is marked in blue in Table 2.2.

Crystal I of Ni								
Slip system [40]	Burgers vector (nm)	Unit normal vector of slip plane	Schmid factor	RSS/IS* <sup>1</sup>	$\theta_{Up}$ (°)	$\theta_{Side}$ (°)	Image force (N/m)* <sup>2</sup>	MTF/CSS* <sup>3</sup>
A2	[0.04; 0.21; 0.13]	[-0.56; 0.51; -0.65]	0.0910	0.0246	132.16	40.98	-0.0075	0.8129/C5
A3	[-0.15; 0.06; 0.18]		0.3500	0.2960			0.0196	0.8919/C3
A6	[0.19; 0.15; -0.06]		0.4410	0.3205			0.0133	0.7393/C1
B2	[0.04; 0.21; 0.13]	[-0.58; -0.35; 0.74]	0.0929	0.1054	58.87	142.12	-0.0035	0.8635/B5
B4	[0.19; 0.011; 0.16]		0.4461	0.3624			0.0162	0.8892/B2
B5	[-0.15; 0.19; -0.03]		0.3532	0.2570			0.0084	0.8435/B4
C1	[0.00; 0.13; -0.21]	[-0.70; -0.60; -0.38]	0.0051	0.0419	49.30	61.63	-0.0121	0.9179/C1
C3	[-0.15; 0.06; 0.18]		0.4355	0.3354			0.0077	0.9594/C3
C5	[-0.15; 0.19; -0.03]		0.4304	0.2935			-0.0002	0.7803/C5
D1	[0.00; 0.13; -0.21]	[-0.44; 0.77; 0.47]	0.0032	0.0390	150.26	137.01	-0.0110	0.7801/B4
D4	[0.19; 0.01; 0.16]		0.3394	0.2689			0.0065	0.8984/B2
D6	[0.19; 0.01; 0.16]		0.3394	0.2689			0.0065	0.8984/B2
Crystal II of Ni								
Slip system [40]	Burgers vector (nm)	Unit normal vector of slip plane	Schmid factor	RSS/IS* <sup>1</sup>	$\theta_{Up}$ (°)	$\theta_{Side}$ (°)	Image force (N/m)* <sup>2</sup>	MTF/CSS* <sup>3</sup>
A2	[-0.15; -0.11; -0.17]	[0.09; -0.86; 0.51]	0.0536	0.1087	6.11	10.27	0.0042	0.7108/A2
A3	[0.10; -0.11; -0.20]		0.0373	0.0051			0.0010	0.8250/A3
A6	[-0.25; -0.01; 0.03]		0.0909	0.1138			-0.0329	0.7049/A6
B2	[-0.15; -0.11; -0.17]	<b>[0.73; 0.07; -0.68]</b>	0.4263	0.5068	<b>95.09</b>	<b>133.01</b>	-0.0052	0.8984/D4
<b>B4</b>	<b>[0.15; -0.13; 0.15]</b>		<b>0.4377</b>	<b>0.5270</b>			<b>0.0103</b>	<b>0.8435/B5</b>
B5	[0.00; -0.25; -0.02]		0.0113	0.0202			0.0062	0.8635/B2
C1	[-0.10; -0.14; 0.18]	[0.89; -0.02; 0.46]	0.3468	0.4131	88.56	62.62	0.0140	0.9179/C1
C3	[0.10; -0.11; -0.20]		0.3606	0.4269			-0.0096	0.9594/C3
C5	[0.00; -0.25; -0.02]		0.0138	0.0137			0.0041	0.8129/A2
D1	[-0.10; -0.14; 0.18]	[0.07; 0.77; 0.63]	0.0259	0.0151	175.07	5.97	0.0098	0.6515/A6
D4	[0.15; -0.13; 0.15]		0.0398	0.0950			-0.0049	0.6161/B5
D6	[-0.25; -0.01; 0.03]		0.0658	0.0799			-0.0416	0.6715/A6

Table 2.1: Slip analyses of Ni micro-beam. The compressive direction is along X, the GB normal along Y and the upper face normal along Z as presented in Figure 2.17.

Crystal I of $\alpha$ -Brass								
Slip system [40]	Burgers vector (nm)	Unit normal vector of slip plane	Schmid factor	RSS/IS*1	$\theta_{Up}$ (°)	$\theta_{Side}$ (°)	Image force (N/m)*2	MTF/CSS*3
A2	[0.07; 0.22; -0.10]	<b>[-0.86; 0.41; 0.30]</b>	0.2339	0.2075	<b>115.22</b>	<b>109.00</b>	0.0229	0.7850/B5
A3	[-0.06; 0.05; -0.24]		0.2010	0.1073			-0.0248	0.7433/C1
<b>A6</b>	<b>[0.13; 0.17; 0.14]</b>		<b>0.4349</b>	<b>0.3148</b>			<b>-0.0213</b>	<b>0.7750/B2</b>
B2	[0.07; 0.22; -0.10]	[-0.11; -0.39; -0.91]	0.0305	0.0522	16.08	7.04	-0.0107	0.7253/B5
B4	[0.25; 0.05; -0.05]		0.1086	0.0218			0.0057	0.9287/A6
B5	[-0.18; 0.18; -0.05]		0.0781	0.0740			0.0012	0.7785/D4
C1	[-0.12; 0.13; 0.19]	<b>[-0.71; -0.70; 0.02]</b>	0.3262	0.3366	<b>45.20</b>	<b>91.97</b>	0.0029	0.9197/C3
C3	[-0.06; 0.05; -0.24]		0.1650	0.0084			-0.0097	0.8949/C1
<b>C5</b>	<b>[-0.18; 0.18; -0.05]</b>		<b>0.4913</b>	<b>0.3450</b>			<b>0.0064</b>	<b>0.7182/C5</b>
D1	[-0.12; 0.13; 0.19]	[-0.27; 0.72; -0.64]	0.1228	0.1813	159.65	22.64	0.0053	0.9214/A3
D4	[0.25; 0.05; -0.05]		0.2573	0.1376			-0.0009	0.9417/D6
D6	[0.13; 0.17; 0.14]		0.1345	0.0437			0.0001	0.9326/A2
Crystal II of $\alpha$ -Brass								
Slip system [40]	Burgers vector (nm)	Unit normal vector of slip plane	Schmid factor	RSS/IS*1	$\theta_{Up}$ (°)	$\theta_{Side}$ (°)	Image force (N/m)*2	MTF/CSS*3
A2	[-0.18; -0.16; -0.07]	[0.22; -0.60; 0.77]	0.1578	0.3233	20.11	15.87	0.0010	0.9326/D6
A3	[0.05; -0.19; -0.16]		0.0460	0.0431			0.0042	0.9214/D1
A6	[0.24; -0.03; -0.09]		0.2038	0.2802			0.0032	0.9351/D4
B2	[-0.18; -0.16; -0.07]	[0.55; -0.26; -0.79]	0.3944	0.3717	64.19	145.40	-0.0133	0.7750/A6
B4	[0.19; -0.08; 0.16]		0.3992	0.3585			-0.0371	0.6673/A3
B5	[0.00; -0.24; 0.08]		0.0048	0.0132			0.0228	0.7850/A2
C1	[-0.05; -0.05; 0.25]	[0.97; 0.08; 0.22]	0.1954	0.0783	94.97	77.13	-0.0195	0.8949/C3
C3	[0.05; -0.19; -0.16]		0.2040	0.1278			0.0116	0.9197/C1
C5	[0.00; -0.24; 0.08]		0.0085	0.0495			-0.0020	0.7833/A2
D1	[-0.05; -0.05; 0.25]	[0.20; 0.95; 0.25]	0.0412	0.0299	167.81	39.88	-0.0072	0.7006/D1
D4	[0.19; -0.08; 0.16]		0.1492	0.2738			0.0041	0.7785/B5
D6	[0.24; -0.03; -0.09]		0.1904	0.2439			-0.0011	0.9417/D4

Table 2.2: Slip analyses of  $\alpha$ -Brass micro-beam. The compressive direction is along X, the GB normal along Y and the upper face normal along Z as presented in Figure 2.17.

\*1 RSS: Resolved shear stress normalized by applied stresses when considering elastic incompatibility stresses (IS) [160].

\*2 Image force at a distance  $5|\mathbf{b}|$  from GB due to misorientation effect in bi-crystal configuration with perfect planar GB which is deeply discussed in subsection 3.1 of Chapter 3.

\*3 MTF: Maximum transmission factor based on Eq. 1.26 in Chapter 1 with corresponding slip system (CSS) [40] in the adjacent grain.

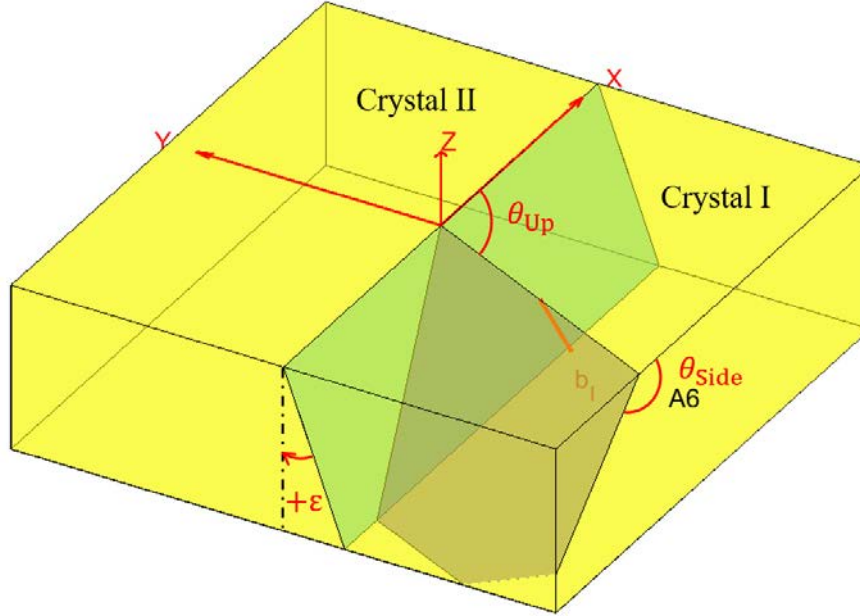


Figure 2.17: Schematic presentation of slip line analyses. The sample coordinates are set as  $y$  perpendicular to GB line on the upper surface pointing to crystal II,  $z$  perpendicular to the upper surface and  $x = y \times z$  parallel to the GB line. The angle between slip line and GB line in positive  $x$  direction on the upper surface is noted as  $\theta_{Up}$ . The angle between slip line and the upper edge of sample in positive  $x$  direction on the side surface is noted as  $\theta_{Side}$ . The inclination angle of GB is noted as  $\epsilon$ .

## 2.5 Micro-pillar compression tests

The in-situ compression tests were carried out in high vacuum at room temperature in a Carl Zeiss  $\Sigma$ IGMA series SEM, by an in-situ nanoindenter (UNAT-SEM II) as shown in Figure 2.18 (a) which has a load noise floor level about 0.002 mN. The micro-beams were compressed by a flat punch of polycrystalline tungsten carbide (WC). Furthermore, in order to well control the orientation of micro-beam for a pure compression test, such as the loading direction parallel to GB and the top surface of sample perpendicular to flat punch, an additional rotation stage for sample holder which can perform rotations in two dimensions was developed as shown in Figure 2.18 (b). This stage is controlled by an Arduino board (Single-board microcontroller) as presented in Figure 2.18 (c). Indeed, the original sample holder can only rotate in one direction. However, it needs to perform three dimensional rotations to correctly position the micro-beam relative to the flat punch. Therefore, combining the original rotation stage with only one degree of freedom, a complementary rotation stage with two degrees of freedom can achieve this goal.

This stage can be used for in-situ mechanical tests. All the compression tests were carried out in displacement controlled mode with several cycles of loading and unloading with small increment as shown in Figure 2.19. The idea of loading and unloading cycles is to have enough time to make a SEM picture of high quality in order to observe the slip lines. Once slip lines were observed or yield stress was reached, the compression test was stopped during the unloading step in order to prevent from the tip shock. The average loading strain rate was about  $0.002 \text{ s}^{-1}$  for Ni and  $0.00133 \text{ s}^{-1}$  for  $\alpha$ -Brass. The loading force and corresponding displacement were recorded during the mechanical test, so that the stress-strain curve can be calculated after the test. Even though the loading was cyclic with small increments, the mechanical test was stopped when the first slip event was activated (slip lines were observed in SEM or yield stress was reached). Thus, only the last cycle (marked as red line in Figure 2.19) contributes to plastic deformation, and all the previous cycles are only in the elastic state.

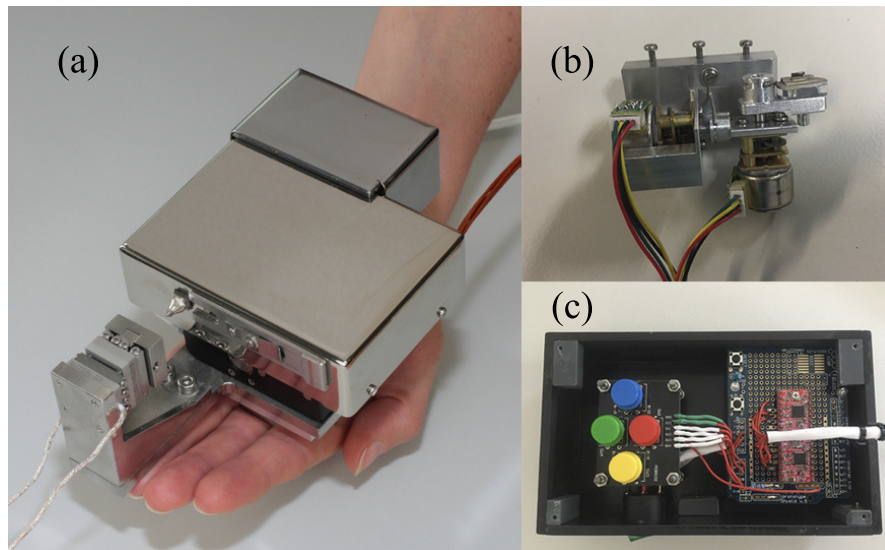


Figure 2.18: (a) In-situ nanoindenter UNAT-SEM II, (b) the developed rotation stage which can perform rotations in two dimensions and (c) the control system with an Arduino board (Single-board microcontroller) of the developed rotation stage.

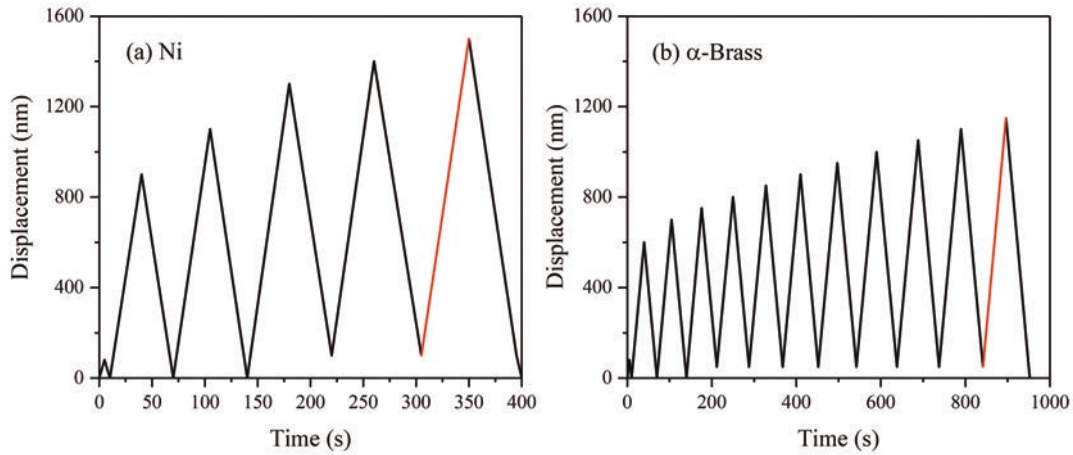


Figure 2.19: Loading curve with displacement control mode for the compression tests of (a) Ni and (b)  $\alpha$ -Brass. Only red lines contribute to plastic deformation, and all the previous cycles are only in the elastic state.

## 2.6 Stress-strain analysis

Figure 2.20 shows the stress-strain curves of the compression test for Ni and  $\alpha$ -Brass. The yield point occurs at about 8.5% strain for Ni and 6.3% for  $\alpha$ -Brass from experimental measurement. These strains are too large for yield point of metals. This error comes from the drift of the tip during the compression test, where the displacement measurement is not accurate, but the force measurement is accurate.

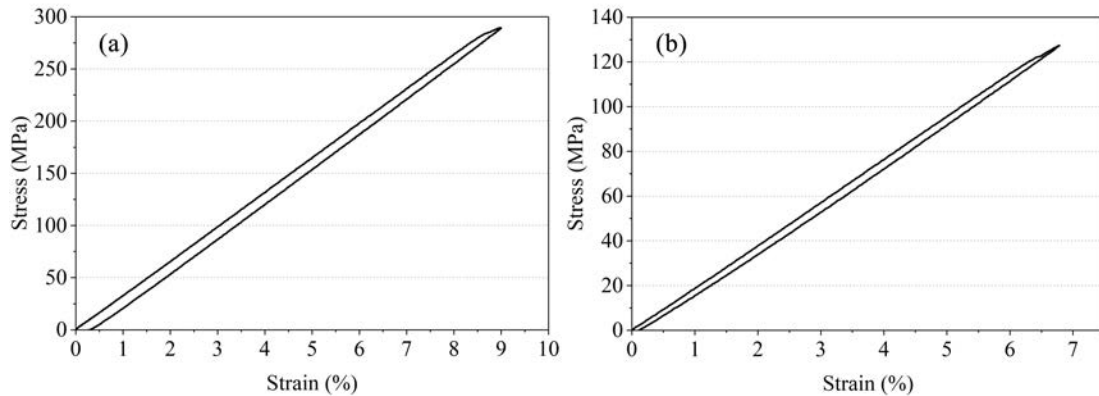


Figure 2.20: Experimental measurement of stress-strain curves for (a) Ni micro-beam and (b)  $\alpha$ -Brass micro-beam.

Therefore, the experimental measured stress-strain curves were calibrated by crys-

tal plasticity finite element method (CPFEM) simulation which are described in section 4.3 of Chapter 4. The compression tests of the same experimental configuration were performed for both Ni and  $\alpha$ -Brass samples, then the strain was calibrated by having the same slope of the stress-strain curves in elastic part. After the calibration, the yield point occurs at the strain about 0.33% for Ni and 0.24% for  $\alpha$ -Brass which are reasonable for metallic material. The applied stress at the final state of compression is about 289.4 MPa for Ni and 127.4 MPa for  $\alpha$ -Brass.

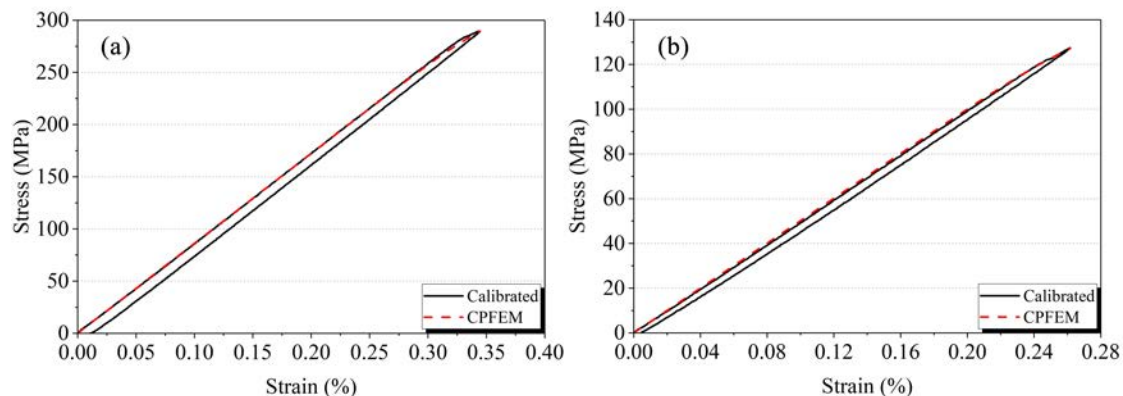


Figure 2.21: Stress-strain curves calibrated by CPFEM for (a) Ni micro-beam and (b)  $\alpha$ -Brass micro-beam.

## 2.7 Slip analysis by SEM and AFM

After the in-situ compression test, the slip lines were firstly analyzed in SEM. Figure 2.22 (a) and Figure 2.23 (a) show the observed slip lines in SEM for Ni and for  $\alpha$ -Brass, respectively. For Ni, the slip lines are very weak on the upper surface and there are only two obvious slip lines in parallel for each crystal. Based on the direction of slip lines on the upper surface and the Schmid factor analysis with local crystalline orientation as described in Table 2.1, the active slip system is determined to be the slip system with maximum Schmid factor or result from incompatibility stress [160] B4 for each crystal as shown in Figure 2.22 (b).



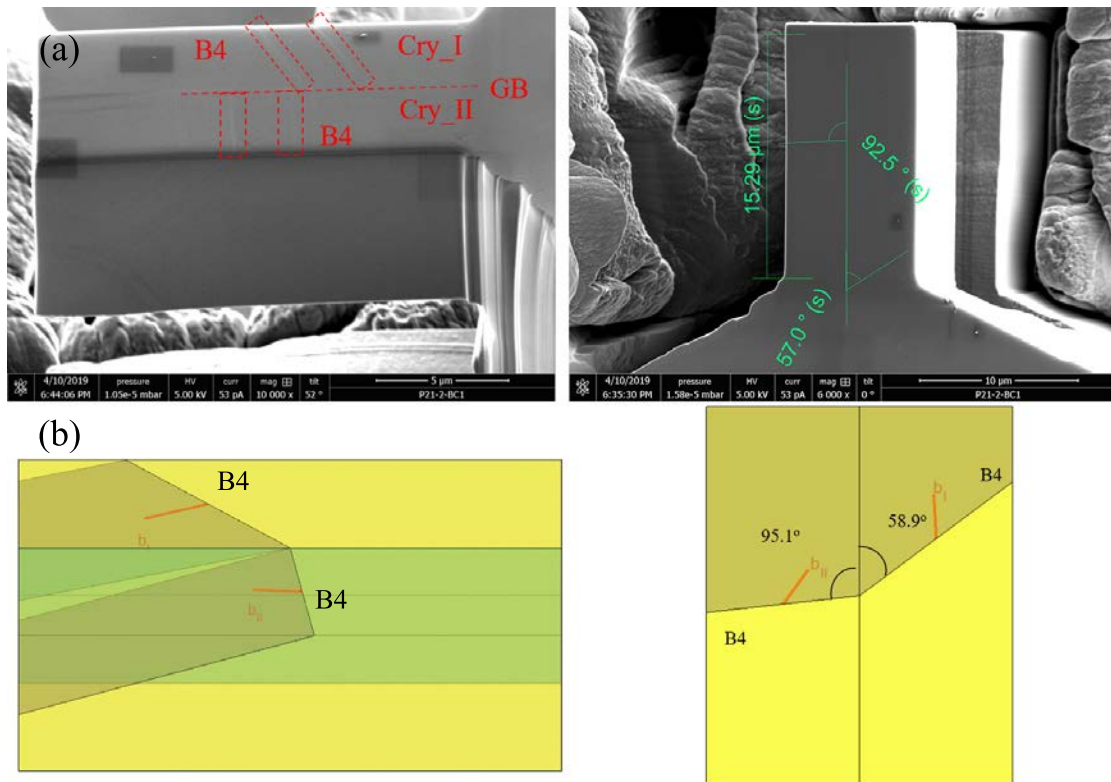


Figure 2.22: Crystallographic analysis of slip lines from SEM picture for Ni sample after compression test. Based on the direction of slip lines, the orientation of each crystal and the Schmid factor (or the incompatibility stress) analysis, the activated slip system is determined as B4 for crystal I and B4 for crystal II.

However, for  $\alpha$ -Brass, there are two obvious slip lines with interaction on the upper surface for crystal I and two obvious slip lines with interaction on the side surface for crystal II. Based on the analysis of the direction of slip lines and the Schmid factor (or the incompatibility stress) for each slip system as described in Table 2.2, the active slip systems are determined as A6, C5 for crystal I and B4, D6 for crystal II as shown in Figure 2.23 (b). Thus there are multiple active slip systems in both grains of the  $\alpha$ -Brass sample.

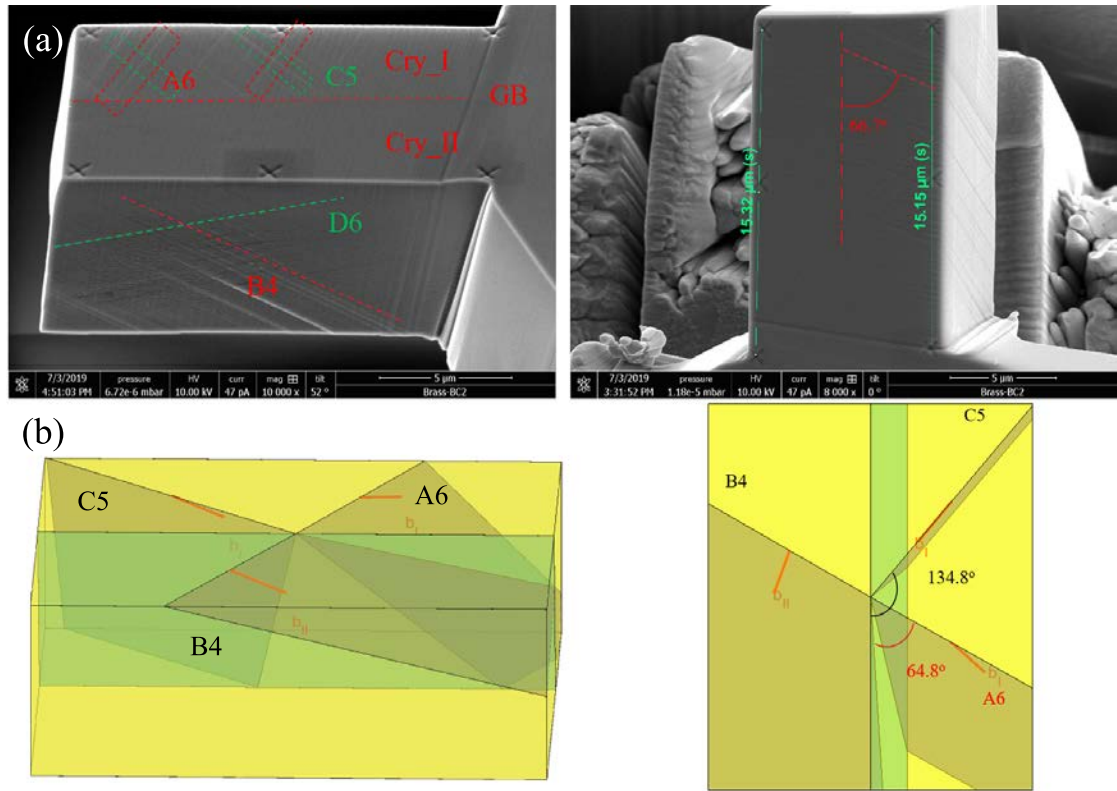


Figure 2.23: crystallographic analysis of slip lines from SEM picture for  $\alpha$ -Brass sample after compression test. Based on the direction of slip lines, the orientation of each crystal and the Schmid factor (or the incompatibility stress) analysis, the activated slip system is determined as A6 and C5 for crystal I and B4 for crystal II.

Then, an AFM measurement was performed on the upper surface by Dimension FastScan with ScanAsyst (BRUKER) with height sensor, so that the 3D topography of slip lines can be obtained and used to analyze dislocations distributions. The step size of scan was 30 nm with a scan rate of 1 Hz. The results were analyzed by NanoScope Analysis. They were first of all flattened by polynomial fit of the second order, and then they were treated by a median filter with  $9 \times 9$  matrix operation. Figure 2.24 and Figure 2.26 show the 3D topography of slip lines of Ni sample and of  $\alpha$ -Brass sample, respectively. The steps of slips are corresponding to the slip lines presented in SEM picture (Figure 2.22 for Ni and 2.23 for  $\alpha$ -Brass). For Ni sample, a slip step with classic features of dislocation pile-ups was selected for analyze. The heights of the top line and the bottom line of this step were measured along the slip direction from GB which are marked as red line and black line in the Figure 2.24, respectively. The measured data was fitted by the polynomial method which is marked as  $h^{Top}$  and  $h^{Bottom}$ . Then the relative height of this step  $\Delta h$  was calculated as the difference of the fitted height between

these two lines as shown in Figure 2.25. It is found that the difference of height between two lines at GB  $\Delta h_{GB} \approx 0.86$  nm is not zero, which corresponds to a weak slip transmission as observed in Figure 2.24 (b) circled by the frame with red dash. The slip step height increases from GB along the slip direction and gets its maximum value  $\Delta h \approx 9.06$  nm at about  $d \approx 3.28$   $\mu\text{m}$ . Furthermore, a GB sliding event is found at the top part of the beam which is presented in Figure 2.24 (a) as the hump part and in Figure 2.24 (b) circled by the frame with green dash dot.

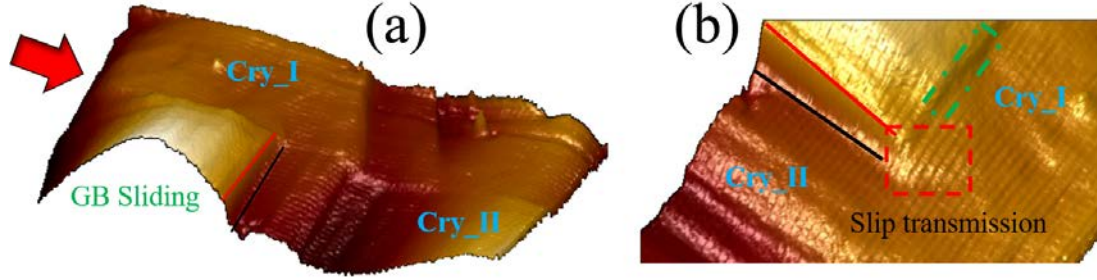


Figure 2.24: AFM topographic measurement of Ni for (a) the whole upper surface and (b) the transmission phenomenon at GB circled by the frame with red dash. The red arrow indicates the loading direction. The hump part in the second crystal shown in (a) and the frame with green dash dot shown in (b) indicate GB sliding.

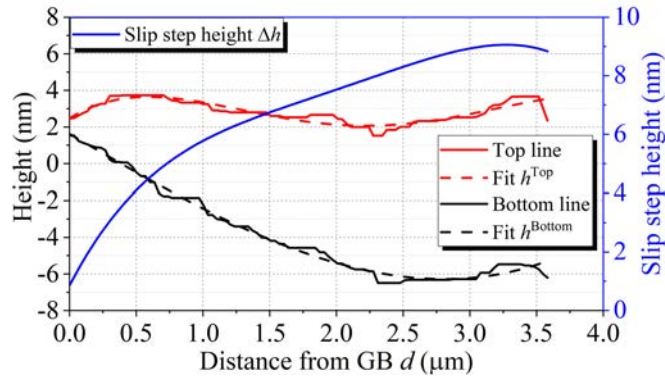


Figure 2.25: Results of slip step height measurement for Ni sample: red and black solid line indicate the measured height of top line and the bottom line of the step, respectively. The dash lines with corresponding color indicate the fitting results by polynomial method with the determinate coefficient  $R^2 = 0.8176$  for top line and  $R^2 = 0.9898$  for bottom line. The blue line indicates the simulated slip step height.

A similar analysis was realized for  $\alpha$ -Brass sample as shown in Figure 2.27. While the slip transmission is more intense compared to Ni sample as  $\Delta h_{GB} \approx 4.29$  nm, but the propagation of dislocations in adjoining grain has a short distance.

The maximum of slip step height is  $\Delta h \approx 10.03$  nm at about  $d \approx 2.44$   $\mu\text{m}$ . There is an obvious peak valley in the middle part of the curve of slip step height which might be caused by the intersect with another non coplanar slip line.

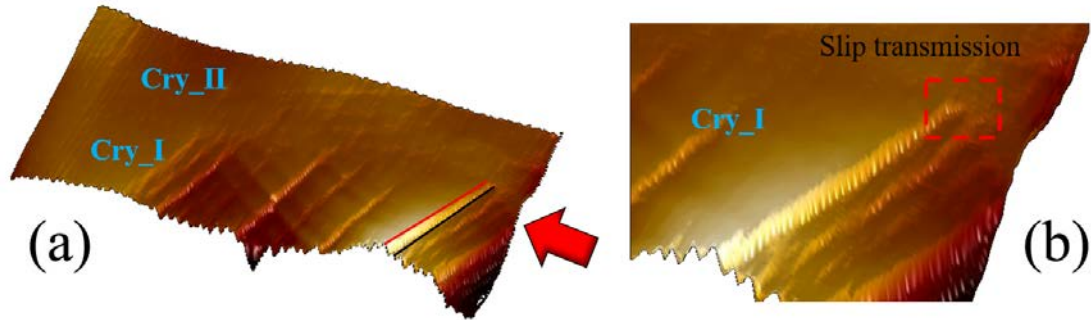


Figure 2.26: AFM measurement of  $\alpha$ -Brass for (a) the whole upper surface and (b) the transmission phenomenon at GB. The red arrow indicates the loading direction.

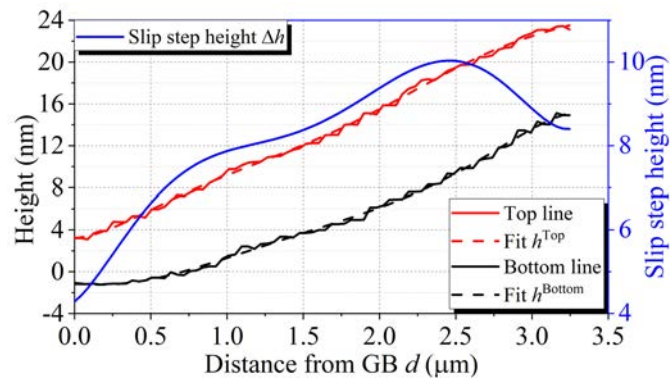


Figure 2.27: Results of slip step height measurement for  $\alpha$ -Brass sample: red and black solid line indicate the measured height of top line and the bottom line of the step, respectively. The dash lines with corresponding color indicate the fitting results by polynomial method with the determinate coefficient  $R^2 = 0.9982$  for top line and  $R^2 = 0.9973$  for bottom line. The blue line indicates the simulated slip step height.

# Chapter 3

## Elastic fields due to single dislocations and dislocation pile-ups in heterogeneous and anisotropic media

### 3.1 Introduction

In this chapter, an analytical approach based on the L-E-S formalism [20, 21, 22] is presented which provides the elastic fields of single straight dislocations in anisotropic homogeneous media, half-spaces, bi- [19] and tri-materials [17] while considering (or not) free surface effects [18]. The bi-material configuration is used to consider perfectly bonded and plane GB without thickness, and the tri-material configuration allows considering a non-zero thickness in the nanometer range and a specific elastic stiffness tensor for the GB region. All the interfaces are considered as perfect ones. Furthermore, the configuration with two free surfaces can be used to study size effects. The equilibrium positions of dislocations in a pile-up have been determined by minimizing the component of the Peach-Koehler (P-K) force along the slip direction for each dislocation with respect to a critical force [105]. The fact to lock or not the leading dislocation of a pile-up is especially discussed. At the end, the computational flow chart of the developed Matlab codes is presented and summarized. This numerical code using vectorial calculation can be used to compute the elastic fields due to single dislocation or dislocation pile-ups in all the configurations presented in this chapter for both anisotropic and isotropic heterogeneous elasticity. The major part of this chapter (without free surface effect described in subsection 3.2.5) are already published in International Journal of Solids and Structures in 2019 [277]. The numerical application of this

chapter will be presented in Chapter 4.

## 3.2 Elastic fields due to one single dislocation in different configurations

In the following, an infinite straight dislocation with Burgers vector  $\mathbf{b}$  and whose line unit vector  $\mathbf{t}$  is parallel to the  $\mathbf{x}_3$ -direction is considered at the position  $(X_1, X_2)$  as shown in Figure 3.1. Through the paper, the so-called FS/RH (Finish Start/Right Hand) convention [28] is used to define the direction of the dislocation line as shown in Figure 3.1. The idea of this section is to find the expression of the vector function  $\mathbf{f}$  (see subsection 1.5.3) for one single dislocation with different configurations.

### 3.2.1 Homogeneous anisotropic medium

In a homogeneous anisotropic medium, the function vector  $\mathbf{f}$  is derived by considering the boundary condition associated to the presence of the dislocation with Burgers vector  $\mathbf{b}$  in the absence of remotely applied force [21, 22]:

$$\int_{\mathcal{C}} d\mathbf{u} = \mathbf{b} \quad (3.1)$$

where  $\mathcal{C}$  is any closed curve (Burgers circuit) enclosing the position  $(X_1, X_2)$ . Following Suo [19], the displacement and stress function vectors can then be expressed as:

$$u_i = 2\text{Re} \left[ A_{i\bar{j}} f_{\bar{j}}^0(z_j) \right] \quad (3.2)$$

$$\Phi_i = 2\text{Re} \left[ B_{i\bar{j}} f_{\bar{j}}^0(z_j) \right] \quad (3.3)$$

The general form of the function vector  $f_j^0(z_i)$  is given by:

$$f_j^0(z_i) = \mathbf{q}_j^0 \ln(z_i - s_j) \quad (3.4)$$

where  $z_i = x_1 + p_i x_2$ ,  $s_j = X_1 + p_j X_2$  and  $\mathbf{q}^0$  is a complex vector expressed as:

$$\mathbf{q}^0 = -\frac{1}{2\pi} \mathbf{i} (\mathbf{B}^T \mathbf{b}) \quad (3.5)$$

where the  $\mathbf{A}$ ,  $\mathbf{B}$  matrices are the Stroh matrices introduced in subsection 1.5.3 of Chapter 1.

### 3.2.2 Heterogeneous anisotropic medium: bi-material

The general problem of anisotropic bi-materials and half-spaces with singularities like dislocations was firstly solved by Gemperlová, Tucker and co-workers [278, 279, 280], then by Tiwari et al. [281] followed by Suo [19] who used analytic continuation arguments. Ting [282], Ting and Barnett [283], Chu and Pan [284] used Green's function technique for anisotropic media [285]. All these methods provide identical solutions (see the proof in Appendix A). It is also noteworthy that many other researchers considered the particular case of an interfacial dislocation in a bi-material with applications to micromechanics problems including interfacial elasticity and interfacial cracks [286, 109, 287, 28, 288, 289, 290, 291].

Let us now consider an anisotropic bi-material (or bi-crystal) with a perfectly bonded interface whose normal is along the  $\mathbf{x}_2$ -direction. The dislocation is supposed to be located in the upper material I ( $x_2 > 0$ ) as shown in Figure 3.1.

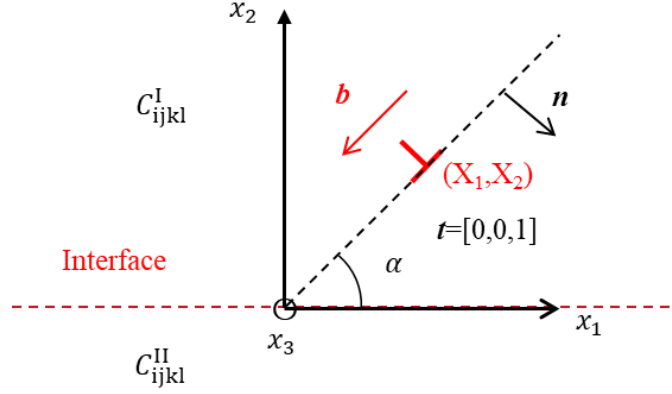


Figure 3.1: Schematic figure of one single infinite straight dislocation in a bi-material, where both crystals I and II have anisotropic elastic stiffness tensors  $C^I_{ijkl}$  and  $C^{II}_{ijkl}$ , respectively.  $x_2 = 0$  corresponds to the interface (GB) position.

In addition to Eq. 3.1, the function vector  $\mathbf{f}$  should also satisfy the continuity conditions at the perfect interface, i.e. the continuity of displacement and traction vectors:

$$u_i^I(x_2 = 0^+) = u_i^{II}(x_2 = 0^-) \quad (3.6)$$

$$\sigma_{i2}^I(x_2 = 0^+) = \sigma_{i2}^{II}(x_2 = 0^-) \quad (3.7)$$

In practice, instead of Eq. 3.7, the continuity of the resultant traction force along an arc of the interface is used. This last condition yields [19, 292]:

$$\Phi_i^{\text{I}}(x_2 = 0^+) = \Phi_i^{\text{II}}(x_2 = 0^-) \quad (3.8)$$

Following the Suo's method [19], the solutions are obtained and recalled in a form similar as for the homogeneous anisotropic case as follows:

$$\begin{cases} u_i = 2\text{Re} \left[ A_{ij} f_j(z_j) \right] = A_{ij} f_j(z_j) + \overline{A_{ij} f_j(z_j)} \\ \phi_i = 2\text{Re} \left[ B_{ij} f_j(z_j) \right] = B_{ij} f_j(z_j) + \overline{B_{ij} f_j(z_j)} \end{cases} \quad (3.9)$$

where  $\overline{\mathbf{A}}$  and  $\overline{\mathbf{B}}$  are the complex conjugate of  $\mathbf{A}$  and  $\mathbf{B}$ , respectively and the function of the homogeneous problem  $f_j^0(z_j)$  is now replaced by a function  $f_j(z_j)$  which is expressed as:

$$f_j(z_j) = \begin{cases} f_j^0(z_j) + f_j^{\text{I}}(z_j) & \text{if } z_j \in \text{I} \ (x_2 > 0) \\ f_j^{\text{II}}(z_j) & \text{if } z_j \in \text{II} \ (x_2 < 0) \end{cases} \quad (3.10)$$

The functions  $f_j^{\text{I}}(z_j)$  and  $f_j^{\text{II}}(z_j)$  are to be determined and are supposed analytic in the upper and lower materials, respectively.  $f_j^0(z_j)$  is calculated from Eq. 3.4 considering the elastic stiffness tensor  $\mathbf{C}^{\text{I}}$  of the upper material I and  $s_j = s_j^{\text{I}} = X_1 + p_j^{\text{I}} X_2$  because the dislocation is present in material I (see Figure 3.1). Moreover, it must be noticed that if  $z_j \in \text{I}$ ,  $z_j = z_j^{\text{I}} = x_1 + p_j^{\text{I}} x_2$  and if  $z_j \in \text{II}$ ,  $z_j = z_j^{\text{II}} = x_1 + p_j^{\text{II}} x_2$  where  $p_j^{\text{I}}$  and  $p_j^{\text{II}}$  are components of the vectors containing the roots with positive imaginary parts of the sextic equation Eq. 1.54 solved in materials I and II, respectively.

By combining Eqs. 3.9 and 3.10 together with the interface continuity conditions (Eqs. 3.6 and 3.8), the following equations can be obtained:

$$\begin{cases} A_{ij}^{\text{I}} f_j^0(x_1) + \overline{A_{ij}^{\text{I}} f_j^0(x_1)} + A_{ij}^{\text{I}} f_j^{\text{I}}(x_1) + \overline{A_{ij}^{\text{I}} f_j^{\text{I}}(x_1)} = A_{ij}^{\text{II}} f_j^{\text{II}}(x_1) + \overline{A_{ij}^{\text{II}} f_j^{\text{II}}(x_1)} \\ B_{ij}^{\text{I}} f_j^0(x_1) + \overline{B_{ij}^{\text{I}} f_j^0(x_1)} + B_{ij}^{\text{I}} f_j^{\text{I}}(x_1) + \overline{B_{ij}^{\text{I}} f_j^{\text{I}}(x_1)} = B_{ij}^{\text{II}} f_j^{\text{II}}(x_1) + \overline{B_{ij}^{\text{II}} f_j^{\text{II}}(x_1)} \end{cases} \quad (3.11)$$

From our notation, it is noteworthy that  $\overline{f_j(x_j)} = \overline{f_j}(x_j)$  when  $x_j$  is real. Hence, Eq. 3.11 can be rewritten as:

$$\begin{cases} A_{ij}^{\text{I}} f_j^0(x_1) + \overline{A_{ij}^{\text{I}} f_j^0(x_1)} + A_{ij}^{\text{I}} f_j^{\text{I}}(x_1) + \overline{A_{ij}^{\text{I}} f_j^{\text{I}}(x_1)} = A_{ij}^{\text{II}} f_j^{\text{II}}(x_1) + \overline{A_{ij}^{\text{II}} f_j^{\text{II}}(x_1)} \\ B_{ij}^{\text{I}} f_j^0(x_1) + \overline{B_{ij}^{\text{I}} f_j^0(x_1)} + B_{ij}^{\text{I}} f_j^{\text{I}}(x_1) + \overline{B_{ij}^{\text{I}} f_j^{\text{I}}(x_1)} = B_{ij}^{\text{II}} f_j^{\text{II}}(x_1) + \overline{B_{ij}^{\text{II}} f_j^{\text{II}}(x_1)} \end{cases} \quad (3.12)$$

By construction,  $f_j^0(z_i)$ ,  $\overline{f_j^{\text{I}}}(z_i)$  and  $f_j^{\text{II}}(z_i)$  are analytic in the lower material II whereas  $\overline{f_j^0}(z_i)$ ,  $\overline{f_j^{\text{II}}}(z_i)$  and  $f_j^{\text{I}}(z_i)$  are analytic in the upper material I [19]. With this background, Eq. 3.12 can be rewritten as [292]:



$$\begin{cases} \theta_i^u(x_2^+) = \theta_i^u(x_2^-) \\ \theta_i^\sigma(x_2^+) = \theta_i^\sigma(x_2^-) \end{cases} \quad (3.13)$$

where:

$$\theta_i^u = \begin{cases} -\overline{A_{ij}^I} \overline{f_j^0}(z_i) - A_{ij}^I f_j^I(z_i) + \overline{A_{ij}^{II}} \overline{f_j^{II}}(z_i) & \text{if } z_i \in \text{I} \\ A_{ij}^I f_j^0(z_i) + \overline{A_{ij}^I} \overline{f_j^I}(z_i) - A_{ij}^{II} f_j^{II}(z_i) & \text{if } z_i \in \text{II} \end{cases} \quad (3.14)$$

$$\theta_i^\sigma = \begin{cases} -\overline{B_{ij}^I} \overline{f_j^0}(z_i) - B_{ij}^I f_j^I(z_i) + \overline{B_{ij}^{II}} \overline{f_j^{II}}(z_i) & \text{if } z_i \in \text{I} \\ B_{ij}^I f_j^0(z_i) + \overline{B_{ij}^I} \overline{f_j^I}(z_i) - B_{ij}^{II} f_j^{II}(z_i) & \text{if } z_i \in \text{II} \end{cases} \quad (3.15)$$

The new functions  $\theta_i^u(z_i)$  and  $\theta_i^\sigma(z_i)$  are analytic both in the upper and lower materials, and are continuous across the interface. As a consequence,  $\theta_i^u(z_i)$  and  $\theta_i^\sigma(z_i)$  are analytic in all the plane including the points at infinity. By Liouville's theory,  $\theta_i^u(z_i)$  and  $\theta_i^\sigma(z_i)$  are thus constant functions [292]. Since in the absence of remotely applied force, the displacements and the stresses should vanish at infinity, it is required that  $\theta_i^u(z_i) = 0$  and  $\theta_i^\sigma(z_i) = 0$ . From Eqs. 3.14 and 3.15, this condition leads to:

$$\begin{cases} -\overline{A_{ij}^I} \overline{f_j^0}(z_i) - A_{ij}^I f_j^I(z_i) + \overline{A_{ij}^{II}} \overline{f_j^{II}}(z_i) = 0 \\ -\overline{B_{ij}^I} \overline{f_j^0}(z_i) - B_{ij}^I f_j^I(z_i) + \overline{B_{ij}^{II}} \overline{f_j^{II}}(z_i) = 0 \end{cases} \quad \text{if } z_i \in \text{I} \quad (3.16)$$

$$\begin{cases} A_{ij}^I f_j^0(z_i) + \overline{A_{ij}^I} \overline{f_j^I}(z_i) - A_{ij}^{II} f_j^{II}(z_i) = 0 \\ B_{ij}^I f_j^0(z_i) + \overline{B_{ij}^I} \overline{f_j^I}(z_i) - B_{ij}^{II} f_j^{II}(z_i) = 0 \end{cases} \quad \text{if } z_i \in \text{II} \quad (3.17)$$

By solving the two linear systems of Eqs. 3.16 and 3.17, the expressions of  $f_j^I(z_j)$  and  $f_j^{II}(z_j)$  are obtained as a function of  $f_k^0(z_j)$ :

$$\begin{cases} f_j^I(z_j) = \overline{V_{jk}^{I,II}} \overline{f_k^0}(z_j) & \text{if } z_j \in \text{I} \\ f_j^{II}(z_j) = W_{jk}^{I,II} f_k^0(z_j) & \text{if } z_j \in \text{II} \end{cases} \quad (3.18)$$

where:

$$\begin{cases} \mathbf{V}^{I,II} = \left( \mathbf{B}^{II} \mathbf{A}^{II^{-1}} \overline{\mathbf{A}^I} - \overline{\mathbf{B}^I} \right)^{-1} \left( \mathbf{B}^I - \mathbf{B}^{II} \mathbf{A}^{II^{-1}} \mathbf{A}^I \right) \\ \mathbf{W}^{I,II} = \left( \overline{\mathbf{B}^I} \mathbf{A}^{I^{-1}} \mathbf{A}^{II} - \mathbf{B}^{II} \right)^{-1} \left( \overline{\mathbf{B}^I} \mathbf{A}^{I^{-1}} \mathbf{A}^I - \mathbf{B}^I \right) \end{cases} \quad (3.19)$$

Displacement and stress fields are then deduced from Eqs. 3.9, 3.10, 3.18 and 3.19. It is noteworthy that when  $z_j \in \text{II}$ ,  $f_k^0(z_j) = f_k^0(z_j^{\text{II}}) = q_k^0 \ln(z_j^{\text{II}} - s_k^{\text{I}})$  with  $s_k^{\text{I}} = X_1 + p_k^{\text{I}} X_2$  since  $f^0$  is associated to material I (just as  $\mathbf{q}^0$ ). Ting [285] has also given the solutions of displacement and stress fields due to one single dislocation

in a bi-material configuration, under however a different form compared to the one of Suo [19]. However they are proved to be equivalent (see the proof in Appendix A).

In the case where the dislocation is assumed to be located in the lower material II, the solution is obtained by a similar procedure yielding:

$$f_j(z_j) = \begin{cases} f_j^I(z_j) & \text{if } z_j \in \text{I } (x_2 > 0) \\ f_j^0(z_j) + f_j^{\text{II}}(z_j) & \text{if } z_j \in \text{II } (x_2 < 0) \end{cases} \quad (3.20)$$

$$\text{with } \begin{cases} f_j^I(z_j) = W_{j\underline{k}}^{\text{II,I}} f_{\underline{k}}^0(z_j) & \text{if } z_j \in \text{I} \\ f_j^{\text{II}}(z_j) = V_{j\underline{k}}^{\text{II,I}} f_{\underline{k}}^0(z_j) & \text{if } z_j \in \text{II} \end{cases} \quad (3.21)$$

where  $f_{\underline{k}}^0(z_j)$  is still calculated from Eq. 3.4 but now considering the stiffness tensor  $\mathbf{C}^{\text{II}}$  of the lower material II and  $s_k = s_k^{\text{II}} = X_1 + p_k^{\text{II}} X_2$ .

### 3.2.3 Anisotropic half-space with rigid or free surface

The problem of a singularity in a half-space I with a surface at  $x_2 = 0$  can be solved in a similar manner as the bi-material problem, see section 3.2.2. If the surface is assumed to be rigid, the displacement boundary condition is:

$$u_i^I(x_2 = 0) = 0 \quad (3.22)$$

Displacement and stress fields are then obtained by considering Eq. 3.9, along with:

$$f_j(z_j) = f_j^0(z_j) + f_j^I(z_j) \quad (3.23)$$

where from first equations in Eqs. 3.16:

$$f_j^I(z_j) = -A_{j\underline{k}}^{\text{I}}{}^{-1} \overline{A_{\underline{k}l}^{\text{I}}} \overline{f_l^0}(z_j) \quad (3.24)$$

If the surface is assumed to be traction-free, the continuity of the resultant traction force becomes:

$$\phi_i^I(x_2 = 0) = 0 \quad (3.25)$$

Displacement and stress fields are then obtained by considering Eq. 3.23 with:

$$f_j^I(z_j) = -B_{j\underline{k}}^{\text{I}}{}^{-1} \overline{B_{\underline{k}l}^{\text{I}}} \overline{f_l^0}(z_j) \quad (3.26)$$

### 3.2.4 Heterogeneous anisotropic medium: tri-material

In section 3.2.2, the bi-material was regarded as the combination of two materials perfectly bonded to each other through an interface without thickness. In the case where the considered interface is a GB, the real thickness is finite. Hence, it may be interesting to investigate the effect of the GB thickness as well as the effect of its elastic stiffness on the elastic fields in a tri-material. Among several studies for multilayered anisotropic elastic media, the method of Choi and Earmme [17] is first applied.

#### 3.2.4.1 Tri-material configuration

Figure 3.2 shows the considered tri-material configuration. There are two planar interfaces  $\Gamma_1$  and  $\Gamma_2$  whose normals are directed along the  $x_2$ -axis. These interfaces are located, respectively, at  $x_2 = h$  and at  $x_2 = -d$ . The interphase (or GB) thickness is thus denoted  $H = h + d$ . Material I corresponds to  $x_2 \geq h$ , material II to  $-d < x_2 < h$  and material III to  $x_2 \leq -d$ . All the materials are assumed to be perfectly bonded to each other (i.e. perfect interfaces).

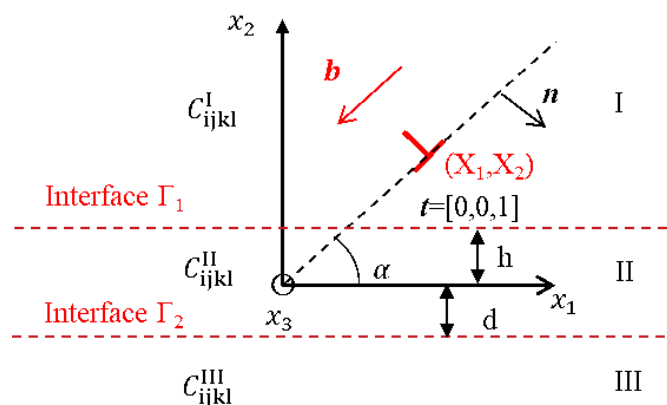


Figure 3.2: Schematic figure of one single infinite straight dislocation in a tri-material configuration with three different stiffness tensors and two perfectly bonded interfaces. The GB region is supposed to be material II between two plane interfaces  $\Gamma_1$  located at  $x_2 = h$  and  $\Gamma_2$  located at  $x_2 = -d$ . In addition, Material I corresponds to  $x_2 \geq h$  and material III corresponds to  $x_2 \leq -d$ .  $C^I_{ijkl}$ ,  $C^{II}_{ijkl}$  and  $C^{III}_{ijkl}$  are elastic stiffness tensors of crystals I, II and III, respectively.

#### 3.2.4.2 A coordinate translation

In contrast with section 3.2.2, it is noteworthy that the interfaces are no more located at  $x_2 = 0$ . Hence, a coordinate translation should be performed first in order to be able to use correctly the bi-material expressions of elastic fields. Let

us then consider a bi-material configuration where the dislocation is located in the upper material I and where the interface is located at  $x_2 = h > 0$ . In this case, the change of coordinates  $x_2 \rightarrow x_2 - h$  and  $X_2 \rightarrow X_2 - h$  must be performed in order to retrieve the same bi-material configuration as the one of section 3.2.2, i.e. such that the interface would be at  $x_2 = 0$  within the new coordinate system. Hence,  $z$  and  $s$  must be modified as  $z_i \rightarrow z_i - hp_i^I$  and  $s_j \rightarrow s_j - hp_j^I$ , which leads to the following change of coordinates for  $f_j^0(z_i)$  [17]:

$$\left\{ \begin{array}{l} f_i^0(z_i^I) \rightarrow q_i^0 \ln((z_i^I - p_i^I h) - (s_i - p_i^I h)) = q_i^0 \ln(z_i^I - s_i) = f_i^0(z_i^I) \\ \overline{f_j^0}(z_j^I) \rightarrow \overline{q_j^0 \ln((z_j^I - p_j^I h) - (s_j - p_j^I h))} = \overline{q_j^0 \ln((z_j^I - p_j^I h + \overline{p_j^I h}) - s_j)} \\ \hspace{15em} = \overline{f_j^0}(z_j^I - p_j^I h + \overline{p_j^I h}) \\ f_j^0(z_j^{II}) \rightarrow q_j^0 \ln((z_j^{II} - p_j^{II} h) - (s_j - p_j^I h)) = q_j^0 \ln((z_j^{II} - p_j^{II} h + p_j^I h) - s_j) \\ \hspace{15em} = f_j^0(z_j^{II} - p_j^{II} h + p_j^I h) \end{array} \right. \quad (3.27)$$

It can be observed that the expression of  $f_i^0(z_i^I)$  remains unchanged since it corresponds to the case of a dislocation in a homogeneous anisotropic material (no interface). However, the two other terms,  $\overline{f_j^0}(z_j^I)$  and  $f_j^0(z_j^{II})$ , have been modified because they depend on the position of the interface. The solutions for a bi-material with the interface located at  $x_2 = h > 0$  are then deduced from Eqs. 3.9, 3.10 and 3.18 along with:

$$\left\{ \begin{array}{l} f_j^I(z_j^I) = \overline{V_{j\mathbf{k}}^{I,II}} \overline{f_{\mathbf{k}}^0}(z_j^I - p_j^I h + \overline{p_{\mathbf{k}}^I h}) \\ f_j^{II}(z_j^{II}) = W_{j\mathbf{k}}^{I,II} f_{\mathbf{k}}^0(z_j^{II} - p_j^{II} h + p_{\mathbf{k}}^I h) \end{array} \right. \quad (3.28)$$

Thanks to a similar procedure, the solutions for the different cases displayed in Table 3.1 are also derived, i.e. when the dislocation is located in the lower material II or when the interface is located at  $x_2 = -d < 0$ .

	Interface $x_2 = h > 0$	Interface $x_2 = -d < 0$
Dislocation in upper material I	$f_j^I(z_j^I) = \overline{V_{j\mathbf{k}}^{I,II}} \overline{f_{\mathbf{k}}^0}(z_j^I - p_j^I h + \overline{p_{\mathbf{k}}^I h})$ $f_j^{II}(z_j^{II}) = W_{j\mathbf{k}}^{I,II} f_{\mathbf{k}}^0(z_j^{II} - p_j^{II} h + p_{\mathbf{k}}^I h)$	$f_j^I(z_j^I) = \overline{V_{j\mathbf{k}}^{I,II}} \overline{f_{\mathbf{k}}^0}(z_j^I + p_j^I d - \overline{p_{\mathbf{k}}^I d})$ $f_j^{II}(z_j^{II}) = W_{j\mathbf{k}}^{I,II} f_{\mathbf{k}}^0(z_j^{II} + p_j^{II} d - p_{\mathbf{k}}^I d)$
Dislocation in lower material II	$f_j^I(z_j^I) = W_{j\mathbf{k}}^{II,I} f_{\mathbf{k}}^0(z_j^I - p_j^I h + p_{\mathbf{k}}^{II} h)$ $f_j^{II}(z_j^{II}) = \overline{V_{j\mathbf{k}}^{II,I}} \overline{f_{\mathbf{k}}^0}(z_j^{II} - p_j^{II} h + \overline{p_{\mathbf{k}}^{II} h})$	$f_j^I(z_j^I) = W_{j\mathbf{k}}^{II,I} f_{\mathbf{k}}^0(z_j^I + p_j^I d - p_{\mathbf{k}}^{II} d)$ $f_j^{II}(z_j^{II}) = \overline{V_{j\mathbf{k}}^{II,I}} \overline{f_{\mathbf{k}}^0}(z_j^{II} + p_j^{II} d - \overline{p_{\mathbf{k}}^{II} d})$

Table 3.1: Bi-material solution functions for different locations of the interface and for dislocation position in crystal I or crystal II.

### 3.2.4.3 Alternating technique with standard analytic continuation arguments

In the tri-material configuration, there are two interfaces and the difficulty is thus to satisfy the continuity of displacements and forces across the two interfaces at the same time. Choi and Earmme [17] overcame this difficulty by applying the alternating technique, which consists in satisfying alternatively the continuity conditions across each interface until a convergence is obtained. That means that both materials which are on the same side of the considered interface are regarded as a homogeneous material. The latter corresponds to the material adjacent to the interface. At each step  $\beta$ , the function which is used as a homogeneous solution to perform the computation is updated (see details in [17]).

Still considering the case of a dislocation located in the material I and by using the same procedure as the one of Choi and Earmme [17], the following series solution is obtained:

$$f_j(z_j) = \begin{cases} f_j^0(z_j) + f_j^{I0}(z_j) + \sum_{\beta=1}^{\infty} f_j^{I\beta}(z_j) & \text{if } z_j \in \text{I} \\ \sum_{\beta=1}^{\infty} f_j^{\beta}(z_j) + \sum_{\beta=1}^{\infty} f_j^{II\beta}(z_j) & \text{if } z_j \in \text{II} \\ \sum_{\beta=1}^{\infty} f_j^{III\beta}(z_j) & \text{if } z_j \in \text{III} \end{cases} \quad (3.29)$$

where:

$$\left\{ \begin{array}{l} f_k^0(z_j) = q_k^0 \ln(z_j - s_k) \\ f_j^{I0}(z_j) = \overline{V_{j\bar{k}}^{I,II}} \overline{f_{\bar{k}}^0} \left( z_j - p_j^I h + \overline{p_{\bar{k}}^I} h \right) \\ f_j^{I\beta}(z_j) = W_{j\bar{k}}^{II,I} \overline{V_{\bar{k}l}^{II,III}} \overline{f_l^{\beta}} \left( z_j - p_j^I h + p_{\bar{k}}^{II} (h + d) - \overline{p_l^{II}} d \right) \\ f_j^{II\beta}(z_j) = \overline{V_{j\bar{k}}^{II,III}} \overline{f_{\bar{k}}^{\beta}} \left( z_j + p_j^{II} d - \overline{p_{\bar{k}}^{II}} d \right) \\ f_j^{III\beta}(z_j) = W_{j\bar{k}}^{II,III} f_{\bar{k}}^{\beta} \left( z_j + p_j^{III} d - p_{\bar{k}}^{II} d \right) \\ f_k^{\beta}(z_j) = \begin{cases} W_{kl}^{I,II} \overline{f_l^0} \left( z_j - p_j^I h + \overline{p_l^I} h \right) & \text{if } \beta = 1 \\ \overline{V_{kl}^{II,I}} \overline{V_{lm}^{II,III}} f_m^{\beta-1} \left( z_j - p_j^{II} h + \overline{p_l^{II}} (h + d) - \overline{p_m^{II}} d \right) & \text{if } \beta > 1 \end{cases} \end{array} \right. \quad (3.30)$$

In the above equations,  $f_j^0(z_j)$  is associated to material I and so  $s_j = s_j^I = X_1 + p_j^I X_2$ . The series solution  $f_j^{I\beta}(z_j)$ ,  $f_j^{II\beta}(z_j)$  and  $f_j^{III\beta}(z_j)$  are all expressed as functions of  $f_{\bar{k}}^{\beta}(z_j)$  which is itself determined by a recurrence equation based on  $f_{\bar{k}}^0(z_j)$ . In particular, when the material III is not-existent, the solutions still remain valid with:

$$\mathbf{V}^{\text{II,III}} = -\overline{\mathbf{B}^{\text{II}}}^{-1} \mathbf{B}^{\text{II}} \quad (3.31)$$

In that case, a lower free surface is presented.

In a similar manner, when the dislocation is located in the material II (inter-phase, i.e. GB region), the series solution is:

$$f_j(z_j) = \begin{cases} \sum_{\beta=1}^{\infty} f_j^{\text{I}\beta}(z_j) & \text{if } z_j \in \text{I} \\ \sum_{\beta=1}^{\infty} f_j^{\beta}(z_j) + \sum_{\beta=1}^{\infty} f_j^{\text{II}\beta}(z_j) & \text{if } z_j \in \text{II} \\ f_j^{\text{III}0}(z_j) + \sum_{\beta=1}^{\infty} f_j^{\text{III}\beta}(z_j) & \text{if } z_j \in \text{III} \end{cases} \quad (3.32)$$

where:

$$\left\{ \begin{array}{l} f_k^0(z_j) = q_k^0 \ln(z_j - s_k) \\ f_j^{\text{III}0}(z_j) = W_{j\bar{k}}^{\text{II,III}} f_{\bar{k}}^0(z_j + p_j^{\text{III}}d - p_{\bar{k}}^{\text{II}}d) \\ f_j^{\text{I}\beta}(z_j) = W_{j\bar{k}}^{\text{II,I}} f_{\bar{k}}^{\beta}(z_j - p_j^{\text{I}}h + p_{\bar{k}}^{\text{II}}h) \\ f_j^{\text{II}\beta}(z_j) = \overline{V_{j\bar{k}}^{\text{II,I}}} \overline{f_{\bar{k}}^{\beta}}(z_j - p_j^{\text{II}}h + \overline{p_{\bar{k}}^{\text{II}}h}) \\ f_j^{\text{III}\beta}(z_j) = W_{j\bar{k}}^{\text{II,III}} \overline{V_{k\bar{l}}^{\text{II,I}}} \overline{f_{\bar{l}}^{\beta}}(z_j + p_j^{\text{III}}d - p_{\bar{k}}^{\text{II}}(h+d) + \overline{p_{\bar{l}}^{\text{II}}h}) \\ f_k^{\beta}(z_j) = \begin{cases} f_k^0(z_j) + \overline{V_{kl}^{\text{II,III}}} \overline{f_{\bar{l}}^0}(z_j + p_j^{\text{II}}d - p_{\bar{l}}^{\text{II}}d) & \text{if } \beta = 1 \\ \overline{V_{kl}^{\text{II,III}}} \overline{V_{lm}^{\text{II,I}}} \overline{f_{\bar{m}}^{\beta-1}}(z_j + p_j^{\text{II}}d - \overline{p_{\bar{l}}^{\text{II}}(h+d)} + \overline{p_{\bar{m}}^{\text{II}}h}) & \text{if } \beta > 1 \end{cases} \end{array} \right. \quad (3.33)$$

In the above equations,  $f_k^0(z_j)$  is now associated to material II and so  $s_k = s_k^{\text{II}} = X_1 + p_k^{\text{II}}X_2$ . When the material I is non-existent, a upper free surface is presented with:

$$\mathbf{V}^{\text{II,I}} = -\overline{\mathbf{B}^{\text{II}}}^{-1} \mathbf{B}^{\text{II}} \quad (3.34)$$

#### 3.2.4.4 Convergence of series solution through three criteria

Choi and Earmme [17] proved that the above series solutions are indeed convergent (see the discussion in the section 6 of their paper). However, for numerical applications, it is important to discuss the definition of different convergence criteria in order to analyze the rate of convergence of the series. When the truncation of the series  $\beta$  becomes large, the computation is very time-consuming or even unrealizable for large values of mechanical contrasts between materials. To study numerical convergence, Choi and Earmme [17] considered a criterion based on the

image force acting on the dislocation and discussed the effect of the elastic stiffness of the different materials as well as the one of the thickness of the second material. Their criterion is expressed as:

$$\epsilon_f^{\beta+1} = \frac{|f^{\beta+1} - f^\beta|}{|f^{\beta+1}|} \quad (3.35)$$

where  $(\beta + 1)$  is the component of the image force along the  $\mathbf{x}_2$ -axis at the position of the dislocation. They considered that convergence was achieved for  $\epsilon_f^{\beta+1} < 10^{-4}$ . This criterion is based only on stress and disregards the solutions outside the dislocation, in particular in the other materials.

In the present thesis and as reported in [277], two new convergence criteria are developed. The first one considers the norm of the displacement vector difference between two steps summed at every point  $(P, Q)$  of the simulation plane (which includes the three materials):

$$\epsilon_u^{\beta+1} = \frac{\sum_{P,Q} \sqrt{\sum_i [u_i^{\beta+1}(P, Q) - u_i^\beta(P, Q)]^2}}{\sum_{P,Q} \sqrt{\sum_i [u_i^{\beta+1}(P, Q)]^2}} \quad (3.36)$$

The second one considers the norm of the stress tensor difference between two steps summed at every point  $(P, Q)$  of the simulation plane:

$$\epsilon_\sigma^{\beta+1} = \frac{\sum_{P,Q} \sqrt{\sum_{ij} [\sigma_{ij}^{\beta+1}(P, Q) - \sigma_{ij}^\beta(P, Q)]^2}}{\sum_{P,Q} \sqrt{\sum_{ij} [\sigma_{ij}^{\beta+1}(P, Q)]^2}} \quad (3.37)$$

Through the combination of these two criteria, both displacement and stress distributions are considered. Contrary to the criterion of Choi and Earmme [17] which focuses on only one material point, the above criteria depends on the size and the spatial discretization (mesh resolution) of the simulation plane. Indeed, it can be observed that the elastic field differences between two steps are larger close to the singularity than far away. However, the numerical calculations reported in section 4.2.2 will show that the influence of the simulation plane's characteristics was actually negligible.

### 3.2.5 Heterogeneous anisotropic medium: multilayer material with free surfaces

In the case of real objects, like the micro-beam shown in Figure 2.12 (see Chapter 2), free surfaces are always present. At small scale, the free surfaces have

an obvious influence on the dislocation behavior. Hence, besides the interphase, it may be necessary to consider the effect of free surfaces on the elastic fields of a multilayer material. The tri-material method of Choi and Earmme [17] can also take into account free surface effects but only in the case of a bi-material with one free surface or a homogeneous material with two free surfaces. In order to handle more complicated cases, like a tri-material with one or two free surfaces, a new method is needed. Therefore, the image decomposition method developed by Wang et al. [18] has been used.

### 3.2.5.1 Multilayered material configuration

Figure 3.3 shows the tri-material configuration with two free surfaces. There are four planar faces whose normals are directed along the  $x_2$ -axis. These faces are located at  $x_2 = 0$ ,  $x_2 = -h_1$ ,  $x_2 = -(h_1 + h_2)$  and  $x_2 = -(h_1 + h_2 + h_3)$  for, respectively upper free surface, first interface, second interface and bottom free surface. The interphase (or GB) is located in the second layer of thickness  $h_2$ . Material I corresponds to  $-h_1 < x_2 < 0$ , material II to  $-(h_1 + h_2) < x_2 < -h_1$  and material III to  $-(h_1 + h_2 + h_3) < x_2 < -(h_1 + h_2)$ . Thus, the thickness of the whole material is marked as  $H' = h_1 + h_2 + h_3$ . All the materials are assumed to be perfectly bonded to each other. In order to discuss the effects of both surfaces, the free surface on the side of the material containing the dislocations is referred to be the first free surface, and the another one is called the second free surface.



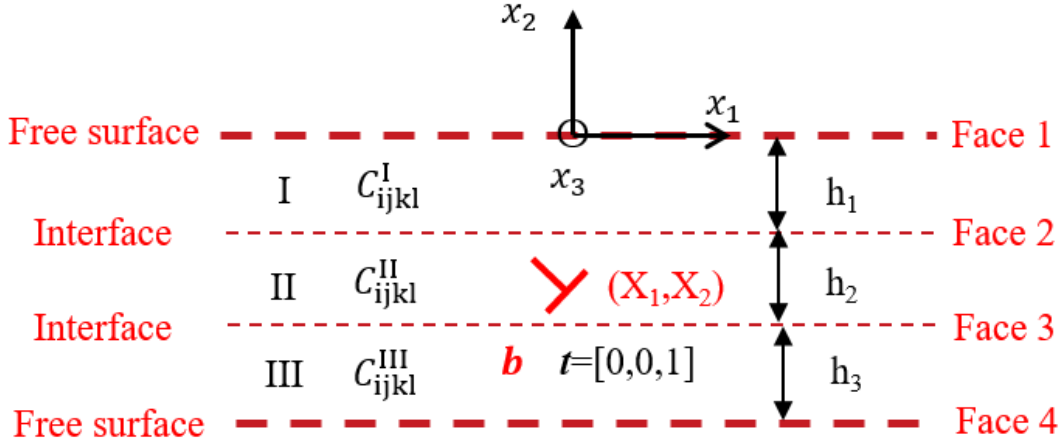


Figure 3.3: Schematic figure of one single infinite straight dislocation in a tri-material configuration with three different stiffness tensors  $C^I_{ijkl}$ ,  $C^{II}_{ijkl}$  and  $C^{III}_{ijkl}$  for material I, II and III, respectively. There are two planar free surfaces at faces 1 located at  $x_2 = 0$  and 4 located at  $x_2 = -(h_1 + h_2 + h_3)$  and two perfectly bonded interfaces at faces 2 located at  $x_2 = -h_1$  and 3 located at  $x_2 = -(h_1 + h_2)$ . Material I corresponds to  $-h_1 < x_2 < 0$ , material II to  $-(h_1 + h_2) < x_2 < -h_1$  and material III to  $-(h_1 + h_2 + h_3) < x_2 < -(h_1 + h_2)$ . The GB region is supposed to be material II.

### 3.2.5.2 Image decomposition method

In the 3-layers configuration with free surfaces, there are 2 interfaces that must satisfy the continuity of tractions and displacements, and two free surfaces that must be free of tractions. For a multilayer system, it is too complicated to use the alternating technique. Wang et al. [18] have proposed an image decomposition method, which can be used to satisfy all the boundary conditions at the same time. The principle of this method is to decompose the multilayer problem into several subproblems of infinite homogeneous medium for each material. Two types of image dislocation densities are distributed on each interface while one image dislocation density is distributed on each surface as shown in Figure 3.4 (left). The densities of these image dislocations are denoted  $\rho^t$ , where  $t=1,2$  and 3 denote the  $x_1$ -,  $x_2$ - and  $x_3$ -components, respectively. Thus, there are in total 18 image dislocation densities  $\rho^t_{1U}$ ,  $\rho^t_{1L}$ ,  $\rho^t_{2U}$ ,  $\rho^t_{2L}$ ,  $\rho^t_{3U}$  and  $\rho^t_{3L}$  which are located at  $x_2 = 0^-$ ,  $-h_1^+$ ,  $-h_1^-$ ,  $-(h_1 + h_2)^+$ ,  $-(h_1 + h_2)^-$  and  $-(h_1 + h_2 + h_3)^+$ , respectively.

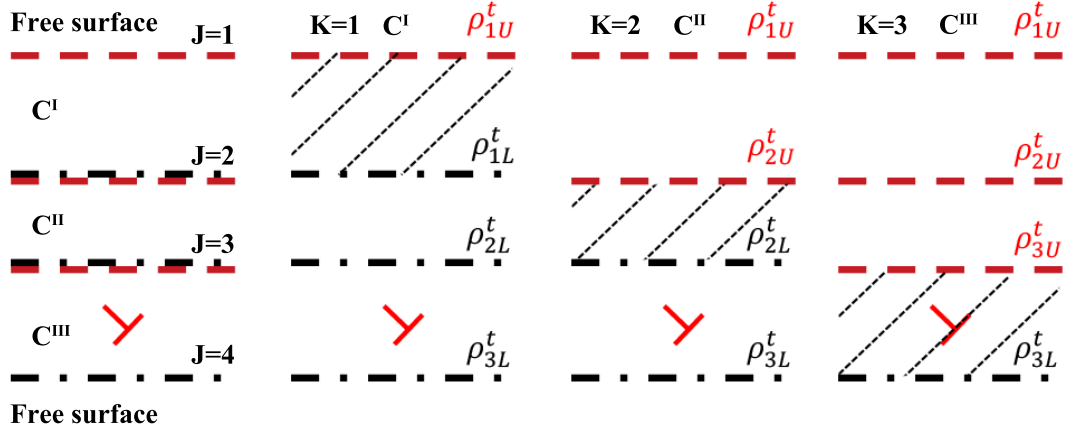


Figure 3.4: Decomposition of a 3-layers problem (left) with 2 free surfaces and 2 interfaces into three infinite homogeneous subproblems. Source dislocation is marked with a red dislocation symbol.

These densities can be resolved at the same time by simultaneously considering all boundary conditions: the continuity of tangential displacement gradient and traction continuity across interfaces, traction free for free surfaces or tangential gradient of displacement free for rigid surfaces. Thus, the present 3-layers configuration with free surfaces is decomposed into 3 subproblems and there are in total 18 boundary conditions ( $i=1,2$  and 3) as follows:

- The traction  $\sigma_{i2}$  vanish on the two free surfaces:
  - I.  $\sigma_{i2}(x_1, x_2 = 0) = 0$
  - II.  $\sigma_{i2}(x_1, x_2 = -(h_1 + h_2 + h_3)) = 0$
- The continuity of stresses  $\sigma_{i2}$  and of displacement gradient  $\partial u_i / \partial x_1$  across the two interfaces:
  - III.  $\sigma_{i2}(x_1, x_2 = -h_1^+) = \sigma_{i2}(x_1, x_2 = -h_1^-)$
  - IV.  $\frac{\partial u_i}{\partial x_1}(x_1, x_2 = -h_1^+) = \frac{\partial u_i}{\partial x_1}(x_1, x_2 = -h_1^-)$
  - V.  $\sigma_{i2}(x_1, x_2 = -(h_1 + h_2)^+) = \sigma_{i2}(x_1, x_2 = -(h_1 + h_2)^-)$
  - VI.  $\frac{\partial u_i}{\partial x_1}(x_1, x_2 = -(h_1 + h_2)^+) = \frac{\partial u_i}{\partial x_1}(x_1, x_2 = -(h_1 + h_2)^-)$

The elastic field in each layer is determined by summing the contributions of the dislocation source and all the corresponding image dislocations as shown in Figure 3.4 (right). Based on a consistency requirement that when two contiguous layers are identical the corresponding subproblems must be identical too

(see the full discussion by Wang et al. [18]), the image dislocation densities in the three subproblems are:  $\rho_{J_1}^t = \{\rho_{1U}^t, \rho_{1L}^t, \rho_{2L}^t, \rho_{3L}^t\}$  for the first subproblem,  $\rho_{J_2}^t = \{\rho_{1U}^t, \rho_{2U}^t, \rho_{2L}^t, \rho_{3L}^t\}$  for the second subproblem and  $\rho_{J_3}^t = \{\rho_{1U}^t, \rho_{2U}^t, \rho_{3U}^t, \rho_{3L}^t\}$  for the third subproblem as shown in Figure 3.4 (right).

### 3.2.5.3 Governing integral equations

Based on Stroh formalism, the stress and displacement gradient fields due to a mixed dislocation with Burgers vector components  $b_t$  ( $t = 1, 2, 3$ ) located at  $(x_{1s}, x_{2s})$  in a homogeneous anisotropic solid under plane strain can be written as [28, 18]:

$$\sigma_{ij}(K, b_t, \Delta x_1, \Delta x_2) = 2 [\xi_{K\alpha ij}^{tR} P(\Delta x_1, p_{K\alpha}^R \Delta x_2, p_{K\alpha}^I \Delta x_2) + \zeta_{K\alpha ij}^{tI} Q(\Delta x_1, p_{K\alpha}^R \Delta x_2, p_{K\alpha}^I \Delta x_2)] b_t \quad (3.38)$$

$$\frac{\partial u_i}{\partial x_j}(K, b_t, \Delta x_1, \Delta x_2) = 2 [\zeta_{K\alpha ij}^{tR} P(\Delta x_1, p_{K\alpha}^R \Delta x_2, p_{K\alpha}^I \Delta x_2) + \zeta_{K\alpha ij}^{tI} Q(\Delta x_1, p_{K\alpha}^R \Delta x_2, p_{K\alpha}^I \Delta x_2)] b_t \quad (3.39)$$

where  $\Delta x_1 = x_1 - x_{1s}$  and  $\Delta x_2 = x_2 - x_{2s}$ , the superscript  $R$  and  $I$  indicate the real and imaginary parts of each term, respectively. Meanwhile the subscript  $K$  indicates which subproblem is considered (no sum over  $K$ ). The definition of the symbols  $\xi_{K\alpha ij}^t$ ,  $\zeta_{K\alpha ij}^t$  and the functions  $P$ ,  $Q$  [18] are:

$$\begin{cases} \xi_{K\alpha ij}^t = \frac{C_{Kijkl}(\delta_{l1} + p_{K\alpha} \delta_{l2}) A_{Kk\alpha} B_{Kt\alpha}}{2\pi i} \\ \zeta_{K\alpha ij}^t = \frac{(\delta_{j1} + p_{K\alpha} \delta_{j2}) A_{K i\alpha} B_{Kt\alpha}}{2\pi i} \end{cases} \quad (3.40)$$

$$\begin{cases} P(x_1 - x_{1s}, a, b) = \frac{x_1 - x_{1s} + a}{(x_1 - x_{1s} + a)^2 + b^2} \\ Q(x_1 - x_{1s}, a, b) = \frac{b}{(x_1 - x_{1s} + a)^2 + b^2} \end{cases} \quad (3.41)$$

where  $p_\alpha$ ,  $A_{k\alpha}$  and  $B_{t\alpha}$  with  $\alpha=1,2$  and 3 denote the same eigenvalues and eigenvectors in Stroh sextic formulation as discussed in section 1.5.3 ( $\mathbf{A}$ ,  $\mathbf{B}$  matrices are the Stroh matrices introduced in subsection 1.5.3 of Chapter 1). These two equations 3.38 and 3.39 of the single-crystal are strictly equivalent to Eqs. 3.2, 3.4 and 3.5.

The contribution of image dislocations on elastic fields can be calculated by replacing the Burgers vector  $b_t$  by  $\rho_{JK}^t(x'_1)$  and integrating from  $x'_1 = -\infty$  to  $x'_1 = +\infty$  in Eqs. 3.38 and 3.39:

$$\begin{aligned}
\sigma_{ij} (K, \rho_{JK}^t, \Delta x_1, \Delta x_2) &= \\
&\int_{-\infty}^{+\infty} 2 [\xi_{K\alpha ij}^{tR} P (\Delta x_1, p_{K\alpha}^R \Delta x_2, p_{K\alpha}^I \Delta x_2) + \xi_{K\alpha ij}^{tI} Q (\Delta x_1, p_{K\alpha}^R \Delta x_2, p_{K\alpha}^I \Delta x_2)] \rho_{JK}^t (x'_1) dx'_1 \\
&= 2\pi [\xi_{K\alpha ij}^{tR} H (p_{K\alpha}^R \Delta x_2, p_{K\alpha}^I \Delta x_2) + \xi_{K\alpha ij}^{tI} I (p_{K\alpha}^R \Delta x_2, p_{K\alpha}^I \Delta x_2)] [\rho_{JK}^t (x_1)]
\end{aligned} \tag{3.42}$$

$$\begin{aligned}
\frac{\partial u_i}{\partial x_j} (K, \rho_{JK}^t, \Delta x_1, \Delta x_2) &= \\
&\int_{-\infty}^{+\infty} 2 [\zeta_{K\alpha ij}^{tR} P (\Delta x_1, p_{K\alpha}^R \Delta x_2, p_{K\alpha}^I \Delta x_2) + \zeta_{K\alpha ij}^{tI} Q (\Delta x_1, p_{K\alpha}^R \Delta x_2, p_{K\alpha}^I \Delta x_2)] \rho_{JK}^t (x'_1) dx'_1 \\
&= 2\pi [\zeta_{K\alpha ij}^{tR} H (p_{K\alpha}^R \Delta x_2, p_{K\alpha}^I \Delta x_2) + \zeta_{K\alpha ij}^{tI} I (p_{K\alpha}^R \Delta x_2, p_{K\alpha}^I \Delta x_2)] [\rho_{JK}^t (x_1)]
\end{aligned} \tag{3.43}$$

where  $\Delta x_1 = x_1 - x'_1$ ,  $\Delta x_2 = x_2 - x'_2$  and  $(x'_1, x'_2)$  denote the positions of image dislocations. The definitions of operators  $H$  and  $I$  are:

$$\begin{cases} H (a, b) [\rho (x_1)] = \frac{1}{\pi} \int_{-\infty}^{\infty} P (x_1 - x'_1, a, b) \rho (x'_1) dx'_1 \\ I (a, b) [\rho (x_1)] = \frac{1}{\pi} \int_{-\infty}^{\infty} Q (x_1 - x'_1, a, b) \rho (x'_1) dx'_1 \end{cases} \tag{3.44}$$

Combining with all the equations from Eq. 3.38 to Eq. 3.44, the boundary conditions can be derived with respect to the Burgers vector of the source dislocation and image dislocations densities. For example, for the boundary condition I:

$$\begin{aligned}
& \sigma_{i2}(1, \mathbf{b}, x_1 - x_{1s}, x_2 - x_{2s}) + \sum_{J=1}^{J=4} \sigma_{i2}(1, \boldsymbol{\rho}_{J1}, x_1 - x'_1, x_2 - x_{2J}) = 0 \rightarrow \\
& 2 \left[ \xi_{1\alpha i2}^{tR} P(x_1 - x_{1s}, -p_{1\alpha}^R x_{2s}, -p_{1\alpha}^I x_{2s}) + \xi_{1\alpha i2}^{tI} Q(x_1 - x_{1s}, -p_{1\alpha}^R x_{2s}, -p_{1\alpha}^I x_{2s}) \right] b_t \\
& + 2\pi \left[ \xi_{1\alpha i2}^{tR} H(0, 0) + \xi_{1\alpha i2}^{tI} I(0, 0^+) \right] [\rho_{1U}^t(x_1)] \\
& + 2\pi \left[ \xi_{1\alpha i2}^{tR} H(p_{1\alpha}^R h_1, p_{1\alpha}^I h_1) + \xi_{1\alpha i2}^{tI} I(p_{1\alpha}^R h_1, p_{1\alpha}^I h_1) \right] [\rho_{1L}^t(x_1)] \\
& + 2\pi \left[ \xi_{1\alpha i2}^{tR} H(p_{1\alpha}^R (h_1 + h_2), p_{1\alpha}^I (h_1 + h_2)) + \right. \\
& \quad \left. \xi_{1\alpha i2}^{tI} I(p_{1\alpha}^R (h_1 + h_2), p_{1\alpha}^I (h_1 + h_2)) \right] [\rho_{2L}^t(x_1)] \\
& + 2\pi \left[ \xi_{1\alpha i2}^{tR} H(p_{1\alpha}^R (h_1 + h_2 + h_3), p_{1\alpha}^I (h_1 + h_2 + h_3)) + \right. \\
& \quad \left. \xi_{1\alpha i2}^{tI} I(p_{1\alpha}^R (h_1 + h_2 + h_3), p_{1\alpha}^I (h_1 + h_2 + h_3)) \right] [\rho_{3L}^t(x_1)] = 0
\end{aligned} \tag{3.45}$$

where  $(x'_1, x_{2J})$  are the coordinate of image dislocation densities  $\boldsymbol{\rho}_{JK}$  for the subproblem  $K$ .

In the Eq. 3.45, a singularity term is found as  $2\pi \left[ \xi_{1\alpha i2}^{tR} H(0, 0) + \xi_{1\alpha i2}^{tI} I(0, 0^+) \right] [\rho_{1U}^t(x_1)]$ , in which:

$$2\pi \xi_{1\alpha i2}^{tR} H(0, 0) [\rho_{1U}^t(x_1)] = 2\xi_{1\alpha i2}^{tR} \int_{-\infty}^{\infty} P(x_1 - x'_1, 0, 0) \rho_{1U}^t(x'_1) dx'_1 \tag{3.46}$$

$$2\pi \xi_{1\alpha i2}^{tI} I(0, 0^+) [\rho_{1U}^t(x_1)] = 2\xi_{1\alpha i2}^{tI} \int_{-\infty}^{\infty} Q(x_1 - x'_1, 0, 0^+) \rho(x'_1) dx'_1 \tag{3.47}$$

In the case where  $a \rightarrow 0$  and  $b \rightarrow 0$ , the limiting values of the functions  $P$  and  $Q$  are given by [18]:

$$\text{Lim}_{a,b \rightarrow 0} P(x_1 - x'_1, a, b) = P(x_1 - x'_1, 0, 0) = \frac{1}{x_1 - x'_1} \tag{3.48}$$

$$\text{Lim}_{a,b \rightarrow 0} Q(x_1 - x'_1, a, b) = Q(x_1 - x'_1, 0, 0) = \pi \text{sgn}(b) \delta(x_1 - x'_1) \tag{3.49}$$

The Dirac delta function in Eq. 3.49 is particularly important as it is a mathematical carrier of the Burgers vector. The sign of the limit of  $Q$  is dependent on its third argument  $b$ . This must be taken into account in the subsequent formulation

when the limit of a quantity is evaluated at an infinitesimally small distance above and below an interface [18]. Using the expression of Eq. 3.48, Eq. 3.46 can be written as:

$$2\pi\xi_{1\alpha i 2}^{tR}H(0,0)[\rho_{1U}^t(x_1)] = 2\xi_{1\alpha i 2}^{tR}\int_{-\infty}^{\infty}\frac{\rho_{1U}^t(x'_1)}{x_1-x'_1}dx'_1 \quad (3.50)$$

In that case, there will be a singularity in the integral equation. In order to remove this singularity, Wang et al. [293, 294] have developed the technique of the  $H$  and  $I$  integral transforms. These  $H$  and  $I$  transforms can be used on  $P$  and  $Q$  functions or on themselves via residue calculus. In particular, using  $H(0,0)$  on itself can be used to remove the singularity problem in Eq. 3.50 as:

$$H(0,0)H(0,0) = -I(0,0^+) \quad (3.51)$$

Then, combining Eqs. 3.41, 3.44 and 3.49, the transform  $I(0,0^\pm)$  on image dislocation densities can be calculated as:

$$I(0,0^\pm)[\rho(x_1)] = \text{sgn}(0^\pm)\rho(x_1) \quad (3.52)$$

Thus, combining Eqs. 3.51 and 3.52, the singularity terms coming from  $H(0,0)$  can be removed, and the image dislocation densities appear by themselves. However, when the transform  $H(0,0)$  is used on all the terms in order to remove the singularities,  $H(0,0)I(0,0^\pm) = \text{sgn}(0^\pm)H(0,0)$  will produce new singularity terms ( $H(0,0)$  is directly used on image dislocation densities themselves). In order to resolve this problem, Wang et al. [18] have developed a more general method which is described as follows. Combining all 18 boundary conditions, a system of nonlinear equations is formed with 18 Fredholm equations of second kind ( $i=1,2$  and 3) with 18 unknowns  $\boldsymbol{\rho} = [\rho_{1U}^t, \rho_{1L}^t, \rho_{2U}^t, \rho_{2L}^t, \rho_{3U}^t, \rho_{3L}^t]^T$  as shown below:

$$\mathbf{C}\boldsymbol{\rho} + \mathbf{C}_0\mathbf{H}_0\boldsymbol{\rho} + \mathbf{C}_H\mathbf{H}\boldsymbol{\rho} + \mathbf{C}_I\mathbf{I}\boldsymbol{\rho} + \mathbf{C}_R\mathbf{R} = \mathbf{0} \quad (3.53)$$

where  $\mathbf{H}_0, \mathbf{C}_H\mathbf{H}, \mathbf{C}_I\mathbf{I}$  are the matrices of integral operator for the densities of image dislocations  $\boldsymbol{\rho}$  and  $\mathbf{C}, \mathbf{C}_0$  are the matrices of coefficient only depending on materials elastic properties.  $\mathbf{C}_R\mathbf{R}$  is the vector in function of Burgers vector of dislocation source. All the components of these matrices can be found in Appendix B. In Eq. 3.53, the singularities  $\mathbf{C}_0\mathbf{H}_0\boldsymbol{\rho}$  cannot be removed by applying  $H(0,0)$  on all the terms, because it will produce new singularities on the first term, as  $\mathbf{C}\mathbf{H}_0\boldsymbol{\rho}$ . However, the image dislocation densities themselves can be resolved from solving the algebraic equation Eq. 3.53 as:

$$\boldsymbol{\rho} = -\mathbf{C}^{-1}(\mathbf{C}_0\mathbf{H}_0\boldsymbol{\rho} + \mathbf{C}_H\mathbf{H}\boldsymbol{\rho} + \mathbf{C}_I\mathbf{I}\boldsymbol{\rho} + \mathbf{C}_R\mathbf{R}) \quad (3.54)$$

Then, by substituting Eq. 3.54 instead of  $\boldsymbol{\rho}$  in the term  $\mathbf{C}_0\mathbf{H}_0\boldsymbol{\rho}$  of Eq. 3.53, the final expression of the equations without singularity terms can be written as:

$$\begin{aligned} (\mathbf{C} + \mathbf{C}_0\mathbf{C}^{-1}\mathbf{C}_0)\boldsymbol{\rho} + (\mathbf{C}_H\mathbf{H} + \mathbf{C}_I\mathbf{I} - \mathbf{C}_0\mathbf{C}^{-1}\mathbf{C}_H\mathbf{H}_0\mathbf{H} - \mathbf{C}_0\mathbf{C}^{-1}\mathbf{C}_I\mathbf{H}_0\mathbf{I})\boldsymbol{\rho} \\ = -\mathbf{C}_R\mathbf{R} + \mathbf{C}_0\mathbf{C}^{-1}\mathbf{C}_R\mathbf{H}_0\mathbf{R} \end{aligned} \quad (3.55)$$

where the new matrices of integral operator  $\mathbf{C}_H\mathbf{H}_0\mathbf{H}$ ,  $\mathbf{C}_I\mathbf{H}_0\mathbf{I}$  and vector  $\mathbf{C}_R\mathbf{H}_0\mathbf{R}$  can be also found in Appendix B. It should be pointed out that due to the different convention used in the present thesis compared to in the paper of Wang et al. [18], the sign of each term is not exact the same as the one used in their paper. Furthermore, the matrices of integral operator  $\mathbf{C}_H\mathbf{H}$ ,  $\mathbf{C}_I\mathbf{I}$ ,  $\mathbf{C}_H\mathbf{H}_0\mathbf{H}$  and  $\mathbf{C}_I\mathbf{H}_0\mathbf{I}$  are the single independent matrices, not the product of matrices. Meanwhile, the vector  $\mathbf{C}_R\mathbf{R}$  and  $\mathbf{C}_R\mathbf{H}_0\mathbf{R}$  are the single independent vector, not the product of a matrix and a vector. In the final expression Eq. 3.55, there is no term with integral operator  $H(0,0)$  directly applied on the image dislocation densities  $\boldsymbol{\rho}$ . Thus, there is no singularities anymore. Eq. 3.55 is still a system of nonlinear equations with 18 Fredholm equations of second kind. These image dislocation densities can be numerically resolved by using the Nyström method [295]. Essentially, the integrals over infinite space can be approximated thanks to a Gauss-Hermite quadrature method. After substituting the integral terms, approximate analytical expressions of  $\boldsymbol{\rho}$  can be obtained as a function of  $x_1$ . Finally, the elastic fields, such as the stress fields due to one single dislocation in a three layers anisotropic material at any points can be calculated from Eqs. 3.38 and 3.42.

In the present thesis, the three-layer configuration is used to consider both effects of GB stiffness and free surfaces in the simulation of experimental slip step height profiles due to discrete dislocation pile-ups in section 4.4 (see Chapter 4). Thus, the second layer is regarded as a GB region and the thickness is set as 0.9 nm, which was obtained from MD simulation of the Ni bi-crystal studied in experiment and it is also a typical order of magnitude in metals. Meanwhile, the two-layer configuration is used to theoretically investigate the effect of free surfaces on dislocation image forces (see section 4.2).

### 3.3 Discrete dislocation pile-ups theory

Let us consider a single dislocation pile-ups of  $N$  infinite straight dislocations, which are all parallel to the  $\mathbf{x}_3$ -axis, have the same Burgers  $\mathbf{b}$  and lie in the same slip plane as shown in Figure 3.5.

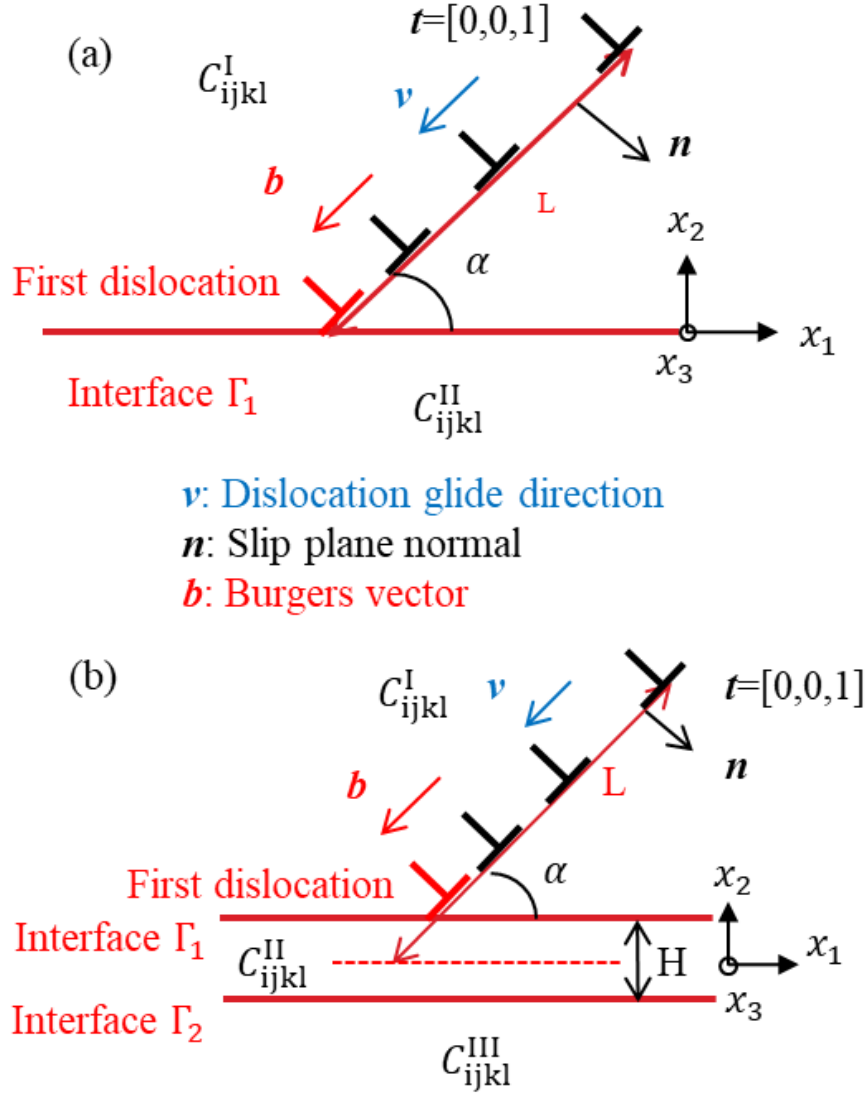


Figure 3.5:  $\alpha$ -inclined dislocation pile-up in a slip plane of unit normal  $\mathbf{n}$  for  $N$  equilibrated edge dislocations with Burgers vector  $\mathbf{b}$  and line vector  $\mathbf{t}$  in a heterogeneous anisotropic (a) bi-material and (b) tri-material [105, 277].

The equilibrium positions of the  $N$  dislocations can be found out by minimizing the component of the Peach-Koehler (P-K) force along the slip direction for each dislocation to a critical force  $F_c$  as follows:

$$F^{(\gamma)} = \text{abs}(\{(\boldsymbol{\sigma}_{int}(X_1(\gamma), X_2(\gamma)) + \boldsymbol{\sigma}_{ext}) \cdot \mathbf{b} \times \mathbf{t}\} \cdot \mathbf{v}) \stackrel{\text{Minimize}}{=} F_c \quad (3.56)$$

where  $(X_1(\gamma), X_2(\gamma))$  denotes the position of the  $\gamma^{\text{th}}$  dislocation.  $\mathbf{v}$  is a unit vector indicating the glide direction of all dislocations, which is considered to be directed



towards the interface so that a pile-up can form. Accordingly,  $F^{(\gamma)} > 0$  means that the  $\gamma^{th}$  dislocation is attracted by the GB (attractive GB) whereas  $F^{(\gamma)} < 0$  means that the  $\gamma^{th}$  dislocation is repelled by the GB (repulsive GB).  $\mathbf{v}$  belongs to the slip plane and is normal to the dislocation line.  $\boldsymbol{\sigma}_{ext}$  is a homogeneous applied stress tensor and  $\boldsymbol{\sigma}_{int} = \boldsymbol{\sigma}_{im} + \boldsymbol{\sigma}_{dis}$  is the internal stress tensor produced by all other dislocations  $\boldsymbol{\sigma}_{dis}$  and image stress  $\boldsymbol{\sigma}_{im}$  on this particular dislocation coming from all heterogeneities. It should be pointed out that in the present work, the applied homogeneous stress tensor  $\boldsymbol{\sigma}_{ext}$  only serves to equilibrate the dislocation pile-up. Even in the absence of singularities like dislocations, an infinite heterogeneously elastic material that is submitted to some (remotely) applied stress will actually display stress heterogeneities due to elastic/plastic incompatibilities that are needed to maintain the continuity conditions at the interfaces (see the derivation of incompatibility stresses in a bi-crystal with a planar GB in subsection 1.5.2.4 of Chapter 1). The critical force  $F_c$  includes the lattice friction force (primary) and other forces due to obstacles to dislocation motion (solutions, precipitates, defects like cavities, etc.). Meanwhile, this critical force can be converted into a shear stress on a dislocation by dividing by the length of standard Burgers vector as  $\tau_c = F_c/|\mathbf{b}|$ . The calculation of the dislocation pile-up equilibrium positions is thus obtained by following an iterative relaxation scheme that minimizes all the  $F^{(\gamma)}$  after an initial configuration is specified [105]. In order to be able to perform such a computation in an infinite homogeneous medium, one dislocation should be considered as locked. Usually, the position of the first (or leading) dislocation ( $X_1(1), X_2(1)$ ) is fixed [97, 105]. As a result, the P-K force on the fixed dislocation is not zero. In a heterogeneous medium, the boundary image force on the leading dislocation may equilibrate the applied stress and the stress contribution coming from other dislocations [105], but only in case of repulsive image force. In such case, the positions of all dislocations, including the leading one, can be found by the iterative relaxation scheme. Most past studies assume  $F_c = 0$  N/m because of the low value of the lattice friction stress in pure FCC crystals which is around  $1 \sim 2$  MPa [296]. However, in the present thesis, it is found that a non zero critical force has a crucial effect on the dislocation pile-up distribution in the presence of GB and free surfaces. This will be discussed more thoroughly in next Chapter 4. The reason is that there are already lattice defects in the material after sample preparation, such as the  $\text{Ga}^+$  ions from FIB which can damage the sample surfaces [139]. Furthermore, for  $\alpha$ -Brass (alloy), the theoretical value of the friction force should be much higher than in pure FCC crystals, like pure Ni. For example, it was found that  $\tau_c \approx 80 \sim 100$  MPa for  $\beta$ -Brass [296]. Thus the critical force cannot be ignored in Eq. 3.56 for realistic calculation.

## 3.4 Computational procedure

A Matlab [297] code has been developed during this thesis, for which the computational flow chart with the different calculation configurations is represented in Figure 3.6.



Figure 3.6: Computational flow chart describing the different procedures in a developed Matlab code.

The developed Matlab code can be used to calculate the elastic fields, such as the image force, the displacement vector, the stress tensor or the induced resolved shear stress, due to one single dislocation or one dislocation pile-up in different configurations. Furthermore, the slip step height profiles due to single slip and measured by AFM can be simulated from the developed code. There are three different types of Matlab code corresponding to the bi-material configuration without free surface (“Ani\_Inf\_Bi\_Homo\_Halfspace” in Figure 3.6), tri-material configuration without free surface (“Ani\_Inf\_Tri” in Figure 3.6) and tri-material configuration with free surfaces (“Ani\_Fini\_Tri\_Bi\_SingleLayer” in Figure 3.6). In particular, the bi-material configuration without free surface can be degenerated to the case of infinite homogeneous single crystal and half space with rigid or free surface. The bi-material code is based on all the theories presented from section 3.2.1 to section 3.2.3 and is fully analytical without any convergence issue. The tri-material configuration without free surface is based on the theory presented in section 3.2.4. For numerical applications, a number of steps  $\beta$  must be chosen for the series solutions based on the convergence analyses. Meanwhile, the tri-material configuration with free surfaces can be degenerated to the case of the bi-material configuration with free surfaces or to the case of one layer material with free surfaces by taking materials with same elastic stiffness tensor. Numerical applications involve infinite integral calculations. Thus, a reasonable number of integration points in the Nyström method with Gauss-Hermite quadrature must be chosen. So, it is semi-analytical.

All the codes are built with some individual functions. The structure of these functions is the same for all the three codes. As presented in Figure 3.6, the first two functions are used to get the input data, including the mechanical properties of materials and the orientation of each grain. The mechanical properties of materials include the elastic stiffness tensor ( $C_{ij}$ ), the length of standard Burgers vector ( $b$ ), the dimension of simulated sample used for simulating experiment (“Dimension” in Figure 3.6), the applied stress for dislocation pile-ups ( $\sigma_{app}$ ), the interesting grain which contains dislocations (“Studied Crystal” in Figure 3.6), the critical force for dislocation pile-ups (“f-CRSS” in Figure 3.6) and the parameter  $\lambda$  which is used to define the elastic stiffness tensor of the interphase considered as a GB by  $C_{ijkl}^{\text{II}} = \frac{\lambda}{2} (C_{ijkl}^{\text{I}} + C_{ijkl}^{\text{III}})$  in the tri-material configuration. At the same time, the effect of incompatibility stresses (presented in section 1.5.2.4) can be chosen to be considered or not (“Schmid/Incompatibility” in Figure 3.6). It should be pointed out that all these codes are based on L-E-S formalism which cannot be used for isotropic elasticity calculation due to the problem of repeated eigenvalues (degenerate solutions). However, these codes can still be used for isotropic elasticity calculation. In that case, the elastic stiffness moduli are firstly represented from isotropic elastic constants by  $C_{11} = 2G(1 - \nu) / (1 - 2\nu)$ ,  $C_{12} = 2G\nu / (1 - 2\nu)$  and

$C_{44} = G$ . Then the  $C_{44}$  is increased a little bit to prevent the problem of degenerate solutions in the L-E-S formalism and is numerically replaced by  $C_{44} = C_{44} \times 1.0001$ . Besides, Choi and Earmme [175] have developed a two dimensional analytical formalism for isotropic elasticity calculation of one single dislocation in a tri-material configuration. Codes that compute the elastic fields of one dislocation or dislocation pile-up in homogeneous media, bi-material and tri-material configurations were also coded using Matlab with the same functions as the one presented in the Figure 3.6. In the present thesis, the isotropic elasticity calculations without free surface have been performed using the analytical formalism [175]. Only the isotropic elasticity calculations with free surfaces are performed using L-E-S formalism with the approximation  $C_{44} = C_{44} \times 1.0001$ . Furthermore, the orientation of each grain can be set from EBSD measurement with the Euler angles  $(\phi_1, \Phi, \phi_2)$  or from a given rotation matrix which will be presented (see section 4.2.1 in Chapter 4).

Based on the orientation of each grain with respect to the direction of applied stress, the Schmid factor (or the resolved shear stress considering incompatibility stress) on each slip system can be calculated. The slip system of FCC crystal can be chosen as perfect dislocation  $[111] \langle 10 - 1 \rangle$  or as partial Shockley dislocation  $[111] \langle 11 - 2 \rangle$ . Then, the active slip system is chosen based on the analysis of Schmid factor/resolved shear stress with the maximum value or based on experimental observation. The details are discussed in section 2.7. After the determination of the active slip system, the coordinates of simulation is built in order to satisfy the conditions of two dimensional calculation, i.e. the dislocation line must be parallel to GB. As presented in section 1.5.3, in the simulation coordinates system, the  $\mathbf{x}_3$ -direction is set to be the direction of dislocation line  $z_S$  as presented in Figure 3.7, and the  $\mathbf{x}_2$ -direction is set to be the direction of GB normal  $y_S$  as presented in Figure 3.7. In agreement with the FS/RH convention, the  $\mathbf{x}_1$ -direction is determined by  $\mathbf{x}_1 = \mathbf{x}_2 \times \mathbf{x}_3$  presented as  $x_S$  in Figure 3.7. Furthermore, all the used vectors and tensors, such as the Burgers vector of active slip systems, the vector of slip direction and the elastic stiffness, etc. are converted into the simulation coordinates system.

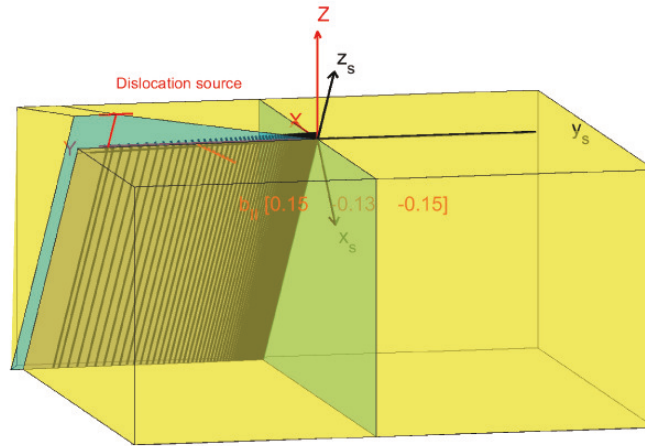


Figure 3.7: Schematic figure of simulation configuration adopted for the experiment.  $(x_s, y_s, z_s)$  indicate the simulation coordinates system, while  $(X, Y, Z)$  indicate the global sample coordinates system.

After that, based on all the necessary information, the elastic fields due to one single dislocation or dislocation pile-ups can be calculated based on the theories and the Matlab code presented in this chapter.

# Chapter 4

## Results and discussions

### 4.1 Introduction

In the present chapter, the following results will be successively presented and discussed. First of all, the pure theoretical and numerical results of the theories described in Chapter 3 for Ni are presented for discussing the role of elastic anisotropy and different boundary conditions (interphase GB and free surfaces) on image forces and discrete dislocation pile-ups, thus the interaction between individual dislocation and GBs. In details, the results are as follows:

- The convergence of series solutions within the tri-material configuration is discussed based on three criteria described in subsection 3.2.4.4.
- Elastic fields (displacements, stresses and image forces) due to one single edge dislocation in different heterogeneous media are calculated.
- The equilibrium positions of edge dislocation pile-ups as well as the resolved shear stress produced by these pile-ups are also performed.

In order to simulate the slip step height profiles of slip lines produced by the compression test on Ni and  $\alpha$ -Brass bi-crystal samples (described in Chapter 2) with considering the effect of incompatibility stresses, the incompatibility stresses of these samples are calculated by CPFEM considering the effect of boundary conditions on finite specimen. These numerical results are also compared with analytical results based on Eqs. 1.44 and 1.45 in subsection 1.5.2.4 considering only anisotropic elasticity and infinite space. Meanwhile, the stress-strain curve due to the compression test of these samples are also calibrated by CPFEM.

At the end of the chapter, the slip step height profiles observed in experiments (presented in the Chapter 2) are simulated for both Ni and  $\alpha$ -Brass samples using

discrete dislocation pile-up calculations (described in Chapter 3). The effects of interfacial dislocations, free surfaces, anisotropic elasticity, incompatibility stresses, applied stress, misorientation and lattice friction are fully discussed.

## 4.2 Theoretical results

### 4.2.1 Computation configurations

In all the following numerical applications presented in the section 4.2, bicrystals of different orientations are considered. In case of a tri-material configuration, the interphase material is supposed to represent the GB region. Furthermore, only edge dislocations with Burgers vector defined by an angle  $\alpha = 45^\circ$  are considered as shown in Figure 3.1, so that the slip direction is  $\mathbf{m} = \mathbf{b}/|\mathbf{b}| = [-\cos 45^\circ, -\sin 45^\circ, 0]$  in global frame  $(\mathbf{x}_1, \mathbf{x}_2, \mathbf{x}_3)$ . Still following the FS/RH convention, the slip plane normal is given by  $\mathbf{n} = \mathbf{t} \times \mathbf{m}$  where  $\mathbf{t} = [0, 0, 1]$ . Meanwhile, the glide direction of dislocations  $\mathbf{v}$  is parallel to  $\mathbf{m}$  for edge dislocations and it always points towards the GB area, so that it is possible to create dislocation pile-ups at GB. The slip system is supposed to be  $\mathbf{m}^0 = 1/\sqrt{2}[1, 1, 0]$  and  $\mathbf{n}^0 = 1/\sqrt{3}[-1, 1, -1]$  in the crystal's frame  $(\mathbf{e}_1, \mathbf{e}_2, \mathbf{e}_3)$ . Thus the orientation of the crystal containing the dislocations is defined by the transformation matrix  $\mathbf{T}$  such that  $[\mathbf{m}, \mathbf{n}, \mathbf{t}]^T = \mathbf{T} [\mathbf{m}^0, \mathbf{n}^0, \mathbf{t}^0]^T$ , where  $\mathbf{t}^0 = \mathbf{m}^0 \times \mathbf{n}^0$ . In the lower crystal, there is no dislocation and thus the choice of its crystallographic orientation is free. For this crystal, two specific orientations are considered in the following:

- orientation A<sup>Ori</sup> with  $\mathbf{T}_A = \begin{bmatrix} 1 & 0 & 0 \\ 0 & 1 & 0 \\ 0 & 0 & 1 \end{bmatrix}$  (Unit matrix)
- orientation B<sup>Ori</sup> with  $\mathbf{T}_B = \begin{bmatrix} -1/2 & \sqrt{2}/2 & 1/2 \\ -1/2 & -\sqrt{2}/2 & 1/2 \\ \sqrt{2}/2 & 0 & \sqrt{2}/2 \end{bmatrix}$

The elastic stiffness tensor in the global frame is then deduced from the transformation matrix  $\mathbf{T}$  by  $C_{ijkl} = T_{ig}T_{jh}C_{ghmn}^0T_{km}T_{ln}$  where  $\mathbf{C}^0$  is the elastic stiffness tensor defined in the crystal's frame. For tri-material and multilayers models, the thickness of the second material as GB is denoted  $H$  which is always equal to  $5|\mathbf{b}|$  in the present section, and its elastic stiffness tensor  $C_{ijkl}^{\text{II}}$  is modeled thanks to a single parameter  $\lambda$  which reflects the GB stiffness as follows:

$$C_{ijkl}^{\text{II}} = \frac{\lambda}{2} (C_{ijkl}^{\text{I}} + C_{ijkl}^{\text{III}}) \quad (4.1)$$



Then, the GB is softer than the grains when  $\lambda < 1$  and stiffer than the grains for  $\lambda > 1$ . In the extreme cases, when  $\lambda = 0$ , the tri-material reduces to a half-space with a free surface, whereas when  $\lambda = +\infty$ , the tri-material reduces to a half-space with a rigid surface. Hence, the single parameter  $\lambda$  allows to study the effect of the GB stiffness on elastic fields of single dislocations and dislocation pile-ups in bi-crystals with GB as a thin interphase region.

For multilayers model with free surfaces, only two-layers configuration is applied in the present section 4.2 with  $h_1 = h_3 = H'/2$  as shown in Figure 4.1, so that the GB is regarded as an interface ( $H = h_2 = 0$ ).

The distance between the GB (or the middle of the GB region) and the  $\gamma^{th}$  dislocation along the glide direction is denoted  $L(\gamma)$ . For dislocation pile-ups, when the leading dislocation is locked,  $L(1) = 5|\mathbf{b}|$ . The pile-up length is defined as the distance between the first and the last dislocation  $L(N) - L(1)$ .

For the forthcoming results in the present section, a regular grid of  $M_x \times M_y$  points and of  $L_x \times L_y$  in size are considered for the simulation plane where the elastic fields are computed. If not specifically stated in the text, the values used for numerical applications are the default values reported in Table 4.1.

$C_{11}$ (GPa)	$C_{12}$ (GPa)	$C_{44}$ (GPa)	$G$ (GPa)	$k$ (GPa)	$ \mathbf{b} $ (nm)
246.5	147.3	124.7	94.7	179.8	0.25
$\sigma_{22}^{ext}$ (MPa)	$\alpha$ ( $^\circ$ )	$L(1)$ ( $ \mathbf{b} $ )	Orientation of the lower crystal		
100	45	5	A <sup>Ori</sup>		
$\lambda$	$H$ ( $ \mathbf{b} $ )	$L_x \times L_y$ ( $ \mathbf{b} ^2$ )		$M_x \times M_y$	
1	5	50 $\times$ 50		100 $\times$ 100	

Table 4.1: Default values of the parameters used for theoretical and numerical simulations in the present section. The elastic constants are for Ni defined in the crystal's frame ( $\mathbf{e}_1, \mathbf{e}_2, \mathbf{e}_3$ ).  $G$ : effective isotropic shear modulus,  $k$ : effective isotropic bulk modulus. The Poisson's ratio can be calculated by  $\nu = (3k - 2G) / (6k + 2G)$ .

Figure 4.1 displays the most general configuration considered. The abbreviations used in the legends of the figures presented in the present section are:

- “Ani”: Anisotropic elasticity.
- “Iso”: Isotropic elasticity.
- “Bi”: Bi-material model with  $H = h_2 = 0$ , materials I and III are infinite (without free surfaces  $\Lambda_1$  and  $\Lambda_2$ ).
- “rigid Half-space”: Half space with rigid surface, material I is infinite (without free surface  $\Lambda_1$ ), materials II and III do not exist (interface  $\Gamma_1$  is regarded as a rigid surface with displacement free).

- “free Half-space”: Half space with free surface, material I is infinite (without free surface  $\Lambda_1$ ), materials II and III do not exist (interface  $\Gamma_1$  is regarded as a free surface with traction free).
- “Tri $\lambda$ ”: Tri-material model, materials I and III are infinite (without free surfaces  $\Lambda_1$  and  $\Lambda_2$ ), the thickness of interphase  $H = h_2 = 5|\mathbf{b}|$ . This value appears to be realistic as following atomistic simulation (see Appendix C). Parameter  $\lambda$  is used to determine the stiffness tensor of material II which is defined in Eq. 4.1.
- “UF $h_1$ ”: Only considering upper free surface  $\Lambda_1$  with  $h_2 = 0$  (using Eqs. 3.32, 3.33 and 3.34, the dislocation is regarded as stored in material II for these equations). Material III is infinite (without free surface  $\Lambda_2$ ).  $h_1$  is the thickness of the material I which is in  $\mu\text{m}$ .
- “LF $h_3$ ”: Only considering lower free surface  $\Lambda_2$  with  $h_2 = 0$  (using Eqs. 3.29, 3.30 and 3.31, the lower material is regarded as the material II for these equations). Material I is infinite (without free surface  $\Lambda_1$ ).  $h_3$  is the thickness of the material III which is in  $\mu\text{m}$ .
- “FS $h_1$ ”: Considering two free surfaces  $\Lambda_1$  and  $\Lambda_2$  without interphase as  $h_2 = 0$ , the thicknesses of materials I and III are always the same ( $h_1 = h_3$ ), thus the thickness of the whole material is  $H' = h_1 + h_3 = 2h_1$ .
- “A<sup>Ori</sup>”: Orientation A<sup>Ori</sup> for lower crystal.
- “B<sup>Ori</sup>”: Orientation B<sup>Ori</sup> for lower crystal.

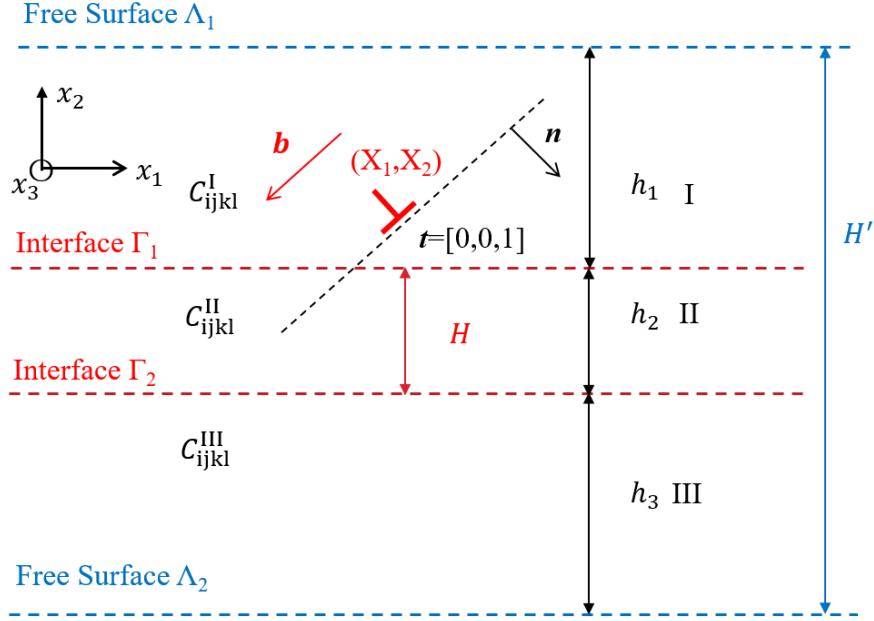


Figure 4.1: Schematic figure of general simulation configurations.

#### 4.2.2 Convergence of the series solutions within the tri-material configuration

In this subsection, the three convergence criteria defined and discussed in subsection 3.2.4.4,  $\epsilon_f^{\beta+1}$  (Eq. 3.35),  $\epsilon_u^{\beta+1}$  (Eq. 3.36) and  $\epsilon_\sigma^{\beta+1}$  (Eq. 3.37) are used to study the influence of three important physical parameters on the convergence of the series solutions in case of a single dislocation within a tri-material configuration of Ni (Figure 3.2). These parameters are the stiffness parameter  $\lambda$  (Eq. 4.1), the thickness of the interphase  $H$  and the distance between the dislocation and the first interface along the glide direction denoted  $L_{\Gamma_1}$  (rather than  $L(1)$  since  $H$  is also varied). To avoid wasting calculation resources, it is indeed important to find out the minimum value of step number  $\beta$  allowing the convergence of the series. It is hereafter considered that the convergence is reached when all the three criteria  $\epsilon_f^{\beta+1}$ ,  $\epsilon_u^{\beta+1}$  and  $\epsilon_\sigma^{\beta+1}$  are smaller than  $10^{-4}$ .

First, the effect of  $\lambda$  was investigated by setting  $H = 5|\mathbf{b}|$ ,  $L_{\Gamma_1} = 2|\mathbf{b}|$ ,  $M_x \times M_y = 200 \times 200$  and  $L_x \times L_y = 200 \times 200|\mathbf{b}|^2$  while the other parameters are given by the default values presented in Table 4.1. Figure 4.2 shows the computed errors by the three criteria for  $\lambda = 0.5, 1$  and  $2$ . It is found that the logarithm of the errors roughly scales with the step number  $\beta$ . When  $\lambda = 1$ , the convergence is reached for  $\beta = 3$  while for  $\lambda = 0.5$  and  $\lambda = 2$ , the convergence is reached for  $\beta = 5$ . It was checked that the convergence becomes more and more difficult when

$\lambda$  departs more and more from unity. However, it is noteworthy that if  $\lambda$  is zero or is infinite, the model equations of subsection 3.2.4.3 reduces to a half-space with a free or a rigid surface and the exact solutions can be obtained directly from Eqs. 3.23, 3.24 and 3.26.

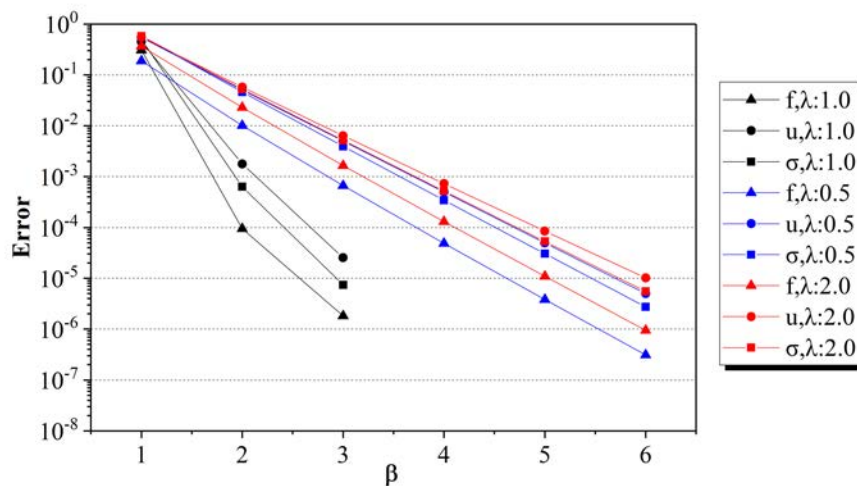


Figure 4.2: Numerical errors computed by the three criteria ( $\epsilon_f^{\beta+1}$ ,  $\epsilon_u^{\beta+1}$  and  $\epsilon_\sigma^{\beta+1}$ ) for  $\lambda = 0.5$ , 1 and 2.

Secondly, the effect of  $H$  was investigated by setting  $\lambda = 2$ ,  $L_{\Gamma_1} = 2|\mathbf{b}|$ ,  $M_x \times M_y = 200 \times 200$  and  $L_x \times L_y = 200 \times 200 |\mathbf{b}|^2$ . Figure 4.3 shows the numerical errors computed by the three criteria for  $H = 5|\mathbf{b}|$ ,  $25|\mathbf{b}|$  and  $50|\mathbf{b}|$ . It is found again that the logarithm of the errors scales with the number of steps  $\beta$ . The error given by  $\epsilon_u^{\beta+1}$  (disk markers in Figure 4.3) is very little dependent on  $H$  while it is easier to get convergence on  $\epsilon_f^{\beta+1}$  and  $\epsilon_\sigma^{\beta+1}$  when  $H$  becomes larger. The reason is that when the thickness of the interphase is larger and larger, the tri-material model gets closer and closer to a bi-material model and the effects of the lower crystal becomes smaller and smaller.

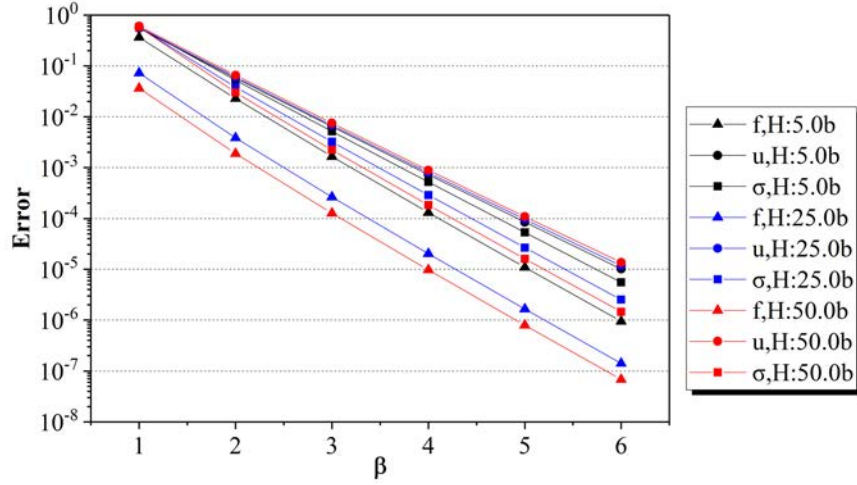


Figure 4.3: Numerical errors computed by the three criteria ( $\epsilon_f^{\beta+1}$ ,  $\epsilon_u^{\beta+1}$  and  $\epsilon_\sigma^{\beta+1}$ ) for  $H = 5|\mathbf{b}|$ ,  $25|\mathbf{b}|$  and  $50|\mathbf{b}|$ .

Finally, the effect of  $L_{\Gamma_1}$  was investigated by setting  $\lambda = 2$ ,  $H = 5|\mathbf{b}|$ ,  $M_x \times M_y = 200 \times 200$  and  $L_x \times L_y = 200 \times 200|\mathbf{b}|^2$ . Figure 4.4 shows the computed numerical errors by the three criteria for  $L_{\Gamma_1} = 2|\mathbf{b}|$ ,  $100|\mathbf{b}|$  and  $150|\mathbf{b}|$ . The error given by  $\epsilon_u^{\beta+1}$  and  $\epsilon_\sigma^{\beta+1}$  (disk and square markers in Figure 4.4) are very little dependent on  $L$ . Contrary to Figure 4.2 and Figure 4.3, when  $L_{\Gamma_1} = 100|\mathbf{b}|$  and  $150|\mathbf{b}|$ , the criterion based on  $\epsilon_f^{\beta+1}$  gives the slowest convergence. The reason is that when the distance between the dislocation and the interface is large, the elastic fields close to the dislocation are weaker than before. Hence, at each step, the relative part of the image force increase is larger compared to the case where the dislocation is close to the interface.

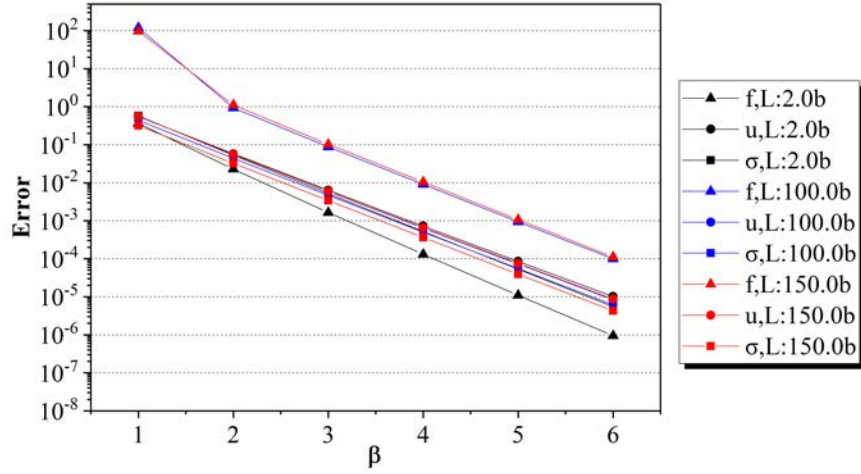


Figure 4.4: Numerical errors computed by the three criteria ( $\epsilon_f^{\beta+1}$ ,  $\epsilon_u^{\beta+1}$  and  $\epsilon_\sigma^{\beta+1}$ ) for  $L_{\Gamma_1} = 2|\mathbf{b}|$ ,  $100|\mathbf{b}|$  and  $150|\mathbf{b}|$ .

As a consequence of these investigations, the convergence criteria based on  $\epsilon_u^{\beta+1}$  and  $\epsilon_\sigma^{\beta+1}$  seem the most appropriate to consider all kinds of situations. Moreover, it was found that only the stiffness parameter  $\lambda$  strongly influences the convergence. Hence, for a same value of  $\lambda$ , a same value of  $\beta$  will be considered in the numerical applications.

The obtained values of  $\beta$  for different  $\lambda$  in case of anisotropic elasticity and isotropic elasticity are presented in Table 4.2. The computations of the elastic fields in a tri-material with heterogeneous isotropic elasticity were also performed for comparisons following the expressions obtained by Choi and Earmme [175]. In this case, the configuration of a Ni bi-crystal is considered such that  $G^{\text{II}} = \lambda G$  and  $k^{\text{II}} = \lambda k$ . Hence, when  $\lambda = 1$ , the configuration reduces to the homogeneous material model and no convergence step is needed ( $\beta = 0$ ). It is found that for a same value of  $\lambda$ , the convergence is fastest in the isotropic elastic case than in the anisotropic elastic case.

		$\lambda$	0.25	0.5	1.0	2.0	4.0
$\beta$	Anisotropic		9	5	3	5	9
	Isotropic		7	4	0	4	7

Table 4.2: Number of steps  $\beta$  to reach convergence according to the criteria ( $\epsilon_f^{\beta+1}$ ,  $\epsilon_u^{\beta+1}$  and  $\epsilon_\sigma^{\beta+1} < 10^{-4}$ ) for different values of  $\lambda$ : anisotropic vs. isotropic elastic cases.

### 4.2.3 Displacements and stresses distribution due to one single dislocation

This subsection considers a single straight edge dislocation in a Ni bi-crystal and compares the induced elastic fields for different kinds of GB modelling characteristics: zero thickness GB (bi-material configuration) or GB with  $H = 5 |\mathbf{b}|$  and different values of the stiffness parameter  $\lambda$  (tri-material configuration). The interface or the middle of the GB is fixed at  $x_2 = 0$  and the distance from the interface or the middle of the GB to the dislocation along the slip direction is  $L = 10 |\mathbf{b}|$ .

Figure 4.3 shows contour plots of the displacement component  $u_1$  (normalized by  $|\mathbf{b}|$ ) and stress components  $\sigma_{12}$  (normalized by  $C_{44}$ ) which are induced by a single edge dislocation in a Ni bi-crystal with a zero thickness GB and with GBs characterized by  $H = 5 |\mathbf{b}|$  and  $\lambda = 0.5, 1$  and  $2$  (tri-material model), as well as the differences between bi-material model and tri-material model. It is remarked that  $u_1$  and  $\sigma_{12}$  are continuous across interfaces with normal along  $\mathbf{x}_2$ , which is consistent with interfacial continuity conditions (Eqs. 3.6 and 3.7). In the case of  $\lambda = 1$ , for both fields, the differences are concentrated in the middle of the GB. In the cases  $\lambda = 0.5$  and  $2$ , the differences are mainly concentrated around the first (or upper) interface and are also much larger compared to the case  $\lambda = 1$ . The cases  $\lambda = 0.5$  (compliant GB) and  $\lambda = 2$  (stiff GB) often display opposite effects. For example, the difference of displacement  $u_1$  is negative below the dislocation when  $\lambda = 0.5$  while it is positive when  $\lambda = 2$ .

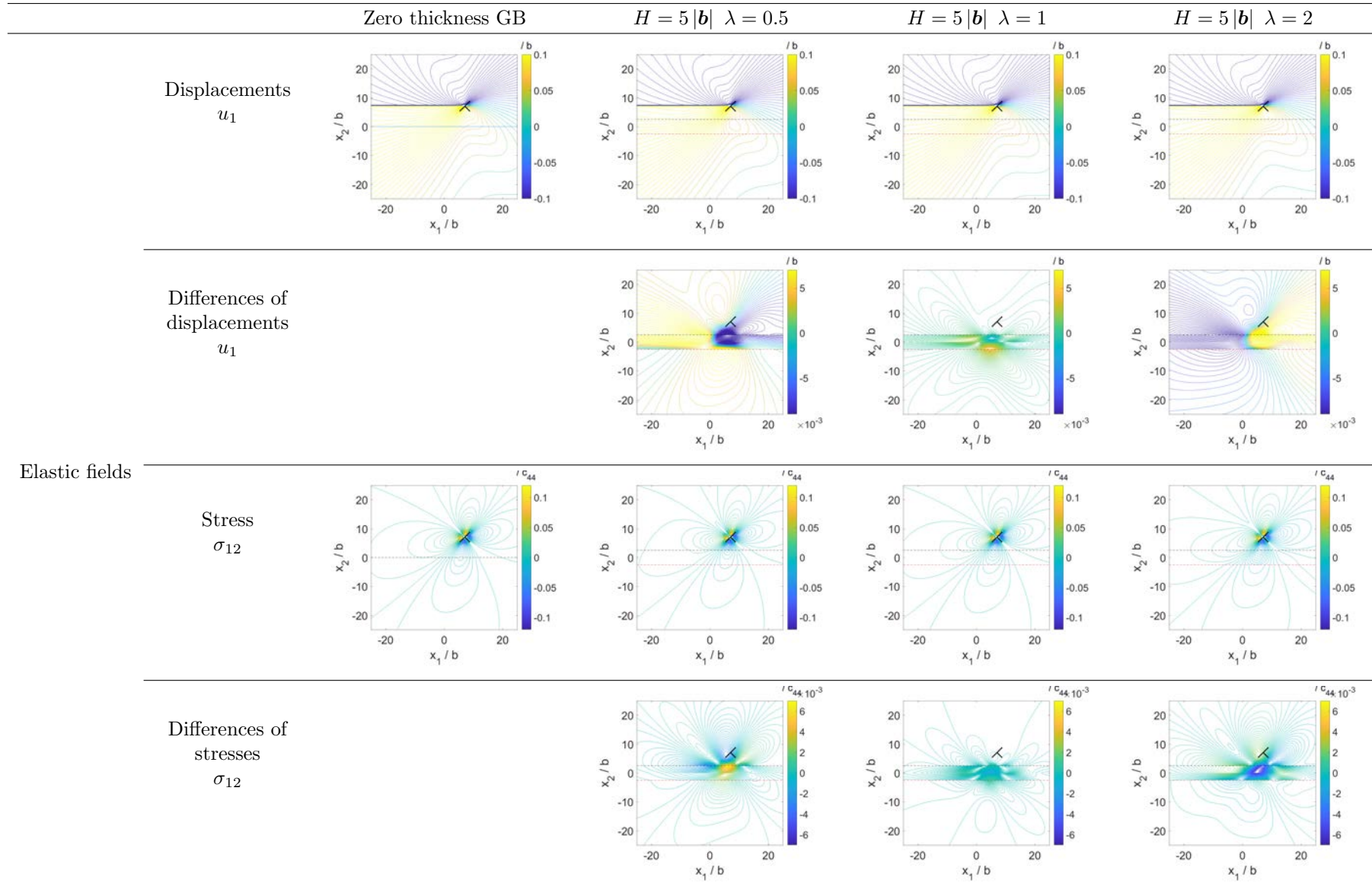


Table 4.3: Elastic fields induced by a single dislocation in a Ni bi-crystal with a zero thickness GB and tri-material with GBs characterized by  $H = 5|b|$  and  $\lambda = 0.5, 1$  and  $2$  and their differences of elastic fields.



#### 4.2.4 Image force on dislocation in heterogeneous media

In a heterogeneous medium, an image force is exerted on the dislocation due to the presence of interface(s) or surface(s). The image force is the Peach-Koehler force at the dislocation position due to its stress field without considering the contribution related to the infinite homogeneous medium, denoted hereafter  $\boldsymbol{\sigma}_{im}$ . The projection of the image force along the slip direction reduces to [28]:

$$F_{im} = [(\boldsymbol{\sigma}_{im} \cdot \mathbf{b}) \times \mathbf{t}] \cdot \mathbf{v} \quad (4.2)$$

With the convention used in Figure 3.1, as  $\mathbf{v}$  always points towards to the GB,  $F_{im} > 0$  means that the dislocation is attracted by the GB whereas  $F_{im} < 0$  means that the dislocation is repelled by the GB.

First, Figure 4.5 (a) considers half-space configurations and Figure 4.5 (b) considers bi-material (i.e., zero thickness GB). It indicates that in a half space, a rigid surface has always a repulsive effect on the dislocation. On the contrary, a free surface has always an attractive effect. Moreover, if the lower crystal is set to orientation A<sup>Ori</sup>, the projected image force  $F_{im}$  is always positive, which means that the zero thickness GB exerts an attractive effect on the dislocation, whereas with orientation B<sup>Ori</sup>, the dislocation is repelled by the GB. It can be also noticed that the magnitude of  $F_{im}$  is far smaller for the bi-crystal than for the half space with free / rigid surfaces, which represent two extreme cases. Besides, considering isotropic elasticity in half-spaces,  $F_{im}$  has nearly the same magnitude as considering anisotropic elasticity (curves are superimposed). Given the chosen orientation of upper crystal, it should be pointed out that orientation A<sup>Ori</sup> and orientation B<sup>Ori</sup> of lower crystal produce the maximum positive and negative projected image forces  $F_{im}$ , respectively.

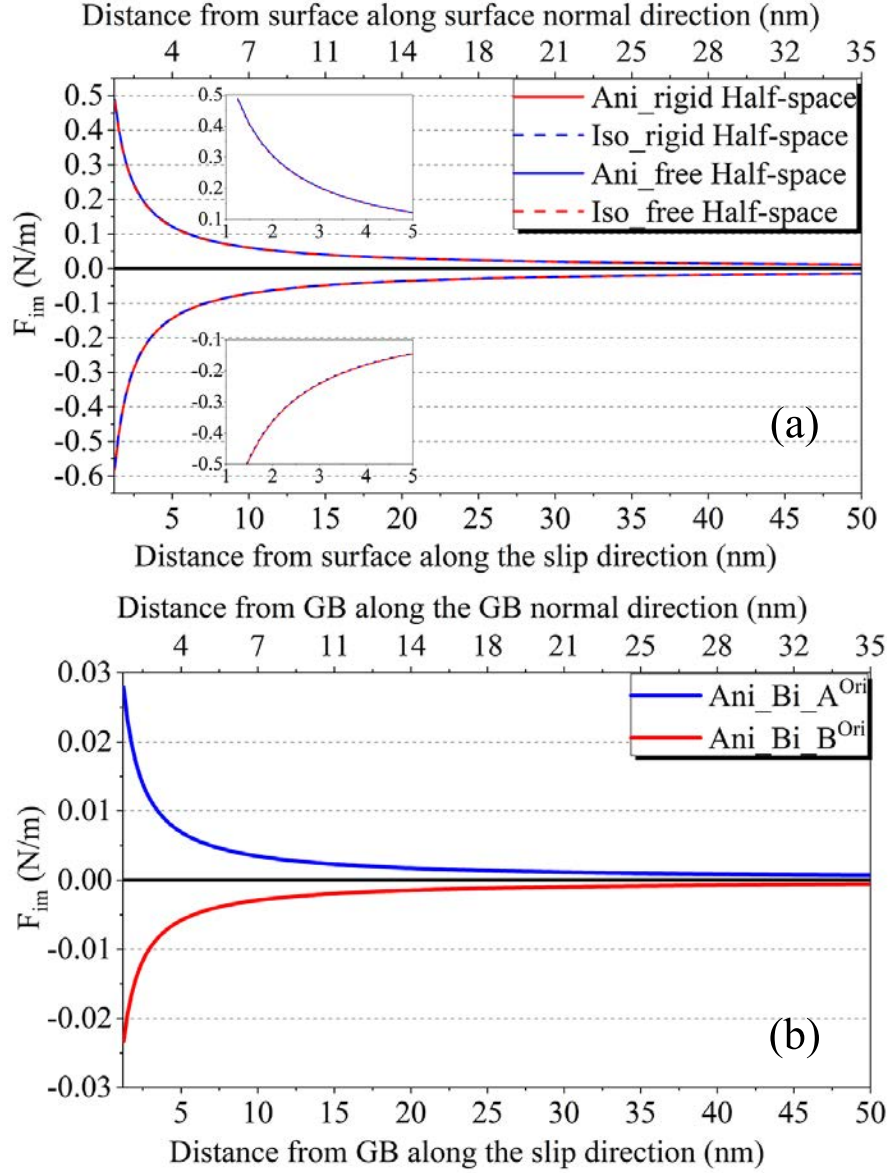


Figure 4.5: Variation of the projected image force  $F_{im}$  with the distance from the GB along the slip direction for different configurations: (a) half space with anisotropic vs. isotropic elasticity and (b) bi-crystal modeled by bi-material configuration.

Figure 4.6 considers only tri-material configurations with  $H = 5 |\mathbf{b}|$  and make comparisons between anisotropic and isotropic elasticity. For  $H = 5 |\mathbf{b}|$ , considering isotropic elasticity, the projected image force  $F_{im}$  is always negative in case of a stiff GB ( $\lambda=2$ ) and positive in case of a soft GB ( $\lambda=0.5$ ). In the case of anisotropic elasticity,  $F_{im}$  exhibits a sign change and extremal points because of

the coupled effects of the image forces arising both from the lower crystal and the GB. For instance, considering a GB characterized by  $\lambda=2$  and orientation  $A^{\text{Ori}}$  for the lower crystal,  $F_{im}$  is negative close to the GB and becomes positive beyond 10.2 nm ( $41|\mathbf{b}|$ ) from the center of GB (Figure 4.6). The repelling effect close to the GB is due to the larger stiffness of the GB ( $\lambda=2$ ) while the attractive effect that becomes predominant at long distance is due to orientation  $A^{\text{Ori}}$  of the lower crystal as shown in Figure 4.5 (b). Accordingly, an equilibrium position for the dislocation can be defined where  $F_{im} = 0$ . In a similar manner, an equilibrium position in the absence of applied stress can also be found by coupling an attractive compliant GB ( $\lambda=0.5$ ) with the repulsive orientation  $B^{\text{Ori}}$  of the lower crystal (Figure 4.6). In this case, the equilibrium position of the dislocation is found around 14.5 nm ( $58|\mathbf{b}|$ ) along the slip direction from the center of GB.

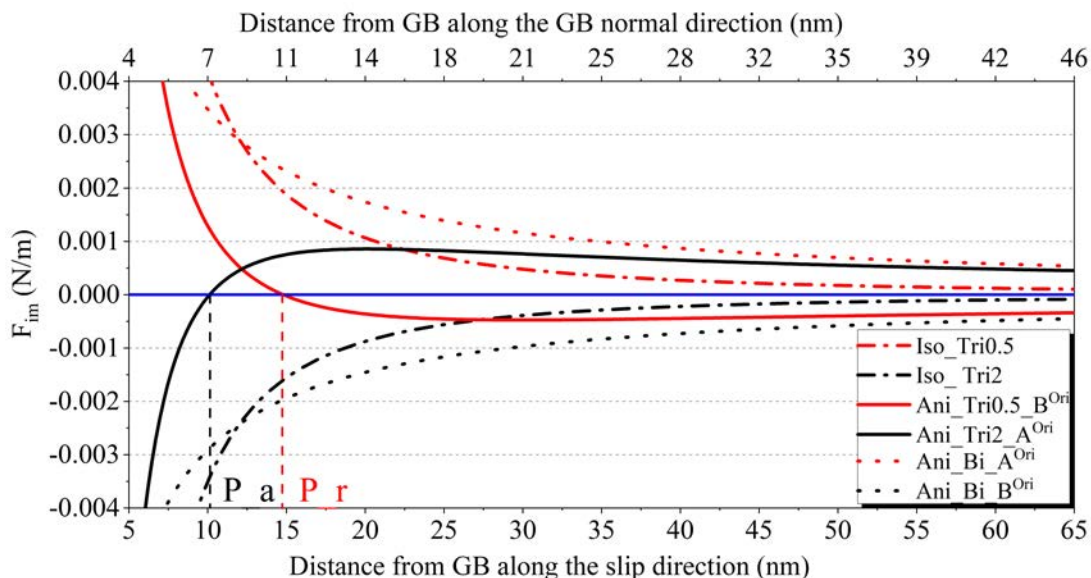


Figure 4.6: Variation of the projected image force  $F_{im}$  with the distance from the GB along the slip direction for different tri-material configurations with  $H = 5|\mathbf{b}|$ . Anisotropic vs. isotropic elasticity.

Besides the effect of misorientation and GB stiffness, the effect of free surfaces  $\Lambda_1$  and  $\Lambda_2$  has been investigated by a two-layers configuration with different misorientations  $A^{\text{Ori}}$ ,  $B^{\text{Ori}}$  and different thicknesses  $H' = h_1 + h_3 = 2\mu\text{m}$  and  $H' = 4\mu\text{m}$  (see Figure 4.1). Figure 4.7 (a) shows that free surfaces have a strong attractive effect on dislocations. In comparison, the effect of misorientation is negligible close to free surface as the value of  $F_{im}$  is quite similar whatever the orientation. A size effect is found after normalizing the distance by half of the thickness as shown in Figure 4.7 (b): at the same relative distance from the GB, the image force is

stronger in the smaller beam. Meanwhile, in case of an attractive misorientation  $A^{\text{Ori}}$ , there is an equilibrium point where the image force on the dislocation is zero. This position is located at nearly the same relative distance from GB for different thicknesses of material as shown in Figure 4.7 (b).

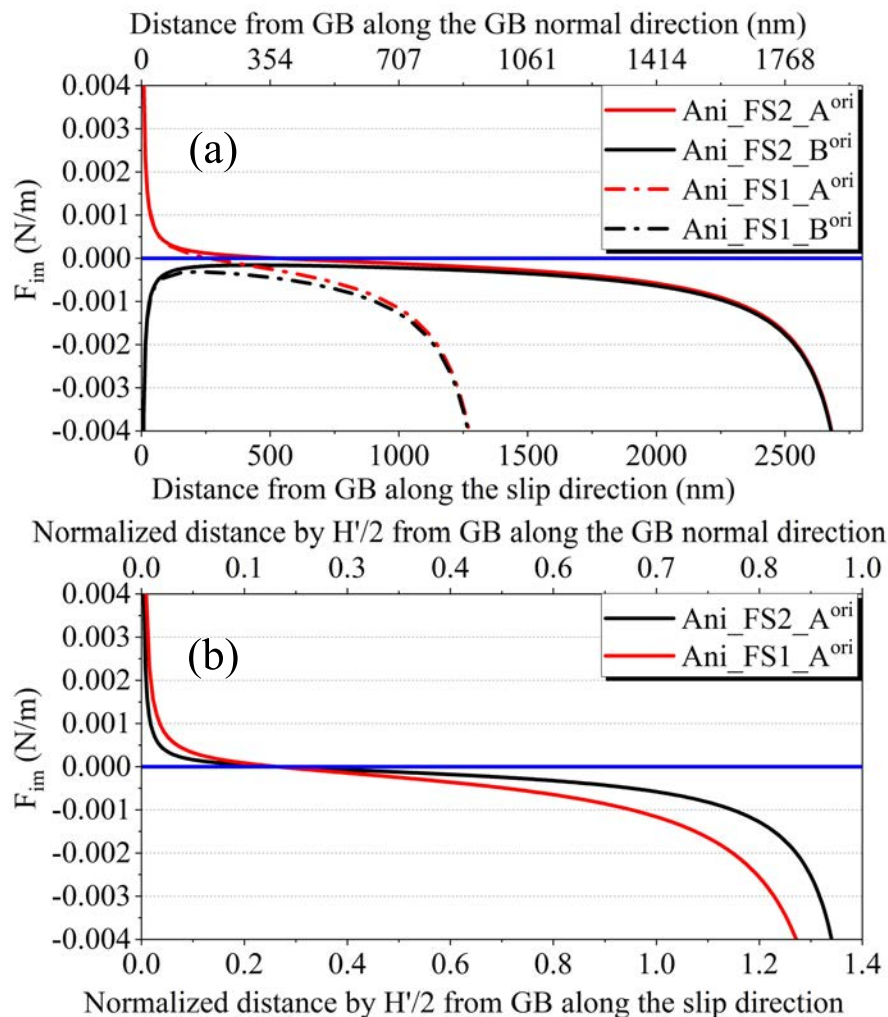


Figure 4.7: Variation of the projected image force  $F_{im}$  for the two-layers model with free surfaces (a) with the distance from the GB along the slip direction and (b) with the distance from GB along the slip direction normalized by  $H'/2$ . “FS1” corresponds to  $h_1 = H'/2 = 1\mu\text{m}$  and “FS2” to  $h_1 = 2\mu\text{m}$ .

Furthermore, in order to specify the effect of each free surface and to compare with misorientation effect,  $F_{im}$  was also computed either with only one upper free surface or with only one lower free surface. Figure 4.8 shows that close to GB,  $F_{im}$  is mainly controlled by misorientation as it is always positive for the

misorientation  $A^{\text{Ori}}$  (see Figure 4.8 (a)) and always negative for the misorientation  $B^{\text{Ori}}$  (see Figure 4.8 (b)) whatever the free surface configuration. The effects of both free surfaces and misorientation can be regarded as the non-linear combination of both effects. As the two free surfaces have an opposite effect on the dislocation, when the dislocation is located at an equal distance from both free surfaces, their contribution becomes negligible. For the configurations with both free surfaces (“Ani\_FS2\_A<sup>Ori</sup>” and “Ani\_FS2\_B<sup>Ori</sup>”), when the dislocation is located close to GB (distance from GB along the slip direction is smaller than about  $0.2 \mu\text{m}$ ),  $F_{im}$  is quite similar to the case of bi-material configuration without free surface for both misorientations  $A^{\text{Ori}}$  and  $B^{\text{Ori}}$  (“Ani\_Bi\_A<sup>Ori</sup>” and “Ani\_Bi\_B<sup>Ori</sup>”). However, if only one free surface is considered, it has an obvious influence on the projected image force even close to GB. Figure 4.8 (a) shows that the positive  $F_{im}$  due to attractive misorientation  $A^{\text{Ori}}$  is enhanced by considering only the lower free surface (“Ani\_LF2\_A<sup>Ori</sup>”) which also has an attractive effect on dislocation. Meanwhile, by considering only the upper free surface, this positive  $F_{im}$  is weakened close to GB (“Ani\_UF2\_A<sup>Ori</sup>”) and an equilibrium position is found ( $F_{im} = 0$ ). In particular, an interesting result is obtained by combining a repulsive misorientation  $B^{\text{Ori}}$  with only an lower free surface (“Ani\_LF2\_B<sup>Ori</sup>”) as shown in Figure 4.8 (b). It shows that  $F_{im}$  is negative close to GB due to repulsive misorientation  $B^{\text{Ori}}$ , then becomes positive away from GB (at a distance of about  $0.2 \mu\text{m}$ ) due to the attractive effect of the lower free surface, whereas the distances between the dislocation and both GB and lower free surface increase at the same time. As discussed for Figure 4.5, the effects of a free surface are felt at a longer distance compared to the misorientation effects. However, Figure 4.8 shows that the misorientation is predominant when the dislocation is close to GB, but only within a short distance. Thus, at a long distance, the free surface effect is predominant. Furthermore, for the case of a repulsive misorientation  $B^{\text{Ori}}$  and only an upper free surface (“Ani\_UF2\_B<sup>Ori</sup>”), even though they have the same repulsive effect, the magnitude of  $F_{im}$  decreases quickly when the dislocation gets away from GB, even at a short distance from GB. Thus, the sign of  $F_{im}$  depends on the relative distances with free surface and GB (misorientation effect), respectively, when they have an opposite effect.

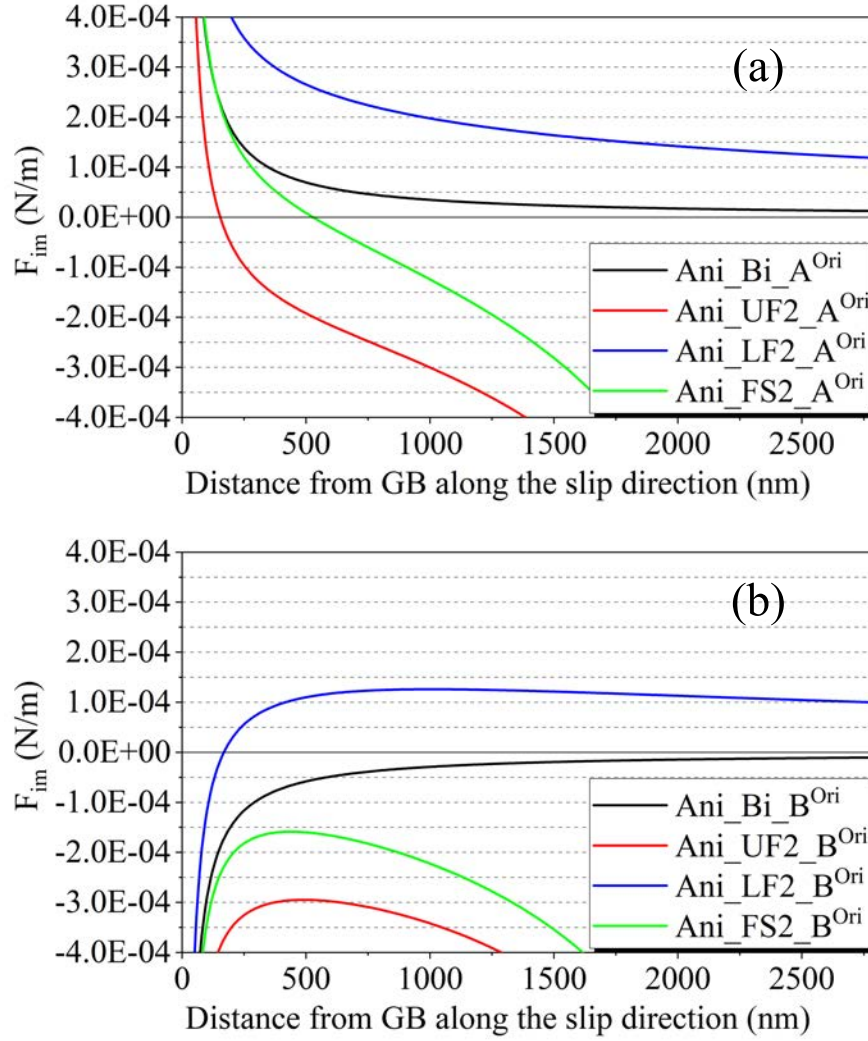


Figure 4.8: Variation of the projected image force  $F_{im}$  considering free surfaces effects with different misorientations: (a) orientation  $A^{Ori}$  and (b) orientation  $B^{Ori}$  of lower crystal.

## 4.2.5 Results for discrete dislocation pile-ups

### 4.2.5.1 Discrete dislocation pile-ups with locked dislocation

As discussed in the section 3.3, in order to always get a stable dislocation pile-up, the first dislocation is locked at  $L(1) = 5|b|$  in a first approach. Comparisons are made for different GB modelling characteristics, as well as between pile-ups having different total number  $N$  of dislocations. As a result, the positions of each dislocation in the pile-up and the resolved shear stress produced by the dislocation pile-up are obtained.

The pile-up lengths computed for different numbers of dislocations are summarized in Table 4.4. From Table 4.4, it can be inferred that the length of dislocation pile-ups increases with the GB stiffness from  $\lambda = 0.5$  to  $\lambda = 2$ , whatever the total number of dislocations considered in the pile-up. This effect is, however, very weak with a variation of less than 1%. As discussed in section 3.3, the P-K force is not zero on the locked leading dislocation. In the present cases where the GB is considered as a small thickness interphase ( $H = 5|\mathbf{b}|$ ), the force on the locked dislocation due to the other dislocations and the applied stress may indeed exceed the image force arising from the GB. Moreover, it is observed that the pile-up length obtained with  $\lambda = 2$  and orientation  $A^{\text{Ori}}$  is smaller than the one obtained for the homogeneous anisotropic crystal (Table 4.4). As discussed in subsection 4.2.4, if the GB with  $\lambda = 2$  exerts a repelling effect, orientation  $A^{\text{Ori}}$  of the lower crystal exerts an attractive effect so that the global effect on dislocations beyond the equilibrium point is attractive. It is noteworthy that the equilibrium distance is about 10.25 nm, which represents a short distance compared to the pile-up length. This means that nearly all the dislocations undergo attractive effects (Figure 4.6). By comparison, in a homogeneous single crystal, there is neither attractive nor repulsive effect due to boundaries and thus the dislocation pile-up length is larger. A similar analysis explains why the dislocation pile-up length obtained with  $\lambda = 0.5$  and orientation  $B^{\text{Ori}}$  is larger than the one obtained for the homogeneous anisotropic crystal since orientation  $B^{\text{Ori}}$  exerts a global repulsive effect on the dislocations of the upper crystal. Table 4.4 indicates clearly that going from an attractive to a repulsive orientation for the lower crystal has much more impact on the pile-up length (variation of about 8%) than changing  $\lambda$  from 0.5 to 2 (variation less than 1%).

In the isotropic case, the dislocation pile-ups length is always larger when considering a GB with  $\lambda = 2$ , and smaller if  $\lambda = 0.5$ , compared to the homogeneous single crystal case since there is no misorientation effect. Meanwhile, in the same configuration with different misorientations, the dislocation pile-up length is always larger when considering a repulsive misorientation  $B^{\text{Ori}}$ , and smaller with an attractive misorientation  $A^{\text{Ori}}$ , compared to the corresponding isotropic case computed from the Voigt-Reuss-Hill average [269, 270]. A significant effect on the pile-up length is only obtained when considering a half-space with a rigid surface (variation of nearly 100%) since such interface displays the strongest repulsive image force on dislocations that one can obtain.

As mentioned in subsection 1.3.2, for a large number of dislocations in isotropic elasticity, the pile-up length can be approximated by  $L = \frac{2NA}{\tau_0}$  with  $A = \frac{G|\mathbf{b}|}{2\pi(1-\nu)}$  for edge dislocations [95]. For  $N = 50$  dislocations in isotropic Ni, the approximated pile-up length is 9.679  $\mu\text{m}$ . Compared with the value presented in Table 4.4 for isotropic homogeneous crystal  $L=8.652 \mu\text{m}$ , the approximated length is longer

about 11.9%.



	N	Homogeneous crystal		Bi-material		Tri-material							Half-space		
						$\lambda = 0.5$			$\lambda = 1$		$\lambda = 2$				
		Ani	Iso	Ani		Ani		Iso	Ani		Ani		Iso	Ani	Iso
				A <sup>Ori</sup>	B <sup>Ori</sup>	A <sup>Ori</sup>	B <sup>Ori</sup>		A <sup>Ori</sup>	B <sup>Ori</sup>	A <sup>Ori</sup>	B <sup>Ori</sup>			
$L$ ( $\mu m$ )	6	0.6976	0.6887	0.6608	0.7262	0.6586	0.7230	0.6878	0.6607	0.7256	0.6629	0.7275	0.6918	1.390	1.361
	9	1.203	1.188	1.144	1.248	1.142	1.245	1.187	1.145	1.248	1.147	1.250	1.192	2.283	2.281
	15	2.260	2.234	2.157	2.337	2.154	2.335	2.232	2.157	2.337	2.160	2.340	2.237	4.161	4.098
	50	8.747	8.652	8.385	9.021	8.382	9.018	8.648	8.385	9.021	8.389	9.024	8.655	15.09	14.78

Table 4.4: Pile-up length  $L$  for different configurations considering anisotropic vs. isotropic elasticity: homogeneous crystal, bi-material, tri-material with GB stiffness characterized by  $\lambda$ , rigid half-space.

Since the orientation of the lower crystal has a stronger effect on dislocations at long distance than GB stiffness, the variation of  $L$  for different orientations of the lower crystal is presented in Figure 4.9 in the case of a pile-up with 50 dislocations and a zero thickness GB. The orientation of the upper crystal (where there is the pile-up) is fixed, still defined by  $\alpha = 45^\circ$  whereas the orientation of lower crystal is given by a rotation  $\psi$  around  $\mathbf{v}$  from  $\psi = 0^\circ$  to  $\psi = 180^\circ$ . In order to always get a stable dislocation pile-up configuration (especially in the case of attractive misorientation), the leading dislocation is always locked to give enough repulsive force on all dislocations. Hence, the homogeneous single crystal case is retrieved for  $\psi = 0^\circ$  and  $\psi = 180^\circ$  for which  $L = 8.75 \mu\text{m}$  (Figure 4.9 (a)). When  $L$  is smaller (resp. larger) than  $8.75 \mu\text{m}$ , the image force has globally an attractive (resp. repulsive) effect on the pile-up which is shown in Figure 4.9 (b). The misorientation angle between both crystals, i.e. the minimum rotation angle to get from one crystal orientation to the other is also presented in Figure 4.9 (a). In the present example, the maximal possible value for misorientation angle in cubic crystal,  $62.8^\circ$  [298], is almost reached but does not correspond to an extremal value of  $L$ . The maximal value of  $L$  corresponds however to a high misorientation angle (about  $60^\circ$ ). Furthermore, it is noteworthy that a same misorientation angle can be related to different elastic behaviors (for example,  $60^\circ$  is retrieved with  $\psi = 60^\circ$  and  $\psi = 120^\circ$ , which give  $L = 9.02 \mu\text{m}$  and  $L = 8.61 \mu\text{m}$ , respectively). Finally, it can be observed that the relative variations of  $L$  compared to the isotropic case in Ni can reach about 7%. The important point is that such significant variations occur in a moderately elastic anisotropic material and cannot be captured considering pile-ups in isotropic elasticity. However, by using the Voigt-Reuss-Hill average [269, 270] to define the isotropic elastic constants, the value of  $L$  is nearly the average length of the different anisotropic configuration. Furthermore, the maximum relative variation of  $L$  for materials with different Zener ratios is presented in Table 4.5. It increases as the anisotropic factor increases. As the effect of rigid half space is much stronger than misorientation effect, both  $L$  and  $F_{im}$  are much larger for the rigid half space configuration than for bi-material configurations with different misorientations.

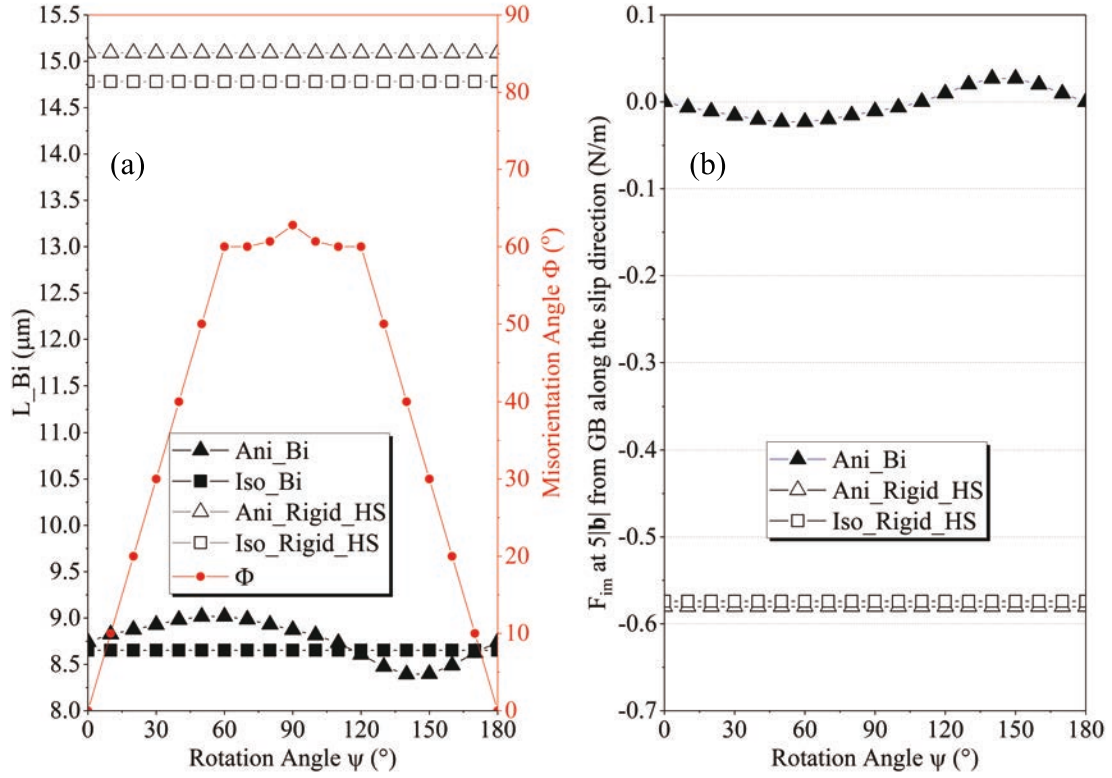


Figure 4.9: Misorientation effect in the case of bi-crystals (Ani\_Bi) on (a) pile-up length  $L$  for a pile-up with 50 dislocations and a zero thickness GB and (b) projected image force along slip direction at a distance  $5|b|$  from GB. The rotation axis is the glide direction  $\boldsymbol{v}$ . Comparisons with the cases of homogeneous isotropic case (Iso\_Bi), isotropic rigid half-space (Iso\_Half space) and the anisotropic rigid half-space (Ani\_Half space).

Material	Al	Ni	Cu	$\alpha$ -Brass
Zener ratio <sup>[1]</sup>	1.22	2.51	3.21	4.11
Maximum relative variation of $L$ (%)	1.2	7.2	9.0	11.5

Table 4.5: Maximum relative variation of the length  $L$  of a pile-up with 50 dislocations in anisotropic elasticity for materials with different Zener ratios. [1] Elastic stiffness moduli of these materials are found in the book “Theory of Dislocations” from Anderson et al. [28].

From Eq. 1.20 combined with Figure 1.30 of subsection 1.3.2, the lower bound estimate of the resolved shear stress in front of a dislocation pile-up can be written in isotropic homogeneous elasticity as:

$$\frac{\tau_{int} + \tau_0}{\tau_0} = \frac{1}{\sqrt{\frac{d}{L}}} \text{ for } \frac{1}{15}l \ll d \ll L \quad (4.3)$$

where  $\tau_{int}$  is the resolved shear stress produced by all the dislocations of the pile-up and  $\tau_0$  is the applied stress. Figure 4.10 show then the variation of  $\frac{\tau_{int} + \tau_0}{\tau_0}$  with respect to  $\frac{d}{L}$  for 50 edge dislocations and different kind of configurations (in the case of a heterogeneous medium,  $\tau_{int}$  includes the effects of image forces). In order to compare the present results with the work of Eshelby et al. [95] in isotropic elasticity, the value of  $L$  used for normalization always corresponds to the approximation  $\frac{2NA}{\tau_0}$ .

From Figure 4.10 (a), it can be seen that the approximation of a shear stress decrease with the inverse of the square root distance from the pile-up remains valid in anisotropic elasticity and for a heterogeneous medium. All the plots are pretty close to each others. The results display also some influence of the second crystal orientation in case of a bi-material model. The resolved shear stress with orientation  $A^{Ori}$  which exerts an attractive effect on dislocations is smaller than the one obtained with orientation  $B^{Ori}$  which exerts a repulsive effect on dislocations. In the studied case of a locked leading dislocation, the repulsive orientation leads thus to slightly higher resolved shear stress in front of the dislocation pile-up compared to the attractive orientation. Figure 4.10 (b) deals with tri-material models. It is found that, with the same orientation of the second crystal, the resolved shear stresses are nearly the same in the area of  $\frac{1}{15}l \ll d \ll L$  for  $\lambda = 0.5$  and  $\lambda = 2$ . The reason is that the thickness of the interphase is very small ( $H = 5|\mathbf{b}|$ ), and its stiffness has not been varied too much. Hence, the effect of the interphase is negligible compared to the one of the misorientation. Similar misorientation effects as obtained with the bi-material model are indeed retrieved: the attractive orientation  $A^{Ori}$  gives lower resolved shear stress than the repulsive orientation  $B^{Ori}$ .

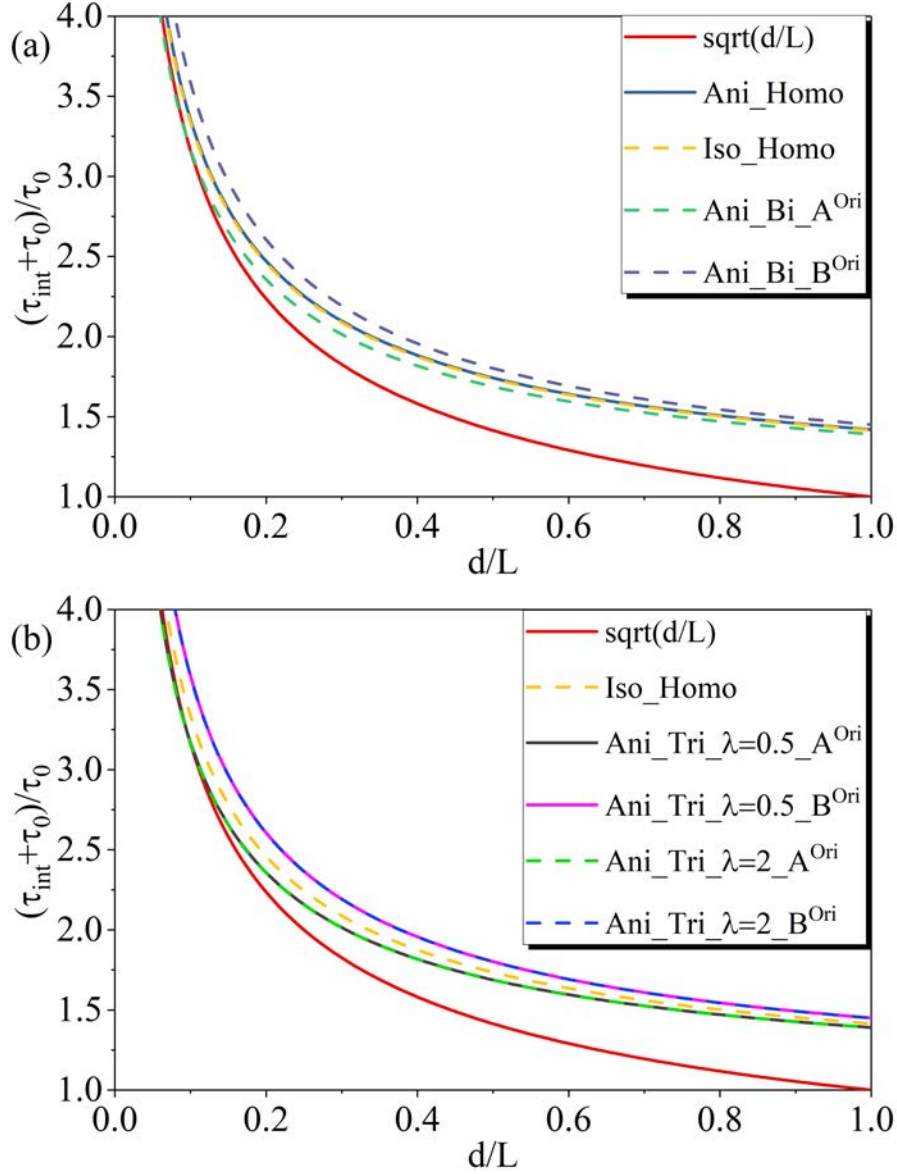


Figure 4.10: Resolved shear stress along the slip direction in front of a dislocation pile-up with 50 edge dislocations for different configurations.

#### 4.2.5.2 Dislocation pile-ups without locked dislocation

As mentioned in section 3.3, in a heterogeneous medium, the boundary image force on the leading dislocation may equilibrate the applied stress and the stress contribution coming from the other dislocations [105], but only in case of repulsive image forces. So in this case, it is not needed to lock the first dislocation in pile-

up. All the dislocation positions, including the leading one, can be found by the iterative relaxation scheme. From the results discussed in subsection 4.2.4, for a tri-material model with a small thickness  $H = 5|\mathbf{b}|$ , the image force is mainly dependent on the orientation of neighboring crystal at long distance from GB. In the region close to GB, a coupled effect is produced from both the neighboring crystal's orientation and GB stiffness occurs. To investigate the influence of GB stiffness on real dislocation positions, the orientation of neighboring crystal is chosen as orientation  $B^{\text{Ori}}$ , which gives a maximum repelling effect. In addition, the GB stiffness varies from  $\lambda = 0.925$  to  $\lambda = 2$ , which could reflect a compliant or a stiff GB. The minimum value of  $\lambda$  is chosen as 0.925 to lead to a stable dislocation pile-up. If  $\lambda$  is too small, the positive image force closed to GB will be very large (attractive effect) and therefore the dislocation pile-up cannot be equilibrated. To study a difference between different GB stiffnesses, the applied stress field is chosen at a lower value with  $\sigma_{22}^{\text{ext}} = 50$  MPa. Comparisons are made for different GB stiffnesses  $\lambda$  and different total number  $N$  of dislocations within the pile-up. As a result, the position of each dislocation in the pile-up and the resolved shear stress in the neighboring grain are obtained.

As the leading dislocation is no longer locked, its position is modified when different GB stiffnesses are considered as well as the positions of the other dislocations and the pile-up lengths. The results are presented in Figure 4.11 where  $L(N) - L(1)$  defines the pile-up length. For a fixed number of dislocations in the pile-up ( $N=5,10$  and  $20$ ), the equilibrium position of each dislocation inside the pile-up are more and more far away from the GB as  $\lambda$  is larger as shown in Figure 4.11. Besides, the pile-up length  $L$  almost linearly scales with  $\lambda$  following the red lines displayed in Figure 4.11 (a)-(c). It is noteworthy that, Lubarda [102] also found an increase of pile-up length  $L$  in the case of stiffer inhomogeneity for isotropic bi-materials. When the number of dislocations in the pile-up increases from  $N = 5$  to  $N = 20$  and for a same  $\lambda$ , the pile-up length also increases following Figure 4.11 (a)-(c). For  $N = 5$ , the pile-up length increases with a magnitude of 1.5 nm when  $\lambda$  varies from 0.925 to 2. For  $N = 10$  and  $N = 20$ , the pile-up length increases with magnitudes 2.0 nm and 2.5 nm, respectively. As a conclusion, the stiffer the GB, the larger the increase of pile-up length with  $N$ .

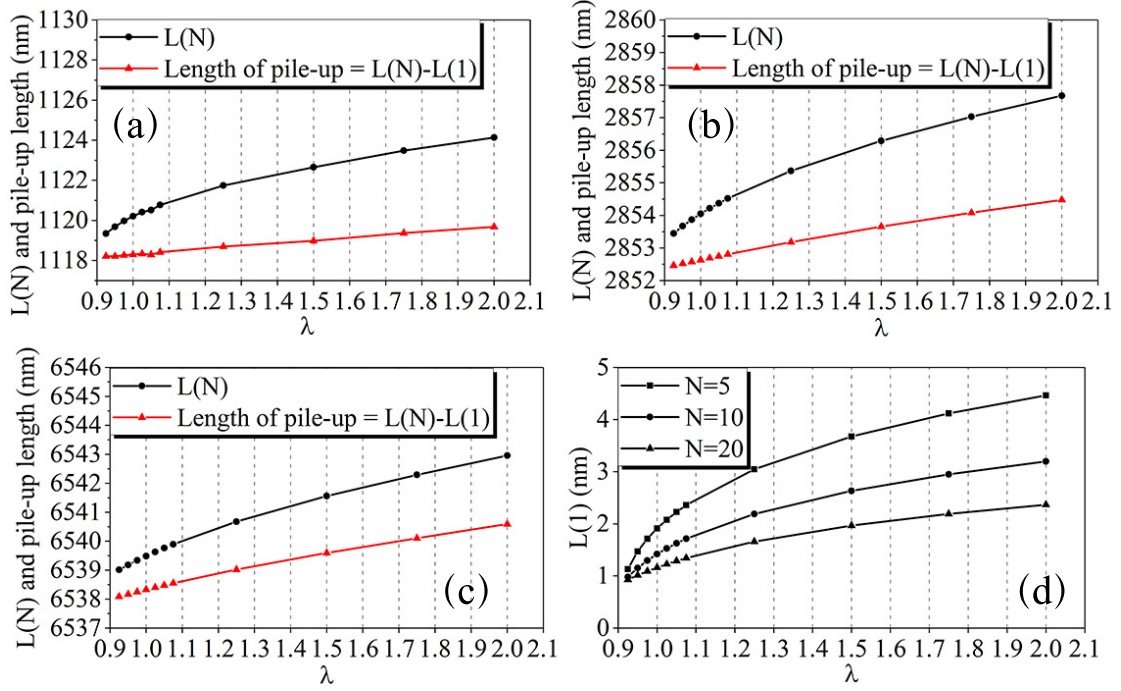


Figure 4.11: (a)-(c) Dislocation pile-up length and position of last dislocation in the pile-up for  $N=5, 10$  and  $20$ , respectively. (d) First dislocation position in the pile-up for  $N=5, 10$  and  $20$  with different GB stiffnesses characterized by  $\lambda = 0.925$  to  $\lambda = 2$ .

As discussed in subsection 4.2.5.1, the resolved shear stress along the slip direction is nearly the same for the same orientation of lower crystal with different  $\lambda$  in the area of  $\frac{1}{15}l \ll d \ll L$ . In GB region, the resolved shear stress along the slip direction will be affected by GB stiffness. The variation of resolved shear stress at a distance of  $|\mathbf{b}|$  from the second interface along the slip direction with  $\lambda$  for different number of dislocations in pile-up are presented in Figure 4.12. It shows that the resolved shear stress always decreases when  $\lambda$  increases for different number of dislocations in pile-up due to the pushing back of dislocations from GB. For  $N=5, 10$  and  $20$ , the resolved shear stress decrease from  $\lambda = 0.925$  to  $\lambda = 2$  is  $1446.3$  MPa,  $1301.6$  MPa and  $1058.4$  MPa, respectively. When  $N$  is large ( $N = 20$ ), Figure 4.12 shows a slower decrease of the resolved shear stress with  $\lambda$ . From Figure 4.12, it is shown that for  $\lambda = 0.9 \sim 1.1$ , the resolved shear stress decreases faster than for  $\lambda > 1.1$ . The influence of  $N$  is more important for a GB stiffness from  $\lambda = 0.9$  to  $\lambda = 1.1$  than for  $\lambda > 1.1$ .

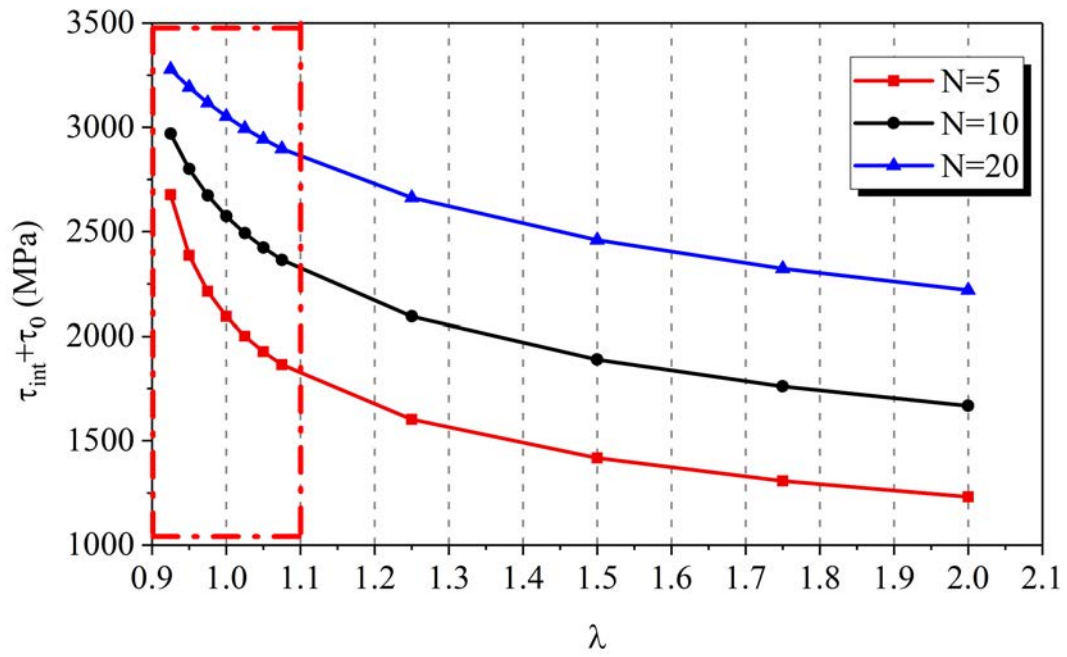


Figure 4.12: Resolved shear stress in the neighboring grain at a distance of  $|b|$  from the second interface along the slip direction.



### 4.3 Prediction of stress-strain curves and study of incompatibility stresses using Crystal Plasticity Finite Element Method (CPFEM)

As discussed in section 2.6, the experimental measurement of displacement during compression test is not accurate due to tip drift. In order to calibrate this displacement measurement, a CPFEM simulation was used to perform the same compression test as described in Chapter 2. At the same time, the incompatibility stresses were numerically calculated by CPFEM and compared with analytical calculations considering only elastic incompatibilities ( $[\epsilon^p] = \mathbf{0}$ ) based on Eqs. 1.44 and 1.45 described in subsection 1.5.2.4. In contrast with analytical expressions, CPFEM simulations can predict plastic incompatibility stresses and their distributions within grains that take into account the finite boundary conditions (free surfaces, bulk material underneath, specimen geometry...).

This section presents the different steps of a micro-pillar compression test using CPFEM simulations. The simulations were performed using the commercial finite element code Abaqus/Standard v.2017 through a user material subroutine (UMAT) [299, 300]. The simulation is based on a constitutive rate hardening law which is described in subsection 1.5.4.1. The geometry of the different parts of the simulation and the mesh are first presented. The boundary conditions are then described. At the end, the numerical results of stress-strain curves and incompatibility stresses are presented and discussed in comparison with experimental measurements and with analytical calculations, respectively.

#### 4.3.1 CPFEM configuration: geometry and mesh

The geometry used in CPFEM simulations is the same as the one of micro-beam used in experiments as shown in Figure 4.13. It contains the tip of the nanoindenter which is a flat punch, the micro-beam and the bulk material. This geometry was meshed using a linear brick element with reduced integration, so-called “C3D8R” solid element in Abaqus as shown in Figure 4.13. Therefore, it consists in 85234 and 52537 finite elements for Ni and  $\alpha$ -Brass samples, respectively. The size of the elements increases when one moves far away from the micro-pillar. In addition, the flat punch indenter was considered perfectly rigid and was meshed by linear triangular element called “S3” 2D element in Abaqus.

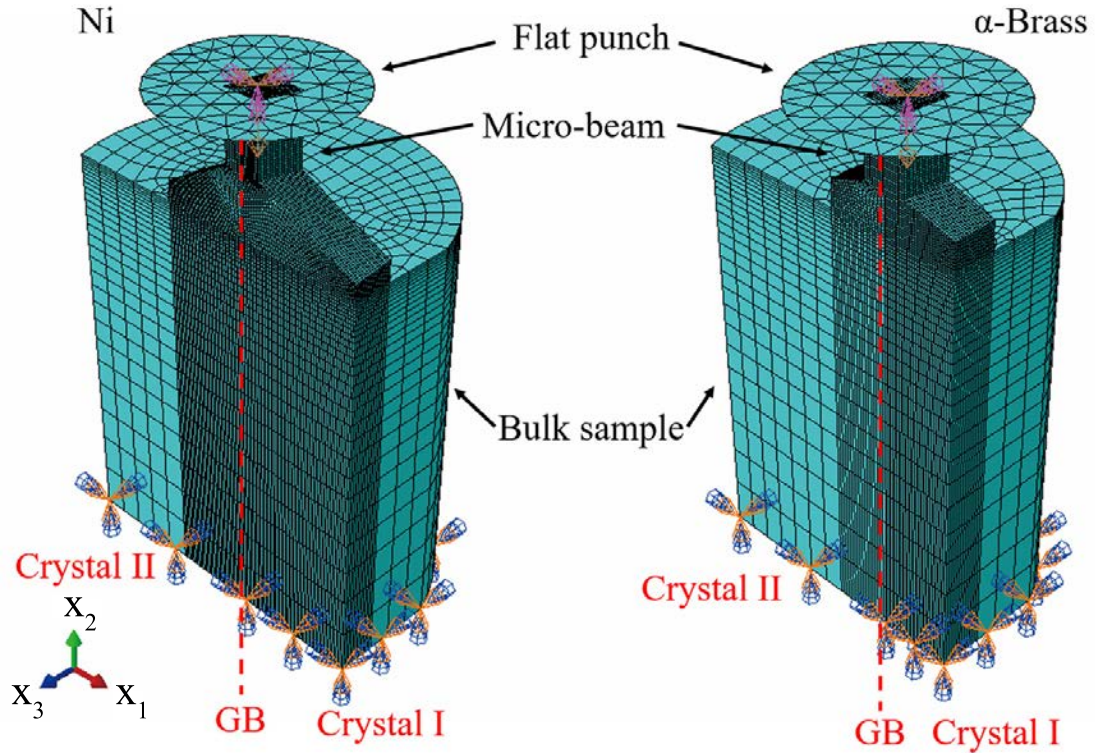


Figure 4.13: Geometry of both Ni and  $\alpha$ -Brass micro-beams used for CPFEM simulation.  $\mathbf{x}_2$  is perpendicular to the flat punch,  $\mathbf{x}_3$  is perpendicular to the upper surface, and  $\mathbf{x}_1 = \mathbf{x}_2 \times \mathbf{x}_3$ .

Based on the experimental data obtained from the compression test detailed in Chapter 2, the boundary conditions were set as follows:

- The displacements and rotations of the lower surface of the bulk material are zero.
- The flat punch is subjected to a constant vertical velocity in the direction parallel to the  $\mathbf{x}_2$ -axis as shown in Figure 4.13 which is also parallel to the GB.
- The lateral surface of the structure is stress free.
- The contact between the nanoindenter and the upper surface of the micro-beam is directly managed by Abaqus, which uses an algorithm based on the penalty method limiting the overlapping of the parts of the assembly.
- The friction between the nanoindenter and the micro-beam is not taken into account in the simulation since its influence is assumed negligible for very low plastic strains and mainly in the elastic regime.

The necessary parameters used in CPFEM include two parts: material properties and experimental conditions. With the present constitutive laws already described in subsection 1.5.4.1, material properties include the elastic stiffness constants ( $C_{11}$ ,  $C_{12}$  and  $C_{44}$ ), the crystallographic orientation of grains, the rate sensitivity exponent ( $n$ ), reference shear strain rate ( $\dot{\gamma}_\alpha^0$ ), the initial hardening modulus ( $h_0$ ), saturation shear stress at stage I ( $\tau^s$ ), initial critical resolved shear stress ( $\tau^0$ ) and latent hardening effect parameter ( $q$ ). For the experimental conditions, only the velocity of the tip  $v_{\text{load}}$  and the loading time  $t_{\text{load}}$  are needed. For the present experiment, the elastic stiffness constants of the material can be found in the literature (presented in section 2.2) and the orientations of grains were measured by EBSD. The coordinates system of the EBSD measurement and the CPFEM simulation are the same, so that the measured Euler angles are coincident with the ones presented in subsection 2.3.4 which are summarized in Table 4.6 and Table 4.7 for Ni and  $\alpha$ -Brass, respectively. The other parameters of the material properties depend on the material's configuration (single crystal or bi-crystal or polycrystal) and the orientation of each grain, which can be fitted from the micro-plastic behavior, in particular by matching experimental and simulated yield stress and final stress at low plastic strain. In addition,  $v_{\text{load}}$  is not accurate due to the drift of the tip, as for displacement measurement. In contrast, the force measurement is accurate. However, the strain simulation in the elastic regime only depends on elastic stiffness constants and on the orientation of the grains. Thus, the measured stress-strain curve can be first calibrated to fit the elastic slope simulated with CPFEM. Then, the real value of  $v_{\text{load}}$  can be deduced by applying the same correction coefficient.

Anisotropic Elastic stiffness constants (GPa)			Orientation of Crystal I Euler-Bunge angles			Orientation of Crystal II Euler-Bunge angles		
$C_{11}$	$C_{12}$	$C_{44}$	$\phi_1$	$\Phi$	$\phi_2$	$\phi_1$	$\Phi$	$\phi_2$
246.5	147.3	124.7	63.8°	14.3°	18.6°	331.1°	9.0°	75.1°

Table 4.6: Anisotropic elastic stiffness constants and orientations of grains for the Ni bi-crystalline micro-beam.

Anisotropic Elastic stiffness constants (GPa)			Orientation of Crystal I Euler-Bunge angles			Orientation of Crystal II Euler-Bunge angles		
$C_{11}$	$C_{12}$	$C_{44}$	$\phi_1$	$\Phi$	$\phi_2$	$\phi_1$	$\Phi$	$\phi_2$
139.21	104.51	71.3	27.7°	35.7°	66.1°	219.5°	28.4°	2.4°

Table 4.7: Elastic stiffness constants and orientations of grains for the  $\alpha$ -Brass bi-crystalline micro-beam.

### 4.3.2 Calibration of displacement and determination of material parameters

First, purely elastic simulations are performed to calibrate the experimental stress-strain curves.  $v_{\text{load}}$  was set to be  $0.031 \mu\text{m/s}$  for Ni and  $0.020 \mu\text{m/s}$  for  $\alpha$ -Brass like in experiments as presented in Figure 2.19 with red lines. The simulated displacement  $u_2$  and force  $f_2$  of the tip along the loading direction were obtained from CPFEM results. Then, the longitudinal strain  $\varepsilon_{22}$  and the loading stress  $\Sigma_{22}$  can be calculated by  $\varepsilon_{22} = \frac{u_2}{L_{\text{beam}}}$  and  $\Sigma_{22} = \frac{f_2}{S_{\text{sec}}}$ , respectively, where  $L_{\text{beam}}$  is the length of the micro-beam and  $S_{\text{sec}}$  is the top cross section area of the micro-beam. For the studied Ni micro-beam,  $L_{\text{beam}} = 15.46 \mu\text{m}$ ,  $S_{\text{sec}} = 71.80 \mu\text{m}^2$  and for the  $\alpha$ -Brass micro-beam,  $L_{\text{beam}} = 15.37 \mu\text{m}$ ,  $S_{\text{sec}} = 88.91 \mu\text{m}^2$  as described in Figure 2.14 and 2.15, respectively. The simulated elastic stress-strain curves are presented in Figure 4.14. Compared to the experimentally measured stress-strain curves presented in Figure 2.20, the elastic slopes of these curves display a huge difference. The experimentally measured slopes  $B_{\text{exp}}$  are 3.3 GPa for Ni, 1.9 GPa for  $\alpha$ -Brass while the simulated slopes  $B_{\text{sim}}$  are 85.9 GPa for Ni, 49.3 GPa for  $\alpha$ -Brass. Therefore, the experimentally measured displacement and  $v_{\text{load}}$  can be calibrated through  $u_2^{\text{cal}} = u_2 \frac{B_{\text{exp}}}{B_{\text{sim}}}$  and  $v_{\text{load}}^{\text{cal}} = v_{\text{load}} \frac{B_{\text{exp}}}{B_{\text{sim}}}$ . After the calibration of displacement and  $v_{\text{load}}$ , the exact time of loading duration can be determined as  $t_{\text{load}} = \frac{u_2^{\text{cal}}}{v_{\text{load}}^{\text{cal}}}$ . After that, the parameters  $n$ ,  $\dot{\gamma}_{\alpha}^0$ ,  $h_0$ ,  $\tau^s$ ,  $\tau^0$  and  $q$  were fitted from the plastic part of the stress-strain curves. All these parameters are presented in Table 4.8 and Table 4.9 for the studied Ni and  $\alpha$ -Brass micro-beam, respectively. We can notice that  $q = 0$  is enough to calibrate the model and  $h_0$  is relatively small. Finally, the calibrated experimental stress-strain curves for the studied micro-beams are presented in Figure 2.21.

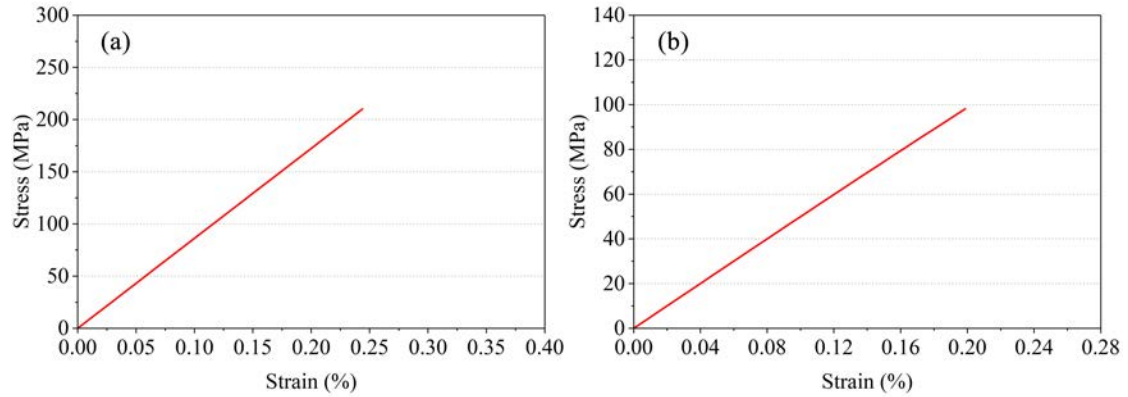


Figure 4.14: Elastic part of stress-strain curves simulated by CPFEM for (a) the Ni micro-beam and (b) the  $\alpha$ -Brass micro-beam.

$n$ (MPa)	$\dot{\gamma}_\alpha^0$ ( $s^{-1}$ )	$h_0$ (MPa)	$\tau^s$ (MPa)	$\tau^0$ (MPa)	$q$	$v_{\text{load}}$ ( $\mu\text{m/s}$ )	$t_{\text{load}}$ (s)
60	0.007	10	250	173	0	0.0012	44.76

Table 4.8: Simulation parameters used in CPFEM for the Ni bi-crystalline micro-beam.

$n$ (MPa)	$\dot{\gamma}_\alpha^0$ ( $s^{-1}$ )	$h_0$ (MPa)	$\tau^s$ (MPa)	$\tau^0$ (MPa)	$q$	$v_{\text{load}}$ ( $\mu\text{m/s}$ )	$t_{\text{load}}$ (s)
60	0.001	10	200	62	0	$7.71 \times 10^{-4}$	52.14

Table 4.9: Simulation parameters used in CPFEM for the  $\alpha$ -Brass bi-crystalline micro-beam.

### 4.3.3 Incompatibility stresses

After determining the parameters for the presented micro-beams, incompatibility stresses were analyzed and compared with analytical calculation considering only elastic incompatibilities ( $[\boldsymbol{\varepsilon}^p] = \mathbf{0}$ ) based on Eqs. 1.44 and 1.45. Incompatibility stresses were first calculated and averaged over all integration points of a specific volume. In order to reduce the influence of the connection part between the beam and bulk material and the influence of contact part between the beam and the tip, the volume for average calculation in each grain was chosen to represent 70% of the micro-beam centered in the middle as shown in Figure 4.15.

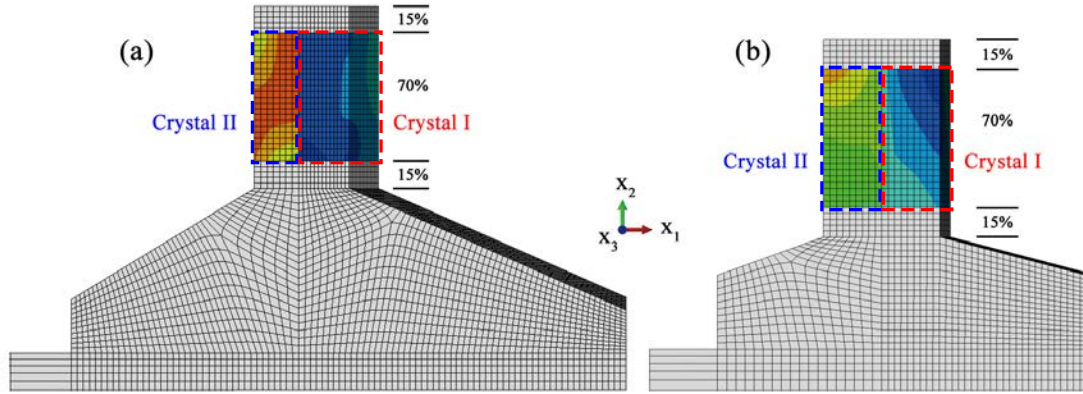


Figure 4.15: Schematic figure of the volume in micro-beam for the average stresses calculations in CPFEM for (a) Ni and (b)  $\alpha$ -Brass.

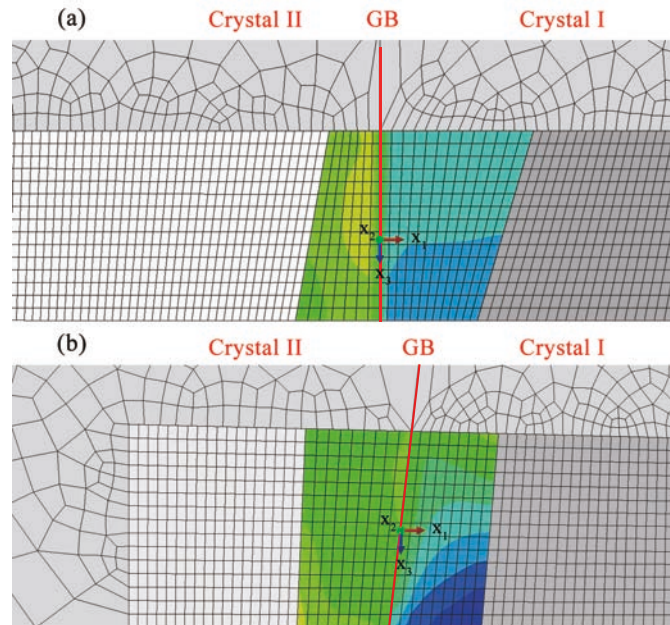


Figure 4.16: Top view of micro-beam in CPFEM coordinates system for (a) Ni and (b)  $\alpha$ -Brass.

Analytical calculations based on the model derived by Richeton and Berbenni [160] were performed considering an uniaxial compression test along the  $\mathbf{x}_2$ -loading direction. Thus, the loading stresses have only one non zero component  $\Sigma_{22}$ , which was obtained from CPFEM calculation. The analytical calculations were performed using the Matlab program described in section 3.4. In this calculation, each grain was regarded as an infinite space, but the volume fraction was set as the real volume fraction which was calculated based on the sectional area of each

grain as presented in Figures 2.14 and 2.15. Thus, the volume fraction  $f$  of crystal I used in Eqs. 1.44 and 1.45 is 0.65 for the Ni micro-beam and 0.4726 for the  $\alpha$ -Brass micro-beam. The inclination angle of GB was also taken into account as  $\varepsilon = 0^\circ$  for the Ni micro-beam and  $\varepsilon = 6.4^\circ$  for the  $\alpha$ -Brass micro-beam as defined in Figure 2.17. In the results, “Analytical\_I” and “Analytical\_II” indicate the analytical results for each grain based on Eqs. 1.44 and 1.45. Meanwhile, “CPFEM\_AVE”, “CPFEM\_I” and “CPFEM\_II” indicate the average stresses calculated from CPFEM over the whole beam, crystal I and crystal II, respectively, as shown in Figure 4.15.

Figure 4.17 shows the variation of  $\sigma_{22}$  with the loading stress  $\Sigma_{22}$  for the Ni micro-beam. In the CPFEM simulation, we can notice that  $\sigma_{22}$  is no more proportional to the loading stress  $\Sigma_{22}$  at the onset of plastic deformation. In the elastic regime, the analytical and numerical solutions for  $\sigma_{22}$  show good agreement. The difference is mainly due to the difference of boundary conditions, in particular the effect of free surfaces and sample geometry. The other components of the stress tensor are non zero but are small and negligible compared to  $\sigma_{22}$ . The stress tensors of each grain ( $\sigma_{\text{Analytical}}^{\text{I}}, \sigma_{\text{Analytical}}^{\text{II}}$ ) and of the whole beam ( $\sigma_{\text{Analytical}}^{\text{Ave}}$ ) calculated at the end of the test from the analytical formulas (Eqs. 1.44 and 1.45) in pure elasticity are given below in the CPFEM coordinates system (see Figures 4.13 and 4.16):

$$\begin{aligned}
\sigma_{\text{Analytical}}^{\text{I}} &= \begin{bmatrix} 0 & 0 & 0 \\ 0 & -222.2 & -1.1 \\ 0 & -1.1 & 23.9 \end{bmatrix} \text{ MPa} \\
\sigma_{\text{Analytical}}^{\text{II}} &= \begin{bmatrix} 0 & 0 & 0 \\ 0 & -415.1 & 2.1 \\ 0 & 2.1 & -44.4 \end{bmatrix} \text{ MPa} \\
\sigma_{\text{Analytical}}^{\text{Ave}} &= \begin{bmatrix} 0 & 0 & 0 \\ 0 & -289.7 & 0 \\ 0 & 0 & 0 \end{bmatrix} \text{ MPa}
\end{aligned} \tag{4.4}$$

As a comparison, the stress tensors obtained from the CPFEM simulations considering a small amount of plasticity ( $\sigma_{\text{CPFEM}}^{\text{I}}, \sigma_{\text{CPFEM}}^{\text{II}}$  and  $\sigma_{\text{CPFEM}}^{\text{Ave}}$ ) are:

$$\begin{aligned}
\sigma_{\text{CPFEM}}^{\text{I}} &= \begin{bmatrix} -3.2 & 0.9 & 0.6 \\ 0.9 & -244.4 & -0.5 \\ 0.6 & -0.5 & 5.8 \end{bmatrix} \text{ MPa} \\
\sigma_{\text{CPFEM}}^{\text{II}} &= \begin{bmatrix} -1.3 & -1.6 & -0.4 \\ -1.6 & -371.3 & 1.0 \\ -0.4 & 1.0 & -7.4 \end{bmatrix} \text{ MPa} \\
\sigma_{\text{CPFEM}}^{\text{Ave}} &= \begin{bmatrix} -2.5 & 0.0 & 0.3 \\ 0.0 & -288.8 & 0.0 \\ 0.3 & 0.0 & 1.2 \end{bmatrix} \text{ MPa}
\end{aligned} \tag{4.5}$$

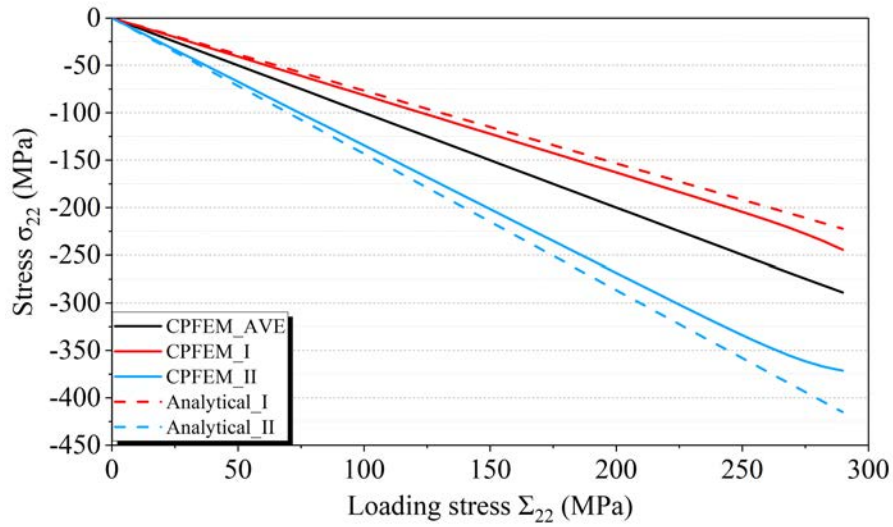


Figure 4.17: Variation of  $\sigma_{22}$  as a function of the loading stress component  $\Sigma_{22}$  for the Ni micro-beam.

Figure 4.18 shows  $\sigma_{22}$  for the  $\alpha$ -Brass micro-beam. Similarly to Ni micro-beam, there is a good match between analytical calculations and numerical simulations from CPFEM. It should be pointed out that plastic deformation begins after  $|\Sigma_{22}| \approx 120$  MPa, even if it is not evidently observed. The stress tensors at the end of the test obtained from analytical calculations and CPFEM simulations for  $\alpha$ -Brass are:



$$\begin{aligned}
\sigma_{\text{Analytical}}^{\text{I}} &= \begin{bmatrix} 0.3 & -2.2 & -3.1 \\ -2.2 & -95.0 & 19.7 \\ -3.1 & 19.7 & 27.5 \end{bmatrix} \text{ MPa} \\
\sigma_{\text{Analytical}}^{\text{II}} &= \begin{bmatrix} -0.3 & 2.0 & 2.8 \\ 2.0 & -156.0 & -17.6 \\ 2.8 & -17.6 & -24.7 \end{bmatrix} \text{ MPa} \\
\sigma_{\text{Analytical}}^{\text{Ave}} &= \begin{bmatrix} 0 & 0 & 0 \\ 0 & -127.1 & 0 \\ 0 & 0 & 0 \end{bmatrix} \text{ MPa}
\end{aligned} \tag{4.6}$$

$$\begin{aligned}
\sigma_{\text{CPFEM}}^{\text{I}} &= \begin{bmatrix} -1.4 & -0.6 & -0.3 \\ -0.6 & -100.9 & 6.5 \\ -0.3 & 6.5 & 6.0 \end{bmatrix} \text{ MPa} \\
\sigma_{\text{CPFEM}}^{\text{II}} &= \begin{bmatrix} -1.9 & 0.6 & 0.6 \\ 0.6 & -150.5 & -5.9 \\ 0.6 & -5.9 & -4.9 \end{bmatrix} \text{ MPa} \\
\sigma_{\text{CPFEM}}^{\text{Ave}} &= \begin{bmatrix} -1.6 & -0.0 & 0.2 \\ -0.0 & -125.7 & 0.3 \\ 0.2 & 0.3 & 0.5 \end{bmatrix} \text{ MPa}
\end{aligned} \tag{4.7}$$

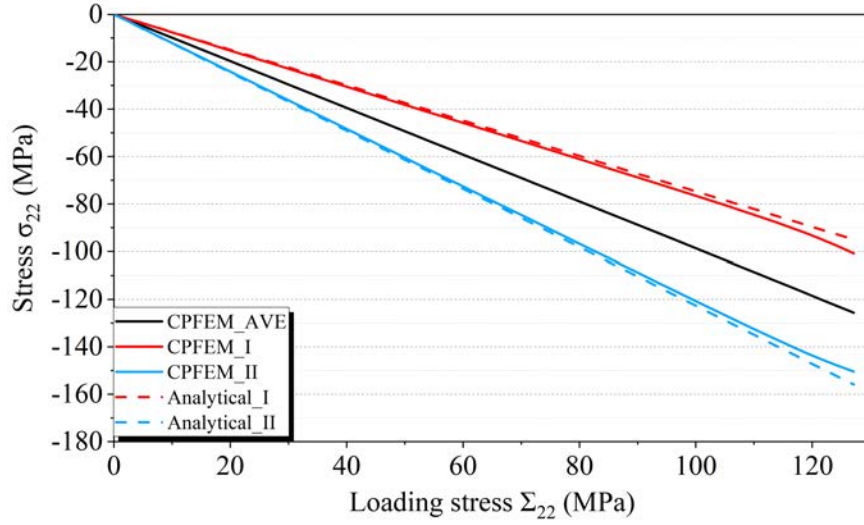


Figure 4.18: Variation of  $\sigma_{22}$  as a function of the loading stress component  $\Sigma_{22}$  for the  $\alpha$ -Brass micro-beam.

In order to consider the effect of applied stress and incompatibility stress coming from elastic anisotropy and heterogeneity on the distribution of dislocations in pile-up, CPFEM simulations were performed in heterogeneous elasticity only until the end of the test. For the results, the final stresses along two specific lines were analyzed for each material. These two specific lines are shown in Figure 4.19 for the Ni micro-beam and in Figure 4.20 for the  $\alpha$ -Brass micro-beam. The first line is the middle line of the whole beam which is marked as “Middle” in the results (Figures 4.21 (a) and 4.22 (a)). The second one is on the upper surface of the micro-beam at the position of the studied slip line for each material, as presented in Figure 2.24 for the Ni micro-beam and in Figure 2.26 for the  $\alpha$ -Brass micro-beam, which is marked as “Surface” in the results (Figure 4.21 (b) and 4.22 (b)). The stress distributions along these lines can be used as accurate estimates of the external stresses that should be considered in addition to the stresses of dislocations for the simulation of slip step heights which will be presented in section 4.4.

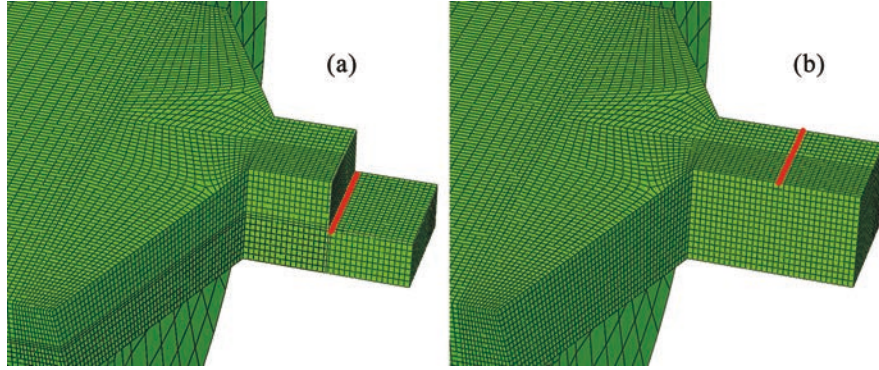


Figure 4.19: Schematic figure of two specific lines along  $x_1$  direction for the Ni micro-beam: (a) the middle line of the whole beam and (b) the middle line of the upper surface which is close to the position of the studied slip line observed in experiment as shown in Figure 2.24.

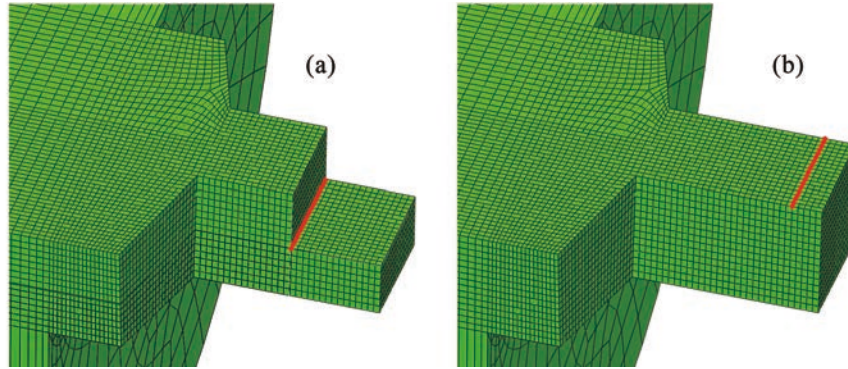


Figure 4.20: Schematic figure of two specific lines along  $x_1$  direction for the  $\alpha$ -Brass micro-beam: (a) the middle line of the whole beam and (b) the line at the top of the upper surface which is close to the position of the studied slip line observed in experiment as shown in Figure 2.26.

Figures 4.21 and 4.22 present the distribution of all the components of the stress tensor along the two special lines as described in Figures 4.19 and 4.20 in each grain obtained from CPFEM simulation, for the Ni and  $\alpha$ -Brass micro-beams, respectively. For the 6 components, there are obvious differences between the middle line and the surface line. In particular, based on the condition of traction continuity across GB, the stress components  $\sigma_{11}$ ,  $\sigma_{12}$  and  $\sigma_{13}$  are continuous across GB along the middle line in the Ni sample as shown in Figure 4.21 with black lines. But these stress components are discontinuous along the surface line (see red lines in Figure 4.21) due to the singularity between free surface and interface, named “T-stress” [301]. However, due to the inclination of GB in the  $\alpha$ -Brass sample as shown in Figure 4.16 (b), all the 6 stress components are discontinuous across GB

even though along the middle line. Meanwhile, there are also the “T-stress” effect of the stress tensor along the surface line in the  $\alpha$ -Brass sample.

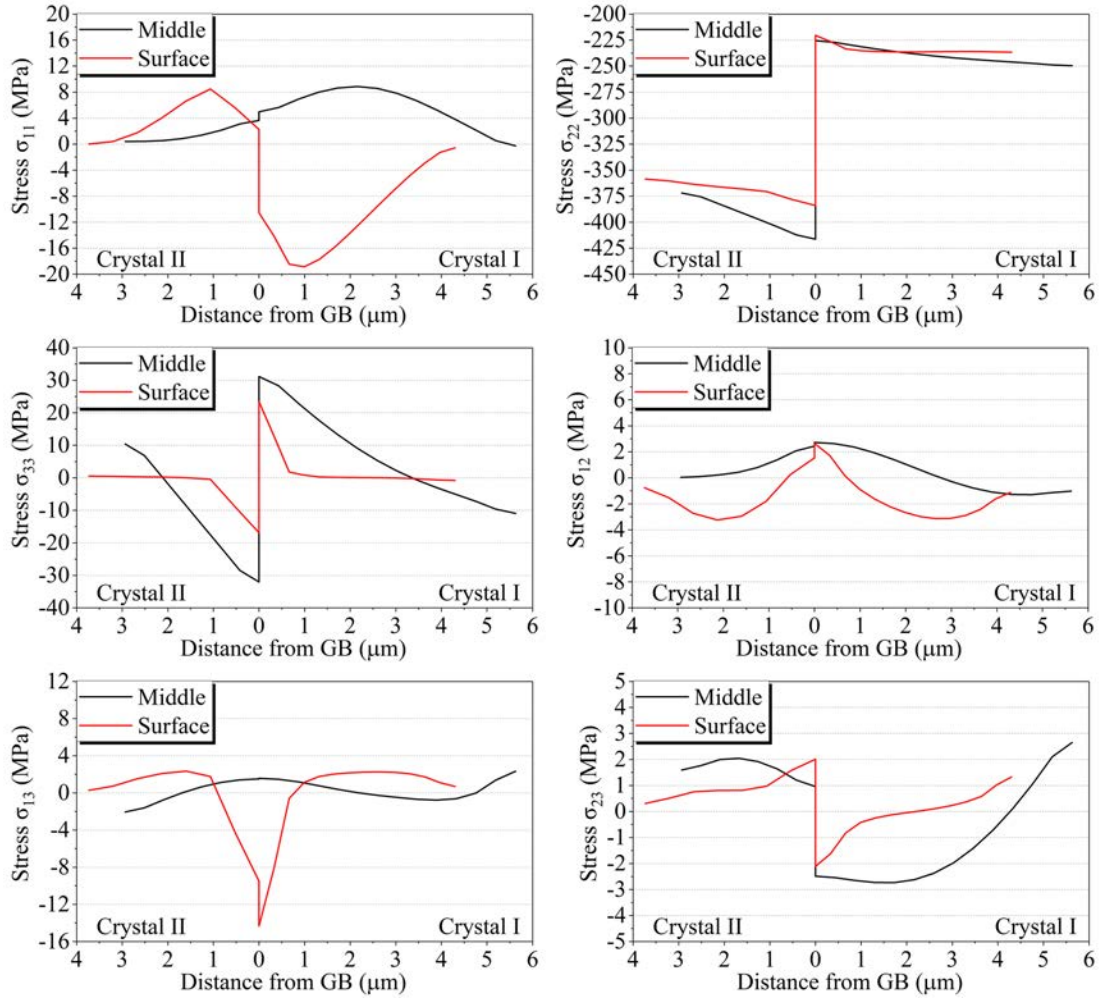


Figure 4.21: Variation of all the components of the stress tensor along two different paths for the Ni micro-beam.

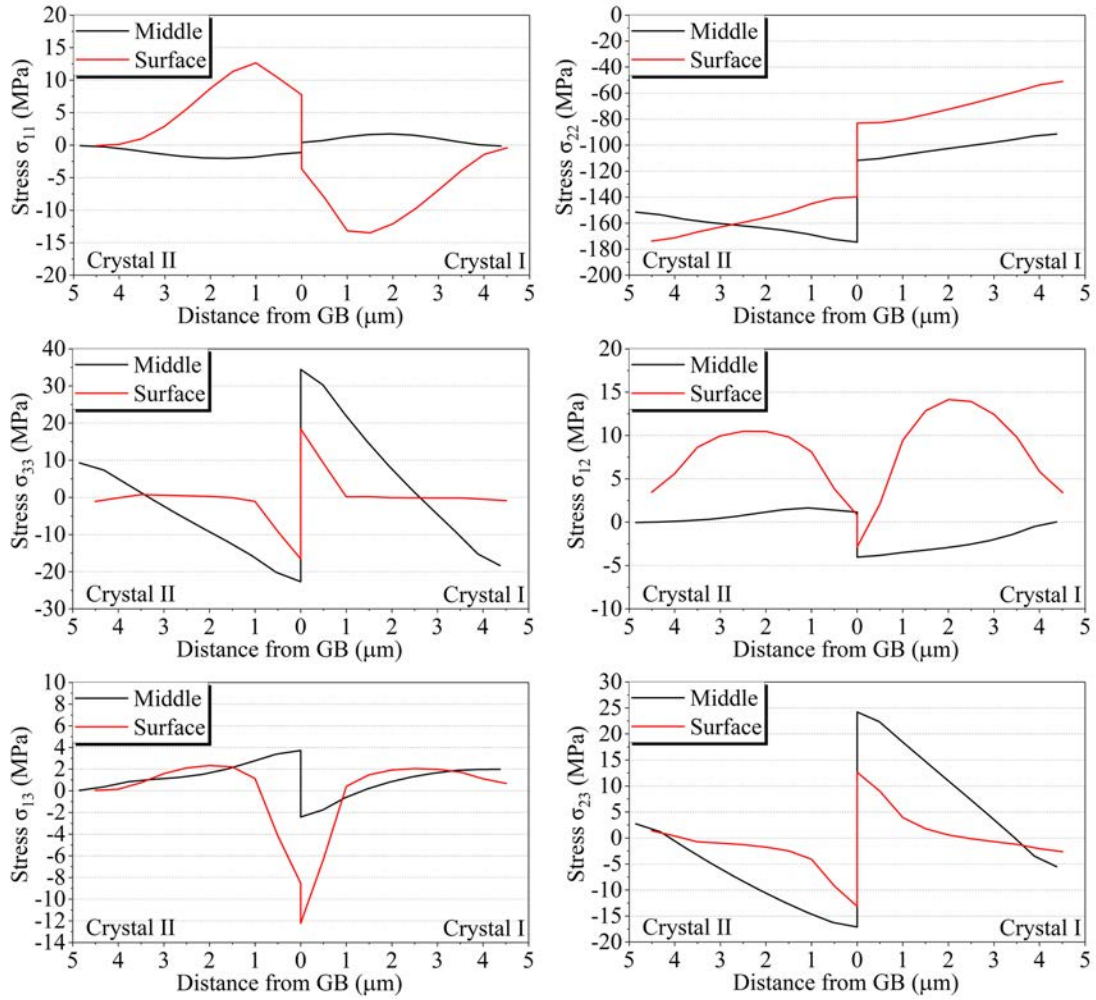


Figure 4.22: Variation of all the components of the stress tensor along two different paths for the  $\alpha$ -Brass micro-beam.

## 4.4 Computations of slip step height compared with experimental observations

### 4.4.1 Simulation configuration for experiment

Based on the models developed in Chapter 3, the slip step heights due to a dislocation pile-up measured in experiment can be simulated in a bi-crystal configuration containing a GB using dislocation pile-ups modelling. The hypotheses and configurations are set as following and presented in Figure 4.23:

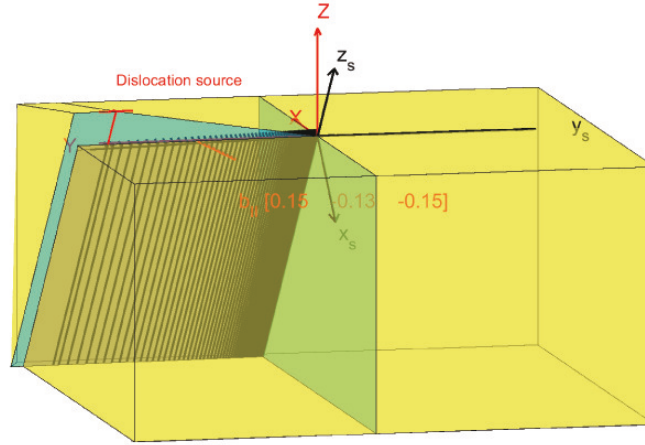


Figure 4.23: Schematic figure of the simulation configuration adopted for the experiment.  $(x_s, y_s, z_s)$  indicate the simulation coordinates system, while  $(X, Y, Z)$  indicates the global sample coordinates system.

- The dislocations lines are supposed to be infinite straight lines. They are parallel to each other and also parallel to GB plane.
- The position of the maximum slip step height measured in the experiment is considered to be the end of the dislocation pile-up. However, in the model, the last dislocation is fixed at the position of the observed maximum slip step height and is considered as the dislocation source.
- The dislocations produced by this source create a pile-up if they move towards GB and will create a step on the side surface if they move also towards the free surface.
- GB is regarded as an elastic interphase with a thickness of 0.9 nm. This value has been obtained from MD simulations (see Appendix C). The stiffness tensor of this interphase can be modeled from Eq. 4.1 with  $\lambda$  equal to 1 or as an isotropic elastic stiffness tensor computed from the Voigt-Reuss-Hill average [269, 270].
- Because the theory is two-dimensional (invariance along the dislocation line), dislocations with different line directions cannot be considered at the same time. Thus, dislocations transferred to the neighboring grain are modeled as an interfacial super-dislocation fixed in the GB interphase. Therefore  $\mathbf{b}^{\text{Tran}} = N^{\text{Tran}} \times \mathbf{b}^{\text{GB}}$ , where  $\mathbf{b}^{\text{Tran}}$  is the Burgers vector of the super-dislocation,  $N^{\text{Tran}}$  the number of transferred dislocations and  $\mathbf{b}^{\text{GB}}$  is the Burgers vector of dislocations stored at GB.  $\mathbf{b}^{\text{GB}}$  can be equal to the Burgers vector of the incoming dislocations, or to the residual Burgers vector between

incoming slip system and one of the 12 outgoing slip systems in the adjacent grain defined as  $\mathbf{b}^{\text{GB}} = \mathbf{b}^{\text{In}} - \mathbf{b}^{\text{Out}}$ .

- As presented in section 3.4, for simulation coordinates system, the  $\mathbf{x}_3$  direction is set to be the direction of dislocation line  $z_S$  as presented in Figure 4.23, and the  $\mathbf{x}_2$  direction is set to be the direction of GB normal  $y_S$  as presented in Figure 4.23.  $\mathbf{x}_1$  is determined by  $\mathbf{x}_1 = \mathbf{x}_2 \times \mathbf{x}_3$  presented as  $x_S$  in Figure 4.23. Furthermore, all the used vectors and tensors, such as the Burgers vector of active slip system, the slip direction vector and the elastic stiffness, etc. are transformed into the simulation coordinates system.
- The equilibrium positions of the dislocations in pile-up are determined by Eq. 3.56, then the slip step height along the slip direction can be calculated by:

$$\Delta h(d) = N(d) \times b(Z) \quad (4.8)$$

where  $d$  is the distance from GB along slip direction,  $N$  the number of dislocations going through this point and  $\mathbf{b}(Z)$  is the out-of-surface component of Burgers vector (along  $Z$  direction which is perpendicular to upper surface as shown in Figure 4.23).

- In the following parts, the measured slip step height is calibrated to be zero at GB, that means  $\Delta h = h^{\text{Top}} - h^{\text{Bottom}} - \Delta h_{\text{GB}}$ . Similarly, the simulated slip step height is considered to be zero at GB as  $\Delta h(0) = 0$ .

For the following results, the default values of the parameters are set as: the Burgers vector of interfacial transferred dislocations is supposed to be the same as the Burgers vector of incoming dislocations and the critical force is set to be  $F_c = 0$  N/m. The external applied stresses are considered by default as homogeneous within the whole bi-crystal. By default, the calculations are performed with anisotropic elasticity. However, the L-E-S formalism cannot be used for isotropic elasticity calculation due to the problem of repeated eigenvalues. In that case, the elastic stiffness moduli are firstly represented from isotropic elastic constants by  $C_{11} = 2G(1 - \nu)/(1 - 2\nu)$ ,  $C_{12} = 2G\nu/(1 - 2\nu)$  and  $C_{44} = G$ . Then, the  $C_{44}$  value is increased a little bit to prevent the problem of repeated eigenvalues in L-E-S formalism by  $C_{44} = C_{44} \times 1.0001$ .

#### 4.4.2 Results of Ni micro-beam

Based on the all above hypotheses, for the studied Ni sample, the out-of-surface component of Burgers vector for the analyzed slip system is about 0.15 nm. The maximum slip step height is about 9.1 nm at  $d \approx 3.28 \mu\text{m}$  and the slip step height

at GB due to transmission is about 0.86 nm. Thus, based on Eq. 4.8, the number of dislocations produced by the dislocation source is 61 and the number of dislocations transferred in the neighboring grain is 6. Therefore, the number of dislocations in the pile-up is equal to 55. The applied stress is 289.4 MPa as measured in experiment. With all these parameters, the slip step height distribution due to dislocations in the pile-up is calculated for different orientations of interfacial Burgers vector and different critical force while considering or not the effect of free surfaces. Furthermore, the effects of incompatibility stresses, of anisotropic elasticity compared to isotropy, of the number of interfacial dislocations, of the applied stress and of the misorientation are studied.

#### **4.4.2.1 Effect of free surfaces**

The results of the tri-material simulations without free surfaces (marked as INF) and with free surfaces (marked as FS) are presented in Figure 4.24. The simulation results are close to experimental measurements, but there are still some discrepancies. Compared to the experimental measurement, the dislocations are closer to GB in INF, while they are closer to the first free surface when considering the effect of free surfaces in FS. From the theory, it is known that free surfaces have always an attractive effect on all the dislocations. When the dislocations are closer to the first free surface than the second one, the total force is always towards the first free surface, and so dislocations are moved towards it. However, the dislocations around GB are nearly in the middle of the two free surfaces, and thus the effects of the two free surfaces are balanced out by each other. Therefore, the free surfaces have much more effects on the dislocations which are near to the free surface rather than them which are located around GB.



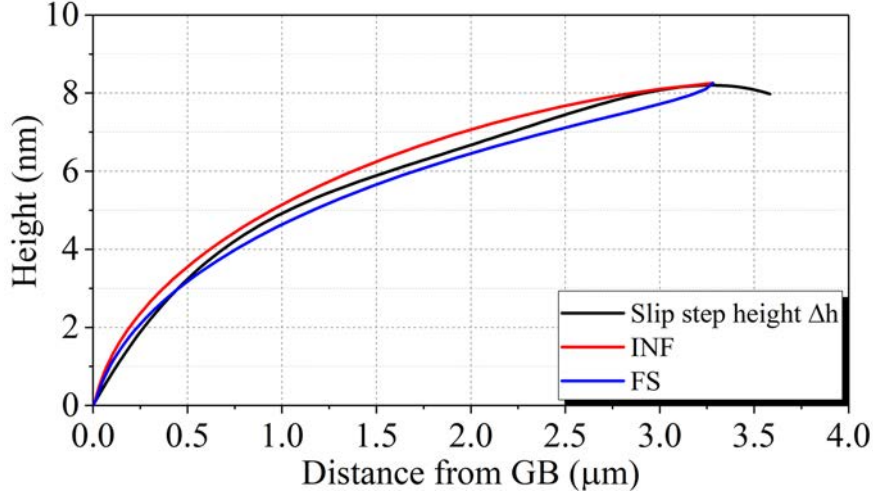


Figure 4.24: Simulation of slip step height in tri-material model without free surfaces (INF) and in three-layers model with free surfaces (FS) and comparisons with the experimental distribution (black line).

#### 4.4.2.2 Effect of interfacial dislocations

In the hypotheses of the simulation, the number of interfacial dislocations is supposed to be the same as the number of transmitted dislocations. So first of all, the number of interfacial dislocations is studied as shown in Figure 4.25 (a). From the experimental measurement, the number of transmitted dislocations is 6. For comparison, the calculation for only 1 interfacial dislocation is also performed. It is well known that the interaction force is repulsive between two parallel dislocations with the same Burgers vector. So compared to the case of 6 interfacial dislocations with the same Burgers vector of incoming dislocation, the repulsive effect is lower in the case of only 1 interfacial dislocation with the same Burgers vector. Thus the equilibrium positions of dislocations in the pile-up are closer to GB in the case of 1 interfacial dislocation compared to the case of 6 interfacial dislocations due to less repulsive force. As the transmission phenomenon is clearly observed by AFM measurement, the Burgers vectors of interfacial dislocations  $\mathbf{b}^{\text{GB}}$  is also studied. The results for two special cases are presented in Figure 4.25 (b). In the first one, the Burgers vector of interfacial dislocation is supposed to be the residual Burgers vector with the outgoing slip system with maximum transmission factor (marked as Residu\_B5). In the other case, the interfacial Burgers vector is supposed to be the residual Burgers vector with the outgoing slip system having the maximum Schmid factor in the adjoining grain (marked as Residu\_B4). Both of them show that the equilibrium positions of dislocations are moved towards GB and are much far away from experimental measurement compared to the case

with the same Burgers vector of incoming dislocation. It seems that the results will be better if the free surfaces are considered for these cases, as the free surfaces will move all the dislocations towards the first free surface side. However, from the results presented in Figure 4.25, it is found that close to GB, the results with 1 interfacial dislocation or with residual Burgers vectors are much far away from experimental measurement compared to the results with 6 interfacial dislocations with the Burgers vector of incoming dislocation. Meanwhile, Figure 4.8 shows that the effects of free surfaces are weak close to GB. Thus, the results will not be better even by considering free surfaces for these cases. It should be pointed out that the Burgers vector of interfacial dislocations has actually been tried with 12 residual Burgers vector corresponding to the 12 FCC slip systems in adjoining grain. Based on these results, the better solution for this sample is still with the Burgers vector of incoming dislocation.

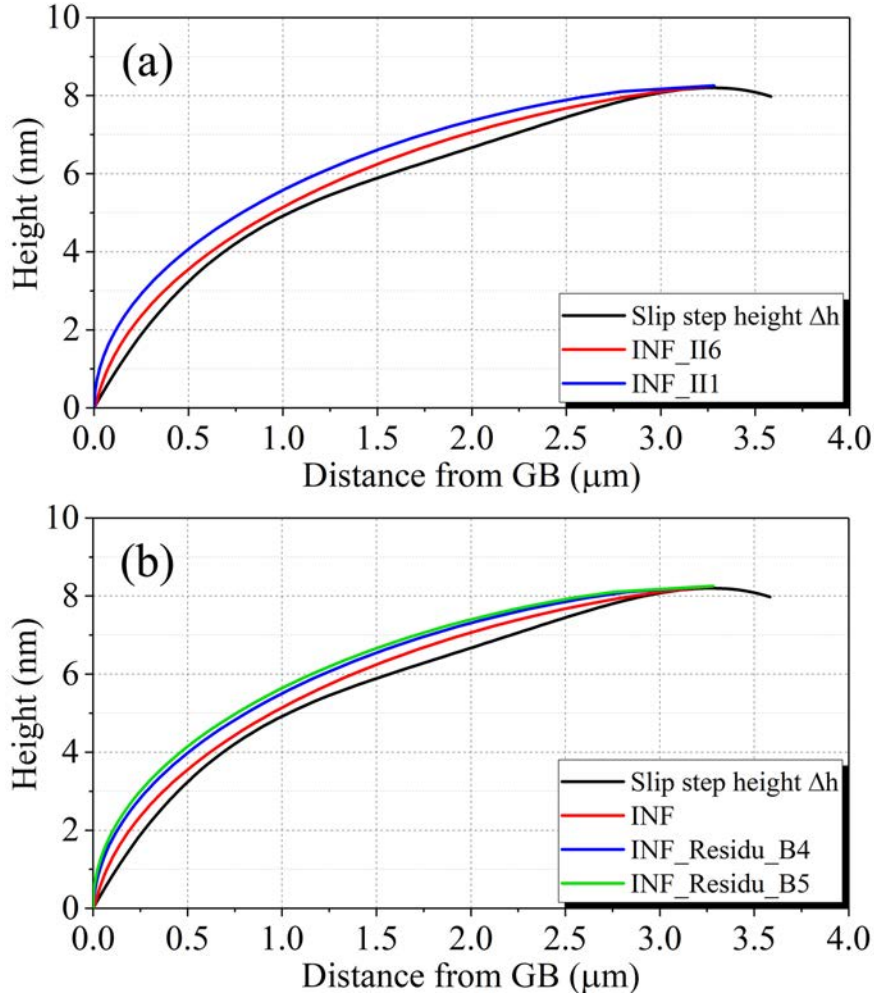


Figure 4.25: Simulation of slip step height in INF for (a) different number of interfacial dislocations: 1 interfacial dislocation (III) and 6 interfacial dislocations (II6), and (b) different Burgers vector of interfacial dislocations: residual Burgers vector between incoming and outgoing slip system with maximum transmission factor (Residu\_B5) and with maximum Schmid factor for outgoing slip system (Residu\_B4).

#### 4.4.2.3 Effect of incompatibility stresses

As discussed in subsection 4.3.3, there are incompatibility stresses due to the heterogeneous elasticity in the present Ni bi-crystal which can be estimated from analytical analyses or numerical simulations (CPFEM). The distribution of stresses due an elastic loading can be calculated from the incompatibility stresses, thus replacing the homogeneous applied stress on the whole bi-crystal as discussed in section 3.3. Incompatibility stresses were first considered as homogeneous in each grain and were calculated from the analytical method based on Eqs. 1.44 and

1.45 considering only elastic incompatibilities ( $[\boldsymbol{\epsilon}^p] = \mathbf{0}$ ). Then, the incompatibility stresses were numerically simulated from CPFEM considering only elasticity (presented in Figure 4.21 with red lines) along a specific line on the upper surface of the micro-beam as presented in Figure 4.19 (b). The latter is more accurate for the present study because the simulated line has the same position on the upper surface as the slip line observed in the experiment. Figure 4.26 presents the results of slip step height considering the effects of incompatibility stresses. Compared to the case of a homogeneous external applied stress, the incompatibility stresses make the equilibrium positions of dislocations closer to GB and much far away from experimental measurement with or without considering free surface effects. For the present Ni bi-crystal, incompatibility stresses increase the applied stress in the grain containing the pile-up. Meanwhile, the results from the analytical method (homogeneous incompatibility stresses in each grain) agree well with the results from the CPFEM simulation (distribution of incompatibility stresses along a special line) for both cases: with or without considering free surface effect.

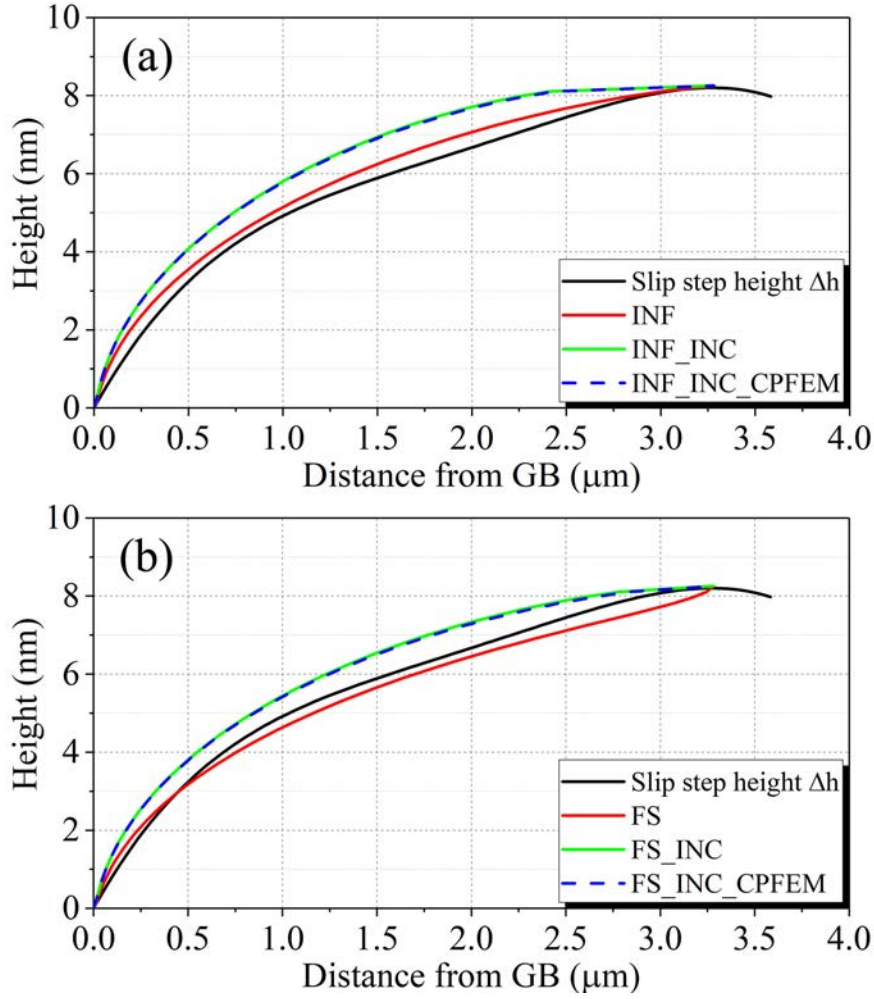


Figure 4.26: Simulation of slip step height considering the effects of incompatibility stresses (a) in INF and (b) in FS. “INC” indicates the incompatibility stresses are calculated by analytical method based on Eqs. 1.44 and 1.45 only for elastic incompatibilities ( $[\epsilon^p] = \mathbf{0}$ ) and they are homogeneous in each grain. “INC\_CPFEF” indicates the incompatibility stresses simulated by CPFEM with considering only elasticity along the line on surface as shown in Figure 4.19 (b).

#### 4.4.2.4 Effect of elastic anisotropy

As the elastic anisotropy factor of Ni  $A = 2.51$  is larger than 1, elastic anisotropy should have some influence on dislocation behavior in the Ni sample. In order to determine the elastic anisotropy effect, the slip step height is calculated considering isotropic elasticity without free surfaces (marked as “INF\_ISO”) and with free surfaces (marked as “FS\_ISO”) which are shown in Figure 4.27 (a) and (b), respectively. The difference between isotropic elasticity and anisotropic elasticity is not too large. One reason is that the image force on one dislocation in the

active slip system at a distance  $5 |\mathbf{b}|$  from GB due to the present misorientation is 0.0103 N/m (see Table 2.1 in Chapter 2). However, with another orientation of the adjoining grain, the maximum image force would be 0.0502 N/m. Moreover, in the present configuration, the dislocations are fixed at two sides of the pile-up which limits the possibilities for the distribution of dislocations. Even so, when considering free surfaces, all dislocations are moved towards the free surface with isotropic elasticity which makes the simulated slip step height profile much far away from experimental measurement. Furthermore, the interphase was also considered as isotropic elastic as shown in Figure 4.27 with name “INF\_InterIso” and “FS\_InterIso”. It is seen that the results are nearly the same as for an anisotropic interphase with  $\lambda = 1$ .

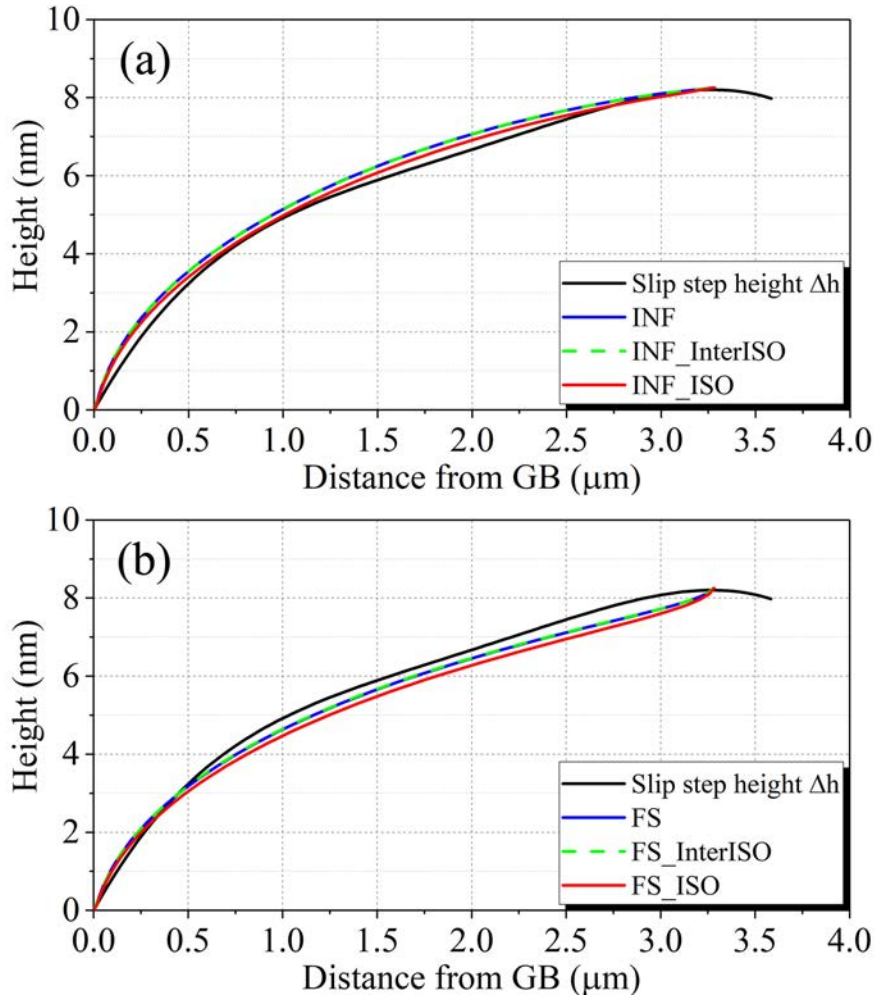


Figure 4.27: Simulation of slip step height between isotropic elasticity and anisotropic elasticity (a) in INF with INF\_InterIso for only the isotropic interphase and INF\_ISO for all layers being isotropic and (b) in FS with all corresponding configurations.

#### 4.4.2.5 Effect of misorientation and applied stress

While the orientation of the grain containing the dislocation pile-up is fixed, the orientation of the adjoining grain is randomly selected in order to investigate the misorientation effect. The results with the maximum attractive misorientation and maximum repulsive misorientation are presented in Figure 4.28 (a). In agreement with the theoretical analysis, the attractive misorientation makes all dislocations move towards GB. Conversely, the repulsive misorientation pushes the dislocations towards the free surface. The applied stress also influences the dislocation behavior as shown in Figure 4.28 (b). A larger applied stress pushes the dislocations towards

GB. Conversely, a smaller applied stress relax the dislocations in the pile-up, and then the distances between dislocations become larger. Therefore, the dislocations are moved towards the free surface with a smaller applied stress.

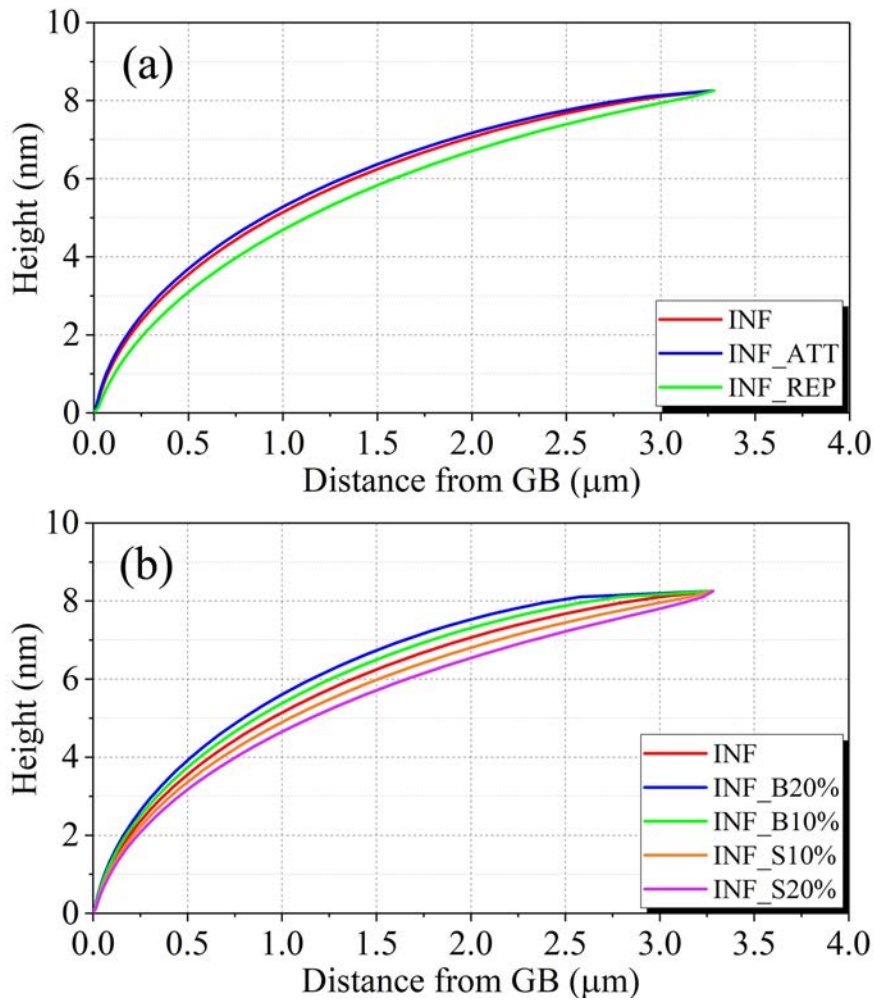


Figure 4.28: Simulation of slip step height in INF (a) with different misorientations: the misorientation with maximum attractive effect (ATT) and with maximum repulsive effect (REP) and (b) with different applied stress : +20% (B20%), +10% (B10%), -10% (S10%) and -20% (S20%) of measured applied stress.

#### 4.4.2.6 Effect of critical force

As discussed in subsection 3.3, it is necessary to consider the effect of critical force  $F_c$  (see Eq. 3.56). The results considering or not the critical force are presented in Figure 4.29. It is found that  $F_c$  moves the dislocation towards the GB. When considering the effect of free surfaces with a critical force  $F_c = 0.003 \text{ N/m}$



(equivalent to a resolved shear stress  $\tau_c = 12$  MPa), the simulation result is closer to the experimental measurement as shown in Figure 4.29 (b) with the red curve of name FS\_Fc0.003. The value here is higher than the theoretical value of lattice friction for pure FCC crystals which is around  $1 \sim 2$  MPa [296]. The reason might be due to the sample preparation, such as the damage coming from FIB polishing. Furthermore, it is found that the critical force does not have obvious effect on dislocations that are located at less than  $0.5 \mu\text{m}$  from GB in the INF model as shown in the Figure 4.29 (a). From Eq. 3.56, it can be found out that this critical force does not have an uniform effect on all the dislocations in the pile-up. For example, when the total force on a dislocation is towards free surface for positions close to free surface, the critical force will point towards GB. However, the stress state is more complicated at regions close to GB. The total force on a dislocation can point towards GB due to repulsive forces from other dislocations, attractive misorientation, compliant GB, attractive force from interfacial dislocations and applied stress. On the contrary, it can point to the opposite direction due to repulsive misorientation, rigid GB, repulsive force from interfacial dislocations or other dislocations in front of this dislocation and free surfaces effect (even if it is weak here). Hence, the total force depends on many parameters. Thus, the critical force could either move the dislocations towards GB or to the opposite direction.

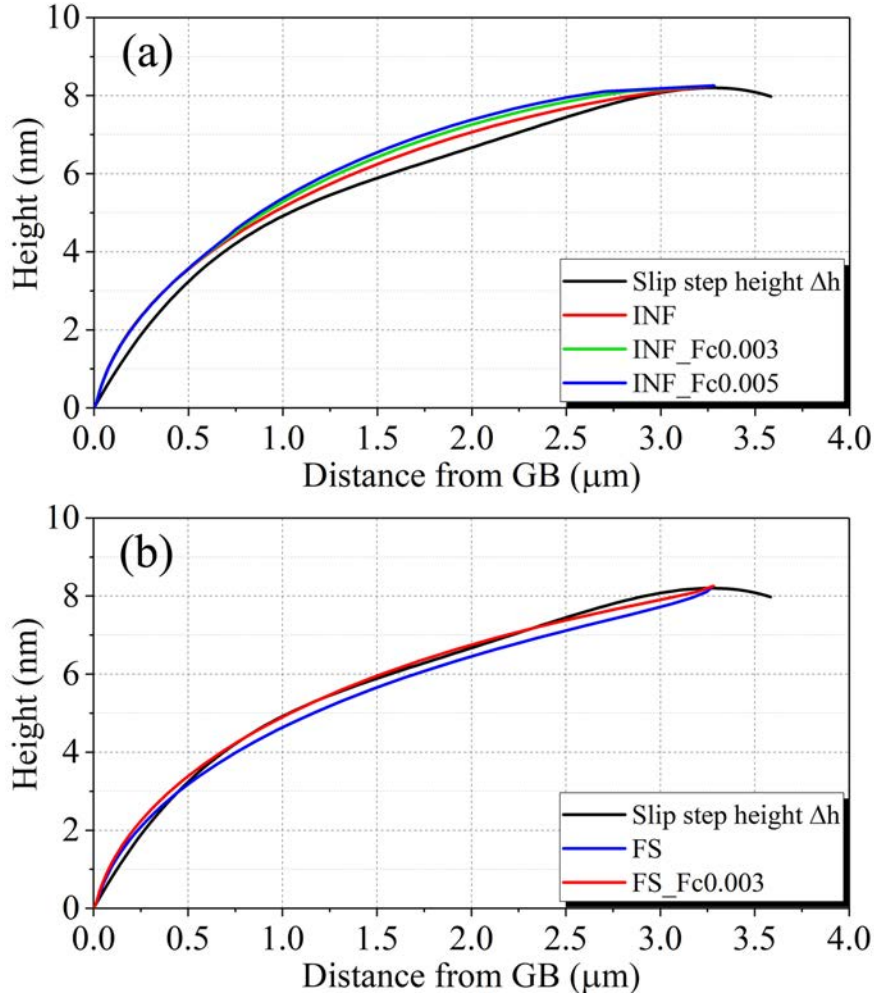


Figure 4.29: Simulation of slip step height (a) in INF and (b) in FS on considering the critical force ( $F_c$ ) on unit N/m.

As a conclusion, the best solution of this simulation is to consider anisotropic elasticity, the effect of free surfaces, a critical force  $F_c = 0.003$  N/m ( $\tau_c = 12$  MPa) and a homogeneous external stress for Ni.

#### 4.4.3 Results of $\alpha$ -Brass micro-beam

Similarly to the Ni sample, the same simulations have been performed for the  $\alpha$ -Brass sample. For the present  $\alpha$ -Brass sample, the out-of-surface component of the Burgers vector of the analyzed slip system is about 0.14 nm. The maximum slip step height is about 10.03 nm at  $d \approx 2.44$  μm and the slip step height at GB due to transmission is about 4.29 nm. Based on Eq. 4.8, the number of

dislocations produced by the dislocation source is 72 and the number of transmitted dislocations is 31. Therefore, the number of dislocations in the pile-up is equal to 41. The applied stress is 127.4 MPa following experimental result. The effects of free surfaces, critical force and anisotropic elasticity for  $\alpha$ -Brass sample are the same as for the Ni sample. However, for this  $\alpha$ -Brass sample, compared to the case of a homogeneous external applied stress, the incompatibility stresses make the equilibrium positions of dislocations closer to free surface and also much far away from experimental measurement with or without considering free surface effects. Thus, the effects of incompatibility stresses for the present  $\alpha$ -Brass micro-beam are inverse compared to the ones for the studied Ni micro-beam. Furthermore, the number of transmitted dislocations is much larger in the  $\alpha$ -Brass sample than in the Ni one, ie. 31 instead of 6. Thus, the repulsive force from these interfacial dislocations is more important if their Burgers vector is considered as the same as the incoming dislocations (see the blue curve in Figure 4.30 (a)). All dislocations are moved far away from GB into the direction of free surface due to this repulsive force. This transmission observed in Figure 2.26 (b) leads us to consider a different residual Burgers vector for interfacial dislocations. After verifying all the possible residual Burgers vectors with 12 slip systems in the adjoining grain, it is found that the best solution is with A6 slip system in the adjoining grain while considering free surfaces and a reasonable critical force  $F_c = 0.011$  N/m ( $\tau_c = 43$  MPa) as shown in Figure 4.30 (b). Furthermore, the theoretical analysis of the slip trace of A6 slip system on the upper surface of adjoining grain agrees well with experimental observation as shown in Figure 2.26 (b) compared to other slip systems, such as B2 slip system with the maximum transmission factor or B4 slip system with the maximum Schmid factor in the adjoining grain. As discussed in section 2.7 for  $\alpha$ -Brass, the peak valley in the middle part of the measured curve is certainly caused by the crossing with a second non coplanar active slip system. In the present two-dimensional anisotropic elasticity calculations, it was not possible to consider the effect of two dislocations whose dislocation lines are not parallel. Thus, this peak valley part cannot be simulated. However, it is important to well identify with the anisotropic pile-up model the part close to GB with  $d < 0.75$   $\mu\text{m}$ . Here, the obtained critical stress is  $\tau_c = 43$  MPa. It is larger than the critical stress for the Ni sample. However, as discussed in subsection 3.3, the theoretical lattice friction stress for  $\beta$ -Brass is about  $\tau_c \approx 80 \sim 100$  MPa [296]. For the  $\alpha$ -Brass, the content of Zinc is lower than for  $\beta$ -Brass, thus the lattice friction stress should be lower. Hence, it is believed that  $\tau_c \approx 43$  MPa is acceptable.

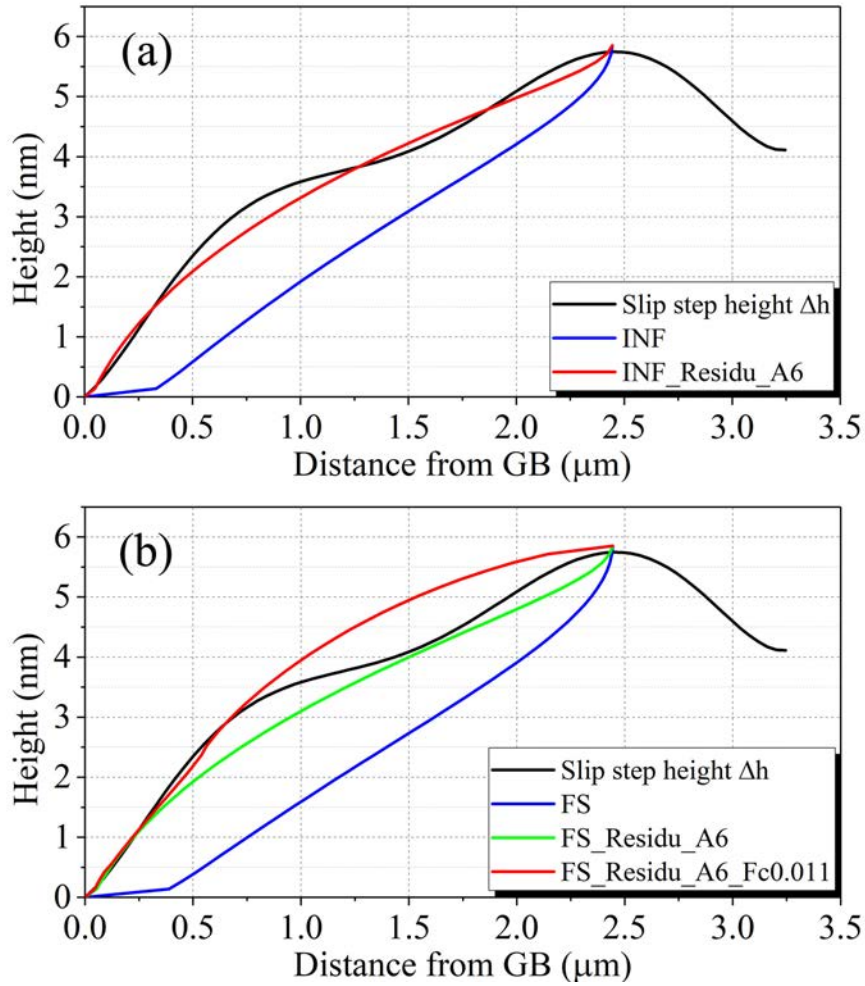


Figure 4.30: Simulation of slip step height for  $\alpha$ -Brass micro-beam (a) in INF considering residual Burgers vector of interfacial dislocations and (b) in FS considering critical force.

As a conclusion, the best solution inferred from these simulations for this  $\alpha$ -Brass sample is to consider anisotropic elasticity, the effect of free surfaces, a critical force  $F_c = 0.011 \text{ N/m}$  ( $\tau_c = 43 \text{ MPa}$ ), the residual Burgers vector for interfacial dislocations as there is a huge number of transmitted dislocations and a homogeneous external stress field.

## 4.5 Conclusions of Chapter 4

In this chapter, numerical applications of the theoretical expressions of elastic fields due to single dislocation and dislocation pile-ups in heterogeneous media as

theoretically presented in Chapter 3 were performed. After studying the convergence of the series solutions for tri-material configuration with two new criteria based on stress and displacement fields in the whole simulation box, the effects of anisotropic elasticity, crystallographic orientation, GB stiffness and free surfaces were studied in the case of a single dislocation in a Ni bi-crystal. Image forces may arise because of both dissimilar grain orientations, the presence of a finite GB region (interphase with finite thickness) and the presence of free surfaces. In particular, it is shown that the Peach-Koehler force projected along the dislocation glide direction can exhibit a change of sign with the dislocation position. In this configuration, an equilibrium position in the absence of applied stress was found as the result of the competition between an attractive compliant GB with a repelling neighboring grain, or, a repelling stiff GB with an attractive neighboring grain. Meanwhile, the effects of free surfaces were individually studied. Free surfaces have always an attractive effect on dislocations and their presence induce thickness size effects on image stresses. Furthermore, it is found that the acting distances of these heterogeneous factors are different. The free or rigid surface has the largest acting distance in the grain and its impact is the largest. The misorientation effect is much lower than the effect of a free or a rigid surface and so the acting distance is shorter. Lastly, the GB stiffness has the shortest acting distance due to the typical thickness of GB which is about 1 nm. However, the GB stiffness effect may still be important, for instance on the equilibrium position of the leading dislocation in pile-up. Then, for discrete edge dislocation pile-ups in Ni bi-crystals, the pile-up length for different configurations considering anisotropic versus isotropic elasticity were computed for different situations: homogeneous crystal, bi-material, tri-material with GB stiffness characterized by  $\lambda$  from 0.5 to 2, rigid half-space. From these configurations and following the numerical results, it was concluded that the first effect on the dislocation pile-up length is the crystallographic misorientation compared to the intrinsic GB stiffness. By using Voigt-Reuss-Hill average [269, 270], the pile-up length in isotropic elasticity is nearly the average length of the considered configurations in anisotropic elasticity as described in subsection 4.2.5.1. Furthermore, the maximum relative variation of pile-up length increases with the anisotropic factor (Zener ratio) of the material (presented in Table 4.5). For a given misorientation, the pile-up length is always much lower than the one resulting from anisotropic or isotropic rigid half-space. From the calculations of resolved shear stress profiles in the neighboring grain, it was shown using Eshelby's diagram that the approximation of a shear stress decrease with the inverse of the square root distance from the pile-up remains valid in the case of anisotropic and heterogeneous elasticity. In the case of stiffer GB (unlocked pile-up configurations), an increase of the dislocation pile-up length was observed to be more important as the number of dislocations in the pile-up and the GB stiffness are higher. The

resolved shear stress at short distance of the GB in the neighboring grain exhibits a decrease in magnitude as the GB stiffness increases. If the parameter  $\lambda$  is low, then a stronger decrease was observed.

In addition to the theoretical results, the results of a numerical method based on CPFEM are presented. Thanks to such CPFEM simulations, the elastic part of the experimental stress-strain curves were first predicted. Then, the incompatibility stresses in each grain of the micro-beam were computed both on average and along some specific lines. The incompatibility stresses calculated from the analytical method were compared to the ones obtained from the FE results and show good agreement for the principal stress  $\sigma_{22}$ .

At the end, the distribution of slip step heights observed in experiment was simulated by dislocation pile-up configuration in bi-crystals with the experimentally measured parameters by considering the effect of misorientation, incompatibility stresses, GB stiffness, free surfaces and critical force. It has been found that the Burgers vector of interfacial dislocations can be regarded as the same of incoming dislocations in case of a low number (6) of transmitted dislocations in the Ni sample. However, in case of a high number (31) of transmitted dislocations in the  $\alpha$ -Brass sample, one should consider the residual Burgers vector of interfacial dislocations. Meanwhile, it appears that the effects of free surfaces and critical force should always be considered. The critical force for the studied Ni sample is  $F_c = 0.003$  N/m ( $\tau_c = 12$  MPa) and for the studied  $\alpha$ -Brass sample is  $F_c = 0.011$  N/m ( $\tau_c = 43$  MPa) which are acceptable due to lattice defects in the material and alloy composition, respectively.

# Conclusions and Perspectives

## General conclusions

The work presented in this thesis was developed on the basis of two complementary approaches:

- a theoretical approach based on micromechanical modeling: anisotropic elasticity, interface (GB), dislocations and dislocation pile-ups.
- an experimental approach based on the micro-compression of Ni and  $\alpha$ -brass bi-crystalline micro-beam processed by FIB and materials characterization with AFM and SEM/EBSD.

Both approaches allowed us to evaluate the distribution of dislocations in a pile-up in Ni and  $\alpha$ -Brass bi-crystal configurations.

The developed models take into account the effect of anisotropic elasticity, misorientation, incompatibility stresses, GB stiffness, free surfaces and critical force. It was established based on the L-E-S formalism [20, 21, 22]. These models provide the explicit analytical or semi-analytical expressions of the elastic fields (displacements and stresses) due to one single dislocation or dislocation pile-ups in anisotropic homogeneous media, half-spaces, bi- and tri-material [17] while possibly considering free surface effects [18]. The tri-material configuration allows considering a more realistic non-zero GB thickness in the nanometer range and a specific stiffness tensor for the GB region. The configuration with two free surfaces can be used to study size effects. These theories were first applied to analyze the effects of misorientation, GB stiffness and free surfaces on image force due to one single dislocation in Ni bi-material configurations. Then, the length of different dislocation pile-ups and the resolved shear stress produced by these dislocation pile-ups were performed with/without locking the leading dislocation of the pile-up by considering all the above effects.

Regarding the experimental work, micro-pillar compression tests were performed on Ni and  $\alpha$ -Brass bi-crystalline micro-beams of diameter 8  $\mu\text{m}$ . The

micro-beams were produced by FIB, characterized by EBSD and deformed in uniaxial compression at displacement control imposed using a flat punch within a nanoindenter. The tests were stopped after a low plastic strain in the material. The active slip lines were analyzed by SEM pictures for geometrical information. Slip step height spatial variations due to localized slip bands terminating at GB were measured by AFM to determine the Burgers vector distribution in the dislocation pile-up.

The stress-strain curves were calibrated by CPFEM simulations in elasticity for both Ni and  $\alpha$ -Brass samples. Then, the incompatibility stresses of the studied micro-beams were analyzed by the analytical method [160] and the present CPFEM simulations. The results showed that the principle component of stress tensor  $\sigma_{22}$  exhibits a good agreement between the two methods. However, it also showed that the geometry and finite size boundary conditions have a strong influence on the stress distributions in the micro-beams, in particular around areas where GB intersects surfaces.

The GB thickness in Ni bi-crystals with different misorientations was also studied by MS/MD simulations (see Appendix C). It showed that this thickness depends on the misorientation and is on average around 1 nm. Meanwhile, the interfacial dislocation structures for these different GB configurations were studied. The atomistic simulations mainly showed three different types of dislocation structures for the studied misorientations.

At the end, the dislocation distributions in the dislocation pile-up were simulated by dislocation pile-up configuration in bi-crystals with the experimentally measured parameters by considering the effect of misorientation, GB stiffness, free surfaces, anisotropic elasticity, incompatibility stresses, interfacial dislocations and critical force. It was found that the Burgers vector of interfacial dislocations can be regarded as the same of incoming dislocations in case of a low number (6) of transmitted dislocations in the Ni sample. However, in case of a high number (31) of transmitted dislocations in the  $\alpha$ -Brass sample, one should consider the residual Burgers vector of interfacial dislocations. Meanwhile, the effects of free surfaces and critical force should always be considered in the theoretical calculations in order to be more predictive regarding the slip step height profile. The critical force for the studied Ni sample is  $F_c = 0.003$  N/m ( $\tau_c = 12$  MPa) and for the studied  $\alpha$ -Brass sample is  $F_c = 0.011$  N/m ( $\tau_c = 43$  MPa) have been found to be acceptable due to lattice defects in the material and alloy composition, respectively.

## Perspectives

The dislocation distribution in dislocation pile-ups can be analyzed more directly and more accurately by ECCI. However, it needs a perfect sample prepa-



ration on the sample surface. In addition to the present analytical approach for dislocation behavior in bi-crystals, the results could be refined using other numerical methods, such as MD simulations and 3D DDD simulations. Meanwhile, the present method could be used to enrich 2D DDD simulations dealing with interfaces in anisotropic elasticity, especially for the GB properties. Even if it is possible to define different elastic properties of GB with anisotropic or isotropic elastic stiffness tensor, the elastic behavior of GBs and their dependence on GB macroscopic and microscopic parameters remain largely unknown. Thus, in a future study, the elastic properties of GB will be investigated by MS/MD simulations.

# Appendix

## A Equivalence between the formulations of T.C.T. Ting and Z. Suo for the elastic fields of a dislocation in bi-materials with perfectly bonded interface

As described in subsection 3.2.2, combining the Eqs. 1.56, 3.4, 3.5, 3.10, 3.18 and 3.19, the displacement fields due to one single dislocation located at  $(X_1, X_2)$  in the crystal I of an anisotropic bi-crystal configuration as shown in Figure 3.1 can be calculated by the formalism proposed by Suo [19]:

$$u_i = 2\text{Re} \left[ A_{ij} f_{\underline{j}}(z_j) \right] \quad (\text{A.1})$$

with

$$f_j(z_j) = \begin{cases} f_j^0(z_j) + \overline{V_{jk}^{\text{I,II}}} f_k^0(z_j) & \text{if } z_j \in \text{I} \ (x_2 > 0) \\ W_{jk}^{\text{I,II}} f_k^0(z_j) & \text{if } z_j \in \text{II} \ (x_2 < 0) \end{cases} \quad (\text{A.2})$$

$$f_j^0(z_i) = q_j^0 \ln(z_i - s_j) \quad (\text{A.3})$$

and

$$\mathbf{q}^0 = -\frac{1}{2\pi} \mathbf{i} (\mathbf{B}^T \mathbf{b}) \quad (\text{A.4})$$

where

$$z_i = \begin{cases} x_1 + p_i^{\text{I}} x_2 & \text{if } z_j \in \text{I} \ (x_2 > 0) \\ x_1 + p_i^{\text{II}} x_2 & \text{if } z_j \in \text{II} \ (x_2 < 0) \end{cases} \quad (\text{A.5})$$

$$s_j = X_1 + p_j^{\text{I}} X_2$$

and

$$\begin{cases} \mathbf{V}^{\text{I,II}} = \left( \mathbf{B}^{\text{II}} \mathbf{A}^{\text{II}-1} \overline{\mathbf{A}^{\text{I}}} - \overline{\mathbf{B}^{\text{I}}} \right)^{-1} \left( \mathbf{B}^{\text{I}} - \mathbf{B}^{\text{II}} \mathbf{A}^{\text{II}-1} \mathbf{A}^{\text{I}} \right) \\ \mathbf{W}^{\text{I,II}} = \left( \overline{\mathbf{B}^{\text{I}} \mathbf{A}^{\text{I}-1} \mathbf{A}^{\text{II}}} - \mathbf{B}^{\text{II}} \right)^{-1} \left( \overline{\mathbf{B}^{\text{I}} \mathbf{A}^{\text{I}-1} \mathbf{A}^{\text{I}}} - \mathbf{B}^{\text{I}} \right) \end{cases} \quad (\text{A.6})$$

Meanwhile, Ting [285] has proposed another equivalent formalism for the same problem, as:

$$\mathbf{u} = \begin{cases} 2\text{Re} \{ \mathbf{A} \langle \ln(z_* - s_*) \rangle \mathbf{q}^0 \} + 2\text{Re} \sum_{k=1}^3 \{ \mathbf{A} \langle \ln(z_* - \overline{s_k}) \rangle \mathbf{q}^{\text{I},k} \} & \text{if } z_j \in \text{I} \ (x_2 > 0) \\ 2\text{Re} \sum_{k=1}^3 \{ \mathbf{A} \langle \ln(z_* - s_k) \rangle \mathbf{q}^{\text{II},k} \} & \text{if } z_j \in \text{II} \ (x_2 < 0) \end{cases} \quad (\text{A.7})$$

with

$$\begin{aligned} \langle \ln(z_* - s_*) \rangle &= \begin{bmatrix} \ln(z_1 - s_1) & 0 & 0 \\ 0 & \ln(z_2 - s_2) & 0 \\ 0 & 0 & \ln(z_3 - s_3) \end{bmatrix} \\ \langle \ln(z_* - s_k) \rangle &= \begin{bmatrix} \ln(z_1 - s_k) & 0 & 0 \\ 0 & \ln(z_2 - s_k) & 0 \\ 0 & 0 & \ln(z_3 - s_k) \end{bmatrix} \end{aligned} \quad (\text{A.8})$$

and

$$\begin{aligned} \mathbf{q}^{\text{I},k} &= \overline{\mathbf{V}} \mathbf{I}^k \overline{\mathbf{q}^0} \\ \mathbf{q}^{\text{II},k} &= \mathbf{W} \mathbf{I}^k \mathbf{q}^0 \\ \mathbf{q}^0 &= -\frac{1}{2\pi} i \mathbf{B}^{\text{T}} \mathbf{b} \end{aligned} \quad (\text{A.9})$$

where

$$\begin{aligned} z_i &= \begin{cases} x_1 + p_i^{\text{I}} x_2 & \text{if } z_j \in \text{I} \ (x_2 > 0) \\ x_1 + p_i^{\text{II}} x_2 & \text{if } z_j \in \text{II} \ (x_2 < 0) \end{cases} \\ s_j &= X_1 + p_j^{\text{I}} X_2 \end{aligned} \quad (\text{A.10})$$

$$\begin{cases} \mathbf{V} = \left( \mathbf{B}^{\text{II}} \mathbf{A}^{\text{II}-1} \overline{\mathbf{A}^{\text{I}}} - \overline{\mathbf{B}^{\text{I}}} \right)^{-1} \left( \mathbf{B}^{\text{I}} - \mathbf{B}^{\text{II}} \mathbf{A}^{\text{II}-1} \mathbf{A}^{\text{I}} \right) \\ \mathbf{W} = \left( \overline{\mathbf{B}^{\text{I}} \mathbf{A}^{\text{I}-1} \mathbf{A}^{\text{II}}} - \mathbf{B}^{\text{II}} \right)^{-1} \left( \overline{\mathbf{B}^{\text{I}} \mathbf{A}^{\text{I}-1} \mathbf{A}^{\text{I}}} - \mathbf{B}^{\text{I}} \right) \end{cases} \quad (\text{A.11})$$

$$\mathbf{I}_{mn}^k = \begin{cases} 1 & m = n = k & (k = 1, 2, 3) \\ 0 & \text{others} & (m, n = 1, 2, 3) \end{cases} \quad (\text{A.12})$$

Thus, it is found that the definitions of  $\mathbf{V}$ ,  $\mathbf{W}$ ,  $z_i$  and  $s_j$  are the same between the formalism of Suo [19] and Ting [285]. Now, the formalism of Ting can be written into index form as Eq. A.1:

$$u_i = 2\text{Re} \left[ A_{i\bar{j}} f_{\bar{j}} \left( z_{\bar{j}} \right) \right] \quad (\text{A.13})$$

where

$$f(z) = \begin{cases} \langle \ln(z_* - s_*) \rangle \mathbf{q}^0 + \sum_{k=1}^3 \left\{ \langle \ln(z_* - \bar{s}_k) \rangle \overline{\mathbf{V}} \mathbf{I}^k \overline{\mathbf{q}^0} \right\} & \text{if } z_j \in \text{I} \ (x_2 > 0) \\ \sum_{k=1}^3 \left\{ \langle \ln(z_* - s_k) \rangle \mathbf{W} \mathbf{I}^k \mathbf{q}^0 \right\} & \text{if } z_j \in \text{II} \ (x_2 < 0) \end{cases} \quad (\text{A.14})$$

When  $z_j \in \text{I} \ (x_2 > 0)$ :

$$\begin{aligned} f_j(z_j) &= \ln(z_j - s_j) q_j^0 + \sum_{k=1}^3 \left\{ \ln(z_j - \bar{s}_k) \overline{V}_{jl} \mathbf{I}_{lm}^k \overline{q_m^0} \right\} \\ &= \ln(z_j - s_j) q_j^0 + \ln(z_j - \bar{s}_1) \overline{V}_{j1} \mathbf{I}_{lm}^1 \overline{q_m^0} + \ln(z_j - \bar{s}_2) \overline{V}_{j2} \mathbf{I}_{lm}^2 \overline{q_m^0} + \ln(z_j - \bar{s}_3) \overline{V}_{j3} \mathbf{I}_{lm}^3 \overline{q_m^0} \\ &= \ln(z_j - s_j) q_j^0 + \ln(z_j - \bar{s}_1) \overline{V}_{j1} \overline{q_1^0} + \ln(z_j - \bar{s}_2) \overline{V}_{j2} \overline{q_2^0} + \ln(z_j - \bar{s}_3) \overline{V}_{j3} \overline{q_3^0} \\ &= \ln(z_j - s_j) q_j^0 + \ln(z_j - \bar{s}_l) \overline{V}_{jl} \overline{q_l^0} \\ &= f_j^0(z_j) + \overline{V}_{jl} f_l^0(z_j) \end{aligned} \quad (\text{A.15})$$

When  $z_j \in \text{II} \ (x_2 < 0)$ :

$$\begin{aligned} f_j(z_j) &= \sum_{k=1}^3 \left\{ \ln(z_j - s_k) W_{jl} \mathbf{I}_{lm}^k q_m^0 \right\} \\ &= \ln(z_j - s_1) W_{j1} \mathbf{I}_{lm}^1 q_m^0 + \ln(z_j - s_2) W_{j2} \mathbf{I}_{lm}^2 q_m^0 + \ln(z_j - s_3) W_{j3} \mathbf{I}_{lm}^3 q_m^0 \\ &= \ln(z_j - s_1) W_{j1} q_1^0 + \ln(z_j - s_2) W_{j2} q_2^0 + \ln(z_j - s_3) W_{j3} q_3^0 \\ &= \ln(z_j - s_l) W_{jl} q_l^0 \\ &= W_{jl} f_l^0(z_j) \end{aligned} \quad (\text{A.16})$$

Thus, Eq. A.14 can be written into:

$$f_j(z_j) = \begin{cases} f_j^0(z_j) + \overline{V_{j\mathbf{k}} f_{\mathbf{k}}^0}(z_j) & \text{if } z_j \in \text{I } (x_2 > 0) \\ W_{j\mathbf{k}} f_{\mathbf{k}}^0(z_j) & \text{if } z_j \in \text{II } (x_2 < 0) \end{cases} \quad (\text{A.17})$$

which is the same as the Eq. A.2 in the formalism of Suo [19]. As a conclusion, both formalisms of Suo [19] and Ting [285] are equivalent.

## B Full coefficient matrix of image decomposition method

For one dislocation in a tri-material configuration with two free surfaces as presented in Figure 3.3 (see subsection 3.2.5 of Chapter 3), the  $18 \times 18$  matrices of coefficient  $\mathbf{C}, \mathbf{C}_0$ , the  $18 \times 18$  matrices of integral operator  $\mathbf{H}_0, \mathbf{C}_H \mathbf{H}, \mathbf{C}_I \mathbf{I}, \mathbf{C}_H \mathbf{H}_0 \mathbf{H}, \mathbf{C}_I \mathbf{H}_0 \mathbf{I}$ , the  $18 \times 1$  vectors in function of Burgers vector  $\mathbf{C}_R \mathbf{R}, \mathbf{C}_R \mathbf{H}_0 \mathbf{R}$  and the image dislocation densities vector  $\boldsymbol{\rho}$  in Eqs. 3.53, 3.54 and 3.55 are expressed in follows:

$$\mathbf{C} = 2\pi \begin{bmatrix} -\xi_{1\alpha i 2}^{tR} & 0 & 0 & 0 & 0 & 0 \\ 0 & 0 & 0 & 0 & 0 & -\xi_{3\alpha i 2}^{tR} \\ 0 & -\xi_{1\alpha i 2}^{tR} & \xi_{2\alpha i 2}^{tR} & 0 & 0 & 0 \\ 0 & \zeta_{1\alpha i 1}^{tI} & \zeta_{2\alpha i 1}^{tI} & 0 & 0 & 0 \\ 0 & 0 & 0 & -\xi_{2\alpha i 2}^{tR} & \xi_{3\alpha i 2}^{tR} & 0 \\ 0 & 0 & 0 & \zeta_{2\alpha i 1}^{tI} & \zeta_{3\alpha i 1}^{tI} & 0 \end{bmatrix} \quad (\text{B.1})$$

$$\mathbf{C}_0 = 2\pi \begin{bmatrix} 0 & 0 & 0 & 0 & 0 & 0 \\ 0 & 0 & 0 & 0 & 0 & 0 \\ 0 & 0 & 0 & 0 & 0 & 0 \\ 0 & \zeta_{1\alpha i 1}^{tR} & -\zeta_{2\alpha i 1}^{tR} & 0 & 0 & 0 \\ 0 & 0 & 0 & 0 & 0 & 0 \\ 0 & 0 & 0 & \zeta_{2\alpha i 1}^{tR} & -\zeta_{3\alpha i 1}^{tR} & 0 \end{bmatrix} \quad (\text{B.2})$$

$$\mathbf{H}_0 = 2\pi \begin{bmatrix} H(0,0) & 0 & 0 & 0 & 0 & 0 \\ 0 & H(0,0) & 0 & 0 & 0 & 0 \\ 0 & 0 & H(0,0) & 0 & 0 & 0 \\ 0 & 0 & 0 & H(0,0) & 0 & 0 \\ 0 & 0 & 0 & 0 & H(0,0) & 0 \\ 0 & 0 & 0 & 0 & 0 & H(0,0) \end{bmatrix} \quad (\text{B.3})$$

$$\begin{aligned}
C_H \mathbf{H}(:, 1:6) &= 2\pi \begin{bmatrix} \mathbf{0} & \boldsymbol{\xi}_{1\alpha i 2}^{tI} \mathbf{H}(p_{1\alpha}^R h_1, p_{1\alpha}^I h_1) \\ -\boldsymbol{\xi}_{3\alpha i 2}^{tI} \mathbf{H}(-p_{3\alpha}^R (h_1 + h_2 + h_3), p_{3\alpha}^I (h_1 + h_2 + h_3)) & \mathbf{0} \\ -\boldsymbol{\xi}_{1\alpha i 2}^{tI} \mathbf{H}(-p_{1\alpha}^R h_1, p_{1\alpha}^I h_1) + \boldsymbol{\xi}_{2\alpha i 2}^{tI} \mathbf{H}(-p_{2\alpha}^R h_1, p_{2\alpha}^I h_1) & \mathbf{0} \\ \boldsymbol{\zeta}_{1\alpha i 1}^{tR} \mathbf{H}(-p_{1\alpha}^R h_1, -p_{1\alpha}^I h_1) - \boldsymbol{\zeta}_{2\alpha i 1}^{tR} \mathbf{H}(-p_{2\alpha}^R h_1, -p_{2\alpha}^I h_1) & \mathbf{0} \\ -\boldsymbol{\xi}_{2\alpha i 2}^{tI} \mathbf{H}(-p_{2\alpha}^R (h_1 + h_2), p_{2\alpha}^I (h_1 + h_2)) + \boldsymbol{\xi}_{3\alpha i 2}^{tI} \mathbf{H}(-p_{3\alpha}^R (h_1 + h_2), p_{3\alpha}^I (h_1 + h_2)) & \mathbf{0} \\ \boldsymbol{\zeta}_{2\alpha i 1}^{tR} \mathbf{H}(-p_{2\alpha}^R (h_1 + h_2), -p_{2\alpha}^I (h_1 + h_2)) - \boldsymbol{\zeta}_{3\alpha i 1}^{tR} \mathbf{H}(-p_{3\alpha}^R (h_1 + h_2), -p_{3\alpha}^I (h_1 + h_2)) & \mathbf{0} \end{bmatrix} \\
C_H \mathbf{H}(:, 7:12) &= 2\pi \begin{bmatrix} \mathbf{0} & \boldsymbol{\xi}_{1\alpha i 2}^{tI} \mathbf{H}(p_{1\alpha}^R (h_1 + h_2), p_{1\alpha}^I (h_1 + h_2)) \\ -\boldsymbol{\xi}_{3\alpha i 2}^{tI} \mathbf{H}(-p_{3\alpha}^R (h_2 + h_3), p_{3\alpha}^I (h_2 + h_3)) & \mathbf{0} \\ \mathbf{0} & \boldsymbol{\xi}_{1\alpha i 2}^{tI} \mathbf{H}(p_{1\alpha}^R h_2, p_{1\alpha}^I h_2) - \boldsymbol{\xi}_{2\alpha i 2}^{tI} \mathbf{H}(p_{2\alpha}^R h_2, p_{2\alpha}^I h_2) \\ \mathbf{0} & \boldsymbol{\zeta}_{1\alpha i 1}^{tR} \mathbf{H}(p_{1\alpha}^R h_2, p_{1\alpha}^I h_2) - \boldsymbol{\zeta}_{2\alpha i 1}^{tR} \mathbf{H}(p_{2\alpha}^R h_2, p_{2\alpha}^I h_2) \\ -\boldsymbol{\xi}_{2\alpha i 2}^{tI} \mathbf{H}(-p_{2\alpha}^R h_2, p_{2\alpha}^I h_2) + \boldsymbol{\xi}_{3\alpha i 2}^{tI} \mathbf{H}(-p_{3\alpha}^R h_2, p_{3\alpha}^I h_2) & \mathbf{0} \\ \boldsymbol{\zeta}_{2\alpha i 1}^{tR} \mathbf{H}(-p_{2\alpha}^R h_2, -p_{2\alpha}^I h_2) - \boldsymbol{\zeta}_{3\alpha i 1}^{tR} \mathbf{H}(-p_{3\alpha}^R h_2, -p_{3\alpha}^I h_2) & \mathbf{0} \end{bmatrix} \\
C_H \mathbf{H}(:, 13:18) &= 2\pi \begin{bmatrix} \mathbf{0} & \boldsymbol{\xi}_{1\alpha i 2}^{tI} \mathbf{H}(p_{1\alpha}^R (h_1 + h_2 + h_3), p_{1\alpha}^I (h_1 + h_2 + h_3)) \\ -\boldsymbol{\xi}_{3\alpha i 2}^{tI} \mathbf{H}(-p_{3\alpha}^R h_3, p_{3\alpha}^I h_3) & \mathbf{0} \\ \mathbf{0} & \boldsymbol{\xi}_{1\alpha i 2}^{tI} \mathbf{H}(p_{1\alpha}^R (h_2 + h_3), p_{1\alpha}^I (h_2 + h_3)) - \boldsymbol{\xi}_{2\alpha i 2}^{tI} \mathbf{H}(p_{2\alpha}^R (h_2 + h_3), p_{2\alpha}^I (h_2 + h_3)) \\ \mathbf{0} & \boldsymbol{\zeta}_{1\alpha i 1}^{tR} \mathbf{H}(p_{1\alpha}^R (h_2 + h_3), p_{1\alpha}^I (h_2 + h_3)) - \boldsymbol{\zeta}_{2\alpha i 1}^{tR} \mathbf{H}(p_{2\alpha}^R (h_2 + h_3), p_{2\alpha}^I (h_2 + h_3)) \\ \mathbf{0} & \boldsymbol{\xi}_{2\alpha i 2}^{tI} \mathbf{H}(p_{2\alpha}^R h_3, p_{2\alpha}^I h_3) - \boldsymbol{\xi}_{3\alpha i 2}^{tI} \mathbf{H}(p_{3\alpha}^R h_3, p_{3\alpha}^I h_3) \\ \mathbf{0} & \boldsymbol{\zeta}_{2\alpha i 1}^{tR} \mathbf{H}(p_{2\alpha}^R h_3, p_{2\alpha}^I h_3) - \boldsymbol{\zeta}_{3\alpha i 1}^{tR} \mathbf{H}(p_{3\alpha}^R h_3, p_{3\alpha}^I h_3) \end{bmatrix}
\end{aligned} \tag{B.4}$$

$$\begin{aligned}
\mathbf{C}_I \mathbf{I}(:, 1:6) &= 2\pi \left[ \begin{array}{ccc}
\mathbf{0} & & -\boldsymbol{\xi}_{1\underline{\alpha}i2}^{tR} \mathbf{I}(p_{1\underline{\alpha}}^R h_1, p_{1\underline{\alpha}}^I h_1) \\
-\boldsymbol{\xi}_{3\underline{\alpha}i2}^{tR} \mathbf{I}(-p_{3\underline{\alpha}}^R (h_1 + h_2 + h_3), p_{3\underline{\alpha}}^I (h_1 + h_2 + h_3)) & & \mathbf{0} \\
-\boldsymbol{\xi}_{1\underline{\alpha}i2}^{tR} \mathbf{I}(-p_{1\underline{\alpha}}^R h_1, p_{1\underline{\alpha}}^I h_1) + \boldsymbol{\xi}_{2\underline{\alpha}i2}^{tR} \mathbf{I}(-p_{2\underline{\alpha}}^R h_1, p_{2\underline{\alpha}}^I h_1) & & \mathbf{0} \\
\boldsymbol{\zeta}_{1\underline{\alpha}i1}^{tI} \mathbf{I}(-p_{1\underline{\alpha}}^R h_1, -p_{1\underline{\alpha}}^I h_1) - \boldsymbol{\zeta}_{2\underline{\alpha}i1}^{tI} \mathbf{I}(-p_{2\underline{\alpha}}^R h_1, -p_{2\underline{\alpha}}^I h_1) & & \mathbf{0} \\
-\boldsymbol{\xi}_{2\underline{\alpha}i2}^{tR} \mathbf{I}(-p_{2\underline{\alpha}}^R (h_1 + h_2), p_{2\underline{\alpha}}^I (h_1 + h_2)) + \boldsymbol{\xi}_{3\underline{\alpha}i2}^{tR} \mathbf{I}(-p_{3\underline{\alpha}}^R (h_1 + h_2), p_{3\underline{\alpha}}^I (h_1 + h_2)) & & \mathbf{0} \\
\boldsymbol{\zeta}_{2\underline{\alpha}i1}^{tI} \mathbf{I}(-p_{2\underline{\alpha}}^R (h_1 + h_2), -p_{2\underline{\alpha}}^I (h_1 + h_2)) - \boldsymbol{\zeta}_{3\underline{\alpha}i1}^{tI} \mathbf{I}(-p_{3\underline{\alpha}}^R (h_1 + h_2), -p_{3\underline{\alpha}}^I (h_1 + h_2)) & & \mathbf{0}
\end{array} \right] \\
\mathbf{C}_I \mathbf{I}(:, 7:12) &= 2\pi \left[ \begin{array}{ccc}
\mathbf{0} & & -\boldsymbol{\xi}_{1\underline{\alpha}i2}^{tR} \mathbf{I}(p_{1\underline{\alpha}}^R (h_1 + h_2), p_{1\underline{\alpha}}^I (h_1 + h_2)) \\
-\boldsymbol{\xi}_{3\underline{\alpha}i2}^{tR} \mathbf{I}(-p_{3\underline{\alpha}}^R (h_2 + h_3), p_{3\underline{\alpha}}^I (h_2 + h_3)) & & \mathbf{0} \\
\mathbf{0} & & -\boldsymbol{\xi}_{1\underline{\alpha}i2}^{tR} \mathbf{I}(p_{1\underline{\alpha}}^R h_2, p_{1\underline{\alpha}}^I h_2) + \boldsymbol{\xi}_{2\underline{\alpha}i2}^{tR} \mathbf{I}(p_{2\underline{\alpha}}^R h_2, p_{2\underline{\alpha}}^I h_2) \\
\mathbf{0} & & \boldsymbol{\zeta}_{1\underline{\alpha}i1}^{tI} \mathbf{I}(p_{1\underline{\alpha}}^R h_2, p_{1\underline{\alpha}}^I h_2) - \boldsymbol{\zeta}_{2\underline{\alpha}i1}^{tI} \mathbf{I}(p_{2\underline{\alpha}}^R h_2, p_{2\underline{\alpha}}^I h_2) \\
-\boldsymbol{\xi}_{2\underline{\alpha}i2}^{tR} \mathbf{I}(-p_{2\underline{\alpha}}^R h_2, p_{2\underline{\alpha}}^I h_2) + \boldsymbol{\xi}_{3\underline{\alpha}i2}^{tR} \mathbf{I}(-p_{3\underline{\alpha}}^R h_2, p_{3\underline{\alpha}}^I h_2) & & \mathbf{0} \\
\boldsymbol{\zeta}_{2\underline{\alpha}i1}^{tI} \mathbf{I}(-p_{2\underline{\alpha}}^R h_2, -p_{2\underline{\alpha}}^I h_2) - \boldsymbol{\zeta}_{3\underline{\alpha}i1}^{tI} \mathbf{I}(-p_{3\underline{\alpha}}^R h_2, -p_{3\underline{\alpha}}^I h_2) & & \mathbf{0}
\end{array} \right] \\
\mathbf{C}_I \mathbf{I}(:, 13:18) &= 2\pi \left[ \begin{array}{ccc}
\mathbf{0} & & -\boldsymbol{\xi}_{1\underline{\alpha}i2}^{tR} \mathbf{I}(p_{1\underline{\alpha}}^R (h_1 + h_2 + h_3), p_{1\underline{\alpha}}^I (h_1 + h_2 + h_3)) \\
-\boldsymbol{\xi}_{3\underline{\alpha}i2}^{tR} \mathbf{I}(-p_{3\underline{\alpha}}^R h_3, p_{3\underline{\alpha}}^I h_3) & & \mathbf{0} \\
\mathbf{0} & & -\boldsymbol{\xi}_{1\underline{\alpha}i2}^{tR} \mathbf{I}(p_{1\underline{\alpha}}^R (h_2 + h_3), p_{1\underline{\alpha}}^I (h_2 + h_3)) + \boldsymbol{\xi}_{2\underline{\alpha}i2}^{tR} \mathbf{I}(p_{2\underline{\alpha}}^R (h_2 + h_3), p_{2\underline{\alpha}}^I (h_2 + h_3)) \\
\mathbf{0} & & \boldsymbol{\zeta}_{1\underline{\alpha}i1}^{tI} \mathbf{I}(p_{1\underline{\alpha}}^R (h_2 + h_3), p_{1\underline{\alpha}}^I (h_2 + h_3)) - \boldsymbol{\zeta}_{2\underline{\alpha}i1}^{tI} \mathbf{I}(p_{2\underline{\alpha}}^R (h_2 + h_3), p_{2\underline{\alpha}}^I (h_2 + h_3)) \\
\mathbf{0} & & -\boldsymbol{\xi}_{2\underline{\alpha}i2}^{tR} \mathbf{I}(p_{2\underline{\alpha}}^R h_3, p_{2\underline{\alpha}}^I h_3) + \boldsymbol{\xi}_{3\underline{\alpha}i2}^{tR} \mathbf{I}(p_{3\underline{\alpha}}^R h_3, p_{3\underline{\alpha}}^I h_3) \\
\mathbf{0} & & \boldsymbol{\zeta}_{2\underline{\alpha}i1}^{tI} \mathbf{I}(p_{2\underline{\alpha}}^R h_3, p_{2\underline{\alpha}}^I h_3) - \boldsymbol{\zeta}_{3\underline{\alpha}i1}^{tI} \mathbf{I}(p_{3\underline{\alpha}}^R h_3, p_{3\underline{\alpha}}^I h_3)
\end{array} \right]
\end{aligned} \tag{B.5}$$



$$\begin{aligned}
C_H H_0 H(:, 1:6) &= 2\pi \begin{bmatrix} \mathbf{0} & -\xi_{1\underline{\alpha}i2}^{tI} \mathbf{I}(p_{1\underline{\alpha}}^R h_1, p_{1\underline{\alpha}}^I h_1) \\ \xi_{3\underline{\alpha}i2}^{tI} \mathbf{I}(-p_{3\underline{\alpha}}^R (h_1 + h_2 + h_3), p_{3\underline{\alpha}}^I (h_1 + h_2 + h_3)) & \mathbf{0} \\ \xi_{1\underline{\alpha}i2}^{tI} \mathbf{I}(-p_{1\underline{\alpha}}^R h_1, p_{1\underline{\alpha}}^I h_1) - \xi_{2\underline{\alpha}i2}^{tI} \mathbf{I}(-p_{2\underline{\alpha}}^R h_1, p_{2\underline{\alpha}}^I h_1) & \mathbf{0} \\ -\zeta_{1\underline{\alpha}i1}^{tR} \mathbf{I}(-p_{1\underline{\alpha}}^R h_1, -p_{1\underline{\alpha}}^I h_1) + \zeta_{2\underline{\alpha}i1}^{tR} \mathbf{I}(-p_{2\underline{\alpha}}^R h_1, -p_{2\underline{\alpha}}^I h_1) & \mathbf{0} \\ \xi_{2\underline{\alpha}i2}^{tI} \mathbf{I}(-p_{2\underline{\alpha}}^R (h_1 + h_2), p_{2\underline{\alpha}}^I (h_1 + h_2)) - \xi_{3\underline{\alpha}i2}^{tI} \mathbf{I}(-p_{3\underline{\alpha}}^R (h_1 + h_2), p_{3\underline{\alpha}}^I (h_1 + h_2)) & \mathbf{0} \\ -\zeta_{2\underline{\alpha}i1}^{tR} \mathbf{I}(-p_{2\underline{\alpha}}^R (h_1 + h_2), -p_{2\underline{\alpha}}^I (h_1 + h_2)) + \zeta_{3\underline{\alpha}i1}^{tR} \mathbf{I}(-p_{3\underline{\alpha}}^R (h_1 + h_2), -p_{3\underline{\alpha}}^I (h_1 + h_2)) & \mathbf{0} \end{bmatrix} \\
C_H H_0 H(:, 7:12) &= 2\pi \begin{bmatrix} \mathbf{0} & -\xi_{1\underline{\alpha}i2}^{tI} \mathbf{I}(p_{1\underline{\alpha}}^R (h_1 + h_2), p_{1\underline{\alpha}}^I (h_1 + h_2)) \\ \xi_{3\underline{\alpha}i2}^{tI} \mathbf{I}(-p_{3\underline{\alpha}}^R (h_2 + h_3), p_{3\underline{\alpha}}^I (h_2 + h_3)) & \mathbf{0} \\ \mathbf{0} & -\xi_{1\underline{\alpha}i2}^{tI} \mathbf{I}(p_{1\underline{\alpha}}^R h_2, p_{1\underline{\alpha}}^I h_2) + \xi_{2\underline{\alpha}i2}^{tI} \mathbf{I}(p_{2\underline{\alpha}}^R h_2, p_{2\underline{\alpha}}^I h_2) \\ \mathbf{0} & -\zeta_{1\underline{\alpha}i1}^{tR} \mathbf{I}(p_{1\underline{\alpha}}^R h_2, p_{1\underline{\alpha}}^I h_2) + \zeta_{2\underline{\alpha}i1}^{tR} \mathbf{I}(p_{2\underline{\alpha}}^R h_2, p_{2\underline{\alpha}}^I h_2) \\ \xi_{2\underline{\alpha}i2}^{tI} \mathbf{I}(-p_{2\underline{\alpha}}^R h_2, p_{2\underline{\alpha}}^I h_2) - \xi_{3\underline{\alpha}i2}^{tI} \mathbf{I}(-p_{3\underline{\alpha}}^R h_2, p_{3\underline{\alpha}}^I h_2) & \mathbf{0} \\ -\zeta_{2\underline{\alpha}i1}^{tR} \mathbf{I}(-p_{2\underline{\alpha}}^R h_2, -p_{2\underline{\alpha}}^I h_2) + \zeta_{3\underline{\alpha}i1}^{tR} \mathbf{I}(-p_{3\underline{\alpha}}^R h_2, -p_{3\underline{\alpha}}^I h_2) & \mathbf{0} \end{bmatrix} \\
C_H H_0 H(:, 13:18) &= 2\pi \begin{bmatrix} \mathbf{0} & -\xi_{1\underline{\alpha}i2}^{tI} \mathbf{I}(p_{1\underline{\alpha}}^R (h_1 + h_2 + h_3), p_{1\underline{\alpha}}^I (h_1 + h_2 + h_3)) \\ \xi_{3\underline{\alpha}i2}^{tI} \mathbf{I}(-p_{3\underline{\alpha}}^R h_3, p_{3\underline{\alpha}}^I h_3) & \mathbf{0} \\ \mathbf{0} & -\xi_{1\underline{\alpha}i2}^{tI} \mathbf{I}(p_{1\underline{\alpha}}^R (h_2 + h_3), p_{1\underline{\alpha}}^I (h_2 + h_3)) + \xi_{2\underline{\alpha}i2}^{tI} \mathbf{I}(p_{2\underline{\alpha}}^R (h_2 + h_3), p_{2\underline{\alpha}}^I (h_2 + h_3)) \\ \mathbf{0} & -\zeta_{1\underline{\alpha}i1}^{tR} \mathbf{I}(p_{1\underline{\alpha}}^R (h_2 + h_3), p_{1\underline{\alpha}}^I (h_2 + h_3)) + \zeta_{2\underline{\alpha}i1}^{tR} \mathbf{I}(p_{2\underline{\alpha}}^R (h_2 + h_3), p_{2\underline{\alpha}}^I (h_2 + h_3)) \\ \mathbf{0} & -\xi_{2\underline{\alpha}i2}^{tI} \mathbf{I}(p_{2\underline{\alpha}}^R h_3, p_{2\underline{\alpha}}^I h_3) + \xi_{3\underline{\alpha}i2}^{tI} \mathbf{I}(p_{3\underline{\alpha}}^R h_3, p_{3\underline{\alpha}}^I h_3) \\ \mathbf{0} & -\zeta_{2\underline{\alpha}i1}^{tR} \mathbf{I}(p_{2\underline{\alpha}}^R h_3, p_{2\underline{\alpha}}^I h_3) + \zeta_{3\underline{\alpha}i1}^{tR} \mathbf{I}(p_{3\underline{\alpha}}^R h_3, p_{3\underline{\alpha}}^I h_3) \end{bmatrix}
\end{aligned} \tag{B.6}$$

$$\begin{aligned}
\mathbf{C}_I \mathbf{H}_0 \mathbf{I}(:, 1 : 6) &= 2\pi \begin{bmatrix} 0 & -\xi_{1\alpha i 2}^{tR} \mathbf{H}(p_{1\alpha}^R h_1, p_{1\alpha}^I h_1) \\ -\xi_{3\alpha i 2}^{tR} \mathbf{H}(-p_{3\alpha}^R (h_1 + h_2 + h_3), p_{3\alpha}^I (h_1 + h_2 + h_3)) & 0 \\ -\xi_{1\alpha i 2}^{tR} \mathbf{H}(-p_{1\alpha}^R h_1, p_{1\alpha}^I h_1) + \xi_{2\alpha i 2}^{tR} \mathbf{H}(-p_{2\alpha}^R h_1, p_{2\alpha}^I h_1) & 0 \\ -\zeta_{1\alpha i 1}^{tI} \mathbf{H}(-p_{1\alpha}^R h_1, -p_{1\alpha}^I h_1) + \zeta_{2\alpha i 1}^{tI} \mathbf{H}(-p_{2\alpha}^R h_1, -p_{2\alpha}^I h_1) & 0 \\ -\xi_{2\alpha i 2}^{tR} \mathbf{H}(-p_{2\alpha}^R (h_1 + h_2), p_{2\alpha}^I (h_1 + h_2)) + \xi_{3\alpha i 2}^{tR} \mathbf{H}(-p_{3\alpha}^R (h_1 + h_2), p_{3\alpha}^I (h_1 + h_2)) & 0 \\ -\zeta_{2\alpha i 1}^{tI} \mathbf{H}(-p_{2\alpha}^R (h_1 + h_2), -p_{2\alpha}^I (h_1 + h_2)) + \zeta_{3\alpha i 1}^{tI} \mathbf{H}(-p_{3\alpha}^R (h_1 + h_2), -p_{3\alpha}^I (h_1 + h_2)) & 0 \end{bmatrix} \\
\mathbf{C}_I \mathbf{H}_0 \mathbf{I}(:, 7 : 12) &= 2\pi \begin{bmatrix} 0 & -\xi_{1\alpha i 2}^{tR} \mathbf{H}(p_{1\alpha}^R (h_1 + h_2), p_{1\alpha}^I (h_1 + h_2)) \\ -\xi_{3\alpha i 2}^{tR} \mathbf{H}(-p_{3\alpha}^R (h_2 + h_3), p_{3\alpha}^I (h_2 + h_3)) & 0 \\ 0 & -\xi_{1\alpha i 2}^{tR} \mathbf{H}(p_{1\alpha}^R h_2, p_{1\alpha}^I h_2) + \xi_{2\alpha i 2}^{tR} \mathbf{H}(p_{2\alpha}^R h_2, p_{2\alpha}^I h_2) \\ 0 & \zeta_{1\alpha i 1}^{tI} \mathbf{H}(p_{1\alpha}^R h_2, p_{1\alpha}^I h_2) - \zeta_{2\alpha i 1}^{tI} \mathbf{H}(p_{2\alpha}^R h_2, p_{2\alpha}^I h_2) \\ -\xi_{2\alpha i 2}^{tR} \mathbf{H}(-p_{2\alpha}^R h_2, p_{2\alpha}^I h_2) + \xi_{3\alpha i 2}^{tR} \mathbf{H}(-p_{3\alpha}^R h_2, p_{3\alpha}^I h_2) & 0 \\ -\zeta_{2\alpha i 1}^{tI} \mathbf{H}(-p_{2\alpha}^R h_2, -p_{2\alpha}^I h_2) + \zeta_{3\alpha i 1}^{tI} \mathbf{H}(-p_{3\alpha}^R h_2, -p_{3\alpha}^I h_2) & 0 \end{bmatrix} \\
\mathbf{C}_I \mathbf{H}_0 \mathbf{I}(:, 13 : 18) &= 2\pi \begin{bmatrix} 0 & -\xi_{1\alpha i 2}^{tR} \mathbf{H}(p_{1\alpha}^R (h_1 + h_2 + h_3), p_{1\alpha}^I (h_1 + h_2 + h_3)) \\ -\xi_{3\alpha i 2}^{tR} \mathbf{H}(-p_{3\alpha}^R h_3, p_{3\alpha}^I h_3) & 0 \\ 0 & -\xi_{1\alpha i 2}^{tR} \mathbf{H}(p_{1\alpha}^R (h_2 + h_3), p_{1\alpha}^I (h_2 + h_3)) + \xi_{2\alpha i 2}^{tR} \mathbf{H}(p_{2\alpha}^R (h_2 + h_3), p_{2\alpha}^I (h_2 + h_3)) \\ 0 & \zeta_{1\alpha i 1}^{tI} \mathbf{H}(p_{1\alpha}^R (h_2 + h_3), p_{1\alpha}^I (h_2 + h_3)) - \zeta_{2\alpha i 1}^{tI} \mathbf{H}(p_{2\alpha}^R (h_2 + h_3), p_{2\alpha}^I (h_2 + h_3)) \\ 0 & -\xi_{2\alpha i 2}^{tR} \mathbf{H}(p_{2\alpha}^R h_3, p_{2\alpha}^I h_3) + \xi_{3\alpha i 2}^{tR} \mathbf{H}(p_{3\alpha}^R h_3, p_{3\alpha}^I h_3) \\ 0 & \zeta_{2\alpha i 1}^{tI} \mathbf{H}(p_{2\alpha}^R h_3, p_{2\alpha}^I h_3) - \zeta_{3\alpha i 1}^{tI} \mathbf{H}(p_{3\alpha}^R h_3, p_{3\alpha}^I h_3) \end{bmatrix}
\end{aligned} \tag{B.7}$$

$$\begin{aligned}
\mathbf{C}_{RR} = 2 & \left[ \begin{aligned}
& \left[ -\xi_{1\underline{\alpha}i2}^{tR} Q(x_1 - x_{1s}, -p_{1\underline{\alpha}}^R x_{2s}, -p_{1\underline{\alpha}}^I x_{2s}) + \xi_{1\underline{\alpha}i2}^{tI} P(x_1 - x_{1s}, -p_{1\underline{\alpha}}^R x_{2s}, -p_{1\underline{\alpha}}^I x_{2s}) \right] b_{\underline{t}} \\
& \left\{ -\xi_{3\underline{\alpha}i2}^{tR} Q[x_1 - x_{1s}, p_{3\underline{\alpha}}^R(x_{24} - x_{2s}), -p_{3\underline{\alpha}}^I(x_{24} - x_{2s})] - \xi_{3\underline{\alpha}i2}^{tI} P[x_1 - x_{1s}, p_{3\underline{\alpha}}^R(x_{24} - x_{2s}), -p_{3\underline{\alpha}}^I(x_{24} - x_{2s})] \right\} b_{\underline{t}} \\
& \left\{ \xi_{2\underline{\alpha}i2}^{tR} Q[x_1 - x_{1s}, p_{2\underline{\alpha}}^R(x_{22} - x_{2s}), |p_{2\underline{\alpha}}^I(x_{22} - x_{2s})|] \right. \\
& \quad - \operatorname{sgn}[p_{2\underline{\alpha}}^I(x_{22} - x_{2s})] \xi_{2\underline{\alpha}i2}^{tI} P[x_1 - x_{1s}, p_{2\underline{\alpha}}^R(x_{22} - x_{2s}), |p_{2\underline{\alpha}}^I(x_{22} - x_{2s})|] \\
& \quad - \xi_{1\underline{\alpha}i2}^{tR} Q[x_1 - x_{1s}, p_{1\underline{\alpha}}^R(x_{22} - x_{2s}), |p_{1\underline{\alpha}}^I(x_{22} - x_{2s})|] \\
& \quad \left. + \operatorname{sgn}[p_{1\underline{\alpha}}^I(x_{22} - x_{2s})] \xi_{1\underline{\alpha}i2}^{tI} P[x_1 - x_{1s}, p_{1\underline{\alpha}}^R(x_{22} - x_{2s}), |p_{1\underline{\alpha}}^I(x_{22} - x_{2s})|] \right\} b_{\underline{t}} \\
& \left\{ -\zeta_{2\underline{\alpha}i1}^{tR} P[x_1 - x_{1s}, p_{2\underline{\alpha}}^R(x_{22} - x_{2s}), p_{2\underline{\alpha}}^I(x_{22} - x_{2s})] - \zeta_{2\underline{\alpha}i1}^{tI} Q[x_1 - x_{1s}, p_{2\underline{\alpha}}^R(x_{22} - x_{2s}), p_{2\underline{\alpha}}^I(x_{22} - x_{2s})] \right. \\
& \quad \left. + \zeta_{1\underline{\alpha}i1}^{tR} P[x_1 - x_{1s}, p_{1\underline{\alpha}}^R(x_{22} - x_{2s}), p_{1\underline{\alpha}}^I(x_{22} - x_{2s})] + \zeta_{1\underline{\alpha}i1}^{tI} Q[x_1 - x_{1s}, p_{1\underline{\alpha}}^R(x_{22} - x_{2s}), p_{1\underline{\alpha}}^I(x_{22} - x_{2s})] \right\} b_{\underline{t}} \\
& \left\{ \xi_{3\underline{\alpha}i2}^{tR} Q[x_1 - x_{1s}, p_{3\underline{\alpha}}^R(x_{23} - x_{2s}), |p_{3\underline{\alpha}}^I(x_{23} - x_{2s})|] \right. \\
& \quad - \operatorname{sgn}[p_{3\underline{\alpha}}^I(x_{23} - x_{2s})] \xi_{3\underline{\alpha}i2}^{tI} P[x_1 - x_{1s}, p_{3\underline{\alpha}}^R(x_{23} - x_{2s}), |p_{3\underline{\alpha}}^I(x_{23} - x_{2s})|] \\
& \quad - \xi_{2\underline{\alpha}i2}^{tR} Q[x_1 - x_{1s}, p_{2\underline{\alpha}}^R(x_{23} - x_{2s}), |p_{2\underline{\alpha}}^I(x_{23} - x_{2s})|] \\
& \quad \left. + \operatorname{sgn}[p_{2\underline{\alpha}}^I(x_{23} - x_{2s})] \xi_{2\underline{\alpha}i2}^{tI} P[x_1 - x_{1s}, p_{2\underline{\alpha}}^R(x_{23} - x_{2s}), |p_{2\underline{\alpha}}^I(x_{23} - x_{2s})|] \right\} b_{\underline{t}} \\
& \left\{ -\zeta_{3\underline{\alpha}i1}^{tR} P[x_1 - x_{1s}, p_{3\underline{\alpha}}^R(x_{23} - x_{2s}), p_{3\underline{\alpha}}^I(x_{23} - x_{2s})] - \zeta_{3\underline{\alpha}i1}^{tI} Q[x_1 - x_{1s}, p_{3\underline{\alpha}}^R(x_{23} - x_{2s}), p_{3\underline{\alpha}}^I(x_{23} - x_{2s})] \right. \\
& \quad \left. + \zeta_{2\underline{\alpha}i1}^{tR} P[x_1 - x_{1s}, p_{2\underline{\alpha}}^R(x_{23} - x_{2s}), p_{2\underline{\alpha}}^I(x_{23} - x_{2s})] + \zeta_{2\underline{\alpha}i1}^{tI} Q[x_1 - x_{1s}, p_{2\underline{\alpha}}^R(x_{23} - x_{2s}), p_{2\underline{\alpha}}^I(x_{23} - x_{2s})] \right\} b_{\underline{t}}
\end{aligned} \right] \tag{B.8}
\end{aligned}$$

$C_R H_0 R = 2$ 

$$\begin{aligned}
& \left[ -\xi_{1\underline{\alpha}i2}^{tR} P(x_1 - x_{1s}, -p_{1\underline{\alpha}}^R x_{2s}, -p_{1\underline{\alpha}}^I x_{2s}) - \xi_{1\underline{\alpha}i2}^{tI} Q(x_1 - x_{1s}, -p_{1\underline{\alpha}}^R x_{2s}, -p_{1\underline{\alpha}}^I x_{2s}) \right] b_t \\
& \left\{ -\xi_{3\underline{\alpha}i2}^{tR} P[x_1 - x_{1s}, p_{3\underline{\alpha}}^R(x_{24} - x_{2s}), -p_{3\underline{\alpha}}^I(x_{24} - x_{2s})] + \xi_{3\underline{\alpha}i2}^{tI} Q[x_1 - x_{1s}, p_{3\underline{\alpha}}^R(x_{24} - x_{2s}), -p_{3\underline{\alpha}}^I(x_{24} - x_{2s})] \right\} b_t \\
& \left\{ \xi_{2\underline{\alpha}i2}^{tR} P[x_1 - x_{1s}, p_{2\underline{\alpha}}^R(x_{22} - x_{2s}), |p_{2\underline{\alpha}}^I(x_{22} - x_{2s})|] \right. \\
& + \operatorname{sgn}[p_{2\underline{\alpha}}^I(x_{22} - x_{2s})] \xi_{2\underline{\alpha}i2}^{tI} Q[x_1 - x_{1s}, p_{2\underline{\alpha}}^R(x_{22} - x_{2s}), |p_{2\underline{\alpha}}^I(x_{22} - x_{2s})|] \\
& - \xi_{1\underline{\alpha}i2}^{tR} P[x_1 - x_{1s}, p_{1\underline{\alpha}}^R(x_{22} - x_{2s}), |p_{1\underline{\alpha}}^I(x_{22} - x_{2s})|] \\
& \left. - \operatorname{sgn}[p_{1\underline{\alpha}}^I(x_{22} - x_{2s})] \xi_{1\underline{\alpha}i2}^{tI} Q[x_1 - x_{1s}, p_{1\underline{\alpha}}^R(x_{22} - x_{2s}), |p_{1\underline{\alpha}}^I(x_{22} - x_{2s})|] \right\} b_t \\
& \left\{ \xi_{2\underline{\alpha}i1}^{tR} Q[x_1 - x_{1s}, p_{2\underline{\alpha}}^R(x_{22} - x_{2s}), |p_{2\underline{\alpha}}^I(x_{22} - x_{2s})|] \right. \\
& - \operatorname{sgn}[p_{2\underline{\alpha}}^I(x_{22} - x_{2s})] \xi_{2\underline{\alpha}i1}^{tI} P[x_1 - x_{1s}, p_{2\underline{\alpha}}^R(x_{22} - x_{2s}), |p_{2\underline{\alpha}}^I(x_{22} - x_{2s})|] \\
& - \xi_{1\underline{\alpha}i1}^{tR} Q[x_1 - x_{1s}, p_{1\underline{\alpha}}^R(x_{22} - x_{2s}), |p_{1\underline{\alpha}}^I(x_{22} - x_{2s})|] \\
& \left. + \operatorname{sgn}[p_{1\underline{\alpha}}^I(x_{22} - x_{2s})] \xi_{1\underline{\alpha}i1}^{tI} P[x_1 - x_{1s}, p_{1\underline{\alpha}}^R(x_{22} - x_{2s}), |p_{1\underline{\alpha}}^I(x_{22} - x_{2s})|] \right\} b_t \\
& \left\{ \xi_{3\underline{\alpha}i2}^{tR} P[x_1 - x_{1s}, p_{3\underline{\alpha}}^R(x_{23} - x_{2s}), |p_{3\underline{\alpha}}^I(x_{23} - x_{2s})|] \right. \\
& + \operatorname{sgn}[p_{3\underline{\alpha}}^I(x_{23} - x_{2s})] \xi_{3\underline{\alpha}i2}^{tI} Q[x_1 - x_{1s}, p_{3\underline{\alpha}}^R(x_{23} - x_{2s}), |p_{3\underline{\alpha}}^I(x_{23} - x_{2s})|] \\
& - \xi_{2\underline{\alpha}i2}^{tR} P[x_1 - x_{1s}, p_{2\underline{\alpha}}^R(x_{23} - x_{2s}), |p_{2\underline{\alpha}}^I(x_{23} - x_{2s})|] \\
& \left. - \operatorname{sgn}[p_{2\underline{\alpha}}^I(x_{23} - x_{2s})] \xi_{2\underline{\alpha}i2}^{tI} Q[x_1 - x_{1s}, p_{2\underline{\alpha}}^R(x_{23} - x_{2s}), |p_{2\underline{\alpha}}^I(x_{23} - x_{2s})|] \right\} b_t \\
& \left\{ \xi_{3\underline{\alpha}i2}^{tR} Q[x_1 - x_{1s}, p_{3\underline{\alpha}}^R(x_{23} - x_{2s}), |p_{3\underline{\alpha}}^I(x_{23} - x_{2s})|] \right. \\
& - \operatorname{sgn}[p_{3\underline{\alpha}}^I(x_{23} - x_{2s})] \xi_{3\underline{\alpha}i2}^{tI} P[x_1 - x_{1s}, p_{3\underline{\alpha}}^R(x_{23} - x_{2s}), |p_{3\underline{\alpha}}^I(x_{23} - x_{2s})|] \\
& - \xi_{2\underline{\alpha}i2}^{tR} Q[x_1 - x_{1s}, p_{2\underline{\alpha}}^R(x_{23} - x_{2s}), |p_{2\underline{\alpha}}^I(x_{23} - x_{2s})|] \\
& \left. + \operatorname{sgn}[p_{2\underline{\alpha}}^I(x_{23} - x_{2s})] \xi_{2\underline{\alpha}i2}^{tI} P[x_1 - x_{1s}, p_{2\underline{\alpha}}^R(x_{23} - x_{2s}), |p_{2\underline{\alpha}}^I(x_{23} - x_{2s})|] \right\} b_t
\end{aligned}$$

(B.9)

$$\boldsymbol{\rho} = \begin{bmatrix} \rho_{1U}^t \\ \rho_{1L}^t \\ \rho_{2U}^t \\ \rho_{2L}^t \\ \rho_{3U}^t \\ \rho_{3L}^t \end{bmatrix} \quad (\text{B.10})$$

Each element in the matrix is a  $3 \times 3$  matrix, for example:

$$\begin{aligned} -\boldsymbol{\xi}_{1\alpha i 2}^{tR} &= \begin{bmatrix} -\xi_{1\alpha 12}^{1R} & -\xi_{1\alpha 12}^{2R} & -\xi_{1\alpha 12}^{3R} \\ -\xi_{1\alpha 22}^{1R} & -\xi_{1\alpha 22}^{2R} & -\xi_{1\alpha 22}^{3R} \\ -\xi_{1\alpha 32}^{1R} & -\xi_{1\alpha 32}^{2R} & -\xi_{1\alpha 32}^{3R} \end{bmatrix} \\ \mathbf{H}(\mathbf{0}, \mathbf{0}) &= \begin{bmatrix} H(0,0) & 0 & 0 \\ 0 & H(0,0) & 0 \\ 0 & 0 & H(0,0) \end{bmatrix} \\ -\boldsymbol{\xi}_{1\alpha i 2}^{tI} (p_{1\alpha}^R h_1, p_{1\alpha}^I h_1) &= \begin{bmatrix} -\xi_{1\alpha 12}^{1I} I(p_{1\alpha}^R h_1, p_{1\alpha}^I h_1) & -\xi_{1\alpha 12}^{2I} I(p_{1\alpha}^R h_1, p_{1\alpha}^I h_1) & -\xi_{1\alpha 12}^{3I} I(p_{1\alpha}^R h_1, p_{1\alpha}^I h_1) \\ -\xi_{1\alpha 22}^{1I} I(p_{1\alpha}^R h_1, p_{1\alpha}^I h_1) & -\xi_{1\alpha 22}^{2I} I(p_{1\alpha}^R h_1, p_{1\alpha}^I h_1) & -\xi_{1\alpha 22}^{3I} I(p_{1\alpha}^R h_1, p_{1\alpha}^I h_1) \\ -\xi_{1\alpha 32}^{1I} I(p_{1\alpha}^R h_1, p_{1\alpha}^I h_1) & -\xi_{1\alpha 32}^{2I} I(p_{1\alpha}^R h_1, p_{1\alpha}^I h_1) & -\xi_{1\alpha 32}^{3I} I(p_{1\alpha}^R h_1, p_{1\alpha}^I h_1) \end{bmatrix} \\ \mathbf{0} &= \begin{bmatrix} 0 & 0 & 0 \\ 0 & 0 & 0 \\ 0 & 0 & 0 \end{bmatrix} \end{aligned} \quad (\text{B.11})$$

Meanwhile, each element in the vector is a  $3 \times 1$  vector, for example:

$$\begin{aligned}
& \left[ -\xi_{1\alpha i2}^{tR} Q(x_1 - x_{1s}, -p_{1\alpha}^R x_{2s}, -p_{1\alpha}^I x_{2s}) + \xi_{1\alpha i2}^{tI} P(x_1 - x_{1s}, -p_{1\alpha}^R x_{2s}, -p_{1\alpha}^I x_{2s}) \right] b_{\underline{t}} \\
& = \begin{bmatrix} \left[ -\xi_{1\alpha 12}^{tR} Q(x_1 - x_{1s}, -p_{1\alpha}^R x_{2s}, -p_{1\alpha}^I x_{2s}) + \xi_{1\alpha 12}^{tI} P(x_1 - x_{1s}, -p_{1\alpha}^R x_{2s}, -p_{1\alpha}^I x_{2s}) \right] b_{\underline{t}} \\ \left[ -\xi_{1\alpha 22}^{tR} Q(x_1 - x_{1s}, -p_{1\alpha}^R x_{2s}, -p_{1\alpha}^I x_{2s}) + \xi_{1\alpha 22}^{tI} P(x_1 - x_{1s}, -p_{1\alpha}^R x_{2s}, -p_{1\alpha}^I x_{2s}) \right] b_{\underline{t}} \\ \left[ -\xi_{1\alpha 32}^{tR} Q(x_1 - x_{1s}, -p_{1\alpha}^R x_{2s}, -p_{1\alpha}^I x_{2s}) + \xi_{1\alpha 32}^{tI} P(x_1 - x_{1s}, -p_{1\alpha}^R x_{2s}, -p_{1\alpha}^I x_{2s}) \right] b_{\underline{t}} \end{bmatrix} \\
\rho_{1U}^t & = \begin{bmatrix} \rho_{1U}^1 \\ \rho_{1U}^2 \\ \rho_{1U}^3 \end{bmatrix}
\end{aligned} \tag{B.12}$$

## C GB thickness and structure analyzed by Molecular Statics (MS) / Molecular Dynamics (MD) simulations

As discussed in the subsection 1.2.2.8, GB is usually not a perfect plane as described in continuum mechanics, but is replaced by an interphase, especially in nanocrystalline materials. This interphase is caused by atomic distortion (inner relaxation) in the vicinity of a GB which strongly depends on the crystalline lattice misorientation (see Chapter 1). In order to analyze the structure of this GB interphase, numerical methods including MS and MD were used to perform a bi-crystal configuration of Ni with different misorientations. As a result, the thickness of the GB interphase and its dislocation structure are obtained for some misorientations.

This section first presents the simulation configurations for a Ni bi-crystal in MS/MD. The simulations were performed by using the open source molecular dynamics code LAMMPS [244]. Then, the results were analyzed by an open visualization tool OVITO [302], including the thickness and the dislocation structure of GB interphase with different misorientations.

### C.1 MD configuration

The geometry of bi-crystal used in MS/MD is presented in Figure C.1. It was set as a parallelepiped with  $25 \times 25 \times 20 \text{ nm}^3$ , including about  $7.3 \times 10^5$  atoms of Ni with lattice parameter 0.352 nm as shown in Figure C.1. GB is perpendicular to  $\mathbf{x}_2$  axis and the thickness of each grain is the same, which is equal to 10 nm. It should be pointed out that the thickness of each grain (10 nm) is large enough to make the GB interphase stable. That means for a comparative simulation with a larger thickness of each grain with all other same conditions, the GB thickness and its dislocation structure do not change. As for simulation configuration, the boundary conditions are set to be periodic in  $\mathbf{x}_1$  and  $\mathbf{x}_3$  directions, and be shrink-wrapped in  $\mathbf{x}_2$  direction. The inter-atomic potential used in this simulation is the embedded atom method (EAM) (Ni\_u3.eam) [303]. The time step is always set to be 1 fs (femtosecond). The orientation configuration is the same as for the discussion of misorientation effect on dislocation pile-ups (see subsection 4.2.5.1). Thus, the orientation of the upper crystal (Crystal I) is fixed, defined by  $\alpha = 45^\circ$  whereas the orientation of lower crystal (Crystal II) is given by a rotation  $\psi$  around rotation axis  $v$  from  $\psi = 0^\circ$  to  $\psi = 180^\circ$ . After the construction of bi-crystal, the overlap atoms within the distance 0.24 nm at GB were first canceled. Then, the energy of whole system was minimized by conjugate gradient minimization at 0 K with parameter  $10^{-15}$  for energy and  $10^{-15}$  eV/Angstrom for force. Then,

the whole system is equilibrated at room temperature (293.15 K) for 20000 ps (picosecond). The integral method is chosen to be the NVE (N: Number of atoms, V: Volume and E: Energy) method. This creates a system trajectory consistent with the microcanonical ensemble as the studied system is regarded to be constant of atoms number, of volume and of energy.

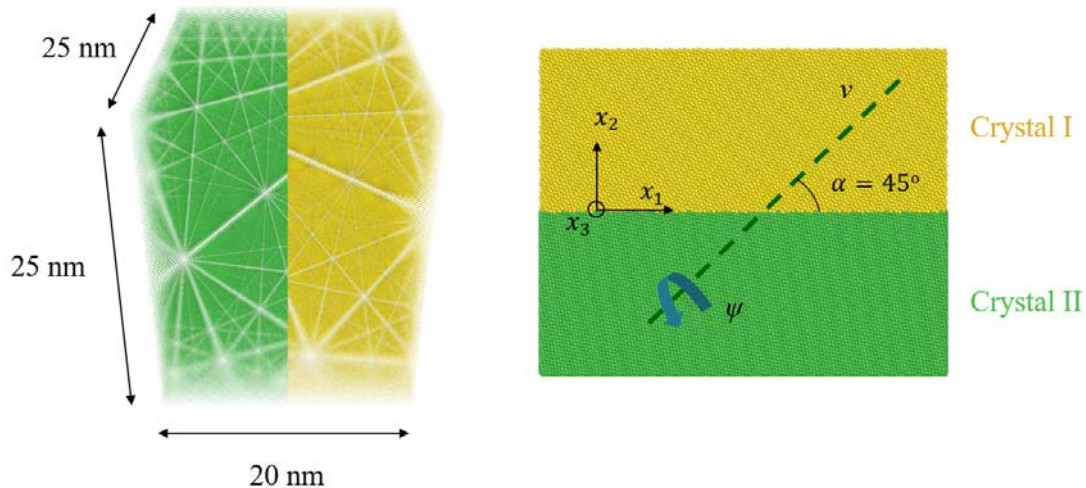


Figure C.1: Geometry of bi-crystal configuration in MS/MD. The bi-crystal is set as a parallelepiped with  $25 \times 25 \times 20 \text{ nm}^3$ . GB is perpendicular to  $\boldsymbol{x}_2$  axis and is at the middle of bi-crystal.

For results analyses, the local crystalline structure was analyzed by Polyhedral Template Matching (PTM) method [304] in OVITO as shown in Figure C.2 (a). The green atoms indicate FCC structure, and the other colors indicate other crystalline structures. As Ni is FCC structure, thus the atoms with other crystalline structures were regarded as GB interphase and were taken out as shown in Figure C.2 (b). Then, a developed Matlab program was performed to simulate a convex outer envelope surface containing all these non FCC structure atoms as shown in Figure C.2 (c). Meanwhile, the volume  $V$  contained by this envelope surface was calculated. Thus, the average thickness of this GB interphase can be calculated as  $H = V/S$ , where  $S$  is the cross sectional area (perpendicular to  $\boldsymbol{x}_2$  axis) of GB interphase. Finally, the GB dislocation structure was analyzed by dislocation analysis (DXA) method [305] in OVITO as shown in Figure C.2 (d). The different colors of dislocation lines indicate different types of dislocations.



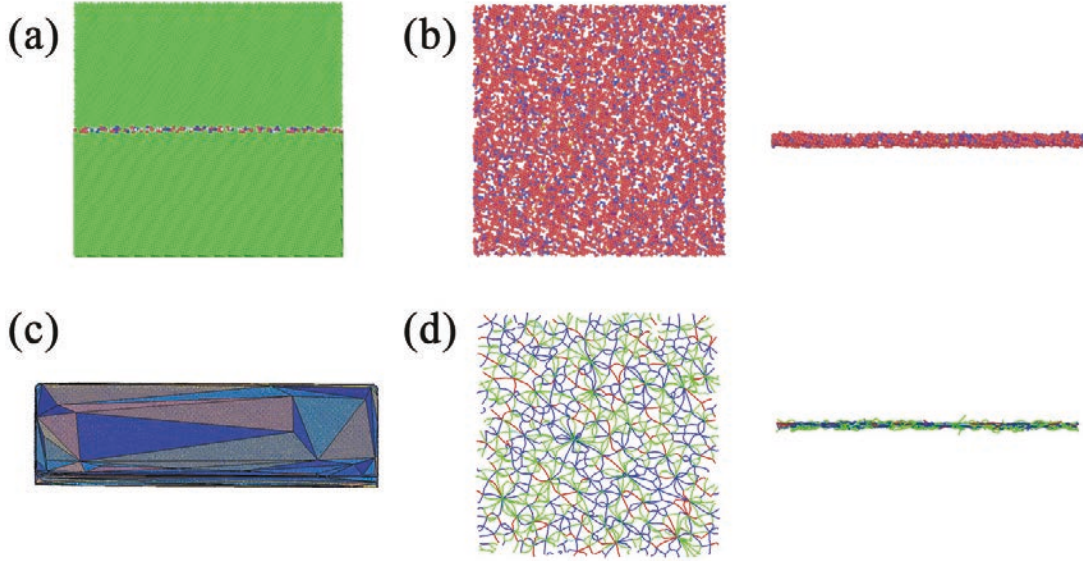


Figure C.2: Results analyses of MS/MD simulations: (a) local crystalline structure are analyzed by PTM in OVITO, the different colors of atoms indicate corresponding crystalline structure (Green: face-centered cubic (FCC), Pink: hexagonal close-packed (HCP), Blue: body-centered cubic (BCC), Orange: icosahedral coordination (ICO), Purple: simple cubic (SC) and White: unknown coordination structure), (b) the non FCC structure atoms at GB area are taken out as GB interphase, (c) a developed Matlab program is performed to simulate a convex outer envelope surface containing all the atoms in GB interphase, meanwhile the volume  $V$  contained by this envelope surface is calculated and (d) the dislocation structure at GB is analyzed by DXA in OVITO, the different colors of dislocation lines indicate corresponding dislocation type (Blue: perfect dislocation, Green: Shockley partial dislocation, Pink: Stair-rod type dislocation, Yellow: Hirth type dislocation and Cyan: Frank type dislocation).

## C.2 Results and discussions

Figure C.3 shows the average thickness of GB interphase in Ni bi-crystal configuration with different rotation angles  $\psi$  at 0 K and at room temperature 293.15 K. The results of 0 K is performed just after energy minimization of the whole system at 0 K. The homogeneous single crystal case is retrieved for  $\psi = 0^\circ$  and  $\psi = 180^\circ$  for which there is no GB, so the thickness of GB interphase  $H$  is 0 nm. With different rotation angles  $\psi$ ,  $H$  is not constant. But there is no evident relationship between  $H$  and  $\psi$ , neither with misorientation angle  $\Phi$ . However, there are three evident high values for  $H$  that occurred at  $\psi = 10^\circ$ ,  $\psi = 110^\circ$  and  $\psi = 170^\circ$ , respectively. With the same rotation angle,  $H$  is always smaller for 0 K compared to room temperature except  $\psi = 30^\circ$ , for which they have the same  $H$ . Furthermore,  $H$  has the same tendency at 0 K and at room temperature. Regardless of homogeneous single crystal case, the average of  $H$  is about 0.87 nm

at 0 K and 1.06 nm at room temperature. In particular, for the Ni bi-crystal micro-beam studied in experiment as described in Figure 2.14,  $H$  is about 0.9 nm which corresponds to about  $4|\mathbf{b}|$ . Thus, the thickness of GB interphase used in theoretical calculations which was  $5|\mathbf{b}|$  (see section 4.2 in Chapter 4) is close to the simulated value from MD and is therefore realistic.

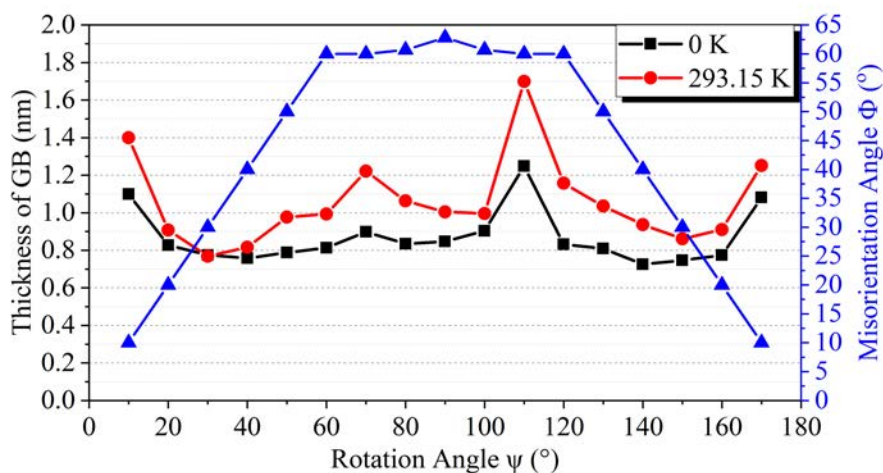
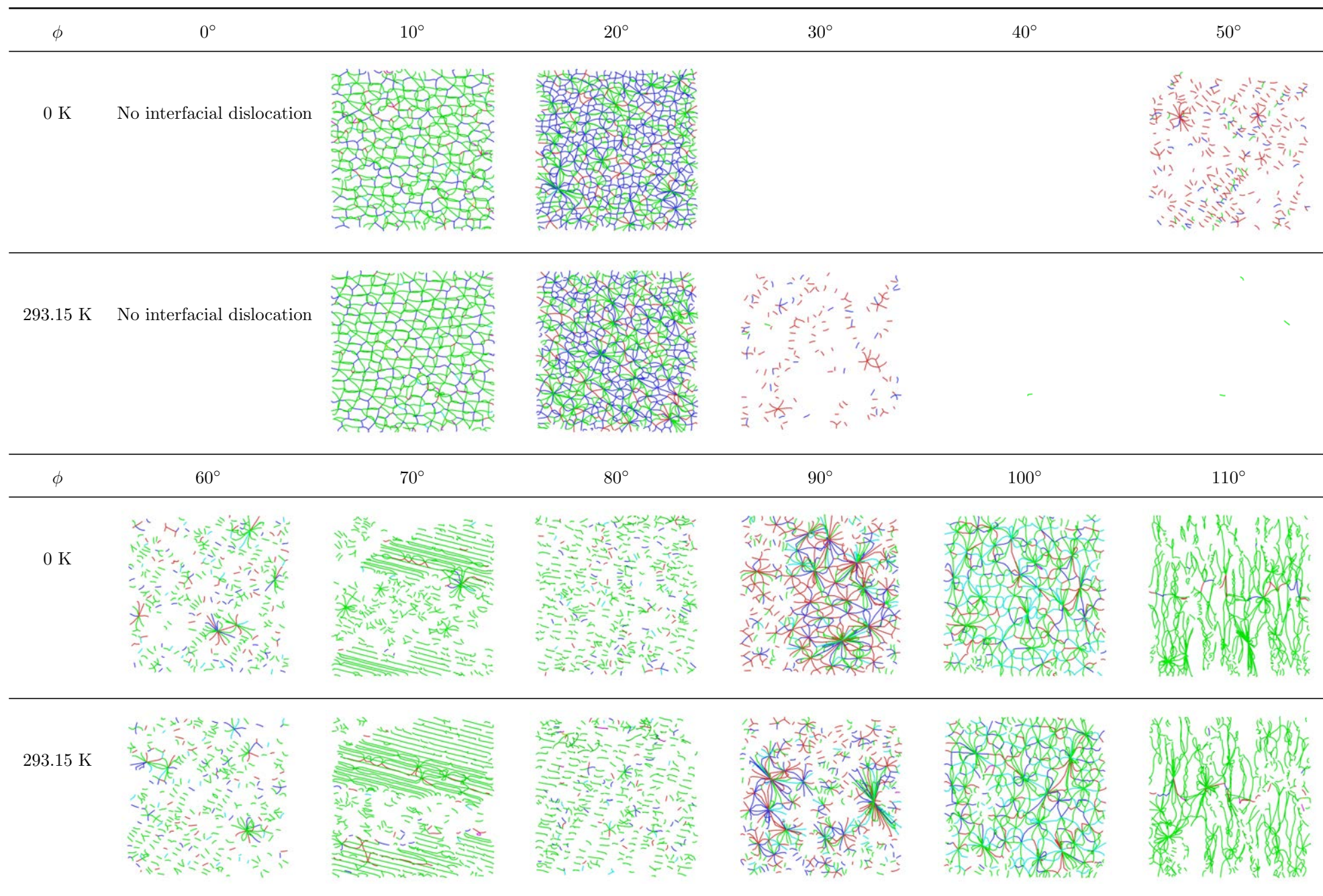


Figure C.3: Average thickness of GB interphase in Ni bi-crystal configuration with different misorientation at 0 K and at room temperature 293.15 K.

For the same configuration, table C.1 presents the interfacial dislocation structure of GB interphase with different rotation angles  $\psi$  at 0 K and at room temperature 293.15 K. With different rotation angles, the interfacial dislocation structures are different. There are mainly three different types of dislocation structures. The first one is dislocation networks as for  $\psi = 10^\circ, 20^\circ, 100^\circ, 120^\circ, 160^\circ$  and  $170^\circ$ . Meanwhile, some of them consist of regular repeating units, such as for  $\psi = 10^\circ$  and  $170^\circ$ . The second one is long dislocation lines without network as for  $\psi = 70^\circ$  and  $110^\circ$ . The third one is just discrete short dislocations as for  $\psi = 30^\circ$  (293.15K),  $50^\circ$  (0K),  $60^\circ, 80^\circ, 90^\circ, 130^\circ$  and  $150^\circ$ . In fact, these structures cannot be called dislocations, as the detected “dislocation” lines are too short. In addition to these structures, there are some cases with no detection of dislocation as for  $\psi = 30^\circ$  (0K),  $40^\circ, 50^\circ$  (293.15K) and  $140^\circ$ . As for  $\psi = 0^\circ$ , it is homogeneous single crystal without GB, thus, there is no dislocation. Considering the misorientation angle as presented in Figure C.3, different from the length of dislocation pile-ups as shown in Figure 4.9, the dislocation structures are similar for the cases with the same misorientation angle  $\Phi$ , but only for  $\Phi < 60^\circ$ , such as  $\psi = 10^\circ$  and  $\psi = 170^\circ$ ,  $\psi = 20^\circ$  and  $\psi = 160^\circ$ ,  $\psi = 30^\circ$  and  $\psi = 150^\circ$ ,  $\psi = 40^\circ$  and  $\psi = 140^\circ$ ,  $\psi = 50^\circ$  and  $\psi = 130^\circ$ . Considering the temperature effect, there is no

evident difference of dislocation structures between 0 K and room temperature. As a conclusion, the GB interphase has different dislocation structures with different misorientations. Different dislocation structures present different mechanical properties, such as dislocation network at GB can easily produce GB sliding [306] or GB migration [307, 308]. Thus, the dislocation-GB interaction strongly depends on the misorientation of bi-crystal and also depends on the incoming/outgoing slip system from the point of view of interfacial dislocations.



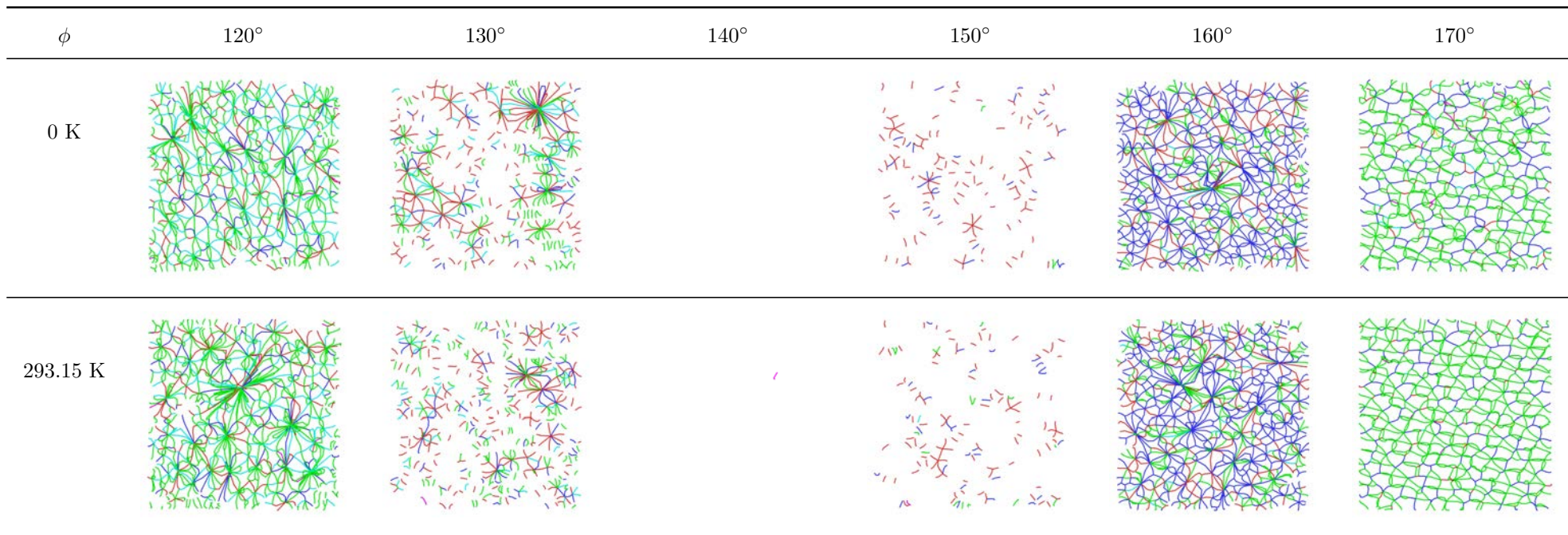


Table C.1: Dislocation structures at GB for Ni bi-crystal with different misorientations.

# Bibliography

- [1] W. Voigt. *Lehrbuch Der Kristallphysik*. B.G. Teubner, Leipzig, Germany, 1928.
- [2] V. Volterra. Sur l'équilibre des corps élastiques multiplement connexes. *Annales Scientifiques de l'Ecole Normale Supérieure*, 24:401–517, 1907.
- [3] E.O. Hall. The deformation and ageing of mild steel: III discussion of results. *Proceedings of the Physical Society. Section B*, 64:747–753, 1951.
- [4] N.J. Petch. The cleavage strength of polycrystals. *The Journal of the Iron and Steel Institute*, 174:25–30, 1953.
- [5] Z. Shen, R.H. Wagoner, and W.A.T. Clark. Dislocation and grain boundary interactions in metals. *Acta Metallurgica*, 36:3231–3242, 1988.
- [6] M. Kamaya, A.J. Wilkinson, and J.M. Titchmarsh. Measurement of plastic strain of polycrystalline material by electron backscatter diffraction. *Nuclear Engineering and Design*, 235:713–725, 2005.
- [7] W. Pantleon. Resolving the geometrically necessary dislocation content by conventional electron backscattering diffraction. *Scripta Materialia*, 58:994–997, 2008.
- [8] C. Perrin, S. Berbenni, H. Vehoff, and M. Berveiller. Role of discrete intra-granular slip on lattice rotations in polycrystalline Ni : Experimental and micromechanical studies. *Acta Materialia*, 58:4639–4649, 2010.
- [9] I. Gutierrez-Urrutia, S. Zaefferer, and D. Raabe. Coupling of electron channeling with EBSD: Toward the quantitative characterization of deformation structures in the SEM. *JOM*, 65:1229–1236, 2013.
- [10] F. Roters, P. Eisenlohr, L. Hantcherli, D.D. Tjahjanto, T.R. Bieler, and D. Raabe. Overview of constitutive laws, kinematics, homogenization and multiscale methods in crystal plasticity finite-element modeling: Theory, experiments, applications. *Acta Materialia*, 58:1152–1211, 2010.
- [11] N.A. Fleck, G.M. Muller, M.F. Ashby, and J.W. Hutchinson. Strain gradient plasticity: Theory and experiment. *Acta Metallurgica et Materialia*, 42:475–487, 1994.
- [12] S.S. Quek, Z. Wu, Y.W. Zhang, and D.J. Srolovitz. Polycrystal deformation in a discrete dislocation dynamics framework. *Acta Materialia*, 75:92–105, 2014.
- [13] S. Khan, H.M. Zbib, and D.A. Hughes. Modeling planar dislocation boundaries using multi-scale dislocation dynamics plasticity. *International Journal of Plasticity*, 20:1059–1092, 2004.
- [14] L. Zhang, C. Lu, and K. Tieu. A review on atomistic simulation of grain boundary behaviors in face-centered cubic metals. *Computational Materials Science*, 118:180–191, 2016.
- [15] R. Asaro. *Mechanics of Solids and Materials*. Cambridge University Press, 2006.
- [16] G.A. Maugin. *Configurational forces: thermomechanics, physics, mathematics and numerics*. CRC Press, Modern Mechanics and Mathematics, Taylor and Francis, 2011.

- [17] S.T. Choi and Y.Y. Earmme. Elastic study on singularities interacting with interfaces using alternating technique: Part I. anisotropic trimaterial. *International Journal of Solids and Structures*, 39:943–957, 2002.
- [18] H.Y. Wang, M.S. Wu, and H. Fan. Image decomposition method for the analysis of a mixed dislocation in a general multilayer. *International Journal of Solids and Structures*, 44:1563–1581, 2007.
- [19] Z. Suo. Singularities, interfaces and cracks in dissimilar anisotropic media. *Proceedings of the Royal Society A: Mathematical, Physical and Engineering Sciences*, 427:331–358, 1990.
- [20] S.G. Lekhnitskii. *Theory of Elasticity of an Anisotropic Elastic Body*. Holden-Day, 1963.
- [21] J.D. Eshelby, W.T. Read, and W. Shockley. Anisotropic elasticity with applications to dislocation theory. *Acta Metallurgica*, 1:251–259, 1953.
- [22] A.N. Stroh. Dislocations and cracks in anisotropic elasticity. *Philosophical Magazine*, 3:625–646, 1958.
- [23] N. Thompson. Dislocation nodes in face-centred cubic lattices. *Proceedings of the Physical Society of London*, 66:481–492, 1953.
- [24] I.L. Dillamore and R.E. Smallman. The stacking-fault energy of f.c.c. metals. *Philosophical Magazine*, 12:191–193, 1965.
- [25] T. Jossang and J.P. Hirth. The energies of stacking-fault tetrahedra in f.c.c. metals. *Philosophical Magazine*, 13:657–670, 1966.
- [26] Joshua Pelleg. *Mechanical Properties of Materials*. Springer Netherlands, 2013.
- [27] M. Peach and J.S. Koehler. The forces exerted on dislocations and the stress fields produced by them. *Physical Review*, 80:436–439, 1950.
- [28] P.M. Anderson, J.P. Hirth, and J. Lothe. *Theory of Dislocations*. Cambridge University Press, 1968.
- [29] C. Coupeau, J. Bonneville, B. Matherstock, J. Grilhé, and J.L. Martin. Slip line analysis in Ni<sub>3</sub>Al by atomic force microscopy. *Scripta Materialia*, 41(9):945 – 950, 1999.
- [30] H. Margolin and M.S. Stanesco. Polycrystalline strengthening. *Acta Metallurgica*, 23:1411–1418, 1975.
- [31] B. Jaoul. *Etude de la plasticité et application aux métaux*. Dunod, 1965.
- [32] F.J. Humphreys. Grain and subgrain characterisation by electron backscatter diffraction. *Journal of Materials Science*, 36:3833–3854, 2001.
- [33] C. Kahloun, R. Badji, B. Bacroix, and M. Bouabdallah. Contribution to crystallographic slip assessment by means of topographic measurements achieved with atomic force microscopy. *Materials Characterization*, 61(9):835 – 844, 2010.
- [34] S. Frechard, F. Martin, C. Clement, and J. Cousty. AFM and EBSD combined studies of plastic deformation in a duplex stainless steel. *Materials Science and Engineering A*, 418:312–319, 2006.
- [35] P. Villechaise, L. Sabatier, and J. Girard. On slip bands features and crack initiation in fatigued 316L austenitic stainless steel : Part 1 : Analysis by electron back-scattered diffraction and atomic force microscopy. *Materials Science and Engineering A*, 323:377–385, 2002.
- [36] M. Zaiser, F.M. Grasset, V. Koutsos, and E.C. Aifantis. Selfaffine surface morphology of plastically deformed metals. *Physical Review Letters*, 93:195507, 2004.
- [37] H. Neuhäuser. *Slip-line formation and collective dislocation motion. 6. ed.* F.R.N. Nabarro, Holland Publishing Company, 1983.
- [38] A. Brinck, C. Engelke, W. Kopmann, and H. Neuhäuser. Structure and development of slip lines during plastic deformation of the intermetallic phases Fe<sub>3</sub>Al and CuZn. *Materials Science and Engineering, A*, 239-240:180–187, 1997.

- [39] C. Perrin. *Etude expérimentale et modélisation des microstructures de déformation plastique intragranulaires discrètes*. PhD thesis, Université Paul-Verlaine de Metz et Université de Saarbrücken, 2010.
- [40] E. Schmid and W. Boas. *Kristallplastizität mit Besonderer Berücksichtigung der Metalle*. Springer, New York, 1935.
- [41] J.C.M. Li. Dislocation sources. In M.F. ASHBY, R. BULLOUGH, C.S. HARTLEY, and J.P. HIRTH, editors, *Dislocation Modelling of Physical Systems*, pages 498 – 518. Pergamon, 1981.
- [42] F.C. Frank and W.T. Read. Multiplication processes for slow moving dislocation. *Physical Review*, 79:722–723, 1950.
- [43] W.C. Dash. Copper precipitation on dislocations in silicon. *Journal of Applied Physics*, 27:1193–1195,, 1956.
- [44] J.M. Marchin and G. Wyon. Observation de spirales sur des surfaces d’aluminium polies électrolytiquement. *Acta Metallurgica*, 10:915–924, 1962.
- [45] E. Orowan and M. Cohen (Ed.). *Dislocations in Metals*. The American Institute of Mining and Metallurgical Engineers, INC, 1954.
- [46] U.F. Kocks, A.S. Argon, and M.F. Ashby. *Thermodynamics and kinetics of slip*. Progress in Materials Science, Pergamon Press, 1975.
- [47] N. Hamao, K. Kataoka, and J. Akimoto. Single-crystal synthesis and structure refinement of  $\text{La}_2\text{Li}_{0.5}\text{Al}_{0.5}\text{O}_4$  with  $\text{K}_2\text{NiF}_4$ -type structure. *Journal of Asian Ceramic Societies*, 3:301–304, 2015.
- [48] B. Berkels, A. Rätz, M. Rumpf, and A. Voigt. *Identification of Grain Boundary Contours at Atomic Scale*. Springer, Berlin, Heidelberg, 2007.
- [49] A. Khorashadizadeh, D. Raabe, S. Zaeferrer, G.S. Rohrer, A.D. Rollett, and M. Winning. Five-parameter grain boundary analysis by 3d EBSD of an ultra fine grained CuZr alloy processed by equal channel angular pressing. *Advanced Engineering Materials*, 13:237–244, 2011.
- [50] A.P. Sutton and R.W. Balluffi. *Interfaces in Crystalline Materials*. OXFORD UNIVERSITY PRESS, 1995.
- [51] Louisette Priester. *Grain Boundaries From Theory to Engineering*. Springer Netherlands, 2013.
- [52] W. Bollmann. *Crystal defects and crystalline interfaces*. Springer-Verlag Berlin Heidelberg GmbH, 1970.
- [53] F.C. Frank. *Symposium on the plastic deformation of crystalline solids*. Carnegie Institute of Technology, Pittsburgh, 1950.
- [54] B.A. Bilby. *Report on the Conference on Defects in Crystalline Solids*. The Physical Society, London,, 1955.
- [55] W.T. Read and W. Shockley. Dislocation models of crystal grain boundaries. *Physical Review*, 78:275–289, 1950.
- [56] A.P. Sutton and V. Vitek. On the structure of tilt grain boundaries in cubic metals I. symmetrical tilt boundaries. *Philosophical Transactions of the Royal Society A: Mathematical, Physical and Engineering Sciences*, 309:1–36, 1983.
- [57] J. Han, V. Vitek, and D.J. Srolovitz. The grain-boundary structural unit model redux. *Acta Materialia*, 133:186–199, 2017.
- [58] G.-J.J. Gao, Y.-J. Wang, and S. Ogata. Studying the elastic properties of nanocrystalline copper using a model of randomly packed uniform grains. *Computational Materials Science*, 79:56–62, 2013.



- [59] P.G. Sanders, J.A. Eastman, and J.R. Weertman. Elastic and tensile behavior of nanocrystalline copper and palladium. *Acta Materialia*, 45:1997, 4019-4025.
- [60] J.E. Carsley, J. Ning, W.W. Milligan, S.A. Hackney, and E.C. Aifantis. A simple, mixtures-based model for the grain size dependence of strength in nanophase metals. *Nanostructured Materials*, 5:441-448, 1995.
- [61] D.J. Benson, H.-H. Fu, and M.A. Meyers. On the effect of grain size on yield stress: extension into nanocrystalline domain. *Materials Science and Engineering: A*, 319-321:854-861, 2001.
- [62] J. Zhou, Y. Li, R. Zhu, and Z. Zhang. The grain size and porosity dependent elastic moduli and yield strength of nanocrystalline ceramics. *Materials Science and Engineering: A*, 445-446:717-724, 2007.
- [63] P. Sharma and S. Ganti. On the grain-size-dependent elastic modulus of nanocrystalline materials with and without grain-boundary sliding. *Journal of Materials Research*, 18:1823-1826, 2003.
- [64] H.S. Kim and M.B. Bush. The effects of grain size and porosity on the elastic modulus of nanocrystalline materials. *Nanostructured Materials*, 11:361-367, 1999.
- [65] X. Qing and X. Guo. The scale effect on the yield strength of nanocrystalline materials. *International Journal of Solids and Structures*, 43:7793-7799, 2006.
- [66] Y. Choi, Y. Park, and S. Hyun. Mechanical properties of nanocrystalline copper under thermal load. *Physics Letters A*, 376:758-762, 2012.
- [67] T.-H. Fang, C.-C. Huang, and T.-C. Chiang. Effects of grain size and temperature on mechanical response of nanocrystalline copper. *Materials Science and Engineering: A*, 671:1-6, 2016.
- [68] B. Mortazavi and G. Cuniberti. Atomistic modeling of mechanical properties of polycrystalline graphene. *Nanotechnology*, 25:215704, 2014.
- [69] J. Schiøtz, T. Vegge, F.D.D. Tolla, and K.W. Jacobsen. Atomic-scale simulations of the mechanical deformation of nanocrystalline metals. *Physical Review B*, 60:11971, 1999.
- [70] B. Jiang and G.J. Weng. A generalized self-consistent polycrystal model for the yield strength of nanocrystalline materials. *Journal of the Mechanics and Physics of Solids*, 52:1125-1149, 2004.
- [71] S. Ramtani, H.Q. Bui, and G. Dirras. A revisited generalized self-consistent polycrystal model following an incremental small strain formulation and including grain-size distribution effect. *International Journal of Engineering Science*, 47:537-553, 2009.
- [72] K. Kowalczyk-Gajewska and M. Maździarz. Atomistic and mean-field estimates of effective stiffness tensor of nanocrystalline copper. *International Journal of Engineering Science*, 129:47-62, 2018.
- [73] D.J. Bacon, D.M. Barnett, and R.O. Scattergood. Anisotropic continuum theory of lattice defects. *Progress in Materials Science*, 23:51-262, 1980.
- [74] J.R. Greer, W.C. Oliver, and W.D. Nix. Size dependence of mechanical properties of gold at the micron scale in the absence of strain gradients. *Acta Materialia*, 53:1821-1830, 2005.
- [75] J.R. Greer and W.D. Nix. Nanoscale gold pillars strengthened through dislocation starvation. *Physical Review B - Condensed Matter and Materials Physics*, 73:1-6, 2006.
- [76] S. Brochard and P. Beauchamp. Dislocation nucleation from surface steps: Atomistic simulation in aluminium. *Philosophical Magazine A*, 80:503-524, 2000.
- [77] I. Ryu, W. Cai, W.D. Nix, and H. Gao. Anisotropic size-dependent plasticity in face-centered cubic micropillars under torsion. *Journal of Mineral, Metals and Materials Society*, 68:253-260, 2016.
- [78] G. Dehm, B.N. Jaya, R. Raghavan, and C. Kirchlechner. Overview on micro-and nanomechanical testing: New insights in interface plasticity and fracture at small length scales. *Acta Materialia*, 142:248-282, 2018.

- [79] W.A.T. Clark, C.E. Wise, Z. Shen, and R.H. Wagoner. The use of the transmission electron-microscope in analyzing slip propagation across interfaces. *Ultramicroscopy*, 30:76–89, 1989.
- [80] H. Gleiter, E. Hornbogen, and G. Ro. The mechanism of grain boundary glide. *Acta Metallurgica*, 16:1053–1067, 1968.
- [81] P.H. Pumphrey and H. Gleiter. Annealing of dislocations in high-angle grain boundaries. *The Philosophical Magazine: A Journal of Theoretical Experimental and Applied Physics*, 30:593–602, 1974.
- [82] J.R. Greer and J.T.M. De Hosson. Plasticity in small-sized metallic systems: intrinsic versus extrinsic size effect. *Progress in Materials Science*, 56:654–724, 2011.
- [83] P.J. Imrich, C. Kirchlechner, C. Motz, and G. Dehm. Differences in deformation behavior of bicrystalline Cu micropillars containing a twin boundary or a large-angle grain boundary. *Acta Materialia*, 73:240–250., 2014.
- [84] N.V. Malyar, J.S. Micha, G. Dehm, and C. Kirchlechner. Dislocation-twin boundary interaction in small scale cu bi-crystals loaded in different crystallographic directions. *Acta Materialia*, 129:91–97, 2017.
- [85] N. Kheradmand, A.F. Knorr, M. Marx, and Y. Deng. Microscopic incompatibility controlling plastic deformation of bicrystals. *Acta Materialia*, 106:219–228, 2016.
- [86] W.A.T. Clark, R.H. Wagoner, Z.Y. Shen, T.C. Lee, I.M. Robertson, and H.K. Birnbaum. On the criteria for slip transmission across interfaces in polycrystals. *Scripta Metallurgica et Materialia*, 26:203–206, 1992.
- [87] A. Kunz, S. Pathak, and J.R. Greer. Size effects in al nanopillars: single crystalline vs. bicrystalline. *Acta Materialia*, 59:4416–4424., 2011.
- [88] K.S. Ng and A.H.W. Ngan. Deformation of micron-sized aluminium bi-crystal pillars. *Philosophical Magazine*, 89:3013–3026, 2009.
- [89] Y. Kim, S. Lee, J.B. Jeon, Y.J. Kim, B.J. Lee, S.H. Oh, and S.M. Han. Effect of a high angle grain boundary on deformation behavior of al nanopillars. *Scripta Materialia*, 107:5–9, 2015.
- [90] T.C. Lee, I.M. Robertson, and H.K. Birnbaum. An in situ transmission electron microscope deformation study of the slip transfer mechanisms in metals. *Metallurgical Transactions A*, 21:2437–2447, 1990.
- [91] S. Kondo, T. Mitsuuma<sup>1</sup>, N. Shibata<sup>1</sup>, and Y. Ikuhara. Direct observation of individual dislocation interaction processes with grain boundaries. *Science Advances*, 2:E1501926, 2016.
- [92] F. Schäfer, L. Weiter, M. Marx, and C. Motz. Quantifying the grain boundary resistance against slip transfer by experimental combination of geometric and stress approach using stage-I-fatigue cracks. *Philosophical Magazine*, 96:3524–3551, 2016.
- [93] Y.T. Chou and J.C.M. Li. *Theory of Dislocation Pileups*, in: *Proceedings of the Symposium on the Mathematical Theory of Dislocations*. ASME Publication, 1969.
- [94] R.E. Voskoboynikov, S.J. Chapman, J.R. Ockendon, and D.J. Allwright. Continuum and discrete models of dislocation pile-ups. I. Pile-up at a lock. *Journal of the Mechanics and Physics of Solids*, 55:2007–2025, 2007.
- [95] J.D. Eshelby, F.C. Frank, and F.R.N. Nabarro. The equilibrium of linear arrays of dislocations. *The London, Edinburgh, and Dublin Philosophical Magazine and Journal of Science*, 42:351–364, 1951.
- [96] G. Leibfried. Verteilung von Versetzungen im statischen Gleichgewicht. *Zeitschrift für Physik. Physik*, 130:214–226, 1951.
- [97] T.E. Mitchell, S.S. Hecker, and R.L. Smialek. Dislocation pile-ups in anisotropic crystals. *Physica Status Solidi (b)*, 11:585–594, 1965.

- [98] Y.T. Chou. Equilibrium of linear dislocation arrays in heterogeneous materials. *Journal of Applied Physics*, 37:2425–2429, 1966.
- [99] D.M. Barnett. The effect of shear modulus on the stress distribution produced by a planar array of screw dislocations near a bi-metallic interface. *Acta Metallurgica*, 15:589–594, 1967.
- [100] H. Kuan and J.P. Hirth. Dislocation pileups near the interface of a bimaterial couple. *Materials Science and Engineering*, 22:113–131, 1976.
- [101] J.G. Kuang and T. Mura. Dislocation pile-up in two-phase materials. *Journal of Applied Physics*, 39:109–119, 1968.
- [102] V.A. Lubarda. An analysis of edge dislocation pileups against a circular inhomogeneity or a bimetallic interface. *International Journal of Solids and Structures*, 129:146–155, 2017.
- [103] M.L. Öveçoğlu, M.F. Doerner, and W.D. Nix. Elastic interactions of screw dislocations in thin films on substrates. *Acta Metallurgica*, 35:2947–2957, 1987.
- [104] I. Vagera. Dislocation pile-up against a grain boundary in an anisotropic material. *Czechoslovak Journal of Physics*, 21:77–82, 1971.
- [105] R.H. Wagoner. Calculating dislocation spacings in pile-ups at grain boundaries. *Metallurgical Transactions A*, 12:2015–2023, 1981.
- [106] S.S. Shishvan, S. Mohammadi, M. Rahimian, and E. Van der Giessen. Plane-strain discrete dislocation plasticity incorporating anisotropic elasticity. *International Journal of Solids and Structures*, 48:374–387, 2011.
- [107] S. Lefebvre, B. Devincere, and T. Hoc. Yield stress strengthening in ultrafine-grained metals: A two-dimensional simulation of dislocation dynamics. *Journal of the Mechanics and Physics of Solids*, 55:788–802, 2007.
- [108] L. Priester. *Grain Boundaries and Crystalline Plasticity*. John Wiley and Sons, Inc., 2011.
- [109] D.M. Barnett and J. Lothe. An image force theorem for dislocations in anisotropic bicrystals. *Journal of Physics F: Metal Physics*, 4:1618–1635, 1974.
- [110] C.-C. Ma and R.-L. Lin. Image singularities of Green’s functions for an isotropic elastic half-plane subjected to forces and dislocations. *Mathematics and Mechanics of Solids*, 6:503–524, 2001.
- [111] K. Davis, E. Teghtsoonian, and A. Lu. Slip band continuity across grain boundaries in aluminum. *Acta Metallurgica*, 14:1677–1684, 1966.
- [112] M. Briceñoa, J. Fenskea, M. Dadfarniab, P. Sofronisb, and I.M. Robertson. Effect of ion irradiation-produced defects on the mobility of dislocations in 304 stainless steel. *Journal of Nuclear Materials*, 409:18–26, 2011.
- [113] Y. Guo, T. Britton, and A. Wilkinson. Slip band-grain boundary interactions in commercial-purity titanium. *Acta Materialia*, 76:1–12, 2014.
- [114] T. Lee, I. Robertson, and Birnbaum H. Prediction of slip transfer mechanisms across grain boundaries. *Scripta Metallurgica*, 23:799–803, 1989.
- [115] I. Beyerlein, N. Mara, J. Wang, J. Carpenter, S. Zheng, W. Han, R. Zhang, K. Kang, T. Nizolek, and T. Pollock. Structure-property-functionality of bimetal interfaces. *JOM*, 64:1192–1207, 2012.
- [116] J. Livingston and B. Chalmers. Multiple slip in bicrystal deformation. *Acta Metallurgica*, 5:322–327, 1957.
- [117] J. Luster and M. Morris. Compatibility of deformation in two-phase Ti-Al alloys: dependence on microstructure and orientation relationships. *Metallurgical and Materials Transactions A*, 26:1745–1756, 1995.

- [118] T. Bieler, P. Eisenlohr, C. Zhang, H. Phukan, and M. Crimp. Grain boundaries and interfaces in slip transfer. *Current Opinion in Solid State and Materials Science*, 18:212–226, 2014.
- [119] P.C. Wo and A.H.W. Ngan. Investigation of slip transmission behavior across grain boundaries in polycrystalline Ni<sub>3</sub>Al using nanoindentation. *Journal of Materials Research*, 19:189–201, 2004.
- [120] T.C. Lee, I.M. Robertson, and H.K. Birnbaum. Tem in situ deformation study of the interaction of lattice dislocations with grain boundaries in metals. *Philosophical Magazine A*, 62:131–153, 1990.
- [121] I. Tiba, T. Richeton, C. Motz, H. Vehoff, and S. Berbenni. Incompatibility stresses at grain boundaries in Ni bicrystalline micropillars analyzed by an anisotropic model and slip activity. *Acta Materialia*, 83:227–238, 2015.
- [122] L. Patriarca, W. Abuzaid, H. Sehitoglu, and H.J. Maier. Slip transmission in bcc FeCr polycrystal. *Materials Science and Engineering: A*, 588:308–317, 2013.
- [123] E. Werner and W. Prantl. Slip transfer across grain and phase boundaries. *Acta Metallurgica et Materialia*, 38:533–537, 1990.
- [124] E. Bayerschen, A.T. McBride, B.D. Reddy, and T. Böhlke. Review on slip transmission criteria in experiments and crystal plasticity models. *Journal of Materials Science*, 51:2243–2258, 2016.
- [125] F. Schäfer, L. Weiter, M. Marx, and C. Motz. Quantifying the grain boundary resistance against slip transfer by experimental combination of geometric and stress approach using stage-I fatigue cracks. *Philosophical Magazine*, 96:3524–3551, 2016.
- [126] J.D. Livingston and B. Chalmers. Difference fatigue cracking behaviors of Cu bicrystals with the same component grains but different twin boundaries. *Acta Metallurgica*, 5:322–327, 1957.
- [127] Y. Zeng, A. Hunter, I.J. Beyerlein, and M. Koslowski. A phase field dislocation dynamics model for a bicrystal interface system: An investigation into dislocation slip transmission across cube-on-cube interfaces. *International Journal of Plasticity*, 79:293–313, 2016.
- [128] V.R. Coffman and J.P. Sethna. Grain boundary energies and cohesive strength as a function of geometry. *Physical Review B*, 77:144111, 2008.
- [129] H.J. Chu, J. Wang, I.J. Beyerlein, and E. Pan. Dislocation models of interfacial shearing induced by an approaching lattice glide dislocation. *International Journal of Plasticity*, 41:1–13, 2013.
- [130] R.G. Hoagland, T.E. Mitchell, J.P. Hirth, and H. Kung. On the strengthening effects of interfaces in multilayer fcc metallic composites. *Philosophical Magazine A*, 82:643–664, 2002.
- [131] J.S. Koehler. Attempt to design a strong solid. *Physical Review B*, 2:547–551, 1970.
- [132] E.S. Pacheco and T. Mura. Interaction between a screw dislocation and a bimetallic interface. *Journal of the Mechanics and Physics of Solids*, 17:163–170, 1969.
- [133] M.A. Shehadeh, G. Lu, S. Banerjee, N. Kioussis, and N. Ghoniem. Dislocation transmission across the Cu/Ni interface: a hybrid atomistic-continuum study. *Philosophical Magazine*, 87:1513–1529, 2007.
- [134] J. Wang, R.G. Hoagland, J.P. Hirth, and A. Misra. Atomistic modeling of the interaction of glide dislocations with “weak” interfaces. *Acta Materialia*, 56:5685–5693, 2008.
- [135] R.G. Hoagland, R.J. Kurtz, and C.H. Henager-Jr. Slip resistance of interfaces and the strength of metallic multilayer composites. *Scripta Materialia*, 50:775–779, 2004.
- [136] C. Blochwitz, R. Richter, W. Tirschler, and K. Obrtlík. The effect of local textures on microcrack propagation in fatigued f.c.c. metals. *Materials Science and Engineering: A*, 234-236:563–566, 1997.
- [137] I. Tiba. *Effets des interfaces cristallines sur les champs mécaniques en plasticité cristalline et conséquences sur le glissement dans des micro-piliers bi-cristallins*. PhD thesis, Université de Lorraine et Université de Saarbrücken, 2015.

- [138] T.B. Britton and A.J. Wilkinson. High resolution electron backscatter diffraction measurements of elastic strain variations in the presence of larger lattice rotations. *Ultramicroscopy*, 114:82–95, 2012.
- [139] N. Kheradmand. *Grain boundary-dislocation interaction : A local investigation via micron-sized bicrystals*. PhD thesis, Universität des Saarlandes, Germany, 2012.
- [140] M.D. Uchic, D.M. Dimiduk, J.N. Florando, and W.D. Nix. Sample dimensions influence strength and crystal plasticity. *Science*, 305:986–989, 2004.
- [141] M.D. Uchic and D.M. Dimiduk. A methodology to investigate size scale effects in crystalline plasticity using uniaxial compression testing. *Materials Science and Engineering A*, 400-401:268–278, 2005.
- [142] K.S. Ng and A.H.W. Ngan. Stochastic nature of plasticity of al micropillars. *Acta Materialia*, 56:1712–1720, 2008.
- [143] D. Kiener, C. Motz, T. Schöberl, M. Jenko, and G. Dehm. Determination of mechanical properties of copper at the micron scale. *Advanced Engineering Materials*, 8:1119–1125, 2006.
- [144] M.D. Uchic, P.A. Shade, and D.M. Dimiduk. Plasticity of micrometerscale single crystals in compression. *Annual Review of Materials Research*, 39:361–386, 2009.
- [145] K.S. Ng and A.H.W. Ngan. Breakdown of schmid’s law in micropillars. *Scripta Materialia*, 59:796–799, 2008.
- [146] D. Kiener. *Understanding nanoscale plasticity using quantitative in situ TEM*. Department Materialphysik, Montanuniversität Leoben, Österreich, 2013.
- [147] J.F. Nye. Some geometrical relations in dislocated crystals. *Acta Metallurgica*, 1:153–162, 1953.
- [148] M.F. Ashby. The deformation of plastically non-homogeneous materials. *Philosophical Magazine*, 21:399–424, 1970.
- [149] S. Berbenni, V. Favier, X. Lemoine, and M. Berveiller. Micromechanical modeling of the elastic-viscoplastic behavior of polycrystalline steels having different microstructures. *Materials Science and Engineering, A*, 372:128–136, 2004.
- [150] L. Tabourot, M. Fivel, and E. Rauch. Generalized constitutive laws for fcc single crystals. *Materials Science and Engineering A*, 234-236:639–642, 1997.
- [151] S. Berbenni, M. Berveiller, and T. Richeton. Intra-granular plastic slip heterogeneities: Discrete vs. Mean field approaches. *International Journal of Solids and Structures*, 45:4147–4172, 2008.
- [152] E. Kroner. Berechnung der elastischen konstanten des vielkristalls aus den konstanten des einkristalls. *Zeitschrift für Physik*, 151:504–518, 1958.
- [153] E. Kroner. *Kontinuumstheorie der Versetzungen und Eigenspannungen*. Springer Verlag, Berlin, 1958.
- [154] V.L. Indenbom. *Internal stresses in crystals*. In *Theory of Crystal Defects*. Academy of Sciences, Prague, 1966.
- [155] J.R. Willis. Second order effects of dislocation in anisotropic crystals. *International Journal of Engineering Science*, 5:171–190, 1967.
- [156] A. Acharya. A model of crystal plasticity based on the theory of continuously distributed dislocations. *Journal of the Mechanics and Physics of Solids*, 49:761–785, 2001.
- [157] T. Mura. Continuous distribution of moving dislocations. *Philosophical Magazine*, 89:843–857, 1963.
- [158] A. Acharya and A. Roy. Size effects and idealized dislocation micro- structure at small scales : predictions of a phenomenological model of mesoscopic field dislocation mechanics : part i. *Journal of the Mechanics and Physics of Solids*, 54:1687–1710, 2006.

- [159] A. Acharya. Constitutive analysis of finite deformation field dislocation mechanics. *Journal of the Mechanics and Physics of Solids*, 52:301–316, 2004.
- [160] T. Richeton and S. Berbenni. Effects of heterogeneous elasticity coupled to plasticity on stresses and lattice rotations in bicrystals: A field dislocation mechanics viewpoint. *European Journal of Mechanics - A/Solids*, 37:231–247, 2013.
- [161] R.E. Hook and J.P. Hirth. The deformation behavior of isoaxial bicrystals of Fe – 3%Si. *Acta Metallurgica*, 15:535–551, 1967.
- [162] R.E. Hook and J.P. Hirth. The deformation behavior of non-isoaxial bicrystals of Fe – 3%Si. *Acta Metallurgica*, 15:1099–1109, 1967.
- [163] J.P. Hirth. The influence of grain boundaries on mechanical properties. *Metallurgical Transactions*, 3:3047–3067, 1972.
- [164] C. Rey and A. Zaoui. Grain boundary effects in deformed bicrystals. *Acta Metallurgica*, 30:523–535, 1982.
- [165] C. Rey and A. Zaoui. Slip heterogeneities in deformed aluminum bicrystals. *Acta Metallurgica*, 28:687–697, 1980.
- [166] K.T. Aust and N.K. Chen. Effect of orientation difference on the plastic deformation of aluminum bicrystals. *Acta Metallurgica*, 2:632–638, 1954.
- [167] J.J. Hauser and B. Chalmers. The plastic deformation of bicrystals of f.c.c. metals. *Acta Metallurgica*, 9:802–818, 1961.
- [168] M. Berveiller. *Contribution à l'étude du comportement plastique et des textures de déformation des polycristaux métalliques - Etude des quaternions et application aux mécanismes spaciaux*. PhD thesis, Université de Paris-Nord-Villetaneuse, France, 1978.
- [169] M. Berveiller. *Thèse d'état: Contribution à l'étude du comportement plastique et des textures de déformation des polycristaux métallique*. Sciences et Techniques de l'Armement, 1980.
- [170] M. Berveiller and A. Zaoui. An extension of the self-consistent scheme to plastically flowing polycrystals. *Journal of the Mechanics and Physics of Solids*, 26:325–344, 1979.
- [171] J. Gemperlová, V. Paidar, and F. Kroupa. Compatibility stresses in deformed bicrystals. *Czech Journal of Physics B*, 39:427–446, 1989.
- [172] J. Turley and G. Sines. The anisotropy of young's modulus, shear modulus and poisson's ratio in cubic materials. *Journal of Physics D: Applied Physics*, 4:264–271, 1971.
- [173] E. Kroner. *Kontinuumstheorie der Versetzungen und Eigenspannungen*. Springer Verlag, Berlin, 1958.
- [174] N.I. Muskhelishvili. *Some Basic Problems of the Mathematical Theory of Elasticity*. Noordhoff, Groningen, pp. 105–175, 1953.
- [175] S.T. Choi and Y.Y. Earmme. Elastic study on singularities interacting with interfaces using alternating technique: Part II. isotropic trimaterial. *International Journal of Solids and Structures*, 39:1199–1211, 2002.
- [176] T.C.T. Ting and H. Chyanbin. Sextic formalism in anisotropic elasticity for almost non-semisimple matrix N. *International Journal of Solids and Structures*, 24:65–76, 1988.
- [177] A.N. Stroh. Steady state problems in anisotropic elasticity. *Journal of Mathematics and Physics*, 41:77–103, 1962.
- [178] P. Chadwick and G.D. Smith. Foundations of the theory of surface waves in anisotropic elastic materials, in: Yih, c.-s. (ed.). *Advances in Applied Mechanics*, Elsevier:303–376, 1977.

- [179] R. Becker and S. Panchanadeswaran. Effects of grain interactions on deformation and local texture in polycrystals. *Acta Materialia*, 43:2701–2719, 1995.
- [180] D.P. Mika and P.R. Dawson. Effects of grain interaction on deformation in polycrystals. *Materials Science and Engineering: A*, 257:62–76, 1998.
- [181] F. Barbe, L. Decker, D. Jeulin, and G. Cailletaud. Intergranular and intragranular behavior of polycrystalline aggregates. Part 1: F.E. model. *International Journal of Plasticity*, 17:513–536, 2001.
- [182] D. Raabe, M. Sachtleber, Z. Zhao, F. Roters, and S. Zaefferer. Micromechanical and macromechanical effects in grain scale polycrystal plasticity experimentation and simulation. *Acta Materialia*, 49:3433–3441, 2001.
- [183] S.J. Park, H.N. Han, K.H. Oh, D. Raabe, and J.K. Kim. Finite element simulation of grain interaction and orientation fragmentation during plastic deformation of BCC metals. *Materials Science Forum*, 408:371–376, 2002.
- [184] A.P. Clarke, F.J. Humphreys, and P.S. Bate. Lattice rotations at large second-phase particles in polycrystalline aluminum. *Materials Science Forum*, 426:399–404, 2003.
- [185] Y.J. Wei and L. Anand. Grain-boundary sliding and separation in polycrystalline metals: application to nanocrystalline fcc metals. *Journal of the Mechanics and Physics of Solids*, 52:2587–2616, 2004.
- [186] L.P. Evers, W.A.M. Brekelmans, and M.G.D. Geers. Scale dependent crystal plasticity framework with dislocation density and grain boundary effects. *International Journal of Solids and Structures*, 41:5209–5230, 2004.
- [187] O. Diard, S. Leclercq, G. Rousselier, and G. Cailletaud. Evaluation of finite element based analysis of 3d multicrystalline aggregates plasticity: application to crystal plasticity model identification and the study of stress and strain fields near grain boundaries. *International Journal of Plasticity*, 21:691–722, 2005.
- [188] P.S. Bate and W.B. Hutchinson. Grain boundary area and deformation. *Scripta Materialia*, 52:199–203, 2005.
- [189] Y.J. Wei, C. Su, and L. Anand. A computational study on the mechanical behavior of nanocrystalline fcc metals. *Acta Materialia*, 54:3177–3190, 2006.
- [190] A. Ma, F. Roters, and D. Raabe. A dislocation density based constitutive model for crystal plasticity fem including geometrically necessary dislocations. *Acta Materialia*, 54:2169–2179, 2006.
- [191] A. Ma, F. Roters, and D. Raabe. On the consideration of interactions between dislocations and grain boundaries in crystal plasticity finite element modeling—theory, experiments, and simulations. *Acta Materialia*, 54:2181–2194, 2006.
- [192] E. Bitzek, P.M. Derlet, P.M. Anderson, and H. Van Swygenhoven. The stress–strain response of nanocrystalline metals: A statistical analysis of atomistic simulations. *Acta Materialia*, 56:4846–4857, 2008.
- [193] R. Hill and J.R. Rice. Constitutive analysis of elastic-plastic crystals at arbitrary strain. *Journal of the Mechanics and Physics of Solids*, 20:401–413, 1972.
- [194] E.H. Lee. Elastic-plastic deformation at finite strains. *Journal of Applied Mechanics*, 36:1–6, 1969.
- [195] M.E. Gurtin. *The Linear Theory of Elasticity*. In: Truesdell, C., Ed., *Handbuch der Physik*, Vol. VIa/2, Springer-Verlag, Berlin, 1-296, 1972.
- [196] D. Peirce, R.J. Asaro, and A. Needleman. An analysis of nonuniform and localized deformation in ductile single crystals. *Acta Metallurgica*, 30:1087–1119, 1982.
- [197] D. Peirce, R.J. Asaro, and A. Needleman. Material rate dependence and localized deformation in crystalline solids. *Acta Metallurgica*, 31:1951–1976, 1983.

- [198] A. Ma and F. Roters. A constitutive model for fcc single crystals based on dislocation densities and its application to uniaxial compression of aluminium single crystals. *Acta Materialia*, 52:3603–3612, 2004.
- [199] J.L. Bassani and T.-Y. Wu. Latent hardening in single crystals II. Analytical characterization and predictions. *Philosophical Transactions of the Royal Society A: Mathematical, Physical and Engineering Sciences*, 435:21–41, 1991.
- [200] G.Z. Voyiadjis and Y. Song. Strain gradient continuum plasticity theories: Theoretical, numerical and experimental investigations. *International Journal of Plasticity*, 121:21–75, 2019.
- [201] E.C. Aifantis. On the microstructural origin of certain inelastic models. *Journal of Engineering Materials and Technology*, 106:326–330, 1984.
- [202] E.C. Aifantis. The physics of plastic deformation. *International Journal of Plasticity*, 3:211–247, 1987.
- [203] K.E. Aifantis, W.A. Soer, J.Th.M. De Hosson, and J.R. Willis. Interfaces within strain gradient plasticity: Theory and experiments. *Acta Materialia*, 54:5077–5085, 2006.
- [204] N.A. Fleck and J.W. Hutchinson. A phenomenological theory for strain gradient effects in plasticity. *Journal of the Mechanics and Physics of Solids*, 41:1825–1857, 1993.
- [205] P. Gudmundson. A unified treatment of strain gradient plasticity. *Journal of the Mechanics and Physics of Solids*, 52:1379–1406, 2004.
- [206] M.E. Gurtin and L. Anand. A theory of strain-gradient plasticity for isotropic, plastically irrotational materials. Part I: Small deformations. *Journal of the Mechanics and Physics of Solids*, 53:1624–1649, 2005.
- [207] M.E. Gurtin. A gradient theory of small-deformation isotropic plasticity that accounts for the burgers vector and for dissipation due to plastic spin. *Journal of the Mechanics and Physics of Solids*, 52:2545–2568, 2004.
- [208] W.D. Nix and H. Gao. Indentation size effects in crystalline materials: A law for strain gradient plasticity. *Journal of the Mechanics and Physics of Solids*, 46:411–425, 1998.
- [209] H. Gao, Y. Huang, W.D. Nix, and J.W. Hutchinson. Mechanism-based strain gradient plasticity—I. Theory. *Journal of the Mechanics and Physics of Solids*, 47:1239–1263, 1999.
- [210] H. Gao, Y. Huang, and W.D. Nix. Modeling plasticity at the micrometer scale. *Naturwissenschaften*, 86:507–515, 1999.
- [211] Y. Huang, H. Gao, W.D. Nix, and J.W. Hutchinson. Mechanism-based strain gradient plasticity—II. Analysis. *Journal of the Mechanics and Physics of Solids*, 48:99–128, 2000.
- [212] Y. Huang, Z. Xue, H. Gao, W.D. Nix, and Z.C. Xia. A study of microindentation hardness tests by mechanism-based strain gradient plasticity. *Journal of Materials Research*, 15:1786–1796, 2000.
- [213] Y. Huang, S. Qu, K.C. Hwang, M. Li, and H. Gao. A conventional theory of mechanism-based strain gradient plasticity. *International Journal of Plasticity*, 20:753–782, 2004.
- [214] Y. Huang, K.C. Hwang, J. Song, and H. Gao. Indentation size effect: a study via the mechanism-based strain-gradient plasticity theory. *International Journal of Surface Science and Engineering*, 1, 2007.
- [215] R.A. Lebensohn and A. Needleman. Numerical implementation of non-local polycrystal plasticity using fast Fourier transforms. *Journal of the Mechanics and Physics of Solids*, 97:333–351, 2016.
- [216] M.E. Gurtin. A gradient theory of single-crystal viscoplasticity that accounts for geometrically necessary dislocations. *Journal of the Mechanics and Physics of Solids*, 50:5–32, 2002.
- [217] R.A. Lebensohn, A.K. Kanjarla, and P. Eisenlohr. An elasto-viscoplastic formulation based on fast Fourier transforms for the prediction of micromechanical fields in polycrystalline materials. *International Journal of Plasticity*, 32–33:59–69, 2012.



- [218] K.S. Djaka, S. Berbenni, V. Taupin, and R.A. Lebensohn. A FFT-based numerical implementation of mesoscale field dislocation mechanics: Application to two-phase laminates. *International Journal of Solids and Structures*, 2019, In Press: doi.org/10.1016/j.ijsolstr.2018.12.027.
- [219] H.M. Zbib, M.A. Shehadeh, S.M.A. Khan, and G. Karami. Multiscale dislocation dynamics plasticity. *International Journal for Multiscale Computational Engineering*, 1:73–90, 2003.
- [220] N.B. Burbery, G.Po, R. Das, N. Ghoniem, and W.G. Ferguson. Dislocation dynamics in polycrystals with atomistic-informed mechanisms of dislocation - grain boundary interactions. *Journal of Micromechanics and Molecular Physics*, 2:1750003, 2017.
- [221] R. Schouwenaars, M. Seefeldt, and P. Van Houtte. The stress field of an array of parallel dislocation pile-ups: Implications for grain boundary hardening and excess dislocation distributions. *Acta Materialia*, 58:4344–4353, 2010.
- [222] L.P. Kubin, B. Devincere, and C. De Sansal. Grain size strengthening in micro-crystalline copper: A three-dimensional dislocation dynamics simulation. *Key Engineering Materials*, 423:25–32, 2010.
- [223] D.S. Balint, V.S. Deshpande, A. Needleman, and E. Van Der Giessen. Discrete dislocation plasticity analysis of the grain size dependence of the flow strength of polycrystals. *International Journal of Plasticity*, 24:2149–2172, 2008.
- [224] L. Nicola, Y. Xiang, J.J. Vlassak, E. Van der Giessen, and A. Needleman. Plastic deformation of freestanding thin films: Experiments and modeling. *Journal of the Mechanics and Physics of Solids*, 54:2089–2110, 2006.
- [225] L.P. Kubin, G. Canova, M. Condat, B. Devincere, V. Pontikis, and Y. Bréchet. Dislocation microstructures and plastic flow: A 3D simulation. *Solid State Phenomena*, 23-24:455–472, 1992.
- [226] E. Van der Giessen and A. Needleman. Discrete dislocation plasticity: a simple planar model. *Modelling and Simulation in Materials Science and Engineering*, 3:689–735, 1995.
- [227] H.D. Espinosa, S. Berbenni, M. Panico, and K.W. Schwarz. An interpretation of size-scale plasticity in geometrically confined systems. *Proceedings of the National Academy of Sciences of the United States of America*, 102:16933–16938, 2005.
- [228] H.D. Espinosa, M. Panico, S. Berbenni, and K.W. Schwarz. Discrete dislocation dynamics simulations to interpret plasticity size and surface effects in freestanding fcc thin films. *International Journal of Plasticity*, 22:2091–2117, 2006.
- [229] S.B. Biner and J.R. Morris. A two-dimensional discrete dislocation simulation of the effect of grain size on strengthening behaviour. *Modelling and Simulation in Materials Science and Engineering*, 10:617, 2002.
- [230] Z. Li, C. Hou, M. Huang, and C. Ouyang. Strengthening mechanism in micro-polycrystals with penetrable grain boundaries by discrete dislocation dynamics simulation and hall-petch effect. *Computational Materials Science*, 46:1124–1134, 2009.
- [231] R. Kumar, F. Szekely, and E. Van Der Giessen. Modelling dislocation transmission across tilt grain boundaries in 2d. *Computational Materials Science*, 49:46–54, 2010.
- [232] N. Ahmed and A. Hartmaier. Mechanisms of grain boundary softening and strain-rate sensitivity in deformation of ultrafine-grained metals at high temperatures. *Acta Materialia*, 59:4323–4334, 2011.
- [233] J. Robbins and T.E. Voth. Modeling dislocations in a polycrystal using the generalized finite element method. *International Journal of Theoretical and Applied Multiscale Mechanics*, 2:95–110, 2010.
- [234] C. Zhou and R. Lesar. Dislocation dynamics simulations of plasticity in polycrystalline thin films. *International Journal of Plasticity*, 30–31:185–201, 2012.
- [235] B. Devincere, R. Madec, G. Monnet, S. Queyreau, R. Gatti, and L. Kubin. Modeling crystal plasticity with dislocation dynamcis simulations : the «micromegas» code. in: *S. Forest, A.P. (Ed.), Mechanics of Nano-Objects. Presses des Mines*, page 81–100, 2011.

- [236] V. Bulatov, W. Cai, J. Fier, M. Hiratani, G. Hommes, T. Pierce, M. Tang, M. Rhee, K. Yates, and T. Arsenlis. Scalable line dynamics in paradisi. *SC '04: Proceedings of the 2004 ACM/IEEE Conference on Supercomputing*, 2005.
- [237] M. Verdier, M. Fivel, and I. Groma. Mesoscopic scale simulation of dislocation dynamics in fcc metals: Principles and applications. *Modelling and Simulation in Materials Science and Engineering*, 6:755–770, 1998.
- [238] N.M. Ghoniem, S.-H. Tong, and L.Z. Sun. Parametric dislocation dynamics: A thermodynamics-based approach to investigations of mesoscopic plastic deformation. *Physical Review B*, 61:913–927, 2000.
- [239] G. Po and N. Ghoniem. A variational formulation of constrained dislocation dynamics coupled with heat and vacancy diffusion. *Journal of the Mechanics and Physics of Solids*, 66:103–116, 2014.
- [240] G. Po, M. Lazar, D. Seif, and N. Ghoniem. Singularity-free dislocation dynamics with strain gradient elasticity. *Journal of the Mechanics and Physics of Solids*, 68:161–178, 2014.
- [241] G. Daveau. *Interaction dislocations - joints de grains en déformation plastique monotone : étude expérimentale et modélisations numériques*. PhD thesis, Ecole Centrale Paris, 2012.
- [242] M. Jiang, B. Devincere, and G. Monnet. Effects of the grain size and shape on the flow stress: A dislocation dynamics study. *International Journal of Plasticity*, 113:111–124, 2019.
- [243] A. Stukowski. Structure identification methods for atomistic simulations of crystalline materials. *Modelling and Simulation in Materials Science and Engineering*, 20:045021, 2012.
- [244] S. Plimpton. Fast parallel algorithms for short-range molecular dynamics. *Journal of Computational Physics*, 117:1–19, 1995.
- [245] M.S. Daw and M.I. Baskes. Embedded-atom method: Derivation and application to impurities, surfaces, and other defects in metals. *Physical Review B. American Physical Society*, 29:6443–6453, 1984.
- [246] M.D. Koning, R. Miller, V.V. Bulatov, and F.F. Abraham. Modelling grain-boundary resistance in intergranular dislocation slip transmission. *Philosophical Magazine A*, 82:2511–2527, 2002.
- [247] M. de Koning, R.J. Kurtz, V.V. Bulatov, C.H. Henager, R.G. Hoagland, W. Cai, and M. Nomura. Modeling of dislocation–grain boundary interactions in FCC metals. *Journal of Nuclear Materials*, 323:281–289, 2003.
- [248] D.V. Bachurin, D. Weygand, and P. Gumbsch. Dislocation–grain boundary interaction in  $\langle 111 \rangle$  textured thin metal films. *Acta Materialia*, 58:5232–5241, 2010.
- [249] M.P. Dewald and W.A. Curtin. Multiscale modelling of dislocation/grain boundary interactions. II. Screw dislocations impinging on tilt boundaries in Al. *Philosophical Magazine*, 87:4615–4641, 2007.
- [250] M.P. Dewald and W.A. Curtin. Multiscale modelling of dislocation/grain-boundary interactions: I. Edge dislocations impinging on  $\sigma_{11}$  (113) tilt boundary in Al. *Modelling And Simulation In Materials Science And Engineering*, 15:S193–S215, 2007.
- [251] V.B. Shenoy, R. Miller, E.B. Tadmor, R. Phillips, and M. Ortiz. Quasicontinuum models of interfacial structure and deformation. *Physical Review Letters*, 80:742–745, 1998.
- [252] M.P. Dewald and W.A. Curtin. Multiscale modeling of dislocation/grain-boundary interactions: III.  $60^\circ$  dislocations impinging on  $\sigma_3$ ,  $\sigma_9$  and  $\sigma_{11}$  tilt boundaries in Al. *Modelling and Simulation in Materials Science and Engineering*, 19:055002, 2011.
- [253] W. Yu and Z. Wang. Interactions between edge lattice dislocations and  $\sigma_{11}$  symmetrical tilt grain boundaries in copper: A quasi-continuum method study. *Acta Materialia*, 60:5010–5021, 2012.
- [254] H. Van Swygenhoven, P.M. Derlet, and A. Hasnaoui. Atomic mechanism for dislocation emission from nano-sized grain boundaries. *Physical Review B: Covering Condensed Matter and Materials Physics*, 66:241011–241018, 2002.

- [255] P.M. Derlet, H. Van Swygenhoven, and A. Hasnaoui. Atomistic simulation of dislocation emission in nanosized grain boundaries. *Philosophical Magazine*, 83:3569–3575, 2003.
- [256] H. Van Swygenhoven, P.M. Derlet, and A.G. Froseth. Nucleation and propagation of dislocations in nanocrystalline fcc metals. *Acta Materialia*, 54:1975–1983, 2006.
- [257] M.A. Tschopp and D.L. McDowell. Dislocation nucleation in  $\sigma_3$  asymmetric tilt grain boundaries. *International Journal of Plasticity*, 24:191–217, 2008.
- [258] D.E. Spearot, K.I. Jacob, and D.L. McDowell. Nucleation of dislocations from [001] bicrystal interfaces in aluminum. *Acta Materialia*, 53:3579–3589, 2005.
- [259] D.E. Spearot, K.I. Jacob, and D.L. McDowell. Dislocation nucleation from bicrystal interfaces with dissociated structure. *International Journal of Plasticity*, 23:143–160, 2007.
- [260] M.A. Tschopp and D.L. McDowell. Grain boundary dislocation sources in nanocrystalline copper. *Scripta Materialia*, 58:299–302, 2008.
- [261] L. Zhang, C. Lu, K. Tieu, L. Pei, X. Zhao, and K. Cheng. Molecular dynamics study on the grain boundary dislocation source in nanocrystalline copper under tensile loading. *Materials Research Express*, 2:035009, 2015.
- [262] H. Van Swygenhoven and P.M. Derlet. Atomistic simulations of dislocations in FCC metallic nanocrystalline materials. *Dislocations Solids*, 14:1–42, 2008.
- [263] M.A. Tschopp, D.E. Spearot, and D.L. McDowell. Influence of grain boundary structure on dislocation nucleation in fcc metals. *Dislocations Solids*, 14:43–139, 2008.
- [264] D.E. Spearot, M.A. Tschopp, K.I. Jacob, and D.L. McDowell. Tensile strength of  $\langle 100 \rangle$  and  $\langle 110 \rangle$  tilt bicrystal copper interfaces. *Acta Materialia*, 55:705–714, 2007.
- [265] F. Ernst, M.W. Finnis, D. Hofmann, T. Muschik, U. Schonberger, U. Wolf, and M. Methfessel. Theoretical prediction and direct observation of the 9r structure in Ag. *Physical Review Letters*, 69:620–623, 1992.
- [266] L. Zhang, C. Lu, and K. Tieu. Atomistic simulation of tensile deformation behavior of  $\sigma_5$  tilt grain boundaries in copper bicrystal. *Scientific Reports*, 4:5919, 2014.
- [267] J.A. Rayne. Elastic constants of  $\alpha$ -brasses: Room-temperature variation with solute concentration. *Physical Review*, 112:1125, 1958.
- [268] J.A. Rayne. Elastic constants of  $\alpha$ -brasses: Variation with solute concentration from 4.2-300 ok. *Physical Review*, 115:63, 1959.
- [269] R. Hill. The elastic behaviour of a crystalline aggregate. *Proceedings of the Physical Society. Section A*, 65:349, 1952.
- [270] R. Dewit. Elastic constants and thermal expansion averages of a nontextured polycrystal. *Journal of Mechanics of Materials and Structures*, 3:195–212, 2008.
- [271] Y.H. Zhao, X.Z. Liao, Y.T. Zhu, Z. Horita, and T.G. Langdon. Influence of stacking fault energy on nanostructure formation under high pressure torsion. *Materials Science and Engineering A*, 410–411:188–193, 2005.
- [272] L. Remy. *PhD thesis*. PhD thesis, Universite de Paris-Sud, 1975.
- [273] I. Itoh and T. Hikage. Dezincification mechanism of brass in vacuum at high temperature. *Transactions of the Japan Institute of Metals*, 17:165–169, 1976.
- [274] M. Kowalski and P.J. Spencer. Thermodynamic reevaluation of the Cu-Zn system. *Journal of Phase Equilibria*, 14:432–438, 1993.

- [275] H.J. Bunge. *Mathematische Methoden Texturanalyse*. English Edition : Butterworth, 1982.
- [276] T. Richeton, I. Tiba, S. Berbenni, and O. Bouaziz. Analytical expressions of incompatibility stresses at  $\sigma_3(111)$  twin boundaries and consequences on single-slip promotion parallel to twin plane. *Philosophical Magazine*, 95:1:12–31, 2015.
- [277] X. Chen, T. Richeton, C. Motz, and S. Berbenni. Elastic fields due to dislocations in anisotropic bi- and tri-materials: Applications to discrete dislocation pile-ups at grain boundaries. *International Journal of Solids and Structures*, 164:141–156, 2019.
- [278] M.O. Tucker and A.G. Crocker. The plane boundary in anisotropic elasticity. *Mechanics of Generalized Continua*, pages 286–289, 1968.
- [279] J. Gemperlová and I. Saxl. Dislocations in an inhomogeneous anisotropic medium. *Czechoslovak Journal of Physics B*, 18:1085–1093, 1968.
- [280] J. Gemperlová. Force on dislocations in anisotropic bicrystals and half-spaces. *Physica Status Solidi (b)*, 30:261–274, 1968.
- [281] V.N. Tiwari, L.K. Lehri, and A.N. Pathak. Effect of inoculating crops with phospho-microbes. *Experimental Agriculture*, 25:47–50, 1989.
- [282] T.C.T. Ting. Anatomy of Green’s functions for line forces and dislocations in anisotropic media and in degenerate materials. *Physica Scripta*, T44:137–144, 1992.
- [283] T.C.T. Ting and D.M. Barnett. Image force on line dislocations in anisotropic elastic half-spaces with a fixed boundary. *International Journal of Solids and Structures*, 30:313–323, 1993.
- [284] H. Chu and E. Pan. Elastic fields due to dislocation arrays in anisotropic bimaterials. *International Journal of Solids and Structures*, 51:1954–1961, 2014.
- [285] T.C.T. Ting. *Anisotropic Elasticity: Theory and Applications*. Oxford Engineering Science Series. Oxford University Press, 1996.
- [286] S. Nakahara and J.R. Willis. Some remarks on interfacial dislocations. *Journal of Physics F: Metal Physics*, 3:249, 1973.
- [287] J.R. Vinson and T.W. Chou. *Composite Materials and Their Use in Structures*. Wiley, 1975.
- [288] R. Bonnet and M. Dupeux. Stress calculations for interfacial extrinsic and intrinsic dislocation arrays in anisotropic two-phase media. *Philosophical Magazine A*, 42:809–812, 1980.
- [289] J. Qu and J.L. Bassani. Cracks on bimaterial and bicrystal interfaces. *Journal of the Mechanics and Physics of Solids*, 37:417–433, 1989.
- [290] J. Qu and Q. Li. Interfacial dislocation and its applications to interface cracks in anisotropic bimaterials. *Journal of Elasticity*, 26:169–195, 1991.
- [291] P.A. Juan and R. Dingreville. Mechanics of finite cracks in dissimilar anisotropic elastic media considering interfacial elasticity. *Journal of the Mechanics and Physics of Solids*, 99:1–18, 2017.
- [292] C. Hwu. *Anisotropic Elastic Plates*. Springer US, 2010.
- [293] H.Y. Wang and M.S. Wu. Green’s function for an anisotropic film–substrate embedded with a screw dislocation. *Engineering Analysis with Boundary Elements*, 29:624–635, 2005.
- [294] M.S. Wu and H.Y. Wang. Solutions for edge dislocation in anisotropic film–substrate system by the image method. *Mathematics and Mechanics of Solids*, 12:183–212, 2007.
- [295] W.H. Press, S.A. Teukolsky, W.T. Vetterling, and B.P. Flannery. *Numerical recipes: The Art of Scientific Computing. Third edition*. Cambridge University Press, 2007.

- [296] T. Suzuki and S. Takeuchi. Correlation of peierls-nabarro stress with crystal structure. *Revue de Physique Appliquee*, 23:685–685, 1988.
- [297] MATLAB. *9.4.0.813654 (R2018a)*. The MathWorks Inc., Natick, Massachusetts, 2018.
- [298] J.K. Mackenzie and M.J. Thomson. Some statistics associated with the random disorientation of cubes. *Biometrika*, 44:205–210, 1957.
- [299] Y. Huang. A user-material subroutine incorporating single crystal plasticity in the abaqus finite element program. *Mech Report, Harvard University*, 178, 1991.
- [300] J.W. Kysar. Addendum to 'a user-material subroutine incorporating single crystal plasticity in the abaqus finite element program, mech report 178'. *Division of Engineering and Applied Sciences, Harvard University*, 1997.
- [301] M. Gupta, R.C. Alderliesten, and R. Benedictus. A review of T-stress and its effects in fracture mechanics. *Engineering Fracture Mechanics*, 134:218–241, 2015.
- [302] A. Stukowski. Visualization and analysis of atomistic simulation data with OVITO – the open visualization tool. *Modelling and Simulation in Materials Science and Engineering*, 18:015012, 2010.
- [303] S.M. Foiles, M.I. Baskes, and M.S. Daw. Embedded-atom-method functions for the fcc metals Cu, Ag, Au, Ni, Pd, Pt, and their alloys. *PHYSICAL REVIEW B*, 33:7983–7991, 1986.
- [304] P.M. Larsen, S. Schmidt, and J. Schiøtz. Robust structural identification via polyhedral template matching. *Modelling and Simulation in Materials Science and Engineering*, 24:055007, 2016.
- [305] A. Stukowski, V.V. Bulatov, and A. Arsenlis. Automated identification and indexing of dislocations in crystal interfaces. *Modelling and Simulation in Materials Science and Engineering*, 20:085007, 2012.
- [306] R.S. Gates. The role of grain boundary dislocations in grain boundary sliding. *Acta Metallurgica*, 21:855–864, 1973.
- [307] J.W. Cahn, Y. Mishin, and A. Suzuki. Coupling grain boundary motion to shear deformation. *Acta Materialia*, 54:4953–4975, 2006.
- [308] S. Berbenni, B. Paliwal, and M. Cherkaoui. A micromechanics-based model for shear-coupled grain boundary migration in bicrystals. *International Journal of Plasticity*, 44:68–94, 2013.



# English abstract

## 1.1 Introduction

The plasticity of crystalline materials results primarily from the movement and the multiplication of dislocations. Dislocations are line defects that were introduced by Volterra [2] at the beginning of the 20th century. Both theoretical and experimental investigations show that the mechanical properties of metals depend on the density, the distribution, the nucleation and the mobility of dislocations as well as the interactions between dislocations and grain boundaries (GBs). This work will focus on slip mechanisms at GBs. Among the different possible mechanisms involving collective dislocation behavior, dislocation pile-ups at GBs and slip transfer will be essentially studied in this PhD thesis from experimental and theoretical viewpoints. In order to do that, dislocation pile-ups are studied both theoretically and experimentally. It aims to computer forces due to dislocation pile-ups that may induce slip transfer and evaluate the effect of anisotropic elasticity. Regarding experiments, an in-situ compression test was performed on the micro-beams with a low strain, then the topography of the external surface containing the slip step height was measured by atomic force microscopy (AFM) which can be used to identify dislocation pile-up and dislocation transmission at GB. In theoretical analysis, the elastic fields due to single dislocation and dislocation pile-up at GB were calculated using a two-dimensional anisotropic elastic theory by considering misorientation, GB thickness and free surfaces effects. At the end, the slip step height was numerically simulated by the presented theory and was compared with experimental observations.

## 1.2 Experiments

The experiments aim to analyze dislocation pile-ups and dislocation transmission in bi-crystals. In order to study these mechanisms, a particular interesting GB was carefully chosen from macro-specimens by Electron Back Scattered Diffraction (EBSD). Then, a micro-beam of bi-crystal containing this GB was realized

by Focused Ion beam (FIB). Afterwards, a micro-pillar compression test was performed on this micro-beam by a flat punch along GB direction with a low strain in order to create a single slip in one grain of the bi-crystals. At the end of the experimental campaign, the topography of the external surface containing the slip step height was measured by AFM.

### 1.2.1 Materials

The materials for this experimental study are Nickel (Ni) with very high purity (99.999%) and  $\alpha$ -Brass (70%Cu-30%Zn, wt%) with impurities (Fe, Pb, P and As, etc.) less than 0.001%. A chemical analysis by energy dispersive spectroscopy (EDX) was performed to check the purity of the samples before and after the preparation procedures. The elastic stiffness moduli of Ni are  $C_{11} = 246.5$  GPa,  $C_{12} = 147.3$  GPa,  $C_{44} = 124.7$  GPa [28] and those of  $\alpha$ -Brass are  $C_{11} = 139.21$  GPa,  $C_{12} = 104.51$  GPa,  $C_{44} = 71.3$  GPa [267, 268]. Thus, these two materials have an elastic anisotropy factor  $A = \frac{2C_{44}}{C_{11} - C_{12}}$  of the order of 2.51 and 4.11, respectively. The chosen materials have different anisotropy factors which can be used to analyze the effects of anisotropic elasticity. In the case of elastic isotropy, the considered elastic constants are  $G = 86.16$  GPa,  $\nu = 0.294$  for Ni and  $G = 40.75$  GPa,  $\nu = 0.343$  for  $\alpha$ -Brass. The latter are deduced from the anisotropic elastic stiffness moduli by applying the Voigt-Reuss-Hill average [269, 270]. Furthermore, the stacking fault energy for  $\alpha$ -Brass and Ni are about 14 mJ/m<sup>2</sup> [271] and 90 mJ/m<sup>2</sup> [272], respectively. The stacking fault energy of  $\alpha$ -Brass is low which promotes planar slip and thus facilitates the observation of slip lines. Although the stacking fault energy of Ni is higher, the planar slip was still observed in Ni bi-crystals during compression tests [137]. Thus, Ni is also suitable for the present experiments.

### 1.2.2 Sample preparation and choice of bi-crystals

The samples, usually in the form of cubes of  $20 \times 20 \times 5$  mm<sup>3</sup>, were cut by electrical discharge machining (EDM) using a bronze wire. Then the six faces of the samples were mechanically polished with coarse abrasive papers up to the particle size index P2500 with water. This polishing phase was followed by a polishing using a diamond suspension of particle sizes 6, 3, and 1 micron on zeta cloth to eliminate hardening and damage achieved during the mechanical polishing, including scratches. At the end, the sample surfaces were finally polished by OP-U-NonDry solution with water on chem-cloth for 5 mins. After the polishing of macro-samples, the thickness was around 2.0 ~ 2.5 mm. With this range of thickness, it is possible to keep GBs relatively perpendicular to the upper surface



thanks to a heat treatment process. Then the polished samples were homogenized by heat treatment. For Ni, the produced samples were homogenized at 1100 °C for three days in a vacuum oven to minimize the risk of contamination and oxidation. However, for  $\alpha$ -Brass, in order to prevent dezincified phenomenon in vacuum environment [273], the heat treatment was realized in argon environment at 980 °C for 1 min with a special sample holder. After heat treatment, the samples were mechanically polished again until getting a “mirror surface”. At the end, the samples were electropolished at a voltage of 24V for 20s. Then the GBs could be clearly observed under optical microscopy.

The orientation of each grain was measured by EBSD in a SEM. It was carried out with a high resolution camera from Oxford Instruments in Zeiss Sigma VP SEM. For the acquisition of the orientation maps, the SEM was set with a 20 kV acceleration voltage, a working distance of 15 mm. Orientation maps were acquired with a spatial step size of 20  $\mu\text{m}$  for macro-samples and of 0.1  $\mu\text{m}$  for micro-samples. Data processing was performed by Flamenco Channel 5 software (HKL Technology) for macro-samples and by AZtec software for micro-samples. The indexing rate was always greater than 99%. The microstructures of the sample were represented by inverse pole figures (IPF) as shown in Figure 1.1. The GBs are marked as black lines in the EBSD orientation mapping and correspond to misorientation angle between adjacent pixels higher than 2°.

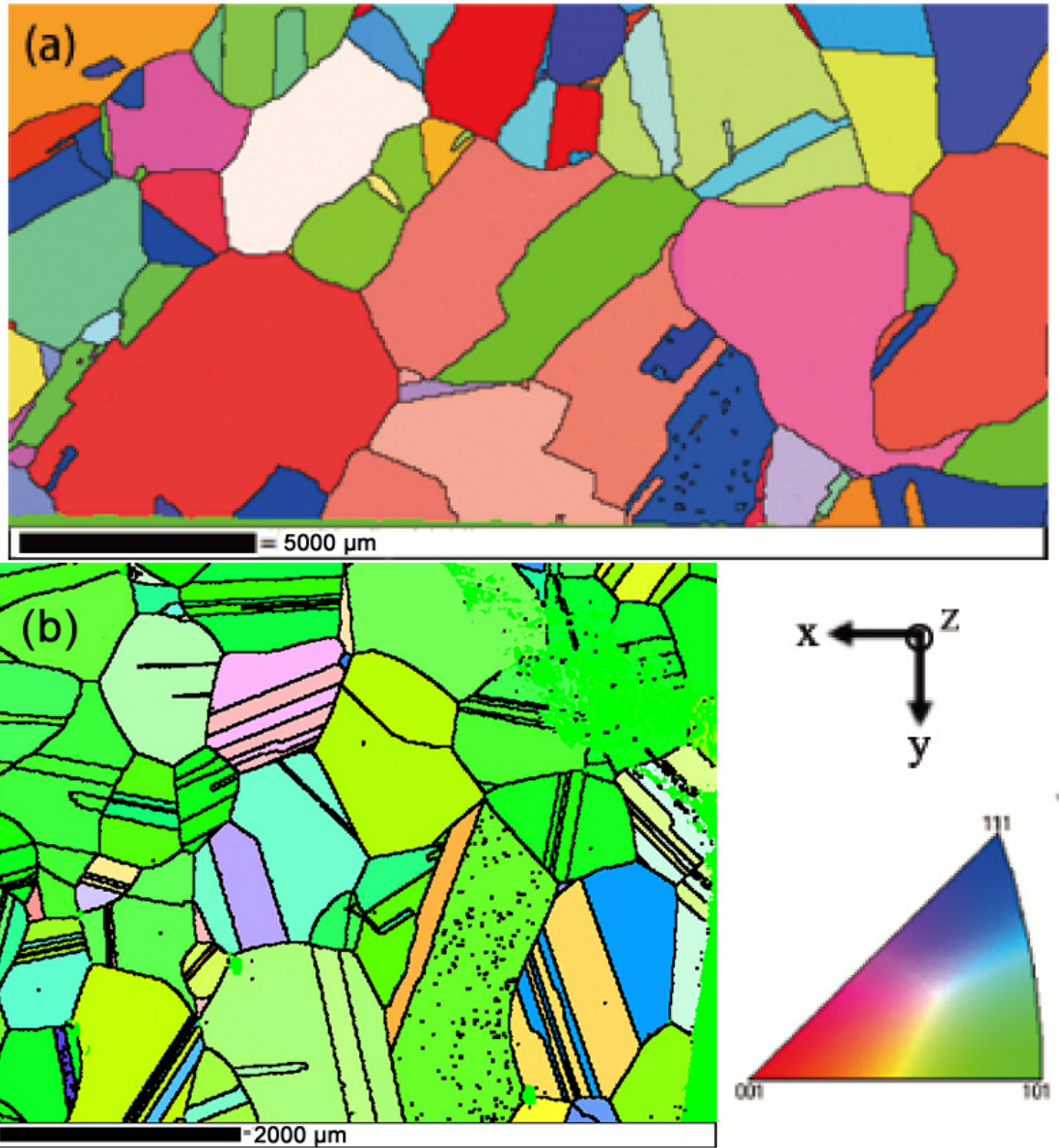


Figure 1.1: EBSD orientation mapping of the macroscopic sample: (a) Ni and (b)  $\alpha$ -Brass. The orientations are given in the IPF in the direction of z axis which is perpendicular to upper surface. The black lines represent GBs and correspond to misorientation angle between adjacent pixels higher than  $2^\circ$ .

Based on the orientation of each grain, the interesting GBs were chosen from the following conditions with the surface configuration is presented in Figure 1.2:

- GB should be, or close to be, perpendicular to upper surface.

- With a mechanical loading parallel to GB plane, for the target grain, the Burgers vector of the slip system with the maximum Schmid factor should not be perpendicular to GB. Meanwhile the slip plane of this slip system should not be parallel to the upper surface. These conditions ensure that the Burgers vector has a component perpendicular to the upper surface where AFM measurements are performed.

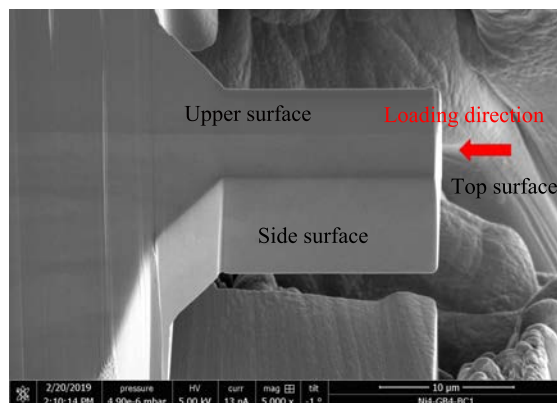


Figure 1.2: The upper surface is defined as the surface containing the GB where AFM measurements are performed. The top surface is the one contacted by plate punch in compression test. The side surface is the lateral surface which does not contain GB.

Then, it is better that the ratio between the maximum Schmid factor and the second maximum Schmid factor is higher than 1.1 in order to get a high probability to only activate single slip at low strain. Furthermore, when considering incompatibility stresses due to heterogeneous anisotropic elasticity [160], the most favourable active slip system can be different from the one predicted by a simple Schmid analysis. This condition can be used to identify the effect of incompatibility stresses. Thus, the twin GB is not used in the present study as there is no incompatibility stresses if type-I twin boundaries are parallel or perpendicular to the loading axis [276]. Based on all the above conditions, several GBs were chosen. However, due to a matter of time, only one GB of each material could be used to analyze the distribution of dislocations in single slip and transmission phenomenon. These GBs are presented in Figure 1.3 and 1.4.

The macro-sample was cut into pieces containing the interesting GBs by EDM. The side surface of small pieces was mechanically polished in order to make the GB close and parallel to side surface which is helpful for FIB cutting. The mechanical polishing was stopped when the distance between GB and side surface was reduced to about 1 mm in order to prevent damage of GB. Then this side surface was polished again by ion slicing technique with low energy  $\text{Ar}^+$  ions in IM4000 system

until the distance from GB to side surface was reduced to about  $40 \mu\text{m}$ . Finally the pre-prepared sample was cut into a micro-beam with length of about  $16 \mu\text{m}$ , width of about  $8 \mu\text{m}$  and thickness of about  $8 \mu\text{m}$  by FIB with FEI Versa 3D Dual Beam system using ion beam currents of  $15 \text{ nA}$  for rough cutting and  $1 \text{ nA}$  at  $30 \text{ kV}$  for fine polishing as shown in Figure 1.3 (c) for Ni and in Figure 1.4 (c) for  $\alpha$ -Brass. The orientation of bi-crystals was measured again by EBSD measurement. The results are presented in Figure 1.3 (a-b) and Figure 1.4 (a-b) for Ni and  $\alpha$ -Brass, respectively.

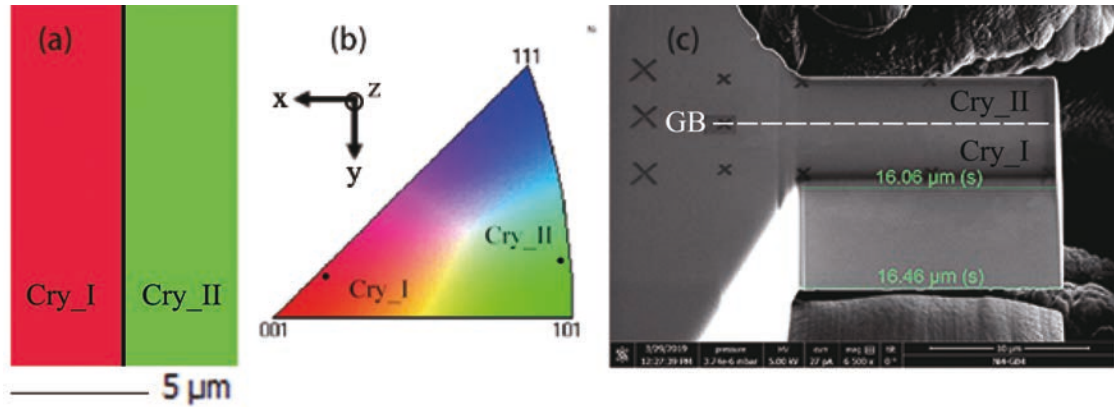


Figure 1.3: (a) EBSD mapping of Ni bi-crystal, orientation of crystal I:  $\phi_1^I = 63.8^\circ$ ,  $\Phi^I = 14.3^\circ$ ,  $\phi_2^I = 18.6^\circ$ , orientation of crystal II:  $\phi_1^{II} = 331.1^\circ$ ,  $\Phi^{II} = 9.0^\circ$ ,  $\phi_2^{II} = 75.1^\circ$ . (b) The crystallographic orientations of both crystals, Cry\_I and Cry\_II, are given on the standard IPF in the direction of y axis which is parallel to GB and is also the loading direction of the compression test. (c) SEM micrograph of a micro-beam containing GB cut by FIB. The average length of micro-beam is about  $15.46 \mu\text{m}$  and the average section area is about  $71.80 \mu\text{m}^2$  with  $46.67 \mu\text{m}^2$  for crystal I and  $25.13 \mu\text{m}^2$  for crystal II.

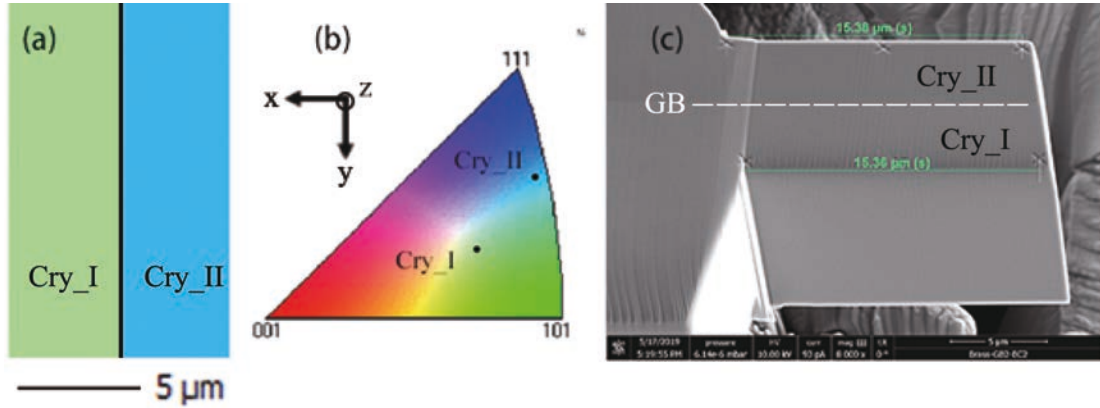


Figure 1.4: (a) EBSD mapping of  $\alpha$ -Brass bi-crystal, orientation of crystal I:  $\phi_1^I = 27.7^\circ$ ,  $\Phi^I = 35.7^\circ$ ,  $\phi_2^I = 66.1^\circ$ , orientation of crystal II:  $\phi_1^{II} = 219.5^\circ$ ,  $\Phi^{II} = 28.4^\circ$ ,  $\phi_2^{II} = 2.4^\circ$ . (b) The crystallographic orientations of both crystals, Cry\_I and Cry\_II, are given on the standard IPF in the direction of y axis which is parallel to GB and is also the loading direction of the compression test. (c) SEM micrograph of a micro-beam containing GB cut by FIB. The average length of micro-beam is about  $15.37 \mu\text{m}$  and the average section area is about  $88.91 \mu\text{m}^2$  with  $42.02 \mu\text{m}^2$  for crystal I and  $46.89 \mu\text{m}^2$  for crystal II.

### 1.2.3 Micro-pillars compression test

The in-situ compression tests were carried out in high vacuum at room temperature in a Carl Zeiss  $\Sigma$ IGMA series scanning electron microscope (SEM), by an in-situ nanoindenter (UNAT-SEM II) which has a load noise floor level about 0.002 mN. The micro-beams were compressed by a flat punch of polycrystalline tungsten carbide (WC). All the compression tests were carried out in displacement controlled mode with several cycles of loading and unloading with small increment. The idea of loading and unloading cycles is to have enough time to make a SEM picture of high quality in order to observe the slip lines. Once slip lines were observed or yield stress was reached, the compression test was stopped during unloading step which prevents the tip shock. The average loading strain rate is about  $0.002 \text{ s}^{-1}$  for Ni and  $0.00125 \text{ s}^{-1}$  for  $\alpha$ -Brass. The mechanical test was stopped when the first slip event was observed. Thus, only the last cycle contributes to plastic deformation, and all the previous cycles are only in the elastic state. According to the raw experimental data, the yield point occurs at about 8.5% strain for Ni and 6.3% for  $\alpha$ -Brass. These strains are too large for yield point of metals. This error comes from the drift of the tip during the compression test, where the displacement measurement is not accurate. However, the force measurement is accurate. Thus, the stress-strain curves were calibrated by a crystal plasticity finite element (CPFEM) simulation as shown in Figure 1.5. The compression tests of the same experimental configuration were performed for both Ni and  $\alpha$ -Brass samples,

then the strain was calibrated by having the same slope of the stress-strain curves in elastic part. Then the yield point occurs at the strain about 0.33% for Ni and 0.24% for  $\alpha$ -Brass which are reasonable for metallic materials. The applied stress at the final state of compression is about 289.4 MPa for Ni and 127.4 MPa for  $\alpha$ -Brass.

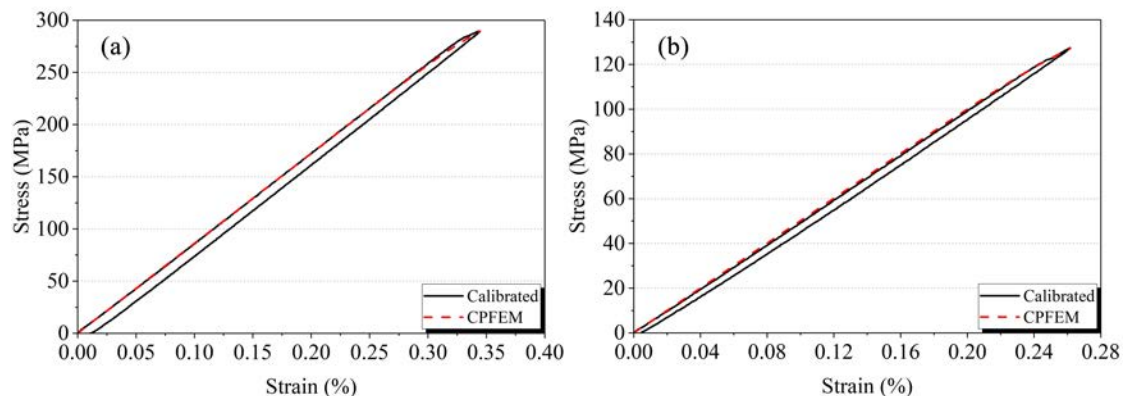


Figure 1.5: Stress-strain curves calibrated by CPFEM for (a) Ni micro-beam and (b)  $\alpha$ -Brass micro-beam.

#### 1.2.4 Slip analyses by AFM

After in-situ compression test, the slip lines were firstly analyzed in SEM. The SEM picture can show the trace of slip line on the upper and side surfaces of micro-beam which can be used to analyze the active slip system based on orientation of each grain. Then, an AFM measurement was performed on the upper surface by Dimension FastScan with ScanAsyst (BRUKER) with height sensor, so that the topography of slip lines can be obtained and used to analyze dislocations distributions. The step size of scan is 30 nm with a scan rate of 1 Hz. The results were analyzed by NanoScope Analysis as shown in Figure 1.6. They were first of all flattened by polynomial fit of the second order, and then they were treated by a median filter with  $9 \times 9$  matrix operation.



Figure 1.6: An example of AFM measurement on the surface of a Ni bi-crystal analyzed by NanoScope Analysis.

## 1.3 Theory

### 1.3.1 2D anisotropic elasticity framework

In order to consider the effect of anisotropic elasticity, the so-called L-E-S (Lekhnitskii [20] - Eshelby [21] - Stroh [22]) analytical formalism for two-dimensional anisotropic elastic problem is used. It is very efficient but it cannot handle the case of a perfectly isotropic crystal since the problem becomes singular due to repeated eigenvalues.

The general solutions for displacement field  $\mathbf{u}$  and stress function vector  $\Phi$  can be calculated by:

$$u_i = 2\text{Re} \left[ A_{i\bar{j}} f_{\bar{j}} \left( z_{\bar{j}} \right) \right] \quad (1.1)$$

$$\Phi_i = 2\text{Re} \left[ B_{i\bar{j}} f_{\bar{j}} \left( z_{\bar{j}} \right) \right] \quad (1.2)$$

where  $\mathbf{A}$  and  $\mathbf{B}$  are  $3 \times 3$  matrix containing the eigenvector components  $a_{k\alpha}$  ( $\alpha = 1, 2, 3$ ),  $B_{ij} = (C_{i2k1} + p_j C_{i2k2}) A_{kj}$  and  $z_j = x_1 + p_j x_2$ .  $p_\alpha$  and  $a_{k\alpha}$  ( $\alpha = 1, 2, 3$ ) denote the eigenvalues and the associated eigenvector components with positive image part of a sextic equation which depends only on the elastic stiffness of the material [21, 22]. Here  $\mathbf{f}$  is a scalar function of  $z$ . Then, the stress fields can be calculated by Hooke's law based on the displacement gradient fields or by stress function vector as following:

$$\sigma_{i1} = -\partial\Phi_i/\partial x_2, \sigma_{i2} = \partial\Phi_i/\partial x_1 \quad (1.3)$$

If needed, component  $\sigma_{33}$  can be computed from the generalized Hooke's law.

The idea of the next sections is to find the expression of the function vector  $\mathbf{f}$  for one single dislocation in different configurations.

### 1.3.2 Dislocation in homogeneous media

In the following, an infinite straight dislocation with Burgers vector  $\mathbf{b}$  and whose line  $\mathbf{t}$  is parallel to the  $\mathbf{x}_3$  direction is considered at the position  $(X_1, X_2)$  as shown in Figure 1.7. Through the paper, the so-called FS/RH (Finish Start/Right Hand) convention [28] is used to define the direction of the dislocation line as shown in Figure 1.7.

In a homogeneous anisotropic medium, the function vector  $\mathbf{f}$  is derived by considering the boundary condition associated to the presence of the dislocation with Burgers vector  $\mathbf{b}$  in the absence of remotely applied force. The displacement and stress function vectors can then be expressed using Eqs. 1.1 and 1.2 with:

$$f_j(z_i) = f_j^0(z_i) = q_j^0 \ln(z_i - s_j) \quad (1.4)$$

where  $z_i = x_1 + p_i x_2$ ,  $s_j = X_1 + p_j X_2$  and  $\mathbf{q}^0$  is a complex vector expressed as  $\mathbf{q}^0 = -\frac{1}{2\pi} \mathbf{i} (\mathbf{B}^T \mathbf{b})$  [19].

### 1.3.3 Dislocation in bi-materials

Let us now consider an anisotropic bi-material (or bi-crystal) with a perfectly bonded interface whose normal is along the  $\mathbf{x}_2$  direction. The dislocation is supposed to be located in the upper material I ( $x_2 > 0$ ) as shown in Figure 1.7.

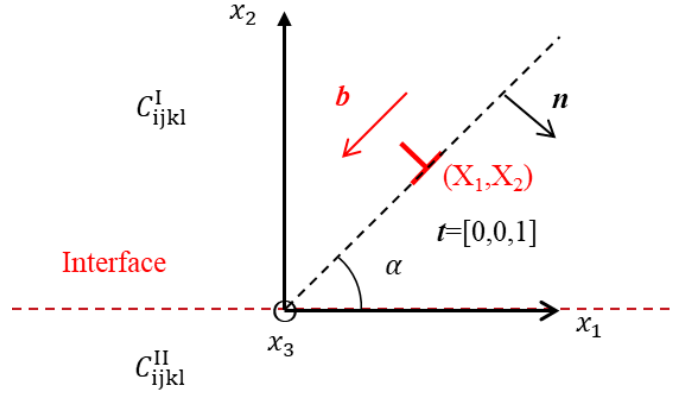


Figure 1.7: Schematic figure of one single infinite straight dislocation in a bi-material.

In addition to the conditions of the homogeneous media case, the function vector  $\mathbf{f}$  should also satisfy the continuity conditions at the perfect interface, i.e. the continuity of displacement  $u_i^I(x_2 = 0^+) = u_i^{II}(x_2 = 0^-)$  and traction vectors  $\sigma_{i2}^I(x_2 = 0^+) = \sigma_{i2}^{II}(x_2 = 0^-)$ . In practice, instead of the continuity of traction



vectors, the continuity of the resultant traction force along an arc of the interface is used. This last condition yields  $\Phi_i^I(x_2 = 0^+) = \Phi_i^II(x_2 = 0^-)$  [19, 292]. Following the Suo's method [19], the solutions are searched in a form similar as Eqs. 1.1 and 1.2:

$$f_j(z_j) = \begin{cases} f_j^0(z_j) + \overline{V_{jk}^{I,II}} \overline{f_k^0}(z_j) & \text{if } z_j \in \text{I} \ (x_2 > 0) \\ \overline{W_{jk}^{I,II}} \overline{f_k^0}(z_j) & \text{if } z_j \in \text{II} \ (x_2 < 0) \end{cases} \quad (1.5)$$

where:

$$\begin{cases} \mathbf{V}^{I,II} = \left( \mathbf{B}^{II} \mathbf{A}^{II-1} \overline{\mathbf{A}^I} - \overline{\mathbf{B}^I} \right)^{-1} \left( \mathbf{B}^I - \mathbf{B}^{II} \mathbf{A}^{II-1} \mathbf{A}^I \right) \\ \mathbf{W}^{I,II} = \left( \overline{\mathbf{B}^I} \mathbf{A}^{I-1} \mathbf{A}^{II} - \mathbf{B}^{II} \right)^{-1} \left( \overline{\mathbf{B}^I} \mathbf{A}^{I-1} \mathbf{A}^I - \mathbf{B}^I \right) \end{cases} \quad (1.6)$$

$f_j^0(z_j)$  is calculated from Eq. 1.4 considering the elastic stiffness tensor  $\mathbf{C}^I$  of the upper material I and  $s_j = s_j^I = X_1 + p_j^I X_2$ . Moreover, it must be noticed that if  $z_j \in \text{I}$ ,  $z_j = z_j^I = x_1 + p_j^I x_2$  and if  $z_j \in \text{II}$ ,  $z_j = z_j^{II} = x_1 + p_j^{II} x_2$ .

Half-space with rigid or free surfaces as special configurations of bi-material, can be easily obtained for  $u_i^I(x_2 = 0) = 0$  or  $\Phi_i^I(x_2 = 0) = 0$  which lead to  $f_j(z_j) = f_j^0(z_j) - A_{jk}^{I-1} \overline{A_{kl}^I} \overline{f_l^0}(z_j)$  for rigid surface and  $f_j(z_j) = f_j^0(z_j) - B_{jk}^{I-1} \overline{B_{kl}^I} \overline{f_l^0}(z_j)$  for free surface.

### 1.3.4 Dislocation in tri-materials

In subsection 1.3.3, the bi-material was regarded as the combination of two materials perfectly bonded to each other through an interface without thickness. In the case where the considered interface is a GB, the real thickness is finite and generally taken about 1 nm using a crude estimation. Hence, it may be interesting to investigate the effect of the thickness of the GB as well as the effect of its elastic stiffness on the elastic fields in a tri-material configuration where the GB is seen as an interphase. Among several studies for multilayered anisotropic elastic media, the method of Choi and Earmme [17] is first applied. Figure 1.8 shows the considered tri-material configuration. There are two planar interfaces  $\Gamma_1$  and  $\Gamma_2$  whose normals are directed along the  $\mathbf{x}_2$  axis. These interfaces are located, respectively, at  $x_2 = h$  and at  $x_2 = -d$ . The interphase (or GB) is the region between  $\Gamma_1$  and  $\Gamma_2$ , thus its thickness is  $H = h + d$ . Material I corresponds to  $x_2 \geq h$ , material II to  $-d < x_2 < h$  and material III to  $x_2 \leq -d$ . All the materials are assumed to be perfectly bonded to each other.

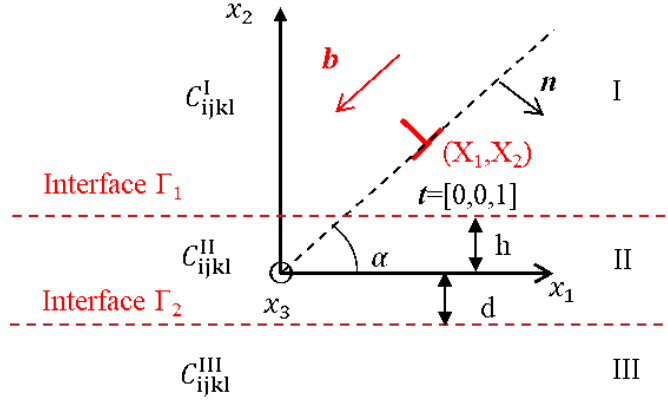


Figure 1.8: Schematic figure of one single infinite straight dislocation in a tri-material with three different stiffness tensors and two perfectly bonded interfaces. The GB region is supposed to be material II.

Choi and Earmme [17] overcame the difficulty of satisfying the continuity of displacements and forces across the two interfaces at the same time by applying the alternating technique, which consists in satisfying alternatively the continuity conditions across each interface until a convergence is obtained. Still considering the case of a dislocation located in the crystal I and by using the same procedure as the one of Choi and Earmme [17], the following series solution is obtained:

$$f_i(z_i) = \begin{cases} f_i^0(z_i) + f_i^{I0}(z_i) + \sum_{\beta=1}^{\infty} f_i^{I\beta}(z_i) & \text{if } z_i \in \text{I} \\ \sum_{\beta=1}^{\infty} f_i^{\beta}(z_i) + \sum_{\beta=1}^{\infty} f_i^{II\beta}(z_i) & \text{if } z_i \in \text{II} \\ \sum_{\beta=1}^{\infty} f_i^{III\beta}(z_i) & \text{if } z_i \in \text{III} \end{cases} \quad (1.7)$$

where:

$$\left\{ \begin{array}{l} f_i^0(z_i) = q_i^0 \ln(z_i - s_i) \\ f_i^{I0}(z_i) = \overline{V_{ij}^{I,II}} \overline{f_j^0} \left( z_i - p_i^I h + \overline{p_j^I} h \right) \\ f_i^{I\beta}(z_i) = W_{ij}^{II,I} \overline{V_{jk}^{II,III}} \overline{f_k^\beta} \left( z_i - p_i^I h + p_j^{II} (h + d) - \overline{p_k^{II}} d \right) \\ f_i^{II\beta}(z_i) = \overline{V_{ij}^{II,III}} \overline{f_j^\beta} \left( z_i + p_i^{II} d - \overline{p_j^{II}} d \right) \\ f_i^{III\beta}(z_i) = W_{ij}^{II,III} \overline{f_j^\beta} \left( z_i + p_i^{III} d - \overline{p_j^{II}} d \right) \\ f_i^\beta(z_i) = \begin{cases} W_{ij}^{I,II} \overline{f_j^0} \left( z_i - p_i^{II} h + \overline{p_j^I} h \right) & \text{if } \beta = 1 \\ \overline{V_{ij}^{II,I}} \overline{V_{jk}^{II,III}} \overline{f_k^{\beta-1}} \left( z_i - p_i^{II} h + \overline{p_j^{II}} (h + d) - \overline{p_k^{II}} d \right) & \text{if } \beta > 1 \end{cases} \end{array} \right. \quad (1.8)$$

In the above equations,  $f_j^0(z_i)$  is associated to crystal I and so  $s_j = s_j^I = X_1 + p_j^I X_2$ . The series solution  $f_i^{I\beta}(z_i)$ ,  $f_i^{II\beta}(z_i)$  and  $f_i^{III\beta}(z_i)$  are all expressed as functions of  $f_j^\beta(z_i)$  which is itself determined by a recurrence equation based on  $f_j^0(z_i)$ .

The above series solutions are proved indeed convergent by Choi and Earmme [17]. The study of the convergence of the series solutions for different GB stiffnesses was explored by using different criteria during this thesis (see Chen et al. [277]).

### 1.3.5 Dislocation in tri-materials with free surfaces

In the nano-mechanical test, especially for micro-beam, there are always free surfaces as shown in Figure 1.2. At small scale, the free surface has an obvious influence on dislocation behavior. Hence besides the interphase, it may be necessary to consider the effect of free surfaces on the elastic fields of multilayers material. The tri-material method of Choi and Earmme [17] can also take into account free surface effects but only in the case of a bi-material with one free surface or a homogeneous material with two free surfaces. In order to handle more complicated cases, like a tri-material with free surfaces, a new method is needed. The image decomposition method inspired from Wang et al. [18] has thus been used. Figure 1.9 (a) shows the configuration of a tri-material with two free surfaces. There are four planar faces whose normals are directed along the  $\mathbf{x}_2$  axis. These faces are located at  $x_2 = 0$ ,  $x_2 = -h_1$ ,  $x_2 = -(h_1 + h_2)$  and  $x_2 = -(h_1 + h_2 + h_3)$  for, respectively upper free surface, first interface, second interface and bottom free surface. The interphase (or GB) is located in the second layer of thickness  $h_2$ . Material I corresponds to  $-h_1 < x_2 < 0$ , material II to  $-(h_1 + h_2) < x_2 < -h_1$  and material III to  $-(h_1 + h_2 + h_3) < x_2 < -(h_1 + h_2)$ . Thus, the thickness of the whole material is marked as  $H' = h_1 + h_2 + h_3$ . All the materials are assumed to be perfectly bonded to each other. In order to discuss the effects of both surfaces, the free surface on the side of the crystal containing the dislocations is referred to be the first free surface, and the another one is called second free surface.

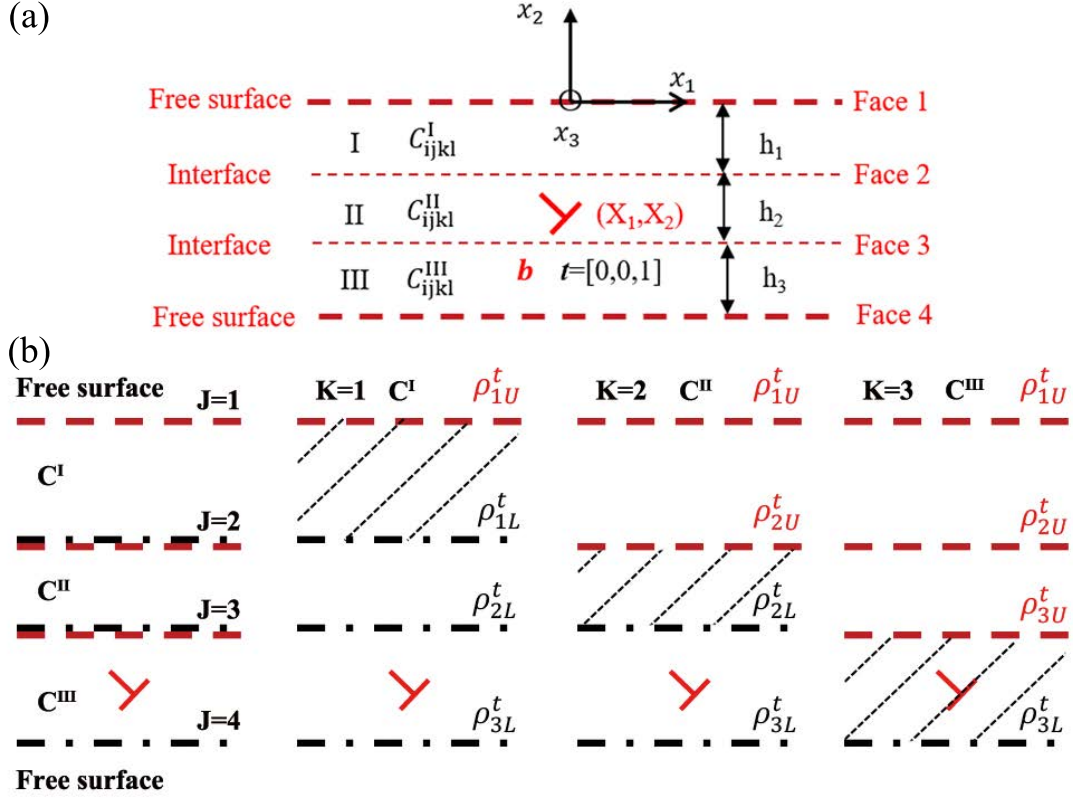


Figure 1.9: (a) Schematic figure of one single infinite straight dislocation in a tri-material with three different stiffness tensors, two planar free surfaces at faces 1 and 4 and two perfectly bonded interfaces at faces 2 and 3. The GB region is supposed to be material II. (b) Decomposition of a 3 layers problem (left) with 2 free surfaces and 2 interfaces into three infinite homogeneous subproblems. Dislocation source is marked with a red dislocation symbol.

In the 3-multilayers configuration with free surfaces, there are 2 interfaces that must satisfied the continuum conditions of perfectly bonded interfaces, and two free surfaces that must satisfied the traction free condition. For a multilayer system, it is too complicated to use the alternating technique. Wang et al. [18] have proposed an image decomposition method, which can be used to satisfy all the boundary conditions at the same time. The principle of this method is to decompose the multilayers problem into several subproblems of infinite homogeneous medium for each material. Two types of image dislocation densities are distributed on each interface while one image dislocation density is distributed on the surface as shown in Figure 1.9 (b) (left). The densities of these image dislocations are denoted  $\rho^t$ , where  $t=1,2$  and 3 denote the  $x_1$ -,  $x_2$ - and  $x_3$ -components, respectively. These densities can be resolved at the same time by considering all boundary conditions: the continuity of tangential gradient of displacements and tractions across interfaces, traction free for free surfaces or tangential gradient of displacement free for

rigid surfaces. Thus, for the present 3-multilayers configuration with free surfaces, it is decomposed into 3 subproblems and there are a total of 18 boundary conditions. The elastic fields in each layer are determined by summing the contributions of the dislocation source and all the corresponding image dislocations as shown in Figure 1.9 (b) (right). Based on consistency requirement fully discussed by Wang et al. [18], the image dislocation densities in the three subproblems are:  $\rho_{J_1}^t = \{\rho_{1U}^t, \rho_{1L}^t, \rho_{2L}^t, \rho_{3L}^t\}$  for the first subproblem,  $\rho_{J_2}^t = \{\rho_{1U}^t, \rho_{2U}^t, \rho_{2L}^t, \rho_{3L}^t\}$  for the second subproblem and  $\rho_{J_3}^t = \{\rho_{1U}^t, \rho_{2U}^t, \rho_{3U}^t, \rho_{3L}^t\}$  for the third subproblem as shown in Figure 1.9 (b) (right).

Based on Stroh's formalism, the stress and displacement gradient fields due to a mixed dislocation with Burgers vector components  $b_t$  ( $t = 1, 2, 3$ ) located at  $(x_{1s}, x_{2s})$  in a homogeneous anisotropic solid can be written as [28, 18]:

$$\begin{aligned} \sigma_{ij}(K, b_t, \Delta x_1, \Delta x_2) = \\ 2 [\xi_{K\alpha ij}^{tR} P(\Delta x_1, p_{K\alpha}^R \Delta x_2, p_{K\alpha}^I \Delta x_2) + \xi_{K\alpha ij}^{tI} Q(\Delta x_1, p_{K\alpha}^R \Delta x_2, p_{K\alpha}^I \Delta x_2)] b_t \end{aligned} \quad (1.9)$$

$$\begin{aligned} \frac{\partial u_i}{\partial x_j}(K, b_t, \Delta x_1, \Delta x_2) = \\ 2 [\zeta_{K\alpha ij}^{tR} P(\Delta x_1, p_{K\alpha}^R \Delta x_2, p_{K\alpha}^I \Delta x_2) + \zeta_{K\alpha ij}^{tI} Q(\Delta x_1, p_{K\alpha}^R \Delta x_2, p_{K\alpha}^I \Delta x_2)] b_t \end{aligned} \quad (1.10)$$

where  $\Delta x_1 = x_1 - x_{1s}$  and  $\Delta x_2 = x_2 - x_{2s}$ , the superscript  $R$  and  $I$  indicate the real and imaginary parts of each term, respectively. Meanwhile the subscript  $K$  indicates which subproblem is considered (no sum over  $K$ ). The definition of the symbols  $\xi_{K\alpha ij}^t$ ,  $\zeta_{K\alpha ij}^t$  and the functions  $P$ ,  $Q$  [18] are:

$$\begin{cases} \xi_{K\alpha ij}^t = \frac{C_{Kijkl}(\delta_{l1} + p_{K\alpha} \delta_{l2}) A_{Kk\alpha} B_{Kt\alpha}}{2\pi \mathbf{i}} \\ \zeta_{K\alpha ij}^t = \frac{(\delta_{j1} + p_{K\alpha} \delta_{j2}) A_{Kt\alpha} B_{Kt\alpha}}{2\pi \mathbf{i}} \end{cases} \quad (1.11)$$

$$\begin{cases} P(x_1 - x_{1s}, a, b) = \frac{x_1 - x_{1s} + a}{(x_1 - x_{1s} + a)^2 + b^2} \\ Q(x_1 - x_{1s}, a, b) = \frac{b}{(x_1 - x_{1s} + a)^2 + b^2} \end{cases} \quad (1.12)$$

where  $p_\alpha$ ,  $A_{k\alpha}$  and  $B_{t\alpha}$  with  $\alpha=1,2$  and  $3$  denote the same eigenvalues and eigenvectors in Stroh's sextic formulation as discussed in section 1.3.1. These two expressions 1.9 and 1.10 of the single-crystal are equivalence to the Eqs. 1.1, 1.2 and 1.4 which can be analytically derived from each other.

The contribution of image dislocations on elastic fields can be calculated by replacing the Burgers vector  $b_t$  by  $\rho_{JK}^t(x'_1)$  and integrating from  $x'_1 = -\infty$  to  $x'_1 = +\infty$  in Eqs. 1.9 and 1.10:

$$\begin{aligned}
\sigma_{ij} (K, \rho_{JK}^t, \Delta x_1, \Delta x_2) &= \\
&\int_{-\infty}^{+\infty} 2 [\zeta_{K\alpha ij}^{tR} P (\Delta x_1, p_{K\alpha}^R \Delta x_2, p_{K\alpha}^I \Delta x_2) + \zeta_{K\alpha ij}^{tI} Q (\Delta x_1, p_{K\alpha}^R \Delta x_2, p_{K\alpha}^I \Delta x_2)] \rho_{JK}^t (x'_1) dx'_1 \\
&= 2\pi [\zeta_{K\alpha ij}^{tR} H (p_{K\alpha}^R \Delta x_2, p_{K\alpha}^I \Delta x_2) + \zeta_{K\alpha ij}^{tI} I (p_{K\alpha}^R \Delta x_2, p_{K\alpha}^I \Delta x_2)] [\rho_{JK}^t (x_1)]
\end{aligned} \tag{1.13}$$

$$\begin{aligned}
\frac{\partial u_i}{\partial x_j} (K, \rho_{JK}^t, \Delta x_1, \Delta x_2) &= \\
&\int_{-\infty}^{+\infty} 2 [\zeta_{K\alpha ij}^{tR} P (\Delta x_1, p_{K\alpha}^R \Delta x_2, p_{K\alpha}^I \Delta x_2) + \zeta_{K\alpha ij}^{tI} Q (\Delta x_1, p_{K\alpha}^R \Delta x_2, p_{K\alpha}^I \Delta x_2)] \rho_{JK}^t (x'_1) dx'_1 \\
&= 2\pi [\zeta_{K\alpha ij}^{tR} H (p_{K\alpha}^R \Delta x_2, p_{K\alpha}^I \Delta x_2) + \zeta_{K\alpha ij}^{tI} I (p_{K\alpha}^R \Delta x_2, p_{K\alpha}^I \Delta x_2)] [\rho_{JK}^t (x_1)]
\end{aligned} \tag{1.14}$$

where  $\Delta x_1 = x_1 - x'_1$ ,  $\Delta x_2 = x_2 - x'_2$  and  $(x'_1, x'_2)$  denote the positions of image dislocations. The definitions of operators  $H$  and  $I$  are:

$$\begin{cases} H(a, b) [\rho(x_1)] = \frac{1}{\pi} \int_{-\infty}^{\infty} P(x_1 - x'_1, a, b) \cdot \rho(x'_1) dx'_1 \\ I(a, b) [\rho(x_1)] = \frac{1}{\pi} \int_{-\infty}^{\infty} Q(x_1 - x'_1, a, b) \cdot \rho(x'_1) dx'_1 \end{cases} \tag{1.15}$$

Combining all 18 boundary conditions, after removing the singularity term by  $H$  and  $I$  operators, a system of nonlinear equations is formed with 18 Fredholm equations of second kind ( $t = 1, 2$  and  $3$ ) with 18 unknowns  $\boldsymbol{\rho} = [\rho_{1U}^t, \rho_{1L}^t, \rho_{2U}^t, \rho_{2L}^t, \rho_{3U}^t, \rho_{3L}^t]^T$  as shown below:

$$\begin{aligned}
(\mathbf{C} + \mathbf{C}_0 \mathbf{C}^{-1} \mathbf{C}_0) \boldsymbol{\rho} + (\mathbf{C}_H \mathbf{H} + \mathbf{C}_I \mathbf{I} - \mathbf{C}_0 \mathbf{C}^{-1} \mathbf{C}_H \mathbf{H}_0 \mathbf{H} - \mathbf{C}_0 \mathbf{C}^{-1} \mathbf{C}_I \mathbf{H}_0 \mathbf{I}) \boldsymbol{\rho} \\
= -\mathbf{C}_R \mathbf{R} + \mathbf{C}_0 \mathbf{C}^{-1} \mathbf{C}_R \mathbf{H}_0 \mathbf{R}
\end{aligned} \tag{1.16}$$

where  $\mathbf{C}_H \mathbf{H}$ ,  $\mathbf{C}_I \mathbf{I}$ ,  $\mathbf{C}_H \mathbf{H}_0 \mathbf{H}$ ,  $\mathbf{C}_I \mathbf{H}_0 \mathbf{I}$  are the matrices of integral operator for the densities of image dislocations  $\boldsymbol{\rho}$  and  $\mathbf{C}$ ,  $\mathbf{C}_0$  are the matrices of coefficient only depending on material property. All the components of these matrices can be found in Appendix B. These unknowns can be numerically resolved by using Gauss-Hermite quadrature with Hermite polynomials. After replacing the integration of  $\boldsymbol{\rho}$ , the analytical expression of  $\boldsymbol{\rho}$  can be obtained as a function of  $x_1$ . Finally, the elastic fields, such as stresses fields due to one single dislocation in a three layers anisotropic material at any points can be calculated based on Eqs. 1.9 and 1.13.

In the present thesis, the three-layers configuration is used to consider both effects of GB stiffness and free surfaces for the simulation of the experiments in

section 1.6. Thus, the second layer is regarded as GB and the thickness is set as about 1nm. Meanwhile the two-layers configuration is used to investigate the effect of free surfaces which will be applied in section 1.4.

### **1.3.6 Application to discrete dislocation pile-up**

Let us consider a single dislocation pile-up of N infinite straight dislocations, which are all parallel to the  $\boldsymbol{x}_3$  axis, have the same Burgers  $\boldsymbol{b}$  and lie in the same slip plane as shown in Figure 1.10.

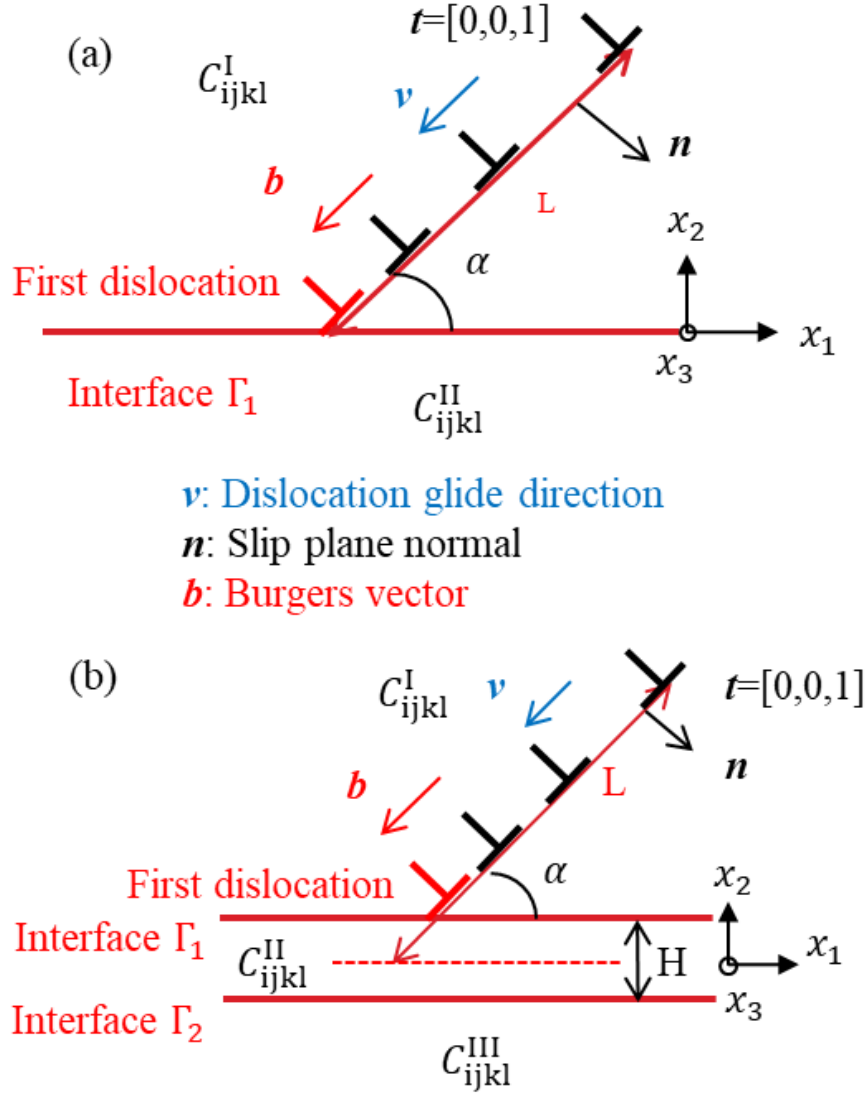


Figure 1.10:  $\alpha$ -inclined dislocation pile-ups in slip plane of unit normal  $\mathbf{n}$  for  $N$  edge dislocations with Burgers vector  $\mathbf{b}$  and line vector  $\mathbf{t}$  in a heterogeneous anisotropic (a) bi-material and (b) tri-material.

The equilibrium positions of the  $N$  dislocations can be found out by minimizing the component of the Peach-Koehler (P-K) force along the slip direction for each dislocation to a critical force denoted  $F_c$  as follows:

$$F^{(\gamma)} = \text{abs}(\{(\boldsymbol{\sigma}_{int}(X_1(\gamma), X_2(\gamma)) + \boldsymbol{\sigma}_{ext}) \cdot \mathbf{b} \times \mathbf{t}\} \cdot \mathbf{v}) \stackrel{\text{Minimize}}{=} F_c \quad (1.17)$$

where  $(X_1(\gamma), X_2(\gamma))$  denotes the position of the  $\gamma^{th}$  dislocation.  $\boldsymbol{\sigma}_{ext}$  is a homogeneous applied stress tensor and  $\boldsymbol{\sigma}_{int} = \boldsymbol{\sigma}_{im} + \boldsymbol{\sigma}_{dis}$  is the internal stress tensor



produced by all the others dislocations  $\sigma_{dis}$  based on the expressions derived in the previous subsections and image stresses  $\sigma_{im}$  on this dislocation coming from all the heterogeneities. The critical force  $F_c$  includes the lattice friction force (primary) and other interactive forces on dislocation, such as the interactive force with cavities, etc. Meanwhile, this critical force can be converted into a critical shear stress on a dislocation by dividing the length of standard Burgers vector as  $\tau_c = F_c/|\mathbf{b}|$ . It should be pointed out that in the present work, the applied homogeneous stress tensor  $\sigma_{ext}$  has only for objective to equilibrate the dislocation pile-up. The calculation of the dislocation pile-ups equilibrium positions is thus obtained by following an iterative relaxation scheme that minimizes all the  $F^{(\gamma)}$  after an initial configuration is specified [105]. In order to be able to perform such a computation in an infinite homogeneous medium, one dislocation should be considered as locked. Usually, the position of the first (or leading) dislocation ( $X_1(1), X_2(1)$ ) is fixed [97, 105]. As a result, the P-K force on the fixed dislocation is not zero. In an heterogeneous medium, the boundary image force on the leading dislocation may equilibrate the applied stress and the stress contribution coming from the other dislocations [105], but only in case of repulsive image forces. In such case, all the dislocation positions, including the leading one, could be found by the iterative relaxation scheme. Most researchers assume  $F_c = 0$  N/m because of low value of the lattice friction stress in pure FCC crystal which is around  $1 \sim 2$  MPa [296]. However, in the present thesis, it is found that a non zero critical force has a crucial effect on dislocation behavior in the presence of GB and free surfaces. The reason is that there are already lattice defects in the material after sample preparation, such as defects due to the  $\text{Ga}^+$  ions from FIB close to the surface [139]. Furthermore, for  $\alpha$ -Brass as an alloy, the theoretical value of the friction force is much higher than pure FCC crystals, like pure Ni. For example, it was found that  $\tau_c \approx 80 \sim 100$  MPa for  $\beta$ -Brass [296]. Thus, the critical force cannot be ignored in Eq. 1.17 for realistic calculations.

## 1.4 Preliminary theoretical results and discussions with single dislocation and dislocation pile-ups for Ni bi-crystals

In order to estimate the effect of several crucial microstructural factors, such as the misorientation, the GB stiffness and the free surface, several simulations with ideal conditions (theoretical study) have been first summarized below. More results are presented in the paper by Chen et al. [277].

In all the following numerical applications, Ni bi-crystals of different orientations are considered. Furthermore, only edge dislocations with Burgers vector

defined by an angle  $\alpha = 45^\circ$  are considered as shown in Figure 1.7, so that the slip direction is  $\mathbf{m} = \mathbf{b}/|\mathbf{b}| = [-\cos 45^\circ, -\sin 45^\circ, 0]$  in global frame  $(\mathbf{x}_1, \mathbf{x}_2, \mathbf{x}_3)$ . Still following the FS/RH convention, the slip plane normal is given by  $\mathbf{n} = \mathbf{t} \times \mathbf{m}$  where  $\mathbf{t} = [0, 0, 1]$ . Meanwhile, the glide direction of dislocations  $\mathbf{v}$  is parallel to  $\mathbf{m}$  for edge dislocations and it always points towards the GB area, so that it is possible to create dislocation pile-ups at GB. The slip system is supposed to be  $\mathbf{m}^0 = 1/\sqrt{2}[1, 1, 0]$  and  $\mathbf{n}^0 = 1/\sqrt{3}[-1, 1, -1]$  in the crystal's frame  $(\mathbf{e}_1, \mathbf{e}_2, \mathbf{e}_3)$ . Thus, the orientation of the crystal containing dislocations is defined by the transformation matrix  $\mathbf{T}$  such that  $[\mathbf{m}, \mathbf{n}, \mathbf{t}]^T = \mathbf{T}[\mathbf{m}^0, \mathbf{n}^0, \mathbf{t}^0]^T$ , where  $\mathbf{t}^0 = \mathbf{m}^0 \times \mathbf{n}^0$ . Two specific orientations are considered in the following:

- orientation A<sup>Ori</sup> with  $\mathbf{T}_A = \begin{bmatrix} 1 & 0 & 0 \\ 0 & 1 & 0 \\ 0 & 0 & 1 \end{bmatrix}$  (Unit matrix)
- orientation B<sup>Ori</sup> with  $\mathbf{T}_B = \begin{bmatrix} -1/2 & \sqrt{2}/2 & 1/2 \\ -1/2 & -\sqrt{2}/2 & 1/2 \\ \sqrt{2}/2 & 0 & \sqrt{2}/2 \end{bmatrix}$

The elastic stiffness tensor in the global frame is then deduced from the transformation matrix  $\mathbf{T}$  by  $C_{ijkl} = T_{ig}T_{jh}C_{ghmn}^0T_{km}T_{ln}$  where  $\mathbf{C}^0$  is the elastic stiffness tensor defined in the crystal's frame. For tri-material and multilayers model, the thickness of the second material as GB is denoted  $H$  which is always equal to  $5|\mathbf{b}|$  in the present section, and its elastic stiffness tensor  $C_{ijkl}^{\text{II}}$  is simply modeled thanks to a single parameter  $\lambda$  which reflects the GB stiffness as:

$$C_{ijkl}^{\text{II}} = \frac{\lambda}{2} (C_{ijkl}^{\text{I}} + C_{ijkl}^{\text{III}}) \quad (1.18)$$

Then the GB is softer than the grains when  $\lambda < 1$  and stiffer than the grains for  $\lambda > 1$ .

For multilayers model with free surfaces, only two-layers configuration is applied in the present section 1.4 with  $h_1 = h_2 = H'/2$ , so that the GB is regarded as an interface with no thickness.

The distance between the GB (or the middle of the GB region) and the  $\gamma^{\text{th}}$  dislocation along the glide direction is denoted  $L(\gamma)$ . For dislocation pile-ups, when the leading dislocation is locked  $L(1) = 5|\mathbf{b}|$  and the pile-up length is defined as the distance between the first and the last dislocation  $L(N) - L(1)$ .

In a heterogeneous medium, an image force is exerted on the dislocation due to the presence of interface(s) or surface(s). The image force is the Peach-Koehler

force at the dislocation position due to its stress field without considering the contribution related to the infinite homogeneous medium, denoted hereafter  $\sigma_{im}$ . The projection of the image force along slip direction reduces to [28]:

$$F_{im} = [(\sigma_{im} \cdot \mathbf{b}) \times \mathbf{t}] \cdot \mathbf{v} \quad (1.19)$$

With the convention used in Figure 1.7, as  $\mathbf{v}$  always points towards to the GB,  $F_{im} > 0$  means that the dislocation is attracted by the GB whereas  $F_{im} < 0$  means that the dislocation is repelled by the GB.

Hereafter, the misorientation effect and the GB stiffness are firstly studied. Both orientations  $A^{Ori}$  and  $B^{Ori}$  are considered for the lower crystal of a bi-material and two different  $\lambda$  values 0.5 and 2, in the case of the tri-material model. The effect of elastic anisotropy vs. isotropy on the projected image forces along the slip direction in bi-material, half space and tri-material configurations are presented in Figure 1.11. Hereafter are the conclusions of this theoretical study, see Chen et al. [277] for more details:

- Orientation  $A^{Ori}$  exerts an attractive effect on the dislocation, whereas with orientation  $B^{Ori}$ , the dislocation is repelled by the GB.
- In a half space, a rigid surface has always a repulsive effect on the dislocation and on the contrary, a free surface has always an attractive effect. It can be also noticed that the magnitude of  $F_{im}$  is far larger for the half space than for the bi-material or tri-material configuration. Besides, considering isotropic elasticity in half-spaces have nearly the same magnitude of  $F_{im}$  as considering anisotropic elasticity.
- A softer GB with  $\lambda = 0.5$  (more compliant interphase) exerts an attractive effect on the dislocation, whereas a stiffer GB with  $\lambda = 2$  (more rigid interphase) presents a repulsive effect on dislocation.
- In the case of anisotropic elasticity, there is an equilibrium position for dislocation where  $F_{im}$  exhibits a sign change because of the coupled effects of the image forces arising both from the lower crystal and the GB with inverse effect, such as  $A^{Ori}$  with  $\lambda = 2$  or  $B^{Ori}$  with  $\lambda = 0.5$ . When the lower crystal and GB have the same effect, their effect will be reinforced. The acting distance of rigid/free surface is larger than misorientation effect.
- The acting distance of GB stiffness is quite short with about  $41 |\mathbf{b}|$  and  $58 |\mathbf{b}|$  for the larger contrast  $\lambda = 2$  and  $\lambda = 0.5$ , respectively. However, it is important in order to be able to equilibrate the leading dislocation of the pile-up. Beyond these distance, the image force is mainly dependent on bi-crystals misorientation.

- For isotropic tri-material configuration, because of no misorientation effect coming from lower crystal, the image force depends only on GB stiffness.

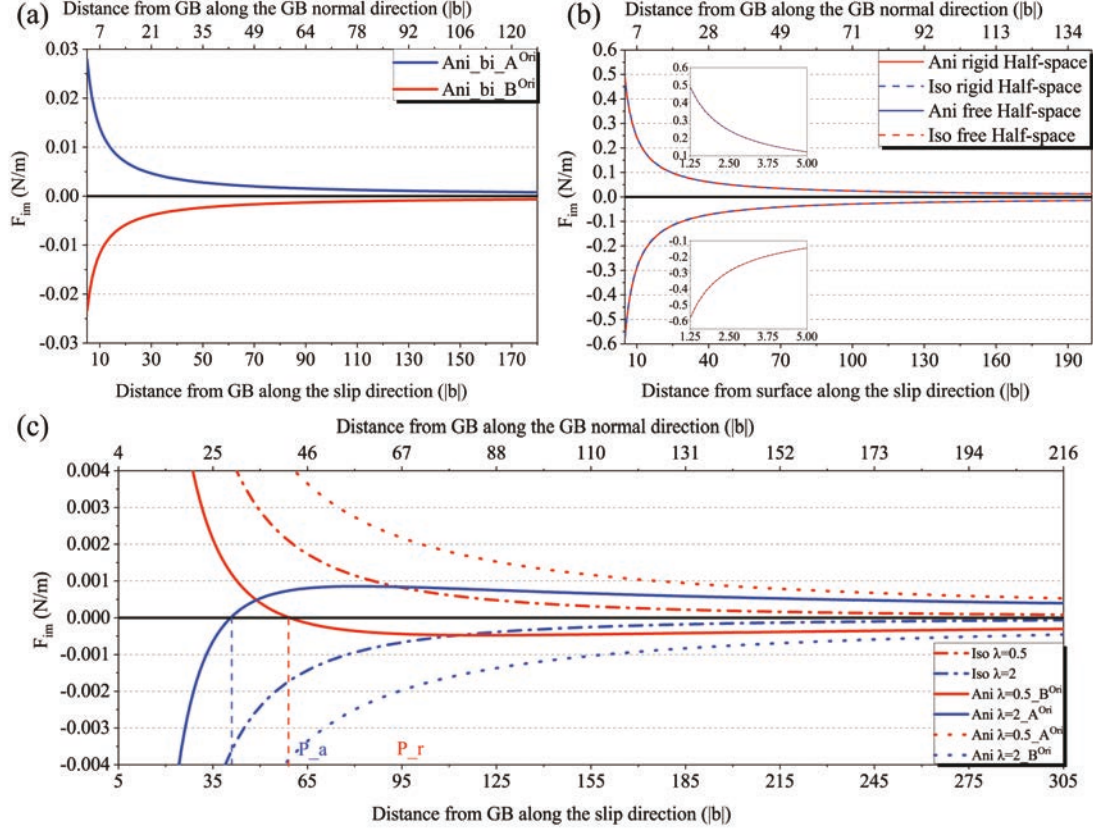


Figure 1.11: Variation of the projected image force  $F_{im}$  with the distance from the GB along the slip direction for different configurations: (a) bi-material configurations, (b) half space configuration and (c) tri-material configurations with anisotropic vs. isotropic elasticity.

Besides the effect of misorientation and GB stiffness, the effect of free surfaces on image force has been theoretically investigated considering a two-layers configuration with different misorientations  $A^{Ori}$ ,  $B^{Ori}$  and different thickness  $H' = 2\mu\text{m}$ ,  $H' = 4\mu\text{m}$ . The results of projected image forces along the slip direction are presented in Figure 1.12. The conclusions are listed below:

- Free surfaces have a strong attractive effect on dislocations. Compared with free surface effect, the effect of misorientation is negligible close to free surface as the P-K force here is quite similar whatever the orientation.
- Close to GB, the image force is mainly controlled by misorientation. Indeed, the two free surfaces have an opposite effect on the dislocation. When the

dislocation lies about an equal distance from the two free surfaces, their contribution becomes negligible.

- A size effect is found after normalizing the distance by the half of thickness: at the same relative distance from the GB, the image force is stronger in the smaller beam.
- Combined with attractive misorientation  $A^{\text{Ori}}$ , there is an equilibrium point where the image force on the dislocation is zero. This position is located at nearly the same relative distance from GB for different thicknesses of material.

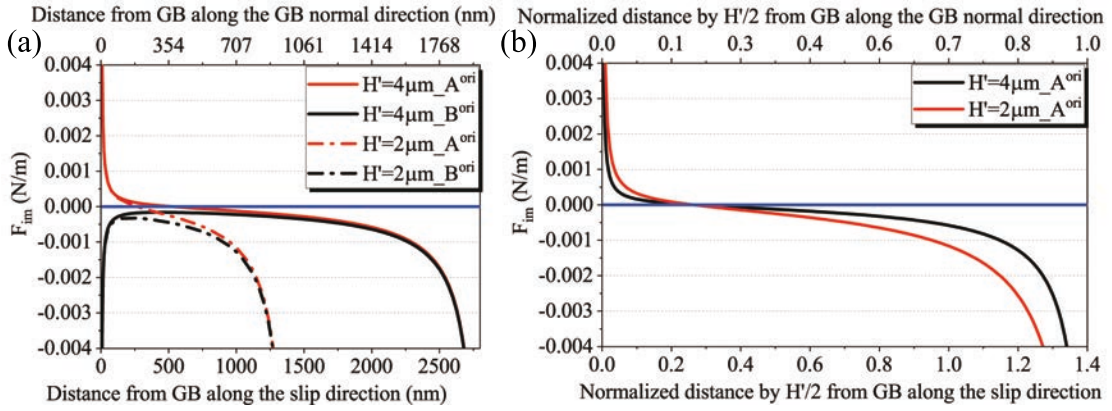


Figure 1.12: Variation of the projected image force  $F_{\text{im}}$  for two-layers model in different thickness (a) with the distance from the GB along the slip direction and (b) with the normalized distance by  $H'/2$  from GB along the slip direction.

Since the orientation of lower crystal has a stronger effect on dislocations at long distance than GB stiffness, here the length of dislocation pile-ups  $L$  with the different orientations of lower crystal is presented in Figure 1.13 in the case of a pile-up with 50 dislocations and a zero thickness GB. The orientation of the upper crystal (where there is the pile-up) is fixed, still defined by  $\alpha = 45^\circ$ , whereas the orientation of lower crystal is given by a rotation  $\psi$  around  $\mathbf{v}$  from  $\psi = 0^\circ$  to  $\psi = 180^\circ$ . In order to always get a stable dislocation pile-up configuration (especially in the case of attractive misorientation), the leading dislocation is always locked to give enough repulsive force on all dislocations. Hence, the homogeneous single crystal case is retrieved for  $\psi = 0^\circ$  and  $\psi = 180^\circ$  for which  $L = 8.75 \mu\text{m}$  (Figure 1.13 (a)). When  $L$  is smaller (resp. larger) than  $8.75 \mu\text{m}$ , the image force has globally an attractive (resp. repulsive) effect on the pile-up which is shown in Figure 1.13 (b). The misorientation angle between both crystals, i.e. the minimum rotation angle to get from one crystal orientation to the other is also presented in

Figure 1.13 (a). In the present example, the maximal possible value for misorientation angle in cubic crystal,  $62.8^\circ$  [298], is almost reached but does not correspond to an extremal value of  $L$ . The maximal value of  $L$  corresponds however to a high misorientation angle (about  $60^\circ$ ). Furthermore, it is noteworthy that a same misorientation angle can be related to different elastic behaviors (for example,  $60^\circ$  is retrieved with  $\psi = 60^\circ$  and  $\psi = 120^\circ$ , which give  $L = 9.02 \mu\text{m}$  and  $L = 8.61 \mu\text{m}$ , respectively). Finally, it can be observed that the relative variations of  $L$  compared to isotropic case in Ni can reach about 7%. The important point is that such significant variations occur in a moderately elastic anisotropic material and cannot be captured considering pile-ups in isotropic elasticity. However, by using Voigt-Reuss-Hill average [269, 270], the value of  $L$  given by isotropic elasticity is nearly the average length considering the anisotropic elasticity with the present rotation configuration (see Figure 1.13 (a)). Furthermore, this maximum relative variation of  $L$  for different materials with different anisotropic factors (Zener ratios) are presented in Table 1.1. It increases as the anisotropic factor increases which reflects the anisotropic effect. As the effect of rigid half space is much stronger than misorientation effect, both  $L$  and  $F_{im}$  are much larger for rigid half space configuration than for bi-material configuration with different misorientations.

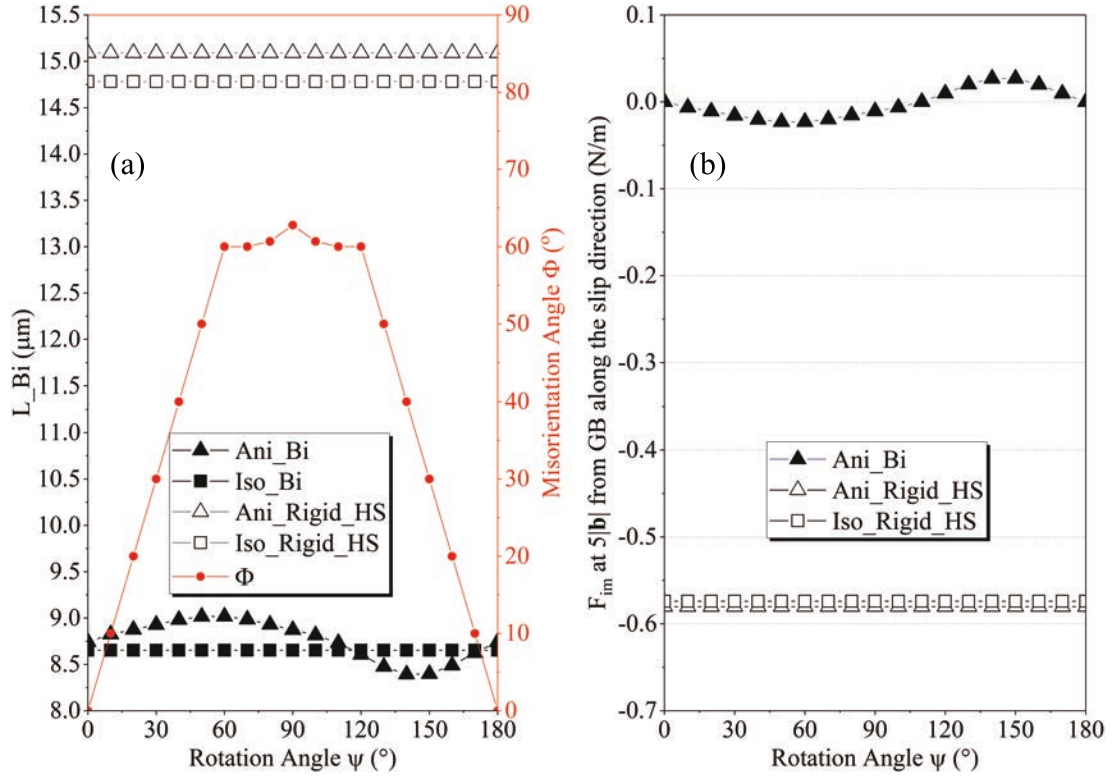


Figure 1.13: Misorientation effect in the case of bi-crystals (Ani\_Bi) on (a) pile-up length  $L$  for a pile-up with 50 dislocations and a zero thickness GB and (b) projected image force along slip direction at a distance  $5|\mathbf{b}|$  from GB. The rotation axis is the slide direction  $\mathbf{v}$ . Comparisons with the cases of homogeneous isotropic case (Iso\_Bi), isotropic rigid half-space (Iso\_Half space) and the anisotropic rigid half-space (Ani\_Half space).

Material	Al	Ni	Cu	$\alpha$ -Brass
Zener ratio <sup>[1]</sup>	1.22	2.51	3.21	4.11
Maximum relative variation of $L$ (%)	1.2	7.2	9.0	11.5

Table 1.1: Maximum relative variation of  $L$  with anisotropic elasticity compared to isotropic elasticity for different materials with different anisotropic factors (Zener ratios). <sup>[1]</sup> Elastic stiffness moduli of these materials are found in the book “Theory of Dislocations” <sup>[28]</sup>.

## 1.5 Experimental results for Ni and $\alpha$ -Brass bi-crystals

First of all, the slip lines were observed by SEM for Ni (see Figure 1.14 (a)) and for  $\alpha$ -Brass (see Figure 1.15 (a)). For Ni, the slip lines are very weak on the upper surface and there are only two obvious slip lines in parallel for each crystal. Based on the direction of slip lines on the upper surface and the Schmid factor analysis with local crystalline orientation, the active slip system is determined to be the slip system with maximum Schmid factor or result from incompatibility stress [160]. The B4 slip system is seen to be the active system using Schmid and Boas's convention [40] for each crystal as shown in Figure 1.14 (b).

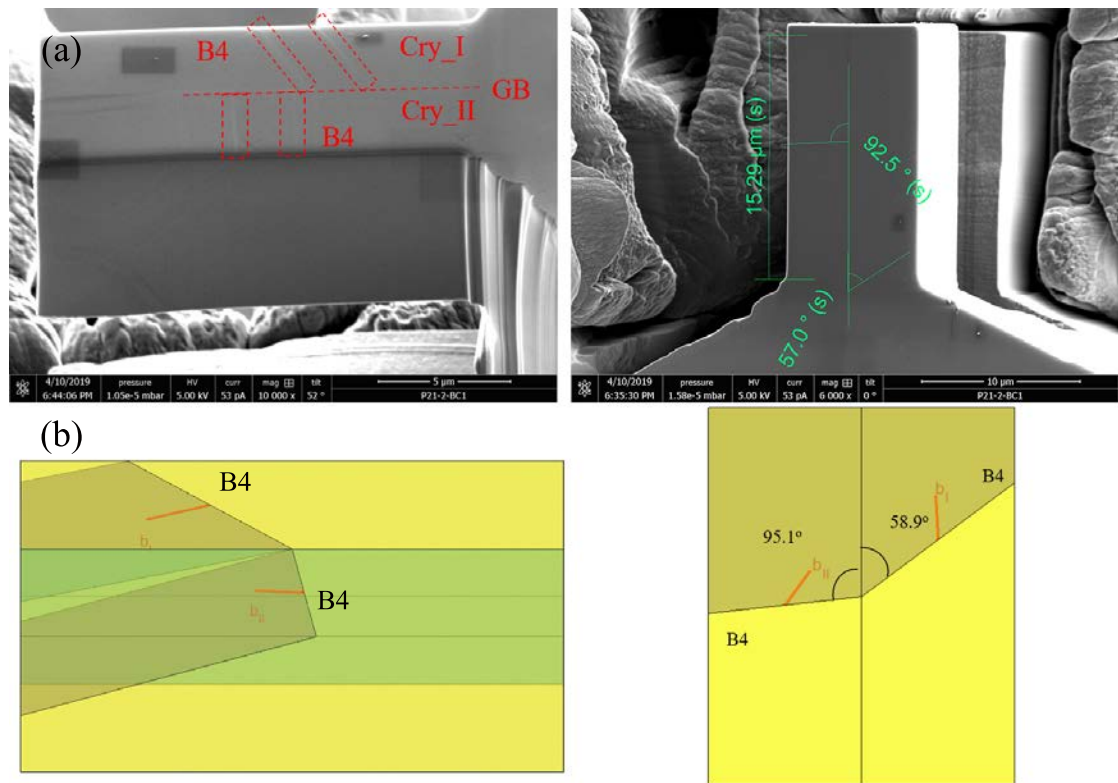


Figure 1.14: Crystallographic analysis of slip lines from SEM picture for Ni sample after compression test. Based on the direction of slip lines, the orientation of each crystal and the Schmid factor (or the incompatibility stress) analysis, the activated slip system is determined as B4 for crystal I and B4 for crystal II.

However, for  $\alpha$ -Brass, there are two obvious slip lines with interaction on the upper surface for crystal I and two obvious slip lines with interaction on the side



surface for crystal II. Based on the analysis of the direction of slip lines and the Schmid factor (or the incompatibility stress) for each slip system as shown in Figure 1.15 (b), the active slip systems are determined as A6, C5 for crystal I and B4, D6 for crystal II using Schmid and Boas's convention [40]. Thus, there are multiple active slip systems in both grains for the  $\alpha$ -Brass sample.

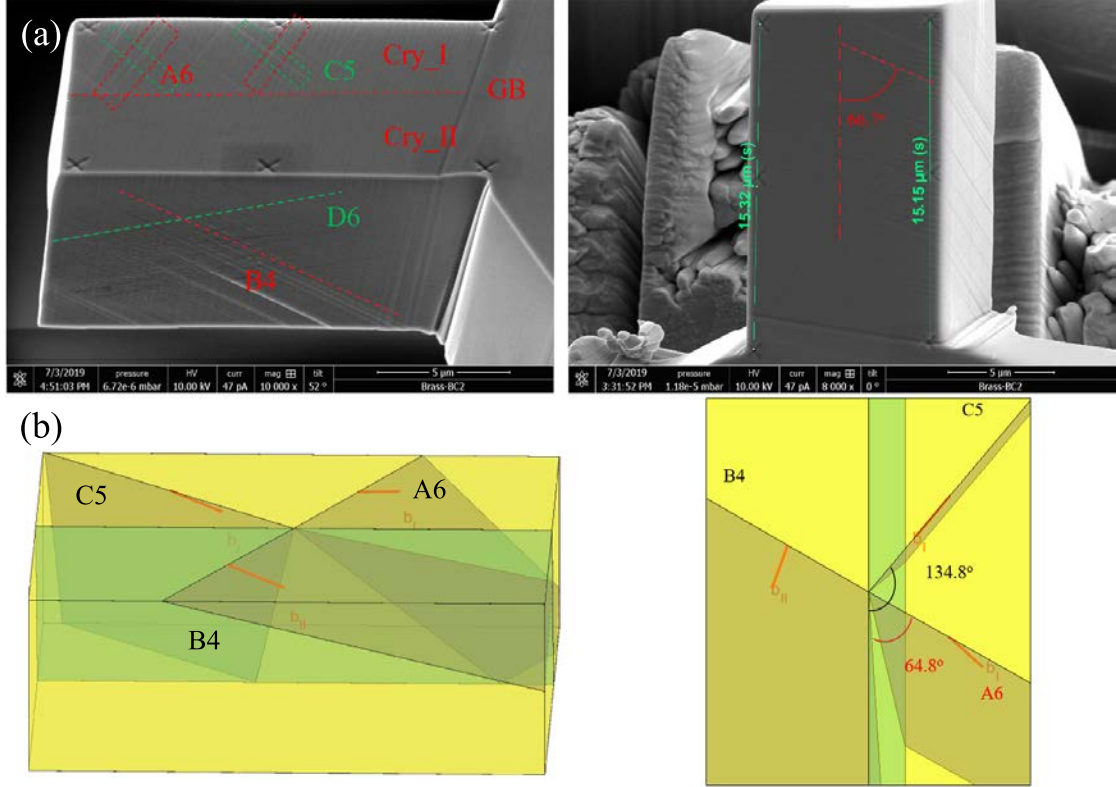


Figure 1.15: Crystallographic analysis of slip lines from SEM picture for  $\alpha$ -Brass sample after compression test. Based on the direction of slip lines, the orientation of each crystal and the Schmid factor (or the incompatibility stress) analysis, the activated slip system is determined as A6 and C5 for crystal I and B4 for crystal II.

An AFM measurement was then performed on the upper surface for both samples in order to get the 3D topography of slip lines as shown in Figure 1.16 for Ni and in Figure 1.18 for  $\alpha$ -Brass. The steps of slips are corresponding to the slip lines presented in SEM picture (Figure 1.14 and 1.15). For Ni sample, a slip step with classic features of dislocation pile-ups was selected for analysis. The heights of the top line and the bottom line of this step were measured along the slip direction from GB which are marked as red line and black line in the Figure 1.16, respectively. The measured data was fitted by the polynomial method, which is marked as  $h^{Top}$  and  $h^{Bottom}$ . Then the relative height of this step  $\Delta h$  was calculated as the

difference of the fitted height between these two lines as shown in Figure 1.17. It is found that the difference of height between two lines at GB:  $\Delta h_{GB} \approx 0.86$  nm is not zero, which corresponds to a weak slip transmission as observed in Figure 1.16 (b) circled by the frame with red dash. The slip step height increases from GB along the slip direction and gets its maximum value  $\Delta h \approx 9.06$  nm at about  $d \approx 3.28$   $\mu\text{m}$ . Furthermore, a GB sliding event is found at the top part of the beam which is presented in Figure 1.16 (a) as the hump part and in Figure 1.16 (b) circled by the frame with green dash dot.

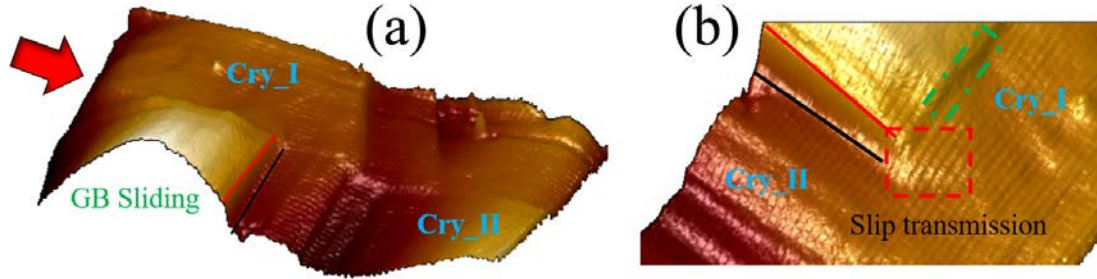


Figure 1.16: AFM topographic measurement of Ni for (a) the whole upper surface and (b) the transmission phenomenon at GB circled by the frame with red dash. The red arrow indicates the loading direction. The hump part in the second crystal shown in (a) and the frame with green dash dot shown in (b) indicate GB sliding.

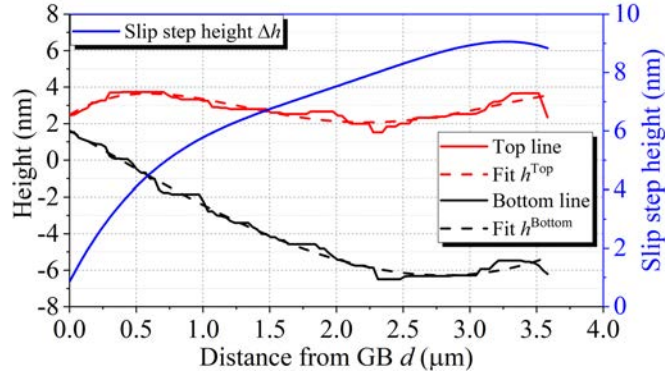


Figure 1.17: Results of slip step height measurement for Ni sample: red and black solid line indicate the measured height of top line and the bottom line of the step, respectively. The dash lines with corresponding color indicate the fitting results by polynomial method with the determinate coefficient  $R^2 = 0.8176$  for top line and  $R^2 = 0.9898$  for bottom line. The blue line indicates the simulated slip step height.

A similar analysis was realized for  $\alpha$ -Brass sample as shown in Figure 1.19. While the slip transmission is more intense compared to Ni sample as  $\Delta h_{GB} \approx 4.29$

nm, the propagation of dislocations in adjoining grain has a short distance. The maximum of slip step height is  $\Delta h \approx 10.03$  nm at about  $d \approx 2.44$   $\mu\text{m}$ . There is an obvious peak valley in the middle part of the curve of slip step height which might be caused by the intersection with another non coplanar slip line.

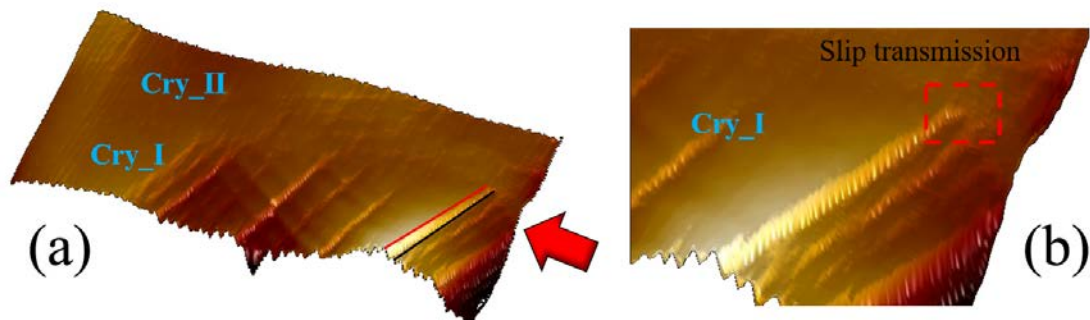


Figure 1.18: AFM measurement of  $\alpha$ -Brass for (a) the whole upper surface and (b) the transmission phenomenon at GB. The red arrow indicates the loading direction.

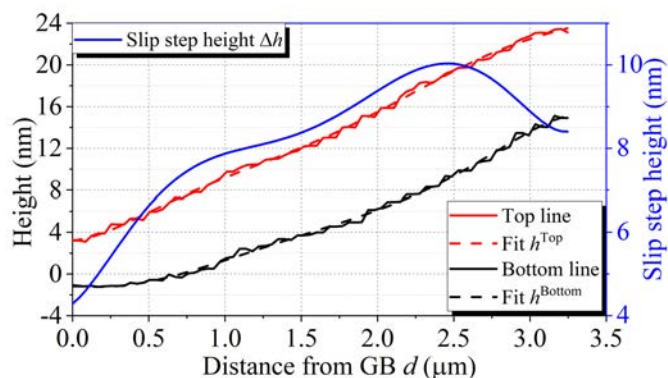


Figure 1.19: Results of slip step height measurement for  $\alpha$ -Brass sample: red and black solid line indicate the measured height of top line and the bottom line of the step, respectively. The dash lines with corresponding color indicate the fitting results by polynomial method with the determinate coefficient  $R^2 = 0.9982$  for top line and  $R^2 = 0.9973$  for bottom line. The blue line indicates the simulated slip step height.

## 1.6 Simulation of slip step height profile using discrete dislocation pile-up calculations and discussions

Based on the models developed in chapter 1.3, the slip step heights due to a dislocation pile-up measured in experiment can be simulated in a bi-crystal configuration containing a GB using dislocation pile-ups modelling. For calculations the hypotheses and configurations are set as follows and presented in Figure 1.20:

- The dislocations lines are supposed to be infinite straight lines. They are parallel to each other and also parallel to the GB plane.
- The position of the maximum slip step height measured in experiment is considered to be the end of the dislocation pile-up. However, in the simulation, it is supposed that there is a fixed dislocation source.
- The dislocations produced by this source will create a pile-up if they move towards GB and will create a step on the side surface if they move also towards free surface.
- GB is regarded as an interphase with a thickness of 0.9 nm which is obtained from MD simulation. This interphase is regarded as anisotropic with  $\lambda$  equal to 1 as defined in Eq. 1.18. For comparison, isotropic properties for GB stiffness were also considered using Voigt-Reuss-Hill average [269, 270], where the stiffness tensor is modeled by:

$$C_{ijkl}^{\text{II}} = 3kJ_{ijkl} + 2GK_{ijkl} \quad (1.20)$$

where  $k = \frac{2G(1+\nu)}{3(1-2\nu)}$  is the bulk modulus,  $G$  the shear modulus,  $\nu$  the Poisson ratio,  $J_{ijkl} = \frac{1}{3}\delta_{ij}\delta_{kl}$ , and  $K_{ijkl} = \frac{1}{2}\left(\delta_{ik}\delta_{jl} + \delta_{il}\delta_{jk} - \frac{2}{3}\delta_{ij}\delta_{kl}\right)$ .

- The transferred dislocations cannot be considered with the dislocations in pile-up at the same time if they have the different directions of dislocation lines because of the two-dimensional L-E-S theory. Thus, the transferred dislocations are supposed to be represented by an interfacial super-dislocation fixed in the GB interphase. Therefore,  $\mathbf{b}^{\text{Tran}} = N^{\text{Tran}} \times \mathbf{b}^{\text{GB}}$ , where  $\mathbf{b}^{\text{Tran}}$  is the Burgers vector of this super-dislocation,  $N^{\text{Tran}}$  the number of transferred dislocations and  $\mathbf{b}^{\text{GB}}$  is the Burgers vector of one dislocation stored in GB. It could be the same as the Burgers vector of incoming dislocations, or it could

be the residual Burgers vector between incoming slip system and one of the 12 outgoing slip systems in the adjacent grain as defined as  $\mathbf{b}^{\text{GB}} = \mathbf{b}^{\text{In}} - \mathbf{b}^{\text{Out}}$ .

- As presented in section 1.3.1, for simulation coordinate, the  $\mathbf{x}_3$  direction is set to be the direction of dislocation line  $z_S$  as presented in Figure 1.20, and the  $\mathbf{x}_2$  direction is set to be the direction of GB normal  $y_S$  as presented in Figure 1.20. Followed by FS/RH convention, the  $\mathbf{x}_1$  is determined to be  $\mathbf{x}_1 = \mathbf{x}_2 \times \mathbf{x}_3$  presented as  $x_S$  in Figure 1.20. Furthermore, all the used vectors and tensors, such as the Burgers vector of active slip systems, the vector of slip direction and the elastic stiffness, etc. are transformed into the simulation coordinates.
- The equilibrium positions of dislocations in pile-up are determined by Eq. 1.17, then the slip step height along the slip direction can be calculated by:

$$\Delta h(d) = N(d) \times b(Z) \quad (1.21)$$

where  $d$  is the distance from GB along slip direction,  $N$  the number of dislocations going through this point and  $b(Z)$  is the out of surface component of Burgers vector (along  $Z$  direction which is perpendicular to upper surface as shown in Figure 1.20).

- In the following parts, the measured slip step height is calibrated to be zero from GB, that means  $\Delta h = h^{\text{Top}} - h^{\text{Bottom}} - \Delta h_{\text{GB}}$ . Similarly, the simulated slip height is considered to be zero at GB as  $\Delta h(0) = 0$ .

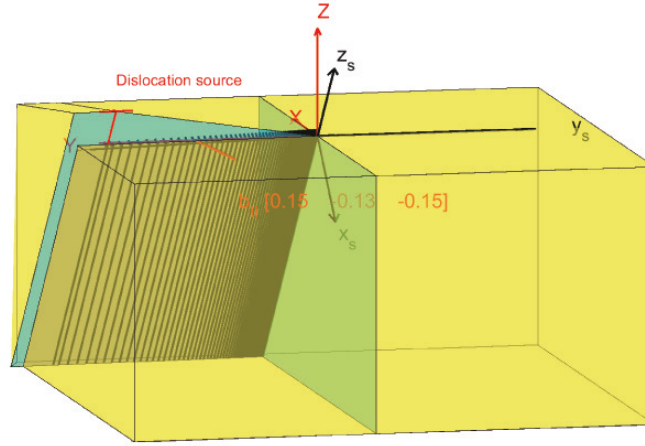


Figure 1.20: Schematic figure of simulation configuration adopted for the experiment.  $(x_S, y_S, z_S)$  indicate the simulation coordinate, while  $(X, Y, Z)$  indicate the global sample coordinate.

For the following results, the default values of the parameters are set as follows: the Burgers vector of interfacial transferred dislocations is supposed to be the same as the Burgers vector of incoming dislocations and the critical force is set to be  $F_c = 0$  N/m. By default, the calculations are performed with anisotropic elasticity. However, the L-E-S formalism cannot be used for isotropic elasticity calculation due to the problem of repeated eigenvalues (degenerated solutions). In that case the elastic stiffness moduli are firstly represented from isotropic elastic constants by  $C_{11} = 2G(1 - \nu) / (1 - 2\nu)$ ,  $C_{12} = 2G\nu / (1 - 2\nu)$  and  $C_{44} = G$ . Then the  $C_{44}$  is increased a little bit to prevent the problem of degenerated solutions in the L-E-S formalism and is replaced by  $C_{44} = C_{44} \times 1.0001$ .

Based on the all above hypotheses, for Ni sample, the out of surface component of Burgers vector for the analyzed slip system is about 0.15 nm. The maximum slip step height is about 9.1 nm at  $d \approx 3.28 \mu\text{m}$  and the slip step height at GB due to transmission is about 0.86 nm. Thus, based on Eq. 1.21, the number of dislocations produced by dislocation source is 61 and the number of transferred dislocations is 6. Therefore, the number of dislocations in the pile-up is equal to 55. The applied stress is 289.4 MPa as measured in experiment. With all these parameters, the slip step height as the distribution of dislocations in pile-up was calculated for different orientations of interfacial Burgers vector and different critical force while considering the effect of free surfaces. Furthermore, the effect of anisotropic elasticity compared to isotropy and the number of interfacial dislocation have been verified.

To summarize, the effects of the different parameters are the following:

- Effect of free surfaces: The results of the tri-material simulations without free surfaces (marked as INF) and with free surfaces (marked as FS) are presented in Figure 1.21. The simulation results are close to experimental measurements, but there are still some discrepancies. Compared to the experimental measurement, the dislocations are closer to GB in INF, while they are closer to the first free surface when considering the effect of free surfaces in FS. This is because the dislocations are closer to the first free surface than the second one, thus the total force coming from both free surfaces is always towards the first free surface. However, the dislocations around GB are nearly in the middle of two free surfaces, the effects of these two free surfaces are balanced out by each other.

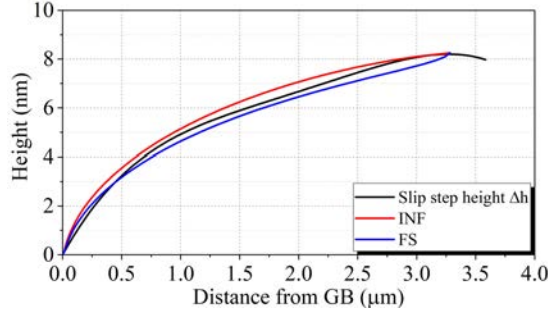


Figure 1.21: Simulation of slip step height in tri-material model without free surfaces (INF) and in three-layers model with free surfaces (FS).

- Effect of interfacial dislocations: In the hypotheses of the simulation, the number of interfacial dislocations is supposed to be the same as the number of transmitted dislocations. So first of all, the number of interfacial dislocations is verified as shown in Figure 1.22 (a). From the experimental measurement, the number of transmitted dislocations is 6. For comparison, the calculation for only 1 interfacial dislocation is also performed. It shows that the equilibrium positions of dislocations in pile-up are closer to GB for 1 interfacial dislocation compared to 6 interfacial dislocations due to less repulsive force. As the transmission phenomenon is clearly observed by AFM measurement, the Burgers vectors of interfacial dislocations  $\mathbf{b}^{\text{GB}}$  is also verified. The results for two special cases are presented in Figure 1.22 (b). The first one is that the Burgers vector of interfacial dislocation is supposed to be the residual Burgers vector with the outgoing slip system of maximum transmission factor (marked as Residu.B5). Another one is supposed to be the residual Burgers vector with the outgoing slip system of maximum Schmid factor in the adjoining grain (marked as Residu.B4). Both of them show that the equilibrium positions of dislocations are moved to GB and are much far away from experimental measurement compared to the case with the same Burgers vector of incoming dislocation. It seems that the results will be better if the free surfaces are considered for these cases, as the free surfaces will move all the dislocations towards the first free surface side. However, from the results presented in Figure 1.22, it is found that close to GB, the results with 1 interfacial dislocation or with residual Burgers vectors are much far away from experimental measurement compared to the results with 6 interfacial dislocations with the Burgers vector of incoming dislocation. Meanwhile, it is known that the effects of free surfaces are weak close to GB. Thus, the results will not be better even by considering free surfaces for these cases. It should be pointed out that the Burgers vector of interfacial dislocations has been tried with 12 residual Burgers vector as

there are 12 slip systems in adjoining grain for FCC crystal. Based on the reasonable analyses, the better solution is still with the Burgers vector of incoming dislocation for this sample.

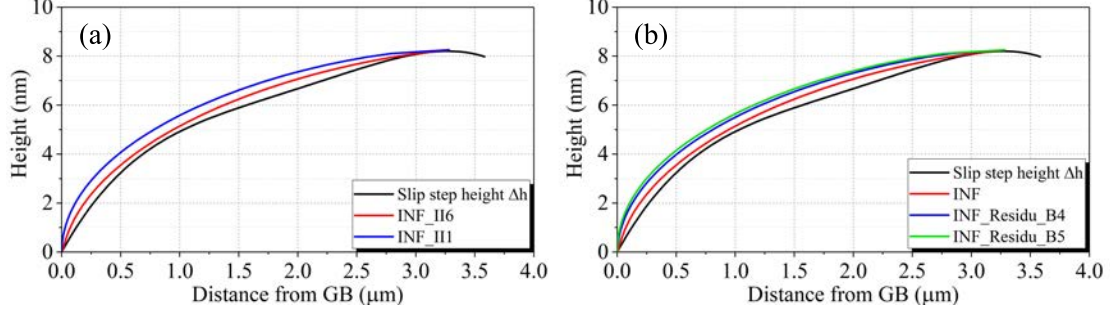


Figure 1.22: Simulation of slip step height in INF for (a) different number of interfacial dislocations: 1 interfacial dislocation (III) and 6 interfacial dislocations (II6), and (b) different Burgers vector of interfacial dislocations: residual Burgers vector between incoming and outgoing slip system with maximum transmission factor (Residu\_B5) and with maximum Schmid factor for outgoing slip system (Residu\_B4).

- Effect of critical force: As discussed in subsection 1.3.6, it is necessary to consider the effect of critical force  $F_c$  (see Eq. 1.17). The results considering or not the critical force are presented in Figure 1.23. It is found that  $F_c$  moves the dislocation towards the GB. When considering the effect of free surfaces with a critical force  $F_c = 0.003 \text{ N/m}$  ( $\tau_c = 12 \text{ MPa}$ ), which leads to a simulation result closer to the experimental measurement as shown in Figure 1.23 (b) the red curve with name FS\_Fc0.003. The value here is higher than the theoretical value for pure FCC crystal around  $1 \sim 2 \text{ MPa}$  [296]. The reason might be due to the sample preparation, such as defects coming from FIB polishing or simply from the fact that only straight dislocations are considered in the L-E-S formalism. Furthermore, it is found that the critical force does not have obvious effect on dislocations from GB until  $d = 0.5 \mu\text{m}$  in the INF model as shown in the Figure 1.23 (a). From Eq. 1.17, it can be found out that this critical force does not have an uniform effect on all the dislocations in pile-up. It depends on the state of the total stresses state and this force will balance them to give an inverse effect. For example, when the total force on dislocation is towards free surface for positions close to free surface, the critical force will point towards GB. However, the stress state is more complicated in the vicinity of GB. The total force on a dislocation could point towards GB due to repulsive forces from other dislocations, attractive misorientation, compliant GB, attractive force from interfacial dislocations and applied stress. On the contrary, it could point to the opposite direction



due to repulsive misorientation, rigid GB, repulsive force from interfacial dislocations or other dislocations in front of this dislocation and free surfaces effect even it is weak here. Hence, the total force here depends on many parameters. Thus, the critical force could either move the dislocations towards GB or to the opposite direction.

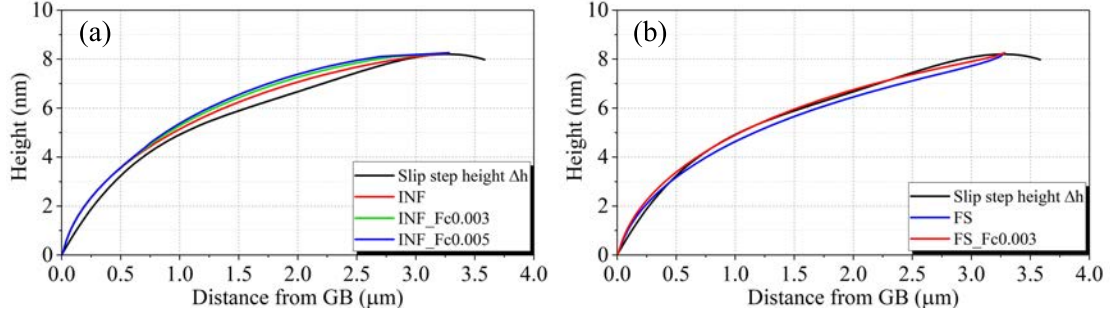


Figure 1.23: Simulation of slip step height (a) in INF and (b) in FS on considering the critical force ( $F_c$ ) on unit N/m.

- Effect of elastic anisotropy: As the elastic anisotropy factor of Ni  $A = 2.51$  is larger than 1, the elastic anisotropy has an influence on dislocation behavior in Ni sample. In order to determine the anisotropy effect, the slip step height is calculated considering isotropic elasticity without free surfaces (marked as “INF\_ISO”) and with free surfaces (marked as “FS\_ISO”) which are shown in Figure 1.24 (a) and (b), respectively. The difference between isotropic elasticity and anisotropic elasticity is not too large. One reason is that the image force due to the present misorientation is 0.0103 N/m. However, with another orientation of the adjoining grain, the maximum image force for this slip system could be 0.0502 N/m. Moreover in the present configuration, the dislocations are fixed at two sides of the pile-up which limits the possibilities for the distribution of dislocations. Even so, when considering free surfaces, all the dislocations are moved towards the free surface with isotropic elasticity which makes the simulated slip height profile much far away from experimental measurement. Furthermore, the microstructure of interphase is more like non-crystalline structure which could be assumed as isotropic elasticity. The slip height was also performed with only the interphase considered to be isotropic elasticity as shown in Figure 1.24 (a) with name “INF\_InterISO” and in Figure 1.24 (b) with name “FS\_InterISO”. However, the result is nearly the same as for an anisotropic interphase with  $\lambda = 1$ .

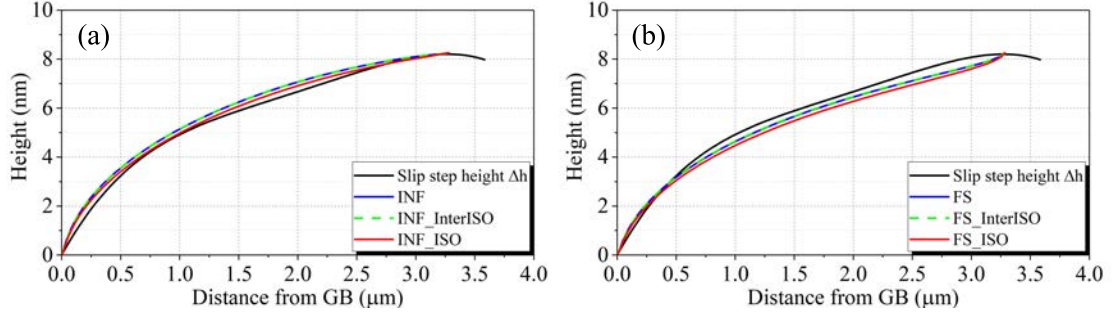


Figure 1.24: Simulation of slip step height between isotropic elasticity and anisotropic elasticity (a) in INF with INF\_InterIso for only the isotropic interphase and INF\_ISO for all layers being isotropic and (b) in FS with all corresponding configurations.

As a conclusion, the best solution of this simulation is to consider anisotropic elasticity, the effect of free surfaces and a critical force  $F_c = 0.003 \text{ N/m}$  ( $\tau_c = 12 \text{ MPa}$ ) for Ni.

Similar to Ni sample, the same simulations have been performed for the  $\alpha$ -Brass sample. For the present  $\alpha$ -Brass sample, the out of surface component of Burgers vector of the analyzed slip system is about 0.14 nm. The maximum slip step height is about 10.03 nm at  $d \approx 2.44 \mu\text{m}$  and the slip step height at GB due to transmission is about 4.29 nm. Based on Eq. 1.21, the number of dislocations in the pile-up produced by the dislocation source is 72 and the number of transmitted dislocations is 31. Therefore, the number of dislocations in the pile-up is equal to 41. The applied stress is 127.4 MPa following experimental result. The effects of free surfaces, critical force and anisotropic elasticity for  $\alpha$ -Brass sample are the same as for the Ni sample. However, the number of transmitted dislocations is much larger than in Ni, i.e. 31 instead of 6. Thus, the repulsive force from these interfacial dislocations is more important if their Burgers vector is considered as the same of the incoming dislocations (see the blue curves in Figure 1.25). All dislocations are moved far away from GB into the direction of free surface due to this repulsive force. This transmission observed in Figure 1.18 (b) leads to consider the residual Burgers vector of interfacial dislocations. After verifying all the possible residual Burgers vectors with 12 slip systems in the adjoining grain, it is found that the best solution is found with an A6 slip system in the adjoining grain while considering free surfaces and a reasonable critical force  $F_c = 0.011 \text{ N/m}$  ( $\tau_c = 43 \text{ MPa}$ ) as shown in Figure 1.25 (b). Furthermore, the theoretical analysis of the slip trace of A6 slip system on the upper surface of adjoining grain agrees well with experimental observation as shown in Figure 1.18 (b). As discussed in subsection 1.5 for  $\alpha$ -Brass, the peak valley in the middle part of the measured curve is certainly caused by the intersection with other non coplanar slip lines. In the present two-dimensional anisotropic elasticity, it was not possible to consider the

effect of two dislocations whose dislocation lines are not parallel. Thus, this peak valley part cannot be predicted by the present model. However, it is important to fit the part close to GB with  $d < 0.75 \mu\text{m}$ . The critical stress here  $\tau_c = 43 \text{ MPa}$  is larger than the critical stress for Ni sample. However, it seems to be acceptable for this alloy as discussed in subsection 1.3.6.

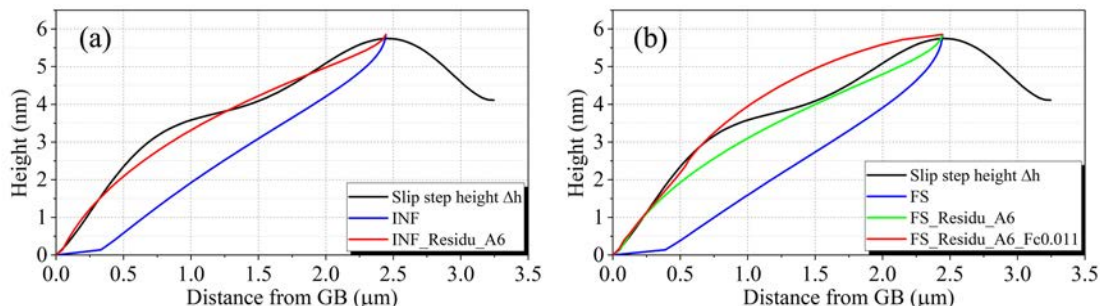


Figure 1.25: Simulation of slip step height (a) in INF considering residual Burgers vector of interfacial dislocations and (b) in FS considering critical force.

As a conclusion, the best solution inferred from these simulations of this  $\alpha$ -Brass sample is to consider anisotropic elasticity, the effect of free surfaces, a critical force  $F_c = 0.011 \text{ N/m}$  ( $\tau_c = 43 \text{ MPa}$ ) and the residual Burgers vector for interfacial dislocations as there is a huge number of transmitted dislocations.

## 1.7 Conclusions and perspectives

In the present thesis, an analytical approach based on the L-E-S formalism [28, 22, 285] has been investigated, which provides the elastic fields of single straight dislocations and different dislocation pile-ups in anisotropic homogeneous media, half-spaces, bi- and tri-material [17] while possibly considering free surface effects [18]. The tri-material configuration allows considering a non-zero thickness in the nanometer range and a specific stiffness tensor for the GB region. The configuration with two free surfaces can be used to study size effects. The effects of anisotropic elasticity, crystallographic orientation, GB stiffness and free surfaces were studied in the case of a single dislocation in a Ni bi-crystal. Image forces may arise because of both dissimilar grain orientations, the presence of a finite grain boundary region and the presence of free surfaces. In particular, it is shown that the Peach-Koehler force projected along the dislocation glide direction can exhibit a change of sign with the dislocation position. Furthermore, it is found that the acting distances of these heterogeneous factors are different. The free or rigid surface has the largest acting distance in the grain and its impact is the

largest. The effect of misorientation is much lower than the effect of free surface and so the acting distance is shorter. Lastly, the GB stiffness has the shortest acting distance. However, GB stiffness is important to change the local stress state in order to equilibrate the leading dislocation in pile-ups. For pile-ups, the dislocation positions were calculated by an iterative relaxation scheme minimizing the Peach-Koehler force on each dislocation. Both GB stiffness and grains misorientation influence pile-up length, but the effect of misorientation is clearly seen to be predominant.

In parallel, in-situ micromechanical tests of micron-sized bi-crystals and observations coupling SEM, AFM and EBSD were performed in the PhD thesis. Ni and  $\alpha$ -Brass bi-crystals were obtained from FIB machining. Slip step height spatial variations due to localized slip bands terminating at GB were measured by AFM to determine the Burgers vector distribution in the dislocation pile-up. This distribution was then simulated by dislocation pile-up configuration in bi-crystals with the experimentally measured parameters by considering the effect of misorientation, GB stiffness, free surfaces and critical force. It is found that the Burgers vector of interfacial dislocations can be regarded as the same of incoming dislocations with a weak dislocation transmission, one should consider the residual Burgers vector of interfacial dislocations in case of a strong dislocation transmission. Meanwhile the effects of free surfaces and critical force should always be considered in calculation to be more predictive regarding slip step height profile. The critical force for studied Ni is  $F_c = 0.003$  N/m ( $\tau_c = 12$  MPa) and for studied  $\alpha$ -Brass is  $F_c = 0.011$  N/m ( $\tau_c = 43$  MPa) which were calculated in the framework of straight dislocation with the L-E-S formalism are acceptable due to lattice defects in the material and alloy composition, respectively.

Compared to the present analytical approach for dislocation behavior in bi-crystals, the results could be verified using other numerical methods, such as molecular dynamics simulations (MD) and 3D discrete dislocation dynamics simulations (DDD). Meanwhile the present method could be used to enrich the DDD simulation for interfacial plasticity considering anisotropic elasticity, especially for the GB properties in bi-crystals or polycrystals. Even if it is possible to define different elastic properties of GB with anisotropic elastic stiffness tensor, the real value of this parameter is more complicated or the GB could be simply supposed to be isotropic. Thus, in a future study, the elastic properties of GB with misorientation dependence will be investigated by molecular static (MS) simulations.

# Résumé français

## 1.1 Introduction

La plasticité des matériaux cristallins résulte principalement du mouvement et de la multiplication des dislocations. Les dislocations sont des défauts linéaires introduits par Volterra [2] au début du XX<sup>e</sup> siècle. Les recherches théoriques et expérimentales montrent que les propriétés mécaniques des métaux dépendent de la densité, de la distribution, de la nucléation et de la mobilité des dislocations ainsi que leurs interactions avec les joints de grains (JDGs). Ces travaux se concentrent sur les mécanismes de glissement aux JDGs. Parmi les différents mécanismes possibles, les empilements des dislocations aux JDGs et la transmission du glissement seront principalement étudiés dans cette thèse, à la fois d'un point de vue expérimental et théorique. Pour ce faire, l'étude théorique des empilements de dislocations se fera en évaluant l'effet de l'élasticité anisotrope sur les positions d'équilibre des dislocations dans un empilement et les forces induites dans le grain voisin. En ce qui concerne les expériences, des essais in-situ de compression seront effectués sur des micro-piliers avec une faible déformation. Ensuite, la topographie de la surface externe contenant les marches de glissement sera mesurée par microscope à force atomique (AFM) et sera utilisée pour caractériser la distribution des dislocations dans l'empilement ainsi que la transmission des dislocations au JDG. Dans la partie théorique, les champs élastiques dus à une dislocation unique et à un empilement de dislocations au JDG seront calculés en utilisant une théorie élastique anisotrope bi-dimensionnelle permettant de considérer la désorientation du réseau cristallin, l'épaisseur et l'élasticité du JDG et les effets des surfaces libres. À la fin, les distributions des hauteurs de marches de glissement seront simulées numériquement par la théorie présentée et comparées aux observations expérimentales.

## 1.2 Expériences

Les expériences visent à caractériser les empilements de dislocations et la transmission des dislocations au joint de grains dans les bi-cristaux. Afin d'étudier ces mécanismes, pour chaque matériau, un JDG particulièrement intéressant a été soigneusement choisi à partir des cartes EBSD (diffraction d'électrons rétrodiffusés) de macro-échantillons. Ensuite, un micro-pilier bi-cristallin contenant ce JDG a été réalisé au FIB (sonde ionique focalisée). Par la suite, un essai de compression a été effectué sur ce micro-pilier à l'aide d'un poinçon plat parallèlement au JDG jusqu'à une faible déformation afin de créer un glissement unique dans un des grains. A la fin de la campagne expérimentale, la topographie de la surface externe contenant les marches de glissement a été mesurée par AFM.

### 1.2.1 Matériaux

Les matériaux pour cette étude expérimentale sont le nickel (Ni) de très haute pureté (99.999 %) et le laiton de structure CFC ( $\alpha$ -Brass, 70%Cu-30%Zn, wt%) avec un taux d'impuretés (Fe, Pb, P et As, etc.) inférieur à 0.001%. Une analyse chimique par spectroscopie à rayons X à dispersion d'énergie (EDX) a été effectuée pour vérifier la pureté des échantillons avant et après les procédures de préparation. Les modules élastique du Ni sont  $C_{11} = 246.5$  GPa,  $C_{12} = 147.3$  GPa,  $C_{44} = 124.7$  GPa [28] et ceux du  $\alpha$ -Brass sont  $C_{11} = 139.21$  GPa,  $C_{12} = 104.51$  GPa,  $C_{44} = 71.3$  GPa [267, 268]. Ainsi, ces deux matériaux CFC ont un facteur d'anisotropie élastique  $A = \frac{2C_{44}}{C_{11} - C_{12}}$  de l'ordre de 2.51 et 4.11, respectivement. Les matériaux choisis ont différents facteurs d'anisotropie, ce qui peut être utile pour analyser les effets de l'anisotropie élastique. Pour les calculs en élasticité isotrope, les constantes élastiques considérées sont  $G = 86.16$  GPa,  $\nu = 0.294$  pour le Ni et  $G = 40.75$  GPa,  $\nu = 0.343$  pour  $\alpha$ -Brass. Ces valeurs sont déduites des constantes élastiques anisotropes en appliquant la moyenne de Voigt-Reuss-Hill [269, 270]. De plus, les énergies de faute d'empilement pour  $\alpha$ -Brass et le Ni sont  $14$  mJ/m<sup>2</sup> [271] et  $90$  mJ/m<sup>2</sup> [272], respectivement. L'énergie de faute d'empilement du  $\alpha$ -Brass est faible, ce qui favorise le glissement planaire et facilite ainsi l'observation des lignes de glissement. Bien que l'énergie de faute d'empilement du Ni soit plus élevée, le glissement planaire a pu être observé dans des bi-cristaux lors de précédents essais de compression [137]. Ainsi, le Ni convient également aux présentes expériences.

### 1.2.2 Préparation des échantillons et choix des bi-cristaux

Les échantillons, généralement sous forme de cubes de  $20 \times 20 \times 5$  mm<sup>3</sup>, ont été découpés par électro-érosion (EDM) à l'aide d'un fil de bronze. Ensuite, les six

faces des échantillons ont été polies mécaniquement avec de l'eau et des papiers abrasifs grossiers jusqu'à une taille des particules P2500. Cette phase a été suivie d'un polissage utilisant une suspension de diamant de granulométrie 6, 3 et 1 micron sur un tissu zêta pour éliminer le durcissement et les dommages obtenus lors du polissage mécanique, y compris les rayures. À la fin, les surfaces des échantillons ont été polies par une solution OP-U-NonDry avec de l'eau sur un chiffon chimique pendant 5 minutes. Après le polissage des macro-échantillons, leur épaisseur était d'environ 2.0 ~ 2.5 mm. Avec cette gamme d'épaisseur, il est possible de maintenir les JDGs presque perpendiculaires à la surface supérieure grâce à un processus de traitement thermique. Ensuite, les échantillons polis ont été homogénéisés par traitement thermique. Pour le Ni, les échantillons produits ont été homogénéisés à 1100 °C pendant trois jours dans un four sous vide pour minimiser le risque de contamination et d'oxydation. Cependant, pour le  $\alpha$ -Brass, afin d'éviter le phénomène de dézincification dans un environnement sous vide [273], le traitement thermique a été effectué sous environnement d'argon à 980 °C pendant 1 min et avec un support d'échantillon spécial. Après traitement thermique, les échantillons ont été à nouveau polis mécaniquement jusqu'à obtenir une "surface de miroir". A la fin, les échantillons ont été électropolis sous une tension de 24V pendant 20 secondes. Ensuite, les JDGs ont pu être clairement observés au microscope optique.

L'orientation de chaque grain a été mesurée par EBSD dans un MEB Zeiss Sigma VP à l'aide d'une caméra à haute résolution d'Oxford Instruments. Pour l'acquisition des cartes d'orientation, le MEB a été réglé avec une tension d'accélération de 20 kV, soit une distance de travail de 15 mm. Les cartes d'orientation ont été acquises avec un pas de 20  $\mu\text{m}$  pour les macro-échantillons et de 0.1  $\mu\text{m}$  pour les micro-échantillons. Le traitement des données a été effectué par le logiciel Flamenco Channel 5 (HKL Technology) pour les macro-échantillons et par le logiciel AZtec pour les micro-échantillons. Le taux d'indexation a toujours été supérieur à 99%. Les microstructures ont été représentées par des figures de pôle inverses (IPF) comme montré sur la Figure 1.1. Les JDGs sont marqués par des lignes noires sur la carte EBSD et correspondent à un angle de désorientation entre pixels adjacents supérieur à 2°.

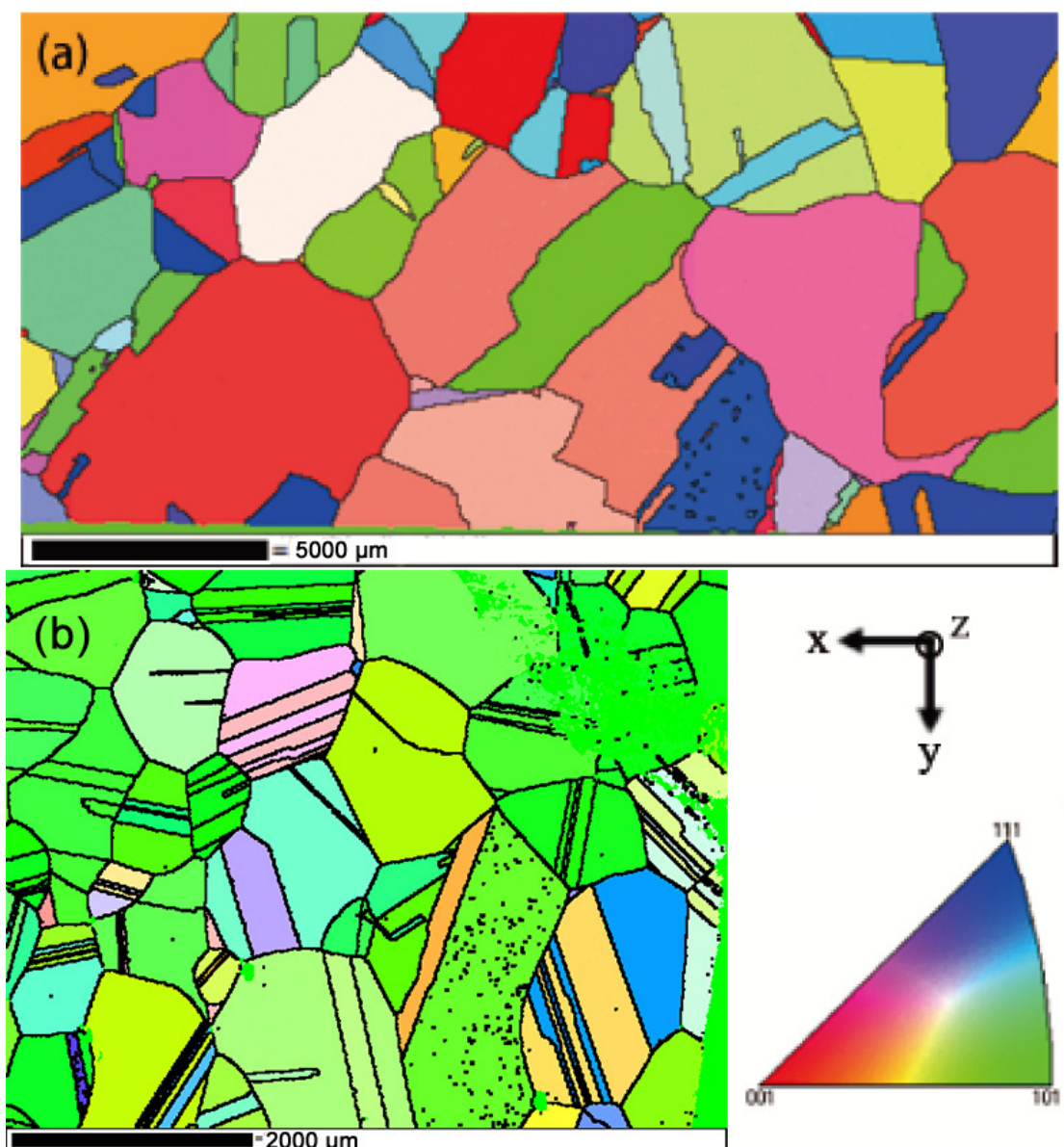


Figure 1.1: Cartographie d'orientation EBSD de l'échantillon macroscopique : (a) Ni et (b)  $\alpha$ -Brass. Les orientations sont représentées dans l'IPF selon la direction de l'axe z qui est perpendiculaire à la surface supérieure. Les lignes noires représentent les JDGs et correspondent à un angle de désorientation entre pixels adjacents supérieur à  $2^\circ$ .

En fonction de l'orientation de chaque grain, les JDGs intéressants ont été choisis en suivant les conditions suivantes par rapport à la configuration présentée dans la Figure 1.2 :

- Le JDG doit être quasi-perpendiculaire à la surface supérieure.



- Le chargement étant parallèle au JDG, le vecteur de Burgers du système de glissement ayant le facteur de Schmid maximum dans le grain cible ne doit pas être perpendiculaire au JDG. Le plan de glissement de ce système ne doit pas être parallèle à la surface supérieure. Ces conditions assurent que le vecteur de Burgers a une composante perpendiculaire à la surface supérieure où les mesures AFM sont effectuées.

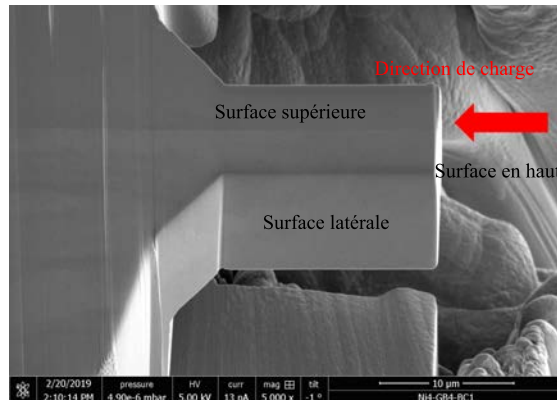


Figure 1.2: La surface supérieure est définie comme la surface contenant le JDG où les mesures AFM sont effectuées. La surface du haut est celle qui est en contact avec le poinçon plat lors de l'essai de compression. La surface latérale est la surface sur le côté qui ne contient pas de JDG.

Ensuite, il est préférable que le rapport entre le facteur Schmid maximum et le second plus élevé soit supérieur à 1.1 afin d'obtenir une probabilité élevée d'activer un seul système à faible déformation. De plus, lorsque l'on considère les contraintes d'incompatibilité dues à l'élasticité anisotrope hétérogène [160], le système de glissement le plus favorable peut être différent de celui prévu par une simple analyse due au facteur de Schmid. Cette condition peut être utilisée pour identifier l'effet des contraintes d'incompatibilité. Les joints de macles ne sont pas considérés dans la présente étude car il n'y a pas de contraintes d'incompatibilité pour des joints de macles de type I parallèles ou perpendiculaires à l'axe de chargement [276]. D'après toutes les conditions susmentionnées, plusieurs JDGs ont été choisis. Cependant, pour un problème de temps, seulement un JDG pour chaque matériau a pu être utilisé pour analyser la distribution des dislocations. Ces JDGs sont présentés sur les Figures 1.3 et 1.4.

Le macro-échantillon a été découpé par EDM en différentes parties contenant les JDGs intéressants. La surface latérale des petites pièces a été polie mécaniquement afin de rendre le JDG proche et parallèle à la surface latérale, ce qui est utile pour la découpe au FIB. Le polissage mécanique a été arrêté lorsque la distance entre le JDG et la surface latérale a été réduite à environ 1 mm afin d'éviter d'endommager

le JDG. Puis, cette surface latérale a été de nouveau polie par la technique de tranchage ionique avec des ions  $\text{Ar}^+$  de faible énergie dans le système IM4000 jusqu'à ce que la distance du JDG à la surface latérale soit réduite à environ  $40 \mu\text{m}$ . Enfin, l'échantillon pré-préparé a été découpé au FIB en un micro-pilier d'une longueur de  $16 \mu\text{m}$  environ, d'une largeur de  $8 \mu\text{m}$  environ et d'une épaisseur de  $8 \mu\text{m}$  environ à l'aide du système FEI Versa 3D Dual Beam utilisant un courant ionique à faisceau de  $15 \text{ nA}$  pour une ébauche de coupe et de  $1 \text{ nA}$  à  $30 \text{ kV}$  pour la finition comme montré dans la Figure 1.3 (c) pour le Ni et dans la Figure 1.4 (c) pour le  $\alpha$ -Brass. Les orientations des bi-cristaux ont été mesurées de nouveau par EBSD. Les résultats sont présentés dans les Figures 1.3 (a-b) et 1.4 (a-b) pour le Ni et le  $\alpha$ -Brass, respectivement.

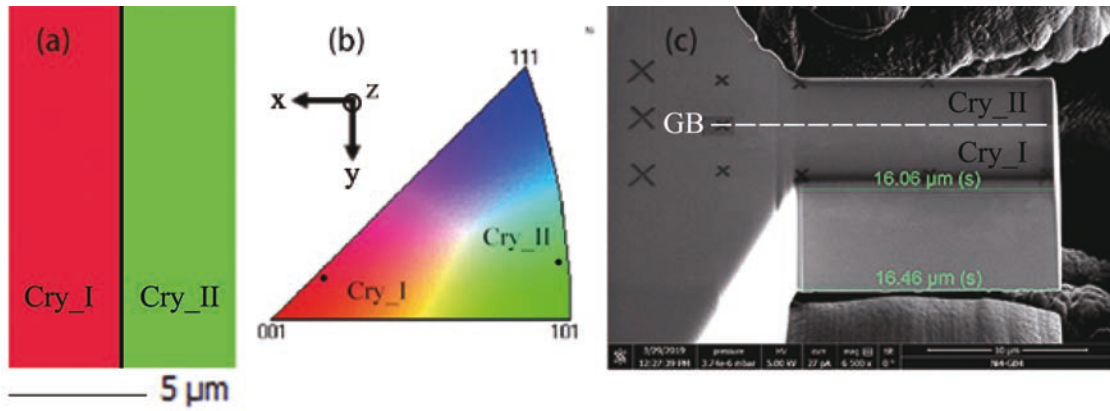


Figure 1.3: (a) Cartographie EBSD du bi-cristal de Ni, orientation du cristal I :  $\phi_1^I = 63.8^\circ$ ,  $\Phi^I = 14.3^\circ$ ,  $\phi_2^I = 18.6^\circ$ , orientation du cristal II :  $\phi_1^{II} = 331.1^\circ$ ,  $\Phi^{II} = 9.0^\circ$ ,  $\phi_2^{II} = 75.1^\circ$ . (b) Les orientations cristallographiques des deux cristaux, Cry\_I et Cry\_II, sont représentées sur la figure de pôle inverse selon la direction de l'axe y qui est parallèle au JDG et qui est aussi la direction de chargement de l'essai de compression. (c) Micrographie MEB d'un micro-pilier contenant le JDG découpé par FIB. La longueur moyenne des micro-piliers est  $15,46 \mu\text{m}$  environ et la surface moyenne des sections est  $71,80 \mu\text{m}^2$  environ avec  $46,67 \mu\text{m}^2$  pour le cristal I et  $25,13 \mu\text{m}^2$  pour le cristal II.

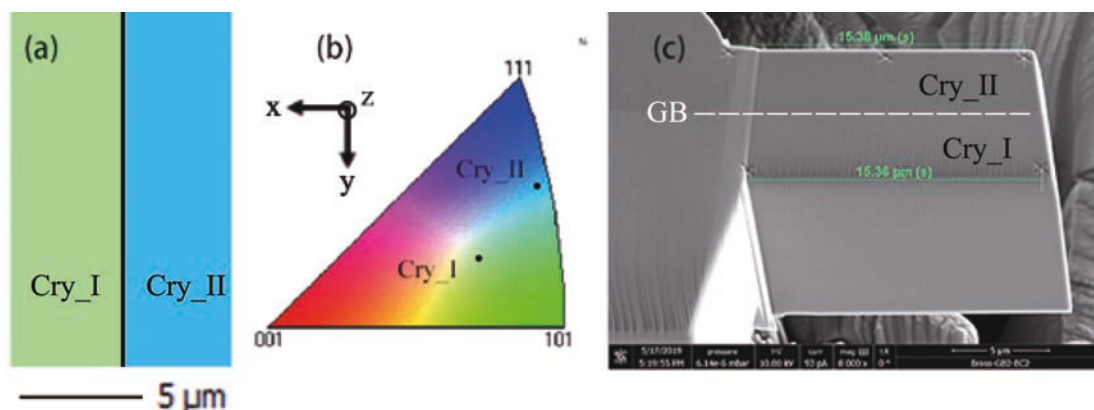


Figure 1.4: (a) Cartographie EBSD du bi-cristal de  $\alpha$ -Brass, orientation du cristal I:  $\phi_1^I = 27.7^\circ$ ,  $\Phi^I = 35.7^\circ$ ,  $\phi_2^I = 66.1^\circ$ , orientation du cristal II:  $\phi_1^{II} = 219.5^\circ$ ,  $\Phi^{II} = 28.4^\circ$ ,  $\phi_2^{II} = 2.4^\circ$ . (b) Les orientations cristallographiques des deux cristaux, Cry\_I et Cry\_II, sont représentées dans l'IPF standard dans la direction de l'axe y qui est parallèle au JDG et qui est aussi la direction de chargement de l'essai de compression. (c) Micrographie MEB d'un micro-poutre contenant le JDG coupé par FIB. La longueur moyenne des micro-poutre est  $15.37 \mu\text{m}$  environ et la surface moyenne des sections est  $88.91 \mu\text{m}^2$  environ avec  $42.02 \mu\text{m}^2$  pour le cristal I et  $46.89 \mu\text{m}^2$  pour le cristal II.

### 1.2.3 Essai de compression sur micro-piliers

Les essais de compression in-situ ont été effectués sous vide à température ambiante dans un MEB Carl Zeiss de la série SIGMA par un nanoindenteur in-situ (UNAT-SEM II) dont le niveau de bruit du fond en charge est d'environ  $0.002 \text{ mN}$ . Les micro-piliers ont été comprimés à l'aide d'un poinçon plat en carbure de tungstène polycristallin (WC). Tous les essais de compression ont été effectués en mode contrôle de déplacement avec plusieurs cycles de charges et de décharges différenciés par de petits incréments. L'idée des cycles de charges et décharges est d'avoir suffisamment de temps pour faire une image de MEB de haute qualité afin d'observer les lignes de glissement. Une fois que les lignes de glissement ont été observées ou que la limite d'élasticité a été atteinte, l'essai de compression a été arrêté au cours de la décharge, ce qui prévient un choc du poinçon. Le taux moyen de déformation en charge est d'environ  $0.002 \text{ s}^{-1}$  pour le Ni et  $0.00125 \text{ s}^{-1}$  pour  $\alpha$ -Brass. L'essai mécanique a été interrompu lorsque la première ligne de glissement a été observée. Ainsi, seul le dernier cycle contribue à la déformation plastique, et tous les cycles précédents sont purement élastiques. Selon les données expérimentales brutes, la limite d'élasticité est d'environ  $8.5\%$  pour le Ni et de  $6.3\%$  pour  $\alpha$ -Brass. Ces déformations sont trop grandes par rapport aux limites d'élasticité connues des métaux. Cette erreur provient de la dérive du poinçon pendant l'essai de compression qui rend la mesure du déplacement imprécise. Cependant, la mesure de la force est précise. Les courbes contrainte-déformation ont

donc été étalonnées à l'aide d'une simulation éléments finis de plasticité cristalline (CPFEM) comme le montre la Figure 1.5. Des essais de compression reproduisant la même configuration expérimentale ont été simulés par CPFEM pour les échantillons de Ni et de  $\alpha$ -Brass, puis la déformation expérimentale a été étalonnée de sorte à avoir la même pente élastique que les courbes simulées. Ainsi, la limite d'élasticité obtenue est d'environ 0.33% pour le Ni et 0.24% pour le  $\alpha$ -Brass, ce qui est raisonnable pour des matériaux métalliques. A la fin de l'essai, la contrainte appliquée est d'environ 289.4 MPa pour le Ni et 127.4 MPa pour le  $\alpha$ -Brass.

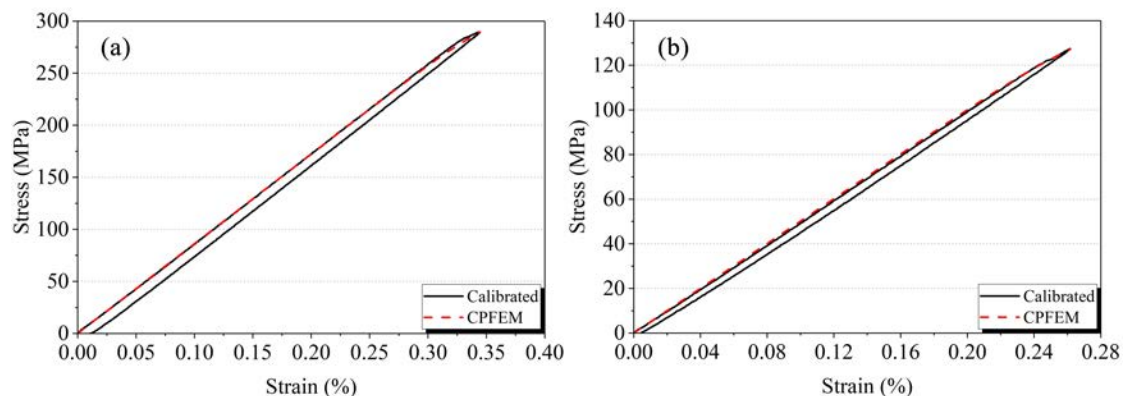


Figure 1.5: Courbes contrainte-déformation étalonnées par CPFEM pour (a) le micro-pilier de Ni et (b) le micro-pilier de  $\alpha$ -Brass.

#### 1.2.4 Analyses des lignes de glissement par AFM

Après un essai in-situ de compression, les lignes de glissement ont tout d'abord été analysées au MEB. L'image MEB permet de voir les traces des lignes de glissement sur les surfaces supérieure et latérale du micro-pilier et ainsi d'identifier les systèmes de glissement actifs d'après l'orientation de chaque grain. Ensuite, une mesure AFM a été effectuée sur la surface supérieure par Dimension FastScan avec ScanAsyst (BRUKER) avec un capteur de hauteur, afin que la topographie des lignes de glissement puisse être utilisée pour analyser les distributions des dislocations. Le pas de balayage est de 30 nm avec une fréquence de balayage de 1 Hz. Les résultats ont été analysés par NanoScope Analysis comme le montre la Figure 1.6. Les images ont d'abord été aplaties à l'aide d'un ajustement polynomial du second ordre, puis traitées par un filtre médian avec une opération matricielle de  $9 \times 9$ .



Figure 1.6: Exemple de mesure AFM sur la surface d'un bi-cristal de Ni analysé par NanoScope Analysis.

## 1.3 Théorie

### 1.3.1 Cadre de l'élasticité anisotrope bi-dimensionnelle

Afin de considérer l'effet de l'anisotropie élastique, on utilise le formalisme analytique L-E-S (Leknitskii [20] - Eshelby [21] - Stroh [22]) pour un problème élastique anisotrope à deux dimensions. Ce formalisme est très efficace mais ne peut pas traiter le cas d'un cristal parfaitement isotrope car le problème devient alors singulier en raison des valeurs propres répétées.

Les solutions générales pour le champ de déplacement  $\mathbf{u}$  et le vecteur fonction de contrainte  $\Phi$  peuvent être calculées par :

$$u_i = 2\text{Re} \left[ A_{i\bar{j}} f_{\bar{j}} \left( z_{\bar{j}} \right) \right] \quad (1.1)$$

$$\Phi_i = 2\text{Re} \left[ B_{i\bar{j}} f_{\bar{j}} \left( z_{\bar{j}} \right) \right] \quad (1.2)$$

où  $\mathbf{A}$  est une matrice  $3 \times 3$  contenant les vecteurs propres  $a_{k\alpha}$  ( $\alpha = 1, 2, 3$ ),  $B_{ij} = (C_{i2k1} + p_j C_{i2k2}) A_{kj}$  et  $z_j = x_1 + p_j x_2$ .  $p_\alpha$  représente les valeurs propres associés à partie imaginaire positive d'une équation sextique dépendant uniquement des constantes élastiques du matériau [21, 22].  $\mathbf{f}$  est une fonction scalaire de  $z$ . Ensuite, les champs de contrainte peuvent être calculés à partir de la loi de Hooke et des gradients du déplacement ou par le vecteur fonction de contrainte comme suit:

$$\sigma_{i1} = -\partial\Phi_i/\partial x_2, \sigma_{i2} = \partial\Phi_i/\partial x_1 \quad (1.3)$$

Si nécessaire, le composant  $\sigma_{33}$  peut être calculé à partir de la loi de Hooke généralisée.

L'idée des sections suivantes est de trouver l'expression du vecteur fonction  $\mathbf{f}$  pour une dislocation seule dans différentes configurations.

### 1.3.2 Dislocation dans un milieu homogène

Dans ce qui suit, une dislocation infinie droite de vecteur de Burgers  $\mathbf{b}$  et dont la ligne  $\mathbf{t}$  est parallèle à la direction  $\mathbf{x}_3$  est considérée à la position  $(X_1, X_2)$  comme indiqué sur la Figure 1.7. La convention FS/RH (Finish Start/Right Hand) [28] est utilisée pour définir la direction de la ligne de dislocation comme indiqué sur la Figure 1.7.

Dans un milieu anisotrope homogène, le vecteur fonction  $\mathbf{f}$  est dérivé en considérant le défaut de fermeture du vecteur de Burgers  $\mathbf{b}$  en l'absence de force appliquée à distance. Les vecteurs de déplacement et de fonction contrainte peuvent alors être exprimés à l'aide des Eqs. 1.1 et 1.2 avec:

$$f_j(z_i) = f_j^0(z_i) = q_j^0 \ln(z_i - s_j) \quad (1.4)$$

où  $z_i = x_1 + p_i x_2$ ,  $s_j = X_1 + p_j X_2$  et  $\mathbf{q}^0$  est un vecteur complexe exprimé comme  $\mathbf{q}^0 = -\frac{1}{2\pi} \mathbf{i} (\mathbf{B}^T \mathbf{b})$  [19].

### 1.3.3 Dislocation dans un bi-matériau

Considérons maintenant un bi-matériau anisotrope (ou bi-cristal) avec une interface parfaite dont la normale est suivant la direction  $\mathbf{x}_2$ . La dislocation est supposée être située dans le matériau supérieur I ( $x_2 > 0$ ) comme indiqué sur la Figure 1.7.

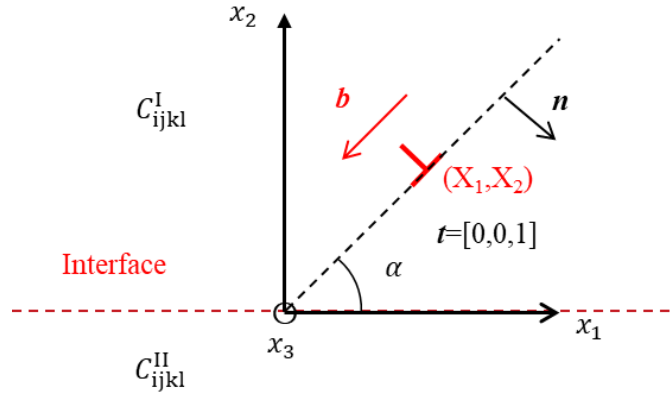


Figure 1.7: Schéma d'une dislocation droite infinie dans un bi-matériau.

En plus des conditions du milieu homogène, le vecteur fonction  $\mathbf{f}$  doit également satisfaire les conditions de continuité à l'interface parfaite, c'est-à-dire la continuité des déplacements  $u_i^I(x_2 = 0^+) = u_i^{II}(x_2 = 0^-)$  et la continuité des vecteurs traction  $\sigma_{i2}^I(x_2 = 0^+) = \sigma_{i2}^{II}(x_2 = 0^-)$ . Dans la pratique, au lieu de la continuité des

vecteurs traction, on utilise la continuité de la force de traction résultante sur un arc de l'interface. Cette dernière condition donne  $\Phi_i^I(x_2 = 0^+) = \Phi_i^{II}(x_2 = 0^-)$  [19, 292]. Suivant la méthode de Suo [19], les solutions sont recherchées sous une forme similaire aux Eqs. 1.1 et 1.2 :

$$f_j(z_j) = \begin{cases} f_j^0(z_j) + \overline{V_{jk}^{I,II}} \overline{f_k^0}(z_j) & \text{si } z_j \in \text{I} \ (x_2 > 0) \\ W_{jk}^{I,II} f_k^0(z_j) & \text{si } z_j \in \text{II} \ (x_2 < 0) \end{cases} \quad (1.5)$$

ou:

$$\begin{cases} \mathbf{V}^{I,II} = \left( \mathbf{B}^{II} \mathbf{A}^{II-1} \overline{\mathbf{A}^I} - \overline{\mathbf{B}^I} \right)^{-1} \left( \mathbf{B}^I - \mathbf{B}^{II} \mathbf{A}^{II-1} \mathbf{A}^I \right) \\ \mathbf{W}^{I,II} = \left( \overline{\mathbf{B}^I} \mathbf{A}^{I-1} \mathbf{A}^{II} - \mathbf{B}^{II} \right)^{-1} \left( \overline{\mathbf{B}^I} \mathbf{A}^{I-1} \mathbf{A}^I - \mathbf{B}^I \right) \end{cases} \quad (1.6)$$

$f_j^0(z_j)$  est calculé à l'aide de l'Eq. 1.4 en considérant le tenseur de rigidité élastique  $\mathbf{C}^I$  du matériau supérieur I et  $s_j = s_j^I = X_1 + p_j^I X_2$ . De plus, il faut notée que si  $z_j \in \text{I}$ ,  $z_j = z_j^I = x_1 + p_j^I x_2$  et si  $z_j \in \text{II}$ ,  $z_j = z_j^{II} = x_1 + p_j^{II} x_2$ .

Les solutions correspondant au problème d'un demi-espace avec des surfaces rigide ou libre,  $u_i^I(x_2 = 0) = 0$  ou  $\Phi_i^I(x_2 = 0) = 0$ , respectivement, peuvent être facilement obtenues comme une configuration spéciale d'un bi-matériau. Elles conduisent à considérer  $f_j(z_j) = f_j^0(z_j) - A_{jk}^I{}^{-1} \overline{A_{kl}^I} \overline{f_l^0}(z_j)$  pour la surface rigide et  $f_j(z_j) = f_j^0(z_j) - B_{jk}^I{}^{-1} \overline{B_{kl}^I} \overline{f_l^0}(z_j)$  pour la surface libre.

### 1.3.4 Dislocation dans un tri-matériau

Dans la sous-section 1.3.3, le bi-matériau était considéré comme la combinaison de deux matériaux parfaitement liés l'un à l'autre par une interface sans épaisseur. Dans le cas où l'interface considérée est un JDG, l'épaisseur réelle est finie et vaut environ 1 nm en utilisant une estimation brute. Par conséquent, il peut être intéressant d'étudier l'effet de l'épaisseur du JDG ainsi que l'effet de sa rigidité élastique sur les champs élastiques dans une configuration tri-matériau où le JDG est considéré comme une interphase. Parmi plusieurs études portant sur les milieux élastiques anisotropes multicouches, la méthode de Choi et Earmme [17] est appliquée dans un premier temps. La figure 1.8 montre la configuration tri-matériau considérée. Il y a deux interfaces planes  $\Gamma_1$  et  $\Gamma_2$  dont les normales sont dirigées le long de l'axe  $\mathbf{x}_2$ . Ces interfaces sont situées, respectivement, à  $x_2 = h$  et à  $x_2 = -d$ . L'interphase (ou JDG) est la région comprise entre  $\Gamma_1$  et  $\Gamma_2$ , donc son épaisseur est  $H = h + d$ . Le matériau I correspond à  $x_2 \geq h$ , le matériau II à  $-d < x_2 < h$  et le matériau III à  $x_2 \leq -d$ . Tous les matériaux sont supposés être parfaitement liés les uns aux autres.

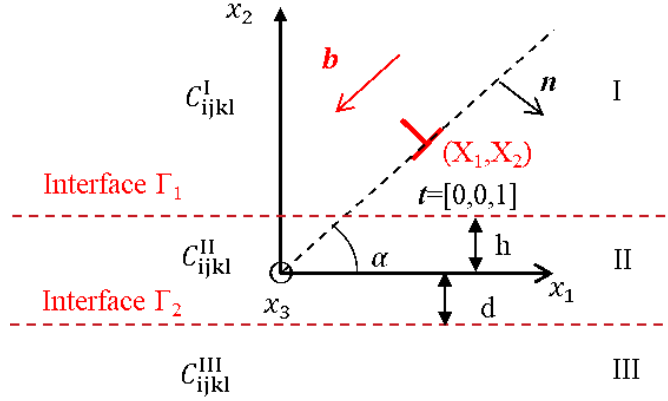


Figure 1.8: Schéma d'une dislocation infinie droite dans un tri-matériau avec trois tenseurs de rigidité différents et deux interfaces parfaitement liées. La zone du JDG est supposée être le matériau II.

Choi et Earmme [17] ont surmonté la difficulté à satisfaire la continuité des déplacements et des forces à travers les deux interfaces en même temps en appliquant une technique dite d'alternance, qui consiste à satisfaire alternativement les conditions de continuité à travers chaque interface jusqu'à ce qu'une convergence soit obtenue. Toujours en considérant le cas d'une dislocation située dans le cristal I et en utilisant la même procédure que celle de Choi et Earmme [17], la solution suivante sous forme de série est obtenue :

$$f_i(z_i) = \begin{cases} f_i^0(z_i) + f_i^{I0}(z_i) + \sum_{\beta=1}^{\infty} f_i^{I\beta}(z_i) & \text{si } z_i \in \text{I} \\ \sum_{\beta=1}^{\infty} f_i^{\beta}(z_i) + \sum_{\beta=1}^{\infty} f_i^{II\beta}(z_i) & \text{si } z_i \in \text{II} \\ \sum_{\beta=1}^{\infty} f_i^{III\beta}(z_i) & \text{si } z_i \in \text{III} \end{cases} \quad (1.7)$$

où:

$$\left\{ \begin{array}{l} f_i^0(z_i) = q_i^0 \ln(z_i - s_i) \\ f_i^{I0}(z_i) = \overline{V_{ij}^{I,II}} \overline{f_j^0}(z_i - p_i^I h + \overline{p_j^I} h) \\ f_i^{I\beta}(z_i) = W_{ij}^{II,I} \overline{V_{jk}^{II,III}} \overline{f_k^\beta}(z_i - p_i^I h + p_j^{II}(h+d) - \overline{p_k^{II}} d) \\ f_i^{II\beta}(z_i) = \overline{V_{ij}^{II,III}} \overline{f_j^\beta}(z_i + p_i^{II} d - \overline{p_j^{II}} d) \\ f_i^{III\beta}(z_i) = W_{ij}^{II,III} \overline{f_j^\beta}(z_i + p_i^{III} d - \overline{p_j^{II}} d) \\ f_i^\beta(z_i) = \begin{cases} W_{ij}^{I,II} \overline{f_j^0}(z_i - p_i^{II} h + \overline{p_j^I} h) & \text{si } \beta = 1 \\ \overline{V_{ij}^{II,I}} \overline{V_{jk}^{II,III}} \overline{f_k^{\beta-1}}(z_i - p_i^{II} h + \overline{p_j^{II}}(h+d) - \overline{p_k^{II}} d) & \text{si } \beta > 1 \end{cases} \end{array} \right. \quad (1.8)$$



Dans les équations ci-dessus,  $f_j^0(z_i)$  est associé au cristal I et donc  $s_j = s_j^I = X_1 + p_j^I X_2$ . Les séries solutions  $f_i^{I\beta}(z_i)$ ,  $f_i^{II\beta}(z_i)$  et  $f_i^{III\beta}(z_i)$  sont toutes exprimées en fonction de  $f_j^\beta(z_i)$  qui est lui-même déterminé par une équation de récurrence basée sur  $f_j^0(z_i)$ .

La convergence des séries solutions a été prouvée par Choi et Earmme [17]. L'étude de la convergence des séries solutions pour différentes rigidités du JDG a été explorée en utilisant différents critères au cours de cette thèse (voir Chen et al. [277]).

### 1.3.5 Dislocation dans un tri-matériau avec surfaces libres

Au cours d'un essai sur un micro-pilier, il y a toujours des surfaces libres comme le montre la Figure 1.2. Aux échelles fines, les surfaces libres ont une influence évidente sur le comportement des dislocations. Par conséquent, en plus de l'interphase, il peut s'avérer également nécessaire de considérer l'effet des surfaces libres sur les champs élastiques au travers d'une modélisation développée pour des matériaux multicouches. La méthode tri-matériau de Choi et Earmme [17] peut également prendre en compte les effets de surface libre mais seulement dans le cas d'un bi-matériau avec une surface libre ou d'un matériau homogène avec deux surfaces libres. Pour traiter des cas plus complexes, comme un tri-matériau avec des surfaces libres, une nouvelle méthode est nécessaire. La méthode de décomposition en densités images développée par Wang et al. [18] a ainsi été utilisée. La Figure 1.9 (a) montre la configuration d'un tri-matériau avec deux surfaces libres. Il y a quatre faces planes dont les normales sont dirigées le long de l'axe  $\mathbf{x}_2$ . Ces faces sont situées à  $x_2 = 0$ ,  $x_2 = -h_1$ ,  $x_2 = -(h_1 + h_2)$  et  $x_2 = -(h_1 + h_2 + h_3)$ , respectivement, pour la surface libre supérieure, la première interface, la deuxième interface et la surface libre inférieure. L'interphase (ou JDG) est située dans la deuxième couche d'épaisseur  $h_2$ . Le matériau I correspond à  $-h_1 < x_2 < 0$ , le matériau II à  $-(h_1 + h_2) < x_2 < -h_1$  et le matériau III à  $-(h_1 + h_2 + h_3) < x_2 < -(h_1 + h_2)$ . Ainsi, l'épaisseur de l'ensemble du matériau est représentée par  $H' = h_1 + h_2 + h_3$ . Tous les matériaux sont supposés parfaitement liés les uns aux autres. Afin de discuter des effets des deux surfaces libres, la surface libre du côté du cristal contenant les dislocations est appelée la première surface libre, et l'autre est appelée la deuxième surface libre.

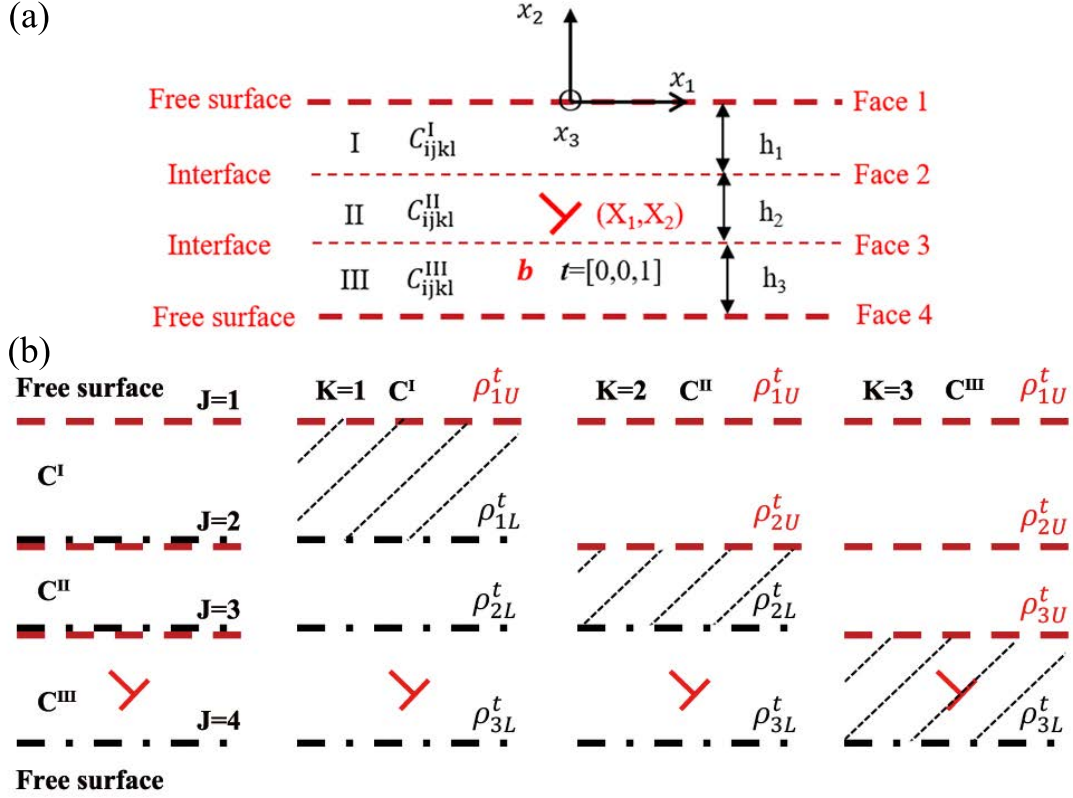


Figure 1.9: (a) Schéma d'une seule infinie dislocation droite dans un tri-matériau ayant trois tenseurs de rigidité élastique différents, deux surfaces libres planes sur les faces 1 et 4 et deux interfaces parfaitement collées sur les faces 2 et 3. La zone du JDG est supposée être le matériau II. (b) Décomposition d'un problème à 3 couches (à gauche) avec 2 surfaces libres et 2 interfaces en trois sous-problèmes infiniment homogènes. La source de dislocation est marquée par un symbole de dislocation en rouge.

Dans une configuration à 3 couches avec surfaces libres, il y a 2 interfaces qui doivent satisfaire les conditions de continuité des interfaces parfaites, et deux surfaces libres qui doivent satisfaire les conditions de traction libre. Pour un système multicouche, il est trop compliqué d'utiliser la technique en alternance. Wang et al. [18] ont proposé une décomposition en densités images, qui peut être utilisée pour satisfaire toutes les conditions limites en même temps. Le principe de cette méthode est de décomposer le problème multicouche en plusieurs sous-problèmes de milieu homogène infini. Deux types de densités de dislocation image sont distribués sur chaque interface tandis qu'une densité de dislocation image est distribuée sur la surface comme le montre dans la Figure 1.9 (b) (à gauche). Les densités de dislocations images sont désignées par  $\rho^t$ , où  $t=1,2$  et  $3$  désigne les composantes  $x_1$ -,  $x_2$ - et  $x_3$ -, respectivement. Ces densités peuvent être résolues en même temps en considérant toutes les conditions aux limites : la continuité du

gradient tangentiel des déplacements et des tractions à travers les interfaces, des tractions nulles pour les surfaces libres ou le gradient tangentiel de déplacement nul pour les surfaces rigides. Ainsi, la configuration actuelle à 3 couches avec surfaces libres est décomposée en 3 sous-problèmes et il y a un total de 18 conditions limites. Les champs élastiques dans chaque couche sont déterminés en additionnant les contributions de la source de dislocation et de toutes les densités de dislocations images correspondantes comme les montre la Figure 1.9 (b) (à droite). D'après une condition de cohérence, discutée en détail par Wang et al. [18], les densités de dislocations images dans les trois sous-problèmes sont :  $\rho_{J_1}^t = \{\rho_{1U}^t, \rho_{1L}^t, \rho_{2L}^t, \rho_{3L}^t\}$  pour le premier sous-problème,  $\rho_{J_2}^t = \{\rho_{1U}^t, \rho_{2U}^t, \rho_{2L}^t, \rho_{3L}^t\}$  pour le deuxième sous-problème et  $\rho_{J_3}^t = \{\rho_{1U}^t, \rho_{2U}^t, \rho_{3U}^t, \rho_{3L}^t\}$  pour le troisième sous-problème comme indiqué sur la Figure 1.9 (b) (à droite).

D'après le formalisme de Stroh, les champs de contrainte et du gradient de déplacement dûs à une dislocation mixte avec des composantes de vecteur de Burgers  $b_t$  ( $t = 1, 2, 3$ ) située à  $(x_{1s}, x_{2s})$  dans un solide anisotrope homogène peuvent être écrits sous la forme [28, 18] :

$$\begin{aligned} \sigma_{ij}(K, b_t, \Delta x_1, \Delta x_2) = \\ 2 [\xi_{K\alpha ij}^{tR} P(\Delta x_1, p_{K\alpha}^R \Delta x_2, p_{K\alpha}^I \Delta x_2) + \xi_{K\alpha ij}^{tI} Q(\Delta x_1, p_{K\alpha}^R \Delta x_2, p_{K\alpha}^I \Delta x_2)] b_t \end{aligned} \quad (1.9)$$

$$\begin{aligned} \frac{\partial u_i}{\partial x_j}(K, b_t, \Delta x_1, \Delta x_2) = \\ 2 [\zeta_{K\alpha ij}^{tR} P(\Delta x_1, p_{K\alpha}^R \Delta x_2, p_{K\alpha}^I \Delta x_2) + \zeta_{K\alpha ij}^{tI} Q(\Delta x_1, p_{K\alpha}^R \Delta x_2, p_{K\alpha}^I \Delta x_2)] b_t \end{aligned} \quad (1.10)$$

où  $\Delta x_1 = x_1 - x_{1s}$  et  $\Delta x_2 = x_2 - x_{2s}$ , les exposants  $R$  et  $I$  indiquent les parties réelle et imaginaire de chaque terme, respectivement. L'indice  $K$  indique le sous-problème considéré (pas de somme sur  $K$ ). La définition des symboles  $\xi_{K\alpha ij}^t$ ,  $\zeta_{K\alpha ij}^t$  et des fonctions  $P$ ,  $Q$  [18] sont :

$$\begin{cases} \xi_{K\alpha ij}^t = \frac{C_{Kijkl}(\delta_{l1} + p_{K\alpha} \delta_{l2}) A_{Kk\alpha} B_{Kt\alpha}}{2\pi i} \\ \zeta_{K\alpha ij}^t = \frac{(\delta_{j1} + p_{K\alpha} \delta_{j2}) A_{Kia} B_{Kt\alpha}}{2\pi i} \end{cases} \quad (1.11)$$

$$\begin{cases} P(x_1 - x_{1s}, a, b) = \frac{x_1 - x_{1s} + a}{(x_1 - x_{1s} + a)^2 + b^2} \\ Q(x_1 - x_{1s}, a, b) = \frac{b}{(x_1 - x_{1s} + a)^2 + b^2} \end{cases} \quad (1.12)$$

où  $p_\alpha$ ,  $A_{k\alpha}$  et  $B_{t\alpha}$  avec  $\alpha=1,2$  et  $3$  désignent les mêmes valeurs propres et les mêmes vecteurs propres que dans la formulation sextique de Stroh comme discuté dans la

section 1.3.1. Les deux expressions 1.9 et 1.10 sont équivalentes aux Eqs. 1.1, 1.2 et 1.4 et peuvent être analytiquement dérivées l'une de l'autre.

La contribution des densités de dislocations images sur les champs élastiques peut être calculée en remplaçant le vecteur de Burgers  $b_t$  par  $\rho_{JK}^t(x'_1)$  et en intégrant de  $x'_1 = -\infty$  à  $x'_1 = +\infty$  dans les Eqs. 1.9 and 1.10:

$$\begin{aligned} \sigma_{ij} (K, \rho_{JK}^t, \Delta x_1, \Delta x_2) &= \\ & \int_{-\infty}^{+\infty} 2 \left[ \xi_{K\alpha ij}^{tR} P (\Delta x_1, p_{K\alpha}^R \Delta x_2, p_{K\alpha}^I \Delta x_2) + \xi_{K\alpha ij}^{tI} Q (\Delta x_1, p_{K\alpha}^R \Delta x_2, p_{K\alpha}^I \Delta x_2) \right] \rho_{JK}^t (x'_1) dx'_1 \\ &= 2\pi \left[ \xi_{K\alpha ij}^{tR} H (p_{K\alpha}^R \Delta x_2, p_{K\alpha}^I \Delta x_2) + \xi_{K\alpha ij}^{tI} I (p_{K\alpha}^R \Delta x_2, p_{K\alpha}^I \Delta x_2) \right] [\rho_{JK}^t (x_1)] \end{aligned} \quad (1.13)$$

$$\begin{aligned} \frac{\partial u_i}{\partial x_j} (K, \rho_{JK}^t, \Delta x_1, \Delta x_2) &= \\ & \int_{-\infty}^{+\infty} 2 \left[ \zeta_{K\alpha ij}^{tR} P (\Delta x_1, p_{K\alpha}^R \Delta x_2, p_{K\alpha}^I \Delta x_2) + \zeta_{K\alpha ij}^{tI} Q (\Delta x_1, p_{K\alpha}^R \Delta x_2, p_{K\alpha}^I \Delta x_2) \right] \rho_{JK}^t (x'_1) dx'_1 \\ &= 2\pi \left[ \zeta_{K\alpha ij}^{tR} H (p_{K\alpha}^R \Delta x_2, p_{K\alpha}^I \Delta x_2) + \zeta_{K\alpha ij}^{tI} I (p_{K\alpha}^R \Delta x_2, p_{K\alpha}^I \Delta x_2) \right] [\rho_{JK}^t (x_1)] \end{aligned} \quad (1.14)$$

où  $\Delta x_1 = x_1 - x'_1$ ,  $\Delta x_2 = x_2 - x'_2$  et  $(x'_1, x'_2)$  indiquent les positions des dislocations images. Les définitions des opérateurs  $H$  et  $I$  sont :

$$\left\{ \begin{array}{l} H(a, b) [\rho(x_1)] = \frac{1}{\pi} \int_{-\infty}^{\infty} P(x_1 - x'_1, a, b) \cdot \rho(x'_1) dx'_1 \\ I(a, b) [\rho(x_1)] = \frac{1}{\pi} \int_{-\infty}^{\infty} Q(x_1 - x'_1, a, b) \cdot \rho(x'_1) dx'_1 \end{array} \right. \quad (1.15)$$

En combinant les 18 conditions aux limites, et après avoir supprimé le terme de singularité grâce aux opérateurs  $H$  et  $I$ , un système d'équations non-linéaires de 18 équations de Fredholm de deuxième type ( $t = 1, 2$  et  $3$ ) avec 18 inconnues  $\boldsymbol{\rho} = [\rho_{1U}^t, \rho_{1L}^t, \rho_{2U}^t, \rho_{2L}^t, \rho_{3U}^t, \rho_{3L}^t]^T$  est obtenu comme indiqué ci-dessous :

$$\begin{aligned} (\mathbf{C} + \mathbf{C}_0 \mathbf{C}^{-1} \mathbf{C}_0) \boldsymbol{\rho} + (\mathbf{C}_H \mathbf{H} + \mathbf{C}_I \mathbf{I} - \mathbf{C}_0 \mathbf{C}^{-1} \mathbf{C}_H \mathbf{H}_0 \mathbf{H} - \mathbf{C}_0 \mathbf{C}^{-1} \mathbf{C}_I \mathbf{H}_0 \mathbf{I}) \boldsymbol{\rho} \\ = -\mathbf{C}_R \mathbf{R} + \mathbf{C}_0 \mathbf{C}^{-1} \mathbf{C}_R \mathbf{H}_0 \mathbf{R} \end{aligned} \quad (1.16)$$

où  $\mathbf{C}_H \mathbf{H}$ ,  $\mathbf{C}_I \mathbf{I}$ ,  $\mathbf{C}_H \mathbf{H}_0 \mathbf{H}$ ,  $\mathbf{C}_I \mathbf{H}_0 \mathbf{I}$  sont des matrices avec opérateur intégral portant sur les densités de dislocations images  $\boldsymbol{\rho}$  et  $\mathbf{C}$ ,  $\mathbf{C}_0$  sont des matrices dont les coefficients dépendent uniquement des propriétés du matériau. Toutes les composantes de ces matrices sont données dans l'annexe B. Ces inconnues peuvent être résolues numériquement en utilisant la méthode de quadrature de Gauss-Hermite

avec des polynômes d’Hermite. Après avoir remplacé l’intégrale de  $\rho$ , l’expression analytique de  $\rho$  peut être obtenue en fonction de  $x_1$ . Enfin, les champs élastiques, tels que les champs de contraintes en tout point dûs à une seule dislocation dans un matériau anisotrope avec trois couches, peuvent être calculés à l’aide des Eqs. 1.9 et 1.13.

Dans la présente thèse, la configuration à trois couches est utilisée dans la section 1.6 pour considérer à la fois les effets de la rigidité du JDG et ceux des surfaces libres dans la simulation des expériences. Ainsi, la deuxième couche est considérée comme un JDG dont l’épaisseur est fixée à 1nm. La configuration à deux couches est utilisée dans la section 1.4 pour étudier théoriquement l’effet des surfaces libres.

### 1.3.6 Applications à un empilement de dislocations discrètes

Considérons un empilement de  $N$  dislocations infinies droites, qui sont toutes parallèles à l’axe  $\mathbf{x}_3$ , ont les mêmes Burgers  $\mathbf{b}$  et se trouvent dans le même plan de glissement comme le montre dans la Figure 1.10.

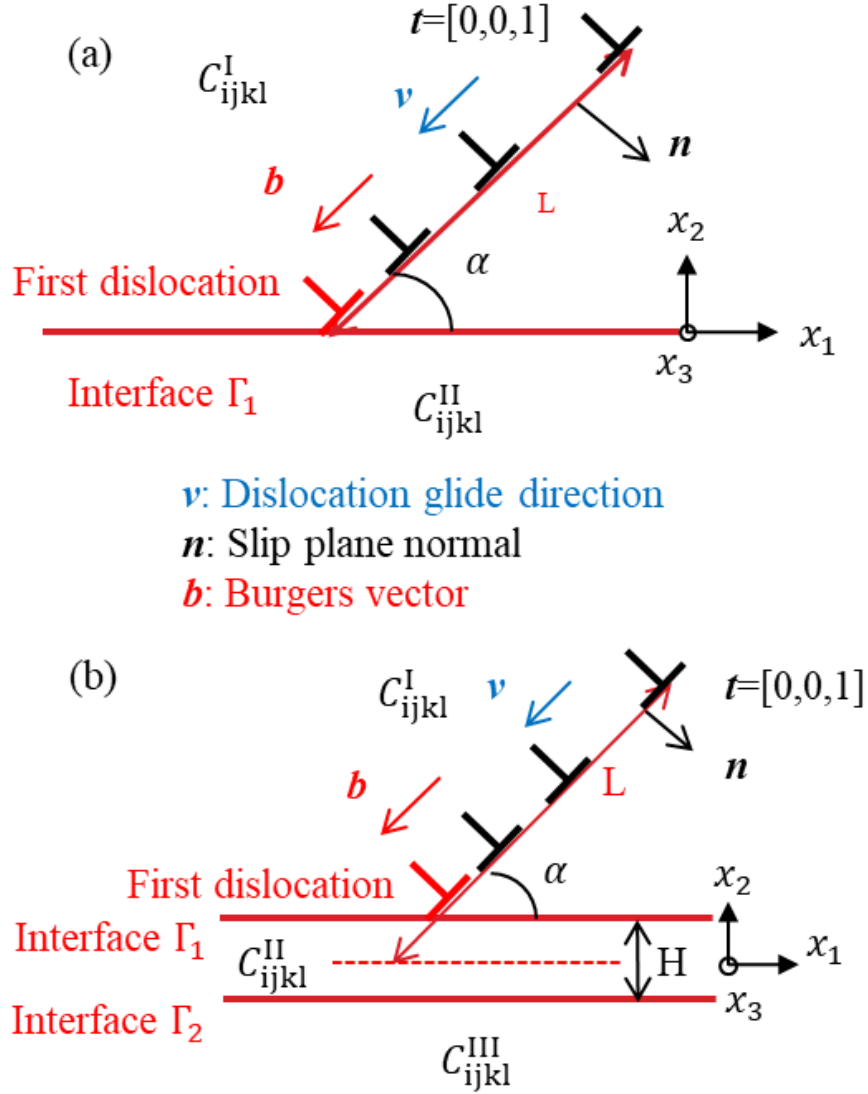


Figure 1.10: Empilements de  $N$  dislocations coins inclinées d'un angle  $\alpha$  par rapport au JDG dans un milieu anisotrope hétérogène de type (a) bi-matériau et (b) tri-matériau.. Leur plan de glissement est donné par la normale unitaire  $n$ . Les dislocations sont caractérisées par leur vecteur de Burgers  $b$  et leur vecteur ligne  $t$ .

Les positions d'équilibre des  $N$  dislocations peuvent être déterminées en minimisant, pour chaque dislocation, la composante de la force de Peach-Koehler (P-K) projetée le long de la direction de glissement jusqu'à une certaine force critique dénommée  $F_c$  comme suit :

$$F^{(\gamma)} = \text{abs}(\{(\sigma_{int}(X_1(\gamma), X_2(\gamma)) + \sigma_{ext}) \cdot b \times t\} \cdot v) \stackrel{\text{Minimiser}}{=} F_c \quad (1.17)$$

où  $(X_1(\gamma), X_2(\gamma))$  indique la position de la dislocation  $\gamma^{th}$ .  $\sigma_{ext}$  est un tenseur de contraintes appliqué homogène et  $\sigma_{int} = \sigma_{im} + \sigma_{dis}$  est le tenseur de contraintes internes produit par toutes les autres dislocations  $\sigma_{dis}$  sur la base des expressions dérivées dans les sous-sections précédentes et des contraintes images  $\sigma_{im}$  s'exerçant sur cette dislocation provenant des différentes hétérogénéités. La force critique  $F_c$  inclut la force de friction de réseau (primaire) et d'autres forces interagissant sur la dislocation, comme la force due aux cavités, etc. Cette force critique peut être convertie en une contrainte de cisaillement critique sur une dislocation en divisant par la longueur du vecteur de Burgers standard :  $\tau_c = F_c/|\mathbf{b}|$ . Il convient de souligner que dans le présent travail, le tenseur des contraintes homogènes appliquées  $\sigma_{ext}$  a pour unique objectif d'équilibrer l'empilement de dislocations. Le calcul des positions d'équilibre des dislocations est obtenu en suivant un schéma de relaxation itératif qui minimise tous les  $F^{(\gamma)}$  après qu'une configuration initiale ait été spécifiée [105]. Afin de pouvoir effectuer un tel calcul dans un milieu homogène infini, une dislocation doit être considérée comme fixe. Habituellement, la position de la première dislocation (ou la dislocation de tête)  $(X_1(1), X_2(1))$  est fixée [97, 105]. Par conséquent, la force P-K sur la dislocation fixée n'est pas nulle. Dans un milieu hétérogène, la force d'image sur la dislocation de tête peut équilibrer la contrainte appliquée et les contraintes provenant des autres dislocations [105], mais seulement dans le cas d'une forces d'image répulsive. Dans ce cas, toutes les positions des dislocations, y compris la dislocation de tête, peuvent être déterminées grâce au schéma de relaxation itératif. La plupart des chercheurs supposent que  $F_c = 0$  N/m à cause de la faible valeur de la contrainte de friction de réseau dans les cristaux CFC pur qui est d'environ  $1 \sim 2$  MPa [296]. Cependant, dans la présente thèse, il est montré qu'une force critique non nulle a un effet crucial sur le comportement des dislocations en présence du JDG et de surfaces libres. La raison est qu'il y a déjà des défauts de réseau dans le matériau après la préparation de l'échantillon, tels que des défauts dus aux ions  $\text{Ga}^+$  du FIB près de la surface [139]. De plus, pour  $\alpha$ -Brass en tant qu'alliage, la valeur théorique de la force de friction de réseau est beaucoup plus élevée que pour les cristaux purs, comme le Ni pur. Par exemple, il a été trouvé que  $\tau_c \approx 80 \sim 100$  MPa pour  $\beta$ -Brass [296]. Ainsi, la force critique ne peut pas être ignorée dans l'équation Eq. 1.17 pour des calculs réalistes.

## 1.4 Résultats théoriques préliminaires et discussion pour des dislocations simples et des empilements de dislocations dans des bi-cristaux de Ni

Afin d'estimer l'effet de plusieurs facteurs microstructuraux cruciaux, tels que la désorientation, la rigidité du JDG et la surface libre, plusieurs simulations avec des conditions idéales (étude théorique) ont d'abord été effectuées et sont résumées ci-dessous. D'autres résultats sont présentés dans l'article de Chen et al. [277].

Dans toutes les applications numériques suivantes, des bi-cristaux de Ni avec différentes orientations sont considérés. De plus, seules les dislocations coin avec un vecteur de Burgers défini par un angle  $\alpha = 45^\circ$  sont prises en compte comme le montre la Figure 1.7. La direction de glissement est donc  $\mathbf{m} = \mathbf{b}/|\mathbf{b}| = [-\cos 45^\circ, -\sin 45^\circ, 0]$  dans le repère global  $(\mathbf{x}_1, \mathbf{x}_2, \mathbf{x}_3)$ . Toujours selon la convention FS/RH, la normale au plan de glissement est donnée par  $\mathbf{n} = \mathbf{t} \times \mathbf{m}$  où  $\mathbf{t} = [0, 0, 1]$ . La direction de glissement des dislocations  $\mathbf{v}$  est parallèle à  $\mathbf{m}$  pour les dislocations coin et elle pointe toujours vers le JDG, de sorte qu'il est possible de créer des empilements de dislocations au JDG. Le système de glissement est supposé être  $\mathbf{m}^0 = 1/\sqrt{2}[1, 1, 0]$  et  $\mathbf{n}^0 = 1/\sqrt{3}[-1, 1, -1]$  dans le repère du cristal  $(\mathbf{e}_1, \mathbf{e}_2, \mathbf{e}_3)$ . Ainsi, l'orientation du cristal contenant les dislocations est définie par la matrice de passage  $\mathbf{T}$  telle que  $[\mathbf{m}, \mathbf{n}, \mathbf{t}]^T = \mathbf{T}[\mathbf{m}^0, \mathbf{n}^0, \mathbf{t}^0]^T$ , où  $\mathbf{t}^0 = \mathbf{m}^0 \times \mathbf{n}^0$ . Deux orientations spécifiques sont considérées dans ce qui suit :

- orientation A<sup>Ori</sup> avec  $\mathbf{T}_A = \begin{bmatrix} 1 & 0 & 0 \\ 0 & 1 & 0 \\ 0 & 0 & 1 \end{bmatrix}$  (Unit matrix)

- orientation B<sup>Ori</sup> avec  $\mathbf{T}_B = \begin{bmatrix} -1/2 & \sqrt{2}/2 & 1/2 \\ -1/2 & -\sqrt{2}/2 & 1/2 \\ \sqrt{2}/2 & 0 & \sqrt{2}/2 \end{bmatrix}$

Le tenseur de rigidité élastique dans le repère global est alors déduit de la matrice de passage  $\mathbf{T}$  par  $C_{ijkl} = T_{ig}T_{jh}C_{ghmn}^0T_{km}T_{ln}$  où  $\mathbf{C}^0$  est le tenseur de rigidité élastique défini dans le repère du cristal. Pour les modèles tri-matériau, l'épaisseur du second matériau représentant le JDG est notée  $H$  et est toujours égal à  $5|\mathbf{b}|$  dans la présente section. Le tenseur de rigidité élastique  $C_{ijkl}^{\text{II}}$  est



simplement modélisé grâce à un unique paramètre  $\lambda$  qui reflète la rigidité du JDG comme :

$$C_{ijkl}^{\text{II}} = \frac{\lambda}{2} (C_{ijkl}^{\text{I}} + C_{ijkl}^{\text{III}}) \quad (1.18)$$

Ainsi, le JDG est plus complaisant que les grains pour  $\lambda < 1$  et plus rigide que les grains pour  $\lambda > 1$ .

Pour les modèles multicouche avec surfaces libres, seule la configuration bi-couche est appliquée dans la présente section 1.4 avec  $h_1 = h_2 = H'/2$ , si bien que le JDG est considéré comme une interface sans épaisseur.

La distance entre le JDG (ou le milieu de la région correspondant au JDG) et la dislocation  $\gamma^{\text{th}}$  le long de la direction de glissement est dénommée  $L(\gamma)$ . Pour les empilements où la dislocation de tête est fixée,  $L(1) = 5|\mathbf{b}|$ , et la longueur de l'empilement est définie comme la distance entre la première et la dernière dislocation  $L(N) - L(1)$ .

Dans un milieu hétérogène, une force image s'exerce sur la dislocation en raison de la présence d'interface(s) ou de surface(s). La force d'image est la force de Peach-Koehler à la position de la dislocation due à son champ de contrainte sans considérer la contribution liée au milieu homogène infini. le tenseur des contraintes images est désigné ci-après  $\sigma_{im}$ . La projection de la force d'image selon la direction de glissement se réduit à [28] :

$$F_{im} = [(\sigma_{im} \cdot \mathbf{b}) \times \mathbf{t}] \cdot \mathbf{v} \quad (1.19)$$

Avec la convention utilisée dans la Figure 1.7, étant donné que  $\mathbf{v}$  pointe toujours vers le JDG,  $F_{im} > 0$  signifie que la dislocation est attirée par le JDG alors que  $F_{im} < 0$  signifie que la dislocation est repoussée par le JDG.

Dans la suite, l'effet de la désorientation et de la rigidité du JDG sont tout d'abord étudiés. Les deux orientations  $A^{\text{Ori}}$  et  $B^{\text{Ori}}$  sont considérées pour le cristal du bas et deux valeurs différentes de  $\lambda$ , 0.5 et 2, sont considérées dans le cas du modèle tri-matériau. L'effet de l'élasticité anisotrope vs. isotrope sur les forces images projetées selon la direction de glissement dans les configurations bi-matériau, demi-espace et tri-matériau est présenté sur la Figure 1.11. Les conclusions de cette étude théorique sont présentées ci-après (voir Chen et al. [277] pour plus de détails) :

- L'orientation  $A^{\text{Ori}}$  exerce un effet attractif sur la dislocation, alors qu'avec l'orientation  $B^{\text{Ori}}$ , la dislocation est repoussée par le JDG.
- Dans un demi-espace, une surface rigide a toujours un effet répulsif sur la dislocation et au contraire, une surface libre a toujours un effet attractif. On peut aussi remarquer que la magnitude de  $F_{im}$  est beaucoup plus grande

pour le demi-espace que pour les configurations bi-matériau ou tri-matériau. Par ailleurs, la valeur de  $F_{im}$  pour un demi-espace ne varie pas beaucoup selon que l'élasticité est supposée isotrope ou anisotrope.

- Un JDG compliant décrit par  $\lambda = 0.5$  exerce un effet attractif sur la dislocation, alors qu'un JDG rigide décrit par  $\lambda = 2$  présente un effet répulsif sur la dislocation.
- Dans le cas de l'élasticité anisotrope, il existe une position d'équilibre pour la dislocation où  $F_{im}$  présente un changement de signe à cause des effets inverses des forces image provenant à la fois du cristal inférieur et du JDG, comme  $A^{Ori}$  avec  $\lambda = 2$  ou  $B^{Ori}$  avec  $\lambda = 0.5$ . Lorsque le cristal inférieur et le JDG ont le même effet, cet effet sera renforcé. La distance d'action de la surface rigide/libre est plus grande que celle liée à l'effet de désorientation.
- La distance d'action de la rigidité du JDG est assez courte avec environ  $41|\mathbf{b}|$  et  $58|\mathbf{b}|$  pour les plus grands contrastes considérés  $\lambda = 2$  et  $\lambda = 0.5$ , respectivement. Cependant, il est important de pouvoir équilibrer la dislocation de tête dans l'empilement. Au-delà de cette distance, la force d'image dépend principalement de la désorientation des bi-cristaux.
- Pour une configuration tri-matériau avec élasticité isotrope, en raison de l'absence d'effet de désorientation provenant du cristal inférieur, la force image dépend uniquement de la rigidité du JDG.

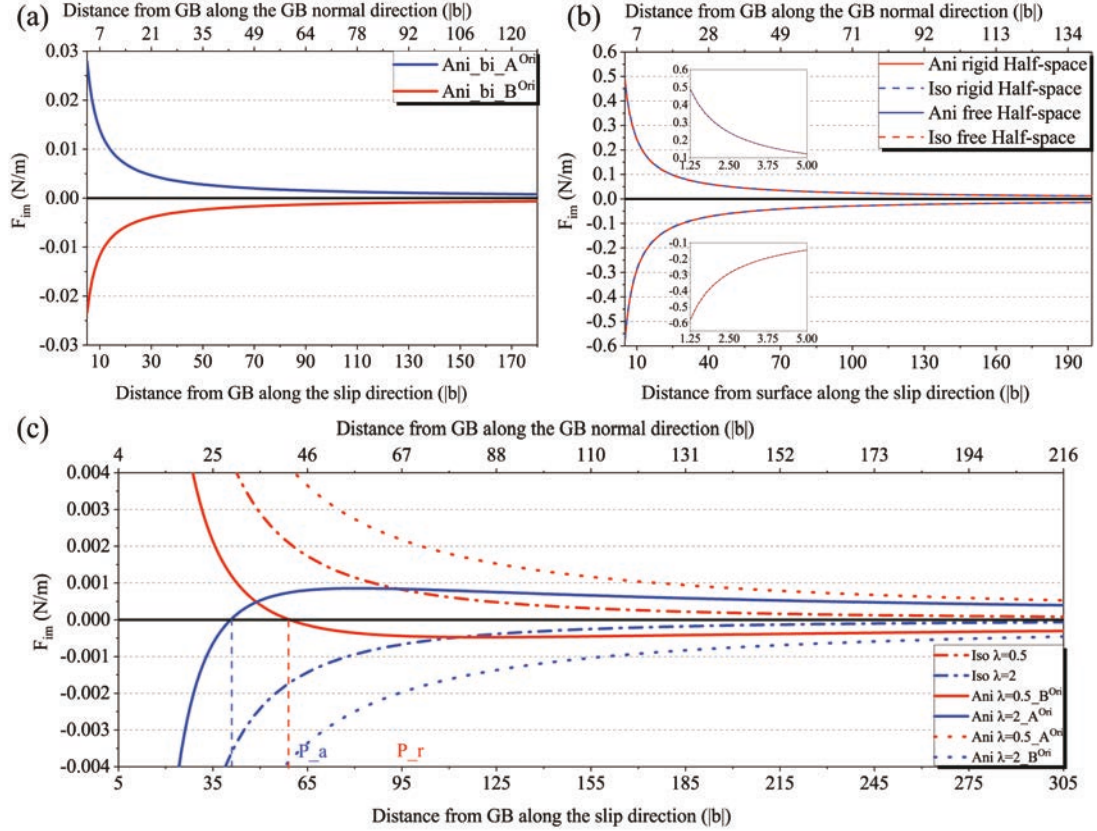


Figure 1.11: Variation de la force d'image projetée  $F_{im}$  avec la distance du JDG le long de la direction de glissement pour différentes configurations: (a) configurations de bi-matériau, (b) configuration de demi-espace et (c) configurations de tri-matériau avec élasticité anisotrope vs. isotrope.

Outre l'effet de la désorientation et de la rigidité du JDG, l'effet des surfaces libres sur la force image a également été étudié théoriquement en considérant une configuration à deux couches avec différentes désorientations  $A^{Ori}$ ,  $B^{Ori}$  et différentes épaisseurs  $H' = 2\mu\text{m}$ ,  $H' = 4\mu\text{m}$ . Les résultats des forces images projetées selon la direction de glissement sont présentés sur la Figure 1.12. Les conclusions sont énumérées ci-dessous :

- Les surfaces libres ont un fort effet attractif sur les dislocations. Comparé à l'effet de surface libre, l'effet de la désorientation est négligeable près de la surface libre car la variation de la force P-K avec l'orientation devient négligeable.
- Près du JDG, la force image est principalement contrôlée par la désorientation. En effet, les deux surfaces libres ont un effet opposé sur la dislocation.

Lorsque la dislocation se trouve à une distance à peu près égale des deux surfaces libres, leurs contributions s'annihilent et deviennent négligeable.

- Un effet de taille est constaté en présence de surfaces libres après normalisation de la distance par la moitié de l'épaisseur : à la même distance relative du JDG, la force image est plus forte dans le pilier le plus petit.
- En présence d'une surface libre et d'une désorientation attractive  $A^{\text{Ori}}$ , il existe un point d'équilibre où la force image sur la dislocation est nulle. Cette position est située à une distance relative presque identique du JDG pour différentes épaisseurs de matériau.

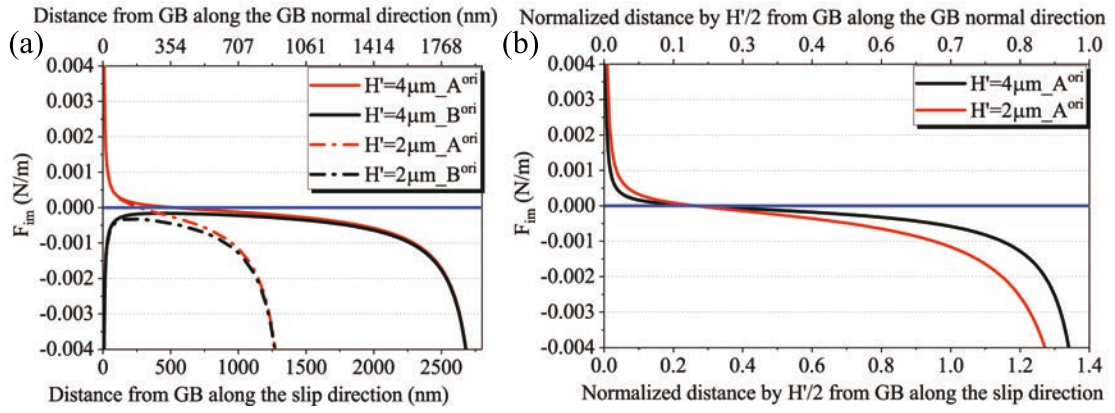


Figure 1.12: Variation de la force image projetée  $F_{im}$  pour un modèle à deux couches et pour deux épaisseurs totales différentes (a) avec la distance au JDG selon la direction de glissement et (b) avec la distance au JDG selon la direction de glissement normalisée par  $H'/2$ .

Puisque l'orientation du cristal inférieur a un effet plus important sur les dislocations à longue distance que la rigidité du JDG, la longueur des empilements de dislocations  $L$  est maintenant présentée sur la Figure 1.13 pour un JDG d'épaisseur nulle et différentes orientations du cristal inférieur dans le cas d'un empilement de 50 dislocations. L'orientation du cristal supérieur (où se trouve l'empilement) est fixée, toujours définie par  $\alpha = 45^\circ$ , alors que l'orientation du cristal inférieur est donnée par une rotation  $\psi$  autour de  $\mathbf{v}$ , de  $\psi = 0^\circ$  à  $\psi = 180^\circ$ . Afin de toujours obtenir une configuration stable (surtout dans le cas d'une désorientation attractive), la dislocation de tête de l'empilement est fixée. Ainsi, le mono-cristal homogène est retrouvé pour  $\psi = 0^\circ$  et  $\psi = 180^\circ$  pour lesquels  $L = 8.75 \mu\text{m}$  (Figure 1.13 (a)). Lorsque  $L$  est inférieure (resp. supérieure) à  $8.75 \mu\text{m}$ , la force image a globalement un effet attractif (resp. répulsif) sur l'empilement, comme le montre la Figure 1.13 (b). L'angle de désorientation entre les deux cristaux, c'est-à-dire l'angle de rotation minimal pour passer d'une orientation à l'autre,

est également présenté sur la Figure 1.13 (a). Dans cet exemple, la valeur maximale possible pour l'angle de désorientation d'un cristal cubique,  $62.8^\circ$  [298], est quasiment atteinte mais ne correspond pas à une valeur extrême de  $L$ . La valeur maximale de  $L$  correspond cependant à un angle de désorientation élevé (environ  $60^\circ$ ). De plus, il est à noter qu'un même angle de désorientation peut être lié à différents comportements élastiques (par exemple,  $60^\circ$  est retrouvé avec  $\psi = 60^\circ$  et  $\psi = 120^\circ$ , ce qui donne respectivement  $L = 9.02 \mu\text{m}$  et  $L = 8.61 \mu\text{m}$ ). Enfin, on peut observer que les variations relatives de  $L$  par rapport au cas isotrope dans le Ni peuvent atteindre environ 7%. Le point important est que de telles variations significatives se produisent dans un matériau possédant une anisotropie élastique modérée et ne peuvent pas être captées en considérant une élasticité isotrope. Cependant, en utilisant la moyenne de Voigt-Reuss-Hill [269, 270], la valeur de  $L$  donnée par l'élasticité isotrope est presque égale à la longueur moyenne des différentes configurations considérées en élasticité anisotrope (voir Figure 1.13 (a)). De plus, la variation relative maximale de  $L$  pour différents matériaux ayant des facteurs d'anisotropie différents (facteur de Zener) est présentée dans le Tableau 1.1. Cette variation relative augmente à mesure que le facteur d'anisotropie augmente. Comme l'effet du demi-espace rigide est beaucoup plus fort que l'effet de la désorientation,  $L$  et  $F_{im}$  sont tous les deux beaucoup plus importants dans le cas d'un demi-espace rigide que dans une configuration bi-matériau avec différentes désorientations.

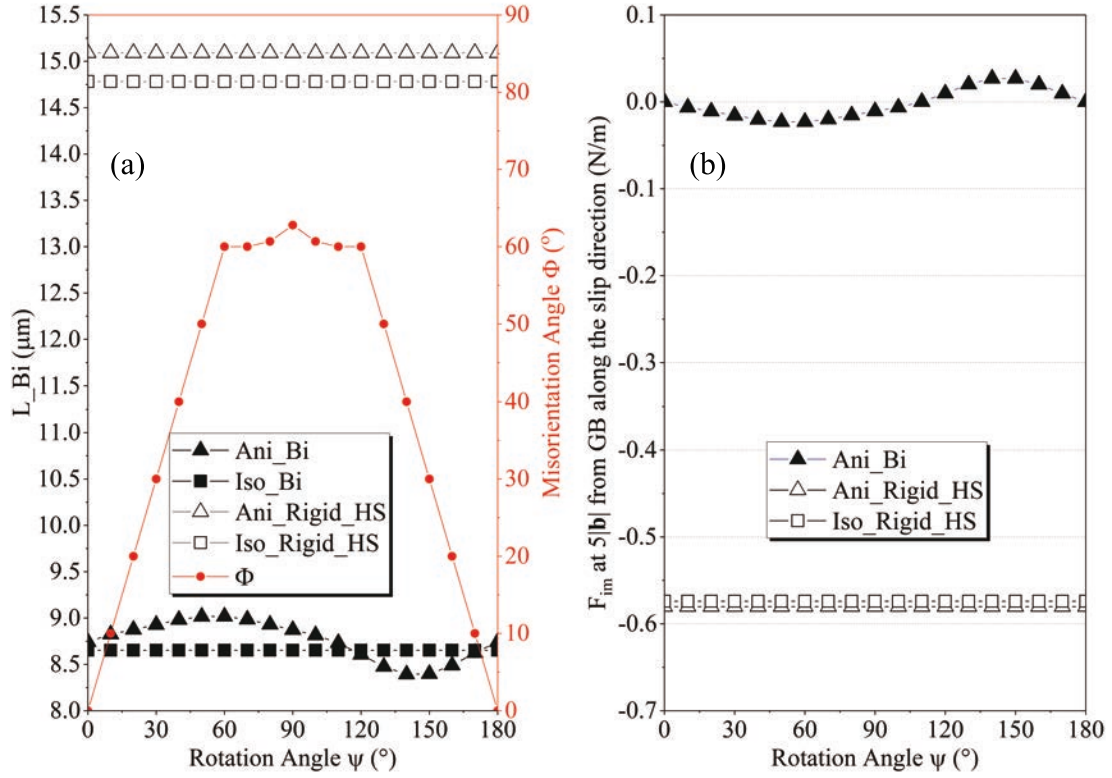


Figure 1.13: Effet de désorientation dans le cas de bi-cristaux (Ani\_Bi) sur (a) la longueur d'empilement  $L$  pour un empilement de 50 dislocations et un JDG d'épaisseur nulle et (b) sur la force image projetée selon la direction de glissement à une distance de  $5|\mathbf{b}|$  du JDG. L'axe de rotation est la direction de glissement  $\mathbf{v}$ . Comparaisons entre les cas de isotrope homogène (Iso\_Bi), demi-espace rigide isotrope (Iso\_Half space) et demi-espace rigide anisotrope (Ani\_Half space).

Matériau	Al	Ni	Cu	$\alpha$ -Brass
Facteur de Zener <sup>[1]</sup>	1.22	2.51	3.21	4.11
Variation relative maximale de $L$ (%)	1.2	7.2	9.0	11.5

Table 1.1: Variation relative maximale de  $L$  par rapport à un calcul en élasticité isotrope pour différents matériaux avec différents facteurs d'anisotropie (facteur de Zener). [1] Les constantes élastiques de ces matériaux se trouvent dans le livre "Theory of Dislocations" [28].

## 1.5 Résultats expérimentaux pour les bi-cristaux de Ni et de $\alpha$ -Brass

Tout d'abord, les lignes de glissement ont été observées par MEB pour le Ni (voir Figure 1.14 (a)) et pour le  $\alpha$ -Brass (voir Figure 1.15 (a)). Pour le Ni, les lignes de glissement sont très peu prononcées sur la surface supérieure et il n'y a que deux lignes de glissement évidentes en parallèle pour chaque cristal. D'après la direction des lignes de glissement sur la surface supérieure et l'analyse du facteur de Schmid d'après l'orientation cristalline locale, le système de glissement actif est déterminé comme celui ayant le facteur de Schmid maximum et reste inchangé en tenant compte des contraintes d'incompatibilité [160]. Pour chaque cristal, il s'agit du système B4 en utilisant la convention de Schmid et Boas [40] comme montré sur la Figure 1.14 (b).

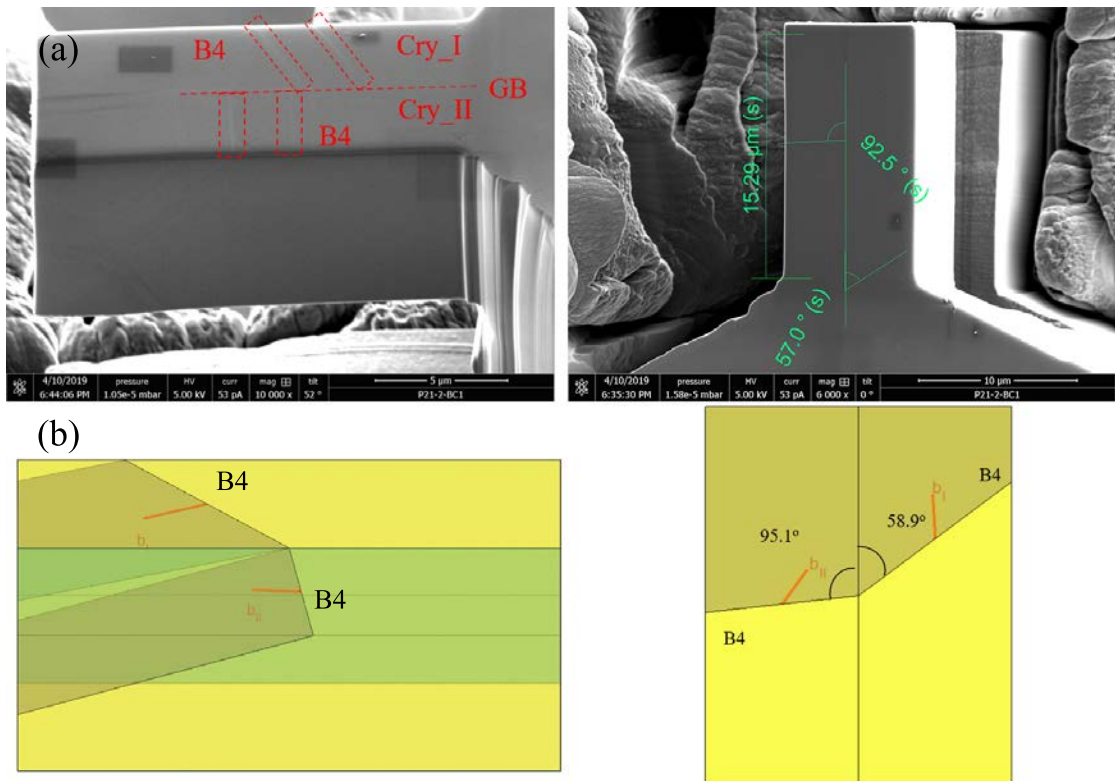


Figure 1.14: Analyse cristallographique des lignes de glissement par imagerie MEB pour l'échantillon de Ni après le test de compression. D'après la direction des lignes de glissement, l'orientation de chaque cristal et l'analyse du facteur de Schmid (ou en tenant compte des contraintes d'incompatibilité), le système de glissement actif est identifié comme le système B4 pour le cristal I et le système B4 pour le cristal II.

Cependant, pour le  $\alpha$ -Brass, il y a deux lignes de glissement évidentes qui s'intersectent sur la surface supérieure pour le cristal I et deux lignes de glissement évidentes qui s'intersectent sur la surface latérale pour le cristal II. D'après l'analyse de la direction des lignes de glissement et du facteur de Schmid (ou en tenant compte des contraintes d'incompatibilité) pour chaque système de glissement, comme montré sur la Figure 1.15 (b), les systèmes de glissement actifs sont déterminés comme suit : A6, C5 pour le cristal I et B4, D6 pour le cristal II en utilisant la convention de Schmid et Boas [40]. Ainsi, il y a plusieurs systèmes de glissement actifs dans les deux grains pour l'échantillon de  $\alpha$ -Brass.

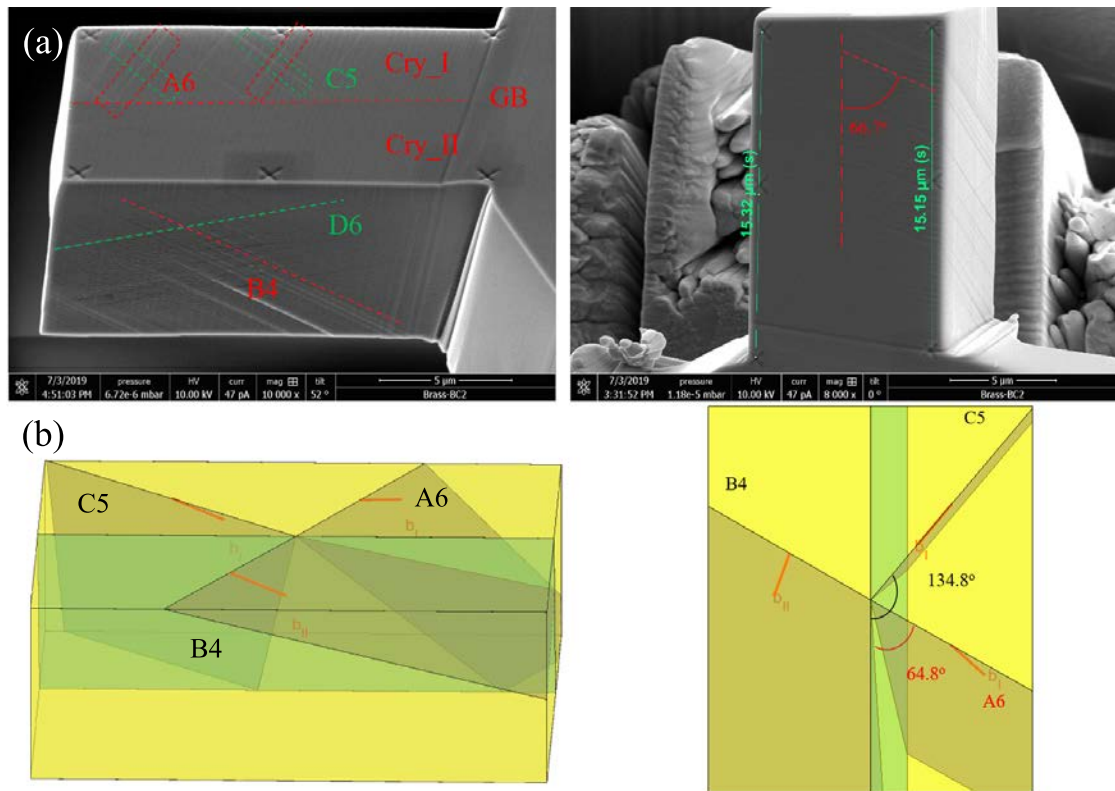


Figure 1.15: Analyse cristallographique des lignes de glissement par imagerie MEB pour l'échantillon de  $\alpha$ -Brass après le test de compression. D'après la direction des lignes de glissement, l'orientation de chaque cristal et l'analyse du facteur Schmid (ou en tenant compte des contraintes d'incompatibilité), les systèmes de glissement actifs sont déterminés comme A6 et C5 pour le cristal I et B4 pour le cristal II.

Une mesure AFM a ensuite été effectuée sur la surface supérieure des deux échantillons afin d'obtenir la topographie 3D des lignes de glissement comme indiquée sur la Figure 1.16 pour le Ni et sur la Figure 1.18 pour le  $\alpha$ -Brass. Les marches de glissement correspondent aux lignes de glissement présentées dans les



images MEB (Figure 1.14 et 1.15). Pour l'échantillon de Ni, une marche ayant les caractéristiques classiques d'un empilement de dislocations a été sélectionnée pour l'analyse. Les hauteurs de la ligne supérieure et de la ligne inférieure de cette marche ont été mesurées dans la direction de glissement à partir du JDG, et sont marquées respectivement par une ligne rouge et une ligne noire sur la Figure 1.16. Les données mesurées ont été ajustées par une méthode polynomiale, et sont marquées comme  $h^{Top}$  et  $h^{Bottom}$ . Ensuite, la hauteur relative de cette marche  $\Delta h$  a été calculée comme étant la différence de la hauteur ajustée entre ces deux lignes, comme le montre la Figure 1.17. On constate que la différence de hauteur entre deux lignes au JDG:  $\Delta h_{GB} \approx 0.86$  nm n'est pas zéro, ce qui correspond à une faible transmission de glissement comme observé sur la Figure 1.16 (b) à l'intérieur du cadre en tirets rouges. La hauteur de marche augmente à partir du JDG dans le sens du glissement et atteint sa valeur maximale  $\Delta h \approx 9.06$  nm à environ  $d \approx 3.28$   $\mu\text{m}$ . De plus, un événement de glissement au JDG peut être observé dans la partie supérieure du pilier, comme le montre la bosse sur la Figure 1.16 (a) et le cadre en pontillés verts sur la Figure 1.16 (b).

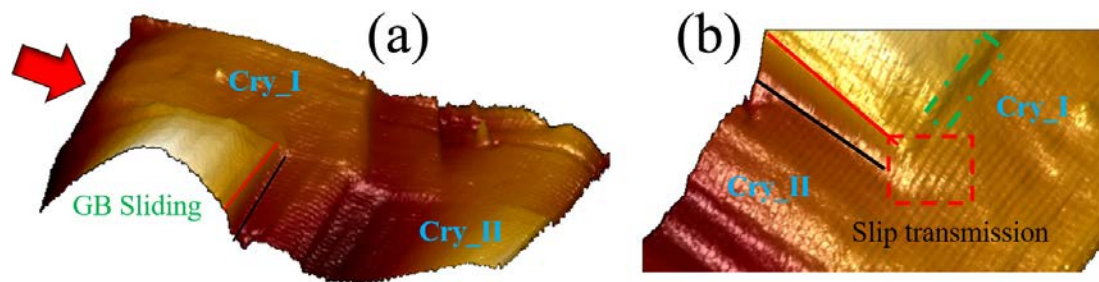


Figure 1.16: Mesure topographique AFM du Ni pour (a) toute la surface supérieure et (b) le phénomène de transmission au JDG au sein du cadre en tirets rouges. La flèche rouge indique la direction du chargement. La bosse dans le cristal II montrée dans (a) et le cadre en pointillés verts montré dans (b) indiquent le glissement au JDG.

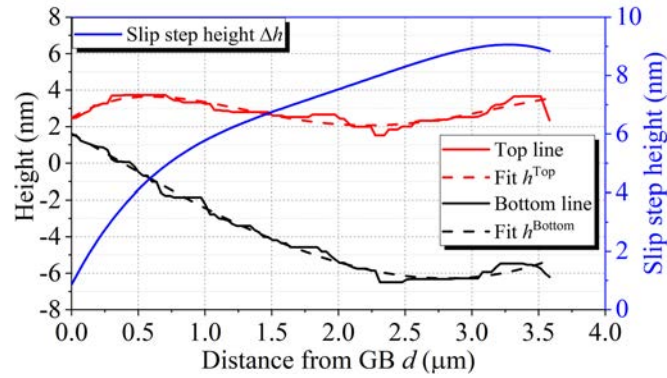


Figure 1.17: Résultats des mesures de hauteur de glissement pour l'échantillon de Ni: la ligne rouge et la ligne noire continues indiquent les hauteurs mesurées pour les lignes supérieures et inférieures de la marche, respectivement. Les lignes en tirets avec la couleur correspondante indiquent les résultats de l'ajustement par méthode polynomiale avec le coefficient de détermination  $R^2 = 0.8176$  pour la ligne supérieure et  $R^2 = 0.9898$  pour la ligne inférieure. La ligne bleue indique la hauteur de marche simulée.

Une analyse similaire a été effectuée pour l'échantillon de  $\alpha$ -Brass comme le montre dans la Figure 1.19. Alors que la transmission de glissement est plus intense par rapport à l'échantillon de Ni,  $\Delta h_{GB} \approx 4.29$  nm, la propagation des dislocations dans le grain adjacent s'effectue elle sur une distance plus courte. Le maximum de la hauteur de marche est  $\Delta h \approx 10.03$  nm à environ  $d \approx 2.44$   $\mu\text{m}$ . Il y a un creux évident dans la partie centrale de la courbe de hauteur de marche qui pourrait être causé par l'intersection avec une ligne de glissement non coplanaire.

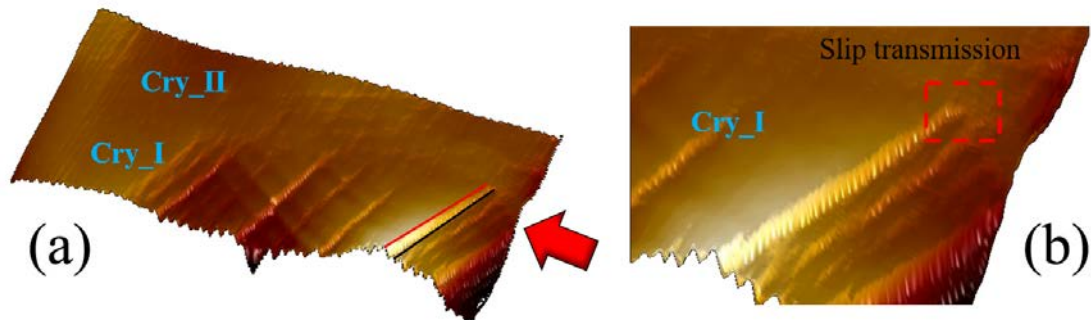


Figure 1.18: Mesure AFM de  $\alpha$ -Brass pour (a) toute la surface supérieure et (b) le phénomène de transmission au JDG. La flèche rouge indique la direction de chargement.

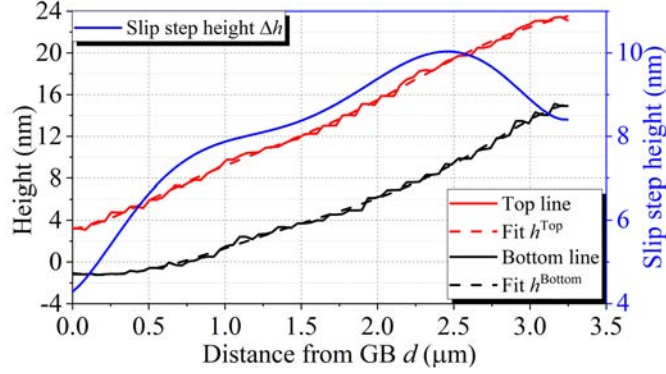


Figure 1.19: Résultats des mesures de hauteur de glissement pour l'échantillon de  $\alpha$ -Brass : la ligne rouge et la ligne noire continues indiquent les hauteurs mesurées pour les lignes supérieures et inférieures de la marche, respectivement. Les lignes en tirets avec la couleur correspondante indiquent les résultats de l'ajustement par méthode polynomiale avec le coefficient de détermination  $R^2 = 0.9982$  pour la ligne supérieure et  $R^2 = 0.9973$  pour la ligne inférieure. La ligne bleue indique la hauteur de marche simulée.

## 1.6 Simulation des profils de hauteur de marche de glissement en utilisant les calculs d'empilement de dislocations discrètes et discussion

Les hauteurs de marche de glissement dues à des empilements de dislocations mesurées dans les expériences peuvent être simulées en utilisant les modèles développés dans le chapitre 1.3. Pour les calculs, les hypothèses et les configurations sont définies comme suit et sont présentées sur la Figure 1.20:

- Les lignes de dislocations sont supposées être des lignes droites infinies. Elles sont parallèles les unes aux autres et également parallèles au plan du JDG.
- La position de la hauteur de marche maximale mesurée dans l'expérience est considérée comme la fin de l'empilement de dislocations. Cependant, dans le modèle, la dernière dislocation est fixée à la position de la hauteur de marche maximale et est considérée comme une dislocation source.
- Les dislocations produites par cette source créeront un empilement si elles se déplacent vers le JDG et créeront une marche sur la surface latérale si elles se déplacent également en direction de la surface libre.
- Le JDG est considéré comme une interphase d'épaisseur 0.9 nm, qui est obtenue à partir d'une simulation MD. Cette interphase est considérée comme

anisotrope avec  $\lambda$  égal à 1 comme défini dans l'Eq. 1.18. Pour comparaison, une élasticité isotrope pour le JDG a également été considérée en utilisant la moyenne de Voigt-Reuss-Hill [269, 270], où le tenseur de rigidité est modélisé par :

$$C_{ijkl}^{\text{II}} = 3kJ_{ijkl} + 2GK_{ijkl} \quad (1.20)$$

où  $k = \frac{2G(1+\nu)}{3(1-2\nu)}$  est le module de compressibilité,  $G$  le module de cisaillement,  $\nu$  le coefficient de Poisson,  $J_{ijkl} = \frac{1}{3}\delta_{ij}\delta_{kl}$ , et  $K_{ijkl} = \frac{1}{2}\left(\delta_{ik}\delta_{jl} + \delta_{il}\delta_{jk} - \frac{2}{3}\delta_{ij}\delta_{kl}\right)$ .

- Etant donné que la théorie est bi-dimensionnelle (invariance le long de la ligne de dislocation), des dislocations avec des directions de ligne différentes ne peuvent pas être considérées en même temps. Ainsi, les dislocations transmises sont supposées être représentées par une super-dislocation interfaciale fixée dans l'interphase du JDG. Par conséquent,  $\mathbf{b}^{\text{Tran}} = N^{\text{Tran}} \times \mathbf{b}^{\text{GB}}$ , où  $\mathbf{b}^{\text{Tran}}$  est le vecteur de Burgers de cette super-dislocation,  $N^{\text{Tran}}$  est le nombre de dislocations transmises et  $\mathbf{b}^{\text{GB}}$  est le vecteur de Burgers d'une dislocation stockée dans le JDG. Ce vecteur de Burgers peut être considéré comme identique au vecteur de Burgers des dislocations entrantes, ou il peut être défini comme le vecteur de Burgers résiduel entre le système de glissement entrant et l'un des 12 systèmes de glissement sortant dans le grain adjacent tel que  $\mathbf{b}^{\text{GB}} = \mathbf{b}^{\text{In}} - \mathbf{b}^{\text{Out}}$ .
- Comme présenté dans la section 1.3.1, en ce qui concerne le système de coordonnées de la simulation, la direction  $\mathbf{x}_3$  est définie comme étant la direction de la ligne de dislocation  $z_S$  comme présenté dans la Figure 1.20, et la direction  $\mathbf{x}_2$  est définie comme étant la direction normale au JDG  $y_S$  comme présenté dans la Figure 1.20. La direction  $\mathbf{x}_1$  est déterminée par  $\mathbf{x}_1 = \mathbf{x}_2 \times \mathbf{x}_3$  et correspond à  $x_S$  dans la Figure 1.20. De plus, tous les vecteurs et tenseurs utilisés, tels que le vecteur de Burgers des systèmes de glissement actifs, le vecteur donnant la direction de glissement, le tenseur de rigidité élastique, etc. sont transformés dans le système de coordonnées de la simulation.
- Les positions d'équilibre des dislocations dans l'empilement sont déterminées d'après l'Eq. 1.17, puis la hauteur des marches de glissement le long de la direction de glissement peut être calculée par :

$$\Delta h(d) = N(d) \times b(Z) \quad (1.21)$$

où  $d$  est la distance au JDG dans la direction de glissement,  $N$  le nombre de dislocations passant par ce point et  $b(Z)$  est la composante hors plan de la surface du vecteur de Burgers (dans la direction  $Z$  qui est perpendiculaire à la surface supérieure comme indiqué sur dans Figure 1.20).

- Dans les parties suivantes, la hauteur de marche mesurée est étalonnée pour être nulle au JDG, c'est-à-dire  $\Delta h = h^{Top} - h^{Bottom} - \Delta h_{GB}$ . De même, la hauteur de glissement simulée est considérée comme nulle au JDG, c'est-à-dire  $\Delta h(0) = 0$ .

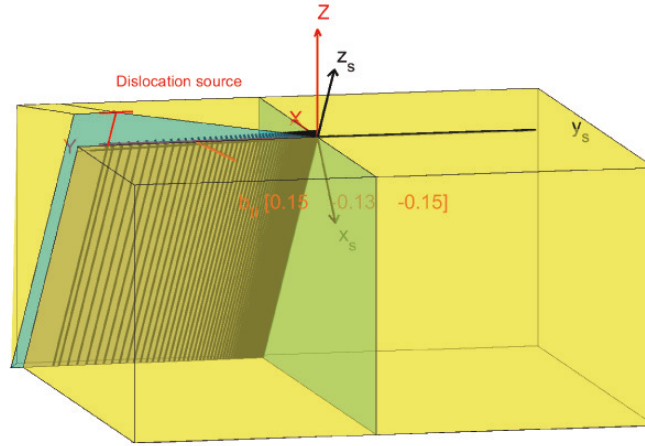


Figure 1.20: Schéma de la configuration adoptée pour simuler l'expérience.  $(x_s, y_s, z_s)$  indique le système de coordonnées de la simulation, tandis que  $(X, Y, Z)$  indique le système de coordonnées globales de l'échantillon.

Pour les résultats qui suivent, les valeurs par défaut des paramètres sont définies comme suit : le vecteur de Burgers des dislocations transmises interfaciales est supposé identique au vecteur de Burgers des dislocations entrantes et la force critique est définie comme étant  $F_c = 0$  N/m. Par défaut, les calculs sont effectués avec une élasticité anisotrope. Cependant, le formalisme L-E-S ne peut pas être utilisé pour un calcul en élasticité isotrope en raison du problème des valeurs propres répétées (solutions dégénérées). Dans ce cas, les modules de rigidité élastique sont d'abord déterminés à partir des constantes d'élasticité isotrope avec  $C_{11} = 2G(1 - \nu) / (1 - 2\nu)$ ,  $C_{12} = 2G\nu / (1 - 2\nu)$  et  $C_{44} = G$ . Ensuite, la valeur de  $C_{44}$  est très légèrement modifiée afin d'éviter le problème des solutions dégénérées dans le formalisme L-E-S et est remplacé par  $C_{44} = C_{44} \times 1.0001$ .

D'après les hypothèses ci-dessus, pour l'échantillon de Ni, la composante hors plan de la surface du vecteur de Burgers pour le système de glissement analysé est environ 0.15 nm. La hauteur de marche maximale est environ 9.1 nm à  $d \approx 3.28 \mu\text{m}$

et la hauteur de marche au JDG due à la transmission est environ 0.86 nm. Ainsi, d'après l'Eq. 1.21, le nombre de dislocations produites par la source de dislocations est de 61 et le nombre de dislocations transmises est de 6. Par conséquent, le nombre de dislocations dans l'empilement est égal à 55. La contrainte appliquée est de 289.4 MPa telle que mesurée dans l'expérience. Avec tous ces paramètres, le profile de la hauteur de marche ainsi que la distribution des dislocations dans l'empilement ont été calculés pour différentes orientations du vecteur de Burgers interfacial et différentes forces critiques tout en considérant l'effet des surfaces libres. De plus, l'effet de l'élasticité anisotrope par rapport à une hypothèse d'élasticité isotrope ainsi que le nombre de dislocations interfaciales ont été étudiés.

Pour résumer, les effets des différents paramètres sont les suivants :

- Effet des surfaces libres : Les résultats des simulations tri-matériau sans surfaces libres (marquées INF) et avec surfaces libres (marquées FS) sont présentés dans la Figure 1.21. Les résultats des simulations sont proches des mesures expérimentales, mais il y a encore quelques divergences. Par rapport à la mesure expérimentale, les dislocations sont plus proches du JDG dans INF, tandis qu'elles sont plus proches de la première surface libre lorsqu'on considère l'effet des surfaces libres dans FS. Cela s'explique par le fait que les dislocations sont plus proches de la première surface libre que de la seconde, de sorte que la force totale provenant des deux surfaces libres est toujours dirigée vers la première surface libre. Cependant, les dislocations autour du JDG sont presque au milieu de deux surfaces libres, ainsi les effets de ces deux surfaces libres se compensent l'un l'autre.

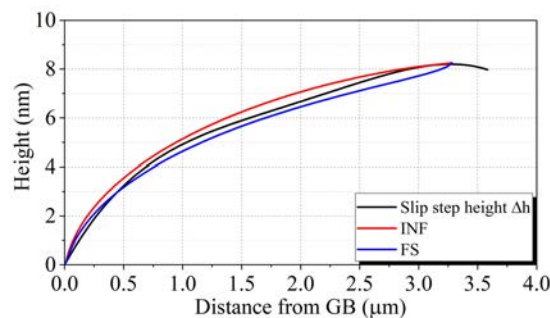


Figure 1.21: Simulation de la hauteur de marche dans le modèle tri-matériau sans surfaces libres (INF) et dans le modèle trois couches avec surfaces libres (FS).

- Effet des dislocations interfaciales : Avec les hypothèses de la simulation, le nombre de dislocations interfaciales est supposé égal au nombre de dislocations transmises. Ainsi, l'effet du nombre de dislocations interfaciales est tout d'abord étudié comme le montre la Figure 1.22 (a). A partir de la

mesure expérimentale, le nombre de dislocations transmises est de 6. Pour comparaison, le calcul est également effectué pour une unique dislocation interfaciale. Les calculs montrent que les positions d'équilibre des dislocations dans l'empilement sont plus proches du JDG pour 1 unique dislocation interfaciale que pour 6 dislocations interfaciales en raison d'une force de répulsion moindre. Comme le phénomène de transmission est clairement observé par la mesure AFM, le vecteur de Burgers des dislocations interfaciales  $\mathbf{b}^{\text{GB}}$  est également étudié. Les résultats pour deux cas particuliers sont présentés sur la Figure 1.22 (b). Pour le premier cas, le vecteur de Burgers de la dislocation interfaciale correspond au vecteur de Burgers résiduel avec le système de glissement sortant ayant le facteur de transmission maximum (marqué comme Residu\_B5). Pour l'autre cas, le vecteur de Burgers résiduel est calculé avec le système de glissement sortant ayant le facteur de Schmid maximum dans le grain adjacent (marqué comme Residu\_B4). Dans les deux cas, les résultats montrent que les positions d'équilibre des dislocations sont déplacées vers JDG et sont très éloignées de la mesure expérimentale par rapport au cas où le même vecteur de Burgers que la dislocation entrante est considéré. Il semble que les résultats seront meilleurs si l'on considère les surfaces libres pour ces cas, car les surfaces libres déplaceront toutes les dislocations vers la première surface libre. Cependant, d'après les résultats présentés sur la Figure 1.22, on constate qu'à proximité du JDG, les résultats avec 1 seule dislocation interfaciale ou avec des vecteurs de Burgers résiduels sont très éloignés de la mesure expérimentale par rapport aux résultats avec 6 dislocations interfaciales de même vecteur de Burgers que la dislocation entrante. Hors, on sait que les effets des surfaces libres sont faibles à proximité du JDG. Ainsi, les résultats ne seront pas meilleurs même en considérant les surfaces libres pour ces cas. Il faut souligner que les 12 vecteurs de Burgers résiduels calculés d'après les 12 systèmes de glissement dans le grain CFC adjacent ont été testés. Ainsi, d'après ces analyses et pour cet échantillon, la meilleure solution reste celle de considérer le même vecteur de Burgers que la dislocation entrante pour les dislocations interfaciales.

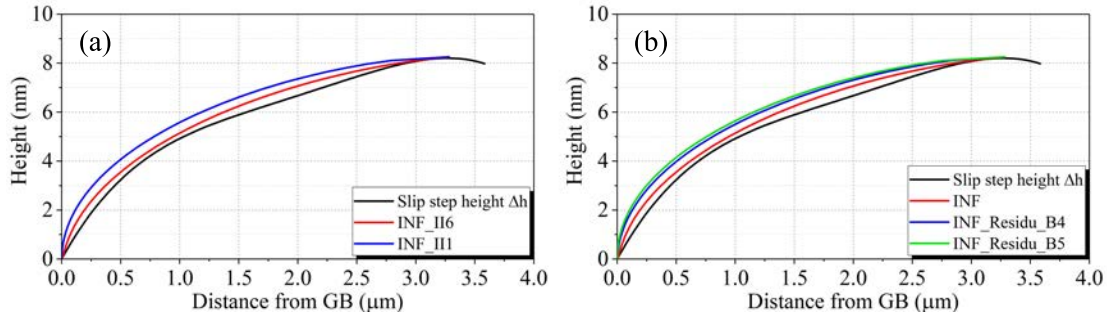


Figure 1.22: Simulation de la hauteur de marche dans INF pour (a) différents nombres de dislocations interfaciales: 1 dislocation interfaciale (III) et 6 dislocations interfaciales (II6), et (b) différents vecteurs de Burgers pour les dislocations interfaciales: vecteur de Burgers résiduel déterminé entre le système de glissement entrant et le système sortant ayant un facteur de transmission maximal (Residu\_B5) et le système sortant ayant un facteur de Schmid maximal (Residu\_B4).

- Effet de la force critique : Comme on l'a vu dans la sous-section 1.3.6, il faut tenir compte de l'effet de la force critique  $F_c$  (voir Eq. 1.17). Les résultats tenant compte ou non de la force critique sont présentés dans la Figure 1.23. On constate que  $F_c$  déplace la dislocation vers le JDG. En considérant l'effet des surfaces libres avec une force critique  $F_c = 0.003$  N/m ( $\tau_c = 12$  MPa), un résultat de simulation plus proche de la mesure expérimentale est obtenu comme le montre la courbe rouge avec le nom FS\_Fc0.003 sur la Figure 1.23 (b). La valeur de  $F_c$  est dans ce cas supérieure à la valeur théorique pour un cristal CFC pur, généralement autour de  $1 \sim 2$  MPa [296]. La raison peut provenir de la préparation de l'échantillon, du fait des défauts provenant du polissage FIB ou simplement du fait que seules les dislocations droites sont prises en compte dans le formalisme L-E-S. De plus, on constate que la force critique n'a pas d'effet évident sur les dislocations distantes du JDG jusqu'à  $d = 0.5 \mu\text{m}$  dans le modèle INF comme le montre la Figure 1.23 (a). D'après l'Eq. 1.17, on peut voir que cette force critique n'a pas un effet uniforme sur toutes les dislocations de l'empilement. Par exemple, lorsque la force totale sur la dislocation est dirigée vers la surface libre pour les positions proches de la surface libre, la force critique pointera vers le JDG. Cependant, l'état de contrainte est plus compliqué au voisinage du JDG. La force totale sur une dislocation peut pointer vers le JDG en raison des forces répulsives des autres dislocations, d'une désorientation attractive, d'un JDG complaisant, de la force attractive des dislocations interfaciales et de la contrainte appliquée. Au contraire, elle peut pointer dans la direction opposée en raison d'une désorientation répulsive, d'un JDG rigide, de la force répulsive des dislocations interfaciales ou des autres dislocations devant cette



dislocation et de l'effet des surfaces libres même si elle est faible ici. Ainsi, la force totale dépend ici de nombreux paramètres. La force critique peut donc soit déplacer les dislocations vers le JDG ou dans la direction opposée.

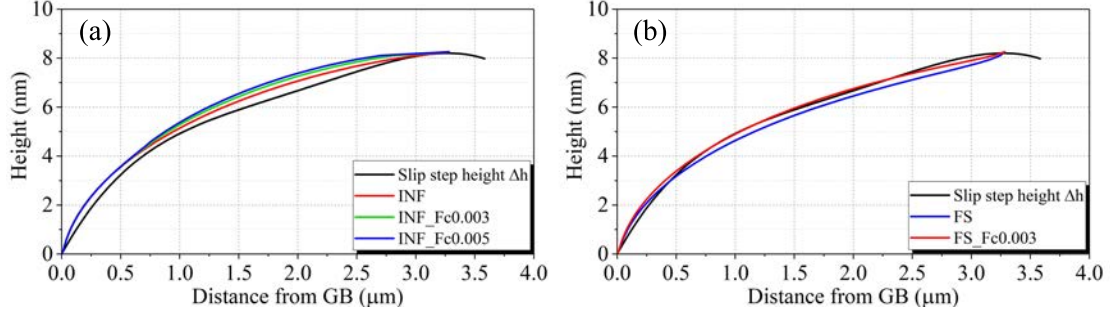


Figure 1.23: Simulation de la hauteur de marche dans (a) INF et (b) FS en considérant différentes forces critiques ( $F_c$ ) (N/m).

- Effet de l'anisotropie élastique : Comme le facteur d'anisotropie élastique du Ni  $A = 2.51$  est supérieur à 1, l'anisotropie élastique a une influence sur le comportement des dislocations dans l'échantillon de Ni. Afin de déterminer l'effet de l'anisotropie élastique, la hauteur de marche est calculée en considérant une élasticité isotrope sans surfaces libres (marquées comme "INF\_ISO") et avec des surfaces libres (marquées comme "FS\_ISO") qui sont montrées dans la Figure 1.24 (a) et (b), respectivement. La différence entre les cas avec élasticité isotrope et élasticité anisotrope n'est pas trop grande. L'une des raisons est que la force image due à la désorientation actuelle est de 0.0103 N/m. Cependant, avec une autre orientation du grain adjacent, la force image maximale pour ce système de glissement pourrait être de 0.0502 N/m. De plus, dans la configuration actuelle, les dislocations sont fixées des deux côtés de l'empilement, ce qui limite les possibilités pour la distribution des dislocations. En considérant les surfaces libres avec une élasticité isotrope, toutes les dislocations sont déplacées vers la surface libre et le profil de hauteur de glissement simulé devient très éloigné de la mesure expérimentale. Par ailleurs, l'interphase a également été considérée comme élastique isotrope comme montré sur la Figure 1.24 (a) avec le nom "INF\_InterISO" et dans la Figure 1.24 (b) avec le nom "FS\_InterISO". On peut voir que le résultat est quasiment le même que pour une interphase anisotrope avec  $\lambda = 1$ .

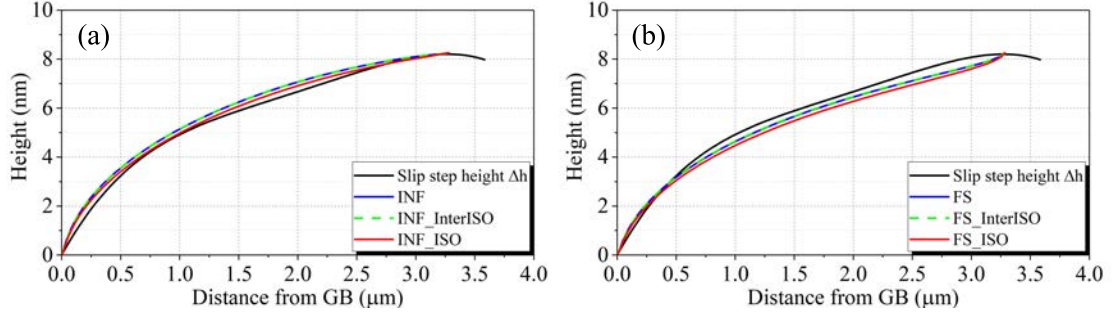


Figure 1.24: Simulation de la hauteur de marche en supposant une élasticité isotrope ou anisotrope (a) dans INF avec INF\_InterIso pour des grains élastiques anisotropes et une interphase élastique isotrope et INF\_ISO pour le cas où toutes les couches sont élastiques isotropes et (b) dans FS avec toutes les configurations correspondantes.

En conclusion, la meilleure solution pour cette simulation sur un échantillon de Ni est de considérer une élasticité anisotrope, l'effet des surfaces libres et une force critique  $F_c = 0.003 \text{ N/m}$  ( $\tau_c = 12 \text{ MPa}$ ).

Comme pour l'échantillon de Ni, les mêmes simulations ont été effectuées pour l'échantillon de  $\alpha$ -Brass. Pour l'échantillon actuel de  $\alpha$ -Brass, la composante hors plan de la surface du vecteur de Burgers du système de glissement analysé est environ  $0.14 \text{ nm}$ . La hauteur de marche maximale est environ  $10.03 \text{ nm}$  à  $d \approx 2.44 \mu\text{m}$  et la hauteur de marche au JDG due à la transmission est environ  $4.29 \text{ nm}$ . D'après l'Eq. 1.21, le nombre de dislocations dans l'empilement produit par la source de dislocations est de 72 et le nombre de dislocations transmises est de 31. Par conséquent, le nombre de dislocations dans l'empilement est égal à 41. La contrainte appliquée est de  $127.4 \text{ MPa}$  selon la mesure expérimentale. Les effets des surfaces libres, de la force critique et de l'élasticité anisotrope pour l'échantillon de  $\alpha$ -Brass sont les mêmes que pour l'échantillon de Ni. Cependant, le nombre de dislocations transmises est beaucoup plus important que pour le Ni, 31 au lieu de 6. Ainsi, la force répulsive de ces dislocations interfaciales est plus importante si leur vecteur de Burgers est considéré comme identique à celui des dislocations entrantes (voir les courbes bleues sur la Figure 1.25). Toutes les dislocations sont éloignées du JDG dans la direction de la surface libre en raison de cette force répulsive. Cette transmission observée sur la Figure 1.18 (b) conduit à considérer un vecteur de Burgers résiduel pour les dislocations interfaciales. Après avoir étudié tous les vecteurs de Burgers résiduels possibles avec les 12 systèmes de glissement dans le grain adjacent, la meilleure solution est trouvée pour le système de glissement A6 dans le grain adjacent tout en considérant les surfaces libres et une force critique raisonnable  $F_c = 0.011 \text{ N/m}$  ( $\tau_c = 43 \text{ MPa}$ ) comme le montre la Figure 1.25 (b). En outre, l'analyse théorique des traces de glissement du système A6 sur la surface supérieure du grain adjacent concorde bien avec l'observation expérimentale

comme le montre la Figure 1.18 (b). Comme on l'a vu dans la sous-section 1.5 pour  $\alpha$ -Brass, le creux dans la partie centrale de la courbe mesurée est certainement causée par l'intersection avec des lignes de glissement non coplanaires. Dans la présente théorie d'élasticité anisotrope bi-dimensionnelle, il n'est pas possible de considérer l'effet de dislocations ayant des lignes non parallèles. Ainsi, ce creux ne peut pas être prédit par le présent modèle. Cependant, il est important d'ajuster la partie de la courbe proche du JDG correspondant à  $d < 0.75 \mu\text{m}$ . La contrainte critique trouvée vaut  $\tau_c = 43 \text{ MPa}$  et est ainsi plus grande que la contrainte critique pour l'échantillon de Ni. Cependant, elle semble être acceptable pour cet alliage comme discuté dans la sous-section 1.3.6.

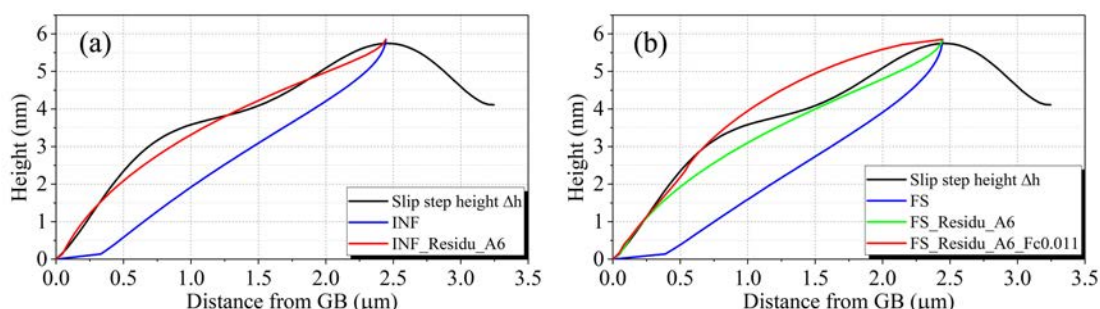


Figure 1.25: Simulation de la hauteur de marche (a) dans INF en tenant compte du vecteur de Burgers résiduel des dislocations interfaciales et (b) dans FS en tenant compte de la force critique.

En conclusion, la meilleure solution déduite de ces simulations pour l'échantillon de  $\alpha$ -Brass est de considérer l'élasticité anisotrope, l'effet des surfaces libres, une force critique  $F_c = 0.011 \text{ N/m}$  ( $\tau_c = 43 \text{ MPa}$ ) et un vecteur de Burgers résiduel pour les dislocations interfaciales étant donné qu'il y a un nombre très grand de dislocations transmises.

## 1.7 Conclusions et perspectives

Dans la présente thèse, une approche analytique basée sur le formalisme L-E-S [28, 22, 285] a été utilisée pour étudier les champs élastiques d'une unique dislocation droite et de différents empilements de dislocations dans des milieux homogènes anisotropes, des demi-espaces, des bi- et tri-matériaux [17] tout en considérant éventuellement les effets des surfaces libres [18]. La configuration tri-matériau permet de considérer une épaisseur non nulle de l'ordre du nanomètre et un tenseur de rigidité spécifique pour la région du JDG. La configuration avec deux surfaces libres peut être utilisée pour étudier les effets de taille. Les effets de l'élasticité anisotrope, de l'orientation cristallographique, de la rigidité du JDG

et des surfaces libres ont été étudiés dans le cas d'une unique dislocation dans un bi-cristal de Ni. Des forces image peuvent apparaître en raison, à la fois des différences d'orientation entre grains, de la présence d'un JDG d'épaisseur finie et de la présence de surfaces libres. En particulier, il est montré que la force de Peach-Koehler projetée le long de la direction de glissement peut présenter un changement de signe avec la position de la dislocation. En outre, on constate que les distances d'action de ces facteurs hétérogènes sont différentes. La surface libre ou rigide a la plus grande distance d'action dans le grain et son impact est le plus important. L'effet de la désorientation est beaucoup plus faible que l'effet de la surface libre et donc la distance d'action est plus courte. Enfin, la rigidité du JDG a la distance d'action la plus courte. Cependant, la rigidité du JDG est importante pour modifier l'état de contrainte local afin, par exemple, d'équilibrer la dislocation de tête dans les empilements. Pour les empilements, les positions des dislocations ont été calculées par un schéma de relaxation itératif minimisant la force de Peach-Koehler sur chaque dislocation. La rigidité du JDG et la désorientation des grains influencent la longueur des empilements, mais l'effet de la désorientation est clairement prédominant.

En parallèle, des essais in-situ sur des bi-cristaux de taille micrométrique et des observations couplant MEB, AFM et EBSD ont été effectués dans la présente thèse. Des bi-cristaux de Ni et  $\alpha$ -Brass ont été obtenus par usinage FIB. Les variations spatiales de hauteur de marche dues aux lignes de glissement localisées se terminant au JDG ont été mesurées par AFM afin de déterminer la distribution des vecteurs de Burgers dans l'empilement de dislocations. Cette distribution a ensuite été simulée à l'aide des paramètres mesurés expérimentalement en considérant l'effet de la désorientation, de la rigidité du JDG, des surfaces libres et de la force critique. On constate que le vecteur de Burgers des dislocations interfaciales peut être considéré comme identique à celui des dislocations entrantes pour un faible nombre de dislocations transmises, et qu'il est nécessaire de considérer un vecteur de Burgers résiduel pour les dislocations interfaciales dans le cas d'un nombre élevé de dislocations transmises. Les effets des surfaces libres et de la force critique doivent eux toujours être considérés dans les calculs pour être plus prédictifs en ce qui concerne le profil de hauteur de marche. La force critique obtenue pour le Ni étudié est  $F_c = 0.003$  N/m ( $\tau_c = 12$  MPa) et  $F_c = 0.011$  N/m ( $\tau_c = 43$  MPa) pour le  $\alpha$ -Brass étudié. Ces valeurs, calculées dans le cadre de dislocations droites infinies avec le formalisme L-E-S, sont acceptables en raison des défauts de réseau dans la composition du matériau et de l'alliage, respectivement.

Par rapport à l'approche analytique actuelle pour le comportement des dislocations dans les bi-cristaux, les résultats peuvent être raffinés en utilisant d'autres méthodes numériques, telles que les simulations de dynamique moléculaire (MD) et les simulations 3D de dynamique des dislocations discrètes (DDD). En atten-

dant, la présente méthode pourrait être utilisée pour enrichir les simulations DDD en présence d'interfaces en tenant compte de l'élasticité anisotrope hétérogène, en particulier ce qui concerne les propriétés du JDG. Même s'il est possible de définir différentes propriétés élastiques du JDG avec un tenseur de rigidité élastique anisotrope ou isotrope, le comportement élastique des JDGs et leur dépendance aux paramètres microscopiques et macroscopiques reste mal connu. Ainsi, dans une étude future, les propriétés élastiques des JDGs seront étudiées à l'aide de simulations de statique moléculaire (MS).



# Deutsche Zusammenfassung

## 1.1 Einführung

Die Plastizität kristalliner Materialien resultiert in erster Linie aus der Bewegung und der Multiplikation von Versetzungen. Versetzungen sind Linienfehler, die von Volterra [2] zu Beginn des 20. Jahrhunderts eingeführt wurden. Sowohl theoretische als auch experimentelle Untersuchungen zeigen, dass die mechanischen Eigenschaften von Metallen von der Dichte, der Verteilung, der Keimbildung und der Mobilität von Versetzungen sowie den Wechselwirkungen zwischen Versetzungen und Korngrenzen (KGs) abhängen. Im Mittelpunkt dieser Arbeit stehen Gleitmechanismen an den Korngrenzen. Unter den verschiedenen möglichen Mechanismen, in Rahmen dieser Dissertation werden das kollektive Versetzungsverhalten, Pile-ups an KGs und Versetzungstransmission im Wesentlichen aus experimenteller und theoretischer Sicht untersucht. Um dies zu erreichen, werden Pile-ups sowohl theoretisch als auch experimentell untersucht. Das Ziel ist die Kräfte, die Gleittransfer induzieren zu berechnen sowie der Effekt der anisotropen Elastizität zu bewerten. In Bezug auf die Experimente wurden in-situ Druckversuch an Mikro-Bi-Kristalle mit einer geringen Dehnung durchgeführt. Anschließend wurde die Höhe der Gleitlinien auf Oberfläche mit Hilfe vom AFM gemessen, womit Pile-ups und Versetzungstransmission an der Korngrenze identifiziert werden können. In der theoretischen Analyse wurden die elastischen Felder durch Einzelversetzung und Pile-ups an der KG mit Hilfe einer zweidimensionalen anisotropen elastischen Theorie unter Berücksichtigung der Missorientierung, KG-Dicke und freien Oberflächeneffekten berechnet. Am Ende wurde die Höhe der Gleitlinien durch die vorgestellte Theorie numerisch simuliert und mit experimentellen Beobachtungen verglichen.

## 1.2 Experimente

Das Hauptziel der Experimente ist Versetzungs-Pile-ups und Versetzungstransfer in Mikro-Bikristallinen Proben zu analysieren. Für die Untersuchung dieser

Mechanismen wurden zuerst spezielle Korngrenzen nach der EBSD (Electron Back Scatter Diffraction) Messung ausgewählt. Als zweitens wurden Mikro-Bikristalle mit Hilfe des Focused-Ion-Beam-Mikroskops (FIB) hergestellt. Danach folgten die in-situ Druckversuche mit einer Belastungsrichtung parallel zur KG mit Hilfe eines Nanoindenters im Vakuum. Die Druckversuche wurden gestoppt, sobald plastische Verformung bzw. die Aktivierung des Gleitsystems mit dem größten Schmidfaktor beobachtet wurde. Anschließend, für die Charakterisierung der Gleitlinien wurden die Mikroproben mit Hilfe des REMs und des AFMs für die lokale Charakterisierung der Gleitstufen untersucht.

### 1.2.1 Materialien

Die verwendeten Materialien für diese experimentelle Studie sind Nickel (Ni) mit einer hohen Reinheit (99,999%) und  $\alpha$ -Brass (70%Cu-30%Zn, Gew%) mit Verunreinigungen (Fe, Pb, P und As) kleiner als 0,001%. Die chemische Zusammensetzung wurde mittels energiedispersiver Spektroskopie (EDX) durchgeführt, um die Reinheit der Proben zu überprüfen. Die elastischen Steifigkeitsmodule von Ni sind  $C_{11} = 246.5$  GPa,  $C_{12} = 147.3$  GPa,  $C_{44} = 124.7$  GPa [28] und von  $\alpha$ -Brass  $C_{11} = 139.21$  GPa,  $C_{12} = 104.51$  GPa,  $C_{44} = 71.3$  GPa [267, 268]. Der elastische Anisotropiefaktor  $A = \frac{2C_{44}}{C_{11} - C_{12}}$  beträgt 2,51 (Ni) und 4,11 ( $\alpha$ -Brass). Somit konnte die Auswirkung der anisotropen Elastizität analysiert werden. Im Falle der elastischen Isotropie sind die betrachteten elastischen Konstanten  $G = 86,16$  GPa,  $\nu = 0,294$  für Ni und  $G = 40,75$  GPa,  $\nu = 0,343$  für  $\alpha$ -Brass. Die isotrop elastischen Konstanten werden aus den anisotropen elastischen Steifigkeitsmodulen durch Anwendung des Voigt-Reuss-Hill-Annäherung [269, 270] abgeleitet. Die Stapelfehlerenergie für  $\alpha$ -Brass und Ni beträgt jeweils  $14 \text{ mJ/m}^2$  [271] und  $90 \text{ mJ/m}^2$  [272]. Durch die geringere Stapelfehlerenergie von  $\alpha$ -Brass wird das planare Gleiten gefördert und dadurch die Beobachtung von Gleitlinien erleichtert. Trotz der höheren Stapelfehlerenergie von Ni in Vergleich zu  $\alpha$ -Brass, wurde planares Gleiten Ni-Bikristallen beobachtet [137]. Daher wurde Ni für unsere Experimente ausgewählt.

### 1.2.2 Probenvorbereitung und Auswahl von Bikristallen

Mehrere Proben mit einer Größe von etwa  $20 \times 20 \times 5 \text{ mm}^3$  wurden mittels Funkenerosion (EDM) mit Bronzedraht geschnitten. Daher wurden alle Seiten der Proben anschließend grob mit SiC-Schleifpapier mit Körnung von P800 ( $\sim 22 \mu\text{m}$ ) bis P2400 ( $\sim 8 \mu\text{m}$ ) mit Wasser mechanisch geschliffen. Dann wurden die Proben mit einer Diamantsuspension mit einer Korngröße von 6, 3 bis  $1 \mu\text{m}$  auf Zetatuch poliert. Nach jedem Schleif und Polierschritt wurden die Proben mit Ethanol



gespült und anschließend für kurze Zeit im Ultraschallbad gereinigt. Nachdem die Probenoberfläche gründlich geschliffen und poliert wurde, betrug die Dicke etwa  $2,0 \sim 2,5$  mm. Auf dieser Weise ist es möglich, dass die KGs nach einer Wärmebehandlung relativ senkrecht zur Oberfläche sind. Anschließend wurden die polierten Proben durch Wärmebehandlung homogenisiert. Danach wurden die Ni-Proben zur Einstellung der Korngröße bei  $1100$  °C und einer Glühzeit von etwa 70 Stunden Ofen unter Vakuum wärmebehandelt. Die  $\alpha$ -Brass-Probe wurde mit Hilfe einer speziellen Probenhalter bei  $980$  °C und einer Glühzeit von 1 minute unter einer Argon-Umgebung wärmebehandelt, um Entzinkung der  $\alpha$ -Brass-Probe zu vermeiden [273]. Nach der Wärmebehandlung wurden die Proben mechanisch erneut poliert und anschließend für 20s bei einer Spannung von 24 Volt elektroliert, um die durch die mechanische Politur aufgebrachte Oberflächendeformation zu entfernen.

Nach der Elektropolitur wurde die EBSD-Messung durchgeführt, um die Orientierung aller Körner zu bestimmen. Die Messung wurde mit einer hochauflösenden Kamera von Oxford Instruments in einem REM (Sigma VP) von Zeiss durchgeführt. Die EBSD-Messung erfolgte grundsätzlich in zwei Schritten. Eine grobe EBSD-Messung der gesamten Probenoberfläche, die mit einer Beschleunigungsspannung von 20 kV und einer Schrittweite von  $20 \mu\text{m}$  bei einem Arbeitsabstand von 15 mm durchgeführt wurden. Nach der Lokalisierung der gewünschten KG folge eine zweite EBSD-Messung der isolierten KG mit einer Schrittweite von  $0,1 \mu\text{m}$ . Die Indexierungsrate bei der EBSD-Messung war größer als 99%. Die EBSD-Karte in IPF-Ansicht in Abbildung 1.1 liefert Informationen über die Kornorientierung sowie die KG-Charakterverteilung, da die Missorientierung an einer KG aus der Kornorientierung berechnet werden kann. In Abbildung 1.1 sind alle KG als schwarze Linien markiert.

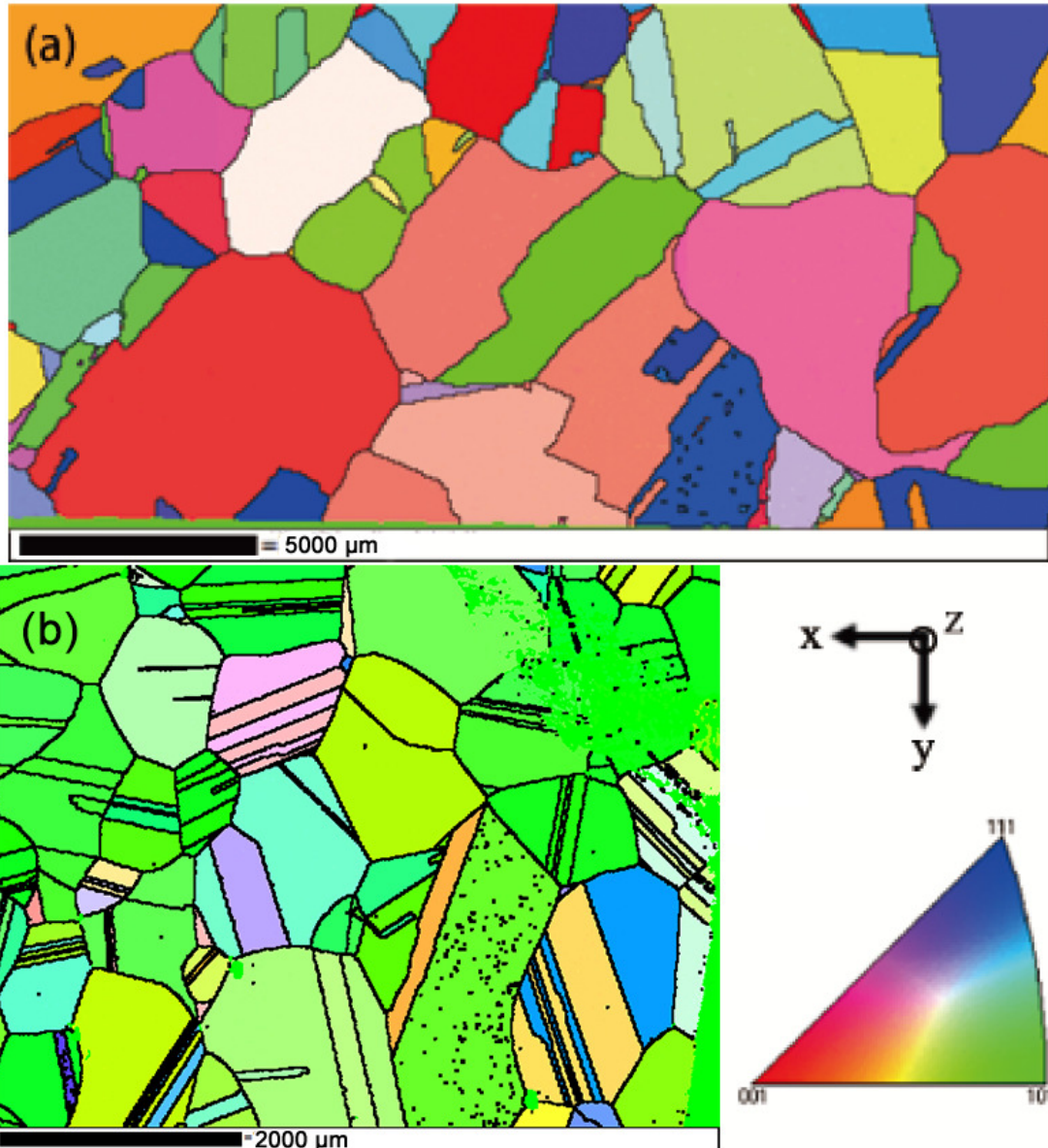


Figure 1.1: EBSD-Karte der gesamten Probenoberfläche: (a) Ni-Probe und (b)  $\alpha$ -Brass-Probe. Die Orientierungen sind in der IPF-Ansicht in Richtung der z-Achse (senkrecht zur Oberfläche) angegeben. Die schwarzen Linien stellen KGs dar und entsprechen dem Missorientierungswinkel zwischen benachbarten Pixeln größer als  $2^\circ$ .

Nach dem Erhalt aller EBSD-Daten wurden die KGs selektiert. Basierend auf der Orientierung der einzelnen Körner wurden die KGs wie folgt ausgewählt:

- KG sollte möglichst senkrecht zur Oberfläche stehen.

- Bei einer Belastung parallel zur KG-Ebene sollte der Burgersvektor des Gleitsystems mit dem maximalen Schmidfaktor nicht senkrecht zur KG stehen. Außerdem sollte die Gleitebene dieses Gleitsystems nicht parallel zur Oberfläche verlaufen. Diese Bedingungen stellen sicher, dass der Burgersvektor eine Komponente senkrecht zur Oberfläche (für die Charakterisierung mit Hilfe vom AFM) zeigt.

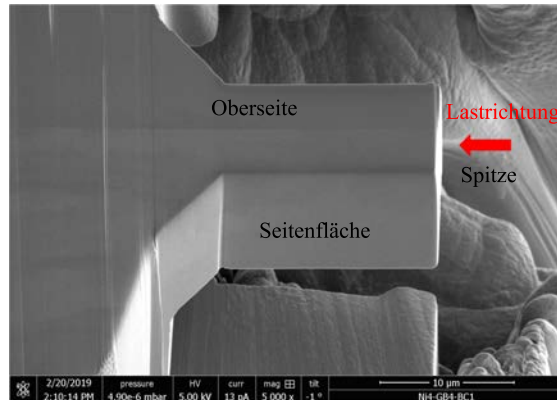


Figure 1.2: Hergestellter Mikro-Bi-Kristall nach der Verformung. Die KG verläuft parallel zur Belastungsrichtung (siehe Pfeil). Die AFM-Messungen wurden auf der Oberfläche nach der Belastung durchgeführt.

Es wurde ebenfalls berücksichtigt, dass das Verhältnis zwischen dem ersten und zweiten maximalen Schmidfaktor höher als 1,1 ist, um die Aktivierung von nur einem Gleitsystem bei einer geringen Dehnung sicher zu stellen. Außerdem, unter Berücksichtigung der Inkompatibilitätsspannungen aufgrund der heterogenen elastischen Anisotropie kann sich das günstigste aktive Gleitsystem (ausgehend von dem Schmidfaktor) unterscheiden [160]. Diese Bedingung kann verwendet werden, um die Auswirkungen von Inkompatibilitätsspannungen zu identifizieren. Daher werden Zwillingskorngrenzen in der vorliegenden Studie nicht untersucht, da diese keine Inkompatibilitätsspannungen aufweisen, wenn die Typ-I-Zwillingsgrenzen parallel oder senkrecht zur Belastungsachse [276] verlaufen. Basierend auf den oben genannten Bedingungen wurden mehrere KGs ausgewählt. In dieser Untersuchung wurde nur eine KG in der Ni-Probe und  $\alpha$ -Brass-Probe zur Analyse der Verteilung von Versetzungen im Einfachgleitung und Transmissionsphänomen verwendet. Die genaue Orientierung der einzelnen Körner des Bi-Kristalls in Ni und  $\alpha$ -Brass sind in Abbildung 1.3 und 1.4 dargestellt.

Um dieses Experiment durchzuführen, sollte die KG sehr nah (etwa  $100 \mu\text{m}$ ) und parallel an der Probenkante präpariert werden. Als erstes wurde die selektierte KG bis zu einem Abstand von etwa  $100 \mu\text{m}$  von der Probenkante mechanisch

vorbereitet. Dann wurde die Probenkante bis zu einem Abstand von etwa  $40 \mu\text{m}$  von der KG mit Hilfe von niederenergetischen  $\text{Ar}^+$ -Ionen poliert, um mechanische Verformungen der KG zu vermeiden/reduzieren. Anschließend wurde die Herstellung der Mikro-Bi-Kristalle wurden mit einem Rasterionmikroskop (FIB) durchgeführt. Für den groben Schnitt wurde  $15 \text{ nA}$  und für die Feinpolitur  $1 \text{ nA}$  bei  $30 \text{ kV}$  verwendet. Nach der Herstellung der Bi-Kristalle wurde eine EBSD-Messung erneut durchgeführt. In Abbildung 1.3 und 1.4 sind die Details der untersuchten KG: die Krystallorientierung vor der Verformung der einzelnen Krystallkomponenten Cry\_I und Cry\_II des Ni-Bi-Kristalls (Abbildung 1.3) bzw.  $\alpha$ -Brass-Bi-Kristalls (Abbildung 1.4).

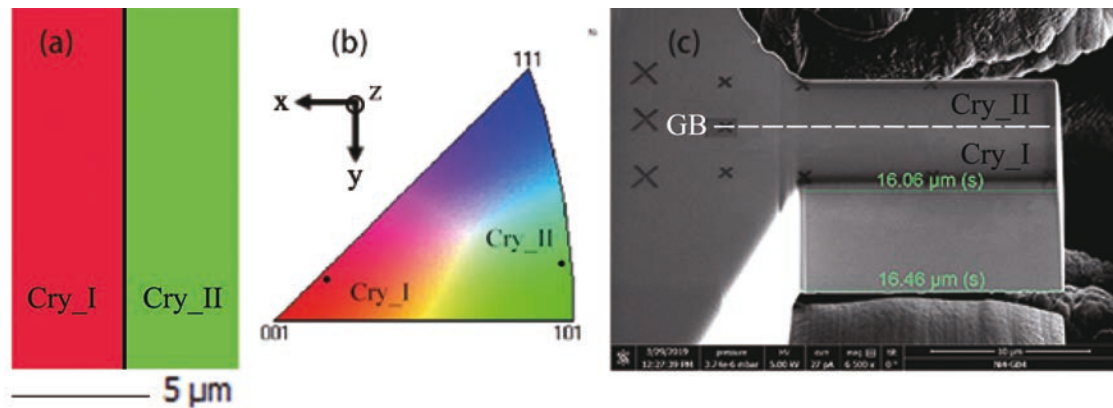


Figure 1.3: (a) EBSD-Karte des Ni-Bi-Kristalls, Euler Winkel des Kristalls I:  $\phi_1^I = 63.8^\circ$ ,  $\Phi^I = 14.3^\circ$ ,  $\phi_2^I = 18.6^\circ$ , Orientierung des Kristalls II:  $\phi_1^{II} = 331.1^\circ$ ,  $\Phi^{II} = 9.0^\circ$ ,  $\phi_2^{II} = 75.1^\circ$ . (b) Die kristallographischen Orientierungen der Krystallkomponenten, CryI und CryII, sind auf dem Standard IPF in Richtung der y-Achse angegeben, die parallel zur KG verläuft und gleichzeitig die Belastungsrichtung ist. (c) REM-Bild eines hergestellten Mikro-Bi-Kristalls vor der Verformung. Die durchschnittliche Länge des Bi-Kristalls beträgt etwa  $15,46 \mu\text{m}$  und die durchschnittliche Querschnittsfläche etwa  $71,80 \mu\text{m}^2$  (Kristall I:  $46,67 \mu\text{m}^2$  und Kristall II:  $25,13 \mu\text{m}^2$ ).

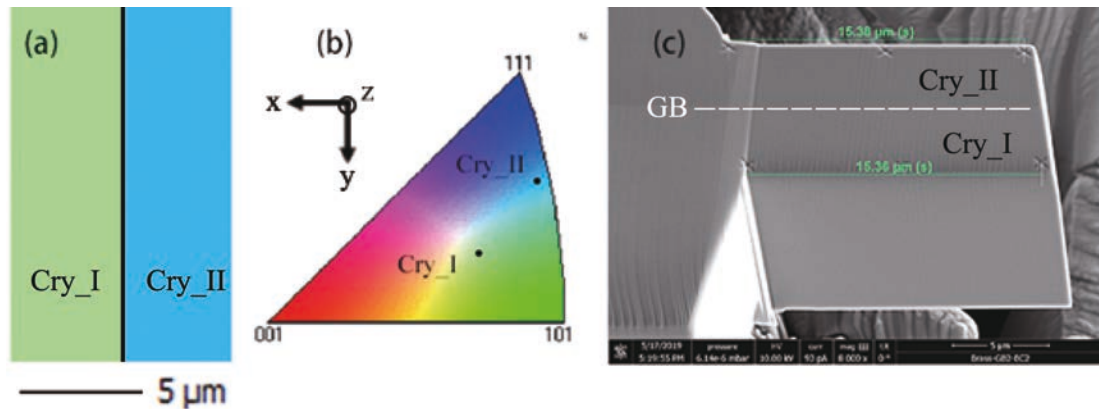


Figure 1.4: (a) EBSD-Karte des  $\alpha$ -Brass-Bi-Kristalls, Euler Winkel des Kristalls I:  $\phi_1^I = 27.7^\circ$ ,  $\Phi^I = 35.7^\circ$ ,  $\phi_2^I = 66.1^\circ$ , Orientierung des Kristalls II:  $\phi_1^{II} = 219.5^\circ$ ,  $\Phi^{II} = 28.4^\circ$ ,  $\phi_2^{II} = 2.4^\circ$ . (b) Die kristallographischen Orientierungen der Krystallkomponenten, CryI und CryII, sind auf dem Standard IPF in Richtung der y-Achse angegeben, die parallel zu KG verläuft und gleichzeitig die Belastungsrichtung ist. (c) REM-Bild eines hergestellten Mikro-Bi-Kristalls vor der Verformung. Die durchschnittliche Länge des Bi-Kristalls beträgt etwa  $15,37 \mu\text{m}$  und die durchschnittliche Querschnittsfläche etwa  $88,91 \mu\text{m}^2$  (Kristall I:  $42,02 \mu\text{m}^2$  und Kristall II:  $46,89 \mu\text{m}^2$ ).

### 1.2.3 Druckversuche der Mikro-Bikristalle

Die in-situ-Druckversuche wurden mit einem Nanoindenter (UNAT-SEM II) mit einem im Vakuum bei Raumtemperatur in einem Rasterelektronenmikroskop (Carl Zeiss SIGMA-Serie (SEM)) der einen Laderauschpegel von etwa  $0,002 \text{ mN}$  aufweist. Die Mikro-Bikristalle wurden mit einer flachen Spitze aus polykristallines Wolframkarbid (WC). Alle Druckversuche wurden Wegeregelt mit einer Belastungsfunktion mit mehreren Be- und Entlastungssegmenten durchgeführt. Die Idee der mehreren Be- und Entlastungssegmenten war, genügend Zeit für eine REM-Bild mit hoher Qualität zu haben, um die Gleitlinien beobachten zu können. Sobald die Gleitlinien beobachtet wurden oder die Streckgrenze erreicht wurde, wurde der Druckversuch während des Entladevorgangs gestoppt. Die durchschnittliche Dehnrates beträgt etwa  $0,002 \text{ s}^{-1}$  für Ni und  $0,00125 \text{ s}^{-1}$  für  $\alpha$ -Brass. Die Belastung während des Druckversuches wurde gestoppt, als die ersten Gleitlinien beobachtet wurde. Somit trägt nur das letzte Belastungssegment zur plastischen Verformung bei, während allen vorherigen Segmenten sind nur im elastischen Zustand. Nach den experimentellen Rohdaten liegt die Fließgrenze bei etwa  $8,5\%$  Dehnung für Ni und  $6,3\%$  für  $\alpha$ -Brass. Diese Dehnungen sind zu groß für die Fließgrenze von Metallen. Dieser Fehler ist durch die Drift der Spitze während des Druckversuches. Die Kraftmessung ist jedoch genau. Daher wurden die Spannungs-Dehnungskurven mit Hilfe einer Kristallplastizitäts-Finite Elemente (CPFEM)-Simulation kalibriert. Diese Ergebnisse sind in Abbildung 1.5

dargestellt. Die CPFEM-Simulation der Druckversuche wurde für die gleiche experimentelle Geometrie-Konfiguration der Ni- und  $\alpha$ -Brass-Bi-Kristalle durchgeführt. Anschließend wurde die Dehnung kalibriert, indem die gleiche Steigung der Spannungs-Dehnungskurven im elastischen Bereich erreicht wurde. Damit ist die Fließgrenze bei etwa 0,33% Dehnung in Ni und 0,24% in  $\alpha$ -Brass, die für metallische Materialien sinnvoll sind. Die angelegte Spannung im Endzustand beträgt etwa 289,4 MPa für Ni und 127,4 MPa für  $\alpha$ -Brass.

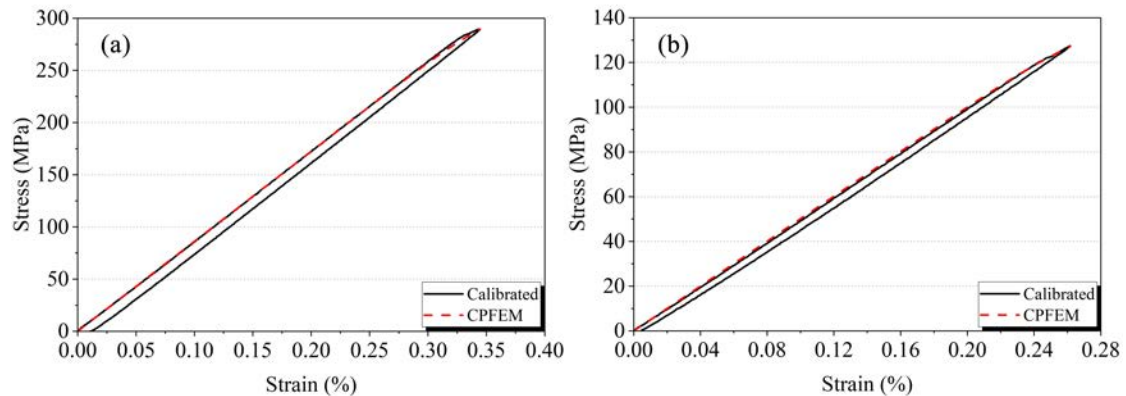


Figure 1.5: Spannungs-Dehnungskurven kalibriert mit Hilfe eines CPFEM-Modells für (a) Ni-Mikro-Bi-Kristalle und (b)  $\alpha$ -Brass-Mikro-Bi-Kristalle.

## 1.2.4 Gleitlinienanalyse mit Hilfe vom AFM

Nach dem In-situ-Druckversuch wurden die Gleitlinien zunächst mit Hilfe des REMs analysiert. So konnten die Gleitlinien auf der Ober- und Seitenfläche eines Bi-Kristalls beobachtet werden und dann die aktivierte Gleitsysteme basierend auf die Orientierung jedes Korns analysiert werden. Anschließend wurde die Oberflächentopografie mit Hilfe vom AFM (mit ScanAsyst (BRUKER) mit Höhensensor so gemessen, dass die Topografie der Gleitlinien erhalten und zur Analyse von Versetzungsverteilungen verwendet werden kann. Die Schrittweite des Scans beträgt 30 nm bei einer Scanrate von 1 Hz. Die Ergebnisse wurden mit dem Software NanoScope Analysis analysiert. Das Ergebnis eines Bi-Kristalls is in Abbildung 1.6 dargestellt.



Figure 1.6: Ein Beispiel für eine AFM-Messung an der Oberfläche eines Ni-Bikristalls, der mit der NanoScope-Analyse analysiert wurde (Da Bild wurde zunächst durch Polynomannpassung zweiter Ordnung geflättet, dann mit einem Medianfilter ( $9 \times 9$  Matrixoperation) behandelt).

## 1.3 Theorie

### 1.3.1 2D anisotropes Elastizitätsgerüst

Um die Wirkung der anisotropen Elastizität zu berücksichtigen, wird der sogenannte L-E-S (Leknitskii [20] - Eshelby [21] - Stroh [22]) analytische Formalismus für ein zweidimensionales anisotropes elastisches Problem verwendet. Es ist sehr effizient, kann aber den Fall eines perfekt isotropen Kristalls nicht aufgrund der Singularität durch die wiederholten Eigenwerte behandeln.

Die allgemeinen Lösungen für das Verschiebungsfeld  $\mathbf{u}$  und den Spannungsfunktionsvektor  $\Phi$  können berechnet werden durch:

$$u_i = 2\text{Re} \left[ A_{i\bar{j}} f_{\bar{j}}(z_{\bar{j}}) \right] \quad (1.1)$$

$$\Phi_i = 2\text{Re} \left[ B_{i\bar{j}} f_{\bar{j}}(z_{\bar{j}}) \right] \quad (1.2)$$

wobei  $\mathbf{A}$  und  $\mathbf{B}$  eine  $3 \times 3$  Matrix sind, die die Komponenten des Eigenvektors  $a_{k\alpha}$  ( $\alpha = 1, 2, 3$ ) enthalten,  $B_{ij} = (C_{i2k1} + p_j C_{i2k2}) A_{kj}$  und  $z_j = x_1 + p_j x_2$ .  $p_\alpha$  und  $a_{k\alpha}$  ( $\alpha = 1, 2, 3$ ) bedeuten die Eigenwerte und die dazugehörigen Komponenten des Eigenvektors mit positivem Bildteil einer Gleichung, die nur von der elastischen Steifigkeit des Materials abhängt [21, 22]. In den Gleichungen 1.1 und 1.2,  $\mathbf{f}$  ist eine skalare Funktion von  $z$ . Anschließend können die Spannungsfelder nach dem Hookeschen Gesetz basierend auf den Verschiebungsgradienten-Felder oder nach dem Spannungsfunktionsvektor wie folgende berechnet werden:

$$\sigma_{i1} = -\partial\Phi_i/\partial x_2, \sigma_{i2} = \partial\Phi_i/\partial x_1 \quad (1.3)$$

Die Komponente  $\sigma_{33}$  können aus dem verallgemeinerten Hookeschen Gesetz berechnet werden.

In den nächsten Abschnitten wird einen Ausdruck für den Funktionsvektor  $\mathbf{f}$  einer einzelnen Versetzung in verschiedenen Konfigurationen gesucht.

### 1.3.2 Versetzung in einem homogenen Medium

Im Folgenden wird eine unendlich gerade Versetzung mit dem Burgersvektor  $\mathbf{b}$ , dessen Versetzungslinie  $\mathbf{t}$  parallel zur Richtung  $\mathbf{x}_3$  ist, an der Position  $(X_1, X_2)$  betrachtet (Abbildung 1.7). Senkrecht zur Papierebene wird die sogenannte FS/RH (Finish Start/Right Hand) Konvention [28] verwendet, um die Richtung der Versetzungslinie zu definieren, wie in Abbildung 1.7 dargestellt.

In einem homogenen anisotropen Medium ist der Funktionsvektor  $\mathbf{f}$  unter Berücksichtigung der Randbedingung, die mit dem Vorhandensein der Versetzung mit dem Burgersvektor  $\mathbf{b}$  verbunden ist und in der Abwesenheit einer Kraft, abgeleitet. Die Verschiebungs- und Spannungsfunktionsvektoren werden mit Hilfe der Gleichungen 1.1 und 1.2 abgeleitet:

$$f_j(z_i) = f_j^0(z_i) = q_j^0 \ln(z_i - s_j) \quad (1.4)$$

wobei  $z_i = x_1 + p_i x_2$ ,  $s_j = X_1 + p_j X_2$  und  $\mathbf{q}^0$  ein komplexer Vektor ist ( $\mathbf{q}^0 = -\frac{1}{2\pi} \mathbf{i} (\mathbf{B}^T \mathbf{b})$  [19], wo  $\mathbf{i} = \sqrt{-1}$  die imaginäre Einheit ist).

### 1.3.3 Versetzungen in Bi-Materialien

Betrachten wir nun ein anisotropes Bi-Material (oder Bi-Kristall) mit einer perfekt gebundenen Grenzfläche mit einem Normalvektor parallel zu  $\mathbf{x}_2$ -Richtung. Hier wird angenommen, dass die Versetzung im oberen Material I ( $x_2 > 0$ ), wie in Abbildung 1.7 dargestellt, liegt.

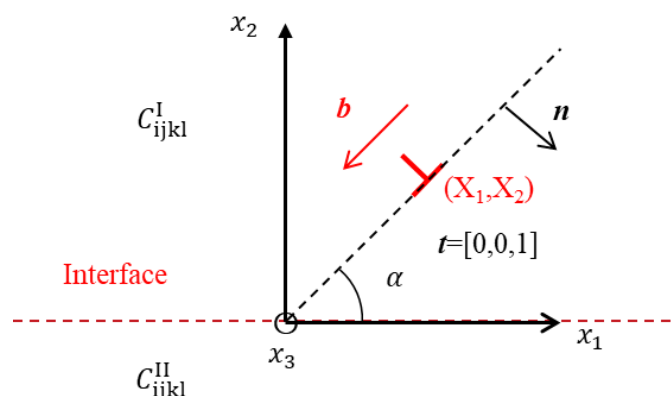


Figure 1.7: Schematische Darstellung einer einzelnen unendlichen geraden Versetzung in einem Bi-Material.



Zusätzlich zu den Bedingungen des homogenen Mediums, der Funktionsvektor  $\mathbf{f}$  sollte die Kontinuitätsbedingungen an der perfekten Grenzfläche auch erfüllen, d.h. die Kontinuität der Verschiebung  $u_i^I(x_2 = 0^+) = u_i^II(x_2 = 0^-)$  und Spannungsvektoren  $\sigma_{i2}^I(x_2 = 0^+) = \sigma_{i2}^II(x_2 = 0^-)$ . In der Praxis wird die Kontinuität der resultierenden Spannungskraft entlang eines Bogens der Grenzfläche allerdings verwendet. Diese letzte Bedingung ergibt  $\Phi_i^I(x_2 = 0^+) = \Phi_i^II(x_2 = 0^-)$  [19, 292]. Nach Suos-Methode [19] werden die Lösungen in einer ähnlichen Form wie die Gleichungen 1.1 und 1.2 gesucht:

$$f_j(z_j) = \begin{cases} f_j^0(z_j) + \overline{V_{jk}^{I,II}} \overline{f_k^0}(z_j) & \text{if } z_j \in I \ (x_2 > 0) \\ W_{jk}^{I,II} f_k^0(z_j) & \text{if } z_j \in II \ (x_2 < 0) \end{cases} \quad (1.5)$$

wo:

$$\begin{cases} \mathbf{V}^{I,II} = \left( \mathbf{B}^{II} \mathbf{A}^{II-1} \overline{\mathbf{A}^I} - \overline{\mathbf{B}^I} \right)^{-1} \left( \mathbf{B}^I - \mathbf{B}^{II} \mathbf{A}^{II-1} \mathbf{A}^I \right) \\ \mathbf{W}^{I,II} = \left( \overline{\mathbf{B}^I \mathbf{A}^{I-1} \mathbf{A}^{II}} - \mathbf{B}^{II} \right)^{-1} \left( \overline{\mathbf{B}^I \mathbf{A}^{I-1} \mathbf{A}^I} - \mathbf{B}^I \right) \end{cases} \quad (1.6)$$

$f_j^0(z_j)$  wird aus Gleichung 1.4 unter Berücksichtigung des elastischen Steifigkeitstensors  $\mathbf{C}^I$  des Materials I und  $s_j = s_j^I = X_1 + p_j^I X_2$ . Außerdem muss folgendes beachtet werden: Wenn  $z_j \in I$  ist, dann ist  $z_j = z_j^I = x_1 + p_j^I x_2$  und wenn  $z_j \in II$  ist, dann ist  $z_j = z_j^{II} = x_1 + p_j^{II} x_2$ .

Ein Halbraum mit starren oder freien Oberflächen als spezielle Konfigurationen von Bi-Material kann leicht für  $u_i^I(x_2 = 0) = 0$  oder  $\Phi_i^I(x_2 = 0) = 0$  erhalten werden, was zu  $f_j(z_j) = \overline{A_{jk}^I}^{-1} \overline{A_{kl}^I} \overline{f_l^0}(z_j)$  für starre Oberfläche und  $f_j(z_j) = f_j^0(z_j) - B_{jk}^I \overline{B_{kl}^I} \overline{f_l^0}(z_j)$  für freie Oberfläche führt.

### 1.3.4 Versetzung in Tri-Materialien

Im Abschnitt 1.3.3 wurde das Bi-Material als die Kombination zweier Materialien betrachtet, die über eine Grenzfläche (ohne Dicke) perfekt miteinander verbunden sind. Für den Fall einer Korngrenze, die reale Dicke einer Grenzfläche ist endlich und daher wird die Grenzfläche hier im Allgemeinen mit einer Dicke von etwa 1 nm berücksichtigt. Daher ist wichtig der Einfluss der Dicke sowie der elastischen Steifigkeit einer KG auf die elastischen Felder in einer tri-materiellen Konfiguration. zu untersuchen, bei der die KG als eine Interphase betrachtet wird. Basierend auf mehrere Untersuchungen für mehrschichtige anisotrope elastische Medien wird zunächst die Methode von Choi und Earmme [17] angewendet. Abbildung 1.8 zeigt die betrachtete tri-Material-Konfiguration. Es gibt zwei planare Grenzflächen  $\Gamma_1$  und  $\Gamma_2$ , deren Normalen entlang der  $\mathbf{x}_2$ -Richtung sind. Diese Grenzflächen befinden sich jeweils bei  $x_2 = h$  und bei  $x_2 = -d$ . Die Interphase

(oder Korngrenze) ist der Bereich zwischen  $\Gamma_1$  und  $\Gamma_2$ , also die gesamte Dicke ist  $H = h + d$ . Material I entspricht  $x_2 \geq h$ , Material II bis  $-d < x_2 < h$  und Material III bis  $x_2 \leq -d$ . Es wird davon ausgegangen, dass alle Materialien perfekt miteinander verbunden sind.

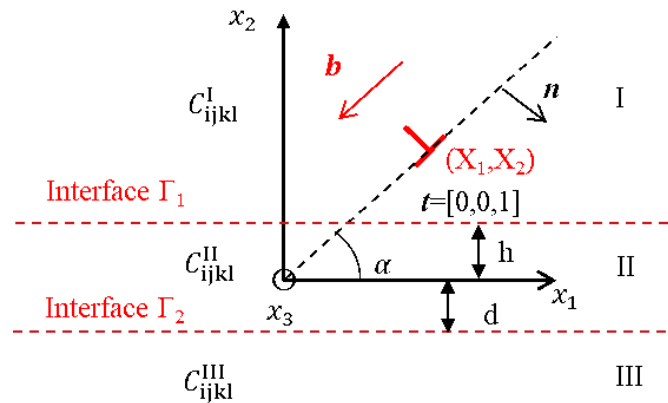


Figure 1.8: Schematische Darstellung einer einzelnen unendlich geraden Versetzung in einem Tri-Material mit drei verschiedenen Steifigkeitstensoren und zwei perfekt verbundenen Grenzflächen. Das Material II soll die Korngrenze der Dicke  $H = h + d$  beschreiben.

Choi und Earmme [17] lösten das Problem bezüglich der Kontinuität der Verschiebungen und Kräften an beiden Grenzflächen gleichzeitig, indem die alternierende Technik verwendet wurde. Diese Technik besteht darin, alternierend die Kontinuitätsbedingungen an jeder Grenzfläche zu erfüllen, bis eine Konvergenz erreicht ist. Unter Berücksichtigung einer Versetzung im Kristall I und unter Verwendung des gleichen Verfahrens von Choi und Earmme [17], wird die folgende Serienlösung erhalten:

$$f_i(z_i) = \begin{cases} f_i^0(z_i) + f_i^{I0}(z_i) + \sum_{\beta=1}^{\infty} f_i^{I\beta}(z_i) & \text{if } z_i \in \text{I} \\ \sum_{\beta=1}^{\infty} f_i^{\beta}(z_i) + \sum_{\beta=1}^{\infty} f_i^{II\beta}(z_i) & \text{if } z_i \in \text{II} \\ \sum_{\beta=1}^{\infty} f_i^{III\beta}(z_i) & \text{if } z_i \in \text{III} \end{cases} \quad (1.7)$$

wo:

$$\left\{ \begin{array}{l}
f_i^0(z_i) = q_i^0 \ln(z_i - s_i) \\
f_i^{I0}(z_i) = \overline{V_{ij}^{I,II}} \overline{f_j^0} \left( z_i - p_i^I h + \overline{p_j^I} h \right) \\
f_i^{I\beta}(z_i) = W_{ij}^{II,I} \overline{V_{jk}^{II,III}} \overline{f_k^\beta} \left( z_i - p_i^I h + p_j^{II} (h + d) - \overline{p_k^{II}} d \right) \\
f_i^{II\beta}(z_i) = \overline{V_{ij}^{II,III}} \overline{f_j^\beta} \left( z_i + p_i^{II} d - \overline{p_j^{II}} d \right) \\
f_i^{III\beta}(z_i) = W_{ij}^{II,III} \overline{f_j^\beta} \left( z_i + p_i^{III} d - \overline{p_j^{II}} d \right) \\
f_i^\beta(z_i) = \begin{cases} W_{ij}^{I,II} \overline{f_j^0} \left( z_i - p_i^{II} h + \overline{p_j^I} h \right) & \text{if } \beta = 1 \\ \overline{V_{ij}^{II,I}} \overline{V_{jk}^{II,III}} \overline{f_k^{\beta-1}} \left( z_i - p_i^{II} h + \overline{p_j^{II}} (h + d) - \overline{p_k^{II}} d \right) & \text{if } \beta > 1 \end{cases}
\end{array} \right. \quad (1.8)$$

In den obigen Gleichungen  $f_j^0(z_i)$  ist dem Kristall I zugeordnet und so ist  $s_j = s_j^I = X_1 + p_j^I X_2$ . Die Serienlösung  $f_i^{I\beta}(z_i)$ ,  $f_i^{II\beta}(z_i)$  und  $f_i^{III\beta}(z_i)$  werden alle als Funktionen von  $f_j^\beta(z_i)$  ausgedrückt, die wiederum durch eine Gleichung basierend auf  $f_j^0(z_i)$  bestimmt wird.

Die Konvergenz der oben genannten Serienlösungen wurden durch Choi und Earmme [17] untersucht. Die Untersuchung der Konvergenz der Serienlösungen für verschiedene KG-Steifigkeiten wurde mit Hilfe verschiedener Kriterien in Rahmen dieser Arbeit untersucht (siehe Chen et al. [277]).

### 1.3.5 Versetzung in Tri-Materialien mit freien Oberflächen

In experimentellen Versuchen, insbesondere bei Mikro-Proben (Abbildung 1.2), gibt es immer freie Oberflächen. Auf der Nano-/Mikroskala hat die freie Oberfläche einen offensichtlichen Einfluss auf das Versetzungsverhalten. Daher ist von Großer Bedeutung, neben der Grenzfläche der Einfluss der freien Oberflächen auf die elastischen Felder von Mehrschichtmaterial zu berücksichtigen. Die Tri-Material-Methode von Choi und Earmme [17] berücksichtigt den Effekt der freien Oberflächen, allerdings nur im Falle eines Bi-Materials mit nur einer freien Oberfläche oder eines homogenen Materials mit zwei freien Oberflächen. Um kompliziertere Fälle, wie z.B. ein Tri-Material mit freien Oberflächen, zu lösen, ist ein neues Verfahren erforderlich. Daher wurde eine nach Wang et al. [18] inspirierte Bild-Aufteilungs-Methode verwendet. Abbildung 1.9 (a) zeigt die Konfiguration eines Tri-Materials mit zwei freien Oberflächen. Es gibt vier planare Ebenen, deren Normalenvektor parallel zur  $\mathbf{x}_2$ -Achse sind. Diese Ebenen befinden sich bei  $x_2 = 0$  (obere freie Oberfläche),  $x_2 = -h_1$  (erste Grenzfläche),  $x_2 = -(h_1 + h_2)$  (zweite Grenzfläche) und  $x_2 = -(h_1 + h_2 + h_3)$  (untere freie Oberfläche). Die Interphase (oder Kongrenz) befindet sich in der zweiten Schicht der Dicke  $h_2$ . Material I befindet

sich zwischen  $-h_1 < x_2 < 0$ , Material II zwischen  $-(h_1 + h_2) < x_2 < -h_1$  und Material III zwischen  $-(h_1 + h_2 + h_3) < x_2 < -(h_1 + h_2)$ . Somit wird die Dicke des gesamten Materials als  $H' = h_1 + h_2 + h_3$  gekennzeichnet. Es wird davon ausgegangen, dass alle Materialien perfekt miteinander verbunden sind. Um die Auswirkungen beider freien Oberflächen zu untersuchen, wird die freie Oberfläche, die die Versetzungen enthält, als die erste freie Oberfläche bezeichnet, und die andere als zweite freie Oberfläche.

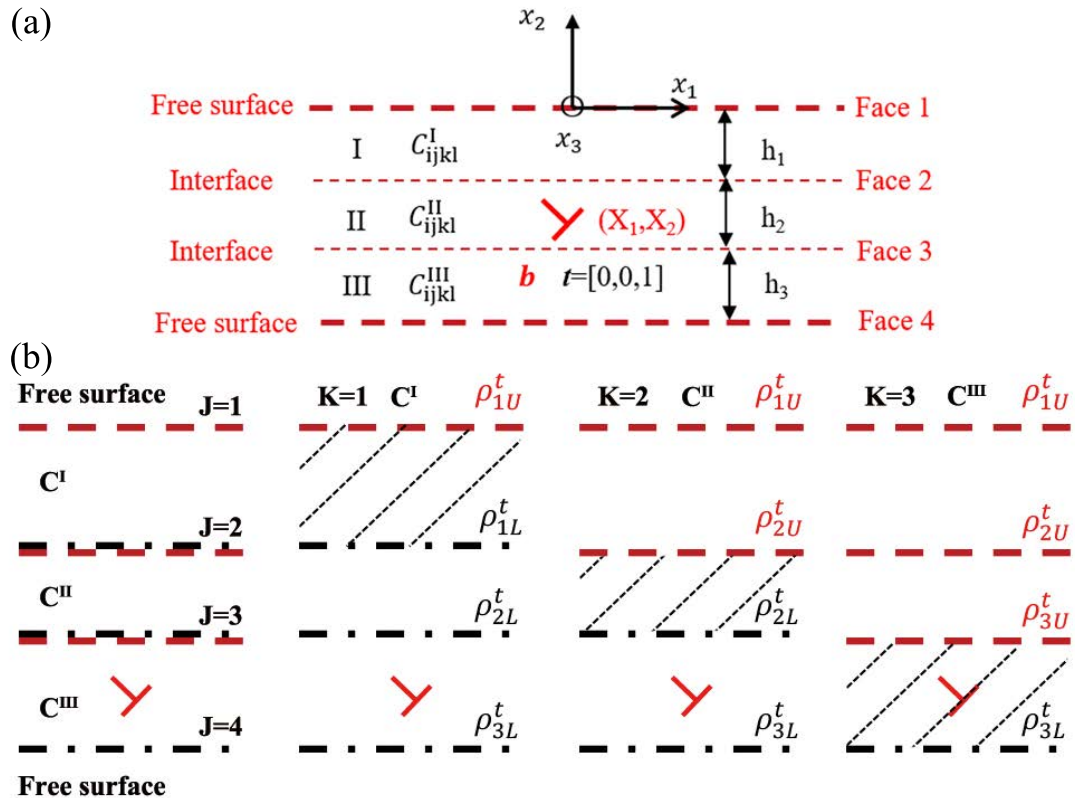


Figure 1.9: (a) Schematische Darstellung einer einzeln unendlich geraden Versetzung in einem Tri-Material mit drei verschiedenen Steifigkeitstensoren, zwei planaren freien Oberflächen an den Ebenen 1 und 4 und zwei perfekt verbundenen Grenzflächen an den Flächen 2 und 3. Der Korngrenzenbereich soll das Material II sein. (b) Zerlegung eines 3-Schichten-Problems (links) mit 2 freien Oberflächen und 2 Grenzflächen in drei unendliche homogene Teilprobleme. Die Versetzungsquelle ist mit einem roten Versetzungssymbol gekennzeichnet.

In der 3-Schichten-Konfiguration mit freien Oberflächen gibt es 2 Grenzflächen, die die Kontinuumsbedingungen von perfekt gebundenen Grenzflächen erfüllen müssen, und 2 freie Oberflächen, die den spannungsfreien Zustand erfüllen müssen. Für ein Mehrschichtensystem ist es zu kompliziert, die alternierende Technik zu verwenden. Wang et al. [18] haben eine Bild-Aufteilungs-Methode vorgeschlagen,

mit der alle Randbedingungen gleichzeitig erfüllt werden können. Das Prinzip dieser Methode besteht darin, das Multilayer-Problem in mehrere Teilprobleme des unendlichen homogenen Mediums für jedes Material zu zerlegen. Zwei Arten von Bildversetzungsdichten sind auf jeder Grenzfläche verteilt, während auf der Oberfläche nur eine Bildversetzungsdichte verteilt ist (siehe Abbildung 1.9 b) (links)). Die Dichten dieser Bildversetzungen werden als  $\rho^t$  bezeichnet, wobei  $t=1,2$  und  $3$  die  $x_1$ -,  $x_2$ - und  $x_3$ -Komponenten bezeichnen. Diese Dichten können gleichzeitig gelöst werden, indem alle Randbedingungen berücksichtigt werden: die Kontinuität des tangentialen Verschiebungsgradienten und Spannungen über die Grenzflächen, freie Oberflächen mit Spannungsfrei oder starre Oberflächen ohne tangentialen Verschiebungsgradienten. So wird sie für die vorliegende 3-Schichten-Konfiguration mit freien Oberflächen in 3 Teilprobleme zerlegt und es gibt insgesamt 18 Randbedingungen. Die elastischen Felder in jeder Schicht werden bestimmt, indem die Beiträge der Versetzungsquelle und alle entsprechenden Bildverschiebungen summiert werden, wie in Abbildung 1.9 b) (rechts) dargestellt. Basierend auf den Konsistenzanforderungen, die von Wang et al. [18] ausführlich diskutiert wurden, sind die Bildversetzungsdichten in den drei Teilproblemen:  $\rho_{J1}^t = \{\rho_{1U}^t, \rho_{1L}^t, \rho_{2L}^t, \rho_{3L}^t\}$  für das erste Teilproblem,  $\rho_{J2}^t = \{\rho_{1U}^t, \rho_{2U}^t, \rho_{2L}^t, \rho_{3L}^t\}$  für das zweite Teilproblem und  $\rho_{J3}^t = \{\rho_{1U}^t, \rho_{2U}^t, \rho_{3U}^t, \rho_{3L}^t\}$  für das dritte Teilproblem, wie in Abbildung 1.9 dargestellt. (b) (rechts).

Basierend auf Strohs Formalismus folgen für die Spannungsfelder und Felder des Verschiebungsgradienten aufgrund einer Mischversetzung mit den Burgersvektorkomponenten  $b_t$  ( $t = 1, 2, 3$ ), die sich bei  $(x_{1s}, x_{2s})$  in einem homogenen anisotropen Solid befinden [28, 18]: geschrieben werden:

$$\sigma_{ij}(K, b_t, \Delta x_1, \Delta x_2) = 2 [\zeta_{K\alpha ij}^{tR} P(\Delta x_1, p_{K\alpha}^R \Delta x_2, p_{K\alpha}^I \Delta x_2) + \xi_{K\alpha ij}^{tI} Q(\Delta x_1, p_{K\alpha}^R \Delta x_2, p_{K\alpha}^I \Delta x_2)] b_t \quad (1.9)$$

$$\frac{\partial u_i}{\partial x_j}(K, b_t, \Delta x_1, \Delta x_2) = 2 [\zeta_{K\alpha ij}^{tR} P(\Delta x_1, p_{K\alpha}^R \Delta x_2, p_{K\alpha}^I \Delta x_2) + \zeta_{K\alpha ij}^{tI} Q(\Delta x_1, p_{K\alpha}^R \Delta x_2, p_{K\alpha}^I \Delta x_2)] b_t \quad (1.10)$$

wobei  $\Delta x_1 = x_1 - x_{1s}$  und  $\Delta x_2 = x_2 - x_{2s}$ , das hochgestellte  $R$  und  $I$  den Real- und Imaginärteil jedes Terms angeben. Der Index  $K$  gibt an, welches Teilproblem berücksichtigt wird (keine Summe über  $K$ ). Die Definition der Symbole  $\xi_{K\alpha ij}^t$ ,  $\zeta_{K\alpha ij}^t$  und der Funktionen  $P$ ,  $Q$  sind [18]:

$$\begin{cases} \xi_{K\alpha ij}^t = \frac{C_{Kijkl} (\delta_{l1} + p_{K\alpha} \delta_{l2}) A_{Kk\alpha} B_{Kt\alpha}}{2\pi i} \\ \zeta_{K\alpha ij}^t = \frac{(\delta_{j1} + p_{K\alpha} \delta_{j2}) A_{Ki\alpha} B_{Kt\alpha}}{2\pi i} \end{cases} \quad (1.11)$$

$$\begin{cases} P(x_1 - x_{1s}, a, b) = \frac{x_1 - x_{1s} + a}{(x_1 - x_{1s} + a)^2 + b^2} \\ Q(x_1 - x_{1s}, a, b) = \frac{b}{(x_1 - x_{1s} + a)^2 + b^2} \end{cases} \quad (1.12)$$

wobei  $i = \sqrt{-1}$  die imaginäre Einheit und  $p_\alpha$ ,  $A_{k\alpha}$  und  $B_{t\alpha}$  mit  $\alpha=1,2$  und  $3$  sind die gleichen Eigenwerte und Eigenvektoren in Strohs Formulierung, wie im Abschnitt 1.3.1 beschrieben. Diese beiden Ausdrücke 1.9 und 1.10 des Einkristalls sind Äquivalenz zu den Gleichungen 1.1, 1.2 und 1.4, die analytisch voneinander abgeleitet werden können.

Der Beitrag von Bildversetzungen auf elastischen Feldern kann berechnet werden, indem der Burgersvektor  $b_t$  durch  $\rho_{JK}^t(x'_1)$  ersetzt wird und von  $x'_1 = -\infty$  zu  $x'_1 = +\infty$  in den Gleichungen 1.9 und 1.10 integriert wird:

$$\begin{aligned} \sigma_{ij}(K, \rho_{JK}^t, \Delta x_1, \Delta x_2) &= \\ \int_{-\infty}^{+\infty} 2 [\xi_{K\alpha ij}^{tR} P(\Delta x_1, p_{K\alpha}^R \Delta x_2, p_{K\alpha}^I \Delta x_2) + \xi_{K\alpha ij}^{tI} Q(\Delta x_1, p_{K\alpha}^R \Delta x_2, p_{K\alpha}^I \Delta x_2)] \rho_{JK}^t(x'_1) dx'_1 & \\ = 2\pi [\xi_{K\alpha ij}^{tR} H(p_{K\alpha}^R \Delta x_2, p_{K\alpha}^I \Delta x_2) + \xi_{K\alpha ij}^{tI} I(p_{K\alpha}^R \Delta x_2, p_{K\alpha}^I \Delta x_2)] [\rho_{JK}^t(x_1)] & \end{aligned} \quad (1.13)$$

$$\begin{aligned} \frac{\partial u_i}{\partial x_j}(K, \rho_{JK}^t, \Delta x_1, \Delta x_2) &= \\ \int_{-\infty}^{+\infty} 2 [\zeta_{K\alpha ij}^{tR} P(\Delta x_1, p_{K\alpha}^R \Delta x_2, p_{K\alpha}^I \Delta x_2) + \zeta_{K\alpha ij}^{tI} Q(\Delta x_1, p_{K\alpha}^R \Delta x_2, p_{K\alpha}^I \Delta x_2)] \rho_{JK}^t(x'_1) dx'_1 & \\ = 2\pi [\zeta_{K\alpha ij}^{tR} H(p_{K\alpha}^R \Delta x_2, p_{K\alpha}^I \Delta x_2) + \zeta_{K\alpha ij}^{tI} I(p_{K\alpha}^R \Delta x_2, p_{K\alpha}^I \Delta x_2)] [\rho_{JK}^t(x_1)] & \end{aligned} \quad (1.14)$$

wobei  $\Delta x_1 = x_1 - x_1 - x'_1$  und  $\Delta x_2 = x_2 - x'_2$  und  $(x'_1, x'_2)$  sind die Positionen von Bild-Versetzungen. Die Definitionen der Operatoren  $H$  und  $I$  sind:

$$\begin{cases} H(a, b) [\rho(x_1)] = \frac{1}{\pi} \int_{-\infty}^{\infty} P(x_1 - x'_1, a, b) \cdot \rho(x'_1) dx'_1 \\ I(a, b) [\rho(x_1)] = \frac{1}{\pi} \int_{-\infty}^{\infty} Q(x_1 - x'_1, a, b) \cdot \rho(x'_1) dx'_1 \end{cases} \quad (1.15)$$

Kombiniert man alle 18 Randbedingungen, so entsteht nach dem Entfernen des singulären Terms durch die Operatoren  $H$  und  $I$  ein System nichtlinearer Gleichungen mit 18 Fredholm-Gleichungen der zweiten Art ( $t = 1, 2$  and  $3$ ) mit 18 Unbekannten  $\boldsymbol{\rho} = [\rho_{1U}^t, \rho_{1L}^t, \rho_{2U}^t, \rho_{2L}^t, \rho_{3U}^t, \rho_{3L}^t]^T$  wie unten gezeigt:

$$\begin{aligned}
(\mathbf{C} + \mathbf{C}_0 \mathbf{C}^{-1} \mathbf{C}_0) \boldsymbol{\rho} + (\mathbf{C}_H \mathbf{H} + \mathbf{C}_I \mathbf{I} - \mathbf{C}_0 \mathbf{C}^{-1} \mathbf{C}_H \mathbf{H}_0 \mathbf{H} - \mathbf{C}_0 \mathbf{C}^{-1} \mathbf{C}_I \mathbf{H}_0 \mathbf{I}) \boldsymbol{\rho} \\
= -\mathbf{C}_R \mathbf{R} + \mathbf{C}_0 \mathbf{C}^{-1} \mathbf{C}_R \mathbf{H}_0 \mathbf{R}
\end{aligned} \tag{1.16}$$

wobei  $\mathbf{C}_H \mathbf{H}, \mathbf{C}_I \mathbf{I}, \mathbf{C}_H \mathbf{H}_0 \mathbf{H}, \mathbf{C}_I \mathbf{H}_0 \mathbf{I}$  sind die Matrizen des integralen Operators für die Dichten von Bildversetzungen  $\boldsymbol{\rho}$  und  $\mathbf{C}, \mathbf{C}_0$  die Matrizen des Koeffizienten, die nur von der materiellen Eigenschaft abhängen. Alle Komponenten dieser Matrizen finden Sie im Anhang B. Diese Unbekannten können numerisch gelöst werden, indem man die Gauß-Hermite-Quadratur mit Hermite-Polynomen verwendet. Nachdem die Integration von  $\boldsymbol{\rho}$  ersetzt wurde, kann der analytische Ausdruck von  $\boldsymbol{\rho}$  als Funktion von  $x_1$  erhalten werden. Schließlich können die elastischen Felder, wie z.B. Spannungsfelder durch eine einzige Versetzung in einem dreischichtigen anisotropen Material an beliebigen Stellen, basierend auf die Gleichungen 1.9 und 1.13 berechnet werden.

In der vorliegenden Arbeit wird die Dreischichtkonfiguration verwendet, um sowohl die Auswirkungen der KG-Steifigkeit als auch die freien Oberflächen für die Simulation der Experimente im Abschnitt 1.6 zu berücksichtigen. Somit wird die zweite Schicht als KG mit einer Dicke von etwa 1nm betrachtet. Währenddessen wird die zweischichtige Konfiguration verwendet, um die Wirkung von freien Oberflächen zu untersuchen, die im Abschnitt 1.4 angewendet wird.

### 1.3.6 Anwendung auf diskrete Versetzungs-Pile-ups

Betrachten wir einen Versetzungs-pile-up aus N unendlichen geraden Versetzungen. Das bedeutet, dass Versetzungen den gleichen Burgersvektor  $\mathbf{b}$  haben und in der gleichen Gleitebene und parallel zur  $\mathbf{x}_3$ -Achse liegen (Siehe Abbildung 1.10).

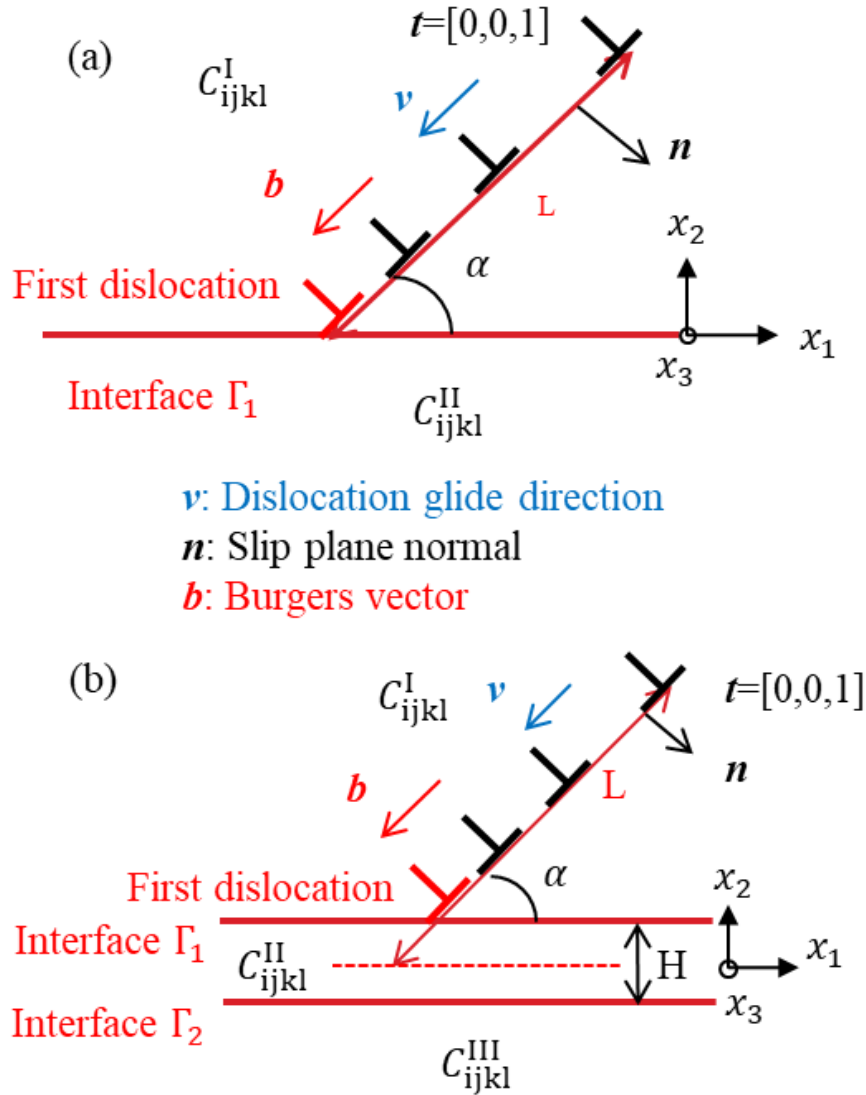


Figure 1.10: Versetzungs-Pile-up in der Gleitebene unter dem Winkel  $\alpha$  und mit dem Normalvektor  $\mathbf{n}$  für  $N$  geraden Versetzungen mit Burgersvektor  $\mathbf{b}$  und Linienvektor  $\mathbf{t}$  in einem heterogenen anisotropen (a) Bi-Material und (b) Tri-Material.

Die Gleichgewichtspositionen der  $N$ -Versetzungen können ermittelt werden, indem die Komponente der Peach-Köhler (P-K)-Kraft entlang der Gleitrichtung für jede Versetzung auf eine kritische Kraft  $F_c$  wie folgt minimiert wird:

$$F^{(\gamma)} = \text{abs}(\{(\boldsymbol{\sigma}_{int}(X_1(\gamma), X_2(\gamma)) + \boldsymbol{\sigma}_{ext}) \cdot \mathbf{b} \times \mathbf{t}\} \cdot \mathbf{v}) \stackrel{\text{abkürzen}}{=} F_c \quad (1.17)$$

wobei  $(X_1(\gamma), X_2(\gamma))$  die Position der  $\gamma^{\text{th}}$  Versetzung bezeichnet.  $\boldsymbol{\sigma}_{ext}$  ist ein homogener angelegter Spannungstensor und  $\boldsymbol{\sigma}_{int} = \boldsymbol{\sigma}_{im} + \boldsymbol{\sigma}_{dis}$  ist der interne



Spannungstensor (erzeugt durch die Spannungswechselwirkungen aller anderen Versetzungen  $\sigma_{dis}$  und die Bildversetzungen  $\sigma_{im}$ ) auf die  $\gamma^{th}$  Versetzung. Die kritische Kraft  $F_c$  beinhaltet die Gitterreibungskraft (primär) und andere Wechselwirkungskräfte, wie z.B. die Wechselwirkungskräfte zwischen einer Versetzung und einer Lerstelle, etc. Dann kann diese kritische Kraft in eine kritische Schubspannung auf eine Versetzung umgewandelt werden, indem  $F_c$  durch die Länge des Burgersvektors  $\tau_c = F_c/|\mathbf{b}|$  geteilt wird. Es sei darauf hingewiesen, dass der angelegte homogene Spannungstensor  $\sigma_{ext}$  in der vorliegenden Arbeit nur zum Gleichgewichtsausgleich des Versetzungs-Pile-ups dient. Die Berechnung der Gleichgewichtspositionen des Versetzungs-Pile-ups erfolgt somit nach einem iterativen Relaxationsschema, das all die kritischen Kräften  $F^{(\gamma)}$ , nachdem eine anfängliche Konfiguration erreicht wurde, minimiert [105]. Um eine solche Berechnung in einem unendlichen homogenen Medium durchführen zu können, sollte eine Versetzung als fixiert betrachtet werden. Normalerweise ist die Position der ersten (oder führenden) Versetzung ( $X_1(1), X_2(1)$ ) fixiert [97, 105]. Infolgedessen ist die P-K-Kraft auf die fixierte Versetzung nicht null. In einem heterogenen Medium kann jedoch diese Bildkraft auf die führende Versetzung die angewandte Spannung und den Spannungsbeitrag aus den anderen Versetzungen ausgleichen werden [105]; Aber nur bei abstoßenden Bildkräften. In diesem Fall könnten alle Versetzungspositionen, einschließlich der führenden, durch das iterative Relaxationsschema gefunden werden. Die meisten Forscher gehen von  $F_c = 0$  N/m aus, da der Wert der Reibspannung im reinen kfz-Kristall gering ist, der etwa  $1 \sim 2$  MPa beträgt [296]. Allerdings, in der vorliegenden Arbeit, wird festgestellt, dass eine nicht Null kritische Kraft hat einen entscheidenden Einfluss auf das Versetzungsverhalten in Anwesenheit von KG und freien Oberflächen. Der Grund dafür ist, dass es bereits nach der Probenvorbereitung Gitterfehler im Material gibt, wie z.B. Defekte nahe der Oberfläche durch die  $\text{Ga}^+$ -Ionen [139]. Darüber hinaus ist der theoretische Wert der Reibkraft für  $\alpha$ -Brass als Legierung viel höher als reine kfz-Kristalle, wie z.B. Ni. Zum Beispiel, es wurde festgestellt, dass Reibkraft  $\tau_c$  für  $\beta$ -Brass zwischen  $80 \sim 100$  MPa liegt [296]. Daher kann die kritische Kraft in Gleichung (1.17) für realistische Berechnungen nicht ignoriert werden.

## 1.4 Vorläufige theoretische Ergebnisse und Diskussion der einzeln Versetzungen und Versetzungs-Pile-ups in Ni-Bikristalle

Um die Wirkung von verschiedenen mikrostrukturellen Faktoren, wie z.B. die Missorientierung, KG-Steifigkeit und freie Oberfläche, abzuschätzen, wurden mehrere Simulationen mit idealen Bedingungen (theoretische Untersuchung) durchgeführt

und sind unten zusammengefasst. Weitere ausführliche Ergebnisse und Diskussion befinden sich in folgender Publikation Chen et al. [277].

In allen folgenden numerischen Anwendungen werden Ni-Bikristalle unterschiedlicher Orientierungen betrachtet. Darüber hinaus werden nur Stufenversetzungen mit einem unter einen Winkel  $\alpha = 45^\circ$  definierten Burgersvektor berücksichtigt (siehe Abbildung 1.7), so dass die Gleitrichtung  $\mathbf{m} = \mathbf{b}/|\mathbf{b}| = [-\cos 45^\circ, -\sin 45^\circ, 0]$  in den globalen Koordinaten  $(\mathbf{x}_1, \mathbf{x}_2, \mathbf{x}_3)$  ist. Nach der FS/RH-Konvention, wird der Normalenvektor der Gleitebene durch  $\mathbf{n} = \mathbf{t} \times \mathbf{m}$  mit  $\mathbf{t} = [0, 0, 1]$  gegeben. Die Gleitrichtung der Versetzungen  $\mathbf{v}$  zeigt parallel zu  $\mathbf{m}$  für Stufenversetzungen und zeigt immer auf den KG-Bereich, so dass es möglich ist, Versetzungs-Pile-ups an der KG zu erzeugen. Das Gleitsystem soll  $\mathbf{m}^0 = 1/\sqrt{2}[1, 1, 0]$  und  $\mathbf{n}^0 = 1/\sqrt{3}[-1, 1, -1]$  im Kristallsystem  $(\mathbf{e}_1, \mathbf{e}_2, \mathbf{e}_3)$  sein. Damit ist die Orientierung des Kristalls, der Versetzungen enthält, durch die Transformationsmatrix  $\mathbf{T}$  so definiert, dass  $[\mathbf{m}, \mathbf{n}, \mathbf{t}]^T = \mathbf{T}[\mathbf{m}^0, \mathbf{n}^0, \mathbf{t}^0]^T$  mit  $\mathbf{t}^0 = \mathbf{m}^0 \times \mathbf{n}^0$  ist. Die betrachteten spezifischen Orientierungen sind wie folgt:

- Orientierung A<sup>Ori</sup> mit  $\mathbf{T}_A = \begin{bmatrix} 1 & 0 & 0 \\ 0 & 1 & 0 \\ 0 & 0 & 1 \end{bmatrix}$  (Einheitsmatrix)

- Orientierung B<sup>Ori</sup> mit  $\mathbf{T}_B = \begin{bmatrix} -1/2 & \sqrt{2}/2 & 1/2 \\ -1/2 & -\sqrt{2}/2 & 1/2 \\ \sqrt{2}/2 & 0 & \sqrt{2}/2 \end{bmatrix}$

Der elastische Steifigkeitstensor im globalen System wird dann aus der Transformationsmatrix  $\mathbf{T}$  durch  $C_{ijkl} = T_{ig}T_{jh}C_{ghmn}^0T_{km}T_{ln}$  hergeleitet, wobei  $\mathbf{C}^0$  der im Kristallsystem definierten elastische Steifigkeitstensor ist. Für das Tri-Material- und Multilayer-Modell wird die Dicke des Materials II (KG) mit  $H$  bezeichnet, die im vorliegenden Abschnitt immer gleich  $5|\mathbf{b}|$  ist, und sein elastischer Steifigkeitstensor  $C_{ijkl}^{\text{II}}$  wird dank eines einzigen Parameters  $\lambda$ , der die KG-Steifigkeit berücksichtigt:

$$C_{ijkl}^{\text{II}} = \frac{\lambda}{2} (C_{ijkl}^{\text{I}} + C_{ijkl}^{\text{III}}) \quad (1.18)$$

Die KG ist dann weicher als die Körner (Material I und III), wenn  $\lambda < 1$  ist und steifer für  $\lambda > 1$ .

Für das Multilayer-Modell mit freien Oberflächen werden zwei Schichten mit  $h_1 = h_2 = H'/2$  nur betrachtet, so dass die KG als eine Grenzfläche (Dicke = null) betrachtet wird.

Der Abstand zwischen der KG (bzw. der Mitte der KG-Region) und der  $\gamma^{th}$  Versetzung entlang der Gleitrichtung wird als  $L(\gamma)$  bezeichnet. Wenn die führende Versetzung in Versetzungs-Pile-Ups fixiert ist, dann ist  $L(1) = 5|\mathbf{b}|$ . Die Versetzungslänge ist definiert als der Abstand zwischen der ersten und der letzten Versetzung  $L(N) - L(1)$ .

In einem heterogenen Medium wird eine Bildkraft auf eine Versetzung ausgeübt, die durch das Vorhandensein von Grenzfläche(n) oder Oberfläche(n) verursacht wird. Die Bildkraft ist die Peach-Köhler-Kraft an einer Versetzungsposition aufgrund ihres Spannungsfeldes ohne Berücksichtigung des unendlichen homogenen Mediums; dessen Beitrag als  $\sigma_{im}$  nachfolgend bezeichnet wird. Die Projektion der Bildkraft entlang der Gleitrichtung reduziert sich basierend auf Gleichung 1.19 [28]:

$$F_{im} = [(\sigma_{im} \cdot \mathbf{b}) \times \mathbf{t}] \cdot \mathbf{v} \quad (1.19)$$

Mit der in Abbildung 1.7 verwendeten Konvention,  $\mathbf{v}$  zeigt immer auf die KG. Für  $F_{im} > 0$  bedeutet die Versetzung wird von der KG angezogen und für  $F_{im} < 0$  die Versetzung wird von der KG abgestoßen.

Im Folgenden werden zunächst der Missorientierungseffekt und die KG-Steifigkeit untersucht. Beide Orientierungen  $A^{Ori}$  und  $B^{Ori}$  werden für den unteren Kristall im Fall eines Bi-Material-Modells verwendet und im Falle des Tri-Material-Modells werden zwei verschiedene  $\lambda$ -Werte 0,5 und 2 berücksichtigt. Der Einfluss der elastischen Anisotropie vs. Isotropie auf die projizierten Bildkräfte entlang der Gleitrichtung in Zweistoff-, Halbraum- und Tri-Material -Konfigurationen ist in Abbildung 1.11 dargestellt. Im Folgenden sind die Schlussfolgerungen dieser theoretischen Untersuchung (siehe Chen et al. [277] für weitere Details):

- In der Orientierung  $A^{Ori}$  hat die KG eine attraktive Wirkung auf die Versetzung, während in der Orientierung  $B^{Ori}$  die KG einen abstoßenden Charakter auf die Versetzung hat.
- In einem Halbraum hat eine starre Oberfläche immer eine abstoßende Wirkung auf die Versetzung, während eine freie Oberfläche zeigt das Gegenteil. Es ist auch zu erkennen, dass die Größe von  $F_{im}$  für den Halbraum viel größer als für die bi- oder tri-materielle Konfiguration ist. Außerdem haben  $F_{im}$  fast die gleiche Größe im Fall isotroper Elastizität in Halbräumen und anisotroper (siehe Abbildung 1.11).
- Eine weichere KG mit  $\lambda = 0,5$  (nachgiebige Grenzfläche) übt einen attraktiven Effekt auf die Versetzung aus, während eine steifere KG mit  $\lambda = 2$  (starre Grenzfläche) einen abstoßenden Effekt auf die Versetzung hat.

- Im Falle einer anisotropen Elastizität gibt es eine Gleichgewichtsposition für die Versetzung, in der  $F_{im}$  eine Vorzeichenänderung aufgrund der gekoppelten Effekte der Bildkräfte aufweist. Die Bildkräfte resultieren sowohl aus dem unteren Kristall als auch aus der KG mit inversem Effekt, wie z.B.  $A^{\text{Ori}}$  mit  $\lambda = 2$  oder  $B^{\text{Ori}}$  mit  $\lambda = 0,5$ . Wenn der untere Kristall und die KG den gleichen Effekt haben, wird ihre Wirkung verstärkt. Der Wirkungsabstand der starren/freien Oberfläche ist größer als der Missorientierungseffekt.
- Die Wirkungsabstand der KG-Steifigkeit ist ziemlich klein mit etwa  $41 |\mathbf{b}|$  für  $\lambda = 2$  und  $58 |\mathbf{b}|$  für  $\lambda = 0,5$ . Es ist jedoch wichtig, die führende Versetzung des Pile-ups ausgleichen zu können. Über diese Abstände hinaus, die Bildkraft ist hauptsächlich von der Missorientierung der Bi-Kristalle abhängig.
- Für isotrope Tri-Materielle-Konfigurationen, die Bildkraft hängt nur von der KG-Steifigkeit aufgrund des Missorientierungs-Effektes durch den unteren Kristall ab.

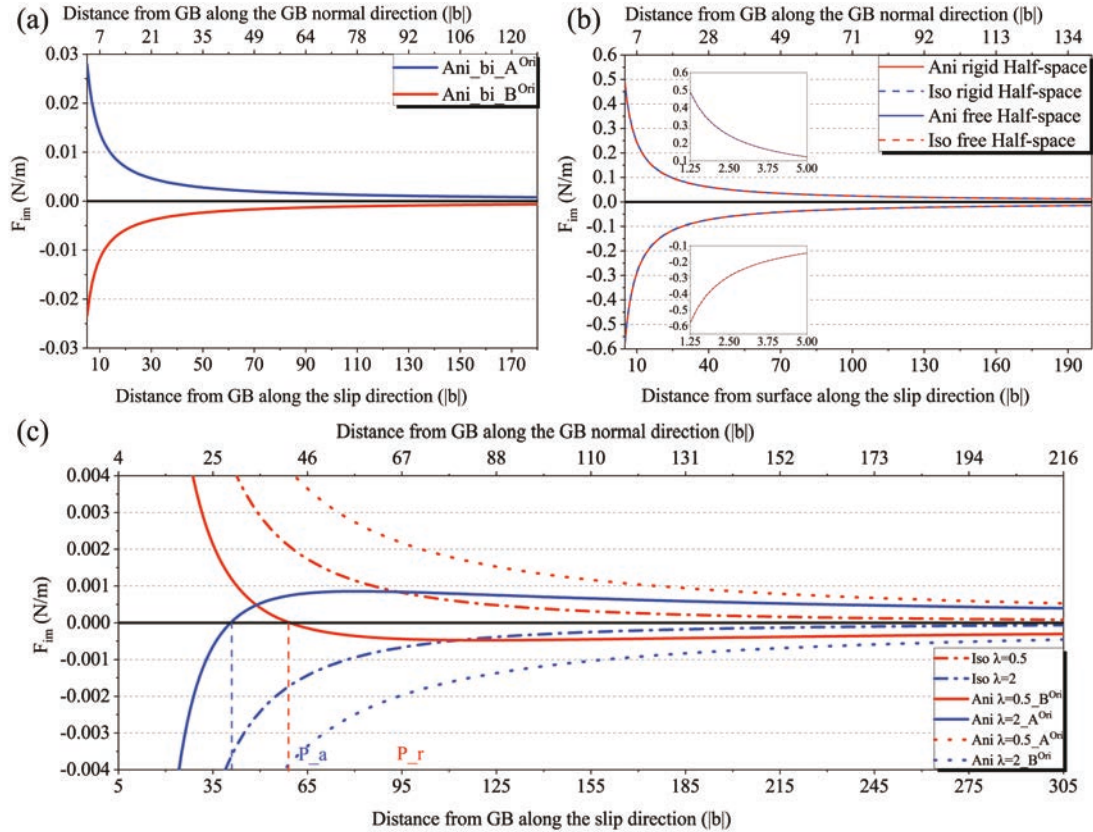


Figure 1.11: Variation der projizierten Bildkraft  $F_{im}$  mit dem KG-Abstand entlang der Gleitrichtung für verschiedene Konfigurationen: (a) Bi-Material-Konfigurationen, (b) Halbraum-Konfigurationen und (c) Tri-Material-Konfigurationen mit anisotroper vs. isotroper Elastizität.

Neben dem Effekt von Missorientierung und KG-Steifigkeit wurde der Effekt von freien Oberflächen auf die Bildkraft theoretisch untersucht, wobei eine Zweischichten-Konfiguration mit unterschiedlichen Missorientierungen  $A^{Ori}$ ,  $B^{Ori}$  und unterschiedlicher Dicke  $H' = 2\mu\text{m}$ ,  $H' = 4\mu\text{m}$  berücksichtigt wurde. Die Ergebnisse der projizierten Bildkräfte entlang der Gleitrichtung sind in Abbildung 1.12 dargestellt. Die Zusammenfassung ist wie folgt:

- Freie Oberflächen haben eine starke attraktive Wirkung auf Versetzungen. Im Vergleich zum freien Oberflächeneffekt ist der Effekt der Missorientierung in der Nähe der freien Oberfläche vernachlässigbar, da die P-K-Kraft nah an der Oberfläche unabhängig von der Orientierung ist.
- In der Nähe der KG wird die Bildkraft hauptsächlich durch Missorientierung gesteuert. Tatsächlich haben die beiden freien Oberflächen einen gegenteiligen Effekt auf die Versetzung. Wenn die Versetzung in etwa gleichem Ab-

stand zu den beiden freien Oberflächen liegt, wird ihr Beitrag vernachlässigt.

- Ein Größeneffekt ergibt sich nach der Normierung des Abstands durch die Hälfte der Dicke: Bei gleichem relativem Abstand von der Korngrenze ist die Bildkraft größer in den kleineren Bi-Kristallen.
- Kombiniert man mit attraktiver Missorientierung  $A^{\text{Ori}}$ , so gibt es einen Gleichgewichtspunkt, bei dem die Bildkraft auf die Versetzung Null ist. Diese Position befindet sich bei der nahezu gleichem relativen Abstand von KG für unterschiedliche Materialdicken.

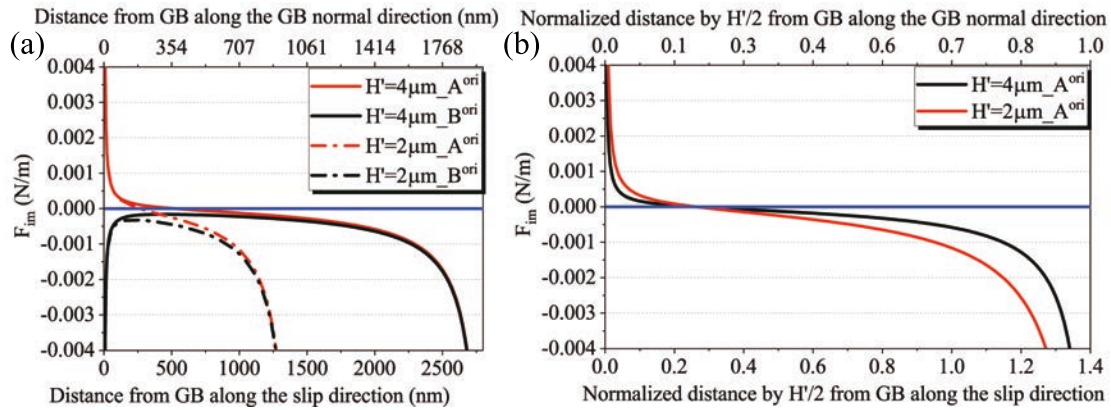


Figure 1.12: Variation der projizierten Bildkraft  $F_{\text{im}}$  für Zweischichten-Modelle in unterschiedlicher Dicke (a) mit dem Abstand vom KG entlang der Gleitrichtung und (b) mit dem normierten Abstand durch  $H'/2$  von KG entlang der Gleitrichtung.

Da die Orientierung des unteren Kristalls einen stärkeren Einfluss auf Versetzungen auf große Entfernungen als die KG-Steifigkeit hat, ist hier die Länge der Versetzungs-Pile-ups  $L$  mit den unterschiedlichen Orientierungen des unteren Kristalls in Abbildung 1.13 im Falle eines Pile-ups mit 50 Versetzungen und einer KG der Dicke null dargestellt. Die Orientierung des oberen Kristalls mit dem Pile-Up ist festgelegt, immer noch definiert durch  $\alpha = 45^\circ$ , während die Orientierung des unteren Kristalls durch eine Drehung  $\psi$  von  $0^\circ$  bis  $180^\circ$  um  $\mathbf{v}$  gegeben ist. Um eine stabile Versetzung-Pile-up-Konfiguration zu erhalten (insbesondere im Fall anziehender Missorientierung), wird die führende Versetzung immer fixiert, um Abstoßungskräfte auf alle anderen Versetzungen auszuüben. Daher wird der Fall des homogenen Einkristalls für  $\psi = 0^\circ$  und  $\psi = 180^\circ$  abgerufen, bei der  $L = 8,75 \mu\text{m}$  beträgt (Abbildung 1.13 (a)). Wenn  $L$  kleiner (bzw. größer) als  $8,75 \mu\text{m}$  ist, hat die Bildkraft überall einen attraktiven (bzw. abstoßenden) Effekt auf den Pile-Up (siehe Abbildung 1.13 (b)). Der Missorientierungswinkel

zwischen beiden Kristallen, d.h. der minimale Drehwinkel, um von einer Kristallorientierung zur anderen zu gelangen, ist auch in Abbildung 1.13 (a) dargestellt. Der maximal mögliche Wert für den Missorientierungswinkel  $62.8^\circ$  [298] in kubischem Kristall ist fast erreicht; entspricht aber nicht dem Maximalwert von  $L$ . Der Maximalwert von  $L$  entspricht jedoch dem hohen Missorientierungswinkel (ca.  $60^\circ$ ). Darüber hinaus ist zu beachten, dass ein und derselbe Missorientierungswinkel mit verschiedenen elastischen Verhalten in Verbindung gebracht werden kann (z.B.  $60^\circ$  wird mit  $\psi = 60^\circ$  und  $\psi = 120^\circ$  abgerufen, so hat  $L$  die Werte  $L = 9.02 \mu\text{m}$  und  $L = 8.61 \mu\text{m}$ ). Schließlich kann beobachtet werden, dass die relativen Schwankungen von  $L$  im Vergleich zum isotropen Fall in Ni etwa 7% erreichen können. Wichtig ist, dass solche signifikanten Schwankungen in einem mäßig elastischen anisotropen Material auftreten. Aber unter Berücksichtigung von Pile-ups in der isotropen Elastizität können nicht beobachtet werden. Unter Verwendung der Voigt-Reuss-Hill-Methode [269, 270] ist der Wert von  $L$  (gegeben durch die isotrope Elastizität) jedoch etwa die durchschnittliche Länge in anisotroper Elastizität mit der aktuellen Rotationskonfiguration (siehe Abbildung 1.13 (a)). Darüber hinaus ist diese maximale relative Variation von  $L$  für verschiedene Materialien mit unterschiedlicher Anisotropie (Zener-Verhältnisse) in Tabelle 1.1 dargestellt. Sie nimmt mit zunehmendem anisotropem Faktor zu, was die anisotrope Wirkung widerspiegelt. Wenn der Effekt des starren Halbraums viel stärker als der Effekt der Missorientierung ist, dann sind  $L$  und  $F_{im}$  bei der starren Halbraum-Konfiguration viel größer als bei der Bi-Material-Konfiguration mit unterschiedlichen Missorientierung.

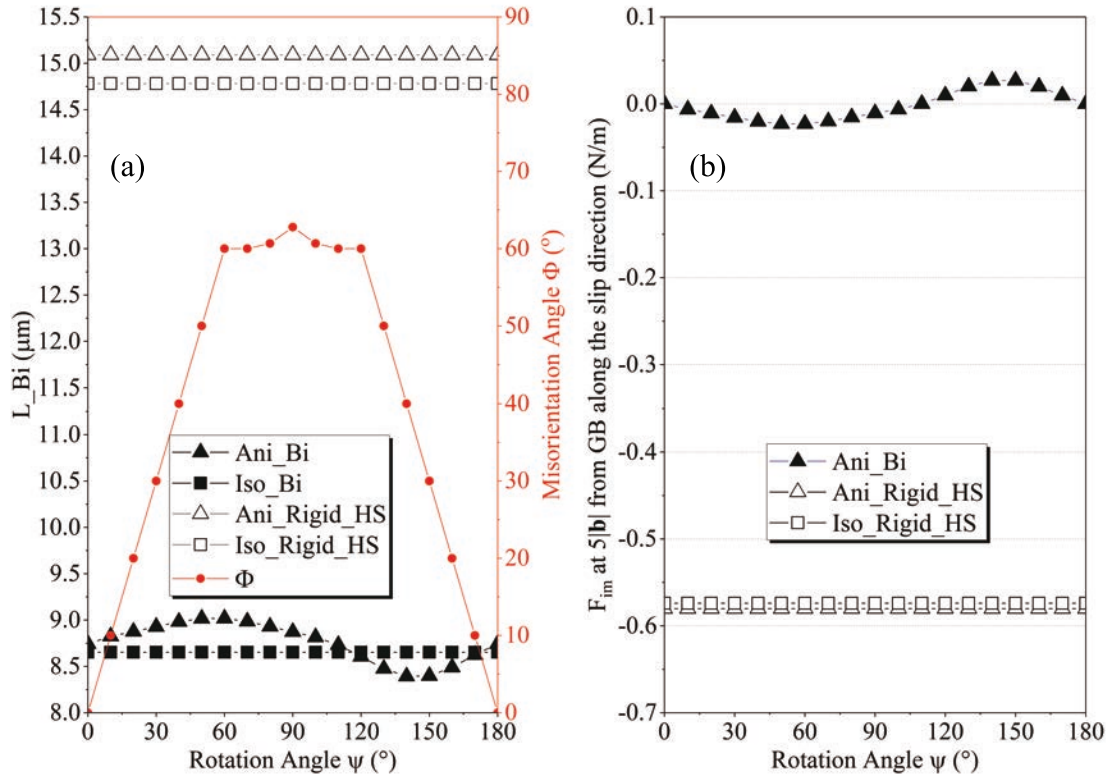


Figure 1.13: Effekt der Missorientierung in anisotropen Bi-Kristallen (Ani\_Bi) auf (a) die Pile-up-länge  $L$  für einen Pile-up mit 50 Versetzungen und einer KG der Dicke null und (b) projizierte Bildkraft entlang der Gleitrichtung in einem Abstand von  $5|b|$  von KG. Die Drehachse ist die Gleitrichtung  $v$ . Vergleiche auch mit den Fällen von homogenem isotropem Fall (Iso\_Bi), isotropem starrem Halbraum (Iso\_Rigid\_HS) und anisotropem starrem Halbraum (Ani\_Rigid\_HS).

Material	Al	Ni	Cu	$\alpha$ -Brass
Zener-Verhältnis <sup>[1]</sup>	1.22	2.51	3.21	4.11
Maximale relative Abweichung von $L$ (%)	1.2	7.2	9.0	11.5

Table 1.1: Maximale relative Variation von  $L$  mit anisotroper Elastizität im Vergleich zur isotropen Elastizität für verschiedene Materialien mit unterschiedlichen anisotropen Faktoren (Zener-Verhältnisse <sup>[1]</sup>). Elastische Steifigkeitsmodule dieser Materialien finden sich im Buch "Theory of Dislocations" <sup>[28]</sup>.



## 1.5 Experimentelle Ergebnisse für Ni und $\alpha$ -Brass Bikristalle

Zunächst wurden die Gleitlinien in Ni-Bi-Kristalle mi Hilfe vom REM untersucht (Abbildung 1.14 (a)) dann in  $\alpha$ -Brass (Abbildung 1.15 (a)). In der Ni-Proben sind die Gleitlinien auf der Oberseite sehr schwach und es können nur zwei parallele Gleitlinien in Kristall I und II beobachtet werden. Basierend auf der Richtung der Gleitlinien auf der Oberseite und den berechneten Schmid-Faktoren wird das aktive Gleitsystem mit dem maximalen Schmid-Faktor oder durch die Inkompatibilitätsspannung bestimmt [160]. Das Gleitsystem B4-basierend auf das Schmid und Boas' Konvention [40] für jeden Kristall-wird als das aktivierte System angesehen, wie in Abbildung 1.14 dargestellt.

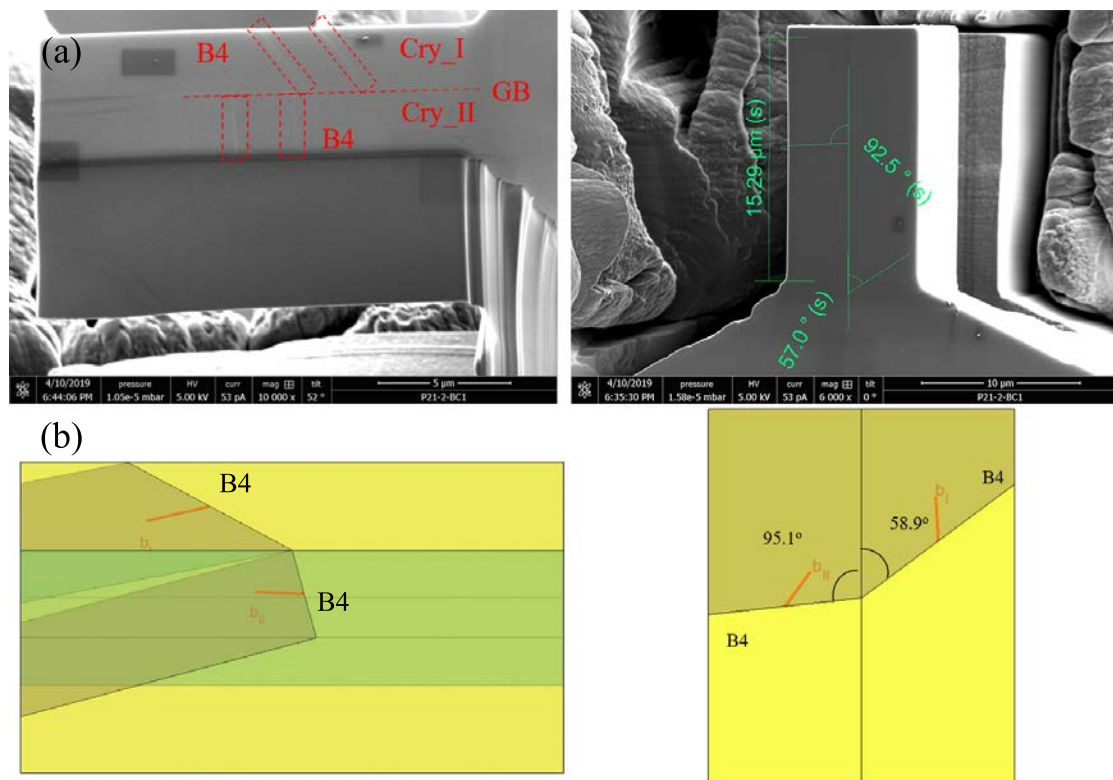


Figure 1.14: REM-Bild eines Ni-Bi-Kristalls nach dem Drucktest zur kristallographischen Analyse der Gleitlinien. Basierend auf der Richtung der Gleitlinien, der Orientierung jedes Kristalls und des Schmid-Faktors (oder der Inkompatibilitätsspannungsanalyse) wird das Gleitsystem B4 im Kristall I und B4 auch im Kristall II aktiviert.

Allerdings im  $\alpha$ -Brass-Bi-Kristall wurden jeweils zwei Gleitsysteme im Krystal I und II aktiviert, die auf der Oberseite im Kristall I (A6 und C5) und auf der

Seitenfläche im Kristall II (B4 und D6) wechselwirken. Basierend auf der Richtung der Gleitlinien und des Schmid-Faktors (oder der Inkompatibilitätsspannung) für jedes Gleitsystem, wie in Abbildung 1.15 dargestellt, die aktiven Gleitsysteme im Kristall I sind A6 und C5 und im Kristall II B4 und D6. Somit gibt es in beiden Körnern in der  $\alpha$ -Brass-Probe Mehrfachgleitung.

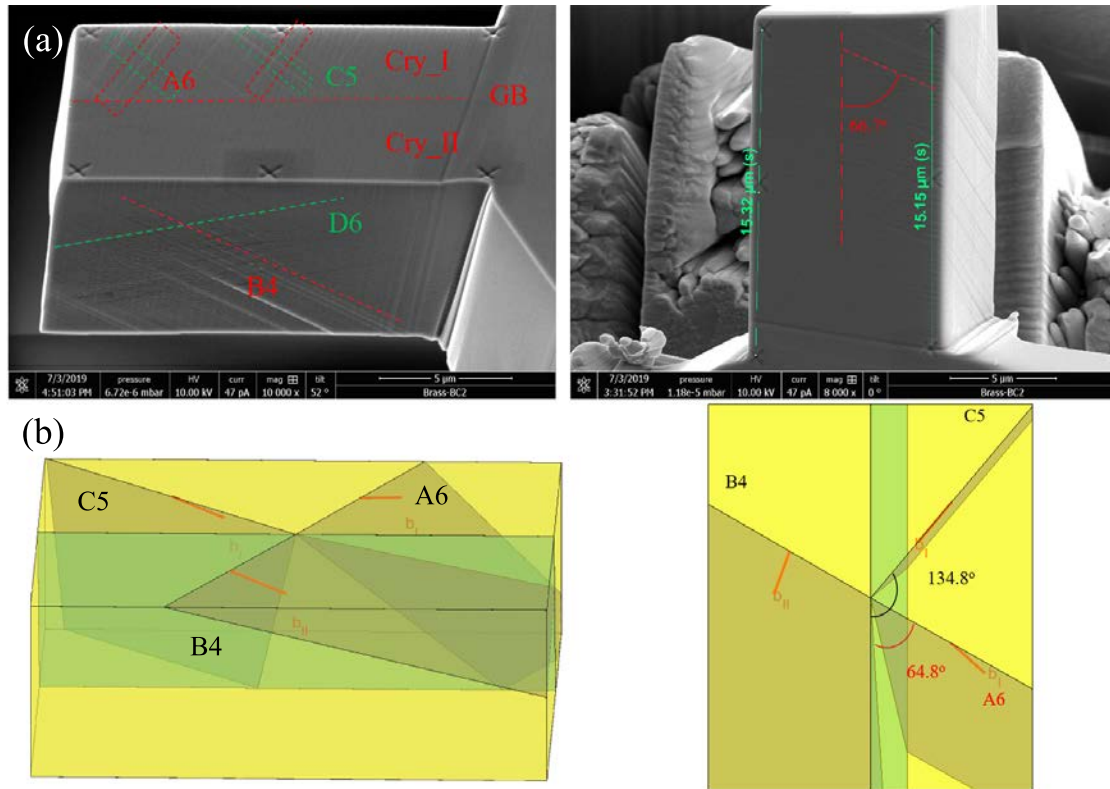


Figure 1.15: REM-Bild eines  $\alpha$ -Brass-Bi-Kristalls nach dem Drucktest zur kristallographischen Analyse der Gleitlinien. Basierend auf der Richtung der Gleitlinien, der Orientierung jedes Kristalls und des Schmid-Faktors (oder der Inkompatibilitätsspannungsanalyse) wird das Gleitsystem A6 und C5 im Kristall I und B4 im Kristall II aktiviert.

Anschließend wurde die Oberflächentopographie der Oberseite der Probe mit Hilfe des AFMs abgebildet, um ein besseres Bild (3D) der Gleitlinien zu erhalten. In Abbildung 1.16 sind die AFM-Ergebnisse der Ni-Probe und in Abbildung 1.18 die AFM-Ergebnisse der  $\alpha$ -Brass-Probe dargestellt. Die Stufen der Gleitlinien entsprechen den Gleitlinien in den REM-Bildern in Abbildung 1.14 und 1.15. Für die Ni-Probe wurde eine Gleitstufe mit klassischen Merkmalen von Pile-up zur Analyse ausgewählt. Die Höhen der oberen und unteren Linie dieser Gleitlinie wurden entlang der Gleitrichtung der KG gemessen (siehe rote Linie schwarze Linie in Abbildung 1.16). Die Messdaten wurden mit Hilfe eines Polynoms gefit-

tet (gekennzeichnet als  $h^{Top}$  und  $h^{Bottom}$ ). Dann wurde die relative Höhe dieser Stufe  $\Delta h$  als Differenz der gefitteten Höhe zwischen diesen beiden Linien berechnet (siehe Abbildung 1.17). Es wird festgestellt, dass der Höhenunterschied zwischen zwei Linien an der KG  $\Delta h_{KG} \approx 0,86$  nm nicht null ist. Dieser Wert entspricht einer schwachen Versetzungstransmission (siehe rote Markierung in Abbildung 1.16 (b)). Die Stufenhöhe steigt von KG entlang der Gleitrichtung an und erhält ihren Maximalwert  $\Delta h \approx 9.06$  nm bei etwa  $d \approx 3.28$   $\mu\text{m}$ . Außerdem wurde lokal Korngrenzengleiten. Dieses Gleiten Mechanismus kann in Abbildung 1.16 (a) und in Abbildung 1.16 (b)(grüne Markierung) beobachtet werden.

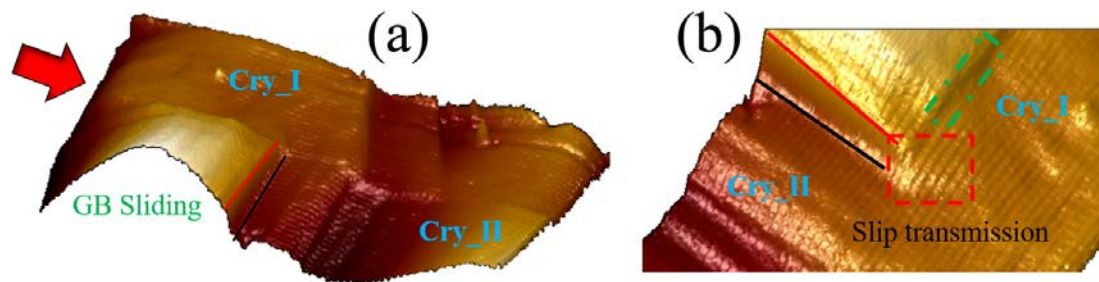


Figure 1.16: AFM-Oberflächentopographie der Ni-Probe: (a) AFM-Scan der gesamten oberen Oberfläche und (b) der AFM-Scan, der lokale Transmission an der KG zeigt (rote viereckige Markierung). Der rote Pfeil zeigt die Belastungsrichtung an. Der Buckelbereich im Kristall II in (a) und die grüne rote Markierung in (b) zeigen KG-Gleiten.

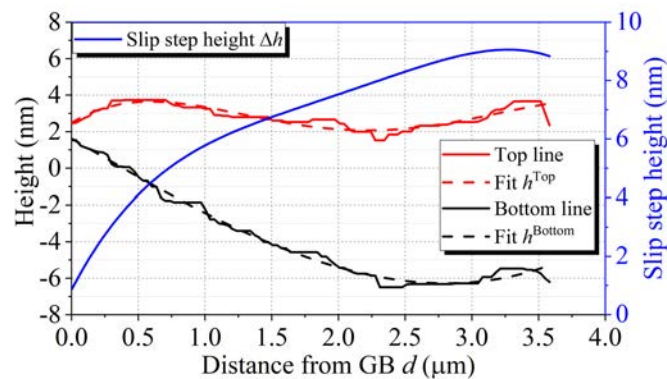


Figure 1.17: Messergebnisse der Gleitstufe in Abbildung 1.16: Rote und schwarze durchgezogene Linie zeigen die gemessene Höhe der oberen Linie bzw. der unteren Linie der Stufe. Die gestrichelten Linien mit der entsprechenden Farbe zeigen die passenden Ergebnisse nach dem Polynomverfahren mit dem Koeffizienten  $R^2 = 0,8176$  für die obere Linie und  $R^2 = 0,9898$  für die untere Linie. Die blaue Linie zeigt die simulierte Stufenhöhe.

Eine ähnliche Analyse wurde für die  $\alpha$ -Brass-Probe durchgeführt, wie in Abbildung 1.19 dargestellt. Während die Transmission in der  $\alpha$ -Brass-Probe stärker aus-

geprägt ( $\Delta h_{KG} \approx 4,29 \text{ nm}$ ) als in der Ni-Probe ist, hat die Ausbreitung von Versetzungen im Nachbarkorn eine kürzere Distanz. Das Maximum der Stufenhöhe ist  $\Delta h \approx 10.03 \text{ nm}$  bei etwa  $d \approx 2.44 \mu\text{m}$ . Im mittleren Teil der Kurve der Stufenhöhe kann eine leichte Vertiefung beobachtet werden, die durch die Überschneidung mit einer nicht-koplanaren Gleitlinie verursacht werden kann.

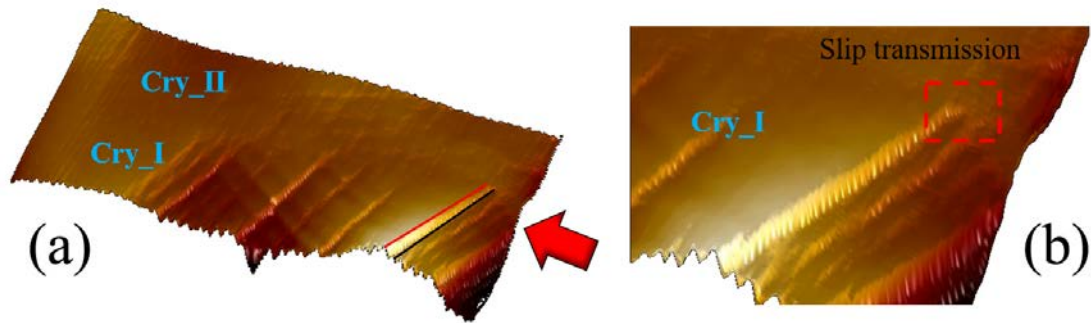


Figure 1.18: AFM-Oberflächentopographie der  $\alpha$ -Brass-Probe: (a) AFM-Scan der gesamten oberen Oberfläche und (b) der AFM-Scan, der lokale Transmission an der KG. Der rote Pfeil zeigt die Lastrichtung.

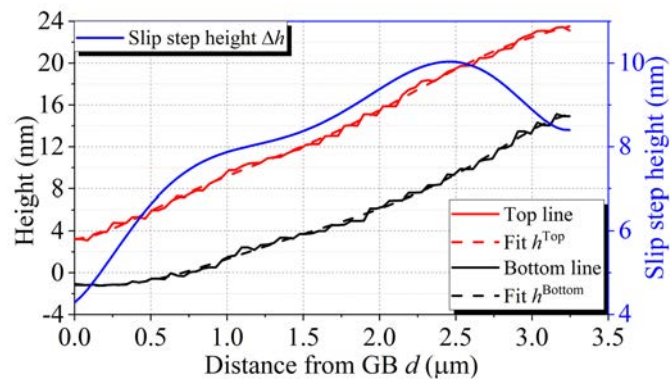


Figure 1.19: Messergebnisse der Gleitstufe in Abbildung 1.18: Rote und schwarze durchgezogene Linie zeigen die gemessene Höhe der oberen Linie bzw. der unteren Linie der Stufe. Die gestrichelten Linien mit der entsprechenden Farbe zeigen die passenden Ergebnisse nach dem Polynomverfahren mit dem Koeffizienten  $R^2 = 0,9982$  für die obere Linie und  $R^2 = 0,9973$  für die untere Linie. Die blaue Linie zeigt die simulierte Stufenhöhe.

## 1.6 Simulation des Stufenhöhenprofils mit Hilfe diskreter Versetzungs-Pile-up-Berechnungen und Diskussionen

Basierend auf den in Kapitel 1.3 entwickelten Modellen können die Stufenhöhen aufgrund eines Versetzungs-Pile-ups an der KG in einem Bi-Kristall mit Hilfe von Versetzungs-Pile-ups-Modelle simuliert werden. Für die Berechnungen werden folgende Hypothesen und Konfigurationen festgelegt und in Abbildung 1.20 dargestellt:

- Die Versetzungslinien sollen unendlich gerade Linien sein. Sie sollen parallel zueinander und auch parallel zur KG-Ebene sein.
- Die im Experiment gemessene Position der maximalen Stufenhöhe gilt als das Ende des Versetzungs-Pile-ups. In der Simulation wird jedoch angenommen, dass es eine feste Versetzungsquelle gibt.
- Die Versetzungen, die von dieser Quelle erzeugt werden, werden einen Pile-up bilden, wenn sie sich in Richtung KG bewegen, und werden eine Stufe auf der Seitenfläche erzeugen, wenn sie sich auch auf die freie Oberfläche bewegen.
- Die KG wird mit einer Grenzflächendicke von 0,9 nm berechnet, die aus der MD-Simulation gewonnen wird. Diese Grenzfläche gilt als anisotrop mit  $\lambda = 1$ , wie in Gleichung 1.18 definiert ist. Zum Vergleich wurden isotrope Eigenschaften für die KG-Steifigkeit auch unter Verwendung der Voigt-Reuss-Hill-Methode [269, 270] berücksichtigt, wobei der Steifigkeitstensor wie folgt modelliert wird:

$$C_{ijkl}^{\text{II}} = 3kJ_{ijkl} + 2GK_{ijkl} \quad (1.20)$$

wobei  $k = \frac{2G(1+\nu)}{3(1-2\nu)}$  der Kompressionsmodul,  $G$  der Schermodul und  $\nu$  das

Poisson-Verhältnis sind mit  $J_{ijkl} = \frac{1}{3}\delta_{ij}\delta_{kl}$ , und  $K_{ijkl} = \frac{1}{2}\left(\delta_{ik}\delta_{jl} + \delta_{il}\delta_{jk} - \frac{2}{3}\delta_{ij}\delta_{kl}\right)$ .

- Die transmittierten Versetzungen können nicht gleichzeitig mit den Versetzungen im Pile-up aufgrund der zweidimensionalen L-E-S-Theorie betrachtet werden, wenn sie unterschiedlichen Richtungen der Versetzungslinien aufweisen. Somit sollen die transmittierten Versetzungen durch eine in der Grenzfläche fixierte Superversetzung dargestellt werden. Deshalb

ist  $\mathbf{b}^{\text{Tran}} = N^{\text{Tran}} \times \mathbf{b}^{\text{GB}}$ , wobei  $\mathbf{b}^{\text{Tran}}$  der Burgersvektor dieser Superversetzung,  $N^{\text{Tran}}$  die Anzahl der transmittierten Versetzungen und  $\mathbf{b}^{\text{GB}}$  der Burgersvektor einer in der KG gespeicherten Versetzung sind. Außerdem,  $\mathbf{b}^{\text{GB}}$  könnte derselbe wie der Burgersvektor der einlaufenden Versetzungen sein oder  $\mathbf{b}^{\text{GB}}$  könnte der Restburgersvektor zwischen dem einlaufenden Gleitsystem und einem der 12 auslaufenden Gleitsysteme im Nachbarkorn sein, wie folgt  $\mathbf{b}^{\text{GB}} = \mathbf{b}^{\text{In}} - \mathbf{b}^{\text{Out}}$  definiert.

- Wie im Abschnitt 1.3.1 vorgestellt, ist die Simulations-Koordinate die  $\mathbf{x}_3$ -Richtung die Richtung der Versetzungslinie  $z_S$ , wie in Abbildung 1.20 dargestellt. Die  $\mathbf{x}_2$ -Richtung ist parallel zur Richtung der KG-Normale  $rm_{y_S}$  (siehe Abbildung 1.20). Basierend auf der FS/RH-Konvention, die  $\mathbf{x}_1$ -Richtung ist  $\mathbf{x}_1 = \mathbf{x}_2 \times \mathbf{x}_3$  und dargestellt als  $x_S$  in Abbildung 1.20. Darüber hinaus werden alle verwendeten Vektoren und Tensoren, wie der Burgersvektor aktiver Gleitsysteme, der Vektor der Gleitrichtung und die elastische Steifigkeit, etc. in die Simulationskoordinaten transformiert.
- Die Gleichgewichtspositionen von Versetzungen im Pile-up werden mit Hilfe der Gleichung 1.17 bestimmt, dann kann die Stufenhöhe entlang der Gleitrichtung wie folgt berechnet werden:

$$\Delta h(d) = N(d) \times b(Z) \quad (1.21)$$

wobei  $d$  der KG-Abstand entlang der Gleitrichtung,  $N$  die Anzahl der Versetzungen, die durch diesen Punkt durchgehen und  $b(Z)$  die außerhalb der Oberfläche liegende Komponente des Burgersvektors (entlang der  $Z$ -Richtung, die senkrecht zur Oberseite steht, wie in Abbildung 1.20 dargestellt) sind.

- In folgenden wird die gemessene Stufenhöhe von KG auf Null kalibriert, das heißt  $\Delta h = h^{\text{Top}} - h^{\text{Bottom}} - \Delta h_{GB}$ . Ebenso wird die simulierte Gleithöhe an der KG gleich Null ( $\Delta h(0) = 0$ ) sein.

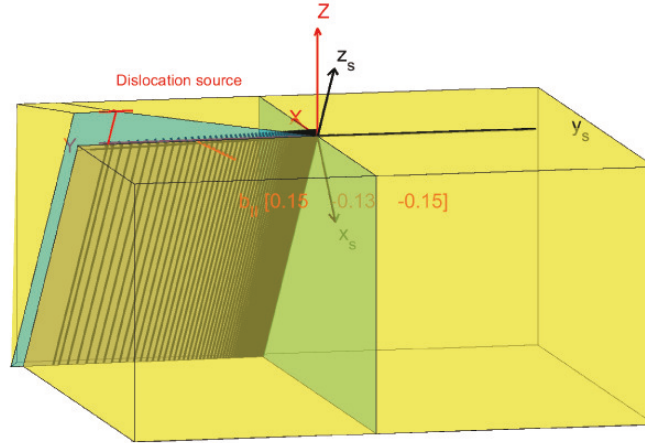


Figure 1.20: Schematische Darstellung der Simulationskonfiguration.  $(x_s, y_s, z_s)$  geben die Simulationskoordinate und  $(X, Y, Z)$  die globale Probenkoordinate an.

Für folgenden Ergebnisse werden die Standardwerte der Parameter wie folgt eingestellt: Der Burgersvektor der transmittierten Versetzungen soll gleich dem Burgersvektor der einlaufenden Versetzungen sein und die kritische Kraft soll  $F_c = 0$  N/m sein. Standardmäßig werden die Berechnungen mit anisotroper Elastizität durchgeführt. Der L-E-S-Formalismus kann jedoch aufgrund des Problems der wiederholten Eigenwerte (entartete Lösungen) nicht für die Berechnung der isotropen Elastizität verwendet werden. In diesem Fall werden die elastischen Steifigkeitsmodule zunächst aus isotropen elastischen Konstanten durch  $C_{11} = 2G(1 - \nu)/(1 - 2\nu)$ ,  $C_{12} = 2G\nu/(1 - 2\nu)$  und  $C_{44} = G$  dargestellt. Dann wird der  $C_{44}$  ein leicht erhöht, um das Problem der entarteten Lösungen im L-E-S-Formalismus zu verhindern und durch  $C_{44} = C_{44} \times 1.0001$  ersetzt.

Basierend auf den oben genannten Hypothesen beträgt die außerhalb der Oberfläche liegende Komponente des Burgersvektors für das analysierte Gleitsystem in der Ni-Probe etwa 0,15 nm. Die maximale Stufenhöhe beträgt etwa 9,1 nm bei  $d \approx 3,28 \mu\text{m}$  und die Stufenhöhe an der KG aufgrund der Transmission etwa 0,86 nm. Basierend auf Gleichung 1.21 beträgt die Anzahl der von der Versetzungsquelle erzeugten Versetzungen 61 und die Anzahl der transmittierten Versetzungen 6, so dass die Anzahl der Versetzungen im Pile-up 55 ist. Die angelegte Spannung wurde aus dem Experiment (289,4 MPa) verwendet. Mit all diesen Parametern, die Stufenhöhe (als Verteilung der Versetzungen im Pile-up) wurde für verschiedene Orientierungen des KG-Burgersvektors und unterschiedliche kritische Kräfte unter Berücksichtigung der Einfluss freier Oberflächen berechnet. Darüber hinaus wurde der Einfluss der anisotropen Elastizität im Vergleich zur Isotropie und die Anzahl der Grenzflächenversetzungen überprüft.

Die Auswirkungen der verschiedenen Parameter sind in folgenden zusammenge-

fasst:

- Effekt freier Oberflächen: Die Ergebnisse der Tri-Material-Simulationen ohne freie Oberflächen (markiert als INF) und mit freien Oberflächen (markiert als FS) sind in Abbildung 1.21 dargestellt. Die Simulationsergebnisse sind vergleichbar mit den experimentellen Ergebnissen mit einigen Diskrepanzen. Im Vergleich zur experimentellen Messung liegen die Versetzungen näher an der KG in INF, während sie näher an der ersten freien Oberfläche liegen, wenn man den Effekt der freien Oberflächen (FS) betrachtet. Der Grund dafür ist, dass die Versetzungen näher an der ersten freien Oberfläche als an der zweiten sind. D.h. die von beiden freien Oberflächen auslaufende Gesamtkraft geht immer in Richtung der ersten freien Oberfläche. Die Versetzungen um die KG liegen jedoch fast in der Mitte der zwei freien Oberflächen. Die Effekte dieser beiden freien Oberflächen werden gegenseitig ausgeglichen.

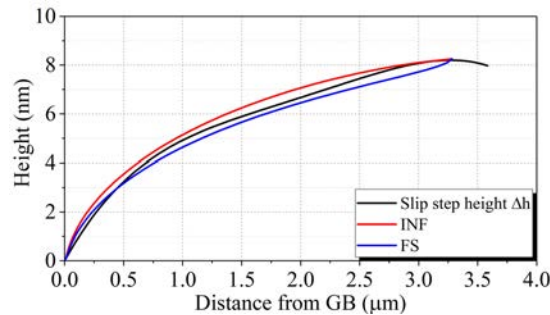


Figure 1.21: Simulation der Stufenhöhe im Tri-Material-Model ohne freie Oberflächen (INF) und im Dreischichtmodell mit freien Oberflächen (FS).

- Effekt von Grenzflächenversetzungen: In den Hypothesen der Simulation soll die Anzahl der Grenzflächenversetzungen gleich der Anzahl der transmittierten Versetzungen sein. Zunächst wird also die Anzahl der Grenzflächenversetzungen überprüft, wie in Abbildung 1.22 (a) dargestellt. Aus der experimentellen Messung, die Anzahl der transmittierten Versetzungen beträgt 6. Zum Vergleich wurde die Berechnung für nur 1 Grenzflächenversetzung durchgeführt. Es zeigt, dass die Gleichgewichtspositionen der Versetzungen in Pile-ups näher an der KG für 1 Grenzflächenversetzung als für 6 Grenzflächenversetzung (aufgrund der geringeren Abstoßungskraft) sind. Transmissionsphänomene wurden mit Hilfe von AFM-Messungen eindeutig gezeigt, sodass die Burgersvektoren der Grenzflächenversetzungen  $\mathbf{b}^{\text{GB}}$  auch überprüft werden konnten. Die Ergebnisse für zwei Sonderfälle sind in Abbildung 1.22 (b) dargestellt. Im ersten Fall es wird folgendes für den Burgersvektor der Grenzflächenversetzung angenommen: Es wird das



auslaufende Gleitsystem mit dem maximalen Transmissionsfaktor berücksichtigt (gekennzeichnet als Residu\_B5). Dann im zweiten Fall: Es wird das auslaufende Gleitsystem mit dem maximalen Schmidfaktor im Nachbarkorn berücksichtigt (gekennzeichnet als Residu\_B4). Beide Fälle zeigen, dass die Gleichgewichtspositionen der Versetzungen zur KG verschoben werden und unterschieden sich somit von experimentellen Messungen, wenn man diese Fälle mit dem Fall mit dem gleichen Burgersvektor der einlaufenden Versetzung vergleicht. Es scheint außerdem, dass die Ergebnisse nähern sich an den experimentellen Ergebnisse, wenn die freien Oberflächen für diese Fälle berücksichtigt werden, da die freien Oberflächen alle Versetzungen in Richtung der ersten freien Oberfläche verschieben. Aus den in Abbildung 1.22 dargestellten Ergebnissen geht jedoch hervor, dass die Ergebnisse mit einer Grenzflächenversetzung nah an der KG weit von der experimentellen Messung entfernt sind, wenn man es mit den Ergebnissen mit 6 Grenzflächenversetzungen mit dem Burgersvektor der einlaufenden Versetzung vergleicht. Mittlerweile ist bekannt, dass die Auswirkungen von freien Oberflächen in der Nähe der KG schwach sind. Daher werden sich die Ergebnisse auch unter Berücksichtigung der freien Oberflächen für diese Fälle nicht viel ändern. Der Burgersvektor der Grenzflächenversetzungen mit 12 Restburgersvektor wurde ebenfalls untersucht, da es 12 Gleitsysteme im Nachbarkorn für kfz-Kristallen gibt. Basierend auf die Analysen, die bessere Lösung ist diejenige mit dem Burgersvektor der einlaufenden Versetzung für diese Probe.

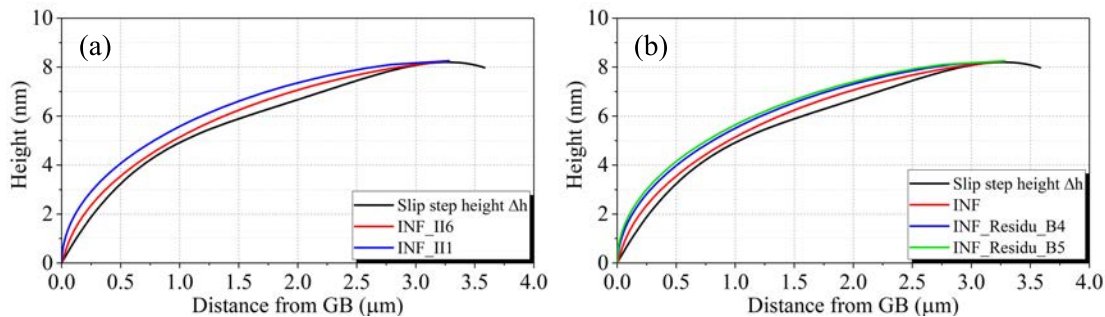


Figure 1.22: Simulation der Gleitstufenhöhe im Tri-Material-Model ohne freie Oberflächen INF für (a) verschiedene Anzahl von Grenzflächenversetzungen: eine Grenzflächenversetzung (III) und 6 Grenzflächenversetzungen (II6), und (b) verschiedene Burgersvektoren von Grenzflächenversetzungen: Restburgersvektor zwischen ein- und auslaufendem Gleitsystem mit maximalem Transmissionsfaktor (Residu\_B5) und mit maximalem Schmidfaktor für das auslaufende Gleitsystem (Residu\_B4).

- Wirkung der kritischen Kraft: Wie im Unterabschnitt 1.3.6 erläutert, ist es wichtig, die Wirkung der kritischen Kraft  $F_c$  zu berücksichtigen (siehe

Gleichung. 1.17). Die Ergebnisse mit und ohne Berücksichtigung der kritischen Kraft sind in Abbildung 1.23 dargestellt. Es wird festgestellt, dass  $F_c$  die Versetzung in Richtung KG verschiebt. Wenn man die Wirkung von freien Oberflächen mit einer kritischen Kraft  $F_c = 0,003 \text{ N/m}$  ( $\tau_c = 12 \text{ MPa}$ ) berücksichtigt, führt dies zu einem Simulationsergebnis, das näher an der experimentellen Messung liegt (Abbildung 1.23 (b) die rote Kurve FS\_Fc0.003). Der Wert ist hier etwas höher als der theoretische Wert für reinen kfz-Kristall ( $1 \sim 2 \text{ MPa}$  [296]). Der Grund dafür kann die durch die Probenherstellung erzeugten Oberflächendefekte sein, die nicht in der Simulation berücksichtigt werden, denn im L-E-S-Formalismus werden nur gerade Versetzungen berücksichtigt. Darüber hinaus wurde festgestellt, dass die kritische Kraft keinen offensichtlichen Einfluss auf Versetzungen um die KG bis zu einem Abstand von  $d = 0,5 \mu\text{m}$  im INF-Modell hat (Abbildung 1.23 (a)). Basierend auf Gleichung 1.17 konnte herausgefunden werden, dass die kritische Kraft keinen einheitlichen Effekt auf alle Versetzungen im Pile-up hat, denn es hängt vom gesamten Spannungszustand ab und die kritische Kraft versucht ihn auszugleichen, um einen umgekehrten Effekt zu erzielen. Beispielsweise, wenn die Gesamtkraft auf einer Versetzung ist in Richtung der freien Oberfläche für Positionen nahe der freien Oberfläche ist, wird die kritische Kraft in die Richtung der KG zeigen. Allerdings ist der Spannungszustand in der Nähe der KG sehr komplex. Die Gesamtkraft auf einer Versetzung kann auch auf die KG aufgrund der abstoßenden Kräfte anderer Versetzungen, attraktive Missorientierung, konformes KG, attraktiven Kräften aus Grenzflächenversetzungen und angelegten Spannung zeigen. Die Gesamtkraft kann auch in die entgegengesetzte Richtung zeigen, wenn abstoßende Missorientierung, starre KG, abstoßende Kraft von Grenzflächenversetzungen oder anderen Versetzungen in der Nähe und freie Oberflächen (auch wenn ihre Wirkung hier schwach ist) vorhanden sind. Daher hängt die Gesamtkraft hier von vielen Parametern ab. Somit könnte die kritische Kraft entweder die Versetzungen in Richtung KG oder in die entgegengesetzte Richtung verschieben.

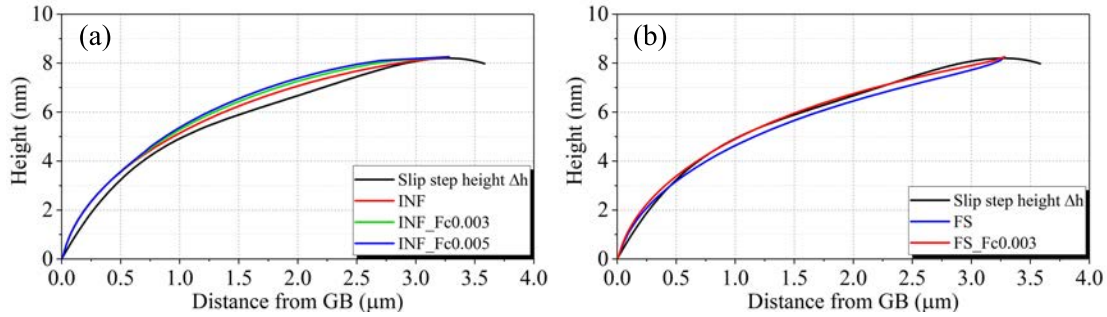


Figure 1.23: Simulation der Höhe einer Gleitstufe: (a) im Tri-Material-Model ohne freie Oberflächen INF und (b) im Dreischichtmodell mit freien Oberflächen FS unter Berücksichtigung der kritischen Kraft ( $F_c$ ) mit N/m.

- Wirkung der elastischen Anisotropie: Die elastische Anisotropie hat einen Einfluss im allgemein auf das Versetzungsverhalten (Anisotropie Faktor in Ni ist 2,51). Um den Anisotropieeffekt zu bestimmen, wird die Stufenhöhe unter Berücksichtigung der isotropen Elastizität ohne freie Oberflächen (gekennzeichnet als “INF\_ISO”) und mit freien Oberflächen (gekennzeichnet als “FS\_ISO”) berechnet (siehe Abbildung 1.24 (a) und (b)). Man kann erkennen, dass der Unterschied zwischen isotroper Elastizität und anisotroper Elastizität nicht zu groß ist. Ein Grund dafür ist, dass die Bildkraft aufgrund der vorliegenden Missorientierung 0,0103 N/m beträgt. Bei einer anderen Orientierung des Nachbarkorns kann die maximale Bildkraft aber für dieses Gleitsystem den Wert 0,0502 N/m erreichen. Darüber hinaus werden in der vorliegenden Konfiguration die Versetzungen an zwei Seiten des Aufstaus fixiert, die die Verteilung der Versetzung limitiert. Dennoch werden alle Versetzungen im Fall der isotropen Elastizität in Richtung der freien Oberfläche bewegt, die dazu führt, dass das simulierte Gleitstufenprofil weit von der experimentellen Messung entfernt ist. Außerdem ist die Mikrostruktur der Grenzfläche eher wie eine nicht-kristalline Struktur, die als isotrop betrachtet werden kann. Die Stufenhöhe wurde auch nur mit der Grenzfläche (als isotrop betrachtet) durchgeführt. Die Ergebnisse unter Berücksichtigung der Grenzfläche als isotrop ohne (INF\_InterISO) und mit (FS\_InterISO) Betrachtung freier Oberfläche sind in Abbildung 1.24 dargestellt. Abbildung 1.24 zeigt, dass die Ergebnisse keinen großen Unterschied im Vergleich zu der anisotropen Fall (Grenzfläche mit  $\lambda = 1$ ) zeigen.

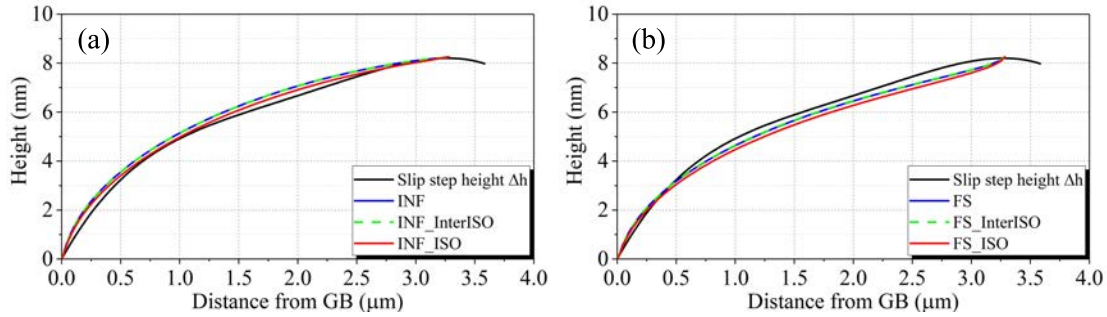


Figure 1.24: Simulation der Stufenhöhe: Grenzfläche mit isotroper Elastizität und anisotroper Elastizität (a) ohne freien Oberflächen (INF) nur für die isotrope Grenzfläche (INF\_InterIso) und für alle isotropen Schichten INF\_ISO und (b) mit freien Oberflächen (FS) mit allen isotropen Schichten.

Als Fazit, die Simulation liefert die beste Lösung, wenn anisotrope Elastizität, die Wirkung freier Oberflächen und eine kritische Kraft  $F_c = 0.003 \text{ N/m}$  ( $\tau_c = 12 \text{ MPa}$ ) für Ni berücksichtigt werden.

Analog zu der Ni-Probe wurden die gleichen Simulationen für die  $\alpha$ -Brass-Probe durchgeführt. Für die  $\alpha$ -Brass-Probe beträgt die Komponente aus der Oberfläche heraus des Burgersvektors des analysierten Gleitsystems etwa  $0,14 \text{ nm}$ . Die maximale Stufenhöhe beträgt etwa  $10,03 \text{ nm}$  bei einem Abstand von  $d \approx 2,44 \mu\text{m}$  und die Stufenhöhe an der KG aufgrund der Transmission etwa  $4,29 \text{ nm}$ . Basierend auf Gleichung 1.21 ist die Anzahl der Versetzungen im Pile-up, die von der Versetzungsquelle erzeugt werden, 72 und die Anzahl der transmittierten Versetzungen 31. Daher ist die Anzahl der Versetzungen im Pile-up 41. Die angelegte Spannung beträgt  $127,4 \text{ MPa}$  (aus den experimentellen Versuchen). Die Auswirkungen freier Oberflächen, kritischer Kraft und anisotroper Elastizität für die  $\alpha$ -Brass-Probe sind die gleichen wie für die Ni Probe. Die Anzahl der transmittierten Versetzungen ist jedoch viel größer als in der Ni-Probe. Das bedeutet, die Abstoßungskraft der Grenzflächenversetzungen ist wichtiger, wenn ihr Burgersvektor als derselbe der einlaufenden Versetzungen betrachtet wird (siehe die blauen Kurven in 1.25). Alle Versetzungen werden aufgrund dieser abstoßenden Kraft weit weg von KG in Richtung freie Oberfläche bewegt. Diese Transmission Abbildung 1.18 (b) führt dazu, dass der Restburgersvektors von Grenzflächenversetzungen berücksichtigt werden sollten. Nach Überprüfung aller möglichen Restburgersvektoren mit 12 Gleitsystemen im Nachbarkorn wurde festgestellt, dass die beste Lösung mit einem A6 Gleitsystem im Nachbarkorn, wenn freie Oberflächen und eine angemessene kritische Kraft  $F_c = 0,011 \text{ N/m}$  ( $\tau_c = 43 \text{ MPa}$ ) wie in Abbildung 1.25 (b) berücksichtigt werden. Die theoretische Analyse der Gleitlinien des A6-Gleitsystems auf der Oberfläche des Nachbarkorns stimmt gut mit den experimentellen Beobachtungen in Abbildung 1.18 (b) überein. Wie bere-

its im Abschnitt 1.5 für  $\alpha$ -Brass erwähnt, wird das Minimum im mittleren Teil der Messkurve durch den Schnittpunkt mit anderen nicht-koplanaren Gleitlinien verursacht. In dem vorliegenden Modell der zweidimensionalen anisotropen Elastizität war es nicht möglich, die im Experiment beobachteten Wechselwirkungen zweier nicht paralleler Gleitlinien zu simulieren. Daher kann dieses im Experiment beobachtete Minimum mit dem vorliegenden Modell nicht vorhergesagt werden. Es ist jedoch wichtig, den Bereich Nahe der KG mit  $d < 0.75 \mu\text{m}$  zu fitten. Die kritische Spannung ( $\tau_c = 43 \text{ MPa}$ ) in diesem Bereich ist größer als die kritische Spannung in den Ni-Proben. Allerdings, es scheint dieser Wert für diese Legierung realistisch zu sein, wie im Abschnitt 1.3.6 bereits beschrieben.

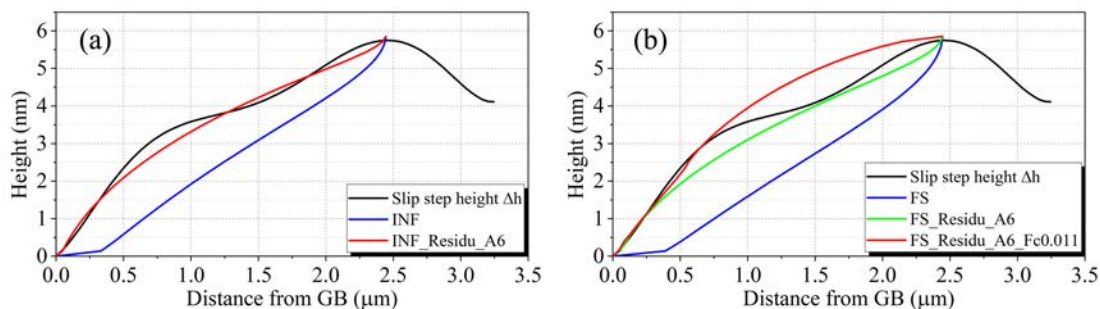


Figure 1.25: Simulation der Stufenhöhe: (a) ohne freie Oberflächen (INF) unter Berücksichtigung des Restburgersvektors der Grenzflächenversetzungen und (b) mit freien Oberflächen (FS) unter Berücksichtigung der kritischen Kraft.

Als Fazit, die Simulationen für die  $\alpha$ -Brass-Probe liefert die beste Lösung, wenn die anisotrope Elastizität, die Wirkung freier Oberflächen, eine kritische Kraft  $F_c = 0.011 \text{ N/m}$  ( $\tau_c = 43 \text{ MPa}$ ) und der Restburgersvektor für Grenzflächenversetzungen berücksichtigt werden, da der Versetzungstransfer groß ist.

## 1.7 Schlussfolgerungen und Perspektiven

In der vorliegenden Arbeit wurde ein analytischer Ansatz auf der Grundlage des L-E-S-Formalismus [28, 22, 285] explicit untersucht, der die elastischen Felder einzelner geraden Versetzungen und verschiedener Versetzungsaufstauungen in anisotropen homogenen Medien, Halbräumen, Bi- und Tri-Material [17] unter Berücksichtigung freier Oberflächen [18] liefert. Die Tri-Material-Konfiguration ermöglicht die Berücksichtigung einer Fläche mit einer Dicke im Nanometerbereich und eines spezifischen Steifigkeitstensors für den KG-Bereich. Die Konfiguration mit zwei freien Oberflächen kann zur Untersuchung von Größeneffekten verwendet werden. Die Auswirkungen von anisotroper Elastizität, kristallographischer Orientierung, KG-Steifigkeit und freien Oberflächen wurden im Falle einer einzelnen

Versetzung in einem Ni-Bikristall untersucht. Bildkräfte können sowohl durch ungleiche Kornorientierung, die Existenz eines endlichen Korngrenzenbereichs und freien Oberflächen entstehen. Insbesondere wird gezeigt, dass die entlang der Versetzungsgleitrichtung projizierte Peach-Köhler-Kraft eine Vorzeichenänderung mit der Versetzungsposition aufweisen kann. Außerdem wurde festgestellt, dass die Wirkungsabstände dieser heterogenen Faktoren unterschiedlich sind. Die freie oder starre Oberfläche hat den größten Wirkungsabstand im Korn und ihre Wirkung ist am größten. Der Effekt der Missorientierung ist viel geringer als der Effekt der freien Oberfläche und somit ist der Wirkungsabstand kürzer. Schließlich hat die KG-Steifigkeit den kürzesten Wirkungsabstand. Die KG-Steifigkeit ist jedoch wichtig, um den lokalen Spannungszustand zu ändern, um die führende Versetzung im Pile-up auszugleichen. Für Pile-Ups wurden die Versetzungspositionen durch ein iteratives Relaxationsschema berechnet, das die Peach-Koehler-Kraft bei jeder Versetzung minimiert. Sowohl die KG-Steifigkeit als auch die Missorientierung der Körner beeinflussen die Länge der Pile-ups, aber der Effekt der Missorientierung wird deutlich als vorherrschend angesehen.

Parallel dazu wurden in Rahmen dieser Dissertation in-situ mikromechanische Druckversuche an Mikro-Bi-Kristallen und Post-mortem-Untersuchungen mit Hilfe vom REM, AFM und EBSD durchgeführt. Die Mikro-Bikristallen aus reinem Ni und  $\alpha$ -Brass wurden mit einem Focused-Ion-Beam-Mikroskop (FIB) hergestellt. Die lokale räumliche Änderung der lokalisierten Gleitbänder, die an der KG enden, wurden mit Hilfe des AFM gemessen, um die Verteilung des Burgersvektors in den Pile-ups zu bestimmen. Diese Verteilung wurde dann durch Pile-up-Konfigurationen in Bikristallen mit den experimentell gemessenen Parametern unter Berücksichtigung des Einflusses der Missorientierung, KG-Steifigkeit, freien Oberflächen und kritischen Kraft simuliert. Es wurde folgendes festgestellt: der Burgersvektor der Grenzflächenversetzungen kann als das gleiche wie die einlaufenden Versetzungen mit einer schwachen Versetzungstransfer angesehen werden und man sollte den verbleibenden Burgersvektor der Grenzflächenversetzungen im Falle einer starken Versetzungstransfer berücksichtigen. Die Auswirkungen von freien Oberflächen und kritischen Kräften sollten in Berechnungen immer als prädiktiver in Bezug auf das Gleithöhenprofil betrachtet werden. Die kritischen Kräften in Ni ( $\tau_c = 12$  ( $\tau_c = 12$  MPa)) und  $\alpha$ -Brass ( $F_c = 0.011$  N/m ( $\tau_c = 43$  MPa)), die in dieser Rahmenbedingungen der geraden Versetzung mit dem L-E-S-Formalismus berechnet wurden, sind akzeptabel aufgrund von Gitterfehlern in der Material- bzw. Legierungszusammensetzung.

Die erreichten Ergebnisse, die mit Hilfe des analytischen Ansatzes für das Versetzungsverhalten in Bikristallen berechnet wurden, konnten mit anderen numerischen Methoden wie molecular dynamics (MD) Simulationen und 3D discrete dislocation dynamic (DDD) Simulationen verifiziert werden. Außerdem könnte

die vorliegende Methode verwendet werden, um DDD-Simulationen für die Grenzflächenplastizität unter Berücksichtigung der anisotropen Elastizität, insbesondere für die KG-Eigenschaften in Bikristallen oder Polykristallen zu unterstützen. Auch wenn es möglich wäre, verschiedene elastische Eigenschaften der KG mit einem anisotropen elastischen Steifigkeitstensor zu definieren, ist der tatsächliche Wert dieses Parameters komplizierter oder die KG könnte einfach als isotrop betrachtet werden. So werden in einer zukünftigen Untersuchung die elastischen Eigenschaften von KG mit Missorientierung mit Hilfe von molecular static (MS) Simulationen untersucht.





# Curriculum Vitae

## **Xiaolei CHEN**

Doctoral student in University of Lorraine-LEM3 / Saarland University-MWW

Date of birth: 05.07.1990

Nationality: Chinese

ORCID: <https://orcid.org/0000-0002-8228-4793>

Address: 022-R+3, 7 rue Félix Savart, F-57070 METZ

e-mail: [cxl900705@gmail.com](mailto:cxl900705@gmail.com)

Telephone: +33 (0)661718024

## **Professional experience and Education**

- From 10.2016: Doctoral student in University of Lorraine-LEM3 / Saarland University-MWW
  - ▷ 06.2019-now: University of Lorraine-LEM3
  - ▷ 06.2017-05.2019: Saarland University-MWW
  - ▷ 10.2016-05.2017: University of Lorraine-LEM3
  - ▷ Research program: Experimental and theoretical studies of incompatibility and dislocation pile-up stresses at grain boundaries accounting for elastic and plastic anisotropies
- 2014-2016: Material Engineering Diploma / Polytech GRENOBLE, Grenoble Alpes University
  - ▷ 04.2016-09.2016: Internship of 6 months in National Laboratory for intense Magnetic Fields (Grenoble)
  - ▷ 01.2016-03.2016: Research project of end study in ESOPP
  - ▷ 04.2015-12.2015: Competition of Technological Challenge Drone-INNOVATEAM
  - ▷ 05.2015-08.2015: Internship of 4 months in Shanghai Metallurgical Laboratory of Shanghai University

▷ 06.2014-07.2014: Internship of 1 month in Institute NEEL (Grenoble)

- 2013-2014: Mundus Integration Program / Polytech GRENOBLE, Joseph Fourier University
- 2009-2013: Bachelor of Applied Chemistry / Dalian University of Technology, China

## **Publications**

- T. Richeton, X. Chen, S. Berbenni. Misorientation dependence of the grain boundary migration rate: role of elastic anisotropy. *Philosophical Magazine*, (2020), 1-22. <https://doi.org/10.1080/14786435.2020.1779368>
- X. Chen, T. Richeton, C. Motz, S. Berbenni. Atomic Force Microscopy Study of Discrete Dislocation Pile-ups at Grain Boundaries in Bi-Crystalline Micro-Pillars. *Crystals*, 10, (2020), 411. <https://doi.org/10.3390/cryst10050411>
- X. Chen, T. Richeton, C. Motz, S. Berbenni. Elastic fields due to dislocations in anisotropic bi- and tri-materials: Applications to discrete dislocation pile-ups at grain boundaries. *International Journal of Solids and Structures*, 164, (2019), 141-156. <https://doi.org/10.1016/j.ijsolstr.2019.01.020>

## **Conference participations**

- 1st Colloquium on Theoretical and Experimental Micro-Mechanics / Metz, France. 18-19 November, 2019. (Oral presentation)
- Nanomechanical Testing in Materials Research and Development VII / Malaga, Spain. 29 September-04 October, 2019. (Poster presentation)
- Intergranular and interphase boundaries in materials (IIB2019) / Paris, France. 01-05 July, 2019. (Oral presentation)
- International conference on material modelling (ICMM6) / Lund, Sweden. 26-28 June, 2019. (Oral presentation)
- E-MRS Spring Meeting 2018 / Strasbourg, France. 15-22 June, 2018. (Oral presentation)
- Colloque Plasticité 2018 / Nancy, France. 09-11 April, 2018. (Poster presentation)

- Summer School on Experimental Nano- and Micromechanics / Max-Planck-Institut Für Eisenforschung GmbH, Düsseldorf, Germany. 11-15 September, 2017 (Poster presentation).

## **Experimental methods**

- SEM, EBSD, EDX, FIB, AFM, Nano-Indentation, Micro-traction, Ion Milling, Electro-polishing, XRD, DSC, IR, HPLC, UV-VIS, NMR, Labview

## **Softwares**

- MATLAB, MATHEMATICA, Python, LAMMPS, OVITO, CrystalMaker, HKL Channel5, NanoScope Analysis, Image J, ABAQUS, COMSOL, CATIA, Auto-cad, Pandat, LABVIEW, Design-Expert, Origin, Microsoft Office, Latex

## **Languages**

- Mandarin: mother language
- French: read, written, spoken
- English: read, written, spoken
- German: level A1

## **Lectures in doctoral school**

- Doctoral school EMMA
  - ▷ Fête de la science 2018: 10 hours
  - ▷ Formation à la culture de prévention Metz: 6 hours
  - ▷ Seminar of doctoral school EMMA: 8 hours
  - ▷ EMMA 05: Modelling of crystal behavior and textures: 24 hours, 5 points
  - ▷ EMMA 09: Méthodes numériques en mécanique des solides déformables: 20 hours, 4 points
- Saarbrücken Graduate School

- ▷ Methodik 7: Nano- und mikromechnische Messmethoden (Vorlesung, 2 points) (Experimental nano and micromechanical methods)
- ▷ Deutschkurse (4 points) (German language course)
- Université de Bordeaux
  - ▷ Intégrité scientifique dans les métiers de la recherche: 8 hours
- Université de Lyon
  - ▷ Éthique de la recherche: 8 hours